Ik-Kyung Jang

Editor

Cardiovascular OCT Imaging

Cardiovascular OCT Imaging

Ik-Kyung Jang

Editor

Cardiovascular OCT Imaging

Editor
Ik-Kyung Jang
Massachusetts General Hospital
Harvard Medical School
Boston, MA
USA

Foreword

Since the first report on OCT over two decades ago, interest in this imaging technology in medicine has exponentially increased, initially in ophthalmology and recently in cardiology. Introduction of this intravascular imaging modality in cardiology coincided with the emergence of a new concept, namely the detection of "vulnerable or high-risk plaque." As vulnerable plaque represents microstructural changes of coronary plaque including thin fibrous cap overlying lipid pool and increased lipid pool, it was thought that this high-resolution imaging modality would be ideal for detecting vulnerable plaques. Indeed, OCT has been proven to be an invaluable tool not only for detecting high-risk plaques, but also for studying in vivo vascular biology, particularly in order to understand the pathophysiology of acute coronary syndromes. With a series of OCT studies, our understanding on the pathogenesis of acute coronary syndrome has made remarkable progress and confirmed many findings, which had been possible only in autopsy studies previously. Since OCT can be used in patients repeatedly, in vivo serial studies have been reported and these studies have provided critical information on the evolution of vascular structure over time and also the vascular response to interventions such as cholesterol lowering therapy.

In addition to the application of OCT to research, OCT has been increasingly used in interventional cardiology, primarily to optimize percutaneous coronary intervention with stenting. Despite gradual adoption of this technology in cardiac catheterization laboratories, the clinical value of OCT remains undefined. How to maximize the information provided by OCT to optimize percutaneous procedures is not widely known. This book will provide background and practical tips for interventional cardiologists.

Since his first report on in vivo OCT application in 2001, in my view, Dr. Jang's group has been the leader in OCT in cardiology. His group brought this technology from bench to bedside through series of preclinical and clinical studies. They for the first time established the OCT criteria for plaque characterization, reported differences in plaque characteristics in patients with various clinical presentations, and recently published the first in vivo demonstration of plaque erosion, one of the important underlying mechanisms for acute coronary syndromes. In addition, his group published the first paper comparing OCT and intravascular ultrasound after stenting, demonstrating the higher sensitivity of OCT in the detection of stent related complications.

This textbook covers all the practical aspects of OCT in current research as well as clinical practice. With the rapidly growing interest in OCT, this book is extremely timely and very relevant for all cardiologists interested in vascular biology or interventional cardiology. My warmest congratulations to Dr. Jang and his group for such outstanding contributions to the field of cardiovascular medicine.

<div align="right">

Valentin Fuster, MD, PhD
Director, Mount Sinai Heart
Past-President American Heart Association
Past-President World Heart Federation

</div>

Contents

Contributors

Desmond C. Adler, PhD Advanced Technology, St. Jude Medical Inc., Westford, MA, USA

Tom Adriaenssens, MD, PhD Cardiovascular Medicine, University Hospitals Leuven, Leuven, Belgium

Takashi Akasaka, MD, PhD Division of Cardiovascular Medicine, Wakayama Medical University, Wakayama, Japan

Mario Albertucci, MD Department of Cardiovascular Surgery, San Giovanni Addolorata Hospital and CLI Foundation, Rome, Italy

Chiara Bernelli, MD Cardiovascular Department, A.O. Papa Giovanni XXIII Hospital, Bergamo, Italy

Brett E. Bouma, PhD Dermatology and Health Sciences and Technology, Harvard Medical School, Associate Physicist, Wellman Center for Photomedicine, Massachusetts General Hospital, Boston, MA, USA

Luca Di Vito, MD, PhD Department of Cardiology, CLI Foundation, Rome, Italy

Marc D. Feldman, MD Department of Medicine, University of Texas Health Science Center at San Antonio, San Antonio, TX, USA

James G. Fujimoto, PhD Department of Electrical Engineering & Computer Science and the Research Laboratory of Electronics, Massachusetts Institute of Technology, Cambridge, MA, USA

Giulio Guagliumi, MD, FESC Cardiovascular Department, A.O. Papa Giovanni XXIII Hospital, Bergamo, Italy

David L. Halaney, BS Department of Medicine, University of Texas Health Science Center at San Antonio, San Antonio, TX, USA

Myeong-Ki Hong, MD, PhD Division of Cardiology, Severance Cardiovascular Hospital, Yonsei University College of Medicine, Seoul, South Korea

Taylor Hoyt, BA Department of Medicine, University of Texas Health Science Center at San Antonio, San Antonio, TX, USA

Ik-Kyung Jang, MD, PhD Division of Cardiology, Massachusetts General Hospital, Harvard Medical School, Boston, MA, USA

Yangsoo Jang, MD, PhD Division of Cardiology, Severance Cardiovascular Hospital, Yonsei University College of Medicine, Seoul, South Korea

Haibo Jia, MD, PhD Department of Cardiology, Hospital of Harbin Medical University, Laboratory of Myocardial Ischemia, Chinese Ministry of Education, Harbin, China
Division of Cardiology, Massachusetts General Hospital, Harvard Medical School, Boston, MA, USA

Soo-Jin Kang, MD, PhD Division of Cardiology, Asan Medical Center, Seoul, South Korea

Antonios Karanasos, MD Department of Cardiology, Erasmus University Medical Center, Rotterdam, The Netherlands

Jung-Sun Kim, MD, PhD Division of Cardiology, Severance Cardiovascular Hospital, Yonsei University College of Medicine, Seoul, South Korea

Kenichi Komukai, MD Cardiovascular Department, A.O. Papa Giovanni XXIII Hospital, Bergamo, Italy

Takashi Kubo, MD, PhD Division of Cardiovascular Medicine, Wakayama Medical University, Wakayama, Japan

Teruyoshi Kume, MD, PhD Division of Cardiology, Kawasaki Medical School, Kurashiki, Okayama, Japan

J. Jacob Mancuso, MD Department of Medicine, University of Texas Health Science Center San Antonio, San Antonio, TX, USA

Valeria Marco, RN Department of Cardiology, CLI Foundation, Rome, Italy

Thomas E. Milner, PhD Department of Biomedical Engineering, The University of Texas at Austin, Austin, TX, USA

Seung Jung Park, MD, PhD Division of Cardiology, Asan Medical Center, Seoul, South Korea

Jennifer E. Phipps, PhD Department of Medicine, University of Texas Health Science Center at San Antonio, San Antonio, TX, USA

Karl Poon, MBBS, FRACP Interventional Cardiologist, Cardiology Program, The Prince Charles Hospital, Chermside, QLD, Australia

Francesco Prati, MD Interventional Cardiology Unit, San Giovanni Addolorata Hospital, Rome, Italy

Evelyn Regar, MD, PhD, FESC Department of Cardiology, Erasmus University Medical Center, Rotterdam, The Netherlands

Joseph M. Schmitt, PhD Advanced Technology, St. Jude Medical Inc., Westford, MA, USA

Vasile Sirbu, MD Cardiovascular Department, A.O. Papa Giovanni XXIII Hospital, Bergamo, Italy

Eric A. Swanson, MSc Research Laboratory of Electronics, Massachusetts Institute of Technology, Cambridge, MA, USA

Shiro Uemura, MD, PhD First Department of Internal Medicine, Nara Medical University, Kashihara, Nara, Japan

Jors Nicolaas van der Sijde, MD Department of Cardiology, Erasmus University Medical Center, Rotterdam, The Netherlands

Nienke Simone van Ditzhuijzen, MSc Department of Cardiology, Erasmus University Medical Center, Rotterdam, The Netherlands

Gijs van Soest, PhD Department of Biomedical Engineering, Erasmus University Medical Center, Rotterdam, The Netherlands

Rocco Vergallo, MD Division of Cardiology, Massachusetts General Hospital, Boston, Harvard Medical School, Boston, MA, USA

Martin L. Villiger, PhD Department of Dermatology, Harvard Medical School, Wellman Center for Photomedicine and Massachusetts General Hospital, Boston, MA, USA

Chenyang Xu, PhD Advanced Technology, St. Jude Medical Inc., Westford, MA, USA

James G. Fujimoto, Joseph M. Schmitt, Eric A. Swanson, and Ik-Kyung Jang

Abstract

Optical coherence tomography (OCT) enables cross sectional and volumetric imaging of internal structure and pathology in biological tissues. OCT can perform an "optical biopsy", imaging pathology *in situ* and in real time without the need for excisional biopsy. OCT imaging has become a standard of care in ophthalmology and is an emerging imaging modality in cardiology, where it provides information that often cannot be obtained by any other means. This chapter reviews the early history of OCT development with an emphasis on basic concepts and the process of technology translation. Early OCT technology and catheter imaging devices as well as advances in imaging speed using swept source/Fourier domain detection are reviewed. The process of clinical translation, beginning with *ex vivo* imaging and histology, preclinical animal studies and progressing to clinical studies in patients is discussed. The history of commercial intravascular OCT development is also summarized.

Keywords

Optical coherence tomography • OCT • Optical biopsy • Intravascular OCT • Swept source OCT • Fourier domain OCT • Optical frequency domain imaging • OFDI • Fiber optic catheter

J.G. Fujimoto, PhD (✉)
Department of Electrical Engineering & Computer Science and the Research Laboratory of Electronics,
Massachusetts Institute of Technology,
77 Massachusetts Avenue, Cambridge, MA 02139, USA
e-mail: jgfuji@mit.edu

J.M. Schmitt, PhD
Advanced Technology, St. Jude Medical Inc., Westford, MA, USA

E.A. Swanson, MSc
Research Laboratory of Electronics,
Massachusetts Institute of Technology, Cambridge, MA, USA

I.-K. Jang, MD, PhD
Division of Cardiology, Massachusetts
General Hospital, Harvard Medical School,
Boston, MA 02114, USA
e-mail: ijang@mgh.harvard.edu

1.1 Introduction

Optical coherence tomography (OCT) has evolved to become a major optical imaging modality in biomedical optics and medicine. OCT performs high resolution, cross-sectional and three dimensional volumetric imaging of the internal microstructure in biological tissues by measuring echoes of backscattered light [1]. Tissue pathology can be imaged *in situ* and in real time with resolutions of 1–15 μm, one to two orders of magnitude finer than conventional ultrasound. The unique features of OCT make it a powerful imaging modality with applications spanning many clinical specialties, fundamental scientific and biological research, as well as non-medical applications.

OCT performs cross-sectional and volumetric imaging by measuring the magnitude and echo time delay of backscattered light. Cross-sectional images are generated by performing multiple axial measurements of reflected light amplitude at different echo time delays (axial scans or A-scans) and scanning the incident optical beam transversely, as shown in
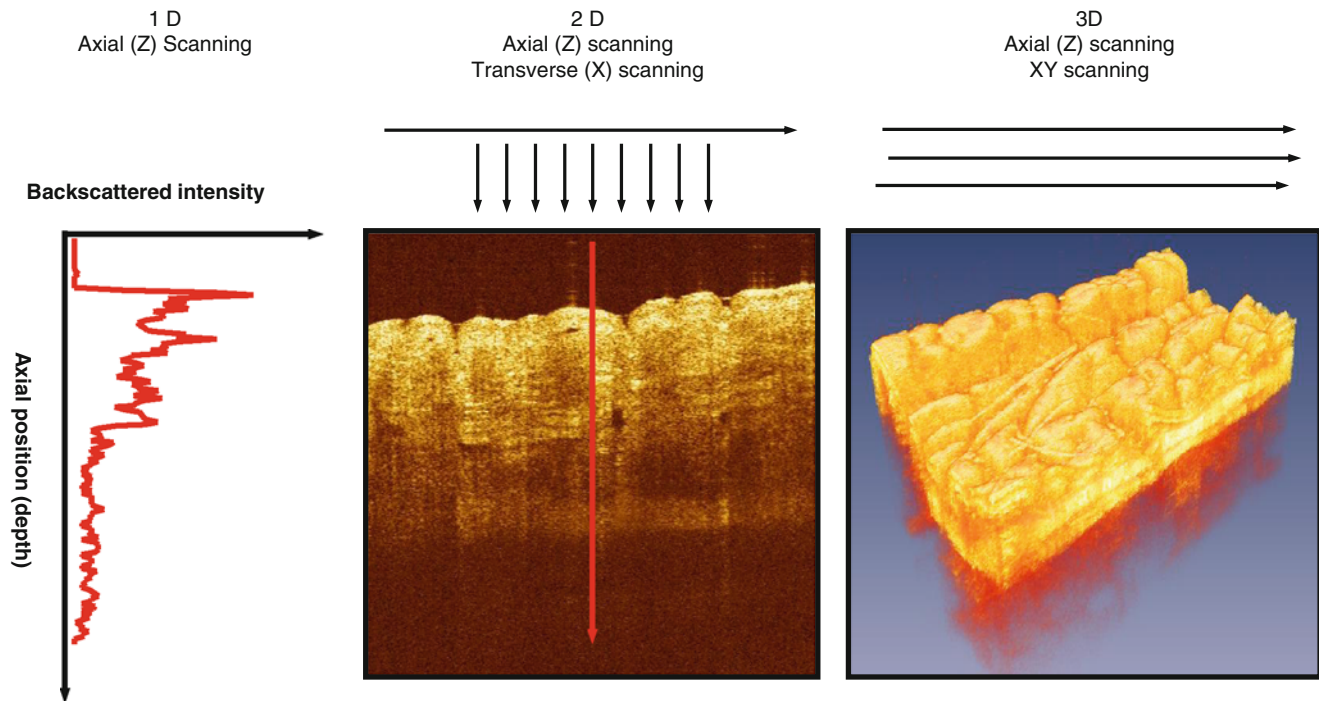
1 D Axial (Z) Scanning	2 D Axial (Z) scanning Transverse (X) scanning	3D Axial (Z) scanning XY scanning

Backscattered intensity

Axial position (depth)

Fig. 1.1 Optical coherence tomography (OCT) generates cross-sectional or three dimensional images by measuring the magnitude and echo time delay of light. Data is composed of axial scans (A-scans) which are measurements of backreflection or backscattering versus delay. Cross-sectional images (B-scan) are generated by transverse scanning the OCT beam, acquiring a series of axial scans. Three dimensional volumetric data sets (3D-OCT) are generated by raster scanning, acquiring a series of cross-sectional images (B-scans)

Fig. 1.1.[1] This produces a two-dimensional data set which represents the optical backscattering in a cross-sectional plane through the tissue. Images, or B-scans, can be displayed in false color or grey scale in order to visualize tissue pathology. Three-dimensional, volumetric data sets are generated by acquiring sequential cross-sectional images, scanning the incident optical beam in a raster, circumferential, or other pattern. Three-dimensional OCT (3D-OCT) data contains comprehensive volumetric structural information and can be digitally manipulated and visualized similar to MR or CT images.

OCT is a powerful imaging technology in medicine because it performs an "optical biopsy"; it provides a real time, *in situ* visualization of tissue microstructure and pathology, without the need to remove and process specimens [2, 3]. Although histopathology is the gold standard for the assessment of pathology, it requires tissue excision, fixation, embedding, microtoming and staining. OCT has applications in several general clinical situations:

1. Where conventional excisional biopsy is hazardous or impossible. Applications include imaging the retina in ophthalmology or coronary arteries in cardiology.
2. Where excisional biopsy has sampling error. Histopathology of biopsy specimens is the gold standard for diagnosis of many diseases including cancer, however, if excisional biopsy misses the lesion, then there is a false negative. OCT can guide excisional biopsy to reduce the number of biopsies required and to improve sensitivity by reducing sampling errors. If sufficient sensitivity and specificity can be achieved, OCT may be used to diagnose pathology in real time. Since imaging is performed *in situ*, OCT has the advantage that much larger regions of tissue can be assessed than with excisional biopsy.
3. For the guidance of interventional procedures. The ability to see cross sectional and three dimensional structure enables the guidance of procedures such as stent placement in intravascular imaging. In ophthalmology, OCT can visualize changes in retinal structure and markers of disease, such as neovascularization or edema, to assess progression or pharmaceutical treatment response. The ability to see beneath the tissue surface enables guidance of ablative therapies such as laser or radio frequency ablation, as well as surgical and microsurgical procedures.
4. For performing functional measurement and imaging. Doppler OCT enables quantitative measurement of blood flow. OCT angiography enables visualization of vasculature. Polarization sensitive OCT enables measurement of birefringence, a marker for cellular and subcellular organization.

Although the imaging depth of OCT is limited by attenuation from light scattering, coupled with medical devices such as catheter, endoscopic, laparoscopic, or needle delivery instruments, OCT can be used to access luminal organ

---

[1]Note there OCT embodiments including full-field OCT that acquire axial data in parallel.

systems such as the coronary arteries, GI tract and airways, as well as solid organs and masses.

OCT has become a standard of care in clinical ophthalmology and promises to have a powerful impact on intravascular imaging as well as other many other clinical specialties and research applications ranging from diagnosis of neoplasia to enabling new minimally invasive therapies or surgical procedures. This chapter reviews the history and early development of OCT including the translation process of *ex vivo* imaging studies, preclinical imaging in animals and the first studies in patients. We present a simplified review of key technological developments that have enabled the use of OCT in intravascular imaging and other applications beyond ophthalmology. Finally, we present an overview of commercial activities in the development of intravascular OCT. Commercialization is a key step in making advances available to the wider clinical community, where new methodologies can ultimately impact clinical care. A more rigorous description of the Physics of Cardiovascular OCT is presented in Chap. 2 and a discussion of Future Developments in OCT is presented in Chap. 15.

1.2 OCT and Ultrasound

OCT has features which are common to both ultrasound and microscopy. Therefore, it is helpful to begin by comparing OCT to these modalities. Figure 1.2 shows the resolution and imaging depth for OCT, ultrasound and microscopy. The resolution of clinical ultrasound imaging is typically 0.1–1 mm and depends on the frequency of the sound wave (3–40 MHz) used for imaging [4–6]. Sound waves at ultrasound frequencies below 10 MHz are transmitted with minimal absorption in biological tissue and it is possible to image structures deep in the body. High frequency ultrasound has been used for intravascular imaging as well as research applications. Resolutions of 15–20 μm and finer have been achieved with frequencies above 100 MHz. However, these high frequencies are strongly attenuated in biological tissues and imaging depths are limited to only a few millimeters.

Microscopy and confocal microscopy are examples of imaging techniques which have extremely high transverse image resolutions of 1 μm or finer. Imaging is typically performed in an *en face* plane and resolutions are determined by optical diffraction. The imaging depth in biological tissue is limited because image signal and contrast are significantly degraded by unwanted scattered light. In most biological tissues, imaging can be performed to depths of only a few hundred microns.[2]

---

[2]In some ways OCT is by definition, always a confocal system. A single spatial optical mode is used for illumination and a single spatial mode is used for detection. However, a long Rayleigh range is often used and the lateral resolution is less than standard confocal microscopes. OCT, with high numerical aperture focusing, is often referred to as Optical Coherence Microscopy (OCM).
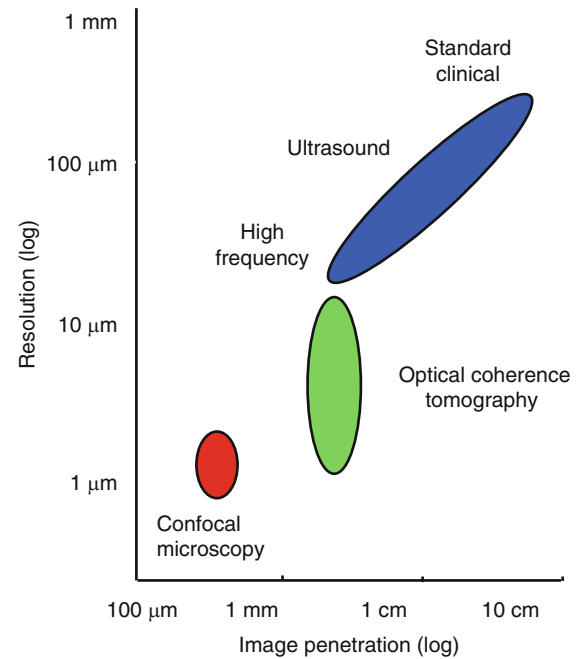

Fig. 1.2 Image resolution and depth. Clinical ultrasound achieves deep imaging depths, but with limited resolution. Higher sound frequencies improve resolution, but increased ultrasonic attenuation reduces imaging depth. Confocal microscopy has submicron resolution, but because it is difficult to reject unwanted scattered light, the imaging depth is a few hundred microns in most tissues. OCT axial image resolution ranges from 1 to 20 μm, according to the coherence length of the light source. In most biological tissues, OCT imaging depth is limited to ~2 mm by attenuation from optical scattering

OCT fills the gap between ultrasound and microscopy. The axial image resolution in OCT is determined by the bandwidth of the light source. OCT technologies have axial resolutions ranging from 1 to 20 μm, approximately 10 to 100 times finer than standard ultrasound imaging. The high resolution of OCT imaging enables the visualization of tissue morphology. OCT has become a clinical standard in ophthalmology, because the transparency of the eye provides easy optical access to the retina, non-contact high-resolution imaging is possible and there is a dearth of other alternative technologies than can acquire quantitative depth information about the retina [7]. The principal limitation of OCT is that light is highly scattered by most tissues and attenuation from scattering limits the imaging depths to ~2 mm in most tissues. However, because OCT uses fiber optics, it can be integrated with a wide range of medical instruments that can bring the light to the tissue region of interest. Instruments such as catheters, endoscopes, laparoscopes, or needles enable imaging in luminal organ systems or even solid tissues inside the body.

OCT imaging is analogous to ultrasound imaging, except that it uses light instead of sound. There are several different detection methods for performing OCT, but essentially imaging is performed by measuring the magnitude and echo time delay of backreflected or backscattered light from internal microstructures in materials or tissues. OCT images are two-

dimensional or three-dimensional data sets which represent optical backreflection or backscattering in a cross-sectional plane or 3D volume. Ultrasound and OCT are analogous in that when a beam of sound or light is incident into tissue, it is back-reflected or backscattered differently from structures which have varying acoustic or optical properties, as well as from boundaries between structures. The dimensions of these internal structures can be determined by measuring the "echo" time it takes for sound or light to travel different axial distances.

In ultrasound imaging, the axial measurement of distance or depth is called A-mode scanning, while cross-sectional imaging is called B-mode scanning. Volumetric or 3D imaging can be performed by acquiring multiple B-mode images. The principal difference between ultrasound and optical imaging is the extremely high speed of light and the fact that light has a much shorter wavelength than sound. The speed of sound in tissue is ~1,500 m/s, while the speed of light is approximately 3×10^8 m/s. The measurement of distances with a 100 μm resolution, a typical resolution for ultrasound imaging, requires a time resolution of ~100 ns which is well within the limits of electronic detection. Ultrasound technology has advanced significantly in recent years with the availability of high performance, low cost analog to digital converters and digital signal processing technology. Unlike sound, the detection of light echoes requires much higher time resolution. Light travels from the moon to the earth in only ~2 s. The measurement of distances with a 10 μm resolution, a typical resolution for OCT imaging, requires a time resolution of ~30 femtoseconds (3×10^{-15} s). A femtosecond is extremely fast; the ratio of one femtosecond to one second is equal to the ratio of one second to the time since the age of dinosaurs. Direct electronic detection is extremely difficult with this time resolution; therefore, measurement methods such as high speed optical gating, optical correlation or interferometry are used.

1.3 Measuring Optical Echoes

1.3.1 Photographing Light in Flight

The use of optical echoes to visualize internal structure in biological tissue was proposed more than 40 years ago by Michel Duguay in 1971 [8, 9]. These pioneering studies demonstrated an ultrafast optical shutter using the laser induced Kerr effect which could "photograph light in flight". Figure 1.3 shows a schematic of Duguay's ultrahigh speed Kerr shutter photographing an ultrashort light pulse propagating though a scattering solution of diluted milk [9]. The Kerr shutter operates by using an intense laser pulse to induce birefringence (the Kerr effect) in an optical medium placed between two crossed polarizers. If the induced birefringence is electronically mediated, it has an extremely

rapid response time and the Kerr shutter can achieve picosecond or femtosecond time resolution.

Optical scattering limits the ability to image biological tissues, and Duguay proposed that an ultrahigh speed shutter could remove the unwanted scattered light and detect light echoes from inside tissue [9]. Ultrahigh speed optical shutters might be used to "see through" tissues and therefore to non-invasively image internal pathology. The principal limitation of the high speed optical Kerr shutter is that it requires high intensity, short laser pulses to induce the Kerr effect and operate the shutter.

1.3.2 Femtosecond Time Domain Measurement

An alternate method for detecting optical echoes is to use nonlinear optical processes such as harmonic generation, sum frequency generation, or parametric conversion [10–12]. Short light pulses illuminate the tissue and the time delay of backscattered light is detected by nonlinear optical cross correlation, mixing the backreflected light with a time delayed reference pulse in a nonlinear optical material. The nonlinear process can measure the intensity and time delay of the optical signal with a time resolution determined by the pulse duration. Figure 1.4 shows a schematic of how light echoes are detected using nonlinear second harmonic generation cross correlation. The reference pulse is generated by the same laser source and is delayed by a variable time delay ΔT using a mechanical optical delay line. The nonlinear mixing process creates an ultrahigh speed optical gate which is like an optical shutter.

The ultrahigh speed optical gate enables measurement of the echo magnitude vs time delay of backreflected or backscattered light, the equivalent of an axial scan in an ultrasound. Figure 1.4 shows a measurement of corneal thickness in an *in vivo* rabbit eye. Very low scattering from the corneal stroma can be detected. The measurement had a 15 μm axial resolution and was performed using 65 femtosecond duration pulses from a femtosecond dye laser at 625 nm wavelength. Sensitivities of −70 dB or 10^{-7} of the incident intensity were achieved. However, these sensitivities were still not high enough to image most biological tissues. Current OCT systems achieve sensitivities 1,000× higher, approaching −100 dB or 10^{-10} of the incident intensity.

1.3.3 Low Coherence Interferometry

The problem of limited sensitivity can be solved using coherent or interferometric detection. Interferometry is a powerful technique for measuring the magnitude and echo time delay of light with very high sensitivity which has the additional
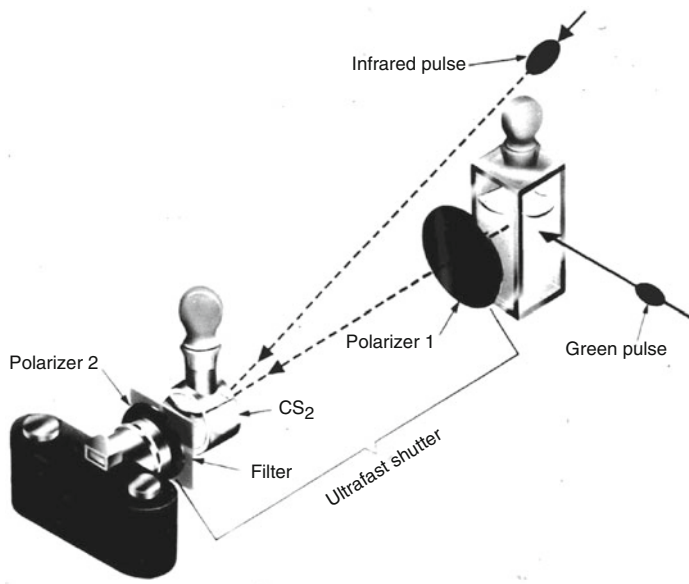
Fig. 1.3 Photographing light in flight. (*left*) A high speed optical shutter is created using a CS_2 cell between crossed polarizers. An intense laser pulse induces transient birefringence (the Kerr effect) to open the shutter. (*right*) Photograph of an ultrashort laser pulse propagating through a cell of milk and water. The shutter speed was ~10 ps. These early studies suggested that high speed optical gating could be used to see inside biological tissues by rejecting unwanted scattered light (From Duguay [8]; and Duguay and Mattick [9])
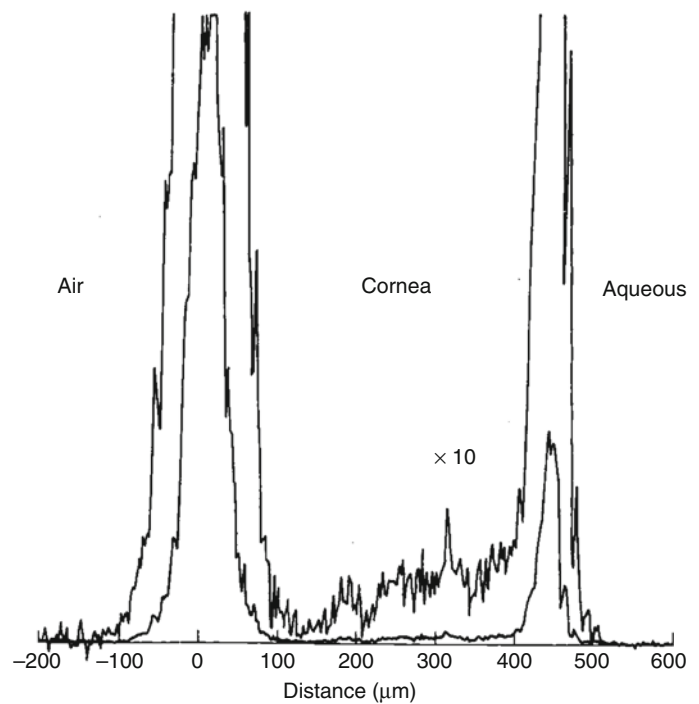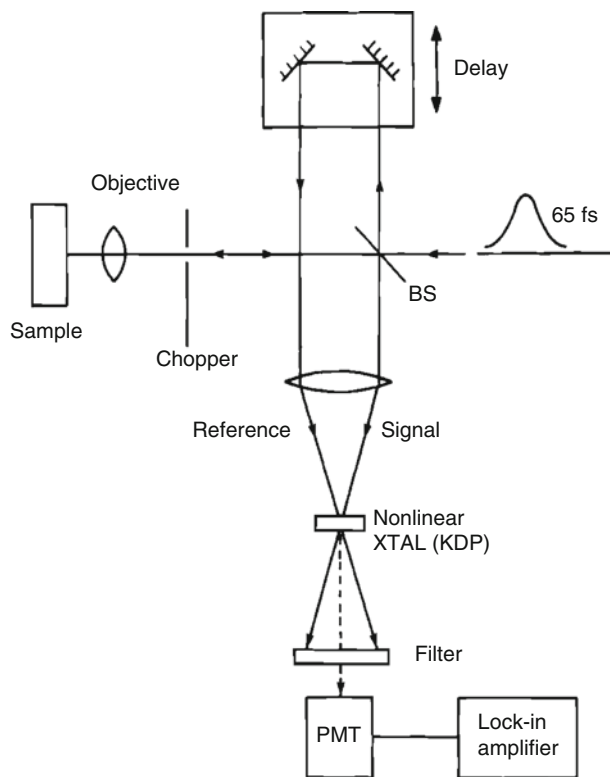
Fig. 1.4 Early demonstration of femtosecond optical ranging in biological systems. (*left*) Femtosecond echoes of light (signal) are detected using nonlinear second harmonic generation, mixing the signal with a delayed reference pulse. (*right*) Femtosecond measurement of corneal thickness in a bovine eye *ex vivo*, showing an axial scan of backscattering versus depth. Using a femtosecond dye laser with a 65 fs pulse duration it was possible to achieve a 15 um axial resolution (in air) with a −70 dB or 10^{-7} detection sensitivity (From Fujimoto et al. [12])
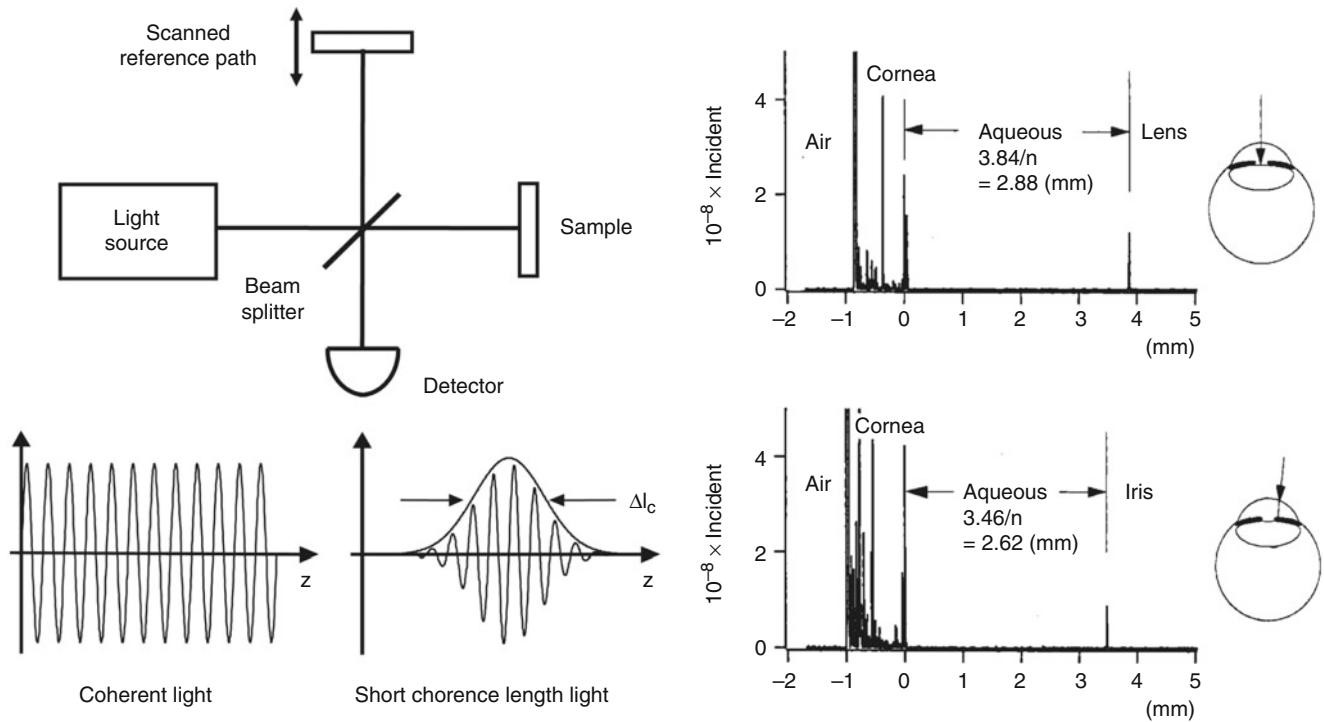
Fig. 1.5 Low coherence interferometry for measuring optical echoes. (*left*) Backreflected or backscattered light signals are interferred with light from a scanning reference path delay. When low coherence length light is used, interference is only observed with the path lengths are matched to within the coherence length. The interferometer output is detected as the reference path delay is scanned (time domain detection).

Axial scan (A-scan) information is obtained by demodulating the inreference signal. (*right*) Measurement of the anterior chamber in an bovine eye *ex vivo*. A 10 µm axial resolution was achieved using a low coherence diode light source at ~800 nm. Interferometry enables high sensitivity detection of optical echoes and is the basis for optical coherence tomography (From Huang et al. [21])

advantage of not requiring short pulse light sources. OCT is based on interferometric imaging and initial embodiments used a classic optical measurement technique known as low coherence interferometry, or white light interferometry, first described by Sir Isaac Newton. Low coherence interferometry was used in photonics to measure optical echoes and backscattering in optical fibers and waveguide devices in the 1980s [13–15]. The first biological application of low coherence interferometry was reported by Fercher et al. in 1988, for the measurement of axial eye length [16]. Different versions of low coherence interferometry were developed for non-invasive measurement in biological tissues [17–20].

Interferometry techniques perform correlation measurements by interfering light that is backscattered from the tissue with light that has traveled a known time delay though a reference path. Interferometry measures the electrical field of the light rather than its intensity. Figure 1.5 shows a schematic diagram of a classic Michelson type interferometer. The incident light is divided into a reference beam and a measurement or signal beam that travels different distances in the two interferometer arms. The path length difference between the interferometer signal and reference arms is ΔL. If the reference path length is scanned, interference fringes will be generated as a function of time. This process can also be understood by noting that scanning the reference arm produces a Doppler shift of the reference field. If a coherent

(narrow line width) light source is used, interference will be observed over a long range of path length differences. However, in order to detect optical echoes from a restricted spatial region, a low coherence (broad bandwidth) light source is required. Low coherence light can be characterized as having a temporal (or longitudinal) autocorrelation function whose width is relatively short. The width of the autocorrelation is inversely proportional to the frequency bandwidth of the light. When low coherence light is used, interference is only observed when the measurement and reference path lengths are matched to within the coherence length. The interferometer essentially measures the field autocorrelation of the light. The magnitude and echo time delay of light can be measured by scanning the reference arm and demodulating, or detecting the interference signal. The coherence length of the light source determines the axial image resolution.[3] Shorter coherence lengths corresponding to broadband light sources provide finer resolution.

Figure 1.5 shows an early *ex vivo* measurement of the anterior chamber of the bovine eye with a 10 µm axial resolution using an 800 nm wavelength, low coherence diode light

---

[3]The longitudinal resolution is actually determined by the product of the coherence (autocorrelation) function and the focusing properties of the incident light beam. But usually the coherence function is the dominate factor.

source with a 29 nm bandwidth [21]. Sensitivities of −100 dB or 10⁻¹⁰ of the incident intensity were achieved. Scanning the beam in the transverse direction yielded information on different structures, such as the lens and iris. The axial measurements of backscatter versus depth using low coherence interferometry provided the foundation for optical coherence tomography. Low coherence interferometry has the advantage that is can be performed without requiring short pulses of light. Since interferometry measures the electric field rather than the intensity, it is equivalent to heterodyne detection in optical communication. Stated another way, interferometry essentially generates a product of electric fields. Weak signals $E_{Signal}(t)$ are multiplied by a strong reference electrical field $E_{Reference}(t)$ to generate an interference output that is proportional to $E_{Signal}(t) \times E_{Reference}(t)$. This multiplication produces homodyne or heterodyne gain and very high, shot noise limited sensitivities (limited by the quantum nature of light) can be achieved and the effects of thermal and other electronic noise sources can be reduced. In addition, since the intensity is proportional to the square of the electric field, very high dynamic ranges are possible because a 10× dynamic range for field corresponds to a 100× dynamic range for intensity. A more comprehensive description of how OCT works can be found in Chap. 2 on the Physics of Cardiovascular OCT.

1.4 The Development of OCT

1.4.1 Early OCT Technology and Systems

Optical coherence tomography imaging was demonstrated in 1991 by Huang et al. [1]. A similar imaging concept was also proposed independently in 1991 by Tanno in Japan [22]. Figures 1.6 and 1.7 show the first OCT images of the retina and human coronary artery *ex vivo* with corresponding histology [1]. These examples demonstrate OCT imaging in transparent as well as optically scattering tissues. Imaging was performed with 15 μm axial resolution in tissue at

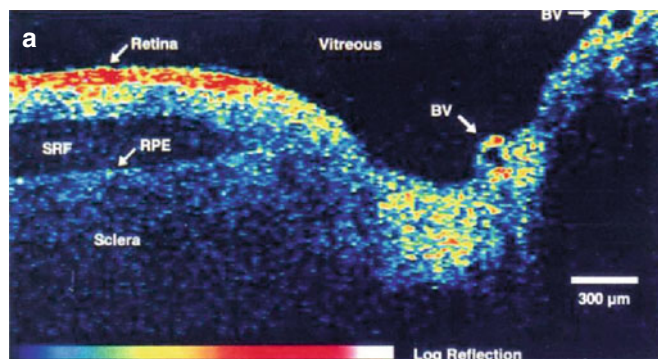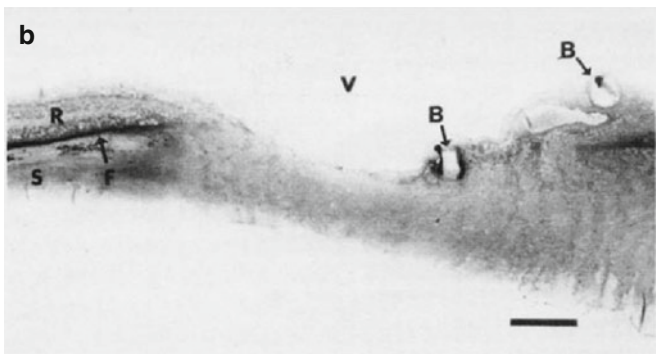830 nm wavelength. The image is displayed using a log false color scale with a signal level ranging from ~ −60 (red color) to −90 dB (dark blue color) of the incident intensity. The OCT image of the retina in Fig 1.6 shows the contour of the optic nerve head as well as retinal vasculature near the nerve head. The retinal nerve fiber layer can also be visualized emanating from the optic nerve head. This image was *ex vivo* and postmortem retinal detachment is evident. The OCT image of the coronary artery in Fig. 1.7 shows fibro-calcific plaque on the right of the specimen and fibroatheromatous plaque on the left. The plaque scatters light and therefore attenuates the OCT beam, limiting the image penetration depth below it.

Optical coherence tomography has the advantage that it can be implemented using fiber optic components and integrated with a wide range of medical devices. OCT systems can be divided into an imaging engine or console (consisting of an interferometer, light source, detector, and support electronics) and imaging devices or probes. Early OCT imaging engines employed time domain detection (TD-OCT) with an interferometer using a low coherence light source and scanning reference delay arm. Figure 1.8 shows an example of a TD-OCT system using a fiber optic Michelson type interferometer with time domain detection. There are many different embodiments of the interferometer and imaging engines which have different power delivery and detection efficiency advantages [23].

1.4.2 Ophthalmic OCT Imaging

Because the eye is optically transparent and optical imaging methods were already widely used in ophthalmology, many of the earliest OCT studies were in the eye. The first *in vivo* retinal images were obtained independently in 1993 by Swanson et al. [24] and Fercher et al. [25]. Figure 1.9 shows an early *in vivo* OCT image of the normal human retina from Hee et al. in 1995 [26]. Imaging was performed with ~10 μm axial resolution in tissue at ~800 nm wavelength. The nerve

Fig. 1.6 OCT image of the human retina ex vivo (**a**) and corresponding histology (**b**). Imaging was performed with 15 μm axial resolution at 830 nm wavelength. The OCT is displayed using a log false color scale ranging from –60 to –90 dB of the incident light intensity. The OCT

shows the optic nerve head contour and vasculature. The retinal nerve fiber layer is visualized and there is postmortem retinal detachment, with subretinal fluid accumulation (From Huang et al. [1])
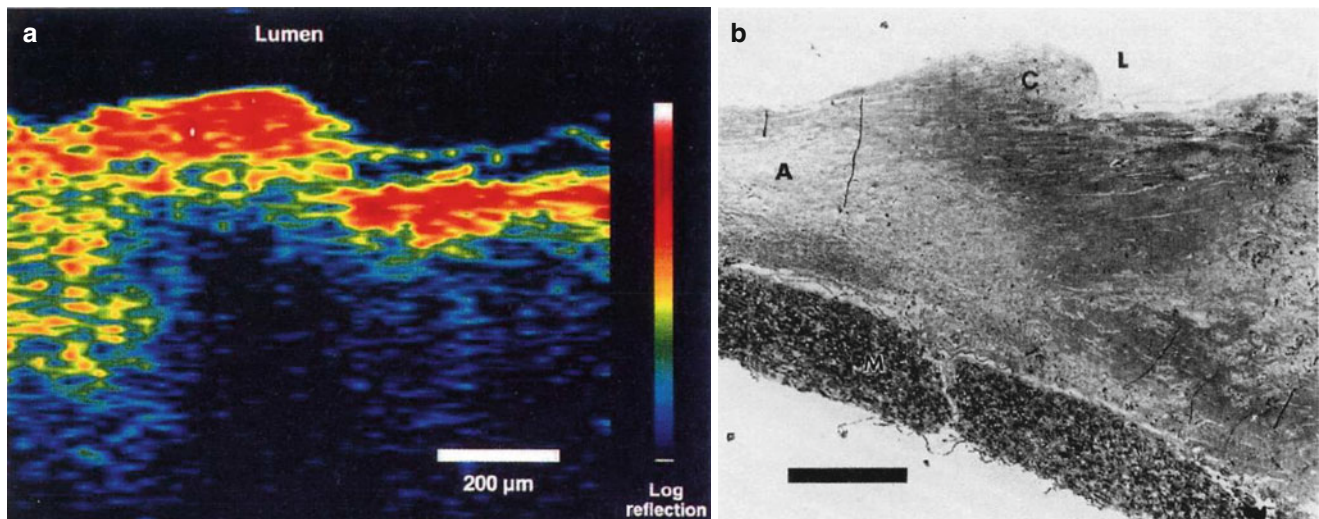
Fig. 1.7 OCT image of human artery *ex vivo* (**a**) and corresponding histology (**b**). The OCT shows fibro-calcific plaque (*right* three-quarters of specimen) and fibroatheromatous plaque (*left* side of specimen).

The fatty-calcified plaque scatters light, limiting the image penetration depth (From Huang et al. [1])

Fig. 1.8 OCT uses photonics and fiber optics technology. This schematic shows a Michelson interferometer implemented using fiber optics. The probe may be interfaced to a variety of medical imaging devices. OCT interferometers can be built in many different configurations depending on design requirements
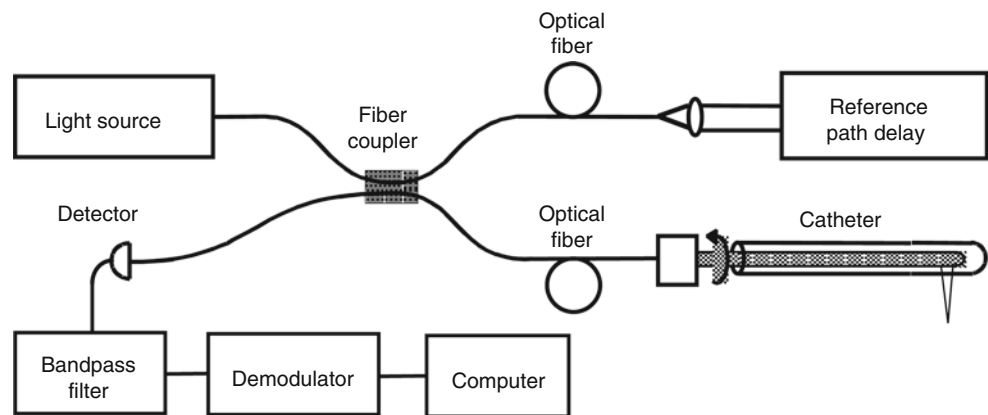
fiber layer as well as other architectural features can be visualized with higher resolution than was previously possible. The high detection sensitivity of OCT enables imaging structures such as the retina which are nominally transparent and have very low optical scattering. For retinal imaging, safety standards govern the maximum permissible light exposure and set limits for OCT imaging speeds [24, 26]. Typical retinal images have signal levels −50 to −90 dB below the incident intensity, but are easily visualized using incident power levels that are well within safe exposure limits.

The earliest clinical studies with OCT were performed in ophthalmology, and OCT has had an extremely large clinical impact in this specialty. Early clinical studies investigated OCT for the diagnosis and monitoring of a variety of macular diseases [27], including macular edema [28, 29], macular holes [30], central serous chorioretinopathy [31], and age-related macular degeneration and choroidal neovascularization [32]. The retinal nerve fiber layer thickness, an indicator of glaucoma, can be quantified in normal and glaucomatous eyes and correlated with conventional measurements of the
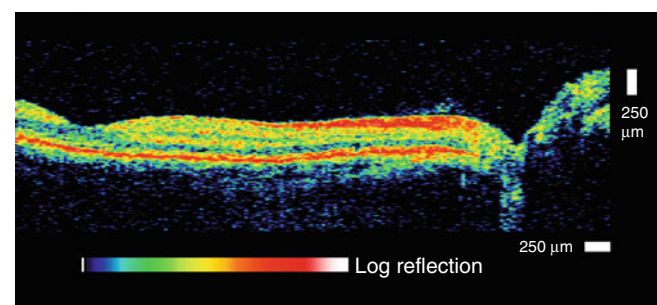
Fig. 1.9 OCT image of the normal human retina *in vivo*. An early OCT image of the normal human retina in vivo. The OCT has 10 µm axial resolution and was acquired at 800 nm wavelength. The retinal pigment epithelium, choriod, and retinal nerve fiber layers are visible as highly backscattering layers. OCT can noninvasively visualize and quantitatively measure retinal pathology and has become a standard of care in ophthalmology (From Hee et al. [26])

optic nerve structure and function [33, 34]. Many of the measurement protocols that were developed in these early studies were adopted in current OCT ophthalmic instruments [7].

OCT is a powerful technique in ophthalmology because it can identify markers of early disease at treatable time points before visual symptoms and irreversible vision loss occurs. Furthermore, repeated imaging can be performed to track disease progression or monitor the response to therapy.

The important process of translating OCT research into the commercial world began in 1992 when an MIT startup company called Advanced Ophthalmic Devices was founded. Advanced Ophthalmic Devices was acquired by Carl Zeiss Meditec in 1994 and Zeiss introduced its first commercial product for ophthalmic diagnostics in 1996. Early instruments had an axial resolution of 10 μm and an imaging speed of 100 A-scans per second. A third generation ophthalmic instrument, the Stratus OCT, was introduced in 2002 which had similar resolution, but a faster speed of 400 A-scans per second. The increased speed enabled an increase in image pixel density. The large number of published clinical studies from previous generation instruments, coupled with technological improvement helped drive the clinical adoption of OCT. By the mid 2000's, OCT became the standard of care in ophthalmology and is considered essential for the diagnosis and monitoring of many retinal diseases as well as glaucoma [7]. With increases in imaging speed provided by spectral/Fourier domain detection (see later section of this chapter), many companies entered the ophthalmic marketplace in the mid 2000s. It is estimated that worldwide, approximately 30 million ophthalmic imaging procedures are currently performed annually [35].

1.4.3   Beyond Ophthalmology to Intravascular and Endoscopic Imaging

In OCT applications, detection sensitivity and tissue optical properties are especially important because light is highly attenuated by scattering and absorption, governing the imaging depth. The eye has the advantage that the path from the cornea to the retina (aqueous, lens, and vitreous) is relatively transparent. Although the retina is nominally transparent, it backscatters a small amount of light, which is detected to form OCT images. Early ophthalmic OCT imaging used 800 nm wavelength light because this wavelength minimizes absorption by water in the lens and vitreous. The use of longer wavelengths for OCT imaging was an important step because it reduced scattering and increased image penetration depths [3, 36, 37]. Figure 1.10 shows an early example from Brezinski et al. 1996 showing OCT imaging in a human epiglottis *ex vivo*, comparing imaging at 800 nm and 1,300 nm wavelengths [3]. At wavelengths shorter than ~1,100 nm, the dominant absorbers in most tissues are melanin and hemoglobin, which absorb at visible and near infrared wavelengths [38]. Water absorption has a peak at 1,450 nm and is extremely high for wavelengths longer than 1,900 nm. In most tissues, scattering at near infrared wavelengths is one to two orders of magnitude higher than absorption (except at the highest absorption peaks), and scattering decreases for longer wavelengths. Therefore, imaging at 1,300 nm improved image

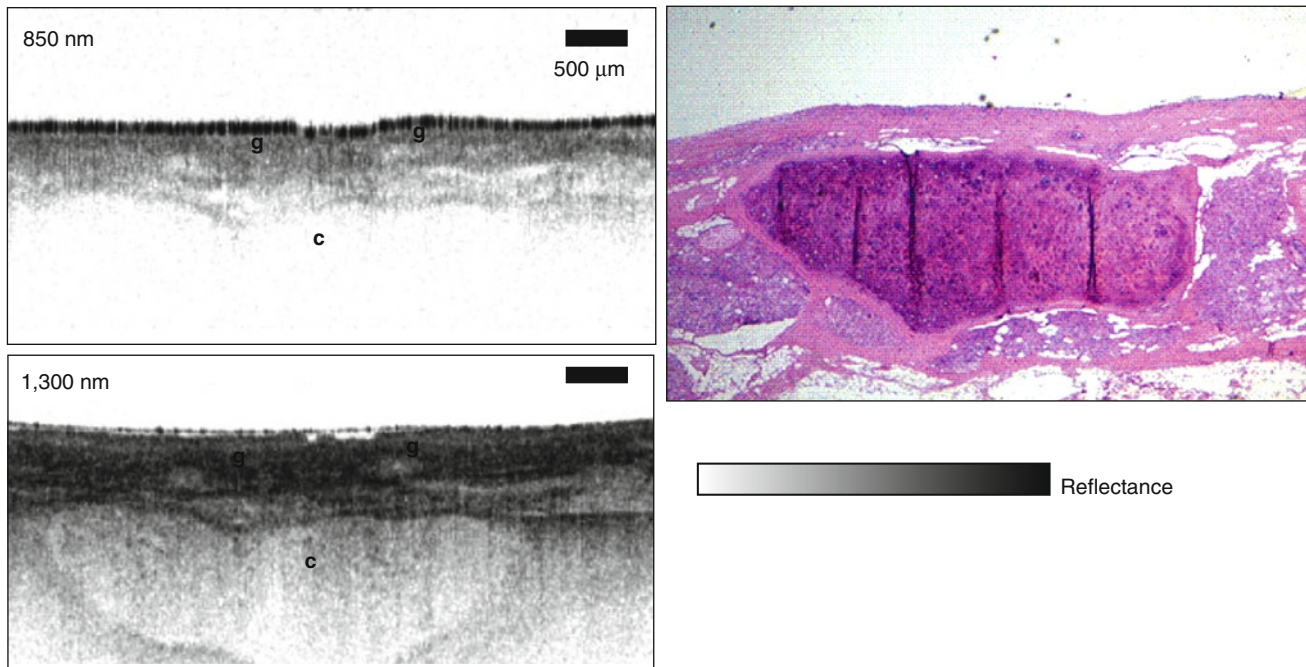**Fig. 1.10**   OCT in scattering tissues is possible using long wavelengths which are less attenuated by scattering. OCT of the human epiglottis *ex vivo* at 850 and 1,300 nm wavelength. Superficial glandular structures (*g*) are visualized with both 850 and 1,300 nm wavelength, but underlying cartilage (*c*) is better visualized with longer 1,300 nm wavelength. Scale = 500 μm (From Brezinski et al. [3])

penetration and has become a standard wavelength for most OCT applications outside of ophthalmology.

Early studies by Schmitt et al. investigated the mechanisms of OCT image contrast which are related to tissue optical properties [36, 39]. In OCT images, tissue structures are visible because they have different optical scattering properties. OCT images show true tissue dimensions (correcting for index of refraction and beam refraction effects) and do not suffer from processing artifacts as in histology. However if the OCT image is displayed using a false color scale, the colors represent different optical properties and not necessarily different tissue morphologies. Histological sections are stained in order to produce selective contrast between different tissue structures. There are multiple histological stains available which are highly specific. OCT relies on intrinsic differences in optical properties of different tissues to produce image contrast. On one hand, this is a limitation because tissue structures, such as cell nuclei, may not have contrast in traditional OCT imaging. However, histology is a time consuming process that requires tissue excision, processing, embedding, sectioning and staining. OCT imaging can be performed on tissue *in situ* and in real time, without the need for excision.

The concept of an "optical biopsy" was explored in several early OCT imaging studies using *ex vivo* surgical specimens [3, 40–51]. These studies developed the paradigm of comparing OCT imaging to the gold standard of histopathology in order to develop a baseline for the interpretation of OCT images. The concept of using OCT to assess vulnerable plaque was first proposed by Brezinski et al. in 1995 [3, 52]. Figure 1.11 shows an example of one of the first OCT images of plaque *ex vivo* and corresponding histology from Brezinski et al. 1996 [3]. The OCT image has an axial resolution of ~15 μm in tissue and imaging was performed at 1,300 nm wavelength to optimize imaging depths. The figure shows an
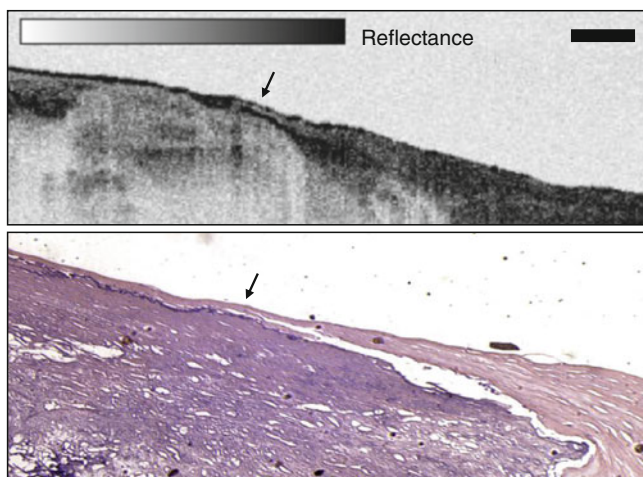

Fig. 1.11 Early OCT image of atherosclerotic plaque *ex vivo* and corresponding histology. The plaque is highly calcified with relatively low lipid content and a thin intimal cap. This result demonstrated that OCT can resolve morphological features associated with unstable plaques. Scale = 500 μm (From Brezinski et al. [3])

unstable plaque characterized by a thin intimal cap layer, adjacent to a heavily calcified plaque with low lipid content. The demonstration that OCT could resolve unstable plaque in *ex vivo* specimens was an important milestone which helped drive the technological and clinical developments of intravascular OCT imaging.

1.4.4 Technology for Catheter and Endoscopic OCT Imaging

The development of flexible fiber optic imaging probes, catheter and endoscopic device technology by Tearney, Bouma et al. at MIT enabled intravascular as well as endoscopic OCT imaging [53, 54]. Figure 1.12 shows one of the first OCT catheter/endoscopes which was a prototype for modern OCT endoscopic probes and intravascular imaging catheters. The catheter/endoscope has a single-mode optical fiber in a hollow rotating torque cable, coupled to a distal lens and microprism that reflects the OCT beam radially outward. The cable and distal optics are contained in a transparent housing. The OCT beam is scanned by rotating the cable to generate a transverse image through luminal structures or hollow organs. Imaging can also be performed in a longitudinal plane by push-pull movement of the fiber optic cable assembly [55]. The early catheter/endoscope shown in Fig. 1.12 had a diameter of 2.9 French or 1 mm, similar to a standard IVUS catheter. The development of catheter imaging devices is challenging because of the simultaneous mechanical, optical and biocompatibility requirements. Early commercial intravascular devices (such as the LightLab Imaging ImageWire™ and Helios™ occlusion balloon catheters) used micro-optic fabrication methods to create lenses and beam-directing elements which have diameters of optical fibers (80–250 μm), significantly smaller than what can be achieved with IVUS catheters [56].

Because of the challenges associated with *in vivo* intravascular OCT, endoscopic OCT initially progressed more rapidly [54, 57]. Figure 1.13 shows an example of OCT imaging of the rabbit esophagus *in vivo* and corresponding histology, from Tearney et al. in 1997 [54]. This image demonstrates visualization of esophageal layers including the mucosa (m), submucosa (sm), inner muscularis (im), outer muscularis (om), serosa (s) and used the rotary probe design of Fig. 1.13. The first clinical studies of endoscopic OCT imaging in human subjects were reported by Sergeev et al. in 1997 [57] and Feldchtein et al. in 1998 [58]. These clinical OCT imaging studies were performed with a flexible forward scanning fiber optic probe in the working channel of a standard endoscope, bronchoscope or trocar. The probe was a 1.5–2 mm diameter and used a miniature magnetic optical scanner to image in the forward direction. These early studies demonstrated the feasibility of performing clinical OCT imaging of organ systems such as the esophagus, larynx,
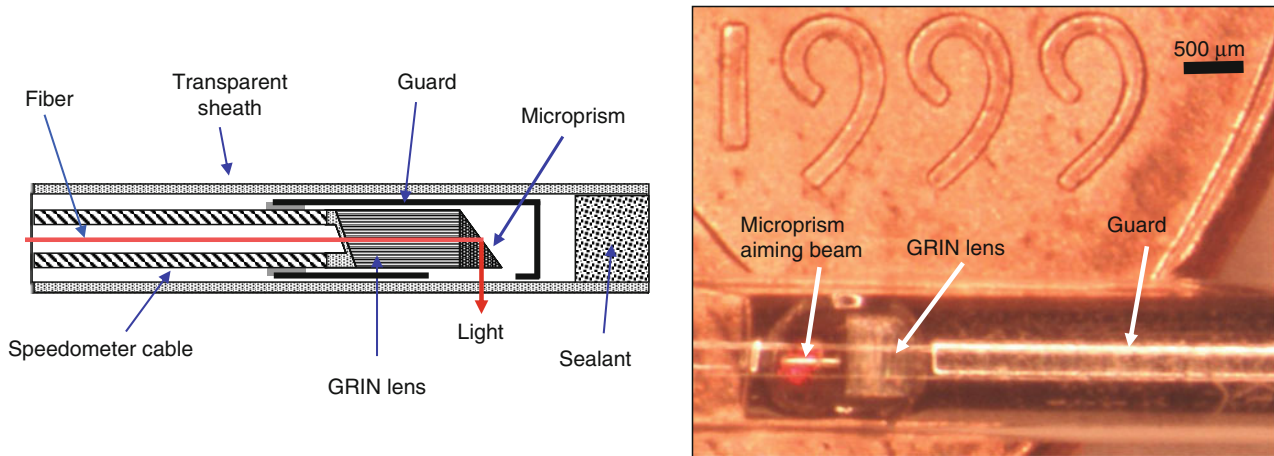
Fig. 1.12 Schematic and photograph of an early OCT catheter/endoscope for intraluminal imaging. A single-mode fiber is housed in a rotating flexible speedometer cable and covered by a transparent plastic sheath. The distal end focuses the beam at ~90° from the catheter axis and scans a rotary pattern and pullback pattern. The catheter diameter is 2.9 French or ~1 mm and is shown on a United States coin for scale. OCT can be integrated with a wide range of diagnostic and interventional devices
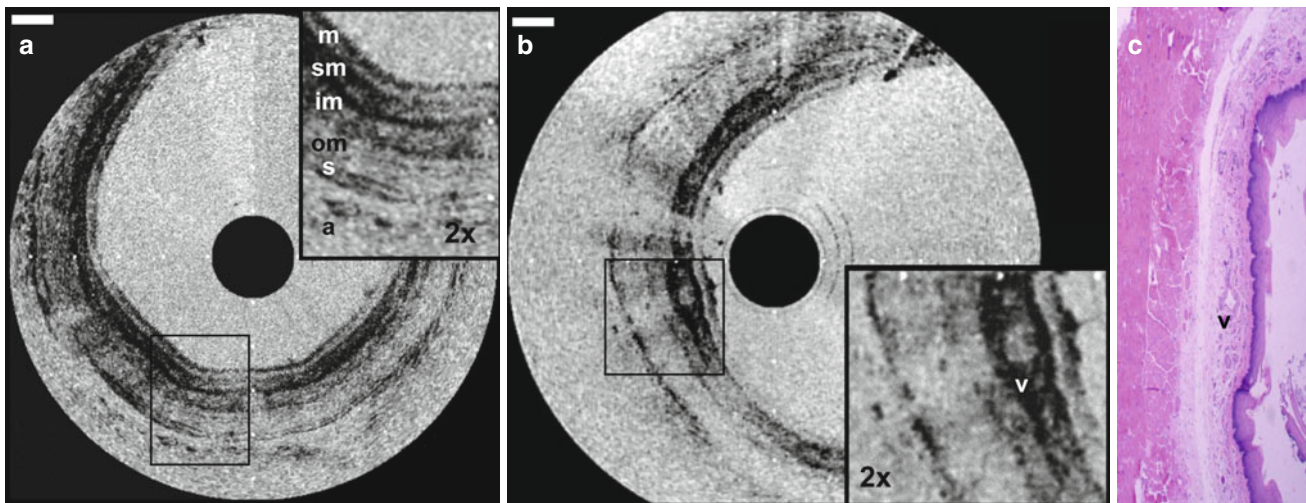
Fig. 1.13 Endoscopic OCT image of the rabbit esophagus in vivo demonstrating internal body imaging. (**a**) Esophageal layers including the mucosa (*m*), submucosa (*sm*), inner muscular layer (*im*), outer muscular layer (*om*), serosa (*s*), and adipose and vascular supportive tissues (a) can be visualized. (**b**) A blood vessel (*v*) can be seen within the submucosa. (**c**) Corresponding histology (**b**) (H&E stain). Scale bars, 500 µm (From Tearney et al. [54])

stomach, urinary bladder and uterine cervix. However, OCT imaging for neoplasia proved to be challenging because of limitations in image resolution and contrast, with associated difficulty in visualizing nuclei.

1.5 Early Intravascular OCT Imaging

The development of intravascular OCT was challenging because it required imaging technology, medical devices, *ex vivo* studies, preclinical studies and clinical imaging studies in patients. Figure 1.14 shows the first catheter-based image of a human coronary artery *ex vivo* using an early prototype 2.9 F OCT catheter from Tearney et al. in 1996 [59]. The figure compares OCT to 30 MHz IVUS. The excellent differentiation of the intima, media, and adventitia and suggested the utility of intravascular OCT.

1.5.1 Preclinical Feasibility Studies

In vivo intravascular OCT imaging required developing improved catheter imaging devices which could be used in animals and human subjects. In addition, since blood scatters and attenuates light, it was necessary to develop saline flushing or balloon occlusion protocols to displace blood, or to significantly dilute the hematocrit in the artery. Preclinical imaging studies in animals were in important step toward

Fig. 1.14 Early OCT image of a human artery *ex vivo* and comparison with intravascular ultrasound (IVUS). The OCT image has 15 μm axial resolution and enables the differentiation of the intima, media, and adventitia. Intimal hyperplasia is evident (From Tearney et al. [59])

developing technology and understanding the feasibility of clinical applications. Intravascular OCT animal imaging studies were performed in a rabbit model by Fujimoto et al. in 1999 [60]. Imaging was performed using a 2.9 F o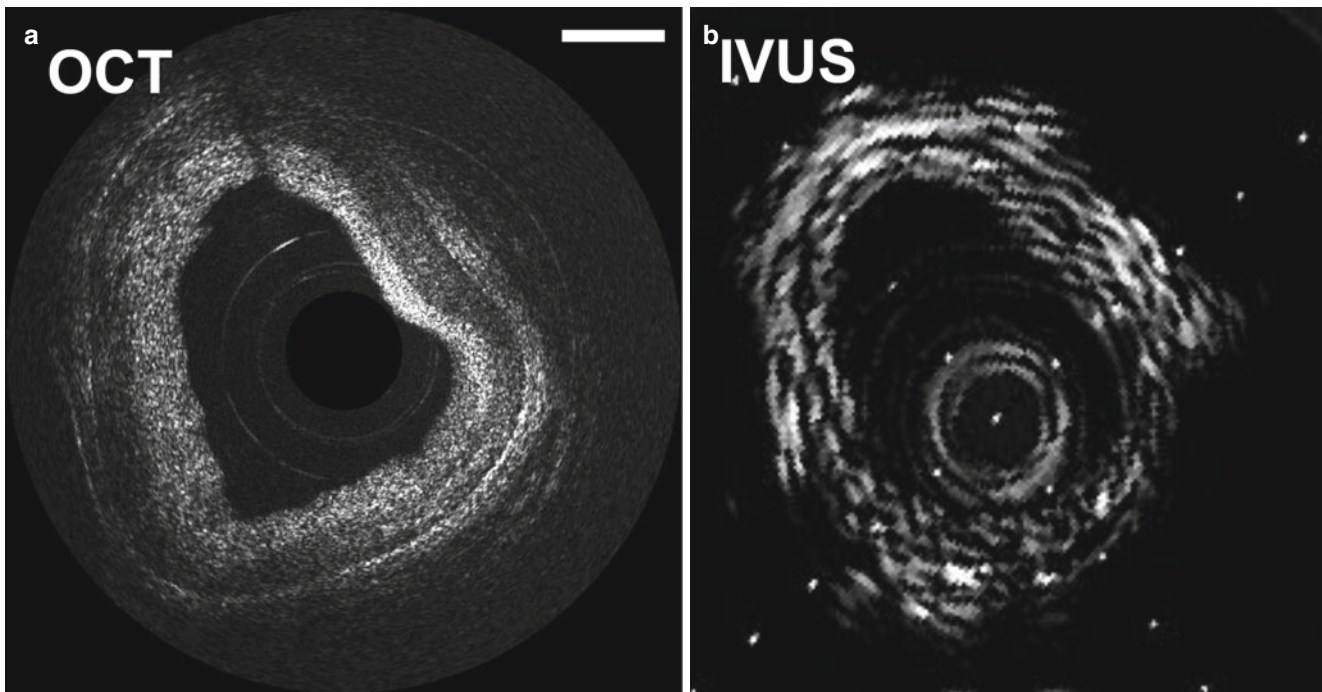ptical catheter using a time domain OCT system with a broadband femtosecond laser at 1,280 nm wavelength to achieve 10 μm axial resolution. Imaging speeds were 4 frames per second with a 512 axial pixels/image. In these studies, saline flushing was used to dilute the hematocrit during imaging. Intravascular OCT in a porcine model was reported by Tearney et al. in 2000 [61]. The study compared OCT and intravascular ultrasound (IVUS) in five swine using an OCT catheter and saline flushing. The study investigated normal coronary architecture, intimal dissections, and stents, demonstrating that OCT could better visualize architectural morphology in dissection and stent apposition than IVUS.

1.5.2 Histological Validation Studies

In parallel with feasibility studies, it was important to investigate OCT image features and their clinical significance. The first step was to establish correspondence of OCT images with histopathology. The early studies by Brezinski et al. investigated the correlation between OCT and histology on *ex vivo* aortic specimens with atherosclerotic plaque [3, 52]. As mentioned previously, the studies demonstrated that the high image resolution of OCT enabled visualization of thin intimal cap layers associated with vulnerable plaques, thin cap fiberatheromas. They also demonstrated that OCT

images had high contrast for lipids with low backscatter compared with fibrous tissues, enabling differentiation of intramural lipid deposits and that OCT could penetrate calcified plaques. A comprehensive study by Yabushita et al. in 2002 investigated the correlation between *ex vivo* OCT images and histology on arterial specimens with fibrous, fibrocalcific, and lipid rich plaques [62]. A blinded reading of OCT images by two readers using a 50 specimen training set and a 307 specimen study set achieved sensitivities ranging from 71 to 97 % and specificities ranging from 90 to 98 % for the three plaque morphologies compared with histology. The highest sensitivities and specificities, (>90 %) with excellent inter and intraobserver agreement, were obtained for fibrocalcific plaques. This study demonstrated that OCT had high sensitivity and specificity compared to histology for identifying plaque morphologies.

1.5.3 Clinical Studies

Intravascular OCT imaging in patients was first reported by Jang et al. in 2001 [63]. This pioneering study used a 3.2 F OCT imaging catheter and compared OCT with IVUS, Fig. 1.15. The OCT image shows tissue prolapse between stent struts, which was not obvious on the IVUS image. The study represents a landmark and was especially significant because it addressed multiple technological, clinical and administrative challenges. Independent clinical demonstrations by Grube et al. at the Sigeberg Heart Center were reported in 2002 using a prototype instrument developed by
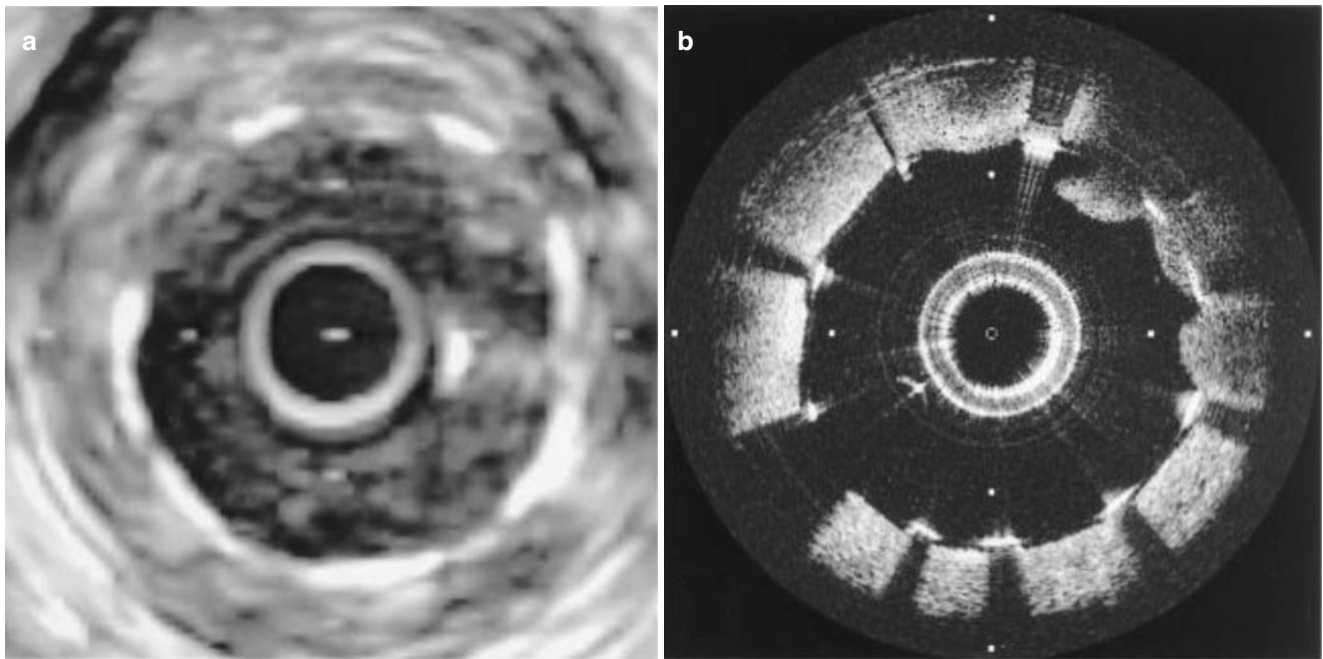
Fig. 1.15 First demonstration of intravascular OCT imaging in humans. IVUS (**a**) and OCT (**b**) images of the stented right coronary artery *in vivo*. OCT clearly visualized tissue prolapse between the stent struts (12–3 o'clock) (From Jang et al. [63])

LightLab Imaging [64]. This study compared OCT to IVUS imaging at 6 months post intervention, showing the ability of OCT to visualize stent-in-stent restenosis of a drug-eluting stent. A study by Jang et al. in 2002 compared intravascular OCT and IVUS in 10 patients [65]. The comparison to IVUS was important because it was the gold standard for intravascular imaging morphological structure. OCT axial image resolution was 13 ± 3 μm, compared to 98 ± 19 μm for IVUS. The comparison of OCT and IVUS showed that all fibrous plaques, calcification and echolucent regions visualized by IVUS were also visualized by OCT and OCT could identify features such as intimal hyperplasia and intramural lipid deposits better than IVUS.

The process of translating cardiovascular OCT for wider spread clinical use began in 1998 when an MIT startup company called LightLab Imaging was founded.[4] More details on commercial cardiovascular OCT efforts are discussed later in this chapter.

1.6 Advances in Imaging Speed

Early intravascular OCT studies demonstrated feasibility, however imaging speed was a serious limitation. Since blood strongly scatters light and attenuates OCT signals, saline flushing or a combination of occlusion with flushing was

required to dilute the hematocrit during OCT imaging. However limitations on the injected saline volume as well as concerns about ischemia restricted the imaging time and the amount of image data that could be acquired. Therefore, increasing OCT imaging speed was important for achieving clinically practical intravascular OCT imaging.

Fortunately, there have been powerful advances in OCT detection technology which enable dramatic increases in imaging speeds. These techniques are known as Fourier domain OCT and there are two variants: Spectral domain OCT (SD-OCT) and swept source OCT (SS-OCT) [66–73]. Swept source OCT, also known as optical frequency domain imaging (OFDI). Early OCT instruments used a low-coherence light source and interferometer with a scanning reference delay arm. This method of low coherence imaging is known as time domain OCT (TD-OCT). However, it is also possible to perform detection in the Fourier domain using a low coherence interferometer with a broadband light source, measuring the interference spectrum with a spectrometer and a high speed line scan camera [66, 74–77]. This method is known as spectral domain OCT and was first proposed by Fercher et al. almost two decades ago in 1995 [66]. In 2003, three different research groups, working independently, demonstrated that spectral domain detection has a powerful sensitivity advantage over time domain detection, since spectral domain detection essentially measures all of the echoes of light simultaneously [71, 78, 79]. This discovery was a powerful advance in OCT research and development. The sensitivity is enhanced by the ratio of the axial resolution to the axial imaging depth. For most OCT systems, this corresponds to a sensitivity increase

---

[4]The original name of the company was Coherent Diagnostic Technology, but the corporate name was later changed to LightLab Imaging.

Fig. 1.16 How swept source
OCT works. Swept source/Fourier
domain OCT uses an
interferometer with a narrow
band, frequency swept laser and
detectors. The Michelson
interferometer interferes two
frequency sweeps which are time
delayed with respect to each other
and generates a beat frequency
which is proportional to the path
length mismatch ΔL. Fourier
transforming the beat signal from
the detector yields axial scan
information (echo magnitude and
time delay). Spatial features are
encoded in frequency, somewhat
analogous to MR imaging
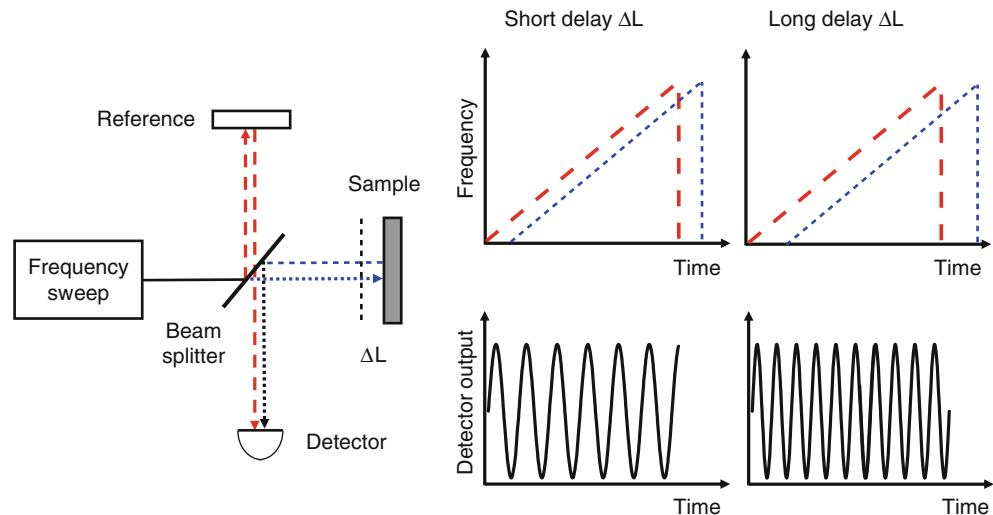
of 50–100 times, enabling a corresponding increase in imaging speeds. Spectral domain detection is well suited for high speed imaging at 800 nm wavelength and has had a powerful impact on clinical ophthalmic OCT.

Swept source OCT, the second type of Fourier domain detection, uses an interferometer with a narrow-bandwidth, frequency-swept light source and detectors which measure the interference output as a function of time. The basic concept of swept source OCT was described in patents as early as 1991 and experimental studies in 1997 [67, 68, 80, 81]. Swept source OCT has the advantage that it does not require a spectrometer and line scan camera as in spectral domain OCT. Furthermore, it can achieve very fast imaging speeds because it is not limited by camera reading speed and is potentially lower in cost and more compact than spectral domain OCT systems. The primary technological challenge in swept source OCT is that it requires high speed, swept light sources with narrow linewidths.

1.6.1 Swept Source/Fourier Domain OCT

Swept source/Fourier domain detection uses an interferometer with a narrowband light source which is frequency swept in time [67–69, 71]. The variation in optical frequency with time essentially encodes different time delays into the light beam, which can then be detected by interference and Fourier transforming. These detection techniques were used in the 1990s to perform measurements in fiber optics and photonics components [82–84]. Even before the basic concepts of a frequency-chirped coherent ranging and imaging, along with the associated fundamental signal-to-noise and performance equations and system tradeoffs, date back to the 1980s when they were widely used in coherent laser radar [85]. OCT using swept source detection was also demonstrated as early as 1997 by Chinn et al. [67] and Golubovic et al. [68], but the sensitivity advantages were not fully recognized and perfor-

mance was limited by the available laser technology. Pioneering studies by Yun et al. in 2003 demonstrated OCT imaging with 19,000 axial scans per second and 13–14 μm axial resolution in air [69]. Record imaging speeds of 115,000 axial scans per second were achieved in 2005 using a novel swept laser technology based on a grating and rotating polygon mirror filter [86].

Figure 1.16 shows a schematic of how swept source detection works. The output from a narrow bandwidth, frequency swept light source is divided into a signal and a reference beam. The signal beam is directed onto the tissue to be imaged and is backreflected or backscattered from internal structures at different depths. The reference beam is reflected from a reference mirror at a fixed delay. The signal and reference beams have a time offset determined by the path length difference, which is related to the depth of the structure in the tissue. Because the frequency of the light is swept as a function of time, the light echoes in the signal beam will have a frequency offset from the reference beam. When the signal and reference beams interfere, a modulation or beat in intensity is produced at a frequency that is given by this frequency offset. Therefore, different echo delays will produce different frequency modulations. The echo delays can be measured by digitizing the photodetector signal over a single frequency sweep of the light source, correcting any nonlinearity in the frequency sweep as a function of time and then Fourier transforming this beat frequency signal. This results in an axial scan measurement of the magnitude and echo delay of light from the tissue.

Fourier domain detection measures all of the optical echoes at the same time, rather than sequentially as in time domain detection. This enables a dramatic improvement in detection sensitivity. Swept source/Fourier domain methods have the advantage that they can be used at wavelength greater than 1,000 nm, where silicon based cameras lack sensitivity and more expensive InGaAs cameras are required.

The axial imaging resolution and axial scan rate in swept source OCT is determined by the sweep range and sweep repetition rate of the laser, respectively. The spectral linewidth of the laser determines the imaging range of imaging depth of the OCT system. If the laser can achieve high sweep repetition rates, imaging can be performed much faster than spectral domain OCT, which is limited by camera read rates. The systems also have the potential to be more compact and lower in cost, since no spectrometer is needed.

1.6.2 Light Sources for High Speed OCT

Because swept source OCT can achieve high imaging speeds at wavelengths of 1,300 nm, it has had a powerful impact on intravascular and endoscopic imaging applications. The performance of swept source OCT systems depends directly on the swept light source; therefore advances in laser technology have become an active area of research in OCT.

Swept source 3D-OCT imaging was demonstrated in the porcine esophagus and coronary artery at speeds of 10,000 and 54,000 axial scans/second, respectively [87, 88] in 2006 and 2007 using swept lasers with a high speed rotating polygon and diffraction grating filter. Frequency swept lasers consist of a laser gain medium and a tunable filter. There is a fundamental limit on the tuning rate of a frequency swept laser because the light at a given frequency must build up from spontaneous emission and be amplified up to a saturation level as the filter is tuned [89]. Therefore, lasers with short cavities, which have a rapid round-trip time. can frequency sweep faster than long cavity lasers. The development of Fourier domain mode locking (FDML) in 2006 by Huber et al. provided a novel approach for breaking the laser speed limit [73]. FDML lasers use a long optical fiber delay inside the laser, which stores the entire frequency sweep in the cavity and synchronously tunes the filter such that a given frequency arrives at the filter when it is tuned to pass it. This avoids the need to build up lasing at each frequency and enables rapid sweep speeds. Early FDML lasers achieved record imaging speeds of 370,000 axial scans per second [90]. FDML technology was enabling for intravascular/ endoscopic as well as ophthalmic applications. Record endoscopic imaging speeds of 100,000 axial scans per second with 5–7 μm axial image resolution were demonstrated in an animal model in 2007 using swept source OCT with FMDL lasers [91]. These high speeds enabled imaging at 50 frames/ second and data rates of 61 megavoxels per second. 3D-OCT enables virtual manipulation of tissue geometry, speckle reduction, synthesis of *en face* views similar to endoscopic images, generation of virtual cross-sectional images with arbitrary orientation, and quantitative measurements of morphology. Swept-source OCT was rapidly adopted in commercial OCT, where LightLabs introduced the first com-
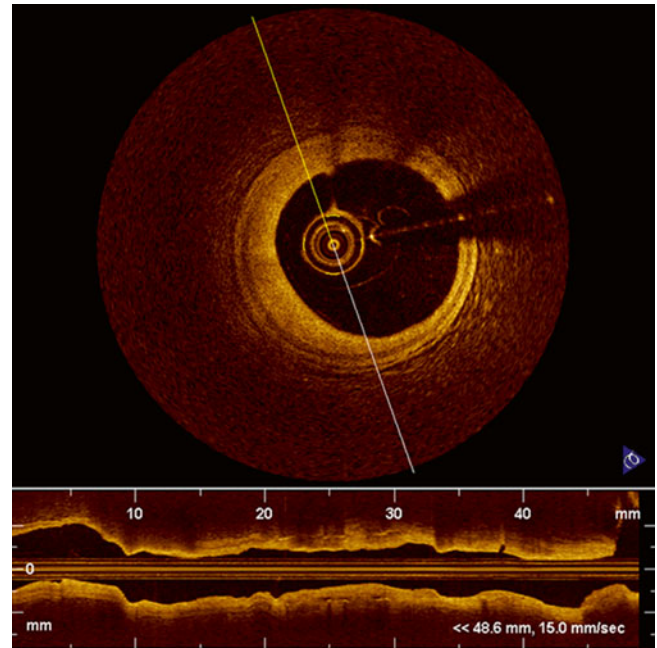

Fig. 1.17 High speed intravascular imaging using swept source OCT. Intravascular OCT pullback image of human coronary artery *in vivo* using manual contrast injection. Imaging was performed at 100 frames per second, at an axial scan rate of 45,000 axial scans per second. Swept source OCT enabled the acquisition of larger data sets with reduced imaging times and contrast volumes

mercial swept-source OCT for intravascular imaging. Figure 1.17 shows an example of high-speed OCT intravascular imaging in an artery *in vivo* using a LightLab prototype instrument with and a FDML laser which operates at 45,000 axial scans/second, acquiring 100 frames per second with a 15 mm/s pullback speed using contrast injection to remove blood from the imaging field. These high imaging speeds enable rapid pullbacks, the mapping of long segments of an artery, while minimizing ischemia. Human endoscopic OCT imaging studies using FDML lasers achieved a 62,000 axial scans/second speed with an axial image resolution of 5 μm in tissue in 2009 [92]. Figure 1.18 shows an example of endoscopic imaging in the normal human colon. A volume of $7 \times 20 \times 1.6$ mm and was acquired in 20 s using a rotary fiber optic probe with pullback. Volumetric data enables the generation of arbitrary cross sections as well as *en face* images which display the uniform crypt pattern in the normal epithelium of the colon. The ability to assess the 3D structure of crypts is of potential value for future applications in cancer detection and treatment. Ophthalmic imaging with speeds greater than 1 million axial scans per second have recently been achieved using swept source OCT with FDML laser technology [93]. These results suggest the future potential of OCT to achieve higher speeds and 3D volumetric imaging.

In addition to research prototype lasers, commercial swept laser technologies also made important advances. The devel-
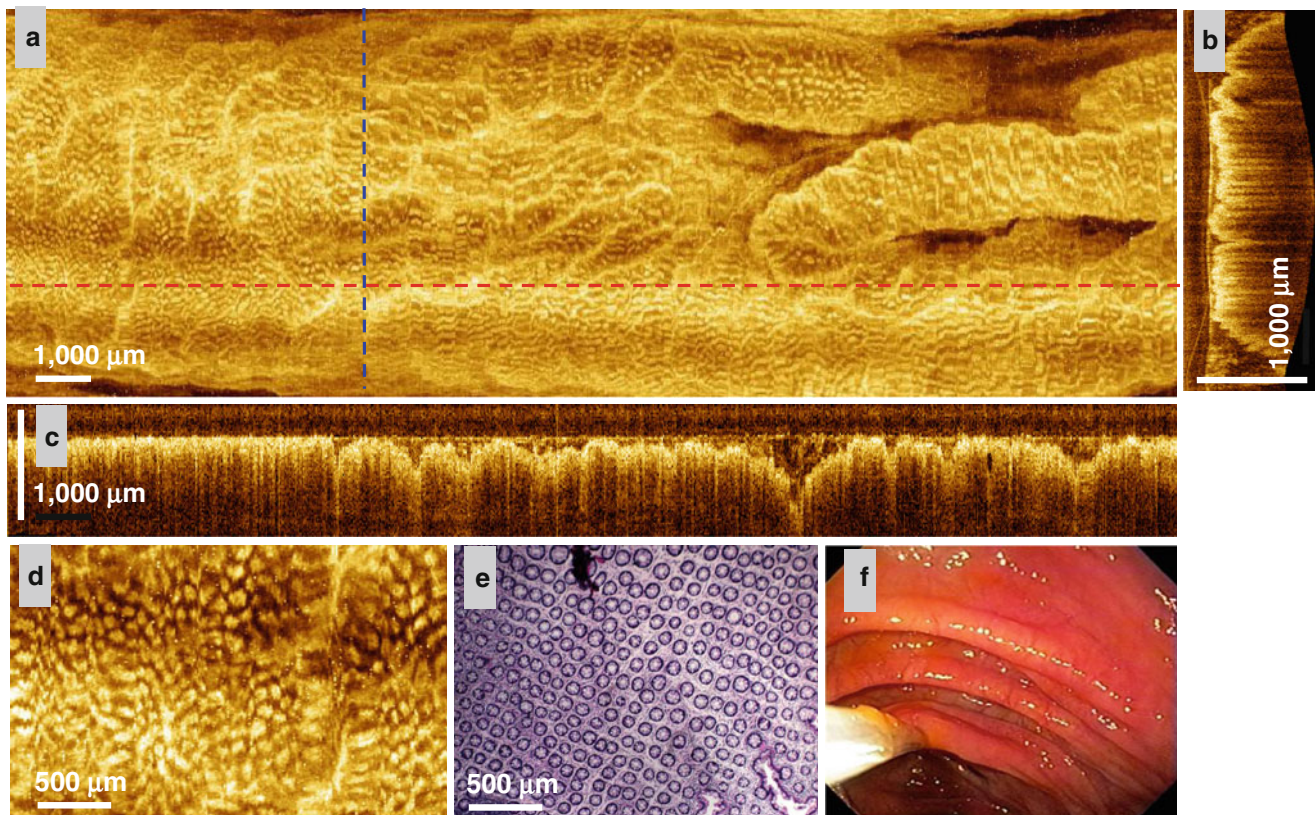
Fig. 1.18 Endoscopic imaging using swept source OCT. 3D-OCT images of the human colon *in vivo*. (**a**) *En face* image constructed by axial summation of volumetric dataset. *Dashed lines* show locations of cross sections. (**b**, **c**) Cross-sections showing columnar epithelial struc-ture. (**d**) Enlarged *en face* view of crypt pattern. (**e**) Representative *en face* histology of human colon. (**f**) White light endoscopy of region imaged by OCT. OCT was performed at 62,000 axial scans per second with 6 um axial image resolution (From Adler et al. [92])

opment of a compact and robust short cavity swept laser by Axsun Technologies enabled intravascular as well as oph-thalmic applications. Their short cavity swept laser uses a tunable filter and a gain medium with a few centimeter cavity length. This laser was used in the LightLab The C7$^{XR\,TM}$ sys-tem introduced in 2009 which operated at 50,000 axial scans per second to achieve imaging speeds of 100 frames per sec-ond. Retinal imaging at a 1,050 nm wavelength with a 5.3 µm axial resolution was demonstrated at 100,000 axial scans per second using the swept laser direct output and 200,000 axial scans per second speed was achieved by multiplexing the laser sweeps [94]. The short cavity laser also enabled nar-rower instantaneous line widths and therefore supported lon-ger imaging ranges than previous swept lasers. This was an important advantage for intravascular OCT which requires a long imaging range for imaging larger diameter arteries as well as for ophthalmic OCT which requires a long image range to achieve wide fields on the retina due to retinal cur-vature. The wide acceptance and large market for ophthalmic OCT promises to drive technological advances that can be utilized in intravascular OCT. Chapter 15 discusses future advances in intravascular OCT.

1.7 Technology Translation and Commercial Development

Commercial development is a key step in the translation of any new medical technology because it puts reliable technol-ogy into the hands of clinicians, enabling widespread clinical access, facilitating multi-center clinical trials which are ulti-mately needed to establish efficacy, support reimbursement and ultimately impact patient care. However the process of technology translation and commercial development is fraught with many technological and clinical challenges, as well as engineering, manufacturing and regulatory hurdles. These factors can make innovation difficult and the path to the market long. Both startups and large corporations have been involved in the development of intravascular OCT.

LightLab Imaging, Inc. (Westford, MA) was founded in 1998 as an MIT startup. LightLab was acquired by Goodman, Ltd. in 2002 and most recently acquired by St. Jude Medical in 2010. LightLab/St. Jude developed multiple generations of intravascular OCT imaging engines and catheters which are summarized in Fig. 1.19. The first generation intravascu-lar OCT instrument was the M2 imaging system with which

2004	2007	2009	2011	2012
M2 System	M3 System	C7XR™ System	ILUMIEN™ System	ILUMIEN™ OPTIS™
First Commercial OCT System 15 fps / 200 lines Occlusion + flush	2nd Generation 20 fps / 240 lines Occlusion + flush	Europe and US only 100 fps / 500 lines Occlusion-free	Commercially available 2011 100 fps / 54 mm pullback Combined FFR and OCT Wireless FFR	Japan launch 2012 180 fps/75 and 54 mm pullback Advanced software tools for PCI Optimization Tableside control from DOC
Occlusion balloon + ImageWire™		Occlusion-free Flush	FFR and OCT System	2nd Gen FFR and OCT System

Fig. 1.19 Multiple generations of intravascular OCT. Development history of commercial LightLab/St. Jude intravascular imaging technology, showing the evolution of OCT systems from time domain to swept source and improvements in performance

the first clinical studies were performed in Europe in 2002. The M2 system used time domain detection and operated at 15 frames per second (200 axial scans per frame at 3,000 axial scans per second) using saline flushing and occlusion. Regulatory approval with CE marking in Europe was obtained in 2004, followed by a release in China in 2006, and Ministry of Health, Labor and Welfare approval in Japan in 2007. The next generation, M3 system, had increased imaging speeds of 20 frames per second (240 axial scans per frame) and was introduced in Japan in 2008. Over 10,000 cases were performed using time domain OCT with the M2 and M3 systems providing key insights on engineering design and clinical utility. An important advance came with the commercial release of swept source domain OCT, which dramatically increased imaging speeds, enabling large pullback data sets to be rapidly acquired within a limited acquisition time required to minimize ischemia. The C7^{XR}™ system achieved imaging speeds of 100 frames per second (500 axial scans per frame) and was introduced in Europe in 2009 and in the U.S. in 2010. The ten times increase in imaging speed enabled higher frame rates for improved pullback speeds and arterial coverage as well as increased axial scan density for improved image quality. Occlusion-free imaging also became possible by using a contrast agent rather than a saline injection to dilute hematocrit. The most recent generation systems (Ilumien™ and Illumien Optis™ OCT Intravascular Imaging Systems, St. Jude Medical, St. Paul,

Minnesota) increased imaging speeds even further to 180 frames per second. These instruments also provide integrated FFR and OCT. The high data acquisition rates enable multiple image modes with pullback speeds of 20 or 36 mm/s over a pullback length of 55 or 75 mm. From 2004 to 2013, Lightlab/St. Jude was the only commercial manufacturer of intravascular OCT; therefore, the majority of clinical cases to date have been performed using these instruments.

Intravascular OCT has also been developed by other companies via startup or industry academic partnerships. Terumo began development of cardiovascular OCT in 2004, establishing a co-development program with MGH. A first-in-man study using the Terumo Lunawave™ was reported by Okamura et al. in 2011 at the Rotterdam Thoraxcenter, comparing OCT with IVUS and quantitative coronary angiography [95]. In 2013, Terumo announced the first commercial release of its intravascular OCT product the Lunawave™ in Europe and Japan. CardioSpectra was a 2005 startup from the University of Texas that was acquired by IVUS leader Volcano in 2007. Unfortunately in 2013 after several years of investment and development, Volcano announced the cancellation of its cardiovascular OCT product development effort for a variety of reasons. Avinger is another startup company founded in 2007 that uses OCT for guiding atherectomy in peripheral arteries and received FDA clearance in 2012. These examples illustrate the complexities and challenges of translating new medical technologies.
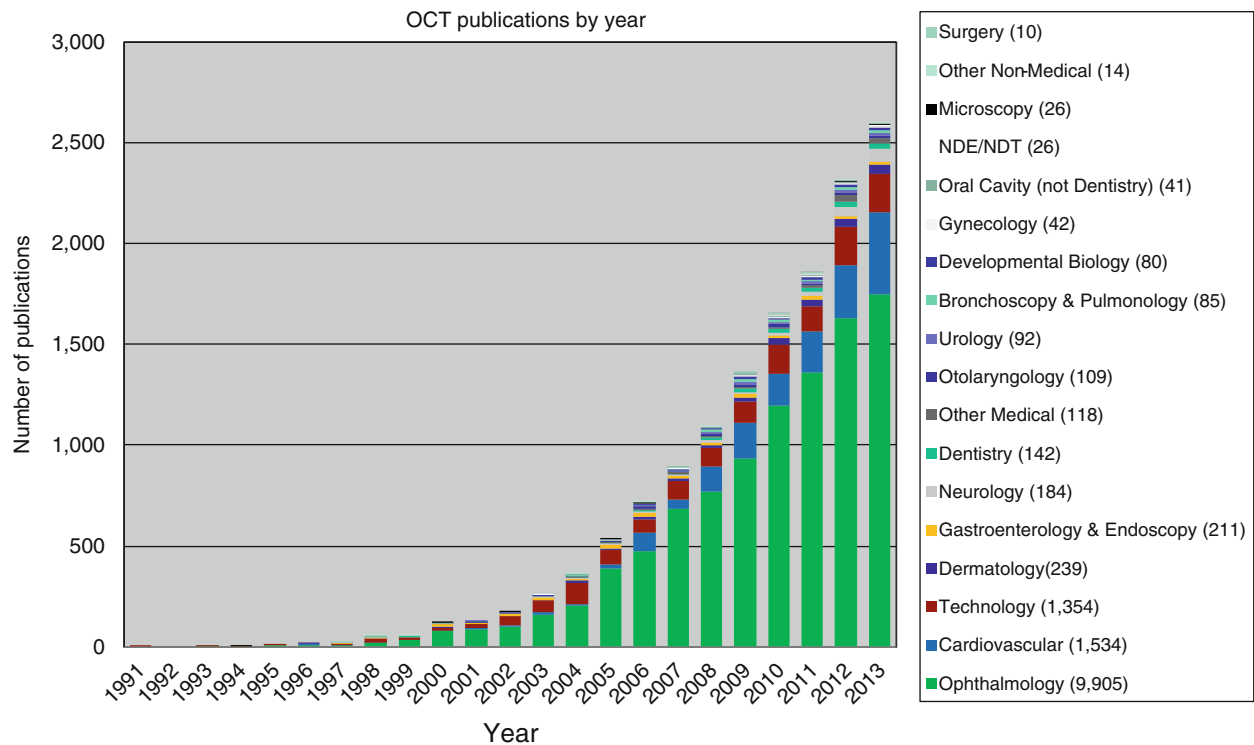
Fig. 1.20 OCT Publication volume versus year. Publications are one indicator of scientific and clinical progress. The largest volume of publications is in ophthalmology, where OCT is now a clinical standard.

Recently, cardiology became the second largest volume of publications and is growing rapidly

Conclusion

OCT is a powerful imaging technology in biomedical research and medicine because it enables high-speed, high-resolution, *in situ* visualization of tissue structure and pathology that often cannot be obtained by any other means. Figure 1.20 shows a yearly plot of journal publications involving OCT. Journal articles are one marker for scientific development as well as clinical adoption. The largest publication volume is in ophthalmology. To date OCT has had the most clinical impact in ophthalmology where it has become the standard of care, providing structural and quantitative information that cannot be obtained by any other modality. OCT improves the diagnosis of retinal disease as well as enables the monitoring of disease progression and response to therapy. In ophthalmology, OCT played a significant role in the development of new pharmaceutical therapies for age-related macular degeneration. The second largest number of publications at the time of this writing is in cardiology. Intravascular OCT has contributed to the understanding of a variety of cardiovascular diseases including plaque morphology and its role in myocardial infarction as well as percutaneous coronary interventions such as stent implantation. OCT is clearly a powerful imaging modality for cardiovascular research and is increasingly being used in everyday clinical decision-making. The number of clinical cases has surpassed ~50,000 case per year; however, this is

a small fraction of the total yearly PCI procedures and the extent to which intravascular OCT will become a more widely used tool in everyday clinical cardiovascular decision making, is still to be determined. Extensive clinical studies are underway in order to establish to what extent OCT will become the standard cardiovascular imaging modality as it has become in ophthalmology. OCT could have a major impact on morbidity and mortality from heart disease and could far surpass its impact in ophthalmology. Even if intravascular OCT does not grow to capture a high percentage of the large number of worldwide PCI procedures (millions per year), it will likely displace a significant fraction of the IVUS market. Its impact in cardiovascular medicine has already been substantial and the underlying technology is constantly improving. Cardiovascular OCT imaging promises to continue to be a key tool for understanding and fighting cardiovascular disease.

References

1. Huang D, Swanson EA, Lin CP, Schuman JS, Stinson WG, Chang W, et al. Optical coherence tomography. Science. 1991;254(5035): 1178–81.
2. Fujimoto JG, Brezinski ME, Tearney GJ, Boppart SA, Bouma BE, Hee MR, et al. Biomedical imaging and optical biopsy using optical coherence tomography. Nat Med. 1995;1:970–2.

3. Brezinski ME, Tearney GJ, Bouma BE, Izatt JA, Hee MR, Swanson EA, et al. Optical coherence tomography for optical biopsy. Properties and demonstration of vascular pathology. Circulation. 1996;93(6):1206–13.

4. Erbel R, Roelandt JRTC, Ge J, Gorge G. Intravascular ultrasound. London: Martin Dunitz; 1998.

5. Szabo TL. Diagnostic ultrasound imaging: inside out. Burlington: Elsevier Academic Press; 2004. xxii, 549 p. p.

6. Hedrick WR, Hykes DL, Starchman DE. Ultrasound physics and instrumentation. 4th ed. St. Louis: Elsevier Mosby; 2005.

7. Schuman JS, Puliafito CA, Fujimoto JG. Optical coherence tomography of ocular diseases. 2nd ed. Thorofare: Slack Inc.; 2004.

8. Duguay MA. Light photographed in flight. Am Sci. 1971;59 (September):551–6.

9. Duguay MA, Mattick AT. Ultrahigh speed photography of picosecond light pulses and echoes. Appl Opt. 1971;10(September):2162–70.

10. Bruckner AP. Picosecond light scattering measurements of cataract microstructure. Appl Opt. 1978;17(October):3177–83.

11. Park H, Chodorow M, Kompfner R. High resolution optical ranging system. Appl Opt. 1981;20(July):2389–94.

12. Fujimoto JG, De Silvestri S, Ippen EP, Puliafito CA, Margolis R, Oseroff A. Femtosecond optical ranging in biological systems. Opt Lett. 1986;11(3):150–3.

13. Takada K, Yokohama I, Chida K, Noda J. New measurement system for fault location in optical waveguide devices based on an interferometric technique. Appl Opt. 1987;26:1603–8.

14. Youngquist R, Carr S, Davies D. Optical coherence-domain reflectometry: a new optical evaluation technique. Opt Lett. 1987;12(3):158–60.

15. Gilgen HH, Novak RP, Salathe RP, Hodel W, Beaud P. Submillimeter optical reflectometry. J Lightwave Techol. 1989;7:1225–33.

16. Fercher AF, Mengedoht K, Werner W. Eye-length measurement by interferometry with partially coherent light. Opt Lett. 1988;13:1867–9.

17. Clivaz X, Marquis-Weible F, Salathe RP. Optical low coherence reflectometry with 1.9 mm spatial resolution. Electron Lett. 1992;28(16):1553–4.

18. Schmitt JM, Knuttel A, Bonner RF. Measurement of optical-properties of biological tissues by low- coherence reflectometry. Appl Opt. 1993;32(30):6032–42.

19. Tanno N, Ichimura T. Reproduction of optical reflection-intensity-distribution using multi-mode laser coherence. Trans Inst Electron Inf Commun Eng C-I. 1994;J77C-I(7):415–22.

20. Wang Y, Funaba T, Ichimura T, Tanno N. Optical multimode time-domain reflectometry. Review of Laser Engineering. 1995;23(4):273–9.

21. Huang D, Wang J, Lin CP, Puliafito CA, Fujimoto JG. Micron-resolution ranging of cornea and anterior chamber by optical reflectometry. Laser Surg Med. 1991;11:419–25.

22. Tanno N, Ichimura T, Saeki A, inventors. Device for measuring the light wave of a reflected image, Japanese Patent Application, 2-300169. 1994.

23. Rollins AM, Izatt JA. Optimal interferometer designs for optical coherence tomography. Opt Lett. 1999;24(21):1484–6.

24. Swanson EA, Izatt JA, Hee MR, Huang D, Lin CP, Schuman JS, et al. In vivo retinal imaging by optical coherence tomography. Opt Lett. 1993;18(21):1864–6.

25. Fercher AF, Hitzenberger CK, Drexler W, Kamp G, Sattmann H. In vivo optical coherence tomography. Am J Opthalmol. 1993;116(1):113–4.

26. Hee MR, Izatt JA, Swanson EA, Huang D, Schuman JS, Lin CP, et al. Optical coherence tomography of the human retina. Arch Ophthalmol. 1995;113(3):325–32.

27. Puliafito CA, Hee MR, Lin CP, Reichel E, Schuman JS, Duker JS, et al. Imaging of macular diseases with optical coherence tomography. Ophthalmology. 1995;102(2):217–29.

28. Hee MR, Puliafito CA, Wong C, Duker JS, Reichel E, Rutledge B, et al. Quantitative assessment of macular edema with optical coherence tomography. Arch Ophthalmol. 1995;113(8):1019–29.

29. Hee MR, Puliafito CA, Duker JS, Reichel E, Coker JG, Wilkins JR, et al. Topography of diabetic macular edema with optical coherence tomography. Ophthalmology. 1998;105(2):360–70.

30. Hee MR, Puliafito CA, Wong C, Duker JS, Reichel E, Schuman JS, et al. Optical coherence tomography of macular holes. Ophthalmology. 1995;102(5):748–56.

31. Hee MR, Puliafito CA, Wong C, Reichel E, Duker JS, Schuman JS, et al. Optical coherence tomography of central serous chorioretinopathy. Am J Opthalmol. 1995;120(1):65–74.

32. Hee MR, Baumal CR, Puliafito CA, Duker JS, Reichel E, Wilkins JR, et al. Optical coherence tomography of age-related macular degeneration and choroidal neovascularization. Ophthalmology. 1996;103(8):1260–70.

33. Schuman JS, Hee MR, Arya AV, Pedut-Kloizman T, Puliafito CA, Fujimoto JG, et al. Optical coherence tomography: a new tool for glaucoma diagnosis. Curr Opin Ophthalmol. 1995;6(2):89–95.

34. Schuman JS, Hee MR, Puliafito CA, Wong C, Pedut-Kloizman T, Lin CP, et al. Quantification of nerve fiber layer thickness in normal and glaucomatous eyes using optical coherence tomography. Arch Ophthalmol. 1995;113(5):586–96.

35. Swanson EA, Huang D. Ophthalmic OCT reaches $1 Billion per year. Retinal Physician. 2011;8(4):45. 58–9, 62.

36. Schmitt JM, Knuttel A, Yadlowsky M, Eckhaus MA. Optical-coherence tomography of a dense tissue: statistics of attenuation and backscattering. Phys Med Biol. 1994;39(10):1705–20.

37. Fujimoto JG, Brezinski ME, Tearney GJ, Boppart SA, Bouma B, Hee MR, et al. Optical biopsy and imaging using optical coherence tomography. Nat Med. 1995;1(9):970–2.

38. Parsa P, Jacques SL, Nishioka NS. Optical properties of rat liver between 350 and 2200 nm. Appl Opt. 1989;28(12):2325–30.

39. Schmitt JM, Knuttel A. Model of optical coherence tomography of heterogeneous tissue. J Opt Soc Am A. 1997;14(6):1231–42.

40. Brezinski ME, Tearney GJ, Boppart SA, Swanson EA, Southern JF, Fujimoto JG. Optical biopsy with optical coherence tomography: feasibility for surgical diagnostics. J Search Res. 1997;71(1): 32–40.

41. Izatt JA, Kulkarni MD, Wang H-W, Kobayashi K, Sivak Jr MV. Optical coherence tomography and microscopy in gastrointestinal tissues. IEEE J Sel Top Quant. 1996;2(4):1017–28.

42. Tearney GJ, Brezinski ME, Southern JF, Bouma BE, Boppart SA, Fujimoto JG. Optical biopsy in human gastrointestinal tissue using optical coherence tomography. Am J Gastroenterol. 1997;92(10): 1800–4.

43. Tearney GJ, Brezinski ME, Southern JF, Bouma BE, Boppart SA, Fujimoto JG. Optical biopsy in human urologic tissue using optical coherence tomography. J Urology. 1997;157(5):1915–9.

44. Boppart SA, Brezinski ME, Pitris C, Fujimoto JG. Optical coherence tomography for neurosurgical imaging of human intracortical melanoma. Neurosurgery. 1998;43(4):834–41.

45. Kobayashi K, Izatt JA, Kulkarni MD, Willis J, Sivak Jr MV. High-resolution cross-sectional imaging of the gastrointestinal tract using optical coherence tomography: preliminary results. Gastrointest Endosc. 1998;47(6):515–23.

46. Tearney GJ, Brezinski ME, Southern JF, Bouma BE, Boppart SA, Fujimoto JG. Optical biopsy in human pancreatobiliary tissue using optical coherence tomography. Digestive Dis Sci. 1998;43(6): 1193–9.

47. Pitris C, Brezinski ME, Bouma BE, Tearney GJ, Southern JF, Fujimoto JG. High resolution imaging of the upper respiratory tract with optical coherence tomography: a feasibility study. Am J Respir Crit Care Med. 1998;157(5 Pt 1):1640–4.

48. Pitris C, Goodman A, Boppart SA, Libus JJ, Fujimoto JG, Brezinski ME. High-resolution imaging of gynecologic neoplasms using

optical coherence tomography. Obstet Gynecol. 1999;93(1): 135–9.

49. Jesser CA, Boppart SA, Pitris C, Stamper DL, Nielsen GP, Brezinski ME, et al. High resolution imaging of transitional cell carcinoma with optical coherence tomography: feasibility for the evaluation of bladder pathology. Brit J Radiol. 1999;72(864):1170–6.

50. Boppart SA, Goodman A, Libus J, Pitris C, Jesser CA, Brezinski ME, et al. High resolution imaging of endometriosis and ovarian carcinoma with optical coherence tomography: feasibility for laparoscopic-based imaging. British J Obstet Gynaec. 1999; 106(10):1071–7.

51. Pitris C, Jesser C, Boppart SA, Stamper D, Brezinski ME, Fujimoto JG. Feasibility of optical coherence tomography for high-resolution imaging of human gastrointestinal tract malignancies. J Gastroenterol. 2000;35(2):87–92.

52. Brezinski ME, Tearney GJ, Bouma BE, Boppart SA, Hee MR, Swanson EA, et al. High-resolution imaging of plaque morphology with optical coherence tomography. Circulation. 1995;92(8):103.

53. Tearney GJ, Boppart SA, Bouma BE, Brezinski ME, Weissman NJ, Southern JF, et al. Scanning single-mode fiber optic catheter-endoscope for optical coherence tomography. Opt Lett. 1996;21(7):543–5.

54. Tearney GJ, Brezinski ME, Bouma BE, Boppart SA, Pitvis C, Southern JF, et al. In vivo endoscopic optical biopsy with optical coherence tomography. Science. 1997;276(5321):2037–9.

55. Bouma BE, Tearney GJ. Power-efficient nonreciprocal interferometer and linear-scanning fiber-optic catheter for optical coherence tomography. Opt Lett. 1999;24(8):531–3.

56. Swanson EA, Petersen C, McNamara E, Lamport R, Kelly D, inventors. Ultra-small optical probes, imaging optics, and methods for using same. US patent 6,445,939. 1999.

57. Sergeev AM, Gelikonov VM, Gelikonov GV, Feldchtein FI, Kuranov RV, Gladkova ND, et al. In vivo endoscopic OCT imaging of precancer and cancer states of human mucosa. Opt Express. 1997;1(13):432–40.

58. Feldchtein FI, Gelikonov GV, Gelikonov VM, Kuranov RV, Sergeev A, Gladkova ND, et al. Endoscopic applications of optical coherence tomography. Opt Express. 1998;3(6):257.

59. Tearney GJ, Brezinski ME, Boppart SA, Bouma BE, Weissman N, Southern JF, et al. Catheter-based optical imaging of a human coronary artery. Circulation. 1996;94(December):3013.

60. Fujimoto JG, Boppart SA, Tearney GJ, Bouma BE, Pitris C, Brezinski ME. High resolution in vivo intra-arterial imaging with optical coherence tomography. Heart. 1999;82(2):128–33.

61. Tearney GJ, Jang IK, Kang DH, Aretz HT, Houser SL, Brady TJ, et al. Porcine coronary imaging in vivo by optical coherence tomography. Acta Cardiol. 2000;55(4):233–7.

62. Yabushita H, Bouma BE, Houser SL, Aretz HT, Jang IK, Schlendorf KH, et al. Characterization of human atherosclerosis by optical coherence tomography. Circulation. 2002;106(13):1640–5.

63. Jang IK, Tearney G, Bouma B. Visualization of tissue prolapse between coronary stent struts by optical coherence tomography: comparison with intravascular ultrasound. Circulation. 2001; 104(22):2754.

64. Grube E, Gerckens U, Buellesfeld L, Fitzgerald PJ. Images in cardiovascular medicine. Intracoronary imaging with optical coherence tomography: a new high-resolution technology providing striking visualization in the coronary artery. Circulation. 2002;106(18):2409–10.

65. Jang IK, Bouma BE, Kang DH, Park SJ, Park SW, Seung KB, et al. Visualization of coronary atherosclerotic plaques in patients using optical coherence tomography: comparison with intravascular ultrasound. J Am Coll Cardiol. 2002;39(4):604–9.

66. Fercher AF, Hitzenberger CK, Kamp G, Elzaiat SY. Measurement of intraocular distances by backscattering spectral interferometry. Opt Commun. 1995;117(1–2):43–8.

67. Chinn SR, Swanson EA, Fujimoto JG. Optical coherence tomography using a frequency-tunable optical source. Opt Lett. 1997;22(5):340–2.

68. Golubovic B, Bouma BE, Tearney GJ, Fujimoto JG. Optical frequency-domain reflectometry using rapid wavelength tuning of a Cr4+:forsterite laser. Opt Lett. 1997;22(22):1704–6.

69. Yun SH, Tearney GJ, Bouma BE, Park BH, de Boer JF. High-speed spectral-domain optical coherence tomography at 1.3 mu m wavelength. Opt Express. 2003;11(26):3598–604.

70. Yun SH, Tearney GJ, de Boer JF, Iftimia N, Bouma BE. High-speed optical frequency-domain imaging. Opt Express. 2003;11(22): 2953–63.

71. Choma MA, Sarunic MV, Yang CH, Izatt JA. Sensitivity advantage of swept source and Fourier domain optical coherence tomography. Opt Express. 2003;11(18):2183–9.

72. Huber R, Taira K, Ko TH, Wojtkowski M, Srinivasan V, Fujimoto JG, editors. High-speed, amplified, frequency swept laser at 20 kHz sweep rates for OCT imaging. Conference on Lasers and Electro-Optics/Quantum Electronics and Laser Science and Photonic Applications, Systems and Technologies 2005. Baltimore: Optical Society of America; 2005.

73. Huber R, Wojtkowski M, Fujimoto JG. Fourier Domain Mode Locking (FDML): a new laser operating regime and applications for optical coherence tomography. Opt Express. 2006;14(8): 3225–37.

74. Wojtkowski M, Leitgeb R, Kowalczyk A, Bajraszewski T, Fercher AF. In vivo human retinal imaging by Fourier domain optical coherence tomography. J Biomed Opt. 2002;7(3):457–63.

75. Nassif N, Cense B, Park BH, Yun SH, Chen TC, Bouma BE, et al. In vivo human retinal imaging by ultrahigh-speed spectral domain optical coherence tomography. Opt Lett. 2004;29(5):480–2.

76. Cense B, Nassif N, Chen TC, Pierce MC, Yun S, Park BH, et al. Ultrahigh-resolution high-speed retinal imaging using spectral-domain optical coherence tomography. Opt Express. 2004;12:2435–47.

77. Wojtkowski M, Srinivasan VJ, Ko TH, Fujimoto JG, Kowalczyk A, Duker JS. Ultrahigh-resolution, high-speed, Fourier domain optical coherence tomography and methods for dispersion compensation. Opt Express. 2004;12(11):2404–22.

78. Leitgeb R, Hitzenberger CK, Fercher AF. Performance of Fourier domain vs. time domain optical coherence tomography. Opt Express. 2003;11(8):889–94.

79. de Boer JF, Cense B, Park BH, Pierce MC, Tearney GJ, Bouma BE. Improved signal-to-noise ratio in spectral-domain compared with time-domain optical coherence tomography. Opt Lett. 2003;28(21):2067–9.

80. Swanson EA, Huang D, Fujimoto JG, Puliafito CA, Lin CP, Schuman JS, inventors. Method and apparatus for optical imaging with means for controlling the longitudinal range of the sample. US patent 5,321,501. 1994.

81. Swanson EA, Chinn SR, inventors. Method and apparatus for performing optical measurements using a rapidly frequency tuned laser. US patent 5,956,355.

82. Eickhoff W, Ulrich R. Optical frequency-domain reflectometry in single-mode fiber. Appl Phys Lett. 1981;39(9):693–5.

83. Barfuss H, Brinkmeyer E. Modified optical frequency-domain reflectometry with high spatial-resolution for components of integrated optic systems. J Lightwave Technol. 1989;7(1):3–10.

84. Glombitza U, Brinkmeyer E. Coherent frequency-domain reflectometry for characterization of single-mode integrated-optical wave-guides. J Lightwave Technol. 1993;11(8):1377–84.

85. Kachelmyer AL. Range-Doppler imaging: waveforms and receiver design. Laser Radar III. SPIE the International Society for Optics and Photonics PO Box 10 Bellingham WA 98227-0010 USA; 1998.

86. Oh WY, Yun SH, Tearney GJ, Bouma BE. 115 kHz tuning repetition rate ultrahigh-speed wavelength-swept semiconductor laser. Opt Lett. 2005;30(23):3159–61.

87. Yun SH, Tearney GJ, Vakoc BJ, Shishkov M, Oh WY, Desjardins AE, et al. Comprehensive volumetric optical microscopy in vivo. Nat Med. 2006;12(12):1429–33.

88. Vakoc BJ, Shishko M, Yun SH, Oh WY, Suter MJ, Desjardins AE, et al. Comprehensive esophageal microscopy by using optical frequency-domain imaging (with video). Gastrointest Endosc. 2007;65(6):898–905.

89. Huber R, Wojtkowski M, Taira K, Fujimoto JG, Hsu K. Amplified, frequency swept lasers for frequency domain reflectometry and OCT imaging: design and scaling principles. Opt Express. 2005;13(9):3513–28.

90. Huber R, Adler DC, Fujimoto JG. Buffered Fourier domain mode locking: unidirectional swept laser sources for optical coherence tomography imaging at 370,000 lines/s. Opt Lett. 2006;31(20):2975–7.

91. Adler DC, Chen Y, Huber R, Schmitt J, Connolly J, Fujimoto JG. Three-dimensional endomicroscopy using optical coherence tomography. Nat Photonics. 2007;1(12):709–16.

92. Adler DC, Zhou C, Tsai TH, Schmitt J, Huang Q, Mashimo H, et al. Three-dimensional endomicroscopy of the human colon using optical coherence tomography. Opt Express. 2009;17(2):784–96.

93. Klein T, Wieser W, Eigenwillig CM, Biedermann BR, Huber R. Megahertz OCT for ultrawide-field retinal imaging with a 1050 nm Fourier domain mode-locked laser. Opt Express. 2011;19(4):3044–62.

94. Potsaid B, Baumann B, Huang D, Barry S, Cable AE, Schuman JS, et al. Ultrahigh speed 1050 nm swept source/Fourier domain OCT retinal and anterior segment imaging at 100,000 to 400,000 axial scans per second. Opt Express. 2010;18(19):20029–48.

95. Okamura T, Onuma Y, Garcia-Garcia HM, Van Geuns RJM, Wykrzykowska JJ, Schultz C, et al. First in man evaluation of intravascular optical frequency domain imaging (OFDI) of Terumo: a comparison with intravascular ultrasound. Eur Heart J. 2010;31:788.

Martin L. Villiger and Brett E. Bouma

Abstract

Optical Coherence Tomography (OCT) measures the delay of light scattered from different depths within biological tissue using low coherence interferometry in order to reconstruct the axial reflectivity profile of the sample. With miniature side-looking fiber optic probes, deployed through a narrow, flexible catheter, intravascular OCT investigates the wall of the coronary arteries. The optical probe rotates within a transparent sheath and with a combined pullback motion performs a helical scanning pattern on the luminal surface of the vessel. During acquisition, blood – which is translucent and obscures optical image formation – is temporarily displaced by the infusion of saline or contrast agent through the guide catheter. With current state-of-the-art OCT systems, however, imaging speed is sufficient so that full coronary scans can be registered in just a few seconds. The physics of OCT and of light propagation in biological tissues underpins both the qualitative and quantitative aspects of images as well as subtleties of interpretation of image features and artifacts. The objective of this chapter is to provide a thorough introduction to the physics necessary for the correct and accurate application of intravascular OCT.

Keywords

Optical coherence tomography • Interferometry • Rotary junction • Fiber-optic probe • Scattering • Optical tissue properties • Sensitivity • Speckle

2.1 Introduction

This chapter explains the working principles of state of the art intravascular OCT and introduces the relevant parameters to assess the performance of an OCT instrument. Correct interpretation of a tomogram requires a basic understanding of the underlying physics, especially in the presence of potential artifacts. This chapter attempts to present this physical background in a language accessible to non-physicists.

OCT provides cross-sectional views of the subsurface microstructure of biological tissue. It employs interferometric detection and broad bandwidth laser light to discriminate the signal from different depths. Intravascular OCT uses an optical fiber-based catheter to deliver a focused laser beam onto the vessel wall. The laser spot is scanned over the surface of the lumen by rotation of the catheter to generate a cross-sectional view of the vessel. After the basic concepts of OCT, we discuss the individual components of an intravascular OCT instrument. Next, light-tissue interactions and optical properties of biological tissue are reviewed. Scattering is the origin of the OCT signal, but also the mechanism that limits imaging depth. We then proceed with elaborating on the signal processing steps required to reconstruct a tomo-

M.L. Villiger, PhD
Department of Dermatology, Harvard Medical School, Wellman Center for Photomedicine and Massachusetts General Hospital, Boston, MA, USA

B.E. Bouma, PhD (✉)
Dermatology and Health Sciences and Technology, Harvard Medical School, Wellman Center for Photomedicine, Massachusetts General Hospital,
BAR 814 50 Blossom Street, Boston, MA 02171, USA
e-mail: Bouma@mgh.harvard.edu

gram. Finally, we discuss noise and detection sensitivity in OCT and develop the concept of speckle in coherent imaging.

2.2 Principle of Operation of OCT

2.2.1 Frequency Domain Signal

OCT measures the subsurface microstructure of biological tissue by discerning light reflected from different depths within the sample. Similar to ultrasound imaging, the signal from a deeper-lying structure has travelled a longer distance and reaches the detector with a delay. The speed of sound is sufficiently low to directly record the delay between the various echoes from the sample. In contrast, light travels at much greater speed that precludes direct detection of the delay. Instead, OCT employs interferometric detection and compares the signal reflected from the sample with a static reference signal. Figure 2.1 displays the basic configuration of an OCT instrument. Light from a source covering a wide wavelength spectrum is separated by a beam splitter into a reference and a sample arm. Biological tissue is partially transparent at the employed wavelength range in the near infrared. Accordingly, the probing light propagates through the sample tissue, and is scattered and reflected by internal structure at different depths. Part of this backscattered light

Fig. 2.1 Basic OCT setup, with a beam splitter (*BS*) separating the light into the sample arm towards the tissue, and the reference arm towards the mirror, respectively. The plots display the source spectrum as well as the resulting interference pattern, and illustrate the reconstruction process. The tomogram $t(z)$ broadens the discrete reflections in the reflection profile $f(z)$ to a full width at half maximum (fwhm) characteristic of the OCT system

will reach the detector where it interferes with the light from the reference arm that was simply reflected off a mirror. The interference signal is converted by the detector into an electrical signal and is of the form

$$P_{det} = \underbrace{\left|U_r\right|^2 + \left|U_s\right|^2}_{P_{dc}} + \underbrace{U_s^* U_r + U_s U_r^*}_{P_{ac}} = P_{dc} + P_{ac} \qquad (2.1)$$

where U_r and U_s are proportional to the electromagnetic field from the reference and the sample, respectively, and the star indicates the complex conjugate. A plane wave of wavelength λ, propagating along z is expressed as $U = U_0 \exp(ikz)$, where $i = \mathrm{sqrt}(-1)$, and $k = 2\pi/\lambda$ the wavenumber. The reference field U_r in Eq. 2.1 has simply travelled the distance from the source to the reference mirror and back to the detector. The sample field U_s, however, was reflected at several depths, and is the superposition of these individual reflections with their respective travelled path lengths. Written as an integral over the sample reflectivity profile $f(z)$:

$$U_s = U_0 \int f(z) e^{i2kz} dz \qquad (2.2)$$

The relevant axial distance is the path length difference compared to that travelled by the reference field, and the origin of z is set at the axial location corresponding to the reference arm length, as indicated in Fig. 2.1.

P_{dc} in Eq. 2.1 corresponds to the light reflected individually from the reference and the sample arm. Of interest for OCT are the two interference signals in P_{ac}.

Optical Frequency Domain Imaging (OFDI) [1] and other swept source implementations of OCT use a wavelength-swept laser source that sweeps a broad wavelength range in a short time. As a result, the interference signal recorded as a function of time corresponds to the signal as a function of the wavenumber $k = 2\pi/\lambda$. The first interference term of Eq. 2.1 can then be expressed as

$$U_s^* U_r(k) \propto \alpha(k) \int f(z) e^{-i2kz} dz \qquad (2.3)$$

Here, $\alpha(k)$ is the spectral shape of the source spectrum, and $f(z)$ is the reflectivity profile. For a single reflector at depth z, the signal varies periodically as a function of the wavenumber. The rate of this variation increases linearly with z.

The integral of Eq. 2.3 can be identified as the Fourier transformation of the depth profile of the sample reflectivity. Recording the signal as a function of the wavenumber is equivalent to taking the Fourier transform of the axial reflectivity profile. Accordingly, inverse Fourier transformation of the recorded signal will reconstruct the tomogram $t(z)$ of the sample reflectivity profile:

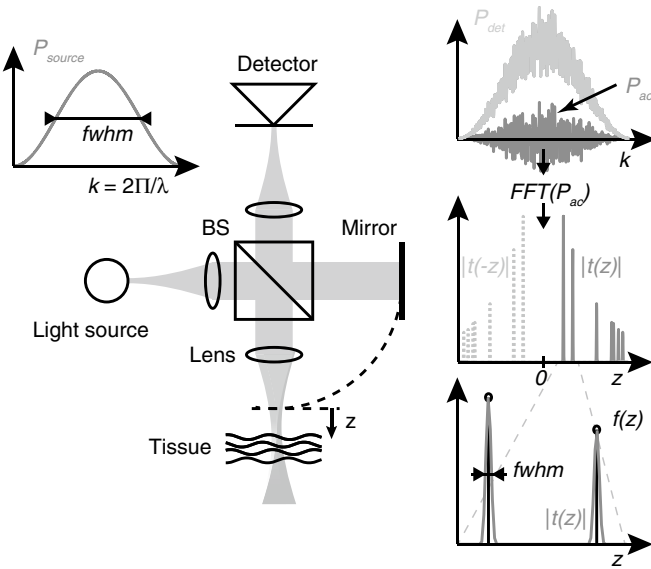$$t(z) = \int U_s^* U_r(k) e^{i2kz} dk = FT^{-1}\left\{U_s^* U_r(k)\right\} \qquad (2.4)$$

The Fourier transformation connects the spatial domain (z) with the spatial frequency or wavenumber domain k. This transformation is a standard operation and can be performed numerically with very high efficiency using the Fast Fourier Transform (FFT). The reconstructed amplitude $|t(z)|$ is proportional to the amplitude of the electromagnetic field scattered from the sample at the same depth. Generally, one is interested in the squared norm $T(z) = |t(z)|^2$, which is proportional to the intensity scattered from the sample as a function of depth. Because of the large dynamic range covered by the OCT signal, tomograms are displayed in logarithmic scale:

$$T(z) = |t(z)|^2 \quad T_{dB}(z) = 10\log_{10}(T(z)) = 20\log_{10}(|t(z)|)$$

(2.5)

The fringe signal P_{ac} contains two interference terms with mirror symmetry. If the first term results in a tomogram $t(z)$, then the second term produces a tomogram $t(-z)$, mirrored about the zero differential path length, as illustrated in Fig. 2.1. Generally, this results in a disturbing overlap that can be avoided by adjusting sufficient path length difference between the reference and the sample arm, or by employing additional strategies to separate the two terms.

Although the reconstructed tomogram is a close image of the original structure, the spectral shape of the source effectively performs a weighting of the spatial frequency spectrum. Only the range of spatial frequencies covered by the employed light source is accessible. As a result, the reconstructed signal is a filtered image of the original structure, expressed by the convolution of the original reflectivity profile with the point spread function (PSF) of the OCT system. This PSF is equivalent to the inverse Fourier transform of the spectral shape function $a(z) = \text{FT}^{-1}\{\alpha(k)\}$. The tomogram $t(z)$ can be expressed as

$$t(z) = \int U_s^* U_r(k) e^{i2kz} dk \propto \int f(z') a(z - z') dz' = f(z) * a(z)$$

(2.6)

with the star symbol indicating the convolution operator. $a(z)$ is the coherence function of a light source with the power spectral density $\alpha(k)$, explaining the origin of the term 'optical coherence tomography'.

As illustrated in Fig. 2.1, a single reflector in the original sample reflectivity function results in a peak of a finite width in the reconstructed tomogram. Assuming a source spectrum with a Gaussian shape, the full width at half maximum (fwhm) of the spectrum as a function of wavenumber is related to the fwhm of the peak in the reconstructed tomogram by

$$\Delta z_{fwhm} = \frac{4\ln(2)}{\Delta k_{fwhm}} = \frac{2\ln(2)\lambda_c^2}{\pi \Delta \lambda_{fwhm}}$$

(2.7)

The wider the spectrum covered by the light source, the better the structure of the axial tomogram is resolved. Indeed, the axial resolution scales with $1/\Delta\lambda$ and the square of the central wavelength λ_c^2. Although the central wavelength of the source should be minimized to increase axial resolution, tissue absorption and scattering are increased at shorter wavelengths and diminish imaging penetration depth, as discussed in more detail in Sect. 2.4.2. Most OCT sources for intravascular imaging operate at a center wavelength close to 1,300 nm and have spectral widths of ~100 nm fwhm, providing an axial resolution below 10 μm.

Real OCT sources do not produce Gaussian spectral shapes, but aim at providing a very broad spectrum with a smooth shape. Because of the Fourier relation between the spectral shape and the PSF of OCT, any ripples or spikes in the spectrum would severely degrade the resulting tomogram.

2.2.2 Imaging Lateral Structure

In order to resolve structure in the lateral direction, the probe beam is focused into a small spot. It is then scanned in the lateral direction while constantly acquiring A-lines. At each scan location, the axial depth profile is acquired by one wavelength-sweep of the light source, resulting in one A-line. Assembling all A-lines of a lateral scan into a B-scan results in a cross-sectional image. The collection of multiple B-scans while scanning along the remaining spatial coordinate represents a three dimensional tomogram and is sometimes referred to as C-scan.

For intravascular imaging and probe-based imaging of other luminal organs, the natural way to scan a spot over the cylindrical inner surface of the organ is by rotating a side-looking imaging probe in the center of the lumen, as illustrated in Fig. 2.2. In a similar way, the collection of A-lines recorded during one rotational scan can then be assembled into the cross-sectional view of the vessel. In combination with a pull-back of the imaging probe, a helical scan pattern over the lumen surface is finally obtained, recording a full three-dimensional image of the organ.

The shape of the laser spot on the tissue determines the lateral resolution of the imaging instrument. Light emitted from a laser source is characterized by its high spatial coherence, resulting in well-defined wavefronts, whose

propagation can be accurately modeled with the Gaussian beam formalism, summarized in Fig. 2.3. A Gaussian beam is characterized by a Gaussian-shaped amplitude and intensity distribution in the lateral direction, with w designating the beam radius at the point where the field amplitude has diminished to e^{-1} of the peak value and accordingly the intensity has dropped to e^{-2}, where e is Euler's number. The minimum radius or waist, at the focus, is designated w_0. The collapse of a beam approaching a focus is mirrored symmetrically by expansion of the diameter (diffraction) as the beam propagates beyond the focus. The smaller the focal spot diameter, the more rapid the collapse and expansion. At a distance $z_0 = (1/2)kw_0^2$, the waist has increased by a factor sqrt(2). The Rayleigh-range of length $2z_0$, centered on the focal plane is used to define the depth of field (DOF). Structure within the DOF is imaged with a lateral definition of within a factor of sqrt(2) of that at the focal plane. Sample regions outside the DOF are considered out of focus, and
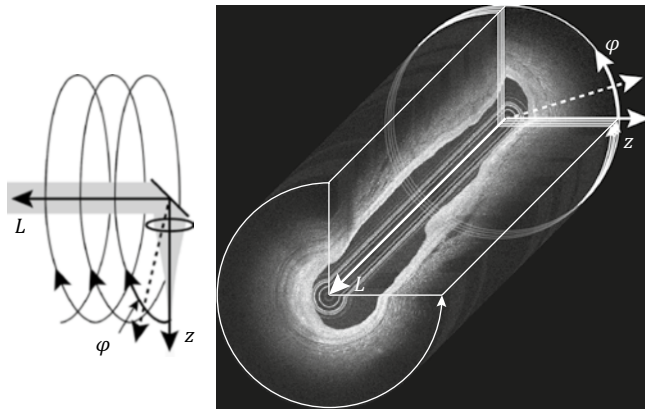
suffer from dramatically reduced lateral resolution and signal amplitude. If the DOF is matched to the typical image penetration depth of OCT within coronary tissue (~2 mm), then the lateral resolution is limited to approximately 20 μm.

A key feature of OCT is the decoupling of axial and lateral resolution. Whereas the source characteristics determine the axial resolution, the lateral resolution is defined through the focusing optics. The DOF and the lateral focus are directly coupled, however, and impose a limit on the lateral focusing.

2.3 Instrumentation

2.3.1 Interferometer

The ability to couple a coherent laser beam into a glass fiber and propagate the light within this fiber with only minimal loss has enabled modern telecommunication technology and facilitated many other applications involving laser light.

A single mode fiber consists in a thin glass core of 5–10 μm diameter, embedded in a slightly lower refractive index glass cladding. Although it is made of glass, the very small diameter of this structure ensures that the fiber remains flexible on the scale of centimeters and can be conveniently manipulated and configured.

The refractive index difference between the core and the cladding confines the light close to the core, similar to total internal reflection. Because the diameter of the core is so small, it accepts only a single spatial mode. This ensures that the light propagating along the fiber remains coherent and the beam emerging from the fiber is identical to the beam that was coupled into the fiber. The spatial shape of this

Fig. 2.2 Principle of helical beam scanning and volumetric scanning
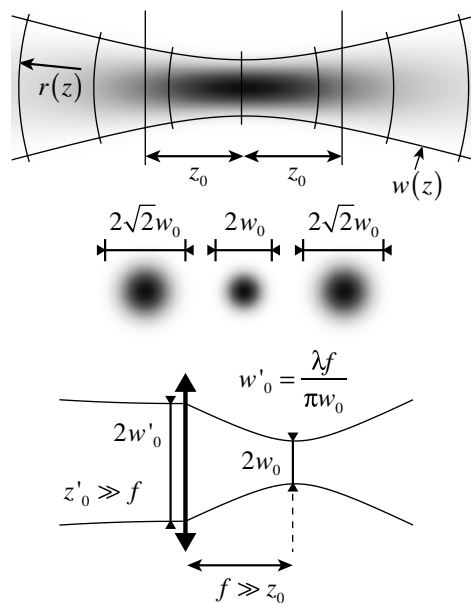
Fig. 2.3 Principle of Gaussian beam propagation

$$U(\rho, z) = \sqrt{\frac{2P}{\pi}} \frac{1}{w(z)} e^{-\frac{\rho^2}{w^2(z)}} e^{-ikz - ik\frac{\rho^2}{2r(z)} + i\tan^{-1}\left(\frac{z}{z_0}\right)}$$

$$I(r, z) = \frac{2P}{\pi w^2(z)} e^{-\frac{2\rho^2}{w^2(z)}}$$

$$w(z) = w_0 \sqrt{1 + \left(\frac{z}{z_0}\right)^2}$$

$$r(z) = z \left(1 + \left(\frac{z_0}{z}\right)^2\right)$$

$$w_0 = \sqrt{\frac{\lambda z_0}{\pi}}$$

$$w'_0 = \frac{\lambda f}{\pi w_0}$$

mode can be approximated by a Gaussian mode. At the fiber facet, this mode exits the fiber and emerges as focused Gaussian spot that will inevitably diffract according to Gaussian beam propagation. Within the fiber, however, this intensity profile propagates unaltered, confined by the fiber structure.

Unlike free space components, fiber optics do not have to be aligned as the light is inherently guided within the fiber, and make robust and rugged optical systems. Catheter-based imaging probes are only possible due to the flexibility of optical fibers and offer the ability to relay an optical signal to and from the coronary arteries.

Figure 2.4 displays the schematic of a fiber-based intravascular OCT system [2]. The fiber carrying the source light is divided into two fibers, creating the sample and reference paths. Both signals are then fed through a fiber circulator. These non-reciprocal elements enable to efficiently relay the signals to the sample and the reference mirror, and the signals reflected from there to the detector. Unlike the double pass through the beam splitter of the free-space configuration, which directs half of the reflected signal back towards the light source, the circulators prevent this signal loss and provide an inherent signal advantage.

The optical path length of the sample and the reference arm must match precisely. Accordingly, the reference arm consists of several meters of fiber to compensate the catheter length of the sample arm. The reference mirror is mounted on a translation stage to enable rapid and easy adjustment of the precise path length.

At the detector, the sample field is combined with the reference field to interfere, by means of a fiber coupler or free-space beam splitter. In the Mach-Zehnder configuration displayed in Fig. 2.4, both outputs of the beam splitter feature an interference signal. Due to the law of energy conversation, the intensity of the two output signals together equal the intensity of the two input signals. Accordingly, a sample reflection that interferes constructively in one exit port features destructive interference in

Fig. 2.4 Schematic layout of fiber-based interferometer for catheter-based imaging. *RJ* Rotary Junction, *BS* Beam Splitter, *PBS* Polarizing Beam Splitter, *PC* Polarization controller, *LP* Linear Polarizer, *BR* Balanced Receiver, *A/D* Analog to Digital converter

the other port. Mathematically, the sign of the interference terms in Eq. 2.1 is inverted between the two outputs. This opens the possibility of balanced detection: Detecting independently both interference signals, but digitizing only their difference effectively eliminates the P_{dc} of Eq. 2.1 and conserves only the interference terms of interest. This approach also removes amplitude noise that is common to both channels. The reference signal frequently exceeds the sample signal by orders of magnitude and makes this detection scheme attractive by using the entire available dynamic range of the electronics for the interference signal.

It is important to consider that electromagnetic waves are vector waves and their oscillations are beating in a spatial direction. In the realm of paraxial optics, which is well suited to describe OCT and only excludes very tightly focused beams, the field oscillations are orthogonal to the direction of the beam propagation. If the vibrations are confined to a single direction along the entire propagating beam, the light is said to be linearly polarized. In general, a field oscillates in an elliptical fashion and can be described as the superposition of a beam with linear polarization along the horizontal direction and an identical beam, but polarized in the vertical direction and with a specific delay with respect to the horizontally polarized beam:

$$\vec{U}(z) = \begin{bmatrix} U^h(z) \\ U^v(z) \end{bmatrix} = \begin{bmatrix} \cos\gamma \\ \sin\gamma\, e^{i\delta} \end{bmatrix} U(z) \qquad (2.8)$$

γ determines the ratio between the two orthogonal polarization states, and δ defines the phase offset. Equation 2.7 describes the "Jones vector" of the field U. At the detector, only the part of the sample field that is polarized identical to the reference field will interfere with that reference signal. Writing the interference term for vector fields gives

$$\vec{U}_s^\dagger \cdot \vec{U}_r = \left(\vec{U}_s^\parallel + \vec{U}_s^\perp\right)^\dagger \cdot \vec{U}_r = \vec{U}_s^{\parallel\dagger} \cdot \vec{U}_r \qquad (2.9)$$

where the dagger denotes the complex transpose. The sample field can be decomposed into a component parallel to the reference field, and a component orthogonal to it. The product with this latter cancels out and does not contribute to the interference signal.

Although its spatial profile is confined, the polarization state of light generally alters upon propagation along a single mode fiber. Indeed, this phenomenon is quite sensitive to bending and pressure applied to the fiber. A controlled amount of bending and twisting enables effectively to control and align the polarization state of the reference signal. In the practical case of catheter-based imaging, however, the sample fiber is manipulated and moved during the acquisition, and it is impossible to control the polarization state of the sample light. Further, the imaged tissue might exhibit
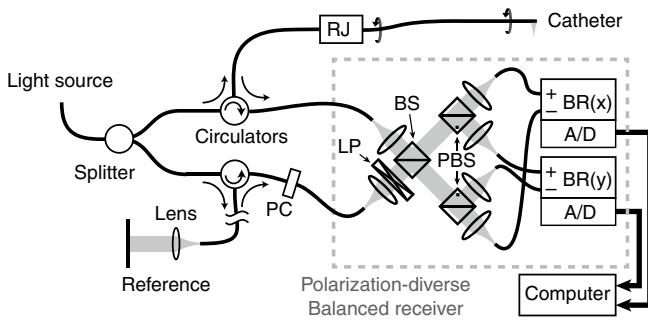
birefringence and specifically alter the polarization state of the propagating probe beam.

To overcome the inability to control the polarization state of the sample light and avoid artifacts in the tomogram due to changes in the polarization state of the sample light, polarization diverse detection, as displayed in Fig. 2.4, is needed. The combined reference and sample signal is projected along two orthogonal linear polarizations by means of polarizing beam splitters. The reference light is adjusted to be linearly polarized at 45° in front of the detector with polarization controllers and a linear polarizer. This ensures an equal splitting of the reference signal into both polarization channels. The unknown sample polarization state is split into the same polarization basis. Each part of the sample light is now polarized in parallel with the local reference signal and creates the desired interference signal:

$$\text{h - channel}: \left(U_s^h\right)^* U_r^h = \left(U_s^h\right)^* U_r$$
$$\text{v - channel}: \left(U_s^v\right)^* U_r^v = \left(U_s^v\right)^* U_r \tag{2.10}$$

Taking the sum of the tomograms of both polarization channels $T^{tot}(z) = T^v(z) + T^h(z)$ provides a signal that is invariant of the precise sample polarization and is robust with respect to movement of the sample fiber.

2.3.2 Light Source

The ideal OCT light source for intravascular imaging should provide a rapid sweep of wavelengths over a wide spectrum centered around 1,300 nm. The width of the spectrum together with the smoothness of the spectral shape will define the axial width of the OCT PSF.

Developments in source technology have enabled a dramatic increase in OCT imaging speed. Although A-lines rates in the MHz range have been demonstrated, the digitization of the resulting interference signal becomes challenging [3, 4]. Also, at constant source power, an increase of sweep speed translates directly to a reduced number of photons, and results in a decreased signal strength and depth of imaging penetration. Current commercial instruments operate at A-line rates around 100 kHz.

The working principle of all sources is a broadband gain medium combined with a wavelength-tunable filter, which selects a narrow wavelength range at each instant in time. There is a wide range of physical implementations, ranging from fiber-based sources consisting in a combination of fiber-optic elements, to fully integrated micro-electro-mechanical systems (MEMS). Most sources produce an output power between 20–60 mW, resulting typically in ~8–20 mW power incident on the tissue.

Besides the A-line rate and the output power, important characteristics of a source are its duty cycle, the sweep linearity, and the instantaneous line width. The duty cycle expresses how much dead time passes between consecutive scans and should be high to optimally use the bandwidth of the detection electronics. The ideal sweep varies the wave-number linearly with time. Any deviation has to be compensated with either a non-uniform sampling clock or interpolation of the digitized signal. Both can become challenging for strong non-linearity.

At each instant in time, any source will generate a spectral line of finite width, rather than a pure monochromatic signal. In consequence, the interference pattern does not sample a single spatial frequency at each time, but a narrow peak with a finite width. The larger the path length difference between a sample feature and the reference arm, the faster the modulation of its wavenumber signal. Variations within the finite spectral width of the source wash out and result in a decreased signal amplitude in the reconstructed tomogram. Mathematically, the sample spatial frequency spectrum is convolved with the instantaneous spectral shape. After reconstruction of the tomogram, this convolution translates into multiplication with the Fourier transform of the finite line width in the spatial domain, which is illustrated in Fig. 2.5.

The best signal amplitude is obtained at zero path length difference. However, to separate the tomogram from its mirror term, an additional path length difference is frequently introduced. This works well for sources with a very low roll-off and a very narrow instantaneous line width. Alternatively, it is possible to place an acousto-optic modulator in the reference arm [5]. Modulating the reference signal at a ¼ of the acquisition frequency has a similar effect as moving the reference arm by a distance equivalent to ¼ of the entire imaged depth range. Unlike a physical increase of the path difference, this reference arm modulation does not alter the spatial frequency spectrum and avoids a signal wash out. Instead, it axially shifts both the tomogram and the roll-off curve, and enables a separation of the two mirror terms, without trading off any sensitivity, as demonstrated in Fig. 2.5.

2.3.3 Catheter

The catheter is connected through the rotary junction with the interferometer and relays the signal to and from the probe tip. It consists in a stationary narrow diameter (typically 0.87 mm) sheath that contains the rotating probe. The probe is fabricated from a single mode fiber and at its distal tip the light emerging from the core of the fiber is reflected to the side and focused through the transparent sheath material onto the lumen surface. The fiber does not tolerate rotational shear forces well and is embedded in a drive shaft. It consists

Fig. 2.5 Measurement of single reflector placed at various depths to assess the signal roll-off with depth. The roll-off curve is the Fourier transform of the instantaneous spectral line of the wavelength-swept laser source. Also note the non-uniformity in the noise floor
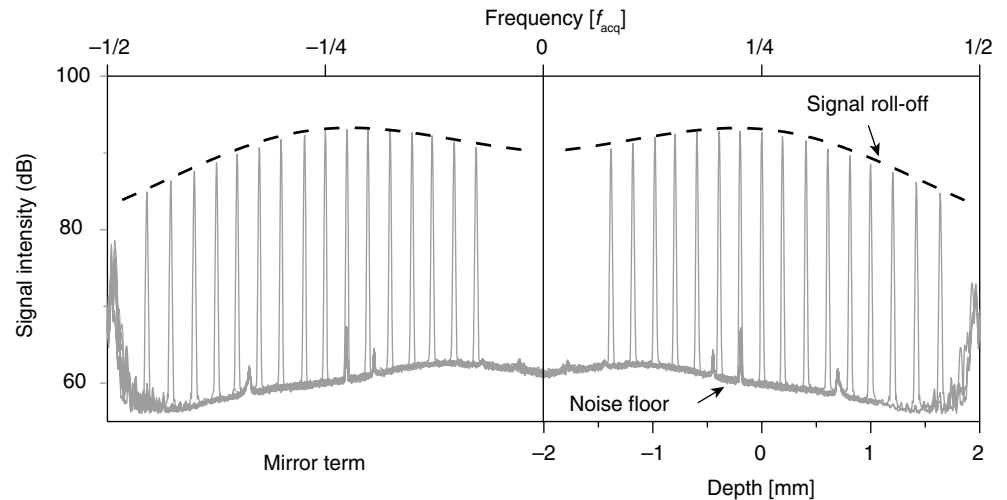
of a coiled spring to preserve the flexibility of the catheter and transmit the torque from the rotary junction to the probe tip. This probe assembly can also be translated in the axial direction within the sheath to perform the required pull-back.

There are two types of distal optics to focus the fiber mode onto the lumen. One uses a ball lens design, and the other a graded index (GRIN) lens. The ball lens is fabricated by splicing a segment of pure, homogenous glass fiber (or "core-less" fiber) to the single mode fiber facet. The tip is then melted to create a drop-shaped glass ball by surface tension. Light emerging from the fiber core diffracts in the core-less medium and is refracted at the ball lens surface to converge into a focused spot. To obtain a side looking probe, the ball lens is angle polished to reflect the light by total internal reflection and to use the side of the glass-ball as the refracting surface.

Alternatively, a GRIN lens or GRIN fiber consists in a fiber-like element with a radially varying refractive index distribution. Propagation through this element is similar to propagation through a classical lens. Splicing an optimized sequence of core-less fiber, GRIN fiber and again core-less fiber at the facet of the probe fiber enables to generate the desired focal spot. Reflection to the side is achieved by a microprism, glued to the distal tip of the fiber optics.

Both probe types achieve focused spots having radii of 20–25 μm, and corresponding fwhm of the lateral PSF of 25–30 μm. However, the refraction of the beam at the curved sheath-tissue interface induces aberrations on the beam that can degrade its focusing and introduce an asymmetry between the direction along and transverse to the catheter axis. Interestingly, the imperfect shape of the ball lens in the lateral direction may be used to compensate for these aberrations. Ideally, the focus should be located just beneath the surface of the vessel lumen to match the depth-of-field to the available image penetration, and is targeted at ~1.5 mm from the sheath surface.

In order to suppress strong reflections from the sheath interface and guarantee total internal reflection in case of an angle polished reflector, the beam is usually reflected at an angle smaller than 90 deg. Accordingly, the resulting cross-sectional views correspond to conical cross-sections through the tissue volume.

Figure 2.6 displays schematics and photographs of two commercial catheters. The catheters have radio-opaque markers for visualization on the angiogram, and a provision for a thin (0.0014″) guide-wire for deployment.

2.3.4 Rotary Junction

The rotary junction connects the interferometer with the catheter and defines the helical scan pattern of the optical probe. As schematically displayed in Fig. 2.7, it consists in a static collimation lens on the interferometer side, and a second lens on the catheter side that rotates together with the probe and couples the collimated beam back into a single-mode fiber. The alignment of these lenses is very sensitive and critical to avoid a strong rotational variation of the power coupled to the fiber probe. Physically, the proximal end of catheter is connected to this rotating fiber.

The rotation speed of the probe is matched to B-scan rate of the imaging system. Current commercial instruments image at up to 158 rotations per second, acquiring 1,000 A-scans per B-scan, and performing pull-backs at speeds of up to 40 mm/s over a length of 150 mm.

The rotational torque generated by the rotary junction is coupled to the drive shaft. The friction of the probe rotating inside the sheath can generate a backlash between the probe base and the probe tip, because the drive shaft acts as a spring. The angular position of the motor therefore may not accurately represent the angular position of the probe tip, which can complicate the interpretation of the acquired volume. If, in addition, the friction depends on the angular

Fig. 2.6 (**a**) Working principle of fiber-optic probes, for a ball-lens probe (*top*) and a graded index lens (*bottom*). Photographs of commercial catheters from Terumo (**b**) and St Jude Medical (**c**)
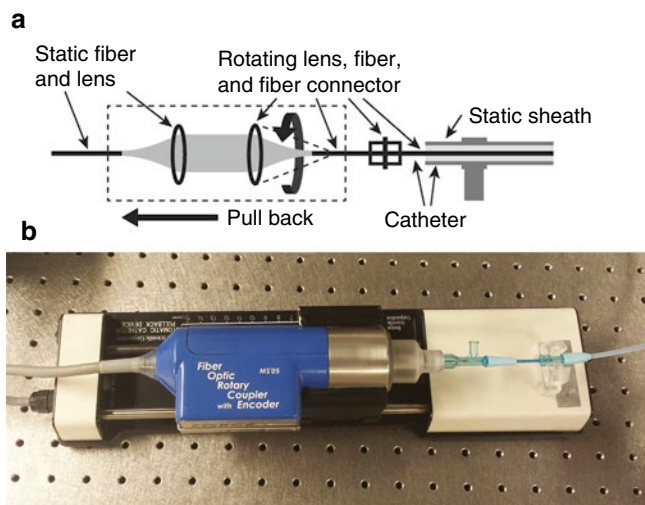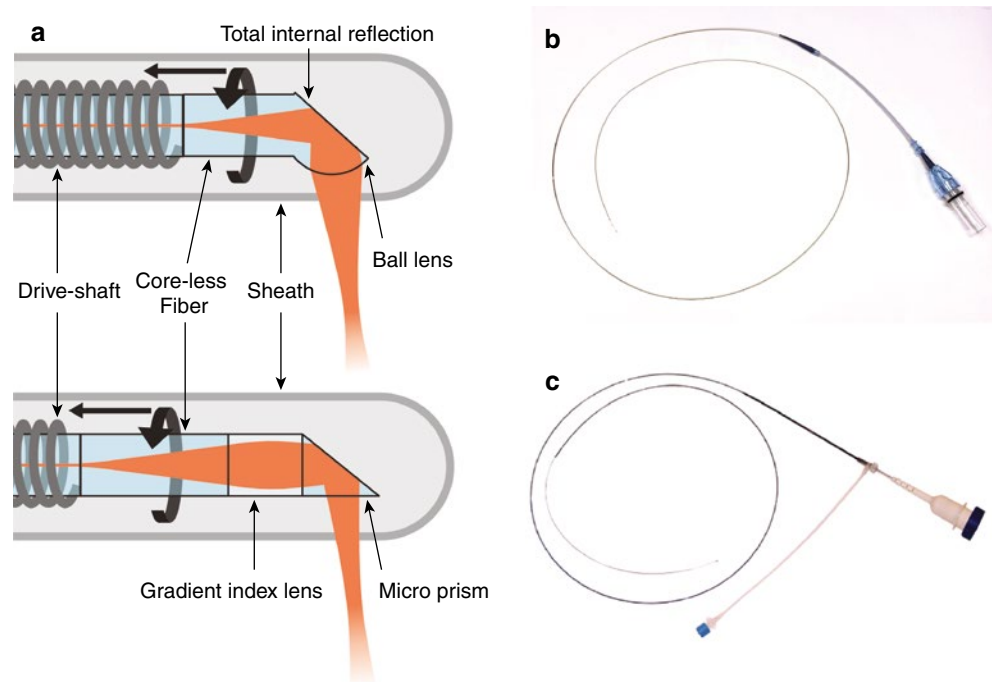

Fig. 2.7 (**a**) Schematic presentation of the rotary junction. (**b**) Photograph of rotary junction

position of the probe, then the probe movement might induce a non-uniform rotational distortion (NURD) in the acquired cross-sections [6, 7]. Small amounts of NURD might not be apparent in a cross-sectional image, but can alter the perceived geometry of the lumen surface.

2.4 Light Tissue Interaction

2.4.1 Light Propagation in Biological Tissue

Inside an optical medium, the propagation of light is impacted by the spatial distribution of the refractive index. At a discrete interface between two regions with distinct refractive indices, part of the incident light is reflected and the transmitted part is refracted. The effect of reflection and refraction for more complex geometries of the refractive index distribution is described as elastic scattering. Unlike non-linear effects and fluorescence, elastic scattering conserves the wavelength of the scattered field. Scattering is the origin of the OCT signal, and the scattering properties of tissue define its appearance in OCT. At the same time, scattering also deteriorates the propagating beam and limits the imaging depth. Figure 2.8 illustrates scattering of the probe light by a tissue sample.

Maxwell's equations describe the propagation of an electromagnetic field [8]. Inside a dielectric medium, such as biological tissue at optical frequencies, these equations depend solely on the refractive index distribution. In a homogeneous medium with a constant refractive index n, Maxwell's equations reduce to the wave equation. For a monochromatic field it is expressed as:

$$\nabla^2 U(\mathbf{r}) + k_0^2 n^2 U(\mathbf{r}) = \nabla^2 U(\mathbf{r}) + k^2 U(\mathbf{r}) = 0 \qquad (2.11)$$

Here, $k = k_0 n$ relates the wavenumber in vacuum to the wavenumber inside the medium, and ∇^2 is the Laplacian. As discussed previously, the plane wave $U = U_0 \exp(ikz) = U_0 \exp(ik_0 nz)$ and the Gaussian beam are particular solutions to this equation. The refractive index shortens the effective wavelength inside the medium, and two consecutive wavefronts are only an axial distance of $\Delta z = \lambda_0/n$ apart. Alternatively, the refractive index can be added to the geometric distance, defining the optical path length (OPL) as the product $OPL = nz$. In this view, the two consecutive
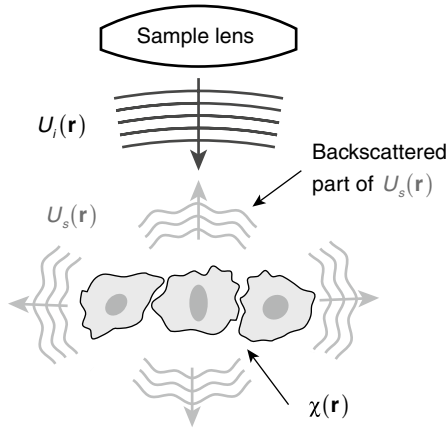
Fig. 2.8 The incident light $U_i(\mathbf{r})$ illuminates the sample and creates the scattered field $U_s(\mathbf{r})$. Only light scattered in the backward direction is collected by the sample lens and contributes to the OCT signal

wavefronts are still an OPL of λ_0 apart from each other. In OCT, a signal originating from a depth L_1 inside a medium of refractive index n_1 is indiscernible from a signal created with different n_2 and L_2, but identical $OPL = n_1 L_1 = n_2 L_2$. OCT measures effectively the OPL, and deriving the geometric distances L requires knowledge of n.

Absorption is an additional light-tissue interaction that reduces the energy of the propagating beam by transforming part of the energy into heat. At OCT wavelengths, its effect can be generally ignored, but it can be included into the refractive index by defining a complex valued refractive index $n' = n + i\kappa$. Substituting into the plane wave expression and converting to intensity results in $I(z) = |U_0|^2 \exp(-2k_0 \kappa z)$ and reveals the Beer-Lambert's law of absorption with the absorption coefficient $\mu_a = 2 k_0 \kappa$.

At a discrete interface between two distinct dielectric media, the boundary conditions, imposed by the continuity of the electromagnetic field expressions, define the ratio of reflected and transmitted light. It is a function of both the incident angle and the polarization state, and is summarized by Fresnel's equations for a planar boundary. The transmitted light is refracted according to Snell's law.

The geometry of the refractive index variations in biological tissue is more involved. Different tissue components, down to sub-cellular compartments, feature distinct refractive indices and locally reflect and refract, i.e. scatter, light. The size of these features is below the resolution of OCT, and for many features even smaller than the wavelength.

The spatial refractive index distribution in biological tissue can be modeled as a continuous function, defined by its autocorrelation function, with the organization of its spatial fluctuations following a fractal mechanism, where large variations dominate over smaller scale variations according to a power law [9–11]. This matches well with the architecture of tissue, being composed of cells, which are similar to each other, comprising themselves smaller compartments that again are self-similar. It is also possible to model tissue as an agglomeration of discrete particles with fractal size distributions [12, 13].

In a dielectric medium with a continuously varying refractive index, the scalar wave equation transforms to:

$$\nabla^2 U(\mathbf{r}) + k_0^2 n^2(\mathbf{r}) U(\mathbf{r}) = 0 \qquad (2.12)$$

The shape of the propagating wave is influenced by the refractive index distribution, and analytical solutions for this inhomogeneous differential equation become involved.

Assuming that the refractive index $n = <n> + \delta n$ varies only slightly around its average value $<n>$ and that δn is small, the first order Born approximation expresses the scattered field as [14]:

$$\begin{aligned}\nabla^2 U_s(\mathbf{r}) + k_0^2 \langle n \rangle^2 U_s(\mathbf{r}) &= -k_0^2 \chi(\mathbf{r}) U_i(\mathbf{r}) \\ \nabla^2 U_i(\mathbf{r}) + k_0^2 \langle n \rangle^2 U_i(\mathbf{r}) &= 0 \end{aligned} \qquad (2.13)$$

In this approximation, the incident field U_i propagates in a homogeneous medium of refractive index $<n>$. At each location it creates a light source proportional to the incident field and the scattering potential $\chi = (n - <n>)^2$ that emits the scattered field U_s, which propagates again in a homogeneous medium of refractive index $<n>$.

Using this model, it can be shown that OCT creates an image of the scattering potential $\chi(\mathbf{r})$ [15, 16]. The tomogram is a convolution of the scattering potential with the lateral beam profile in the lateral direction, and the axial PSF $a(z)$ in the axial direction. $a(z)$ is defined through the spectrum of the light source and only gives access to the corresponding axial spatial frequencies. It excludes low frequencies, and makes the OCT signal sensitive to abrupt variations of the scattering potential. The axial reflectivity profile $f(z)$ from Eqs. 2.2, 2.3, 2.4, 2.5 and 2.6 could be replaced with the scattering potential $\chi(z)$.

The first order Born approximation ignores the impact of the refractive index variations on the propagating beam, and likewise on the scattered field. In reality, the continuous scattering degrades the advancing beam and severely impairs the ability to image deep into a scattering sample.

2.4.2 Tissue Optical Properties

Instead of describing tissue as a local refractive index distribution, its optical properties are generally expressed on a larger scale. This is equivalent to analyzing an entire slab of tissue and measuring the scattered and absorbed light without attempting to resolve any spatial structure. It is then possible to express in a statistical way, how frequently and in what way incident light interacts with the tissue. In this view, the incident beam is split into many independent beams, each of which experiences a sequence of random interactions with

the medium. The combined effect on the independent beams matches the large-scale observations.

The scattering mean free path (MFP) expresses the average distance between two scattering and absorption events as the inverse of the attenuation coefficient μ_t:

$$MFP = \frac{1}{\mu_t} = \frac{1}{\mu_s + \mu_a} \approx \frac{1}{\mu_s} \qquad (2.14)$$

Here, μ_a is the absorption coefficient, and μ_s the scattering coefficient of the tissue. As shown in Fig. 2.9, in the near infrared wavelength range and for biological tissues, absorption is generally low, $\mu_s \gg \mu_a$, and scattering dominates. Typical scattering coefficients for biological tissue, such as the coronary artery wall, are in the range of 5–10 mm^{-1}, corresponding to a MFP of 100–200 μm. A comprehensive review of tissue optical properties is given for instance by Jacques [17].

Conceptually, the tissue can be visualized as a distribution of discrete scattering particles having a characteristic cross-section. The MFP is the average distance travelled before hitting another particle. The scattering coefficient depends both on the density and the cross-section of the particles. At the scattering site, the light is deflected by a random angle, defined by the scattering function – a probability density function characteristic for the particle. Particles many times smaller than the wavelength, such as individual molecules, scatter light uniformly in all directions, giving rise to Rayleigh scattering. For particles of a size similar to the wavelength, however, the phase difference between light scattered from different locations on the particle can create interference effects, resulting in the strong angular variations of Mie-scattering. For even larger particles the scattering is directed primarily in the forward direction. The anisotropy

factor g, ranging from −1 to 1, expresses the degree of forward scattering, which is dominant in biological tissue with a g typically in the range 0.8–1.

The OCT signal arises from light that is scattered in the backward direction and is captured by the imaging optics. According to the high anisotropy of biological tissue, only a small fraction of the light is backscattered, whereas the majority of the light is scattered in the forward direction. The precise amount of backscattering, however, depends on the scattering function of the specific sample, and can vary substantially between different tissues.

Most efforts on modeling attenuation in OCT rely on a single-scattering model, which assumes that light contributing to the OCT signal experienced a single backscattering event [18–20]. In this case, the incident beam was not altered by forward scattering and retained its original shape. However, this signal can only originate from within the MFP of the tissue, i.e. 100–200 μm. A series of forward-directed scattering events, followed by one backscatter and again several forward scattering events also contributes to the OCT tomogram, and would be difficult to distinguish from a single backscattered signal. The strong forward scattering gradually degrades the propagating wave, but its general shape and propagation direction is retained for several scattering events. This is accounted for in the transport mean free path (*TMFP*)

$$TMFP = \frac{1}{\mu_s'} = \frac{1}{\mu_s(1-g)} \qquad (2.15)$$

and is consistent with the imaging depths of 1–2 mm and the resolution degradation with depth frequently encountered in OCT. Beyond the *TMFP*, an incident waveform is truly randomized, and although it might still contribute to the OCT signal, it no longer conveys spatial information.

The optical properties of the arterial wall and atherosclerotic lesions are quite amenable to optical imaging. The characteristics used to identify different plaque types rely on the visual recognition of their tissue properties. Quantitative analysis of the attenuation coefficient has also been investigated [19, 21, 22]. The arterial layers of a healthy vessel feature a low attenuation, which is barely noticeable over the thickness of the layers. The amount of backscattering, however, is decreased in the media, accounting for its lower signal compared to the intima and the adventitia. Fibrous plaques give rise to strong backscattering and moderate attenuation, whereas calcifications appear as nearly signal void regions, with both very low backscattering and attenuation. The typical feature of a lipid plaque is a rapid signal decay, masking any deeper lying structure, consistent with high attenuation.

Absorption is almost negligible in the employed wavelength range of OCT, as indicated in Fig. 2.9. Towards the visible wavelengths, blood absorption becomes important, and moving towards longer wavelengths, above 1.36 μm, water
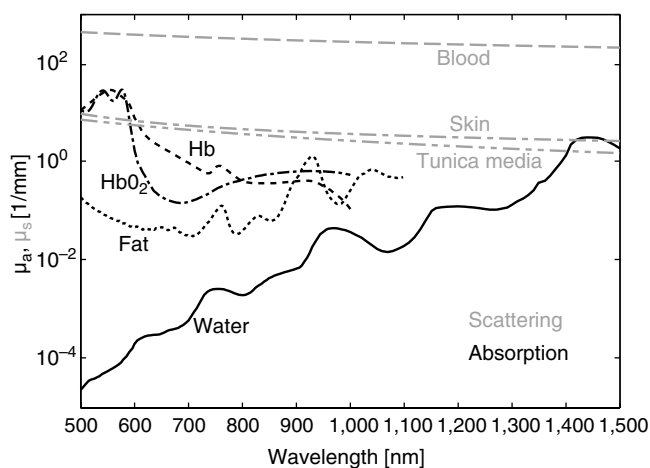

Fig. 2.9 Biological tissue absorption and scattering coefficients as a function of wavelength (Water absorption from Segelstein [24], Blood absorption from Takatani and Graham [25], Fat absorption from van Veen et al. [26], tissue scattering coefficients adapted from Jacques [17], assuming $g_{blood} = 0.995$, $g_{skin} = 0.5$, $g_{media} = 0.8$)

absorption begins to influence penetration depth. Figure 2.9 also displays the scattering coefficients for some tissues. As expected, scattering is stronger than absorption in the wavelength range of OCT. Scattering decreases with increasing wavelength, which could motivate the use of longer wavelength laser sources [23]. Although its absorption is not limiting at OCT wavelengths, imaging through blood is precluded by its strong attenuation due to a high scattering. Saline or contrast agent flushing is required to dilute the hematocrit during imaging and offer a clear view onto the vessel wall.

2.5 Imaging with Intravascular OCT

2.5.1 Tomographic Reconstruction

To summarize and provide a more complete description, in order to obtain a tomographic view of a coronary artery from the acquired interference fringes the following reconstruction steps are performed:

1. Preconditioning of the fringe signal, including eventual background subtraction, depth-degeneracy removal, interpolation in linear wavenumber, dispersion compensation, and spectral shaping:

$$P_{\text{det}}(t) \rightarrow U_s^* U_r(k)$$

2. FFT of the fringe signal from wavenumber to depth coordinate:

$$t(z) = FFT\{U_s^* U_r(k)\}$$

3. Log compression, possibly summing the signal from the two detection channels if polarization diverse detection was performed, and conversion to a gray scale image:

$$T_{\log}(z) = \frac{10 \log_{10}\{T_x(z) + T_y(z)\} - BGR_{\log}}{DR_{\log}}$$

4. Scaling of depth axis and determination of apparent center of catheter:

$$T_{\log}(z') = T_{\log}\left(\frac{z - z_0}{\langle n_g \rangle_{tissue}}\right)$$

5. Interpolation of B-scan in Cartesian coordinates:

$$T_{\log}(x, y) = T_{\log}\left(z' = \sqrt{x^2 + y^2}, \varphi = \tan^{-1}\left(\frac{y}{x}\right)\right)$$

The preconditioning of the fringe signal depends on the specific OCT system. Even if balanced detection is employed, a residual background frequently persists, which can introduce fix-pattern noise in the reconstructed tomogram. This background can be measured at the beginning of an acquisition and subtracted from all recorded signals. The depth-degeneracy removal requires some additional processing steps, if implemented. Next, if the acquisition was not performed at equidistant wavenumber points, the fringe signal is interpolated. The presence of a physical dispersion imbalance between the two interferometer arms can corrupt the tomogram by broadening of the axial PSF. Material dispersion describes the OPL as a function of wavelength. Whereas a linear variation of the OPL simply alters the group velocity and hence the apparent arm length, both arms must have matching group velocity dispersion (GVD) and higher order dispersion. Although fiber optic components have little GVD at 1,310 nm, the effect of variations between different fibers and additional optical components may require correction. This can be achieved numerically by multiplying the fringe signal with a calibrated complex phase signal. Lastly, the fringe spectrum can be multiplied with a window function to favorably tailor its shape and reduce ringing artifacts in the axial point spread function.

The FFT can be zero padded to enhance the appearance of the tomogram. After summing both detection channels in case of polarization diverse detection, the logarithm of the tomogram is adjusted to the background noise level (BGR), and divided by the dynamic range (DR) to obtain a normalized gray scale image. The background value is frequently chosen as the average noise signal, effectively scaling the resulting dB signal to signal to noise ratio. Exporting the final gray scale image with 255 gray levels, a dynamic range of 50–60 dB is most appropriate to maximize the image contrast (see Sect. 2.5.3).

The FFT transforms the wavenumber signal to a tomogram as function of optical path length. In order to derive geometric distances, the group refractive index of the sample medium must be known. Assuming it to be constant throughout the entire imaged region allows to directly scale the recovered OPL to obtain $z' = OPL/n_g$. Here, the group refractive index n_g is used, to extend on the previous discussion of Sect. 2.4.1, which assumed a non-dispersive medium where the phase and group refractive indices are identical $n = n_g$.

Yet, up to the outer surface of the sheath, the catheter consists of a sequence of materials with strongly varying refractive indices (glass, air, sheath material). The axial position of these interfaces is clearly visible in the tomogram and Fig. 2.10 demonstrates the distortions that scaling with a constant $n_g = 1.33$ of saline introduces in areas of distinct n_g. Conveniently, the precise position of these elements is irrelevant for intravascular imaging. However, the measurement of the lumen area and vessel diameters is crucial for the selection of stents and planning of landing zones. For these measurements to be accurate, n_g of the flushing medium should be known, as it can vary between saline and radiocontrast agent. The correct selection of n_g for the flushing
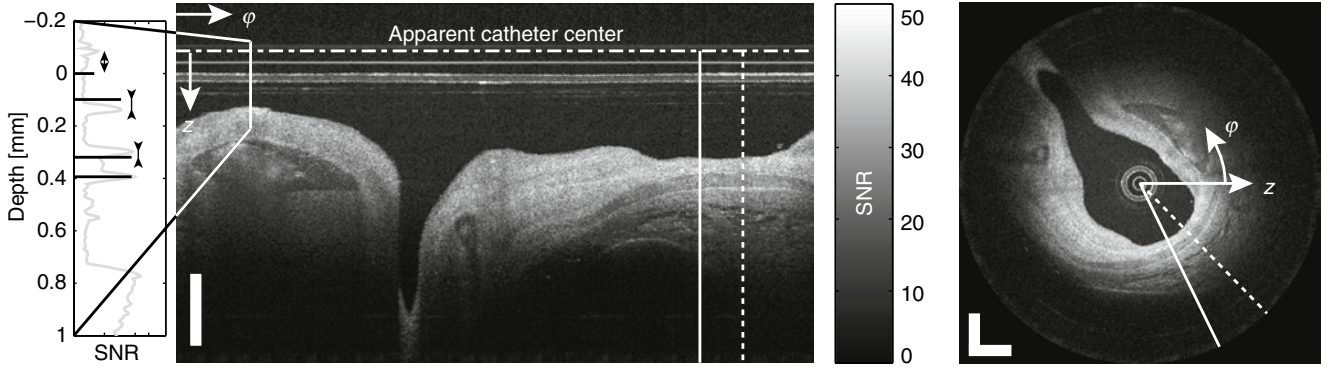
Fig. 2.10 Demonstration of transformation from cylindrical to Cartesian coordinates. In the cylindrical view, the scale bar of 1 mm is only indicated along the depth axiss, as the lateral direction corresponds to the angular catheter position. After circularizing around the determined apparent center of the catheter, an undistorted Cartesian view is obtained. The line plot on the left hand side indicates the axial profile, revealing reflections from the center of the catheter, the ball-lens surface, and the inner and outer sheath surface (from top to bottom). The black lines indicate the geometric positions of these elements, distorted in the axial profile due to effectively measuring the OPL

medium ensures correct measurements of the lumen dimensions. Inside the vessel wall, however, the refractive index might again be different and could result in skewed measurements of plaque geometries.

The last step is the transformation from cylindrical coordinates, in which the A-lines were acquired by circumferential scanning, to Cartesian coordinates. This offers an undistorted cross-sectional view of the coronary arteries. With the employed scaling of the depth coordinate, the origin of the radial z coordinate is selected to match the outer radius of the sheath to its corresponding geometric radius, as illustrated in Fig. 2.10.

2.5.2 Sampling

Because the OCT signal is measured in the frequency domain, there is no risk of under-sampling the axial signal, i.e. the axial points along the reconstructed tomogram are always more densely spaced than the resolution. Taking into account the group refractive index of the sample, the axial resolution from Eq. 2.6 is modified to

$$\Delta z'_{fwhm} = \frac{\Delta z_{fwhm}}{\langle n_g \rangle} = \frac{2\ln(2)\lambda_c^2}{\pi \Delta\lambda_{fwhm} \langle n_g \rangle} \quad (2.16)$$

The axial spacing of two depth pixels in the original tomogram (before transformation to the circular view) and the one-sided maximum depth range, i.e. the depth range of one of the mirror terms are defined by:

$$\delta z' = \frac{\pi}{N_{fft}\delta k \langle n_g \rangle}, \quad \Delta z'_{max} = \frac{\pi}{2\delta k \langle n_g \rangle} \quad (2.17)$$

where δk is the spacing of the equidistant wavenumber sampling points, and N_{fft} is the possibly zero-padded length of an A-line before the FFT.

In the lateral directions, the resolution is given by the dimensions of the focal spot in the sample. The spacing of the A-lines is imposed by the A-line rate f_A and the rotational speed of the catheter, defining N_A, the number of A-lines per B-scan. Because of the rotation of the probe, two adjacent A-lines are separated by an angle $\delta\varphi$, and the lateral offset depends on the radial location along depth:

$$\delta\varphi = \frac{2\pi}{N_{A-lines}}, \quad \Delta x = \delta\varphi z' \quad (2.18)$$

In order to correctly sample lateral structure according to the Nyquist criterion, at least two sampling points per resolution width are required. With a lateral fwhm of 25 μm, and $N_A = 1,024$, the tissue is correctly sampled up to a radial position of ~2 mm.

Along the pull-back direction, the spacing between adjacent B-scans is usually more significant, leading to an under-sampling along this direction. Sampling in this direction is defined by the pull-back speed v_{pb}, divided by the B-scan rate:

$$\delta L = \frac{v_{pb} N_A}{f_A} \quad (2.19)$$

Although longitudinal cross-sectional views offer important insight into the vessel geometry, these views may be unsuitable for investigation of detailed plaque morphology.

Because the true scan pattern is helical, the start and end points of a B-scan do not correspond to the same location on the vessel lumen. Additional heartbeat motion further

differentiates these borders and can lead to additional arti- facts. This points to the benefits of faster imaging, both to overcome motion artifacts and allow denser sampling.

2.5.3 Signal to Noise Ratio and Sensitivity in OCT

The interferometric detection of OCT offers the benefit of coherent amplification. The weak sample signal is mixed with the strong reference signal and lifted above the noise floor. This enables the excellent sensitivity of OCT that translates into the high imaging speeds appreciated and nec- essary for intravascular imaging.

The signal to noise ratio (SNR) in OCT is defined as the power in the amplitude signal $|t(z)|^2$, divided by the variance of the background noise. This translates to the ratio of the intensity signal $T(z)$ divided by the standard deviation of the background signal:

$$SNR = \frac{|t_s|^2}{\sigma_{t,bgr}^2} = \frac{T_s}{\sigma_{T,bgr}} \tag{2.20}$$

In practice, the background signal frequently varies along the depth range, as seen in Fig. 2.5, and its accurate determi- nation may be challenging.

The sensitivity Σ of an OCT system expresses the ratio of a signal corresponding to an SNR of 1, to the signal of a perfectly reflecting mirror that would redirect the entire sam- ple light to the detector:

$$\Sigma = \frac{1}{SNR_{mirror}} \tag{2.21}$$

The amount of light scattered by biological tissue is orders of magnitudes smaller than the reflection of a mirror. To experi- mentally measure the sensitivity, the signal of the mirror is attenuated with an neutral density filter, to avoid saturation of the detection.

The sensitivity of OCT is influenced by three principle sources of noise. First, the electronic noise of the detector and the analog to digital conversion, which are determined by the specific hardware components of the system. The sec- ond is shot-noise, which is intrinsic to any optical signal, due to the statistical nature of the arrival time of individual pho- tons. Shot noise represents the ultimate limit of detection sensitivity and cannot be overcome, but it scales favorably with the number of photons, i.e. increasing the number of photons will improve the SNR. The third term is relative intensity noise, originating primarily in the laser and mani- festing as fluctuations of the optical power. The balanced detection scheme helps in rejecting this noise, because unlike the shot or detector noise, the RIN contribution is identical in both detection channels. All noise terms depend directly on the imaging speed. The faster the A-line rate of the wavelength-swept laser, the higher is the required bandwidth on the detection electronics, and the more is the final signal immersed in noise.

Figure 2.11 displays characteristic sensitivity curves for OCT. The optimal performance of the instrument is deter- mined by the setting of the reference arm power incident on the detector. If the reference arm power is too low, the elec- tronic detector noise dominates the sensitivity. In contrast, too much reference power makes RIN the dominating noise source. At the ideal working point, the sensitivity, and hence the SNR, turn out to be independent of the reference power. At this point, it is only the number of photons returning from the sample that defines the noise level.

In practice, the detector and laser noise characteristics render it difficult to achieve entirely shot-noise limited detec- tion, and it is the combination of the different noise contribu- tions that define the SNR for any given system. Importantly, to achieve higher imaging speeds, a larger detection band- width and faster detectors are required, leading to increased detector noise. Figure 2.11 demonstrates the effect of increasing the A-line rate in combination with doubled detector noise on the resulting sensitivity.

Generally, sensitivity levels greater than 100 dB are required for acceptable intravascular imaging. Decreased sensitivity particularly penalizes the weak signal from deeper tissue struc- ture, limiting the imaging depth. Although the typical sensitiv- ity of OCT exceeds a 100 dB, the dynamic range is limited to ~50 dB. The number of discretization levels of the analog to digital conversion, typically 12–14 bits, physically limits the signal range that can be reconstructed. If the system was
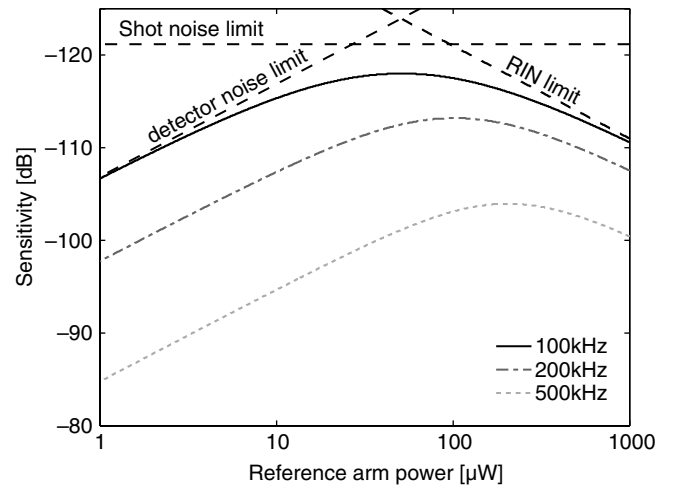

Fig. 2.11 Characteristic theoretical sensitivity curves for OCT sys- tems with different A-line rates. Assumed detector noise currents: 3 pA/ $Hz^{1/2}$, 6 pA/$Hz^{1/2}$, 12 pA/$Hz^{1/2}$ resp., RIN of −120 dB/$Hz^{1/2}$, common mode rejection ratio of −25 dB/$Hz^{1/2}$, 1,536 sampling points and 10 mW of power at the sample

optimized to detect the lowest possible signal and include the noise level in the dynamic range, then this sets a limit on the largest possible signal that can be detected. Whereas tissue is unlikely to produce such strong signals, specular reflection off the sheath interface or stent struts could saturate both the detector and the analog to digital conversion. Specifying the beam exit angle from the catheter to be ~10° away from normal reduces the signal strength from sheath reflections.

2.5.4 Speckle

An important characteristic of OCT is the presence of speckle in its tomograms. Speckle refers to the granular or grainy appearance present in the images of many tissues imaged with OCT [27]. Figure 2.12 displays an example of speckle in an enlarged region of a fibrous plaque. This tissue layer is expected to have a homogeneous appearance, because the size of all its composing features are well below the resolution provided by intravascular OCT. Indeed, the tomogram presents a homogeneous signal without internal structure. However, this signal is strongly textured, exhibiting a grainy pattern with spots or 'speckle' of bright, high intensity signal, alternating with regions of very low signal. This appearance is common for coherent imaging methods such as OCT or ultrasound imaging, and can be misleading

to the viewer by masking meaningful structural details. A detailed discussion of speckle in OCT is provided by Curatolo et al. [28].

Speckle is not noise, but simply unresolved spatial information. Speckle arises from the interference of many sub-resolution spaced scatterers. As discussed in Sect. 2.4, tissue can be modeled as a composition of many small discrete particles. Each such particle scatters a fraction of the incident light back to the detector, encoding its depth location in the path length difference with the reference signal. The argument of the complex-valued interference term of each particle is very sensitive to its axial position and varies by 2π for an axial shift of $\lambda/2$. The tomogram signal at a given depth corresponds to the sum of the contributions of all the particles within one resolution volume centered on this location. The axial dimension of this resolution volume measures several times the wavelength, which makes the phase of each particle essentially random. Mathematically, the summation of these contributions is described as a random walk. It generates a complex signal with a random amplitude and phase, following well-known statistical properties [29]:

$$\sum_{n=1}^{N} t_n e^{i2kz_n} = te^{i\varphi} \quad p(t) = \frac{\pi t}{2\langle t\rangle^2} e^{-\frac{\pi t^2}{4\langle t\rangle^2}} \quad p\left(T = |t|^2\right) = \frac{1}{\langle T\rangle} e^{-\frac{T}{\langle T\rangle}}$$
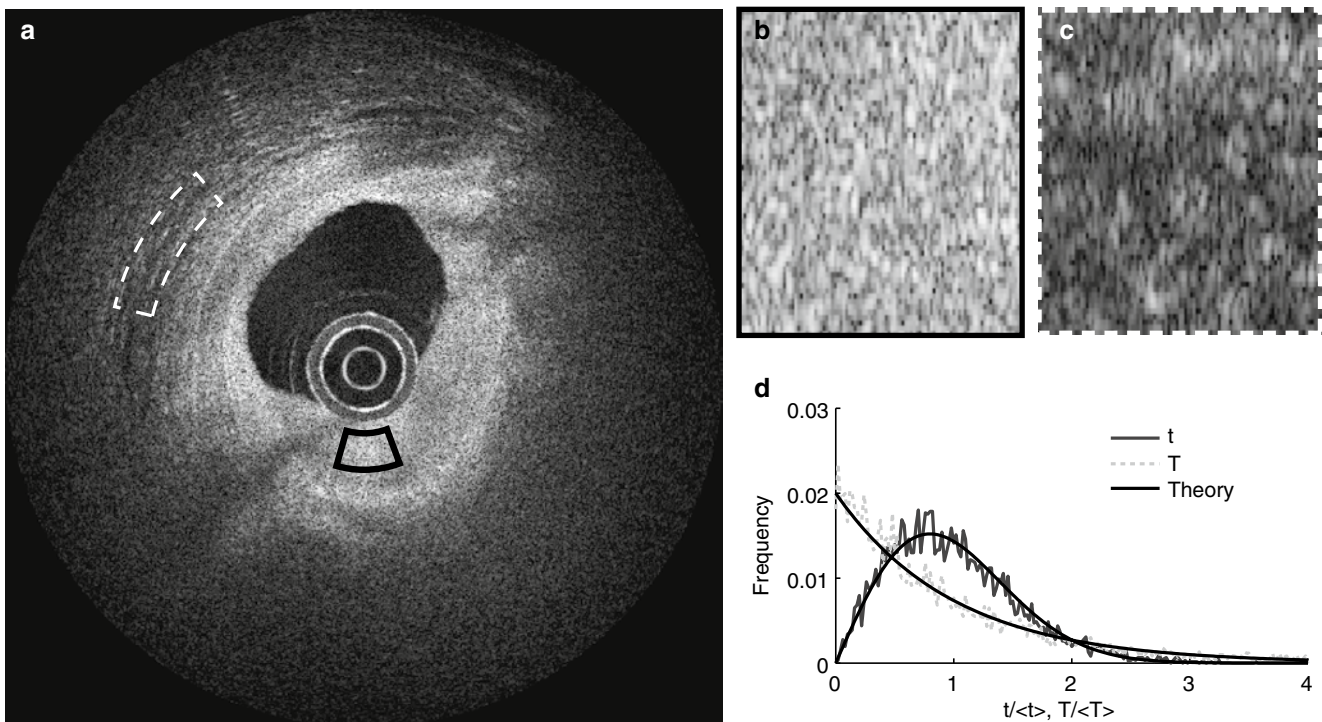
$$(2.22)$$

Fig. 2.12 (**a**) Speckle as perceived in intravascular OCT. The two regions of interest magnified in (**b**, **c**) have equal angular width and demonstrate the invariance of speckle size with depth. Whereas the area in

(**b**) corresponds to a homogeneous tissue region, the region in (**c**) reveals some structural features. (**d**) The amplitude and intensity histograms of the speckle in (**b**) follow accurately the theoretical distributions

Here, $p(t)$ and $P(T)$ are probability density functions of the resulting amplitude and intensity signal, respectively. The resulting phase is uniformly distributed between 0 and 2π, whereas $p(t)$ follows a Rayleigh distribution, with $<t>$ the mean amplitude value. Converting the amplitude signal to the corresponding intensity expression results in $p(T)$, a negative exponential distribution, highlighting the prevalence of dark speckle. Indeed, the contrast of a speckle pattern, expressed as the mean signal divided by its standard deviation is unity for the intensity signal and 0.52 for the amplitude signal [30]. A speckle pattern that produces these predicted statistical properties is termed 'fully developed'. Alternatively, if for instance the generating phase values are not evenly distributed, a more involved, 'partially developed' speckle pattern can arise. As indicated in Fig. 2.12, the speckle of the fibrous plaque follows the theoretical distribution of fully developed speckle very well.

In a sample region with uniform scattering properties the speckle follow the same distribution. However, each point in the tomogram corresponds to a different subset of contributing scatterers, and hence to a different, independent realization of the random walk. This subset is defined by the spatial resolution of the system: only scattering particles from within the resolution volume contribute to the speckle at this specific location. The speckle from two adjacent, but non-overlapping resolution volumes, are statistically independent. At intermediate positions between these two resolution volumes, the contributing particles gradually vary from one subset to the other, resulting in intermediate values. The rate of the spatial variation, i.e. the size of the speckle, is directly defined by the resolution of the imaging system, both along the axial and the lateral directions. A better resolution would result in smaller speckle grains. Intravascular OCT performs circumferential scanning, and the lateral offset between two A-lines is depth-dependent, as seen in Eq. 2.18. One could then expect that the speckle pattern decorrelates faster at larger depth than close to the probe center. However, as can be seen in the subsets of Fig. 2.12, the pattern decorrelates at an equal angular rate, irrespective of radius. Since the circumferential scan also alters the incident angle on the tissue, even if the same subset of scatterers is interrogated the speckle realization becomes statistically independent and the angular speckle size is therefore defined by the angular width of the beam, independent of distance.

The individual layers of the vessel are clearly distinguishable in an OCT tomogram, because their scattering properties are different and result in a speckle pattern with distinct mean values, showing brighter or darker layers. Some tissue layers, such as the periadventitial adipose tissue, feature an architecture that results in an inhomogeneous OCT signal, as shown in Fig. 2.12. The speckle intensity varies locally because the underlying tissue scattering properties vary on this same size scale.

The presence of speckle in OCT can alternatively be explained by reasoning in the spatial frequency domain. As discussed in Sect. 2.2.1, each wavenumber of a wavelength sweep measures a different axial spatial frequency. This resulting spectrum is not centered on zero spatial frequency, but on the central wavenumber k_c. Accordingly, OCT acts as a bandpass filter, suppressing both the low and high spatial frequencies, and measuring only those within the wavelength spectrum. In comparison, most traditional imaging and vision instruments act as low-pass filters and provide a more intuitive image of the sample structure. The missing frequencies of the bandpass filtering of OCT cause speckle [27]. This is very similar to ultrasound imaging, which likewise suffers from speckle. Acoustic waves from different scatterers also interfere and give rise to the similar statistical behavior. There have been many attempts at developing hardware modifications and post-processing algorithms to reduce or remove speckle. Although those that are compatible with catheter-based imaging have not significantly enhanced the information content of intravascular images, future technical improvements are possible.

Conclusions

Although the first demonstration of intracoronary OCT in human subjects was performed with time-domain interferometry, the advent of frequency-domain OCT has greatly improved the clinical utility of this modality by significantly increasing imaging speed. Since the underlying signal for both time-domain and frequency-domain arises from the interference between the electric field scattered from the tissue and that provided by the reference arm, the primary image characteristics of resolution, contrast, and depth of penetration, are essentially unchanged. This chapter has introduced the basic principles underpinning interferometry and optical propagation in biological tissue. It should serve as a basis for understanding the OCT image features presented in other chapters in this book and identifying the origin of artifacts that may arise from phenomenon such as speckle.

References

1. Yun S, Tearney G, de Boer J, Iftimia N, Bouma B. High-speed optical frequency-domain imaging. Opt Express. 2003;11(22): 2953–63.
2. Yun SH, Tearney GJ, Vakoc BJ, Shishkov M, Oh WY, Desjardins AE, et al. Comprehensive volumetric optical microscopy in vivo. Nat Med. 2006;12(12):1429–33.
3. Wojtkowski M. High-speed optical coherence tomography: basics and applications. Appl Optics. 2010;49(16):D30–61.
4. Klein T, Wieser W, Reznicek L, Neubauer A, Kampik A, Huber R. Multi-MHz retinal OCT. Biomed Opt Express. 2013;4(10):1890.
5. Yun S, Tearney G, de Boer J, Bouma B. Removing the depth-degeneracy in optical frequency domain imaging with frequency shifting. Opt Express. 2004;12(20):4822–8.

6. Kawase Y, Suzuki Y, Ikeno F, Yoneyama R. Comparison of nonuniform rotational distortion between mechanical IVUS and OCT using a phantom model. Ultrasound Med Biol. 2007;33:67–73.

7. van Soest G, Bosch JG, van der Steen AFW. Azimuthal registration of image sequences affected by nonuniform rotation distortion. IEEE Trans Inform Technol Biomed. 2008;12(3):348–55.

8. Saleh BEA, Teich MC. Fundamentals of photonics. Hoboken: John Wiley & Sons; 2013.

9. Schmitt JM, Kumar G. Turbulent nature of refractive-index variations in biological tissue. Opt Lett. 1996;21(16):1310. OSA.

10. Xu M, Alfano RR. Fractal mechanisms of light scattering in biological tissue and cells. Opt Lett. 2005;30(22):3051–3.

11. Rogers JD, Capoğlu IR, Backman V. Nonscalar elastic light scattering from continuous random media in the born approximation. Opt Lett. 2009;34(12):1891–3.

12. Schmitt JM, Kumar G. Optical scattering properties of soft tissue: a discrete particle model. Appl Opt. 1998;37(13):2788–97.

13. Schneiderheinze DHP, Hillman TR, Sampson DD. Modified discrete particle model of optical scattering in skin tissue accounting for multiparticle scattering. Opt Express. 2007;15(23):15002–10.

14. Born M, Wolf E. Principles of optics: electromagnetic theory of propagation, interference and diffraction of light. 7th ed. Cambridge/New York: Cambridge University Press; 1999.

15. Coupland JM, Lobera J. Holography, tomography and 3D microscopy as linear filtering operations. Measure Science Technol. 2008;19(7). doi:10.1088/0957-0233/19/7/074012.

16. Villiger M, Lasser T. Image formation and tomogram reconstruction in optical coherence microscopy. J Opt Soc Am A OSA. 2010;27(10):2216–28.

17. Jacques SL. Optical properties of biological tissues: a review. Phys Med Biol. 2013;58(11):R37–61.

18. Schmitt JM, Knuttel A, Yadlowsky M, Eckhaus MA. Optical-coherence tomography of a dense tissue: statistics of attenuation and backscattering. Phys Med Biol. 1994;39(10):1705–20.

19. van der Meer FJ, Faber DJ, Baraznji Sassoon DM, Aalders MC, Pasterkamp G, van Leeuwen TG. Localized measurement of optical attenuation coefficients of atherosclerotic plaque constituents by quantitative optical coherence tomography. IEEE Trans Med Imaging. 2005;24(10):1369–76.

20. Scolaro L, McLaughlin RA, Klyen BR, Wood BA, Robbins PD, Saunders CM, et al. Parametric imaging of the local attenuation coefficient in human axillary lymph nodes assessed using optical coherence tomography. Biomed Opt Express. 2012;3(2):366–79.

21. Xu C, Schmitt JM, Carlier SG, Virmani R. Characterization of atherosclerosis plaques by measuring both backscattering and attenuation coefficients in optical coherence tomography. J Biomed Opt. 2008;13(3):034003.

22. van Soest G, Goderie T, Regar E, Koljenovic S, van Leenders G, Gonzalo N, et al. Atherosclerotic tissue characterization in vivo by optical coherence tomography attenuation imaging. J Biomed Opt. 2010;15(1):011105.

23. Sharma U, Chang EW, Yun SH. Long-wavelength optical coherence tomography at 1.7 microm for enhanced imaging depth. Opt Express. 2008;16(24):19712–23.

24. Segelstein DJ. The complex refractive index of water [PhD thesis]. Kansas City: University of Missouri; 1981.

25. Takatani S, Graham MD. Theoretical analysis of diffuse reflectance from a two-layer tissue model. IEEE Trans Biomed Eng. 1979;26(12):656–64.

26. Van Veen RL, Sterenborg H, Pifferi A, Torricelli A, Cubedddu R. Determination of VIS-NIR absorption coefficient of mammalian fat, with time- and spatially resolved diffuse reflectance and transmission spectroscopy. Biomedical Topical Meeting; OSA Technical Digest 2004.

27. Schmitt JM, Xiang SH, Yung KM. Speckle in optical coherence tomography. J Biomed Opt. 1999;4(1):95–105.

28. Curatolo A, Kennedy BF, Sampson DD, Hillman RH. Speckle in Optical Coherence Tomography. In: Wang RK, Tuchin VV, editors. Advanced Biophotonics. Boca Raton: Taylor & Francis; 2014.

29. Goodman JW. Speckle phenomena in optics: theory and applications. Englewood: Roberts & Co; 2007.

30. Karamata B, Hassler K, Laubscher M, Lasser T. Speckle statistics in optical coherence tomography. J Opt Soc Am A Opt Image Sci Vis. 2005;22(4):593–6.

Teruyoshi Kume, Takashi Kubo, and Takashi Akasaka

Abstract

Optical coherence tomography (OCT) can reliably visualize the microstructure (i.e., 10–50 μm) of normal and atherosclerotic arteries. Typically, the media of the coronary artery appears as a lower signal intensity band relative to that of the intima and adventitia, providing a three-layered appearance (bright-dark-bright). In OCT images, fibrous plaques exhibit homogeneous, signal-rich (highly backscattering) regions; lipid-rich plaques exhibit signal-poor regions (lipid pools) with poorly defined borders and overlying signal-rich bands (corresponding to fibrous caps); and fibrocalcific plaques exhibit signal-poor regions with sharply delineated upper and/or lower borders. Studies have also assessed the ability of OCT to detect vulnerable plaque. A thin fibrous cap of vulnerable plaque, commonly named thin-cap fibroatheroma (TCFA), has fibrous cap thickness <65 μm. Although, the ability of OCT to characterize a lipid pool containing necrotic core needs to be clarified in future histologic studies, OCT could visualize thin (<65 μm) fibrous cap overlying the necrotic core and thus, detect TCFA. Infiltration of macrophages within the fibrous cap is another characteristic of vulnerable plaque. In OCT images, macrophage accumulation is seen as signal-rich, confluent punctuate regions that exceed the intensity of background speckle noise. The unique capabilities of OCT as an investigational tool for high-risk lesions will serve the cardiology community well, as it advances us toward a better understanding of atherosclerotic plaque. This information will improve our ability to more precisely treat our patients, both acutely and in the long term.

3.1 Introduction

High-resolution optical coherence tomography (OCT) can often provide superior delineation of coronary vessel wall structure when compared with intravascular ultrasound (IVUS). OCT can reliably visualize the microstructure (i.e., 10–50 μm, versus 150–200 μm for IVUS) of normal and atherosclerotic arteries [1]. However, OCT images are fundamentally different from histology, and it is not clear whether all characteristics identified by histology can also

T. Kume, MD, PhD
Division of Cardiology, Kawasaki Medical School, Kurashiki, Okayama, Japan

T. Kubo, MD, PhD • T. Akasaka, MD, PhD (✉)
Division of Cardiovascular Medicine, Wakayama Medical University, Kimiidera 811-1, Wakayama 641-8509, Japan
e-mail: akasat@wakayama-med.ac.jp

be characterized by OCT. Therefore, careful interpretation of OCT images is required. This chapter reviews the histological validation of OCT images.

3.2 Normal Vessel Wall Morphology and Intimal Thickening

Typically, the media of the vessel appears as a lower signal intensity band relative to that of the intima and adventitia, providing a three-layered appearance (bright-dark-bright) (Fig. 3.1). Intimal thickening occurs during the early phase of atherosclerosis in the coronary artery [2]. Evaluation of intimal thickening of the coronary artery is clinically important, and recent advancements in IVUS have enabled pathological evaluation of the wall structure of the coronary artery. However, intimal thickening is indirectly evaluated as the intima–media thickness by IVUS, because the boundary of the intima and media cannot be distinguished completely by this method [3]. On the other hand, OCT is superior to IVUS in terms of qualitative delineation of the vessel wall structure, and OCT can differentiate the intima from media. There is good agreement in the intimal thickness between OCT and histological examination (r = 0.98, p < 0.001, mean difference = 0.01 ± 0.04 mm) [4]. Most adults undergoing cardiac catheterization have intimal thickening and a signal-rich thick intimal band, even in angiographically normal segments (Fig. 3.2). OCT signal penetration through the diseased arterial wall is generally more limited (no more than 2 mm with current OCT devices), making it difficult to investigate deeper portions of the artery or to track the entire circumference of the media-adventitia interface.

3.3 Atherosclerotic Plaque

An atherosclerotic plaque is characterized as a mass lesion or a loss of the three-layered structure of the blood vessel. OCT can provide detailed information about plaque composition. Fibrous plaques exhibit homogeneous, signal-rich (highly backscattering) regions (Fig. 3.3); lipid-rich plaques exhibit signal-poor regions (lipid pools) with poorly defined borders and overlying signal-rich bands (corresponding to fibrous caps) (Fig. 3.4); and fibrocalcific plaques exhibit signal-poor regions with sharply delineated upper and/or lower borders (Fig. 3.5). OCT has the advantage of being able to image through calcium without shadowing, as would otherwise occur with IVUS. Plaque characteristics of OCT are listed in Table 3.1. The diagnostic accuracy of OCT for the above plaque characterization criteria was confirmed by an *ex vivo* study of 307 human atherosclerotic specimens, including those from the aorta, carotid arteries, and coronary
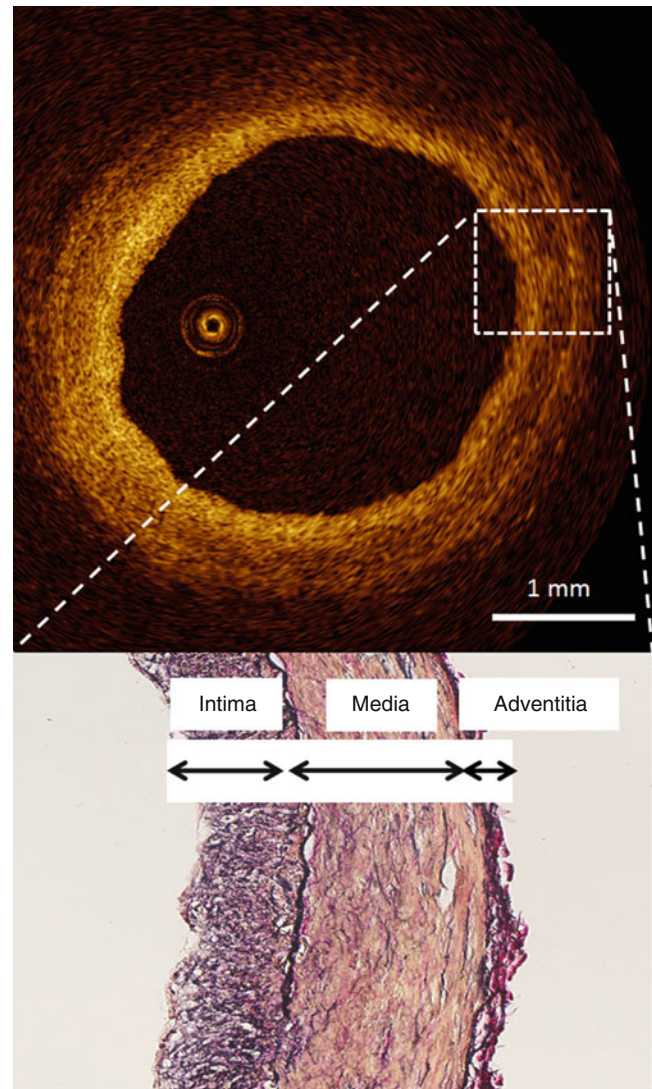

Fig. 3.1 The layered structure of the coronary wall imaged by optical coherence tomography (OCT). This OCT image demonstrates visualization of the intima, media and adventitia. The bright-dark-bright, three-layered appearance is seen in the OCT image with the corresponding anatomy as defined. Histological image is partial enlarged view of the dashed rectangle in OCT image (*bottom*). (Histologic staining Elastica van Gieson stain)

arteries [5]. Independent evaluations by two OCT analysts demonstrated a sensitivity and specificity of 71–79 and 97–98 %, respectively, for fibrous plaques; 90–94 and 90–92 %, respectively, for lipid-rich plaques; and 95–96 and 97 %, respectively for fibrocalcific plaques, (overall agreement versus histopathology, κ values of 0.88–0.84). The interobserver and intraobserver reproducibility of OCT assessment was also high (κ values of 0.88 and 0.91, respectively).

However, the limited depth of penetration of OCT could pose a problem for the imaging of deep vascular structures.
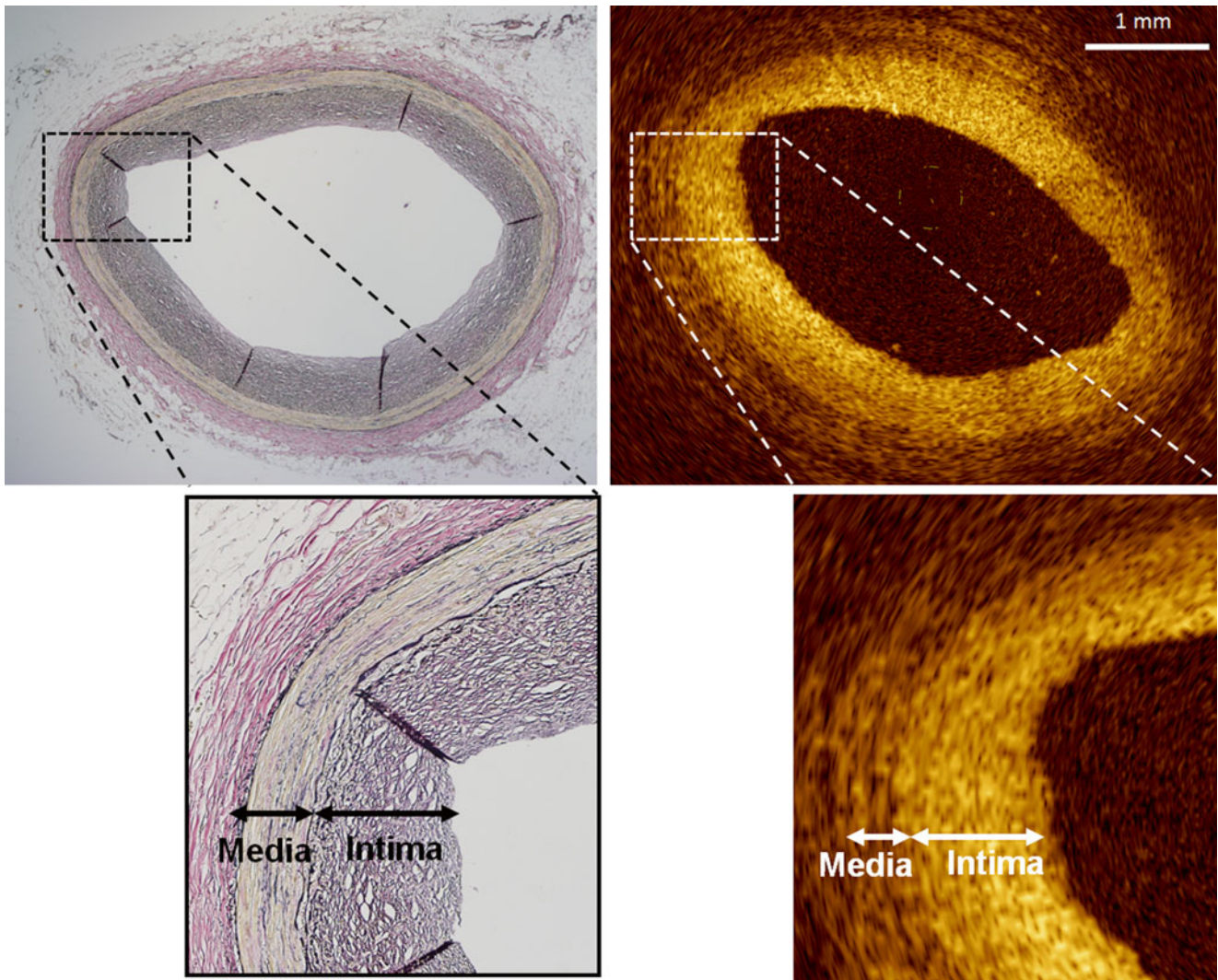
Fig. 3.2 Intimal thickening visualized by optical coherence tomography. Most adults undergoing cardiac catheterization have intimal thickening, represented as a signal-rich thick intimal band in the OCT image, even in angiographically normal segments. Partial enlarged view of the dashed rectangle in top images (*bottom*). (Histologic staining Elastica van Gieson stain)

A previous report showed that OCT assessments of lipid-rich lesion with thin fibrous cap (thickness of the fibrous cap <200 um) were achieved with 92 % sensitivity and 75 % specificity, while overall OCT assessments of lipid-rich lesion were achieved with 77 % sensitivity and 75 % specificity [6]. These data suggest that the superficial penetration of OCT may limit the assessment of entire plaque morphology.

the surface of the calcium due to acoustic shadowing. On the other hand, OCT can identify calcification tissue without shadowing (Fig. 3.6). There is better correlation in areas of calcification between OCT and histological examination when comparing between IVUS and the histological examination ($r = 084$, $p < 0.001$ vs. $r = 0.78$, $p < 0.001$) [7]. These data suggest that superficial calcification can be quantified more accurately using OCT than with IVUS.

3.4 Calcification

Calcification is frequently observed in more advanced atherosclerotic disease and is therefore thought to be a marker of coronary heart disease. IVUS can only visualize

3.5 Fibroatheroma

A fibroatheroma is characterized as necrotic core with an overlying fibrous cap. A fibrous cap is a fibrous tissue layer, which is often a signal-rich band, overlying a signal-poor
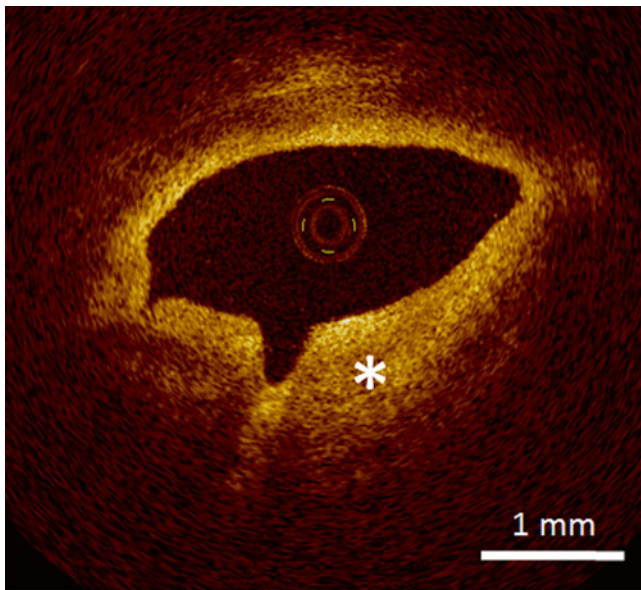
Fig. 3.3 Optical coherence tomography images (*top*) and corresponding histology (*bottom*) for fibrous plaque. In fibrous plaques, the OCT signal is strong and homogeneous (*asterisk*). (Histologic staining Elastica van Gieson stain)
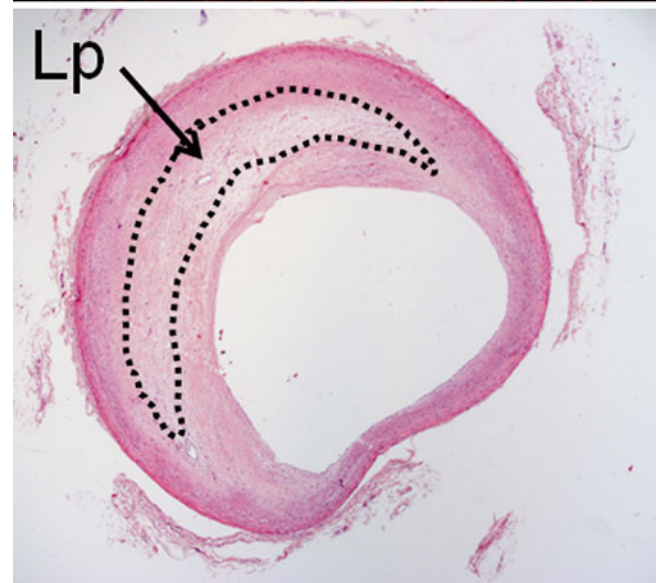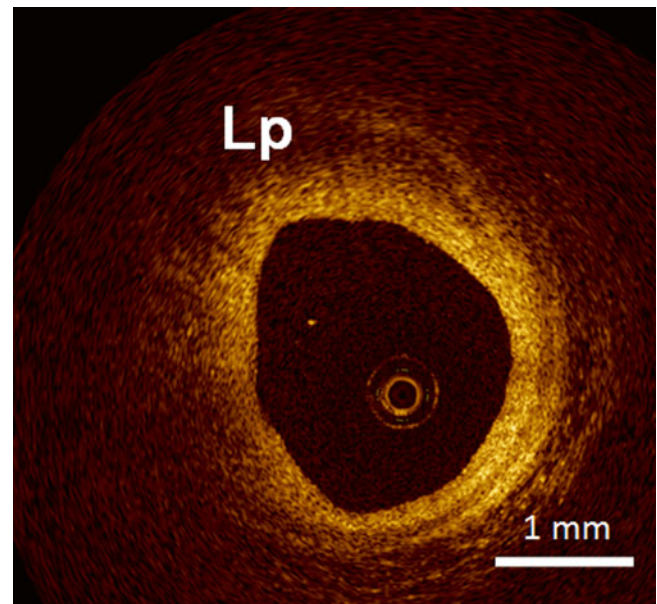

Fig. 3.4 Optical coherence tomography images (*top*) and corresponding histology (*bottom*) for lipid-rich plaque. Lipid-rich (*Lp*) regions appear as a signal-poor region within the vessel wall, and lipid-rich plaques have diffuse or poorly demarcated borders (Histologic staining: hematoxylin and eosin stain)

region indicating the necrotic core (Fig. 3.7). In the OCT image, the necrotic core was characterized as signal-poor regions with poorly defined borders, which is similar to that of a lipid pool. Histologically, a lipid pool is converted to a necrotic core from macrophage infiltration and apoptosis forming the early necrotic core. In a previous histologic study using OCT, there was no attempt to differentiate a necrotic core from a lipid pool, and these structures have different clinical relevance. The ability of OCT to characterize a lipid pool containing necrotic core needs to be clarified in future histologic studies.

3.6   Vulnerable Plaque

Studies have also assessed the ability of OCT to detect vulnerable plaque.

Myocardial infarction, sudden cardiac death and unstable angina arise from coronary thrombosis, which develops as a result of ruptured vulnerable plaque. Autopsy studies have identified several histological characteristics of plaques that correlate with the risk of rupture and subsequent acute
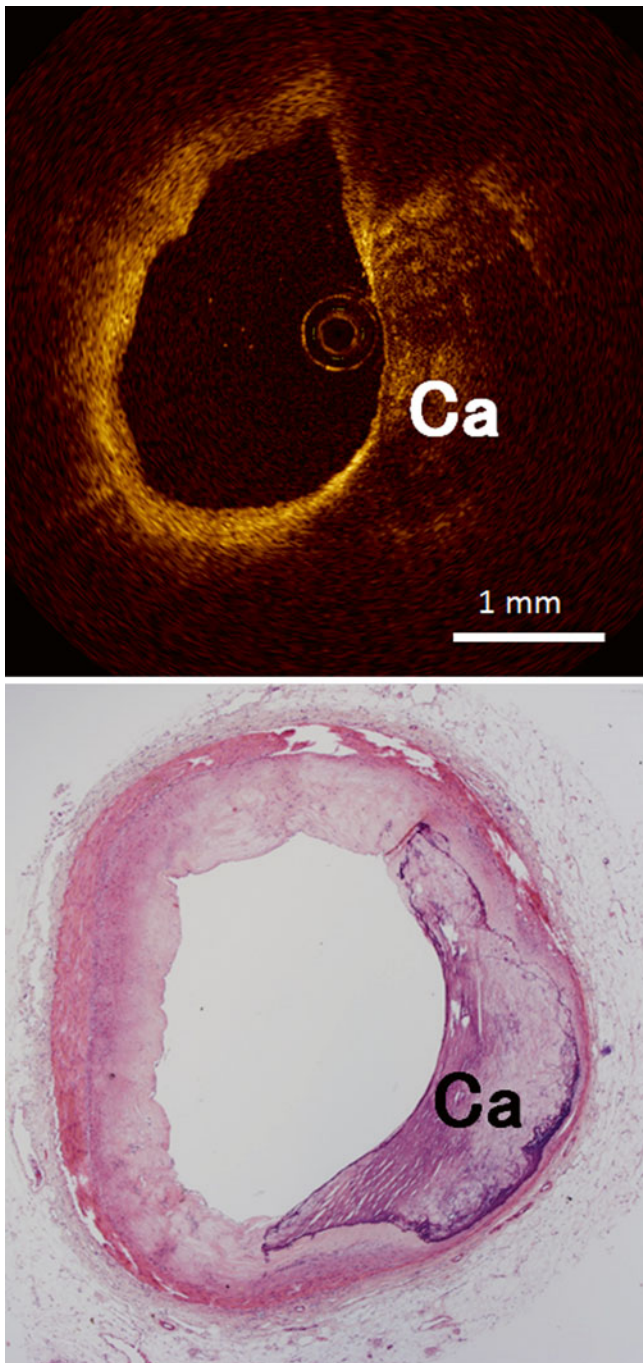
Fig. 3.5 Optical coherence tomography images (*top*) and corresponding histology (*bottom*) for fibrocalcific plaque. Calcific (*Ca*) regions appear as a signal-poor region within the vessel wall, and fibrocalcific plaques have sharply delineated borders (Histologic staining: hematoxylin and eosin stain)

Table 3.1 Plaque characteristics in optical coherence tomography (OCT)

Tissue type	OCT
Fibrous	Homogeneous
	Signal-rich (highly backscattering)
Fibrocalcific	Sharply delineated borders
	Signal-poor
Lipid-rich	Poorly defined borders
	Signal-poor

<65 μm. TCFA is the primary plaque type at the site of plaque rupture but exists both in culprit lesions and non-culprit lesions and is distributed in all three coronary arteries. TCFAs are more commonly observed in patients with acute coronary syndrome than in patients with stable angina. Histologic data show that TCFAs tend to cluster in predictable spots within the proximal segment of the left anterior descending artery but also develop relatively evenly in the left circumflex and right coronary artery [10, 11]. A thin (<65 μm) fibrous cap of vulnerable plaque is technically below the image resolution of IVUS (~150 μm). On the other hand, the resolution of OCT is between 10 and 50 μm, which is significantly greater than any currently available imaging technology. Therefore, OCT could visualize thin fibrous cap (Fig. 3.8) and measure the thickness of the fibrous cap in the lipid-rich plaque (r=090, p<0.001) [12]. Fujii et al. performed a three-vessel OCT examination in patients with ischemic heart disease in the clinical settings and showed that TCFAs tend to cluster in predictable spots within the proximal segment of the left anterior descending artery yet develop relatively evenly in the left circumflex and right coronary artery [13]. These data are similar to those from prior histologic studies.

Infiltration of macrophages within the fibrous cap is another characteristic of vulnerable plaque. A previous report showed that OCT enables the quantification of macrophages within fibrous caps [14]. OCT with a simple image-processing algorithm for macrophage evaluation yielded results that correlated well with histological measurements of fibrous cap macrophage density (r=0.84, p<0.0001). A range of OCT signal standard deviation thresholds (6.15–6.35 %) yielded 100 % sensitivity and specificity for identifying caps containing >10 % CD68 staining. In OCT images, macrophage accumulation is seen as signal-rich, confluent punctuate regions that exceed the intensity of background speckle noise (Fig. 3.9). OCT may provide researchers and clinicians with a valuable tool for the assessment of vulnerable plaque, including the visualization of the thin fibrous cap.

Plaque neoangiogenesis is a morphological characteristic of vulnerable plaque [9]. Neoangiogenesis may promote the
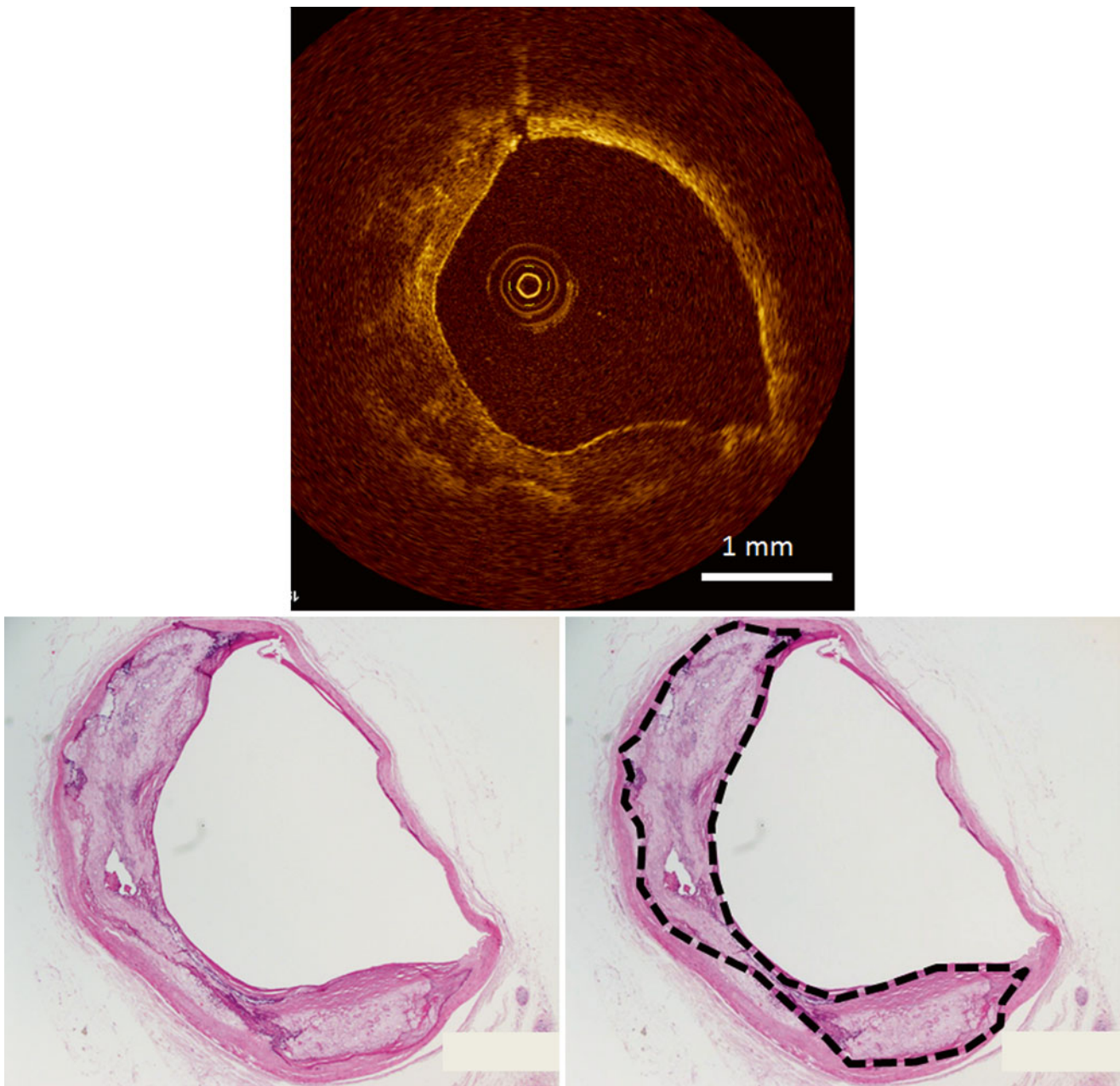
coronary events. These characteristics include: (1) a thin fibrous cap (<65 μm), (2) activated macrophages near the fibrous cap, (3) a large lipid pool, and (4) neoangiogenesis [8, 9].

A thin fibrous cap of vulnerable plaque, commonly named thin-cap fibroatheroma (TCFA), has fibrous cap thickness

Fig. 3.6 Optical coherence tomography images (*top*) and corresponding histology (*bottom*) for heavily calcified plaque. OCT can identify the calcification tissue without shadowing. Dashed lines indicate calcification tissue (*bottom right*). (Histologic staining: hematoxylin and eosin stain)

influx of lipids and the infiltration of inflammatory cells in coronary plaque. In addition, newly formed angiogenic vessels are fragile and tend to break. This may result in an intraplaque hemorrhage, eventually resulting in luminal narrowing [15–17]. In OCT images, neoangiogenesis can be recognized as small black holes (microchannels) (Fig. 3.10) [18]. Microchannels detected by OCT are associated with plaque vulnerability and are predictors of luminal narrowing in clinical studies [19, 20]. However, the accuracy of OCT for the detection of coronary plaque neoangiogenesis has not yet been investigated.

3.7 Thrombus

Rupture of the vulnerable plaque leading to subsequent thrombotic occlusion of the coronary artery accounts for the majority of acute coronary events (Fig. 3.11). Thrombi that form in regions of blood stasis or low flow are composed of red blood cells entrapped within interspersed fibrin and a smaller component of aggregated platelets. These thrombi are colored darkly by abundant hemoglobin and are often referred to as "red" thrombi. In contrast, platelet-rich thrombi, which contain few red cells, appear off-white in color and are called
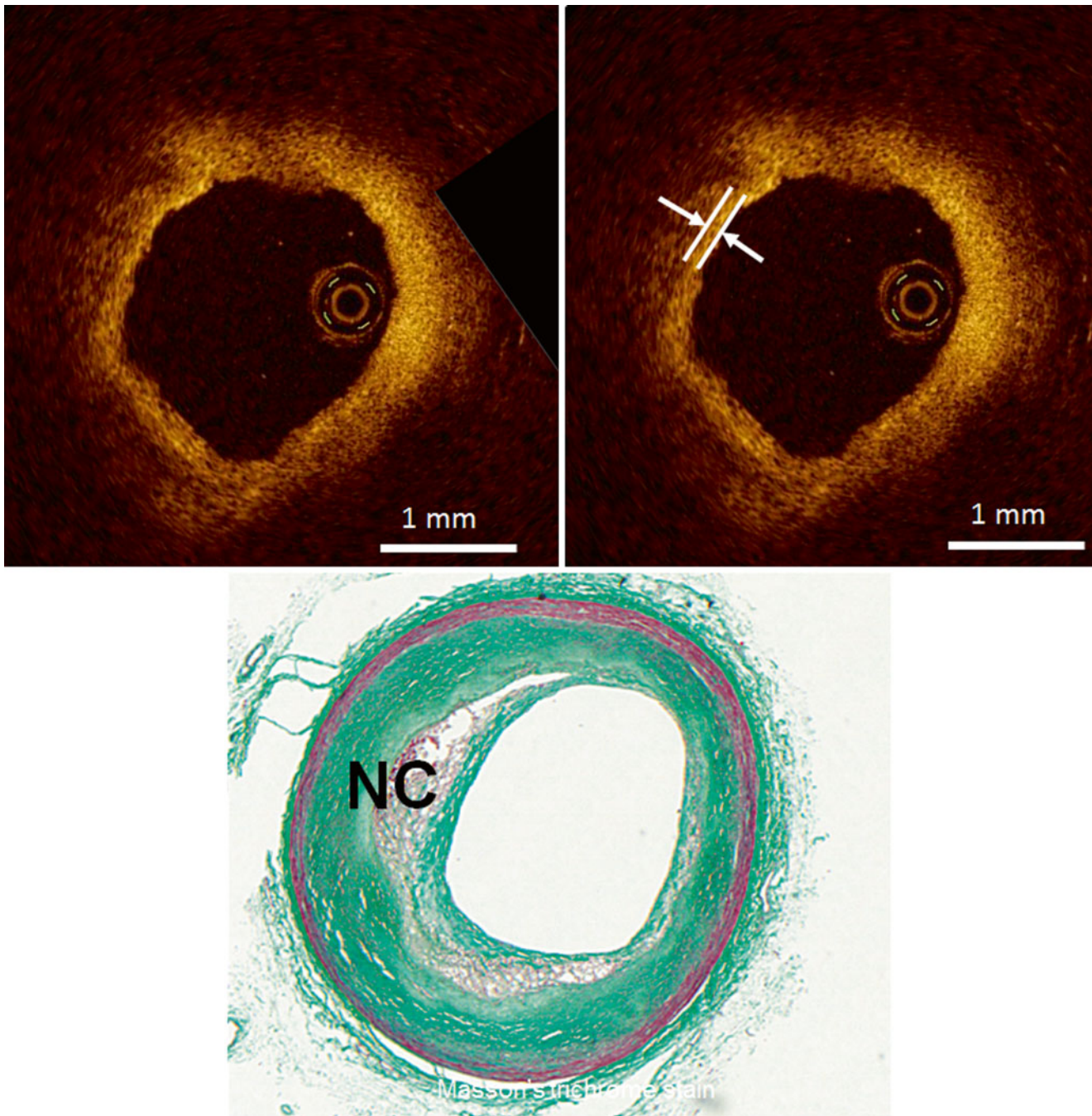
Fig. 3.7 Optical coherence tomography images (*top*) and corresponding histology (*bottom*) for fibroatheroma. A fibrous cap (*arrow*) is a fibrous tissue layer, which is depicted as a signal-rich band overlying a signal-poor region indicating necrotic core (*NC*). (Histologic staining: Masson trichrome stain)

"white" thrombi. Red thrombus is depicted as a high-backscattering protrusion with signal-free shadowing in OCT images (Fig. 3.12). White thrombus is depicted by a signal-rich, low-backscattering projection (Fig. 3.13). There is a significant difference in attenuation of intensity between red and white thrombi [21]. White thrombi associated with ruptured plaque plays a particularly important role in acute coronary syndrome. Identification and characterization of thrombi might help to predict outcome as well as the impact of mechanical interventions and antithrombotic/antiplatelet strategies.

OCT can detect a unique feature of thrombus in the coronary lumen that cannot otherwise be visualized by IVUS [22], namely, white thrombus consisting mainly of platelets and white blood cells (Fig. 3.14). This thin flat white thrombus was attached to the vessel wall without significant lumen stenosis. The clinical impact of this abnormal structure is unclear.
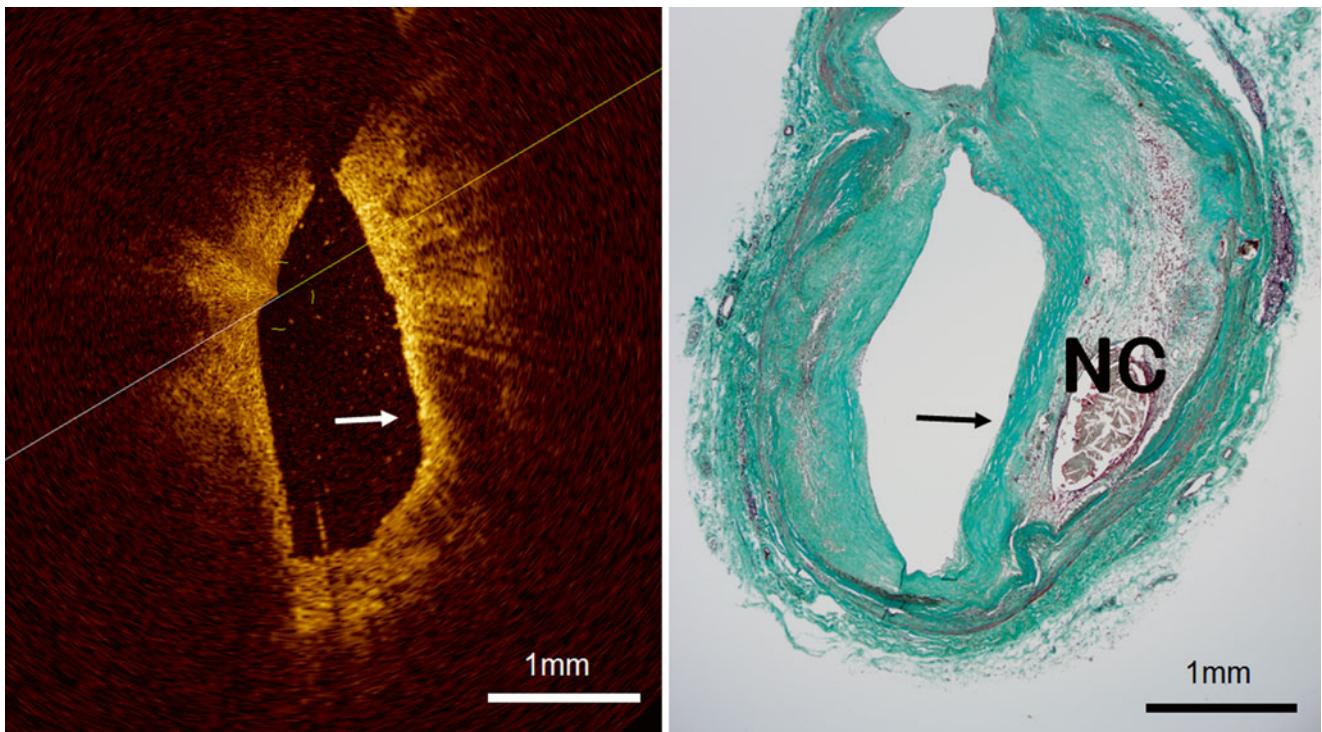
Fig. 3.8 Optical coherence tomography images (*left*) and corresponding histology (*right*) for thin-cap fibroatheroma (TCFA, *arrowhead*). OCT can measure the thickness of the fibrous cap and detect TCFA.

TCFA has a fibrous cap thickness <65 μm and is the primary plaque type at the site of plaque rupture. It exists in both culprit lesions and non-culprit lesions. (Histologic staining: Masson trichrome stain)
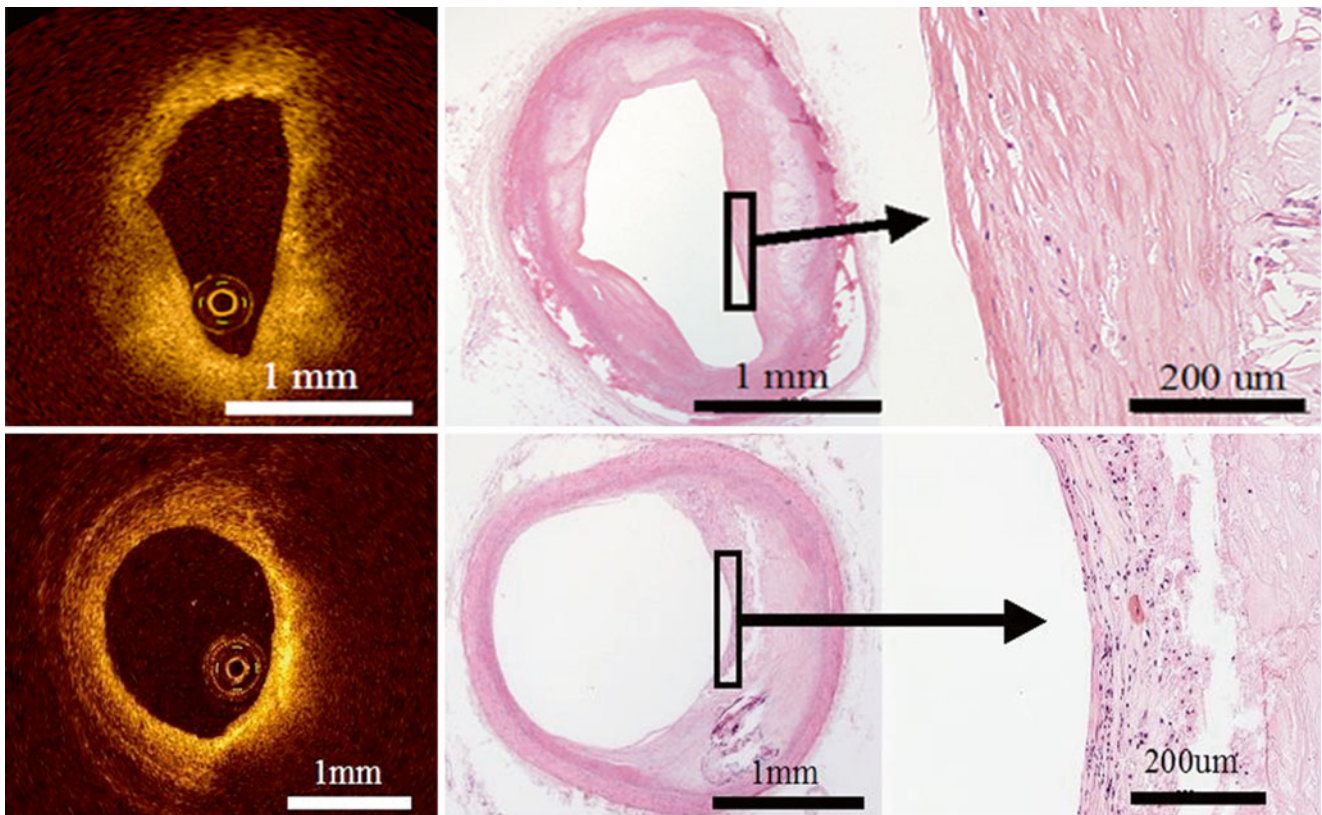

Fig. 3.9 Optical coherence tomography images (*left*) and corresponding histology (*middle and right*) for infiltration of macrophages within the fibrous cap. In the OCT image (*top*), there are no confluent punctate regions that exceed the intensity of background speckle within the fibrous cap. In the OCT image (*bottom*), infiltration of macrophages within the fibrous cap is seen as confluent punctate regions that exceed the intensity of background speckle within the fibrous cap (Histologic staining: hematoxylin and eosin stain)
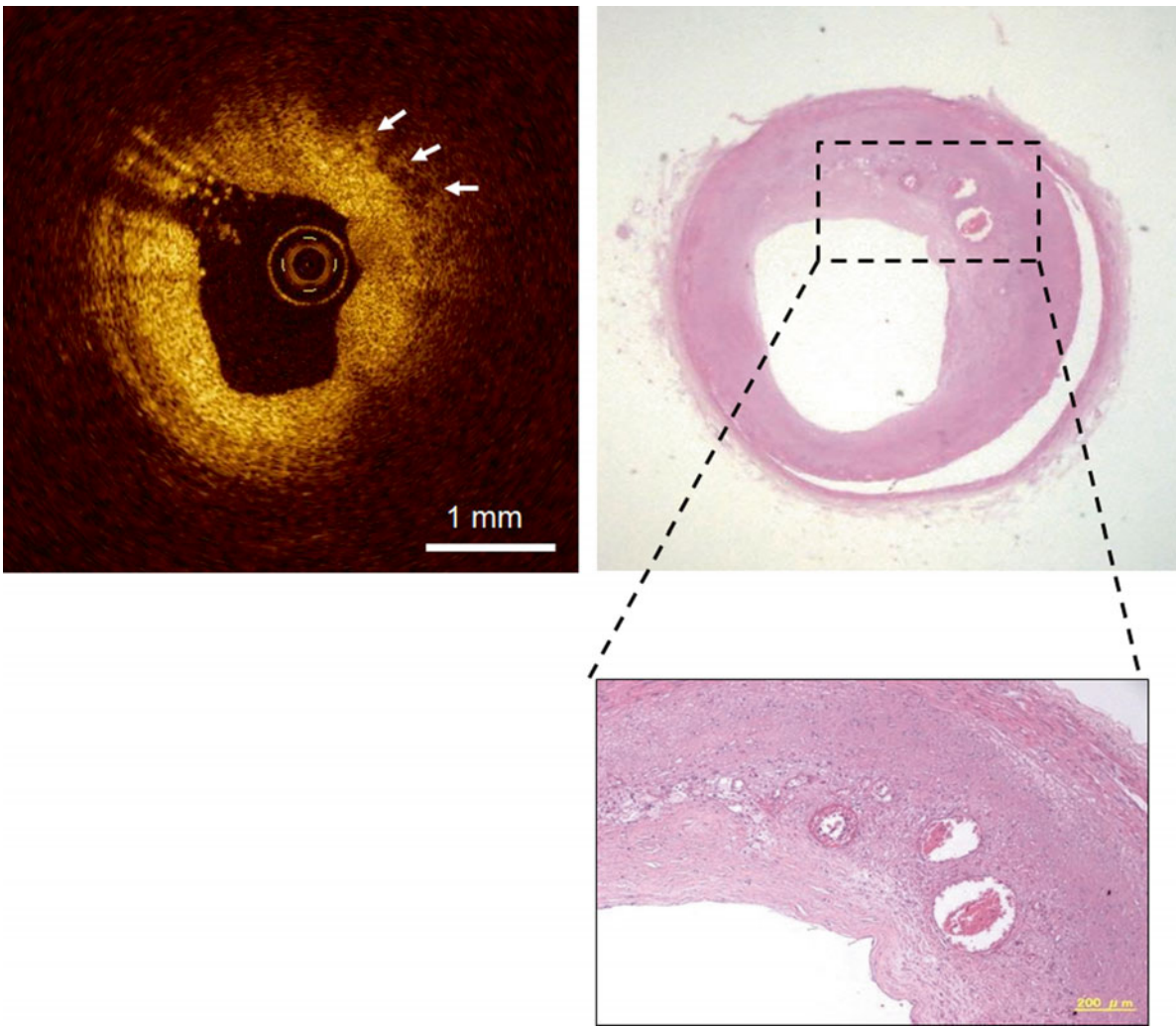
Fig. 3.10 Optical coherence tomography images (*left*) and corresponding histology (*right*) for neoangiogenesis of coronary plaque. Histological examination revealed neoangiogenesis of coronary plaque Partial enlarged view of the dashed rectangle in top images (*bottom*).

In the corresponding OCT image, neovascularization was characterized by no-signal tubululuminal structures (microchannel) in coronary plaque (*arrowhead*) (Histologic staining: hematoxylin and eosin stain)
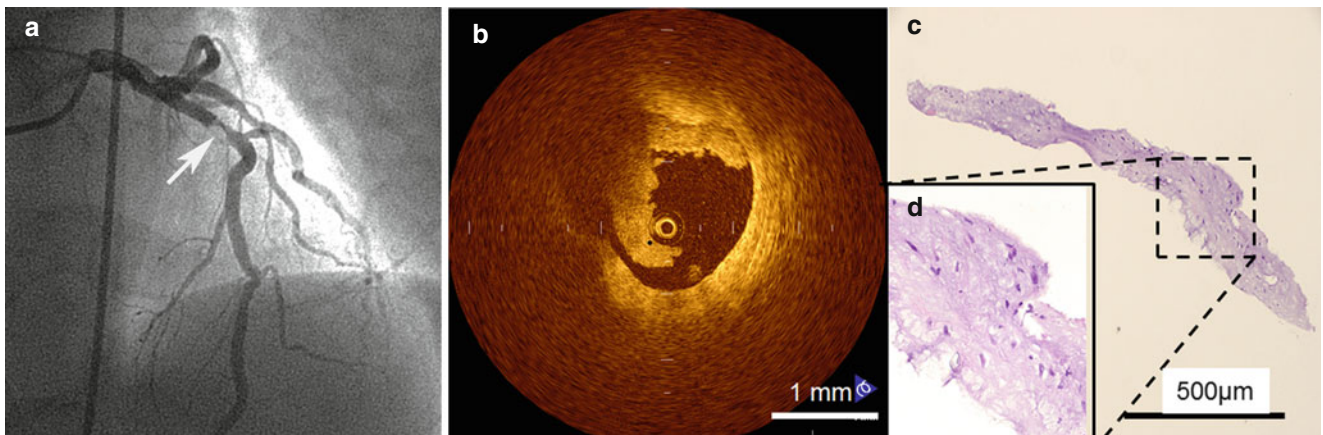

Fig. 3.11 A coronary angiogram shows a filling defect surrounded by contrast medium at the site of a severe stenosis in the left anterior descending coronary artery (panel **a**; *arrow*). Using optical coherence tomography (Image WireTM, LightLab Imaging, Inc.) imaging, a low backscattering protrusion suggestive of white thrombus in the coronary lumen at the site of plaque rupture is clearly visualized (panel **b**). The histopathological examination shows white thrombus composed of fibrin, platelets, and few white blood cells (panel **c** and **d**, hematoxylin and eosin stain). Partial enlarged view of the dashed rectangle in panel c (panel **d**).
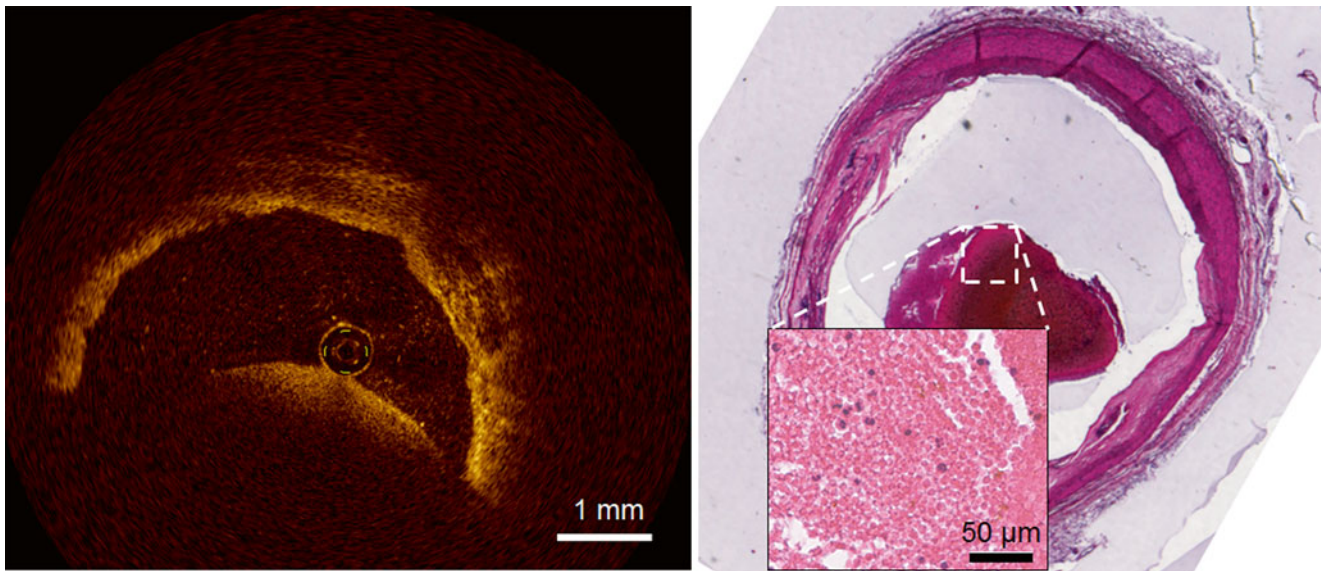
Fig. 3.12 Optical coherence tomography images (*left*) and corresponding histology (*right*) for red thrombus. Red thrombus forms in regions of blood stasis or low flow and is composed of red blood cells entrapped within interspersed fibrin and a smaller component of aggregated platelets. Partial enlarged view of the dashed rectangle (*bottom*). Red thrombus appears in OCT images as a high-backscattering protrusion with signal-free shadowing. (Histologic staining: hematoxylin and eosin stain)
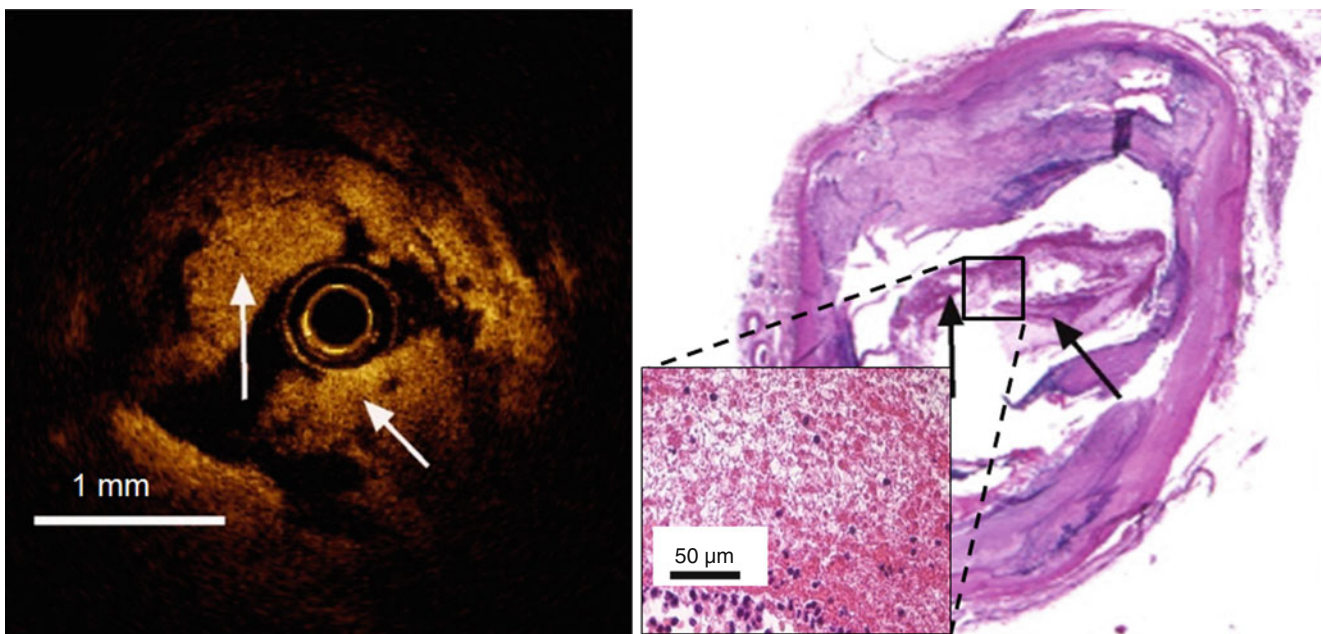

Fig. 3.13 Optical coherence tomography images (*left*) and corresponding histology (*right*) for white thrombus. White thrombus associated with ruptured plaque plays a particularly important role in acute coronary syndrome. Platelet-rich thrombi, which contain few red cells, are off-white in color. White thrombus is characterized by a signal-rich, low-backscattering projection. Partial enlarged view of the dashed rectangle (bottom). Partial enlarged view of the dashed rectangle (*bottom*). (Histologic staining: hematoxylin and eosin stain)

3.8   Neointima

The current capabilities of OCT are well suited for the identification and study of neointima formation, where the relevant morphologic features are primarily localized within 500 μm of the luminal surface (Fig. 3.15). Neointima within a stent is comprised of various tissue components, including collagen, proteoglycan, smooth muscle, fibrin, or thrombus. Because the neointima is composed of different tissues after stent implantation, it displays a variety of different characteristics (Fig. 3.16) [23, 24]. Only a few case reports have studied the relationship between OCT-imaged neointimal characteristics and these tissue components [25, 26]. OCT is useful for monitoring the structural changes that occur in neointima formation after stent implantation.
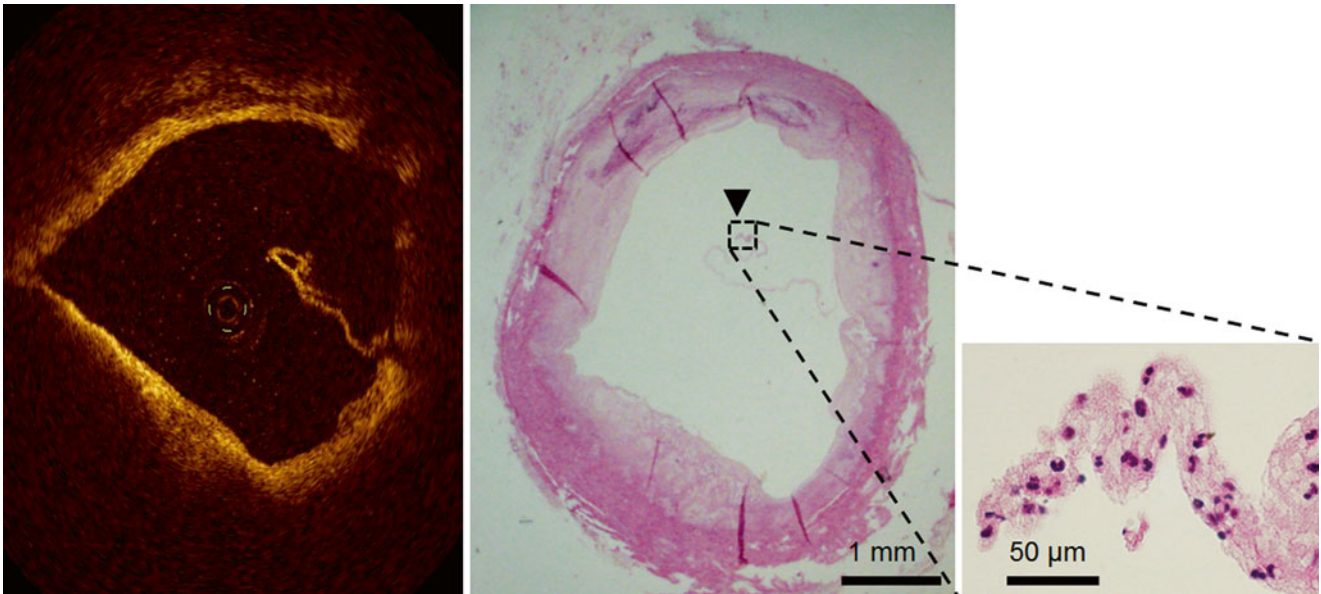
Fig. 3.14 A thin flat structure in the coronary lumen in optical coherence tomography image. Histological images reveal a white thrombus consisting mainly of platelets and white blood cells (*middle and left*). Partial enlarged view of the dashed rectangle (*left*). (Histologic staining: hematoxylin and eosin stain)
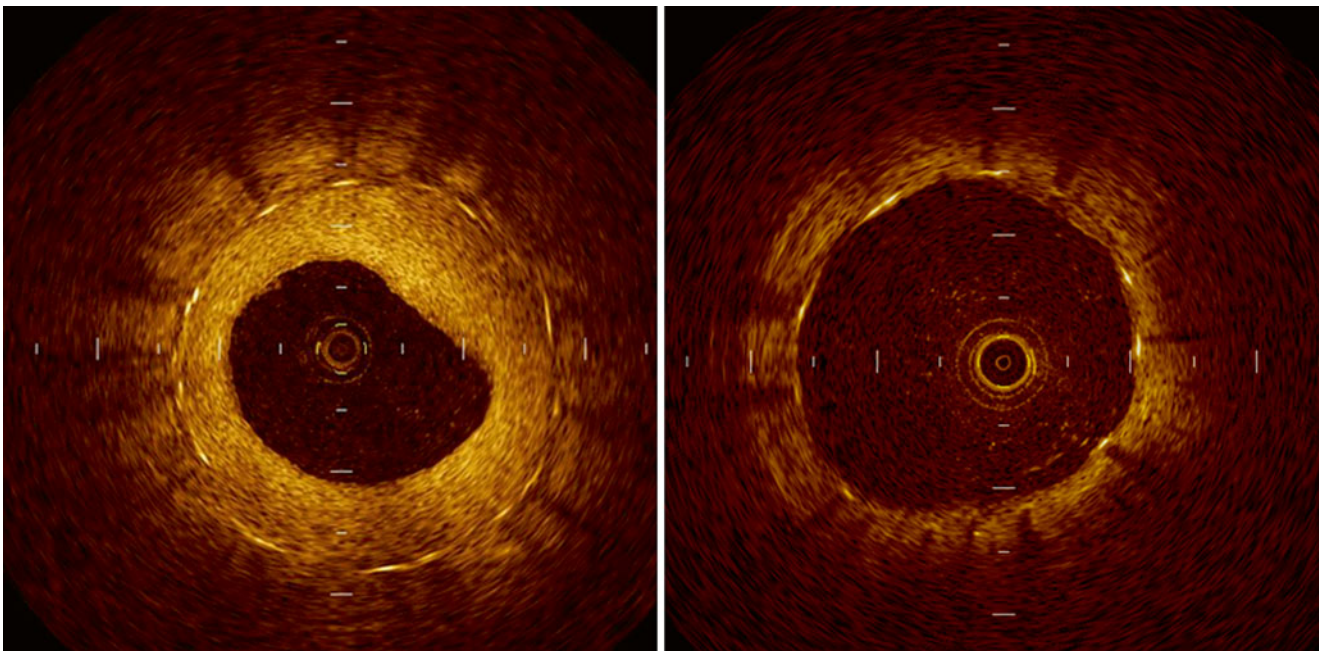

Fig. 3.15 Optical coherence tomography images at 8 months after stent deployment. OCT visualizes the stent struts covered by a thick neointima that appears as a bright luminal layer surrounding the stent struts after bare metal stent implantation (*left*). OCT shows stent struts and thin, bright reflective tissue coverage after drug-eluting stent implantation (*right*)
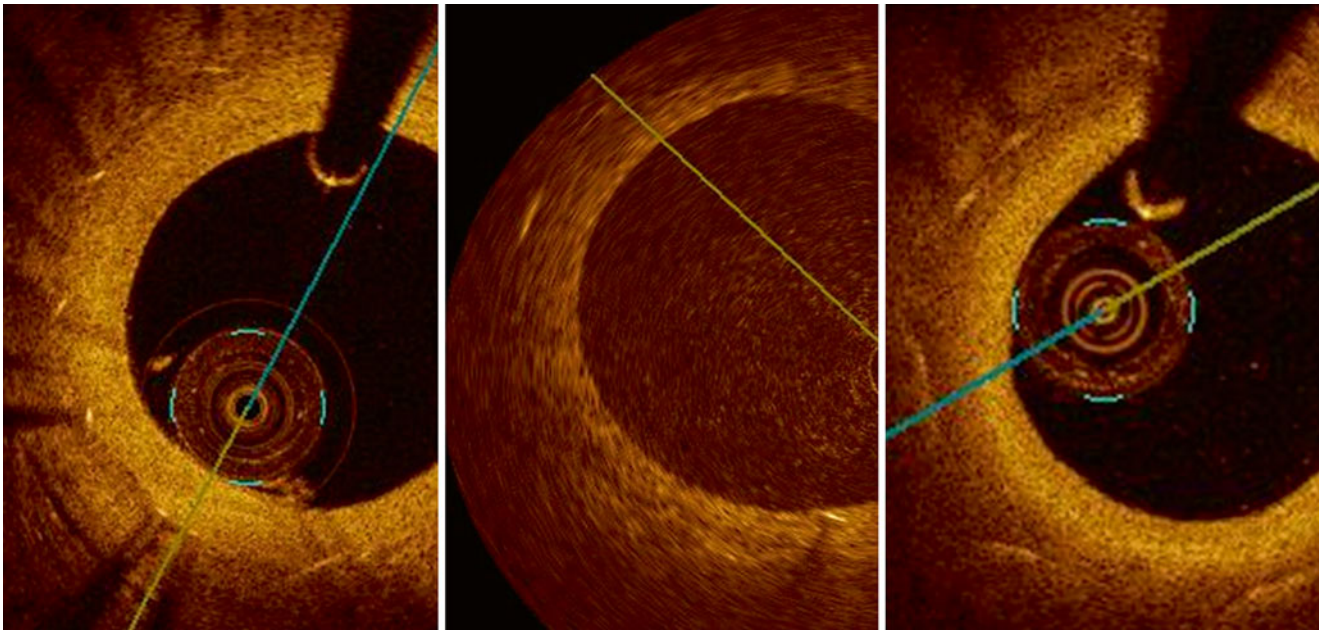
Fig. 3.16 Neointimal optical coherence tomography characteristics. Restenotic tissue structure in the OCT image is classified as homogeneous (*left*), heterogeneous (*middle*) and layered pattern (*right*). Neointima displays a variety of different OCT characteristics

3.9 Summary

This chapter reviewed the histologic validation of OCT images. OCT images are fundamentally different from histology, and it is not clear whether all characteristics identified by histology can also be characterized by OCT. Future studies include a large number of lesions to be used for further comparative investigation of OCT versus histology. However, high-resolution OCT can provide information comparable to histology in some circumstances. For example, OCT can provide a comprehensive assessment of atherosclerotic plaque. The unique capabilities of OCT as an investigational tool for high-risk lesions will serve the cardiology community well, as it advances us toward a better understanding of atherosclerotic plaque. This information will improve our ability to more precisely treat our patients, both acutely and in the long term.

References

1. Tearney GJ, Regar E, Akasaka T, Adriaenssens T, Barlis P, Bezerra HG, et al. Consensus standards for acquisition, measurement, and reporting of intravascular optical coherence tomography studies: a report from the international working group for intravascular optical coherence tomography standardization and validation. J Am Coll Cardiol. 2012;59(12):1058–72.
2. Tuzcu EM, Kapadia SR, Tutar E, Ziada KM, Hobbs RE, McCarthy PM, et al. High prevalence of coronary atherosclerosis in asymptomatic teenagers and young adults: evidence from intravascular ultrasound. Circulation. 2001;103(22):2705–10.
3. Pignoli P, Tremoli E, Poli A, Oreste P, Paoletti R. Intimal plus medial thickness of the arterial wall: a direct measurement with ultrasound imaging. Circulation. 1986;74(6):1399–406.
4. Kume T, Akasaka T, Kawamoto T, Watanabe N, Toyota E, Neishi Y, et al. Assessment of coronary intima–media thickness by optical coherence tomography: comparison with intravascular ultrasound. Circ J. 2005;69(8):903–7.
5. Yabushita H, Bouma BE, Houser SL, Aretz HT, Jang IK, Schlendorf KH, et al. Characterization of human atherosclerosis by optical coherence tomography. Circulation. 2002;106(13):1640–5.
6. Kume T, Okura H, Kawamoto T, Akasaka T, Toyota E, Watanabe N, et al. Relationship between coronary remodeling and plaque characterization in patients without clinical evidence of coronary artery disease. Atherosclerosis. 2008;197(2):799–805.
7. Kume T, Okura H, Kawamoto T, Yamada R, Miyamoto Y, Hayashida A, et al. Assessment of the coronary calcification by optical coherence tomography. EuroIntervention. 2011;6(6):768–72.
8. Virmani R, Kolodgie FD, Burke AP, Farb A, Schwartz SM. Lessons from sudden coronary death: a comprehensive morphological classification scheme for atherosclerotic lesions. Arterioscler Thromb Vasc Biol. 2000;20(5):1262–75.
9. Vancraeynest D, Pasquet A, Roelants V, Gerber BL, Vanoverschelde JL. Imaging the vulnerable plaque. J Am Coll Cardiol. 2011;57(20):1961–79.
10. Cheruvu PK, Finn AV, Gardner C, Caplan J, Goldstein J, Stone GW, et al. Frequency and distribution of thin-cap fibroatheroma and ruptured plaques in human coronary arteries: a pathologic study. J Am Coll Cardiol. 2007;50(10):940–9.
11. Kume T, Okura H, Yamada R, Kawamoto T, Watanabe N, Neishi Y, et al. Frequency and spatial distribution of thin-cap fibroatheroma assessed by 3-vessel intravascular ultrasound and optical coherence tomography: an ex vivo validation and an initial in vivo feasibility study. Circ J. 2009;73(6):1086–91.
12. Kume T, Akasaka T, Kawamoto T, Okura H, Watanabe N, Toyota E, et al. Measurement of the thickness of the fibrous cap by optical coherence tomography. Am Heart J. 2006;152(4):755 e1–4.

13. Fujii K, Kawasaki D, Masutani M, Okumura T, Akagami T, Sakoda T, et al. OCT assessment of thin-cap fibroatheroma distribution in native coronary arteries. JACC Cardiovasc Imaging. 2010;3(2):168–75.

14. Tearney GJ, Yabushita H, Houser SL, Aretz HT, Jang IK, Schlendorf KH, et al. Quantification of macrophage content in atherosclerotic plaques by optical coherence tomography. Circulation. 2003;107(1):113–9.

15. Kolodgie FD, Gold HK, Burke AP, Fowler DR, Kruth HS, Weber DK, et al. Intraplaque hemorrhage and progression of coronary atheroma. N Engl J Med. 2003;349(24):2316–25.

16. Virmani R, Kolodgie FD, Burke AP, Finn AV, Gold HK, Tulenko TN, et al. Atherosclerotic plaque progression and vulnerability to rupture: angiogenesis as a source of intraplaque hemorrhage. Arterioscler Thromb Vasc Biol. 2005;25(10):2054–61.

17. Burke AP, Farb A, Malcom GT, Liang YH, Smialek J, Virmani R. Coronary risk factors and plaque morphology in men with coronary disease who died suddenly. N Engl J Med. 1997;336(18):1276–82.

18. Vorpahl M, Nakano M, Virmani R. Small black holes in optical frequency domain imaging matches intravascular neoangiogenesis formation in histology. Eur Heart J. 2010;31(15):1889.

19. Tian J, Hou J, Xing L, Kim SJ, Yonetsu T, Kato K, et al. Significance of intraplaque neovascularisation for vulnerability: optical coherence tomography study. Heart. 2012;98(20):1504–9.

20. Uemura S, Ishigami K, Soeda T, Okayama S, Sung JH, Nakagawa H, et al. Thin-cap fibroatheroma and microchannel findings in optical coherence tomography correlate with subsequent progression of coronary atheromatous plaques. Eur Heart J. 2012;33(1):78–85.

21. Kume T, Akasaka T, Kawamoto T, Ogasawara Y, Watanabe N, Toyota E, et al. Assessment of coronary arterial thrombus by optical coherence tomography. Am J Cardiol. 2006;97(12):1713–7.

22. Kume T, Okura H, Fukuhara K, Koyama T, Nezuo S, Neishi Y, et al. A unique feature of thin flat thrombus visualised by optical coherence tomography. EuroIntervention. 2013;9(8):1008.

23. Hou J, Jia H, Liu H, Han Z, Yang S, Xu C, et al. Neointimal tissue characteristics following sirolimus-eluting stent implantation: OCT quantitative tissue property analysis. Int J Cardiovasc Imaging. 2012;28(8):1879–86.

24. Gonzalo N, Serruys PW, Okamura T, van Beusekom HM, Garcia-Garcia HM, van Soest G, et al. Optical coherence tomography patterns of stent restenosis. Am Heart J. 2009;158(2):284–93.

25. Kume T, Akasaka T, Kawamoto T, Watanabe N, Toyota E, Sukmawan R, et al. Visualization of neointima formation by optical coherence tomography. Int Heart J. 2005;46(6):1133–6.

26. Nagai H, Ishibashi-Ueda H, Fujii K. Histology of highly echolucent regions in optical coherence tomography images from two patients with sirolimus-eluting stent restenosis. Catheter Cardiovasc Interv. 2010;75(6):961–3.

Basic Interpretation Skills

Tom Adriaenssens

Abstract

Due to its capacity to provide ultra-high detail images in an in vivo setting, intracoronary optical coherence tomography (OCT) has been adopted enthusiastically by the interventional community. For the individual operator, confronted with a set of >200 cross-sectional images after acquisition of a single pullback, sound knowledge of essential aspects of the images is indispensable, as well as appropriate skills for optimal acquisition of OCT images. In this chapter, we present a step by step approach that will help operators to plan the procedure properly, provide high quality OCT pullbacks and gain confidence in systematic and correct image interpretation. Key to interpretation success is the recognition of specific findings, both in the setting of assessing coronary artery disease, as well as studying results after percutaneous coronary intervention and stent or scaffold implantation. Due to important differences in optical characteristics between different components of the vessel wall in healthy and diseased states, different components of atherosclerotic disease (such as fibrous plaques, fibrocalcific plaques and fibroatheromas) can be readily discriminated. Finally, we discuss strengths and limitations of the current technology, and possible pitfalls and artifacts that might carry a risk of over- or misinterpretation.

Keywords

Optical coherence tomography • Acquisition quality • Image interpretation • Fibrous plaque • Calcified plaque • Fibroatheroma

4.1 Introduction

The unsurpassed detail of intracoronary OCT images leads to an increasing use of this relatively young technology in the cardiac catheterization laboratory, both for research and clinical purposes [1]. Although currently available Fourier domain OCT imaging systems have proven their safety, reliability and ease of use, the development of a high level clinical OCT program in the hospital setting poses some challenges as well [2]. With its enormous potential to influence further decision making during diagnostic and interventional procedures, it is critical that operators gain appropriate skills in optimal image acquisition and a solid experience in correct image interpretation, as in many cases, they will be the key responsible person for the correct implementation of OCT in a particular invasive procedure.

Basically, OCT can be used in the clinical setting whenever the operator feels the information obtained by OCT would offer a valuable addition to the angiographic images or physiologic information obtained. Confronted with hazy lesions on angiography, OCT is able to discriminate between intracoronary thrombus, calcification or ulceration [3–5]. In the setting of acute coronary syndrome (ACS) with unclear culprit lesion site, OCT is often able to unravel the culprit mechanism [6, 7]. Due to its capacity to discriminate between different types of vulnerable plaques, such as thin-capped fibroatheroma (TCFA) rupture, plaque

T. Adriaenssens, MD, PhD
Cardiovascular Medicine, University Hospitals Leuven,
Herestraat 49, Leuven 3000, Belgium
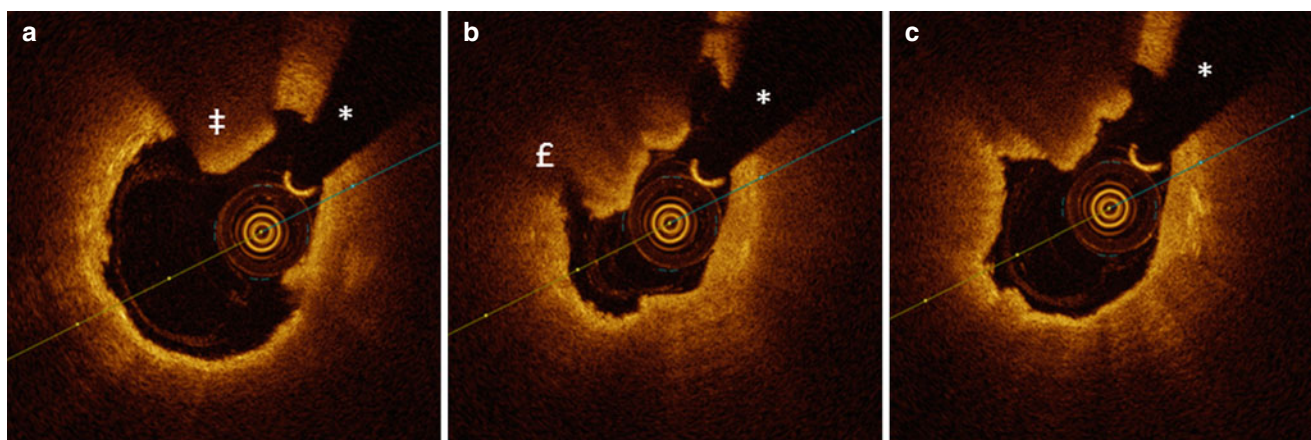e-mail: tom.adriaenssens@uzleuven.be

Fig. 4.1 Ruptured thin-capped fibroatheroma. Consecutive OCT frames in a 73-year-old male patient presenting with anterior STEMI (ST elevation myocardial infarction). After thrombus aspiration, adequate image quality could be obtained. At the culprit lesion site, a thin-capped fibroatheroma (TCFA) was identified. In most cases of ruptured vulnerable plaque causing acute coronary syndrome, there is a varying degree of thrombus accumulation involved. It is not always easy or even possible to discriminate between remnants of the ruptured plaque and thrombus. In panel **a**, a highly backscattering structure with strong attenuation properties is observed at 12 o'clock, compatible with a red thrombus (*double dagger*). In the adjacent frames, the exact site of TCFA rupture becomes evident (panel **b**, indicated by '£' at 10 o'clock). In panel **c**, an image with mixed TCFA characteristics (4–11 o'clock) and possible red thrombus superposition can be observed. The *asterisk* is indicating the guide wire artifact

erosion and calcified nodule, it offers the perspective of a tailored approach towards the individual patient with an ACS [3, 8]. With respect to the assessment of intermediate lesions, the lack of information on functional significance must be balanced against the value of obtaining accurate lumen areas and plaque composition information. In the setting of serial coronary lesions, where functional testing with fractional flow reserve (FFR) is hampered by the influence of proximal on more distal lesions and vice versa, OCT can be of important value for proper diagnosis and intervention planning [9, 10]. There is a separate chapter in this book on the acute effects after stent implantation and the potential of OCT to optimize the acute results of PCI. On the other hand, in the setting of stent failure, such as in-stent restenosis and particularly stent thrombosis, OCT is of great value for correct determination of the mechanisms involved and for adequate guidance of therapy, as will be discussed in Chap. 12.

Apart from not obtaining the informed consent of the patient, there are only few and relative contraindications to the procedure. As the acquisition of an OCT run necessitates the use of around 12–16 ml of contrast medium, care should be taken to avoid excessive contrast administration to the patient, especially when renal or cardiac function is impaired. It is usually very easy to advance the OCT imaging catheter to a distal position in the coronary artery. In the setting of extremely tortuous or calcified vessels, however, this may be challenging. While adjunctive tools such as an extra-support wire or a child-in-a-mother catheter can help to achieve the desired position of the imaging catheter, the operator should refrain from too forceful pushing on the imaging device, as this might cause damage to the imaging catheter or the vessel. The imaging catheter and the accompanying imaging wire starting to separate from each other on angiography, indicates the appropriate moment to relief pressure. Inherent to the use of current generation Fourier Domain OCT systems, the coronary guide wire is causing an artefact precluding assessment of a small sector of the cross section image. The operator should in all cases refrain from retracting the guidewire with the imaging catheter still in place. Such maneuver might lead to kinking and entrapment of the catheter, with potentially serious complications. Final challenges are the assessment of critically or subtotally narrowed lesions, where introduction of the imaging catheter might occlude blood flow in the coronary artery, as well as aortic junctional lesions, with the associated difficulty in engaging the guiding catheter correctly. The imaging catheter occluding the blood flow leads to ischemia in the distal myocardial territory and precludes adequate blood clearance, and hence proper image quality, in the distal part of the vessel. Although there are certain tricks to manage this issues, the assessment of subocclusive and aortic junctional lesions is considered a limitation of the technology [11].

In contrast to histopathologic assessment, which can rely on morphologic examination and additional immunologic and histochemical analysis, the OCT image is generated from the optical characteristics of the tissue and the transition between different layers of tissue [12, 13]. The currently commercially available OCT systems offer no further tools for tissue characterization. Although it is possible in most of the cases and frames to make a clear diagnosis with OCT, there will be uncertainty in selected frames, where no definite diagnosis can be made based on the OCT image. An example of this is the differentiation of thrombus from tissue flaps in the setting of ruptured TCFA (Fig. 4.1).
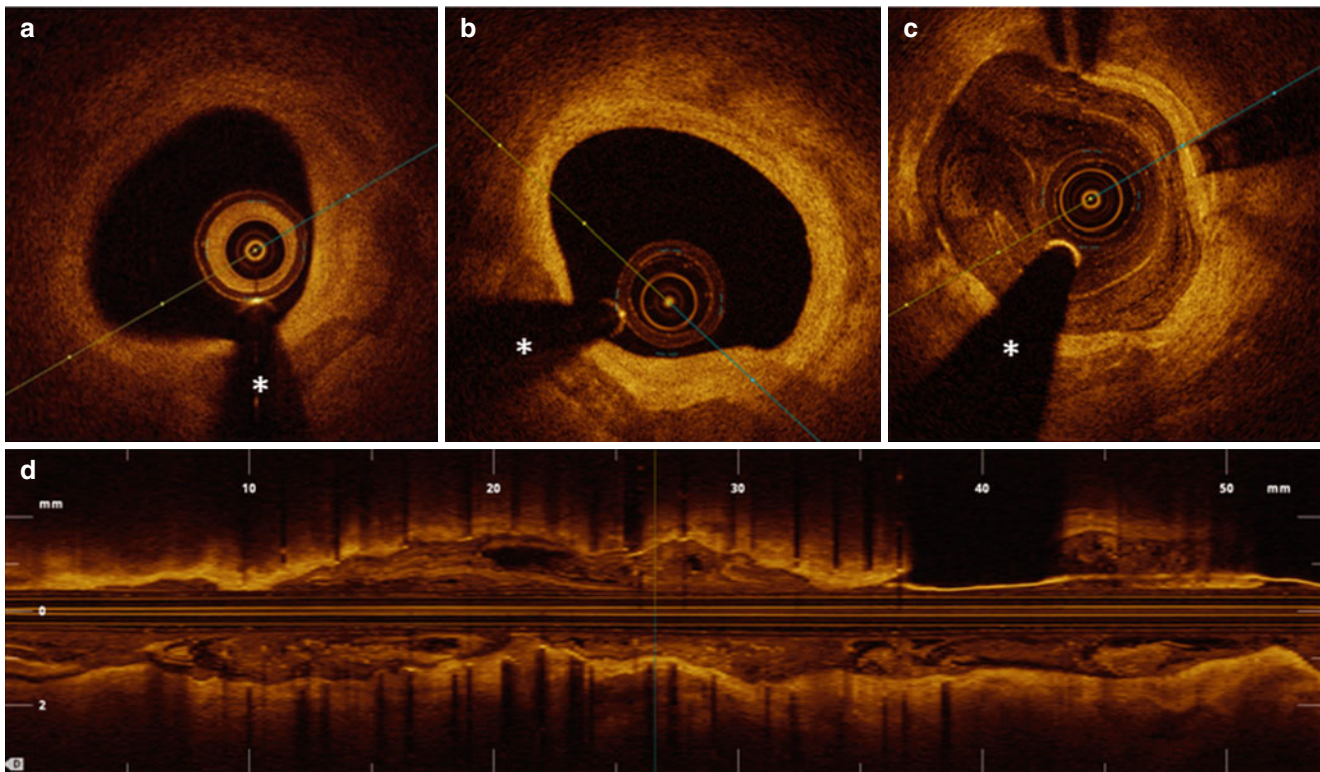
Fig. 4.2 Insufficient quality pullbacks. One of the most common sources of decreased image quality in OCT pullbacks, is the accumulation of blood between the different plastic layers of the imaging catheter, obscuring all emitted light from the laser source due to the strong attenuating capacity of the red blood cells. The imaging catheter should be flushed with a small volume of pure contrast after unpacking. Even after positioning the imaging catheter in the blood vessel for a short period of time, blood accumulation between the different layers of the catheter can occur. It is therefore strongly recommended to check for the presence of blood accumulation in the catheter before starting the pullback run. If blood is detected, it is necessary to flush the catheter again. This must be done without active stationary scanning of the laser lens, as such might lead to damage to the catheter in some instances. In panels **a** and **b**, images acquired at the same site in the coronary artery with bad vs. good catheter flush are depicted, respectively, illustrating the important loss in image quality if no adequate attention is paid to this aspect of image acquisition. Panel **c** (cross sectional view) and **d** (longitudinal view) show images of an OCT acquisition with insufficient clearance of the lumen from blood. In such cases, suboptimal positioning of the guiding catheter or inadequate contrast flush speed can be identified as the cause of insufficient clearance and can be corrected for. In some cases, such as large vessels with big diameter side branches, or in the setting of a tight lesion limiting adequate blood clearance in the distal vessel territory, it is –even with maximal operator effort- impossible to achieve optimal clearance of blood. The *asterisk* is indicating the guide wire artifact

4.2   Systematic Approach to Image Acquisition and Interpretation

For the correct interpretation of individual OCT studies, we propose a systematic and step by step approach. Non-compliance with these basic principles will potentially lead to a waste of time and resources, associated with extra costs and loss of information and negatively reflect on operator performance and patient safety.

1. Baseline characteristics- To fully exploit the huge amount of information from a set of OCT pullbacks, acquired during an interventional procedure, a clear understanding of the purpose of the examination is essential. These include demographic factors (age, sex…), the clinical presentation, and the information from the angiogram (such as haziness, relation of the segment of interest to angiographic landmarks etc…). It is important always to consider what the particular clinical or research question of the investigation is. For example, specific characteristics such as plaque erosion or spontaneous coronary artery rupture predominantly occur in young females [3, 14]. In the setting of stent thrombosis, the time elapsed since the initial implantation of the device is important for the interpretation of the burden of uncovered struts or adverse neointimal reactions, such as neoatherosclerosis [15].

2. Pullback quality- Before starting the interpretation of an acquisition, it is advised to first perform an initial quality check (which can be done in only a couple of seconds) after which feedback can be given to the operator. In case of important and remediable shortcomings, there is always the possibility to perform a second and better OCT run. Key questions are: (a) is the whole segment of interest represented in the specific acquisition? (b) Was adequate blood clearance of the lumen achieved? (c) Was the imaging catheter adequately cleared from blood and air? (Fig. 4.2) (d) Has appropriate and precise calibration of the imaging catheter been performed for this pullback?
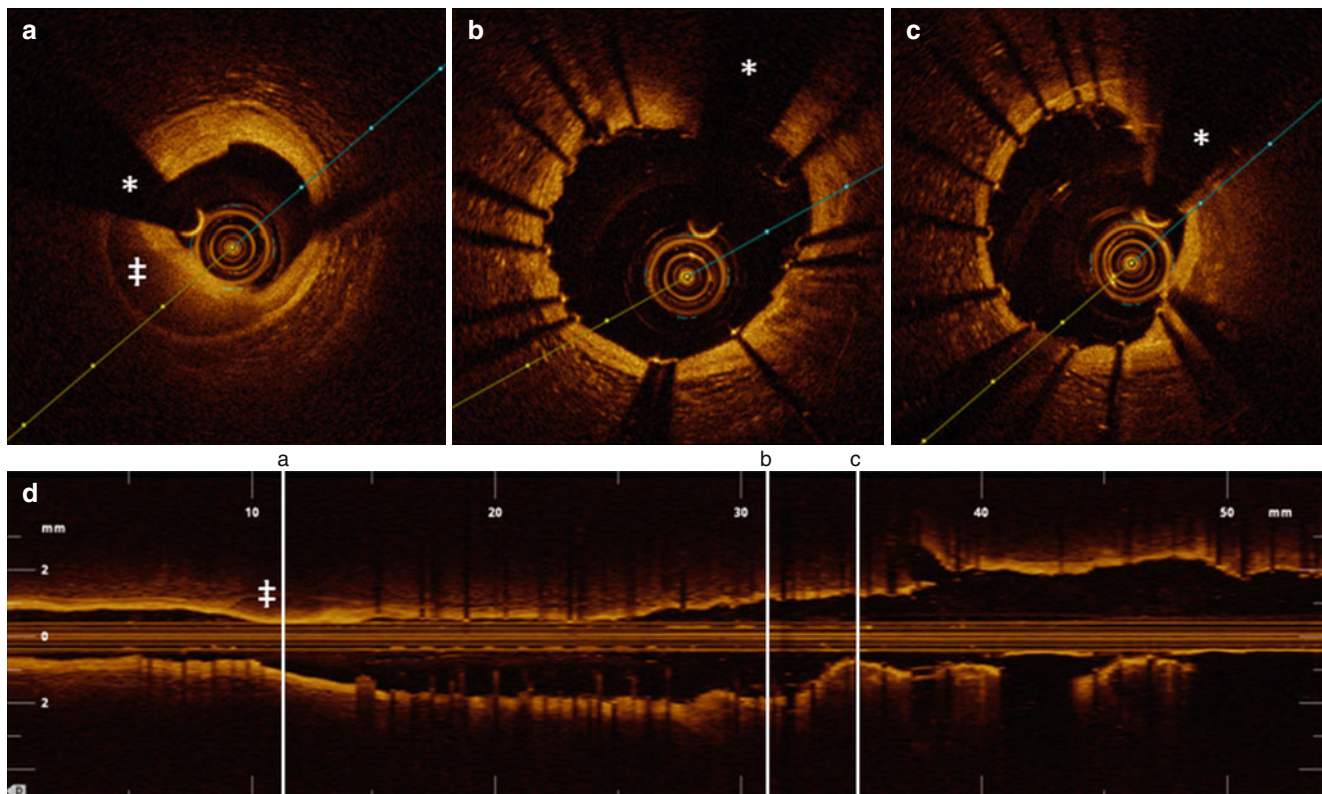
Fig. 4.3 Information obtained from the longitudinal view in OCT pullbacks. OCT acquisition immediately after implantation of two overlapping drug-eluting stents in the mid LAD in a 76-year old male presenting with stable angina. The figure illustrates that with selection of an adequate cutting plane in the longitudinal view, several important observations can already be made before starting a frame by frame analysis of the cross-sectional tomographic images. At the level of the distal stent edge, a zone with strong signal attenuation (indicated with ‡) can be observed. The corresponding cross-sectional image shows a medial dissection with blood accumulation in the vessel wall. In the same longitudinal view, a zone of relative underexpansion can be observed in cross section **c**, compared with better and more symmetrical expansion in panel **b**. Stent areas are 5.6 mm^2 in panel **b** and 4.5 mm^2 in panel **c**. In panel **b**, some malapposed struts can be observed around 2 o'clock, which (after careful inspection), can also be discovered in the longitudinal view. The upper panel figures **a**, **b**, and **c** correspond to **a**, **b**, and **c** with vertical lines on the longitudinal view (*lower panel*). The *asterisk* is indicating the guide wire artifact

3. Longitudinal view- The next step is a general appreciation of the case, based on the longitudinal view of the segment of interest, with selection of an adequate longitudinal cutting plane. The longitudinal view of a pullback is frequently overlooked. However, it usually provides a wealth of information, such as sites of lumen encroachment and their importance, thrombus accumulation and general anatomical information on vessel size, tapering, location of side branches and longitudinal extent of diseased segments. In OCT examinations of stented segments, the longitudinal view can provide important insights on the presence of edge dissections, intramural hematomas and sites of underexpansion or malapposition (Fig. 4.3). Depending on the complexity of the case (such as in the case of a coronary segment with multiple and serial lesions), the longitudinal view of the pullback will be an important help in making a manual registration of the OCT and angiography acquisitions. Awaiting commercially available technology to co-register OCT and angiography pullbacks, the documentation of the position of the imaging catheter at the start of the pullback (or registration of the movement of the optical lens during the pullback) should be advised. Applications for co-registration of angiography and OCT acquisitions will, however, become available soon in software updates from vendors of the technology, which will help focusing on the region of interest and avoid potential mistakes. Furthermore, automatic 3D rendering is emerging and provides additional advantages over the two-dimensional L-view.

4. Images of interest- Finally, a detailed assessment of individual cross-sections of interest can be made. Apart from quality characteristics already discussed before, attention should be paid to the position of the catheter with respect to the specific frame of interest. Certain artifacts can be caused by an eccentric position
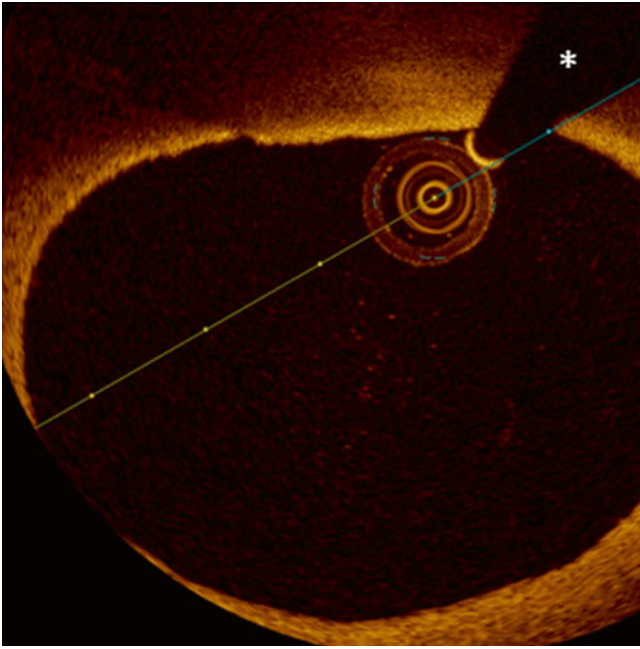
Fig. 4.4 Tangential drop out artifact. In this figure, the eccentric position of the imaging catheter creates an image resembling TCFA at 11–12 o'clock. Although the presence of a lipid pool cannot be excluded, the signal poor area under the thin layer of more intense signal tissue is probably caused by very tangential interrogation of this part of the vessel wall by the laser light. The *asterisk* is indicating the guide wire artifact

of the imaging catheter. As it can lead to the mis- and overdiagnosis of thin-capped fibroatheroma (TCFA), the most important artifact to consider is tangential drop-out [16]. The main characteristic is that the tangential interaction of the light beam with the vessel wall leads to a loss of lateral resolution and the attenuation of the light beam traveling through the vessel wall almost parallel to the luminal border, creating an image closely resembling a thin-capped fibroatheroma (Fig. 4.4). We refer to Chap. 5 for a more detailed description.

5. Lumen morphology- The interpretation at the frame level starts with the appreciation of the lumen area and lumen contour. Is lumen area decreased compared to what would be expected from the reference area in a normal part of the vessel? Has the lumen contour a normal round shape or is there encroachment from the diseased vessel wall? Is the lumen contour regular or irregular? These irregularities most often are small intraluminal thrombi (to be differentiated from insufficient clearance of blood), but small indentations can be observed in lesions with important superficial calcification as well (Fig. 4.5).

Can the normal three-layered appearance (intima-media-adventitia) be recognized circumferentially in the frame? If not, it should be described in which sector this specific pattern is lost.
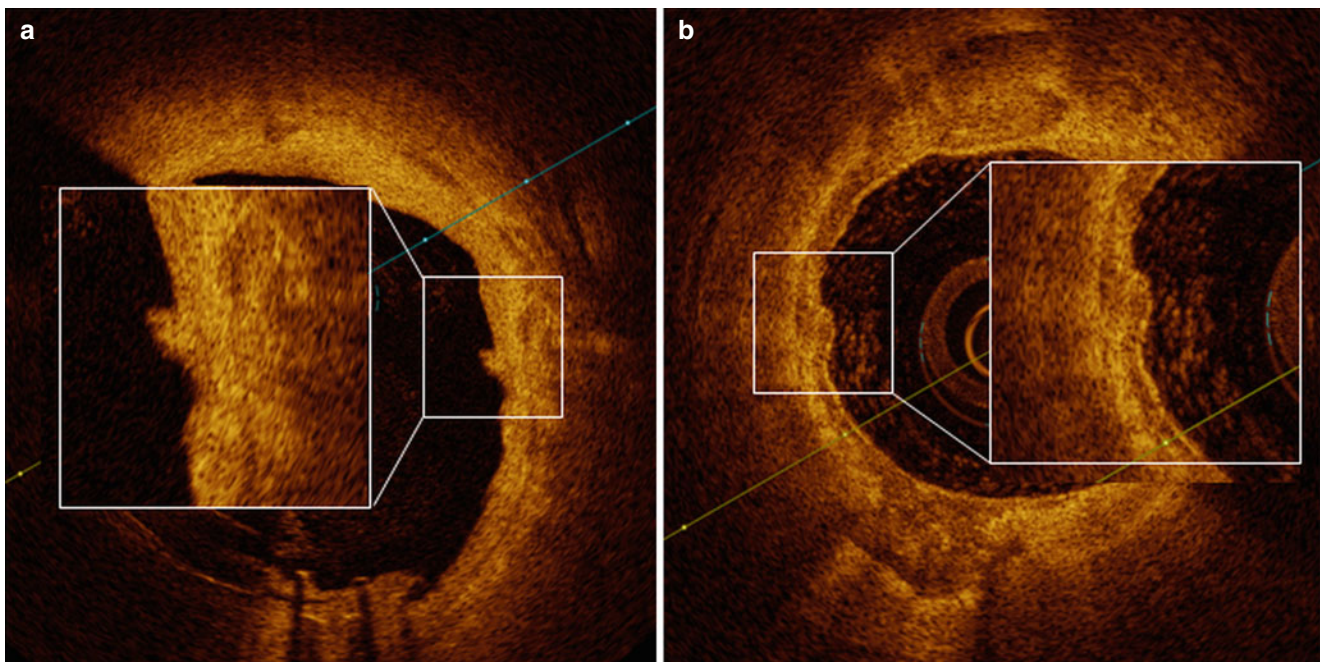

Fig. 4.5 Lumen irregularities. In panel **a**, a small lumen irregularity with low attenuating property is observed around 3 o'clock (magnified). In panel **b**, large and almost circumferential calcium accumulation is observed. Around 9 o'clock (magnified), there is a small protrusion of calcium into the lumen
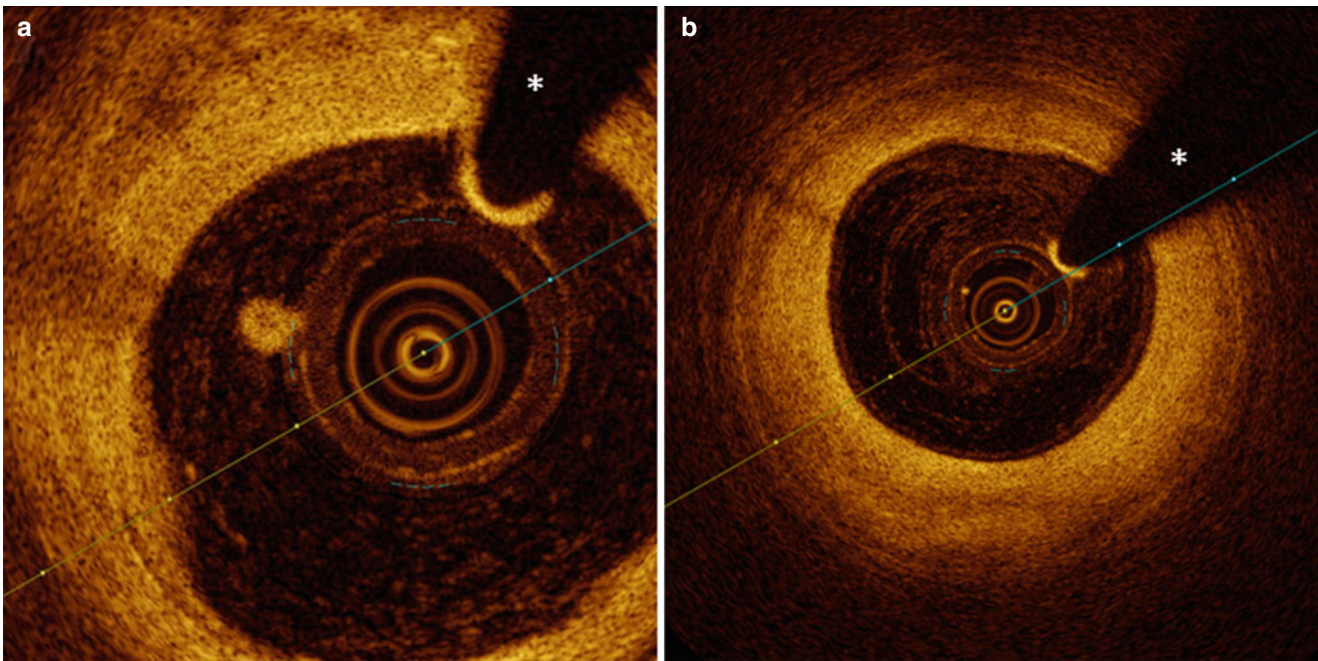
Fig. 4.6 Small luminal adhesions. In panel **a**, a small accumulation of fibrin or blood platelet-rich white thrombus adheres to the imaging catheter and casts a shadow on the underlying vessel wall between 9 and 10 o'clock. In panel **b**, equally around 10 o'clock, a small impurity in the outer plastic sheath of the catheter can be observed, casting a very fine shadow. The *asterisk* is indicating the guide wire artifact

6. Vessel wall- If any abnormal pattern in the lumen or the vessel wall is encountered, it is important to check the trajectory between this particular finding and the center of the imaging catheter. Any abnormality (such as blood or air bubbles in the catheter or thrombus around the imaging catheter or the coronary wire) can cast a shadow on the underlying vessel wall, which sometimes leads to misinterpretation (Fig. 4.6).

   In cases where the normal three-layered aspect of the vessel wall is lost, a systematic approach to describing various states of disease should be used. Key determinants are the intensity of the backscattered light signal, the demarcation between layers with different optical characteristics and the attenuation characteristics of the tissue. Careful attention to these characteristics can almost uniformly discriminate between fibrous, fibrocalcific, lipid plaques and all mixed forms. [13]

   For the interpretation of specific structures, a profound knowledge of the optical characteristics, the pathophysiology of the coronary artery and particularities of different invasive treatment options is required.

   Often, a single frame does not offer reliable insights into a problem at once. It is strongly advised to scroll between adjacent frames before making conclusions.

7. Image quantification- Together with the interpretation of OCT images, measurement of the lumen or stent area and of specific structures is often required. Accuracy of all measurements relies on a careful calibration of the imaging catheter, a frequently overlooked issue [17]. Even small insufficiencies in correct calibration can lead to important deviations in measurements. It is important to mention that catheter calibration can be corrected off-line as well.

8. Multiple frames- In some cases, particular findings can only be observed in a limited number of frames. It could be worthwhile to repeat the acquisition with slower pullback speed, in order to acquire a higher number of frames and enhance sampling in the longitudinal direction.

9. Pullback information- The recording of the findings of the case (including vessel and segment studied, information whether thrombectomy or predilatation was performed) is strongly advised so that later interpretation is not hampered by a lack of crucial information.

Report Form
1. Administrative data (age, sex)
2. Clinical presentation
3. Indication for the examination:
   Diagnosis making, PCI optimization, stent failure (stent thrombosis, in stent restenosis)
4. Pullback vessel-location, pullback length and speed, flush (manual vs. automatic), flush type of contrast (speed, volume)
5. Quality
6. Complications
7. Particular findings (artifacts…)
8. Main finding
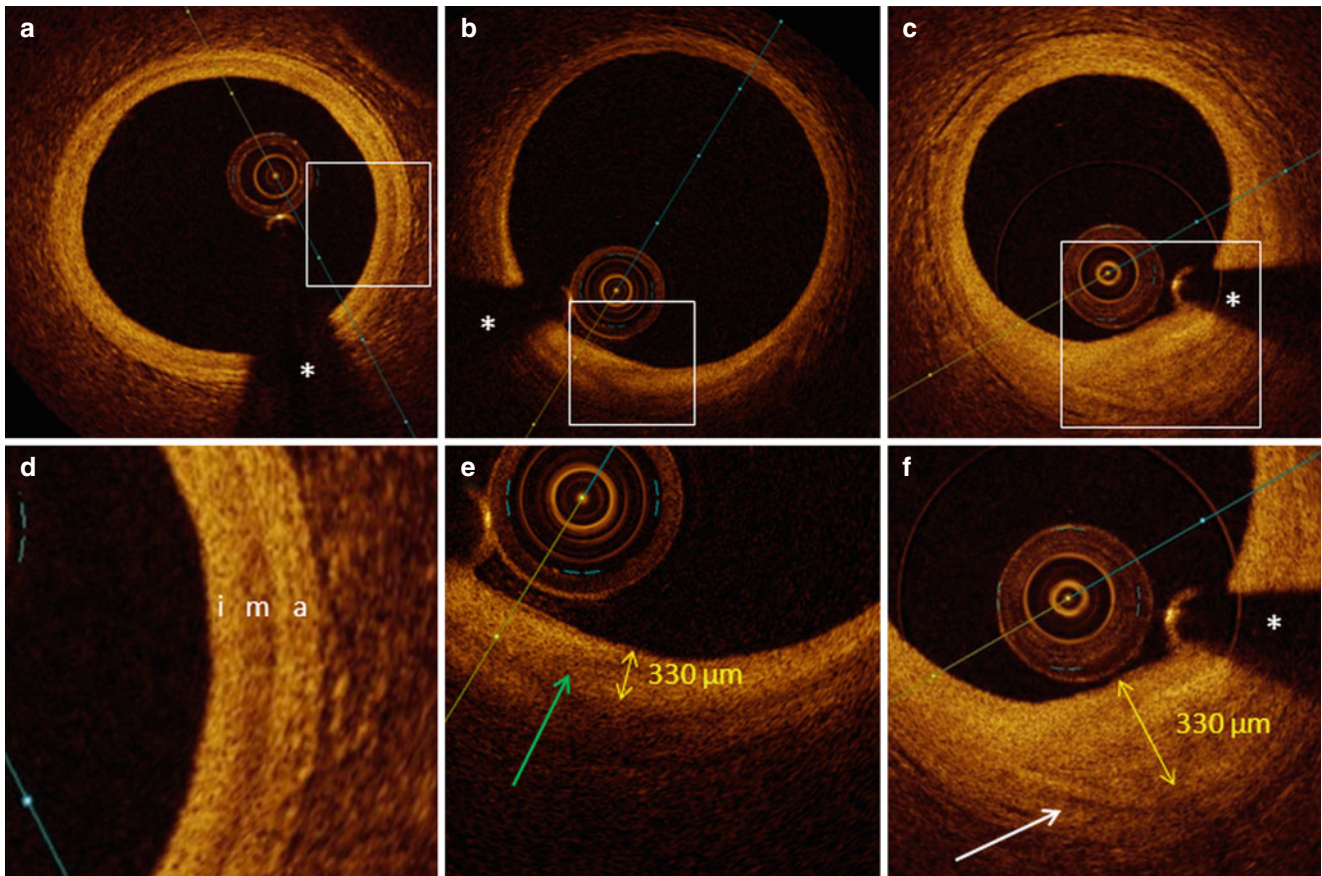9. Impact (did OCT acquisition change practice in this particular patient)

Fig. 4.7 Normal vessel wall, intimal thickening and fibrous plaque. In panel **a** (with magnification in panel **d**), the typical three-layered structure of the vessel wall is visualized, with a thin highly backscattering intima (*i*), a more signal poor media (*m*), which can present with slightly varying thickness and a highly backscattering adventitia (*a*). In panel **b** (magnification in panel **e**), a region with intimal thickening is described between 6 and 7 o'clock. The intimal thickness (measured from the luminal border to the beginning of the media) is 330 μm. The *green arrow* is indicating a zone with lower signal intensity within the region of intimal thickening, compatible with beginning lipid deposition. In panel **c** (magnification in panel **f**), a fibrous plaque is shown. Due to the poorly attenuating properties of the fibrous plaque, it is still possible to see the media bordering the fibrous plaque (*white arrow*) (distance from luminal border to media is 850 μm). The *asterisk* is indicating the guide wire artifact

4.3   OCT Characteristics of Coronary Artery Disease

For discriminating specific OCT characteristics of atherosclerotic disease, we offer a description that follows the classification as described in the first consensus document of the International Working Group for Intravascular Optical Coherence Tomography Standardization and Validation [13].

The normal coronary artery wall is recognized by a typical three-layered structure, where intima, media and adventitia can be clearly defined. The intima, the most inner layer of the vessel wall, is characterized as a signal-rich, highly backscattering layer of tissue. It can be very thin, as is usually the case in young individuals. However, with advancing age, the thickness of the intima gradually increases. Although arbitrarily chosen, a thickness of 300 μm is considered as the cut-off between normal intima and intimal thickening. The OCT appearance of such intimal thickening is usually characterized as a homogenous signal rich area. Small areas of lower signal intensity can sometimes be observed, compatible with small lipid accumulations. It is important to remember that intimal thickening is not considered as a state of atherosclerotic disease (Fig. 4.7).

The media is the second layer of the vessel wall and characteristically has a signal-poor intensity, as it is predominantly composed of smooth muscle cells and extracellular matrix. The third layer, the adventitia, is heterogeneous with a highly backscattering first layer and periadventitial tissue that usually has a very loose structure [18, 19].

Fibrous, fibrocalcific and lipid plaques are the manifestations of atherosclerotic disease. Differences in backscattering (the intensity of the back reflected signal) and attenuation properties (the degree by which the intensity of the light signal decreases gradually by scattering and absorption while traveling into deeper tissue layers) are different between these various types of plaques.

A fibrous plaque, also described as pathologic intimal thickening, is described as a homogeneous highly
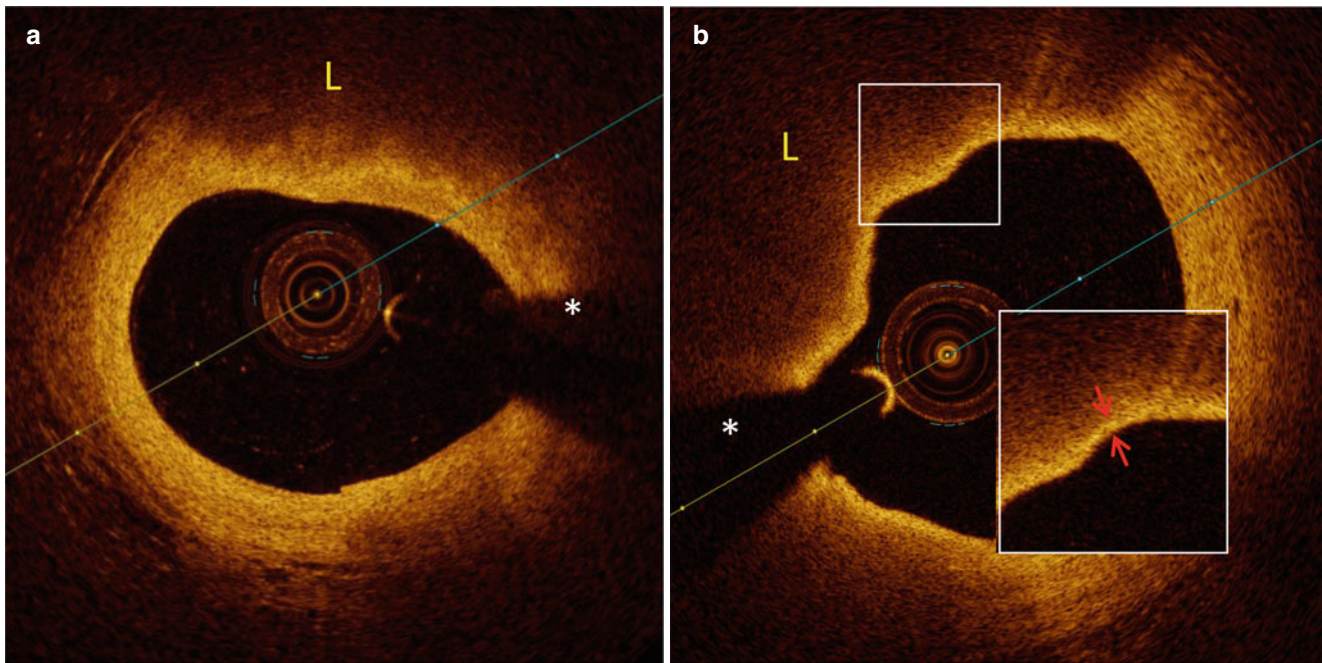
Fig. 4.8 Thick- and thin-capped fibroatheroma. In panel **a**, a thick-capped fibroatheroma is demonstrated as a signal poor, strongly attenuating region from 11 to 3 o'clock, compatible with lipid occumulation (indicated with *L*). In panel **b**, a thin cap fibroatheroma is present from 6 to 1 o'clock, representing a lipid arc of over 180°. At its thinnest point, the fibrous cap (*red arrows*) (magnification in insert) is measuring only 70 μm. The *asterisk* is indicating the guide wire artifact

backscattering region. An intimal thickness of 600 μm is considered as the cut-off between normal and pathologic intimal thickening. Although some lipid or calcified content can be observed in fibrous plaques, these should not occupy more than 1 quadrant. Due to the low attenuation properties of fibrous plaques, it is often possible to visualize the media through the fibrous plaque.

Fibroatheromas are plaques containing lipid pools covered by a fibrous cap. This cap can be thick (thick cap fibroatheroma) or thin (thin-capped fibroatheroma, TCFA) (Fig. 4.8). It is generally accepted that a thin cap overlying a lipid pool, together with the presence of inflammatory cells, is the hallmark of a vulnerable plaque (this means a plaque that is prone to rupture, thus causing an acute coronary syndrome or sudden cardiac death). A fibroatheroma is considered to be present when the lipid pool/necrotic core exceeds >1 quadrant. It is generally agreed upon that lipid accumulation in ≥2 quadrants is required to comply with the definition of TCFA. According to histopathologic definitions, 65 μm has been the historically accepted cut-off to discriminate between thin and thick-capped fibroatheroma. Although challenged by several publications advocating higher cut-off values, this cut-off is still accepted in OCT assessment of fibroatheroma and vulnerable plaques, pending further evidence and consensus in the community [20, 21]. It should be acknowledged as well that there is important interobserver variability in these measurements, especially for choosing the frame with the lowest cap thickness. The typical not sharply demarcated delineation between the fibrous cap and the underlying lipid core adds to the variability in the measurements. In the setting of acute coronary syndrome due to TCFA rupture, a variable amount of (usually red) thrombus is present in the frames of interest, often obscuring parts of the vessel wall with important disease involvement.

The transition between the overlying fibrous cap (with a high intensity signal) and the underlying lipid pool (a signal-poor region due to strong attenuation) is typically smooth and diffusely demarcated. Pathologically, necrotic cores are considered an advanced stage of lipid pools, after destruction of the extracellular matrix. In OCT images, the difference between lipid pool and necrotic core is not easy to make. Due to their content of debris, necrotic cores are thought to have faster signal drop-off than lipid pools due to a slightly higher optical attenuation coefficient [13].

The presence of lipid pools is often overinterpreted. A very thick fibrous intima, causing strong attenuation, may falsely lead to the suspicion of underlying lipid accumulation. The same mistake can be made when the imaging catheter is located far away from the interrogated area. It must be emphasized that the capacity of OCT to detect lipid plaques is at its best close to the lumen border. The larger the distance between the imaging source and the vessel wall, the higher the degree of lipid plaques being misclassified as fibrous ones [18, 22, 23].
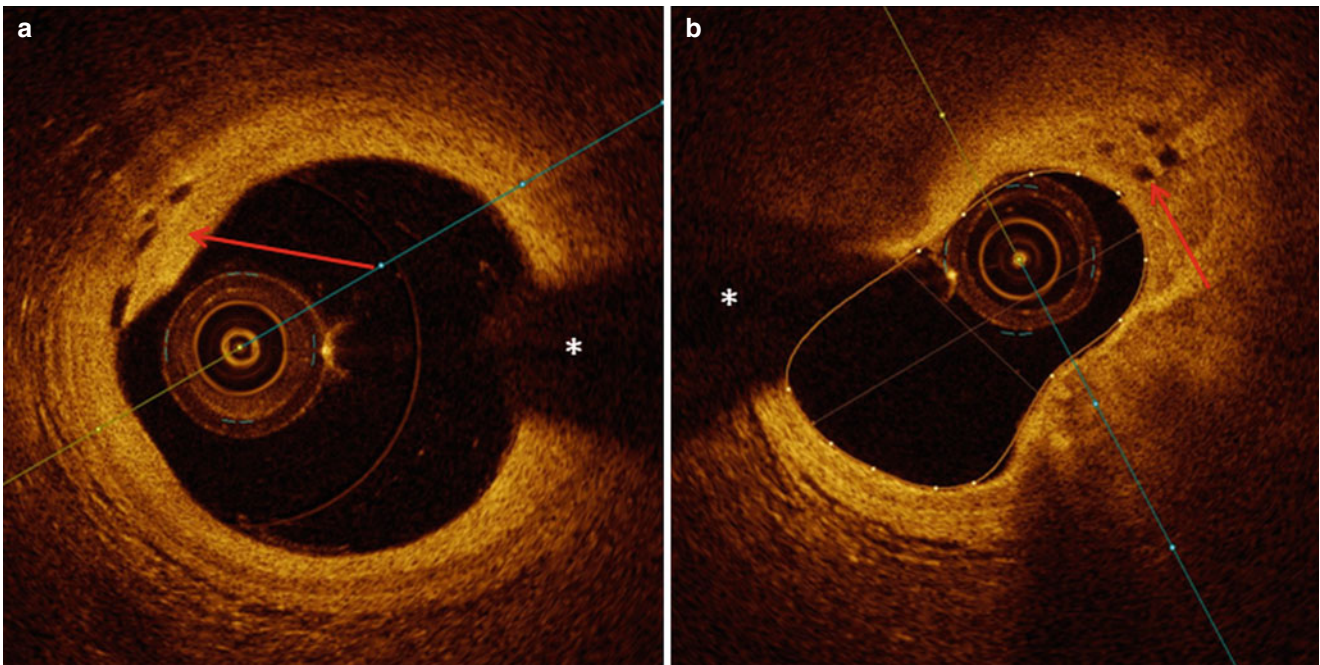
Fig. 4.9 Microvessels. Microvessels representing *round to oval shaped* structures with black content, indicated with *red arrows* and occurring in the setting of intimal thickening (panel **a**) and fibrocalcific plaque (panel **b**). The *asterisk* is indicating the guide wire artifact
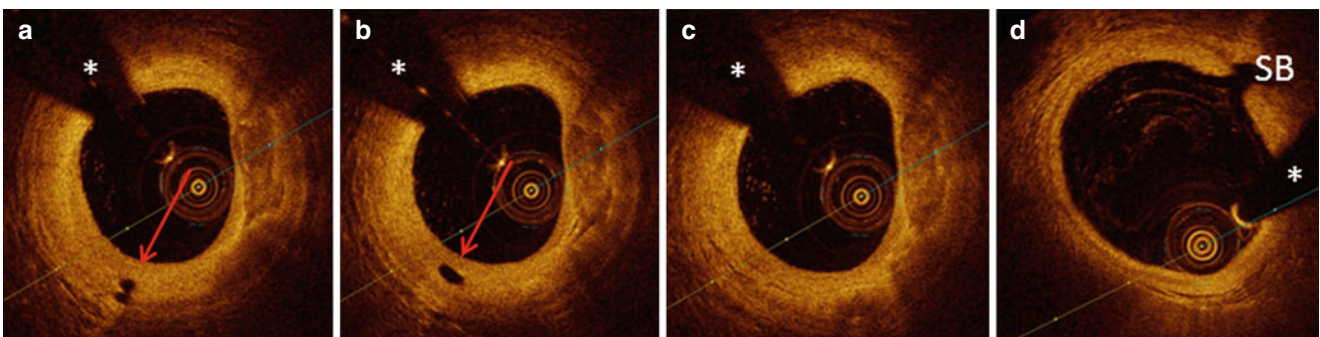

Fig. 4.10 Discrimination between microvessels (*red arrows*) and side branches. Microvessels typically grow in from the periadventitial vessels towards the media and intima, not transversing the luminal border

(7 o'clock panel **a–c**). Panel **d** is showing a sidebranch (SB) coming into the lumen around 2 o'clock. The *asterisk* is indicating the guide wire artifact

With gradually increasing size of the plaque volume, nurturing vessels, known as microvessels, can be observed growing from the adventitia into the inner layers of the vessel wall and the plaque. As these microvessels communicate with the periadventitial vasculature and eventually with the lumen of the coronary artery, their blood content is flushed during an OCT pullback. Therefore, microvessels appear as round or oval shaped (depending if they are cut in a cross-sectional or longitudinal fashion) structures with luminal content comparable to the blood vessel lumen. Microvessels are usually relatively small in size (Fig. 4.9). To discriminate larger microvessels from small side branches, inspection of adjacent frames will show side branches coming in from the vessel lumen and microvessels typically not transversing the intima (Fig. 4.10).

Another characteristic of vulnerable lesions is the presence of macrophages. These are inflammatory cells located in the fibrous tissue covering a fibroatheroma, often occurring in clusters. Due to their high backscatter and attenuation characteristics, macrophages are visualized in OCT images as highly intense structures casting a very dark shadow (Fig. 4.11) [24, 25]. Macrophages can occur isolated and more spread or clustered together, appearing as single dots or bands of highly reflecting tissue, respectively. The strong attenuating properties of macrophage collections cause the casting of a laterally sharply demarcated shadow. This is a typical characteristic which can help to differentiate a band of macrophages overlying a fibroatheroma from a true TCFA. In case of isolated groups of macrophages, causing multiple thin rays of dark shadows, it is advised to inspect

the inner layer of the vessel wall in the gaps between the shadows, to discriminate a fibrous plaque from a lipid pool.

Calcium has low backscatter and low attenuation properties. Fibrocalcific plaques appear as signal-poor or heterogeneous

Fig. 4.11 Macrophages. A thin layer of macrophages is observed from 7 to 10 o'clock. Macrophages exhibit highly intense backscattering properties (magnified box), casting a dark shadow which is sharply bordered laterally. The *asterisk* is indicating the guide wire artifact

regions with a sharply delineated border. When the calcium accumulation is located superficially and does not extend into the deeper layers of the vessel wall, it is most often possible to visualize its entire thickness by OCT and the backside of the plaque can be identified in such cases as well (Fig. 4.12).
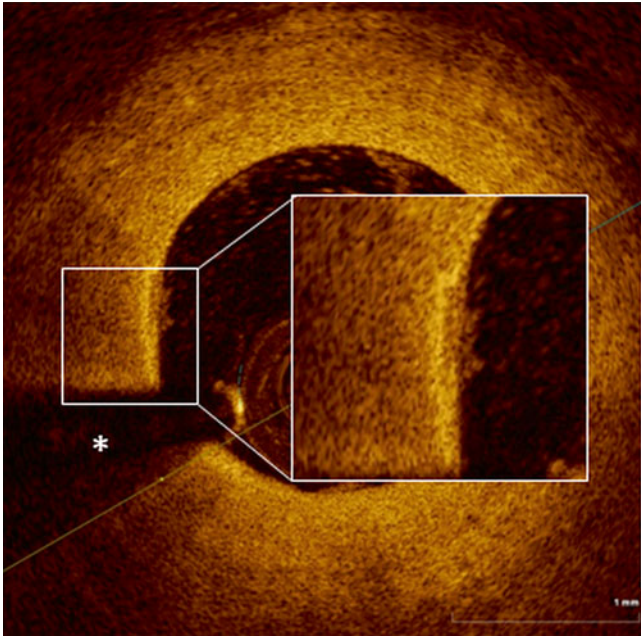
4.4 Acute Coronary Syndrome

Three main categories of vulnerable plaques (which is considered the pathophysiologic substrate for acute coronary syndrome (ACS)) have been described: TCFA with rupture, plaque erosion and calcified nodule, responsible for ACS in 2/3, 1/3 and 1/20 of cases, respectively (Fig. 4.13) [12]. Although not mandatory, small or large intraluminal thrombi are very often observed in the setting of ACS. Thrombi appear on OCT as masses attached to the luminal surface or floating within the lumen. Due to their difference in optical characteristics, it is possible to discriminate between red and white thrombi. Red thrombi contain a lot of red blood cells and demonstrate high backscatter and high attenuation, while white thrombi (rich in white blood cells and blood platelets) show less backscatter and have low attenuation [26]. In many cases, mixed thrombus is present. The strong attenuation by red thrombus precludes any reasonable interpretation of the vessel wall beyond (Fig. 4.14).

It is very important to discriminate intraluminal thrombus from residual blood due to insufficient clearance of the
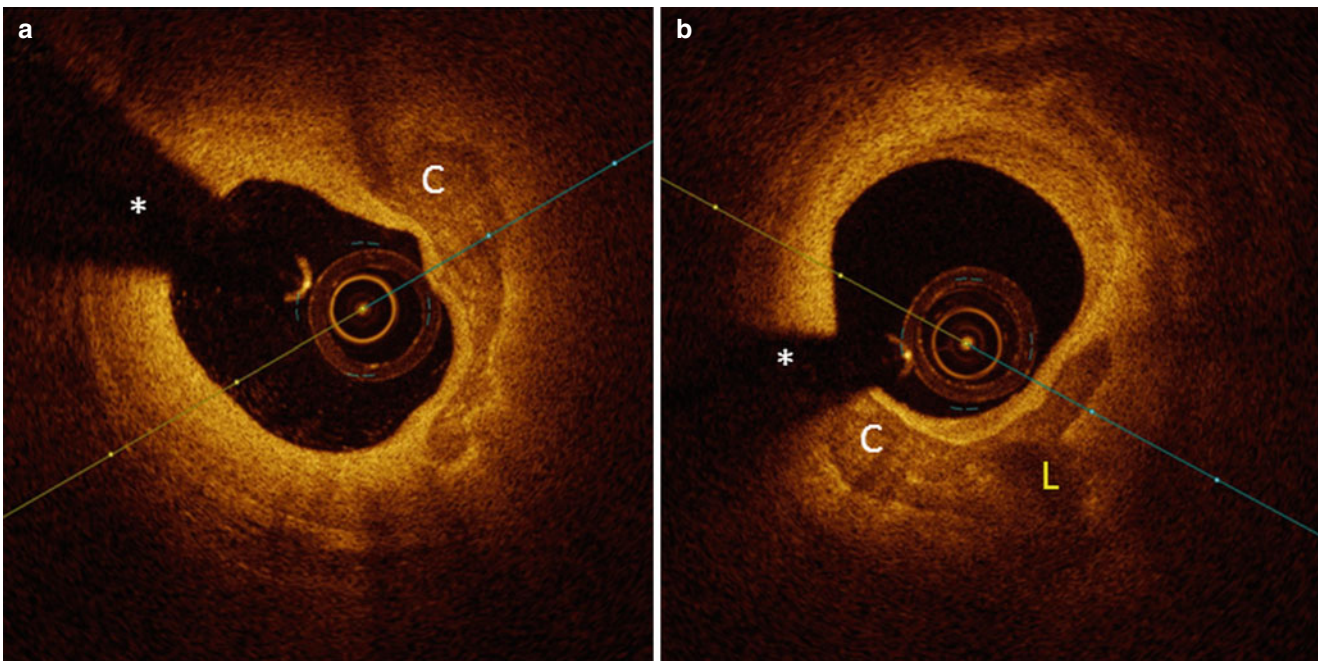

Fig. 4.12 Fibrocalcific and mixed plaque. Sharply demarcated low signal intensity region from 2 to 5 o'clock in panel **a**, compatible with a fibrocalcific plaque. Unless very thick calcium accumulations are present, it is usually possible to visualize the back border of the calcified plaque, due to the weak attenuation properties of calcified tissue. In panel **b**, a calcified plaque (*C*) with some lipidic inclusions (*L*), characterized by stronger attenuation, is present from 4 to 7 o'clock. The *asterisk* is indicating the guide wire artifact
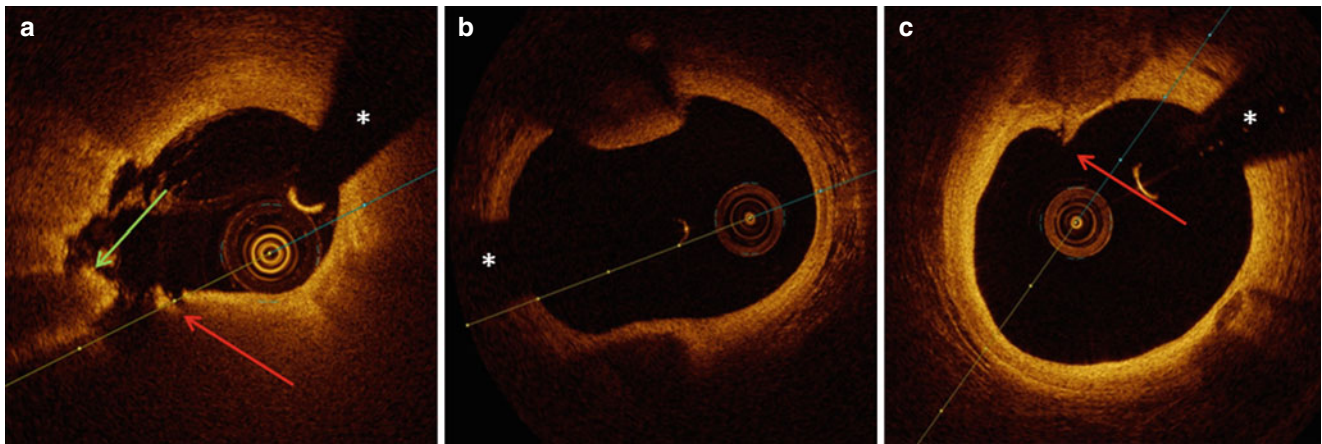
Fig. 4.13 Acute coronary syndrome. Panel **a**: Thin-capped fibroatheroma rupture (the rupture site is indicated with a *red arrow*) with some superimposed thrombus (*green arrow*) around 8 o'clock. Panel **b**: Probable plaque erosion from 11 to 12 o'clock causing acute coronary syndrome in a 64-year old female patient. No signs of lipid pool in the current or adjacent frames. Panel **c**: calcified nodule with penetration into the lumen (*red arrow*) from 11 to 12 o'clock. The *asterisk* is indicating the guide wire artifact
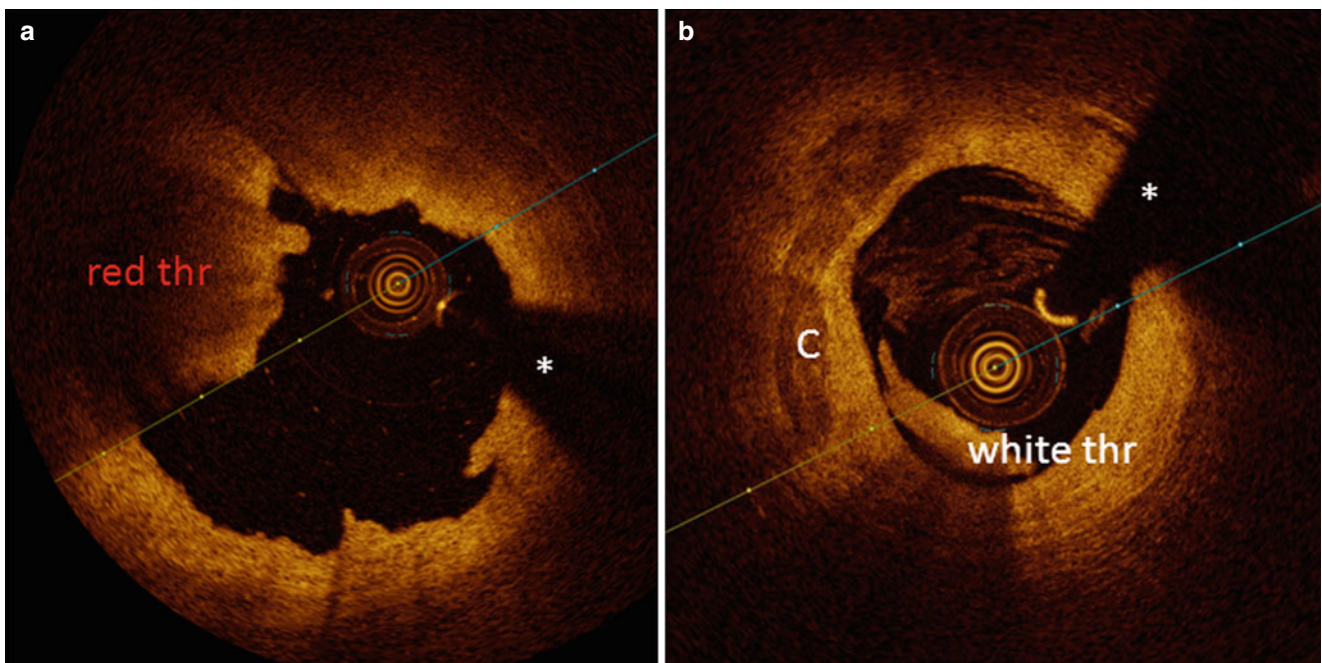

Fig. 4.14 Red and white thrombus. Panel **a**: red thrombus (thr) from 8 to 11 o 'clock characterized by an intense signal layer and casting a dark shadow, precluding interpretation of the underlying tissue. Panel **b**: white thrombus (thr) from 6 to 8 o'clock casting a less dark shadow so that interpretation of the underlying vessel wall is still possible. A calcified plaque is indicated with (*C*). The *asterisk* is indicating the guide wire artifact

vessel. While the former usually has irregular contours, the latter is often characterized by a swirling phenomenon in multiple frames. In several cases of ACS or stent thrombosis, it can be difficult to discriminate between both.

TCFA with rupture shows features of intimal tearing, disruption or dissection. Usually, an underlying cavity is observed, which can be filled with necrotic debris or thrombi, but can be washed out by the contrast flush as well.

Plaque erosion is defined as evidence of thrombus, together with an irregular lumen surface and no evidence of fibrous cap rupture in multiple adjacent frames on OCT [3, 13]. Plaque erosions are predominantly observed in relatively young and female patients. The underlying lesion can be a fibrous plaque or a fibroatheroma, but no cap rupture may be present according to the definition.

Calcified nodule is defined as a calcium accumulation protruding into the lumen, frequently exhibiting sharp angles, capable of puncturing the fibrous layers above and causing subsequent thrombus formation. These lesions are more common in older patients [12].
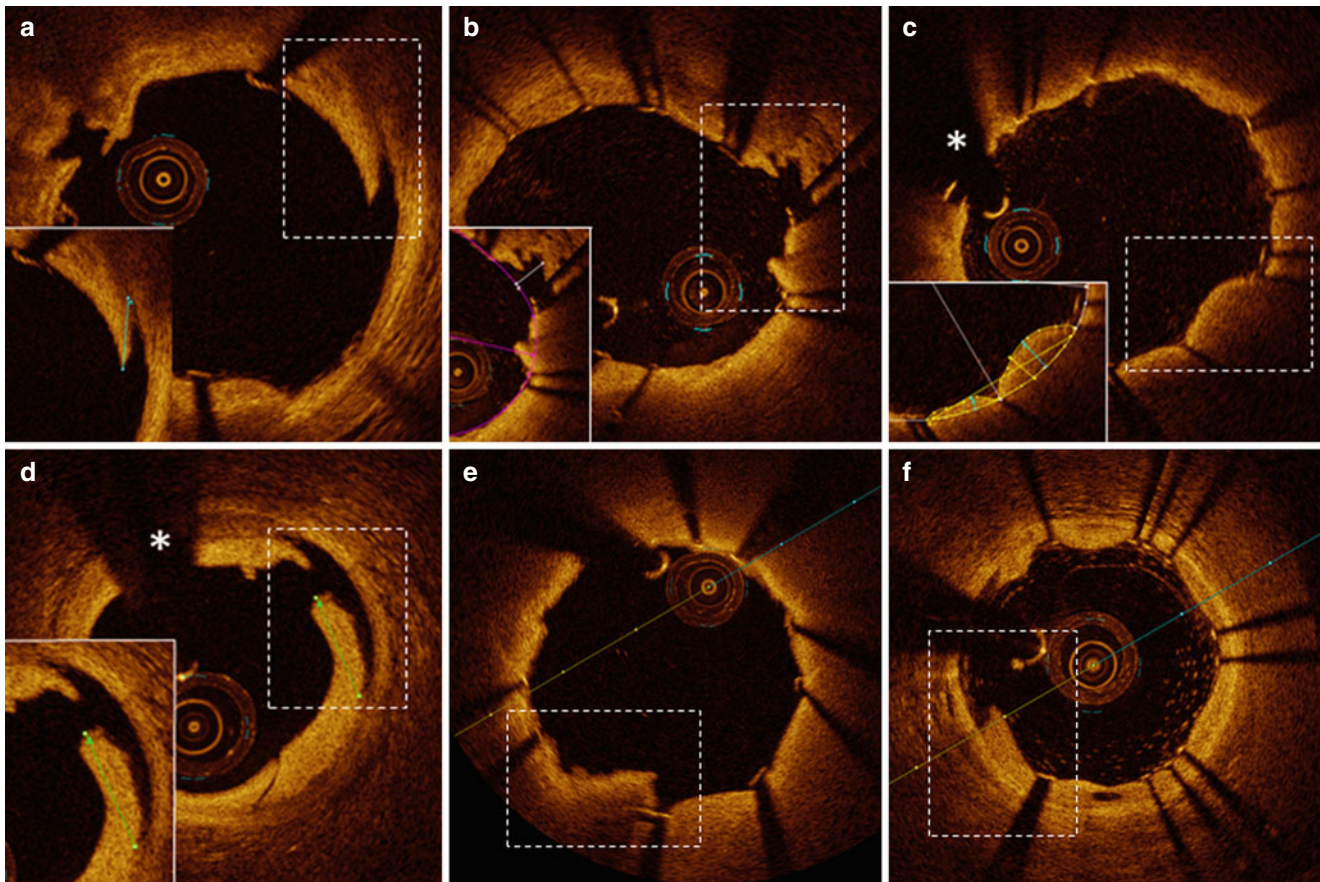
Fig. 4.15 Acute effects of stent implantation. Panel **a** and **b**: Intra-stent dissection with luminal dissection flap in (**a**) and empty cavity in (**b**). Panel **c**: tissue prolapse. Panel **d**: edge dissection. Panel **e** and **f**: exam- ples of tissue protrusion (Panels **a**–**d** from De Cock et al. [27]). The *asterisk* is indicating the guide wire artifact

4.5 Assessment of Coronary Stents After Implantation and at Follow-Up

Metallic stent struts have a typical and easy recognizable appearance on OCT images. They appear as highly intense linear structures with typical blooming (intense signal), casting a dark shadow obscuring the underlying vessel wall. Many characteristics of vessels immediately after stent implantation can be described, such as plaque prolapse, plaque protrusion, edge dissections, intra-stent dissections and intra-stent cavities (Fig. 4.15) [27]. With respect to the struts themselves, their apposition to the vessel wall, both immediately after implantation and at follow-up and the degree of tissue coverage over the stent strut surface at any time after implantation, are the most important parameters in OCT studies.

Tissue prolapse describes convex-shaped tissue with a regular surface protruding between adjacent stent struts towards the lumen, without disruption of the continuity of the luminal vessel surface while tissue protrusion corresponds to masses with an irregular surface attached to the vessel wall or to the stent struts, protruding beyond the struts into the lumen [28].

Intra-stent dissection (ISD) is defined as a disruption of the luminal vessel surface in the stented segment with either a visible dissection flap protruding in the lumen or a cavity in the vessel wall [29].

Malapposition is present when the axial distance between the strut surface and the luminal surface is greater than the thickness of the stent strut (including polymer, if present). The latter is different for each type of stent and varies from around 150 μm in first generation drug-eluting stents (DES) to around 90 μm or even lower in second generation DES.

In contrast to IVUS, hampered by a ten times lower resolution and a higher susceptibility to artifacts, OCT has been proven to be a reliable technique to assess the neointimal coverage above stent struts, even in the more difficult situations where a thin layer of neointima has to be discriminated from a completely uncovered strut. By definition, struts are considered uncovered if no evidence of tissue can be visualized above the struts (Fig. 4.16) [13].
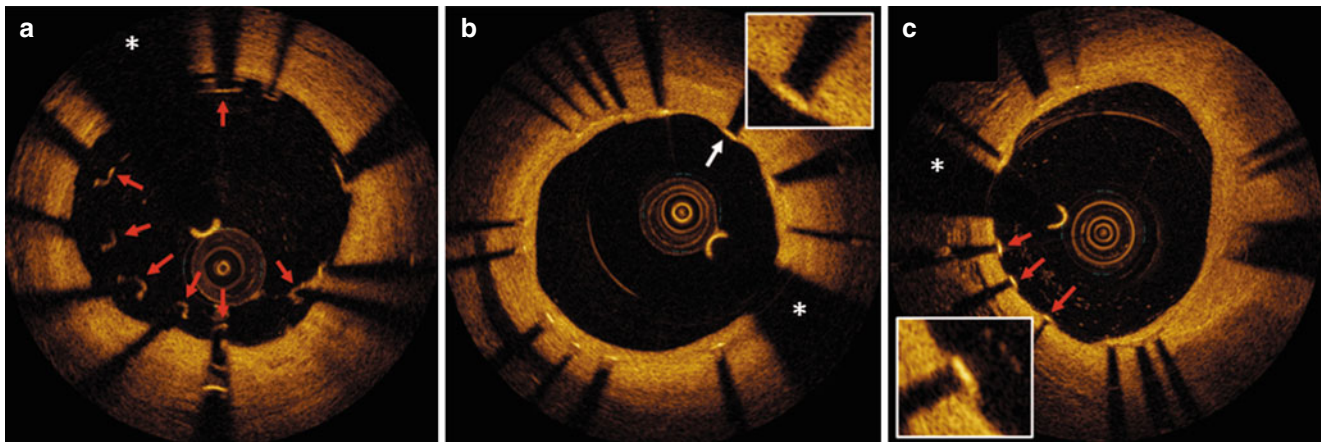
Fig. 4.16 Apposition and coverage. Panel **a**: *red arrows* indicate malapposed struts. Panel **b**: well healed struts 9 months after drug-eluting stent (DES) implantation. Some struts are covered with a very thin layer of neointima (magnification in insert). Panel **c**: some uncovered struts at long-term follow-up after DES implantation (*red arrows*) (magnification in insert). The *asterisk* is indicating the guide wire artifact

4.6 Limitations

The unsurpassed detail of OCT images and the safe and fast acquisition with current technology has led to an enthusiastic adoption by the interventional cardiologists community. It is equally important, however, to be aware of several limitations of current generation OCT systems in order to avoid over- or misinterpretation.

The first issue is the limited penetration depth of OCT (1–2 mm) compared to intravascular ultrasound (IVUS) (8–10 mm). Therefore, in many cases, no reliable assessment of plaque volume or of disease states of the deeper layers of the vessel wall can be made. With respect to the assessment of lumen area and vessel diameters, excellent agreement between IVUS and OCT measurements has been reported in non-diseased vessel segments. However, differences have been observed in lumen and stent areas in diseased segments, with smaller values consistently obtained with OCT, probably due to a better delineation of lumen area and stent area with OCT. When using OCT for guidance of PCI, it is important to rely on lumen criteria, as classical media to media values, as used in IVUS studies, cannot be obtained reliably with OCT.

A second limitation is the interpretation of tissue covered by thrombus. Especially red thrombus casts a complete shadow over the underlying vessel wall, making any reliable interpretation impossible. In such setting, no firm statements on qualification of underlying plaque or characterization of the healing status of stent struts (a common scenario in stent thrombosis) can be formulated.

With respect to long term healing characteristics of stent struts, the assessment of coverage with OCT has been validated against histopathologic data. However, the analysis of struts with an ultra-thin layer of neointima can be difficult.

Moreover, small deposits of fibrin can be misclassified as coverage above struts. In many cases, the neointimal layer above struts has a heterogeneous aspect, with zones with intense backscattering alternating zones with low backscattering. Current OCT technology is not capable of differentiating the exact nature of these lower intensity zones, which can be caused by fibrin deposition around struts, lipid accumulation or accumulation of inflammatory cells. With future technical innovation, such as combined OCT/near infrared fluoroscopy, it might be possible to characterize further between these early stages of neointimal tissue formation in the future.

Finally, it is important to recognize the limitations of 2D OCT imaging (especially in the setting of bifurcation treatment and in cases of stent deformation and stent fracture). The development of on-line available detailed 3D reconstructions is in an advanced stage with the first application already entering the clinical arena. These 3D visualizations offer more insight into these specific stent-related issues in the future.

References

1. Yonetsu T, Bouma BE, Kato K, Fujimoto JG, Jang IK. Optical coherence tomography- 15 years in cardiology. Circ J. 2013;77: 1933–40.
2. Imola F, Mallus MT, Ramazzotti V, Manzoli A, Pappalardo A, Di Giorgio A, Albertucci M, Prati F. Safety and feasibility of frequency domain optical coherence tomography to guide decision making in percutaneous coronary intervention. EuroIntervention. 2010;6:575–81.
3. Jia H, Abtahian F, Aguirre AD, Lee S, Chia S, Lowe H, Kato K, Yonetsu T, Vergallo R, Hu S, Tian J, Lee H, Park SJ, Jang YS, Raffel OC, Mizuno K, Uemura S, Itoh T, Kakuta T, Choi SY, Dauerman HL, Prasad A, Toma C, McNulty I, Zhang S, Yu B,

Fuster V, Narula J, Virmani R, Jang IK. In vivo diagnosis of plaque erosion and calcified nodule in patients with acute coronary syndrome by intravascular optical coherence tomography. J Am Coll Cardiol. 2013;62(19):1748–58.

4. Girassolli A, Carrizo S, Jimenez-Valero S, Sanchez Recalde A, Ruiz Garcia J, Galeotte G, Moreno R. Utility of optical coherence tomography and intravascular ultrasound for the evaluation of coronary lesions. Rev Port Cardiol. 2013;32:925–9.

5. Carrizo S, Salinas P, Jimenez-Valero S, Moreno R. Utility of optical coherence tomography to assess a hazy intracoronary image after percutaneous coronary intervention. Korean Circ J. 2013;43:44–7.

6. Regar E, van Soest G, Bruining N, Constantinescu AA, van Geuns RJ, van der Giessen W, Serruys PW. Optical coherence tomography in patients with acute coronary syndrome. EuroIntervention. 2010;6 Suppl G:G154–60.

7. Kubo T, Ino Y, Tanimoto T, Kitabata H, Tanaka A, Akasaka T. Optical coherence tomography imaging in acute coronary syndromes. Cardiol Res Pract. 2011;2011:312978.

8. Prati F, Uemura S, Souteyrand G, Virmani R, Motreff P, Di Vito L, Biondi-Zoccai G, Halperin J, Fuster V, Ozaki Y, Narula J. OCT-based diagnosis and management of stemi associated with intact fibrous cap. JACC Cardiovasc Imaging. 2013;6:283–7.

9. Gonzalo N, Escaned J, Alfonso F, Nolte C, Rodriguez V, Jimenez-Quevedo P, Banuelos C, Fernandez-Ortiz A, Garcia E, Hernandez-Antolin R, Macaya C. Morphometric assessment of coronary stenosis relevance with optical coherence tomography: a comparison with fractional flow reserve and intravascular ultrasound. J Am Coll Cardiol. 2012;59:1080–9.

10. De Bruyne B, Pijls NH, Heyndrickx GR, Hodeige D, Kirkeeide R, Gould KL. Pressure-derived fractional flow reserve to assess serial epicardial stenoses: theoretical basis and animal validation. Circulation. 2000;101:1840–7.

11. Yamaguchi Y, Kagawa E, Kato M, Sasaki S, Nakano Y, Ochiumi Y, Takiguchi Y, Arakawa Y, Ishimaru A, Ueda A, Dote K. A novel procedure for imaging acute coronary syndrome lesions using frequency-domain optical coherence tomography. EuroIntervention. 2013;9:996–1000.

12. Virmani R, Kolodgie FD, Burke AP, Farb A, Schwartz SM. Lessons from sudden coronary death: a comprehensive morphological classification scheme for atherosclerotic lesions. Arteriosclerosis, thrombosis, and vascular biology. Arterioscler Thromb Vasc Biol. 2000;20:1262–75.

13. Tearney GJ, Regar E, Akasaka T, Adriaenssens T, Barlis P, Bezerra HG, et al. Consensus standards for acquisition, measurement, and reporting of intravascular optical coherence tomography studies: a report from the international working group for intravascular optical coherence tomography standardization and validation. J Am Coll Cardiol. 2012;59:1058–72.

14. Alfonso F, Paulo M, Gonzalo N, Dutary J, Jimenez-Quevedo P, Lennie V, Escaned J, Banuelos C, Hernandez R, Macaya C. Diagnosis of spontaneous coronary artery dissection by optical coherence tomography. J Am Coll Cardiol. 2012;59:1073–9.

15. Park SJ, Kang SJ, Virmani R, Nakano M, Ueda Y. In-stent neoatherosclerosis: a final common pathway of late stent failure. J Am Coll Cardiol. 2012;59:2051–7.

16. van Soest G, Regar E, Goderie TP, Gonzalo N, Koljenovic S, van Leenders GJ, Serruys PW, van der Steen AF. Pitfalls in plaque characterization by OCT: image artifacts in native coronary arteries. JACC Cardiovasc Imaging. 2011;4:810–3.

17. Hebsgaard L, Christiansen EH, Holm NR. Calibration of intravascular optical coherence tomography as presented in peer reviewed publications. Int J Cardiol. 2014;171:92–3.

18. Yabushita H, Bouma BE, Houser SL, Aretz HT, Jang IK, Schlendorf KH, Kauffman CR, Shishkov M, Kang DH, Halpern EF, Tearney GJ. Characterization of human atherosclerosis by optical coherence tomography. Circulation. 2002;106:1640–5.

19. Kume T, Akasaka T, Kawamoto T, Watanabe N, Toyota E, Neishi Y, Sukmawan R, Sadahira Y, Yoshida K. Assessment of coronary intima–media thickness by optical coherence tomography: comparison with intravascular ultrasound. Circ J. 2005;69:903–7.

20. Kume T, Akasaka T, Kawamoto T, Okura H, Watanabe N, Toyota E, Neishi Y, Sukmawan R, Sadahira Y, Yoshida K. Measurement of the thickness of the fibrous cap by optical coherence tomography. Am Heart J. 2006;152:755.e751–4.

21. Cilingiroglu M, Oh JH, Sugunan B, Kemp NJ, Kim J, Lee S, Zaatari HN, Escobedo D, Thomsen S, Milner TE, Feldman MD. Detection of vulnerable plaque in a murine model of atherosclerosis with optical coherence tomography. Catheter Cardiovasc Interv. 2006;67:915–23.

22. Kawasaki M, Bouma BE, Bressner J, Houser SL, Nadkarni SK, MacNeill BD, Jang IK, Fujiwara H, Tearney GJ. Diagnostic accuracy of optical coherence tomography and integrated backscatter intravascular ultrasound images for tissue characterization of human coronary plaques. J Am Coll Cardiol. 2006;48:81–8.

23. Manfrini O, Mont E, Leone O, Arbustini E, Eusebi V, Virmani R, Bugiardini R. Sources of error and interpretation of plaque morphology by optical coherence tomography. Am J Cardiol. 2006;98:156–9.

24. MacNeill BD, Jang IK, Bouma BE, Iftimia N, Takano M, Yabushita H, Shishkov M, Kauffman CR, Houser SL, Aretz HT, DeJoseph D, Halpern EF, Tearney GJ. Focal and multi-focal plaque macrophage distributions in patients with acute and stable presentations of coronary artery disease. J Am Coll Cardiol. 2004;44:972–9.

25. Tearney GJ, Yabushita H, Houser SL, Aretz HT, Jang IK, Schlendorf KH, Kauffman CR, Shishkov M, Halpern EF, Bouma BE. Quantification of macrophage content in atherosclerotic plaques by optical coherence tomography. Circulation. 2003;107:113–9.

26. Kume T, Okura H, Kawamoto T, Akasaka T, Toyota E, Watanabe N, Neishi Y, Sadahira Y, Yoshida K. Images in cardiovascular medicine. Fibrin clot visualized by optical coherence tomography. Circulation. 2008;118:426–7.

27. De Cock D, Bennett J, Ughi GJ, Dubois C, Sinnaeve P, Dhooge J, Desmet W, Belmans A, Adriaenssens T. Healing course of acute vessel wall injury after drug-eluting stent implantation assessed by optical coherence tomography. Eur Heart J Cardiovasc Imaging. 2014;15(7):800–9.

28. Bouma BE, Tearney GJ, Yabushita H, Shishkov M, Kauffman CR, DeJoseph Gauthier D, MacNeill BD, Houser SL, Aretz HT, Halpern EF, Jang IK. Evaluation of intracoronary stenting by intravascular optical coherence tomography. Heart. 2003;89:317–20.

29. Gonzalo N, Serruys PW, Okamura T, Shen ZJ, Onuma Y, Garcia-Garcia HM, Sarno G, Schultz C, van Geuns RJ, Ligthart J, Regar E. Optical coherence tomography assessment of the acute effects of stent implantation on the vessel wall: a systematic quantitative approach. Heart. 2009;95:1913–9.

Intravascular OCT Imaging Artifacts

5

Jennifer E. Phipps, Taylor Hoyt, David L. Halaney,
J. Jacob Mancuso, Thomas E. Milner,
and Marc D. Feldman

Abstract

This chapter discusses many intravascular imaging artifacts that may be encountered when interpreting OCT images from coronary arteries in the clinic or in research settings. All OCT artifacts originate in either the propagation of light in the vessel lumen, signal acquisition or polar-to-rectangular conversion. When these artifacts are recognized and understood, OCT image interpretation can become much more accurate.

Keywords

Light attenuation artifacts • Catheter location or movement artifacts • Stent artifacts

5.1   Introduction

OCT continues to gain use as an imaging tool in the cardiac catheterization laboratory for providing measurements of the vessel diameter, stent apposition, and basic plaque characterization. However, understanding the limitations of OCT imaging technology is critical so that artifacts are correctly interpreted when assessing plaque vulnerability, disease burden, or pre- or post-prognosis of stent deployment. Also, some OCT artifacts can be corrected if the user recognizes the artifact and makes appropriate modifications to the imaging procedure. This chapter is segmented into three parts to describe: (1) artifacts that originate with light propagation in the catheter, lumen or vessel wall, (2) artifacts related to catheter location and movement, and (3) artifacts associated with stents. With the recognition of the artifacts described in this chapter, improved OCT image interpretation can be achieved.

J.E. Phipps, PhD • T. Hoyt, BA • D.L. Halaney, BS
J.J. Mancuso, MD • M.D. Feldman, MD (✉)
Department of Medicine, University of Texas Health
Science Center at San Antonio, 7703 Floyd Curl Drive MSC 7872,
San Antonio, TX 78229, USA
e-mail: feldmanm@uthscsa.edu

T.E. Milner, PhD
Department of Biomedical Engineering,
The University of Texas at Austin, Austin, TX USA

5.2   Light Propagation in the Catheter, Lumen or Vessel Wall

OCT light for intravascular imaging is centered at approximately 1,300 nm and able to penetrate through most constituents of the arterial wall to depths of 1–2 mm. However, some vessel constituents will attenuate OCT light more strongly causing the appearance of shadows that reduce the intensity of the OCT signal in the arterial wall. Features in the shadowed regions may still be decipherable if the intensity is not reduced significantly, but if the intensity is significantly reduced, it will prevent the underlying tissue structure from being accurately interpreted.

5.2.1   Guide Wire Shadow

An artifact that is present in all current clinical OCT images is a shadow caused by the guide wire. The guide wire functions in clinical imaging to direct the OCT imaging catheter to the coronary arteries being imaged. In research settings, the guide wire may or may not be necessary and can even be removed once it has been used to align the imaging wire, though this may cause difficulties if repeated pullbacks are acquired from the same location. The guide wire shadow will completely mask the underlying tissue and stents and is commonly labeled with an asterisk in scientific publications (see asterisk in Fig. 5.10).

5.2.2 Ghost Lines

Ghost lines appear as circular features in the OCT image and should not be considered representative of the vessel wall anatomy (Fig. 5.1) [1]. A ghost line is caused by light reflec-
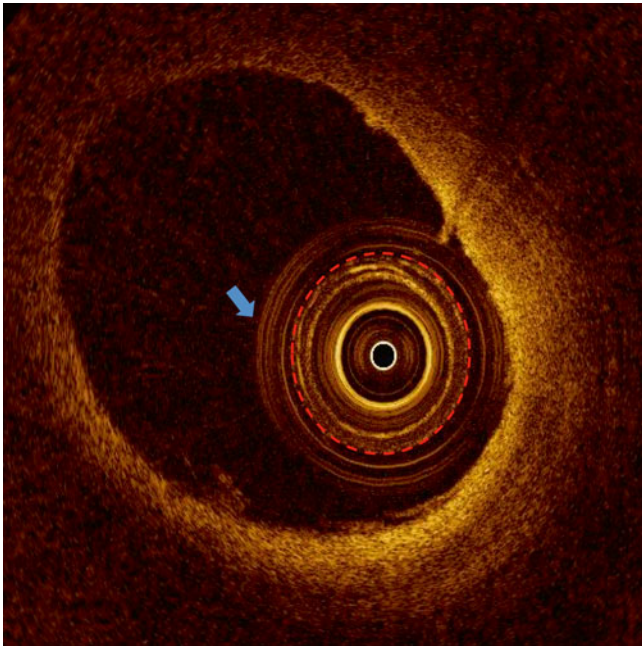

Fig. 5.1 Ghost lines. OCT image with ghost lines between outer catheter (*red dotted line*) and *blue arrow*

tions from at least two interfaces within the interferometer that may include the catheter. Commonly, one or both reflections that cause a ghost line originate from interfaces in the catheter. Position of the ghost line in the OCT image depends on the optical pathlength difference between the two underlying reflections. Typically the edges of the catheter are selected to calibrate any measurements taken of features in OCT images. If the ghost lines are mistaken as the edge of the catheter, features of the OCT image will be artifactually diminished or reduced. For example, vessel cross-sectional areas may be artifactually smaller than their true physical size, and stent strut malapposition may be underestimated.

5.2.3 Residual Blood from Incomplete Lumen Flushing

Blood must be completely flushed from within the lumen during OCT imaging to prevent artifacts resulting from OCT light scattered by red blood cells. When blood is present, lumen artifacts can appear in the OCT image as signal-rich areas instead of a transparent lumen completely free of OCT signal (Fig. 5.2). Scattering of light from within the lumen by blood can cause shadowing that will decrease the intensity of the OCT signal from the arterial wall and can cause difficulty in interpretation of arterial structure. [1–6] Scattering by blood can also introduce significant changes to stent strut appearance including merry-go-round, blooming, and ghost
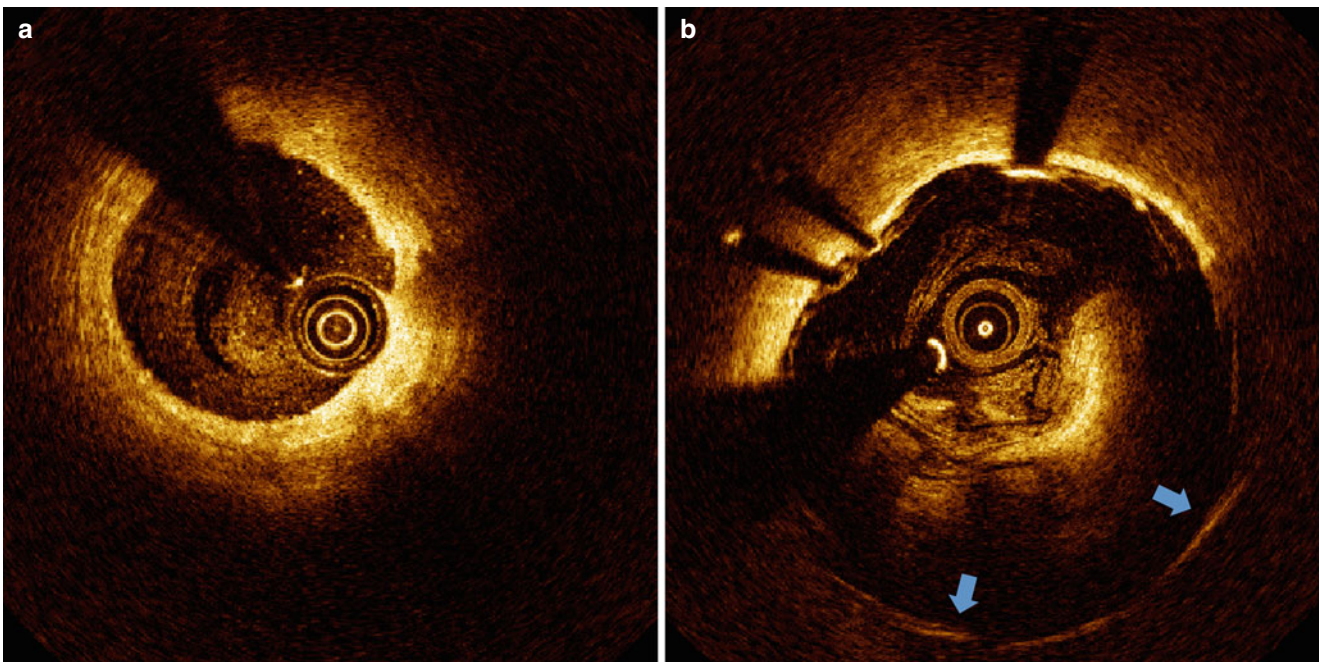

Fig. 5.2 Blood artifact. (**a**) Coronary artery with "spotty" luminal blood due to poor clearance. (**b**) Stented superficial femoral artery with "swirled" luminal blood due to very poor clearance. Stent struts with merry-go-rounding (*blue arrows*) are observed behind the blood
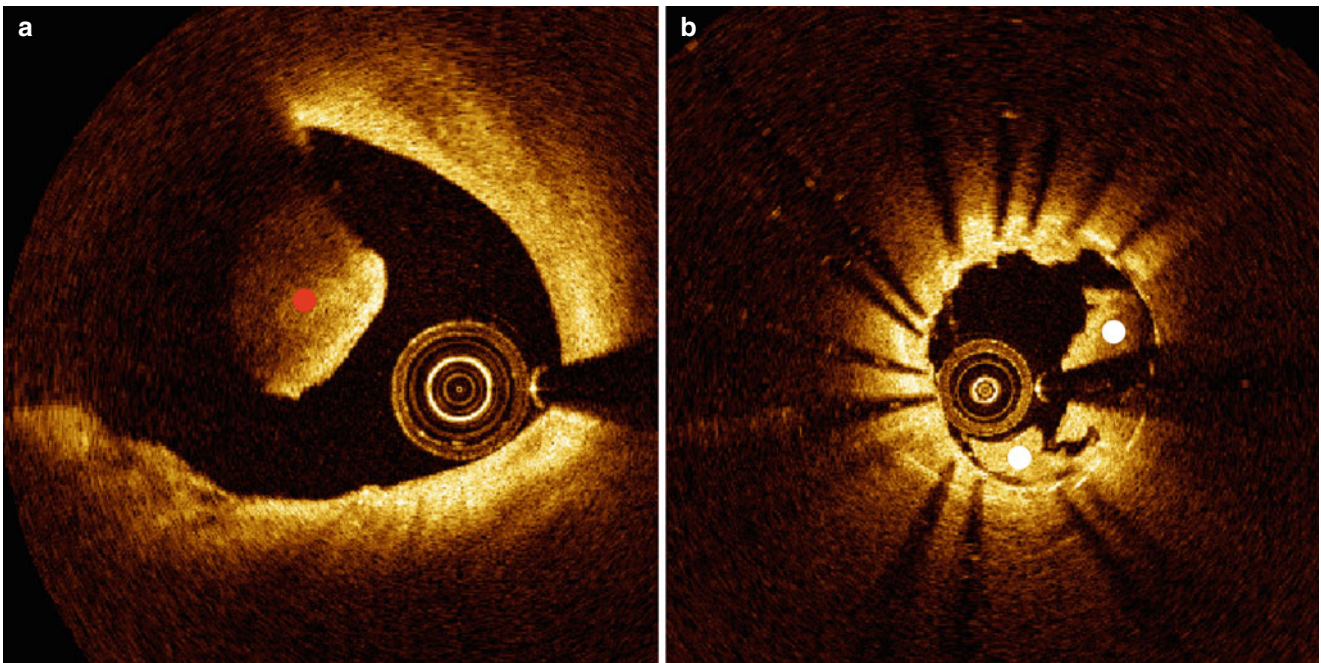
Fig. 5.3 Clots. (**a**) Red blood clot (denoted by *red dot*) causing complete attenuation of the OCT beam. (**b**) White blood clot (denoted by *white dots*) within a stented vessel causing partial attenuation of the OCT beam

strut artifacts (Fig. 5.2b), which are discussed in Sect. 5.4. If OCT signal is observed in the vessel lumen, modifying the flush parameters and repeating the imaging procedure can correct this artifact. At times there is concern that multiple power injections will increase trauma to the coronary wall and complications to the patient, or that the increased contrast volume will result in renal insufficiency. However, literature demonstrating the safety of power injection of coronary arteries mitigate some of these concerns. For trained cardiologists, hand injection is also a suitable alternative to clear blood during intravascular OCT imaging [7]. When concerns regarding contrast induced renal damage exist Dextran-40 can be used to clear the blood instead of contrast [8, 9].

5.2.3.1 Thrombus

Red cell thrombus positioned between the catheter and arterial wall can also cause shadowing. Thrombi can form on the surface of the arterial wall, stent struts or the catheter. Shadow effects are greater for thrombi positioned closer to the catheter. In any of these cases, a shadow will appear beyond the thrombus, diminishing the signal intensity originating from the arterial wall (Fig. 5.3a). Red cell thrombi will typically not only shadow the arterial wall beneath, but also obscure the back side of the clot furthest from the light source and introduce some uncertainty in computing the volume of a red cell thrombus. A white cell thrombus is more translucent (less scattering) to OCT light compared to red thrombi and result in less shadowing (Fig. 5.3b). By

examining the signal attenuation strength within the thrombus, distinguishing between red and white cell thrombi is possible. Reconstruction and volume calculations for white thrombi are generally more accurate than for red thrombi.

5.2.4 Gas Bubbles

Gas bubbles can form inside fluid-filled catheters. These bubbles are highly scattering due to the large refractive index difference between the gas and surrounding fluid and will also cause the appearance of a shadow that will decrease the signal intensity of the arterial wall (Fig. 5.4) [1–4, 6]. They are recognized by a distinct region of brightness inside the catheter and diminished signal in the part of the OCT image in the path of the disrupted region of the catheter. These gas bubbles can form inside the catheter if the operator does not correctly pre-flush the imaging catheter before placement into the patient for imaging. Gas bubbles can also appear in the lumen of the vessel in cadaver heart studies, causing the appearance of a bright outline of the bubble and a shadow in the OCT image behind the bubble.

5.2.5 Metallic and Biodegradeable Stents

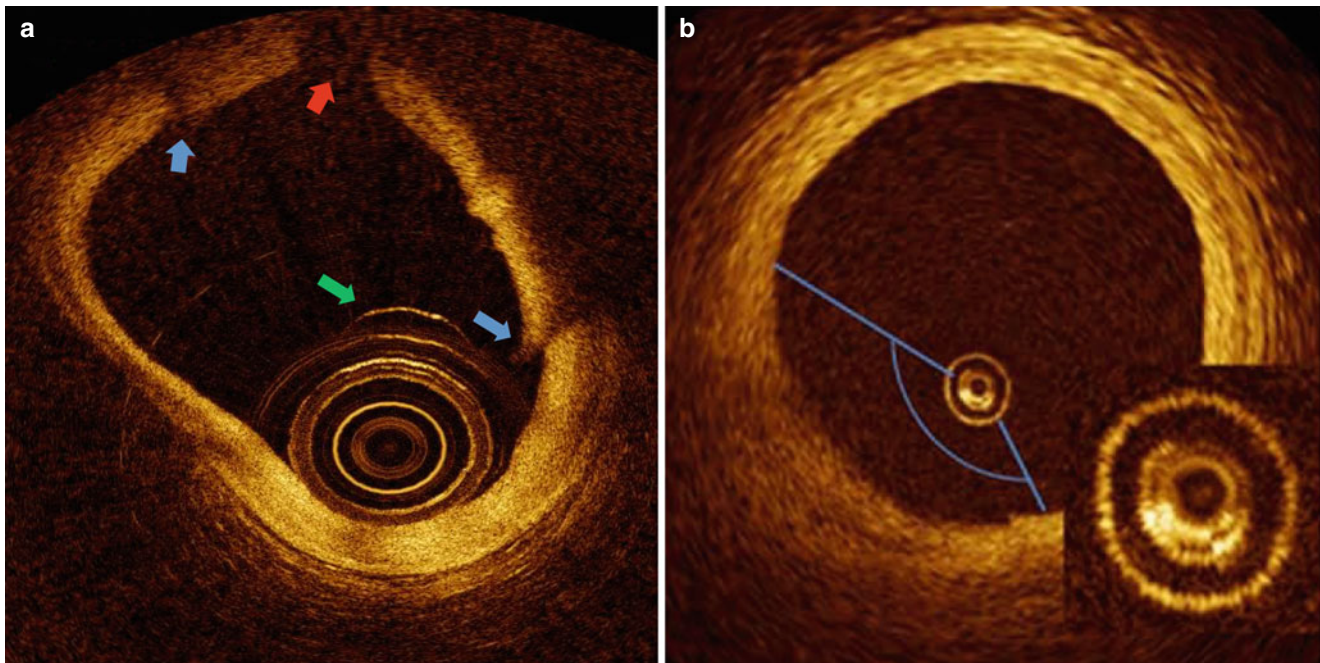Metal stents block incident OCT light and thus cause shadows behind each strut. A substantial fraction of the

Fig. 5.4 Bubble Artifacts. (**a**) *Ex vivo* heart with luminal bubble (*green arrow*) adhered to catheter. Refraction of light at bubble contour results in bubble shadow (*red arrow*) and tissue discontinuities (*blue arrows*).

(**b**) Bubble inside catheter (inset) due to inadequate flushing results in a dimmed sector. (Panel B from Bezerra et al. [2])

arterial cross-section can be disrupted by these shadows, which can then significantly complicate the process of characterizing the underlying tissue structure. Dropout of light occurs behind metallic struts, where struts typically appear as a single leading edge feature that casts a single expanding broad shadow over the arterial wall beginning with the width of the stent strut. This light dropout can often be used as a strategy to recognize the presence of older stents in regions of complex neoimtima and new plaque growth. In contrast to metallic stents, biodegradable stent strut shadows are normally observed along the two lateral sides of the strut, leaving a much greater volume of the native tissue structure (e.g., plaque, intima, media) interpretable for light interrogation.

5.2.6 Superficial Shadowing by Macrophages

Attenuation of light by macrophage accumulations can cause shadows in OCT images that appear falsely as an underlying lipid pool or necrotic core. Thus a relatively normal artery with superficial infiltration of macrophages can even appear as a thin-capped fibroatheroma (Fig. 5.5), causing a non-vulnerable plaque to incorrectly appear vulnerable to rupture. Shadowing is not due to the macrophage itself, but rather is caused by either (1) large pools of lipid-filled macrophages (foam cells) that cause light to attenuate similarly to a lipid pool due to the low index of refraction (IR) of lipid

or (2) its association with compact structures with high IR such as micro-calcification and cholesterol crystals [10]. Increased scattering and shadowing by these structures is anticipated by classical scattering theory (e.g., Mie), which describes the way light scatters from objects. In addition to ingesting lipid, macrophages can engulf microcalcifications [11] and cholesterol crystals [12]. Small cholesterol crystals and microcalcifications, both of which have high IRs compared with surrounding tissue structures can cause shadowing. In general, macrophages do not necessarily have optical properties that would cause a shadow, unless they are a large cluster of lipid-rich foam cells or have engulfed a micro-calcification or plaque component that has an IR substantially higher than that of lipid.

5.2.7 Saturation Artifact

When OCT light is incident on an object that causes a large backscattered signal the OCT detector can saturate. The saturation effect introduces signal energy in much of the OCT signal detection bandwidth so that a bright line appears for that particular A-scan in the OCT image (Fig. 5.6). Polar-to-rectangular conversion causes the saturation artifact to bleed laterally into adjacent A-scans [1–4]. Radial extent of the bright line depends on the artifactual frequencies introduced and can extend beyond the strongly backscattering object deep into the arterial wall and extend to the edge of the OCT image.
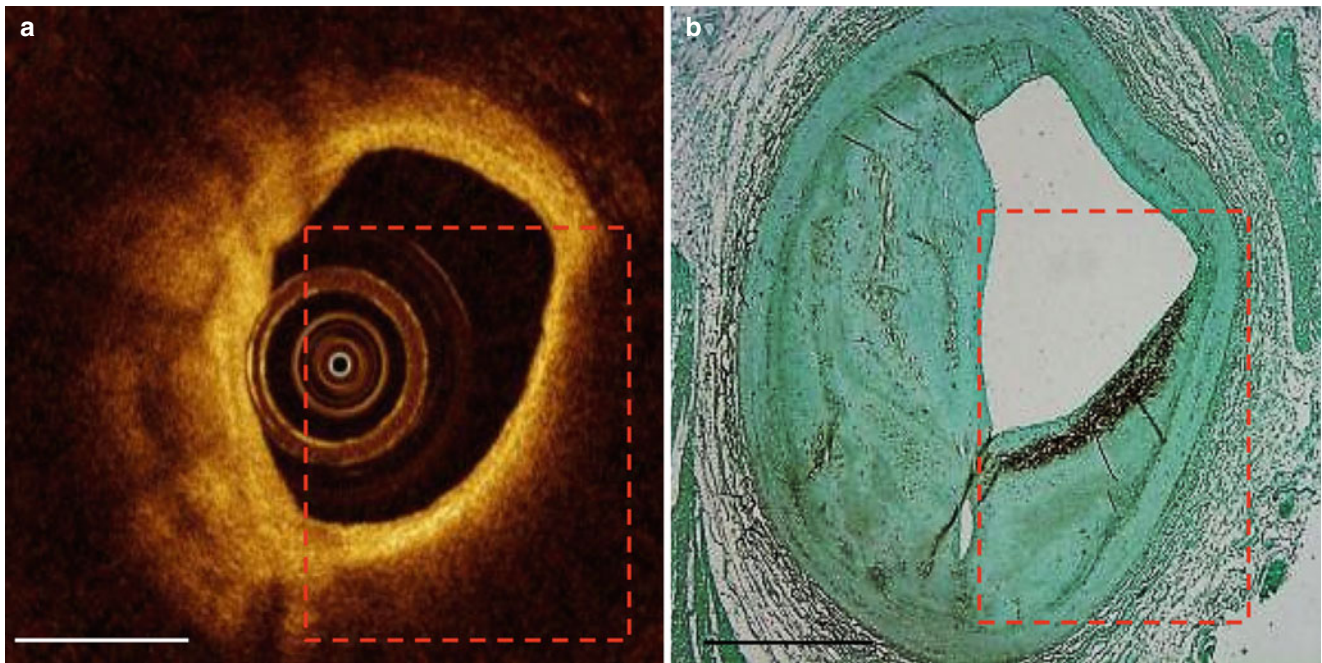
Fig. 5.5 False TCFA. Superficial macrophage infiltration causes appearance of false thin-capped fibroatheroma. The *red dashed line* outlines the region of light dropout in the OCT image (**a**) and the region of macrophages in the CD68 histology section (**b**). Scale bars represent 1 mm
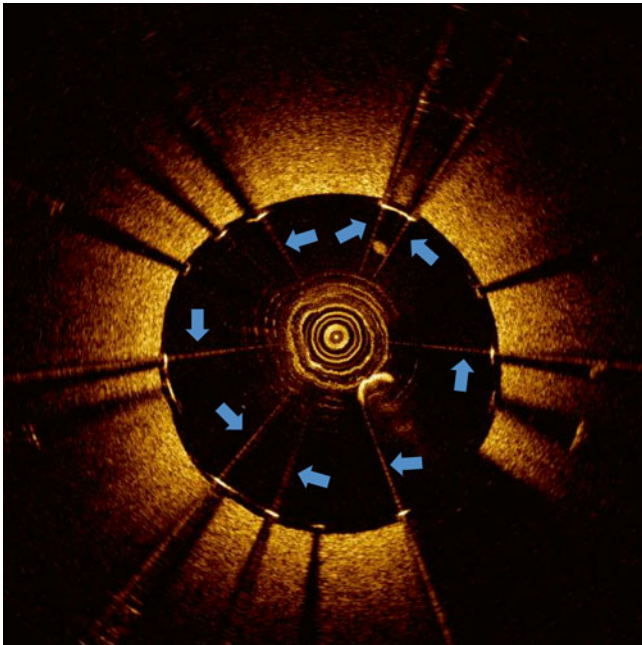

Fig. 5.6 Saturation artifact. OCT image with saturation artifacts (*blue arrows*) occurring at stent struts

At larger radial distances from the catheter, polar-to-rectangular conversion results in broadening of the artifact. Objects that can cause a saturation artifact include stent struts, the guide wire, and sometimes components in the arterial wall or tissue surface such as microcalcifications and cholesterol crystals.

5.3 Catheter Location and Movement

The catheter location within the vessel lumen (center or off-center) and the vessel diameter can affect the OCT image appearance. Additionally, motion of the imaging catheter, due to rotation and pullback speed, can alter the OCT image appearance as well.

5.3.1 Non-Uniform Rotational Distortion (NURD)

NURD is due to a non-constant angular velocity of the mono-fiber optical catheter and appears in OCT images as a blurring or smearing in the lateral (or rotational) direction (Fig. 5.7). [1–3] NURD normally occurs due to mechanical rotational resistance in the catheter due to a either a tortuous or narrow vessel, a tight hemostatic valve, or possibly a crimped catheter sheath. Additionally, NURD can be caused by a defective catheter. The NURD artifact also occurs in other imaging systems that rely on a rotating mechanical element (such as intravascular ultrasound).

5.3.2 Fold-Over Artifact

Fold-over artifact is observed when the vessel diameter is too large for the field-of-view of the imaging catheter. In such a case, OCT signal aliasing occurs and the image appears to
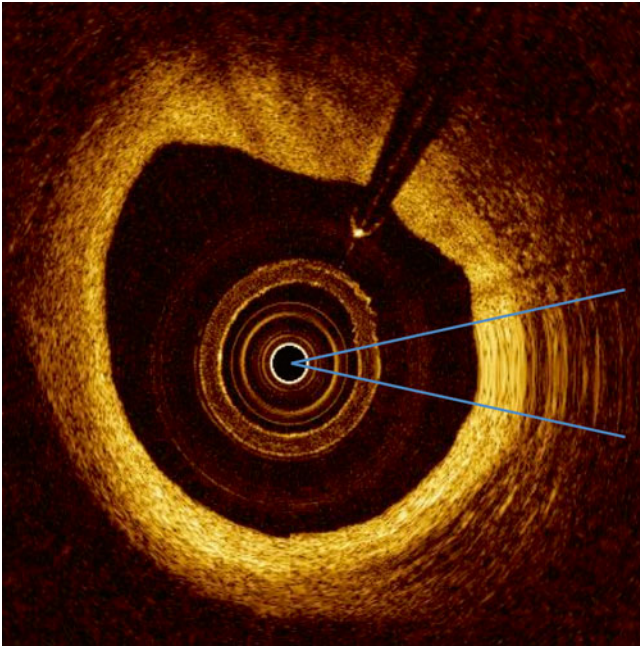
Fig. 5.7 NURD. OCT image with NURD artifact (between two *blue lines*)

Fig. 5.8 Fold-over artifact. OCT image with fold-over artifact (*blue arrow*)

fold back on itself in an inverted reflection of the tissue (Fig. 5.8) [1–3]. The folded-back portion of the image should not be used to assess the tissue geometry of the vessel.

5.3.3 Tangential Light Drop-out

When the imaging catheter is positioned close to the arterial wall so that the light is emitted nearly parallel to the tissue surface, that part of the artery wall may appear to attenuate light when in actuality the optical beam is not penetrating in that region (Fig. 5.9). This artifact may be confused with the appearance of a thin-capped fibroatheroma, superficial accumulation of macrophages, a lipid pool, or a necrotic core and thus the knowledge of this artifact should be considered when assessing the tissue composition in regions of artery that are nearly parallel to the OCT light beam [1].

5.3.4 Sew-up or Seam Artifact

OCT pullbacks are acquired by the light beam tracing a helix on an idealized cylindrical lumen wall during a pullback. For example, at a 1 mm/s pullback speed, an approximately 270 μm longitudinal separation exists between the starting and final A-scans after a single 360° rotation of the catheter. The combined rotational and longitudinal motion of the catheter results in a discontinuity between successive B-scans, which is called a sew-up or seam artifact. The artifact is rep-
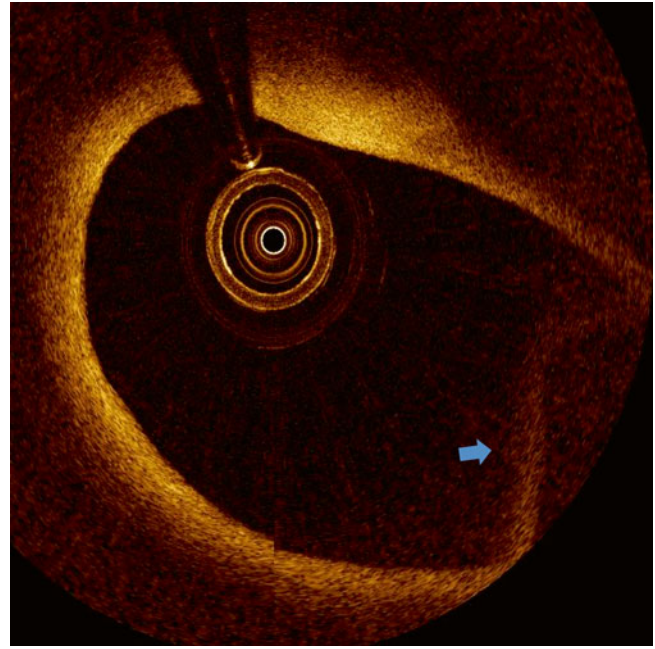
resented as a gradient along the lateral direction and normally is most prominent as a discontinuity of the luminal surface but can be observed within the arterial wall as well. Although the sew-up artifact is always present and can be observed in many images presented in this chapter, different conditions can accentuate the appearance. For example, when the relative position between the imaging catheter and vessel wall exhibits a large longitudinal gradient due to vessel tortuosity, luminal diameter changes or calcified and rigid plaque, sew up artifacts will be observed (Fig. 5.10) [1–6].

5.3.5 Effect of Beam Focus and Catheter Pupil on OCT Signal Strength

OCT signal intensity depends on a number of factors including the beam spot size, backscattering strength of the tissue and solid angle between the backscattering site and pupil of the imaging catheter. Normally, a larger beam spot results in a smaller OCT signal intensity due to the increased amplitude and phase variation over the mode field of the catheter fiber. Light that backscatters from the tissue must enter the pupil of the imaging catheter and be coupled into a single mode optical fiber. A smaller solid angle between the backscattering site and catheter pupil decreases OCT signal strength. The beam exiting from the OCT catheter is normally designed to focus at a position within the arterial wall being imaged. At positions before and after the beam focus, the spot size increases and normally results in less signal intensity. When
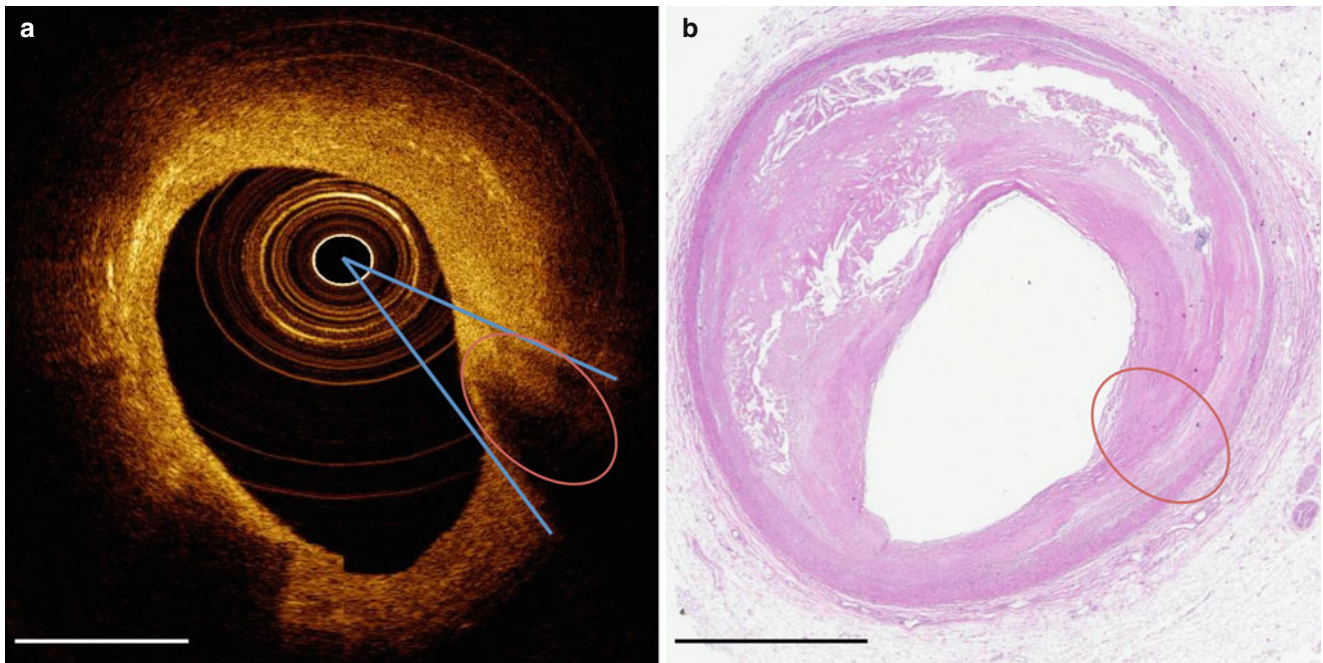
Fig. 5.9 Tangential light drop out. (**a**) OCT image with tangential light drop out. (**b**) Corresponding hematoxylin and eosin histology. *Oval* denotes area where tangential light drop out causes the appearance of a necrotic core that is not revealed by histology. *Blue lines* indicate the direction of light beams tangential to the tissue that appears to have artifactual light dropout. Scale bars represent 1 mm
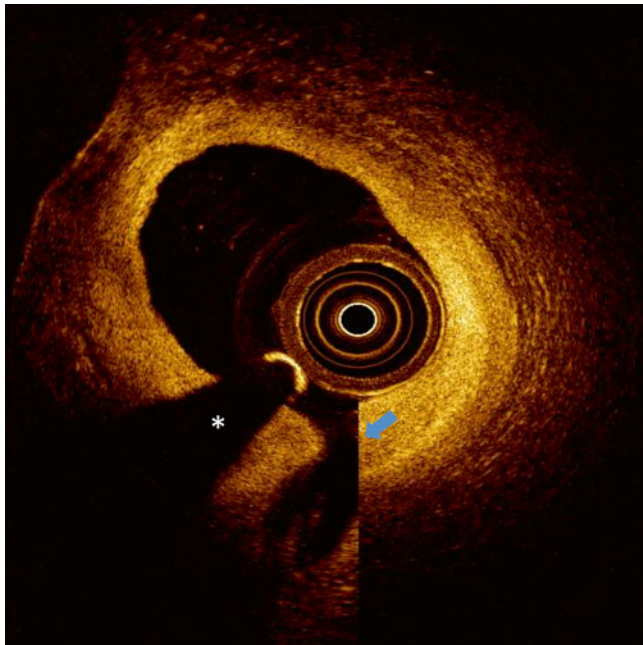

Fig. 5.10 Seam artifact. OCT image with seam artifact occurring at a branch (*blue arrow*). Guidewire shadow denoted by the *asterisk*

Fig. 5.11 Beam divergence. OCT image with beam divergence artifact. The tissue near to the catheter is very bright whereas the rest of the image is dimmer. It can be observed that the brighter region (3 o' clock) has higher resolution compared to the dimmer area (9 o' clock)

the imaging catheter is very near or touching the arterial wall, although the spot size is larger the solid angle between the backscattered light and pupil of the imaging catheter is also increased so that the OCT signal level can be relatively bright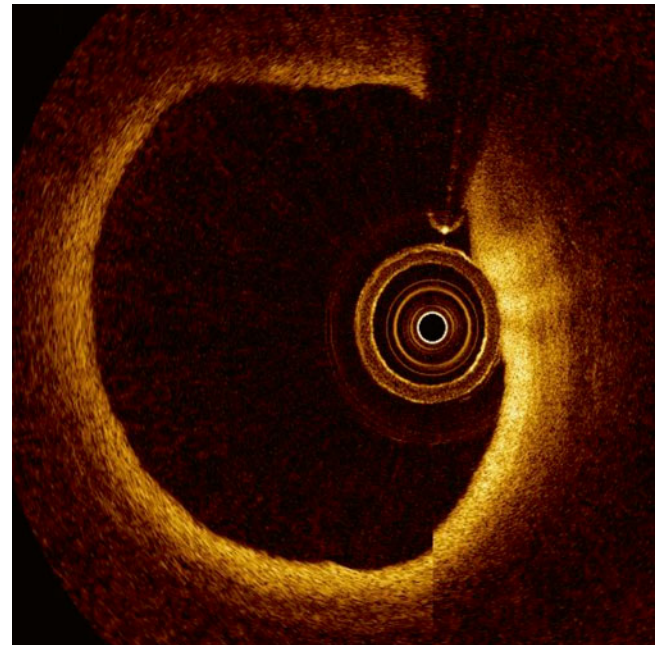er than the light backscattered from tissue regions far from the catheter (Fig 5.11) [1]. Alternatively, when the backscattered light originates from a position farther than the beam focus, the two effects – larger spot size and smaller solid angle – contribute to a reduced OCT signal intensity.

5.3.6 Obliquity/Eccentricity

When the imaging catheter is centered and parallel to a cylindrical vessel, the luminal wall in OCT images will appear circular; however, when the catheter is oblique to the vessel axis, which places it closer to the artery wall in some longitudinal positions and further in others, a circular vessel will appear elliptical. In these cases, the shape of the vessel lumen can appear distorted by an oblique imaging catheter and this effect needs to be taken into account when making measurements of an artery area with OCT images [13, 14]. Moreover if the z-offset is not at the center of the imaging catheter fiber and the catheter is at an eccentric position artifacts may be introduced in the shape of the vessel wall.

5.4 Stent Artifacts

Metal stents strongly backscatter light and normally are clearly observed in OCT images as small bright line segments. Strong scattering by metallic stents is due to the large imaginary component of the index of refraction of the metal which results in intense reflections. Residual blood incompletely flushed from the lumen can introduce various artifacts in the appearance of the metallic stent struts. Bioabsorbable stents, on the other hand, reflect and scatter OCT light more weakly than metal and are dominated by diffuse reflection of light from the strut surface. Diffusely reflected light occurs when incident light returns from a strut in many directions, as, for example, observing light reflected from frosted glass. Bioabsorbable stents exhibit a unique set of artifacts that are distinct from metallic stents.

5.4.1 Merry-Go-Round Artifact

Merry-go-round artifact occurs when the small bright line segments that represent a stent strut appear elongated in the lateral (rotational) direction (Fig. 5.12). Merry-go-rounding has also been described as an artifactual stretching of the stent strut. Two mechanisms have been suggested for merry-go-round artifact: (1) reduced lateral resolution due to an increased lateral distance between A-lines at increasing distances from the catheter [2, 6] and (2) a larger beam spot diameter at increased distances from the focus [1, 6]. However, neither mechanism addresses why merry-go-rounding is sometimes observed when the catheter is in the center of the artery and also does not explain exaggerated merry-go-rounding that can cause strut arc length to increase by up to 400 %. It was proposed that optical scattering in the lumen (primarily due to inadequate blood flushing) between the catheter and arterial wall can cause the light backscattered from the stent strut to appear to originate from a wider arc length than the true strut length [15]. This has been demonstrated experimentally and shown to account for the up to 400 % strut arc length increase in a lumen at 1 % hematocrit and also is demonstrated to cause merry-go-round whether the catheter is centered or eccentric. Due to scattering by red blood cells, OCT light in A-lines that would normally miss the strut on either side may be scattered away
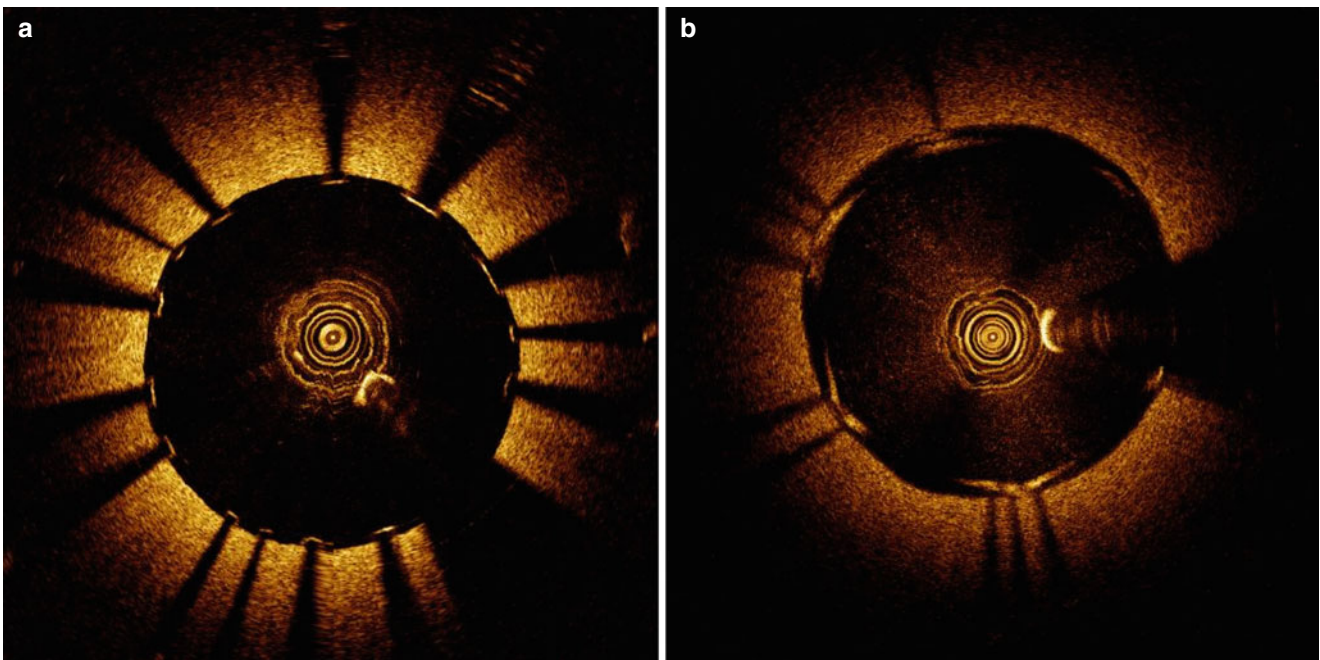
Fig. 5.12 Blood-induced merry-go-round. (**a**) Stented vessel phantom with saline flush. (**b**) Stented vessel phantom with homogenous 0.5 % hematocrit. Blood scatter results in blooming and merry-go-rounding of stent struts. Although the presence of blood is not apparent, it also results in dimming of the image
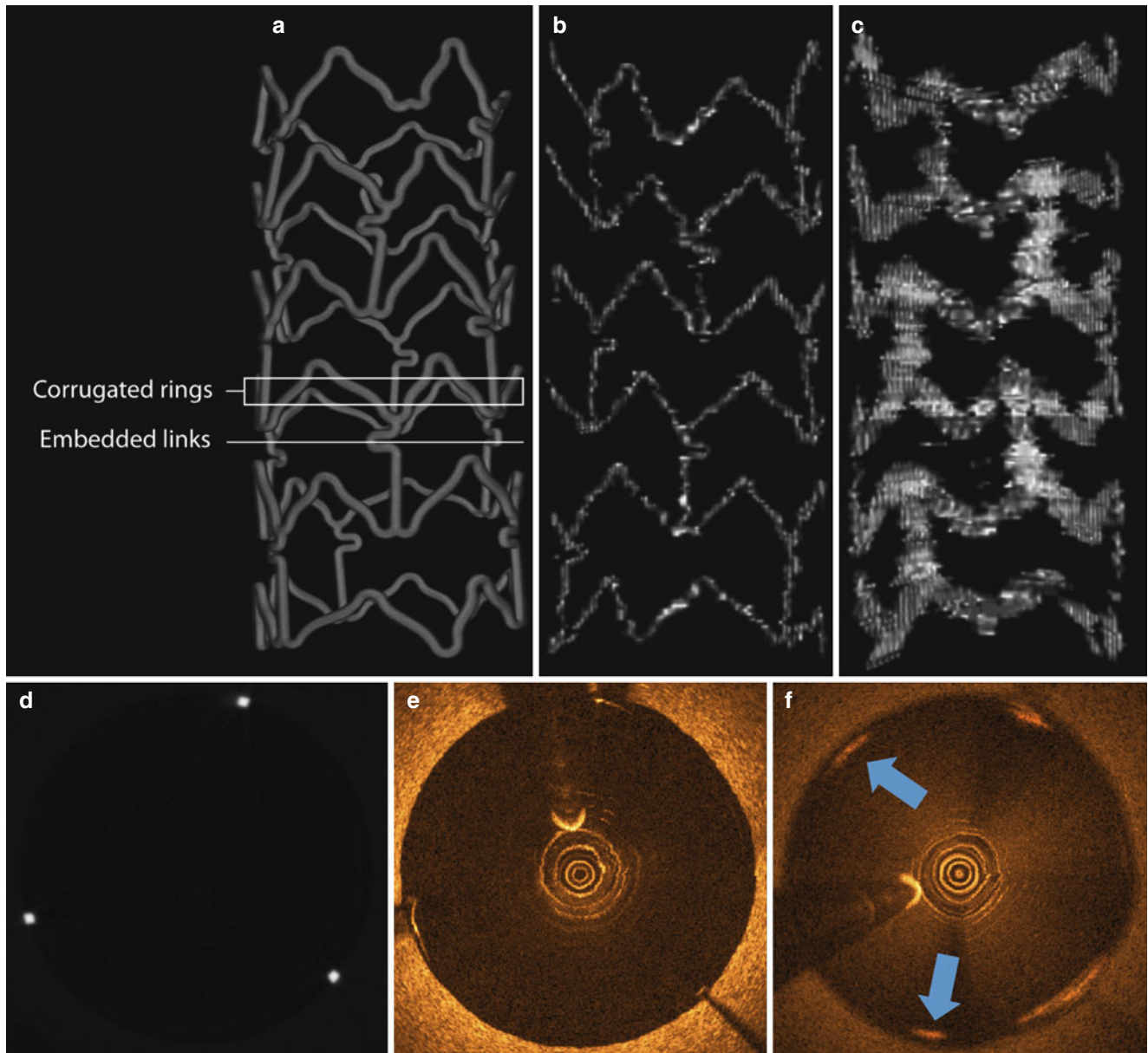
Fig. 5.13 Ghost struts. (**a**) MicroCT of a 3×8mm Xience V stent showing the five repetitive embedded link regions along the longitudinal axis, compared to 3D reconstructions of OCT images of the same stent imaged in (**b**) 0.9 % saline, and (**c**) 1 % Hct. The 1 % Hct causes longitudinal blurring (3D-merry-go-round) of the struts. (**d**–**f**) Corresponding B-scans from the center embedded link region of the 3D reconstructions in (**a**-**c**), respectively. As seen in (**f**), longitudinal blurring can introduce ghost struts (*blue arrows*) where they do not exist

from their normal path and contact the strut. In the reconstructed OCT image, the strut will appear artifactually elongated to include these A-lines (which would have missed the strut in the absence of the scattering by blood).

5.4.2   Blooming

Blooming is the increase in strut reflection thickness in the axial direction of OCT images (Fig. 5.12), causing the small bright line segment that represents the leading edge of a stent strut to appear thicker than normal, making it difficult to locate the true leading edge of the strut [1, 2, 4, 6, 16, 17].

Saturation artifact can sometimes be confused with blooming though they are actually very distinct artifacts. Saturation artifact can cause blooming, but blooming can also be observed in the absence of saturation. For instance, when residual blood attenuates the OCT beam, the saturation artifact may not occur, but the blooming artifact may still be observed (Fig. 5.13f). A mechanism for blooming has been found to be the presence of optical scatterers (again, most likely due to residual blood following insufficient flushing) in the lumen. The scatterers cause variation in the path length that photons of an OCT beam travel between emission from the catheter and collection by the catheter. Due to this range of path lengths, photons of the OCT beam appear to come
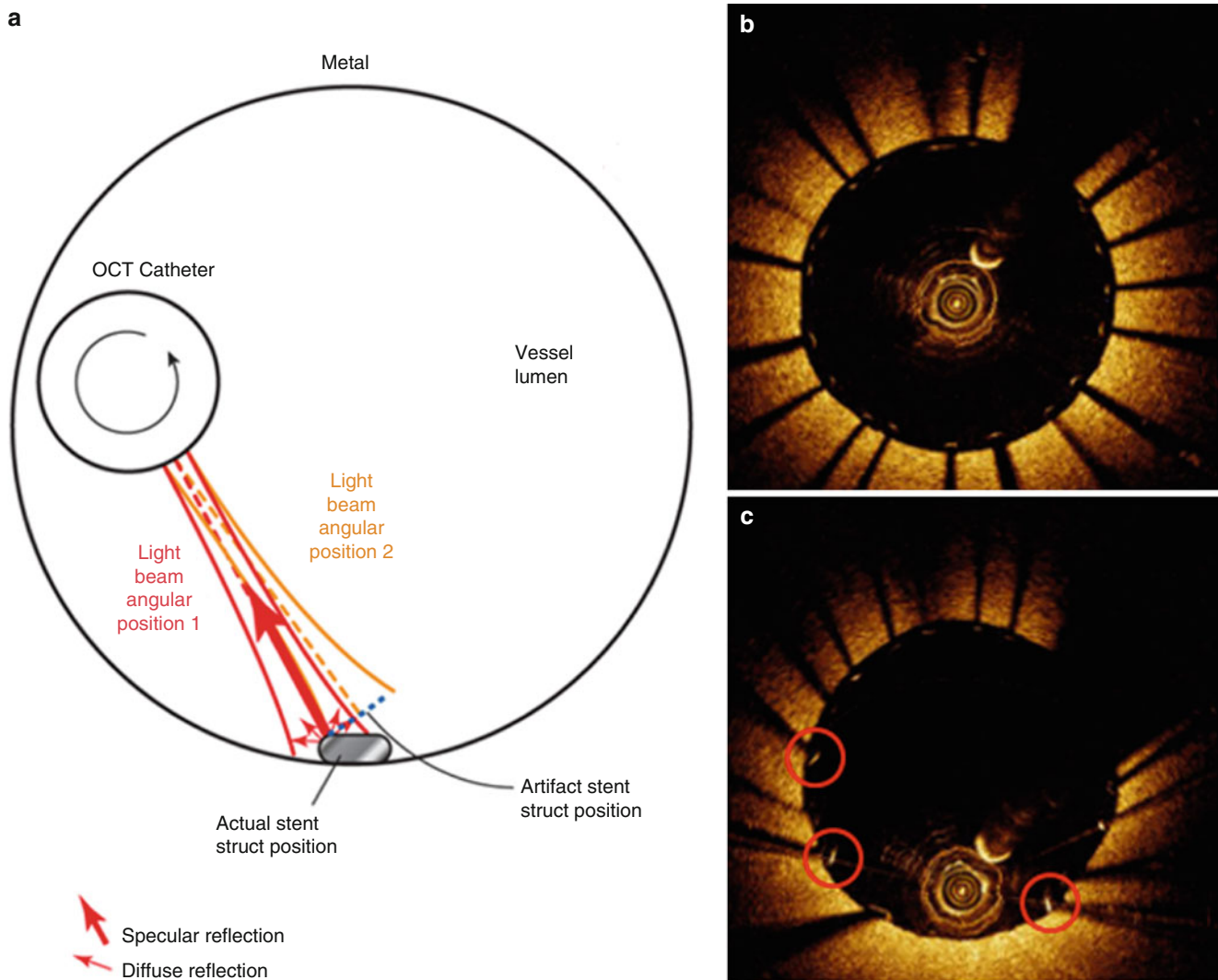
Fig. 5.14 Sunflower mechanism. (**a**) Cartoon showing mechanism of sunflowering with eccentric catheter position. (**b**) Stented phantom vessel with centered OCT catheter showing no sunflowering. (**c**) Stented phantom vessel with eccentric catheter showing sunflowering struts

from different depths than the true strut leading edge, therefore thickening the line feature representing the leading edge of the strut in the OCT image. A hematocrit as low as 0.5 % has been demonstrated to more than double the thickness of the line feature representing the strut, [15] demonstrating both the importance of residual blood and how difficult the effect is to recognize since low hematocrits are difficult to observe in OCT images.

5.4.3 3D Merry-Go-Round ("Ghost Struts")

Not only does artifactual stretching of stent struts occur in the axial (blooming) and lateral (rotational) direction (merry-go-round) due to scatterers in the lumen such as residual blood, it can also occur in the longitudinal direction (3D merry-go-round), along the pullback, and between B-scans.

We have coined the term "ghost struts" because 3D merry-go-round creates the appearance of struts in OCT B-scans when no struts are actually present (Fig. 5.13). Both merry-go-round and blooming are due to optical scatterers (most often red blood cells), and that scattering will occur both azimuthally and longitudinally.

5.4.4 Sunflower Artifact

When the OCT catheter is located in an eccentric position in the presence of metallic stent struts, the sunflower artifact can occur. Sunflower artifact occurs when stent struts appear to bend towards the OCT catheter as sunflowers grow toward the sun (Fig. 5.14) [1–3, 5, 6, 18]. This artifact may cause a well apposed stent to appear malapposed in a vessel. This occurs because with metallic stents, incident OCT light only
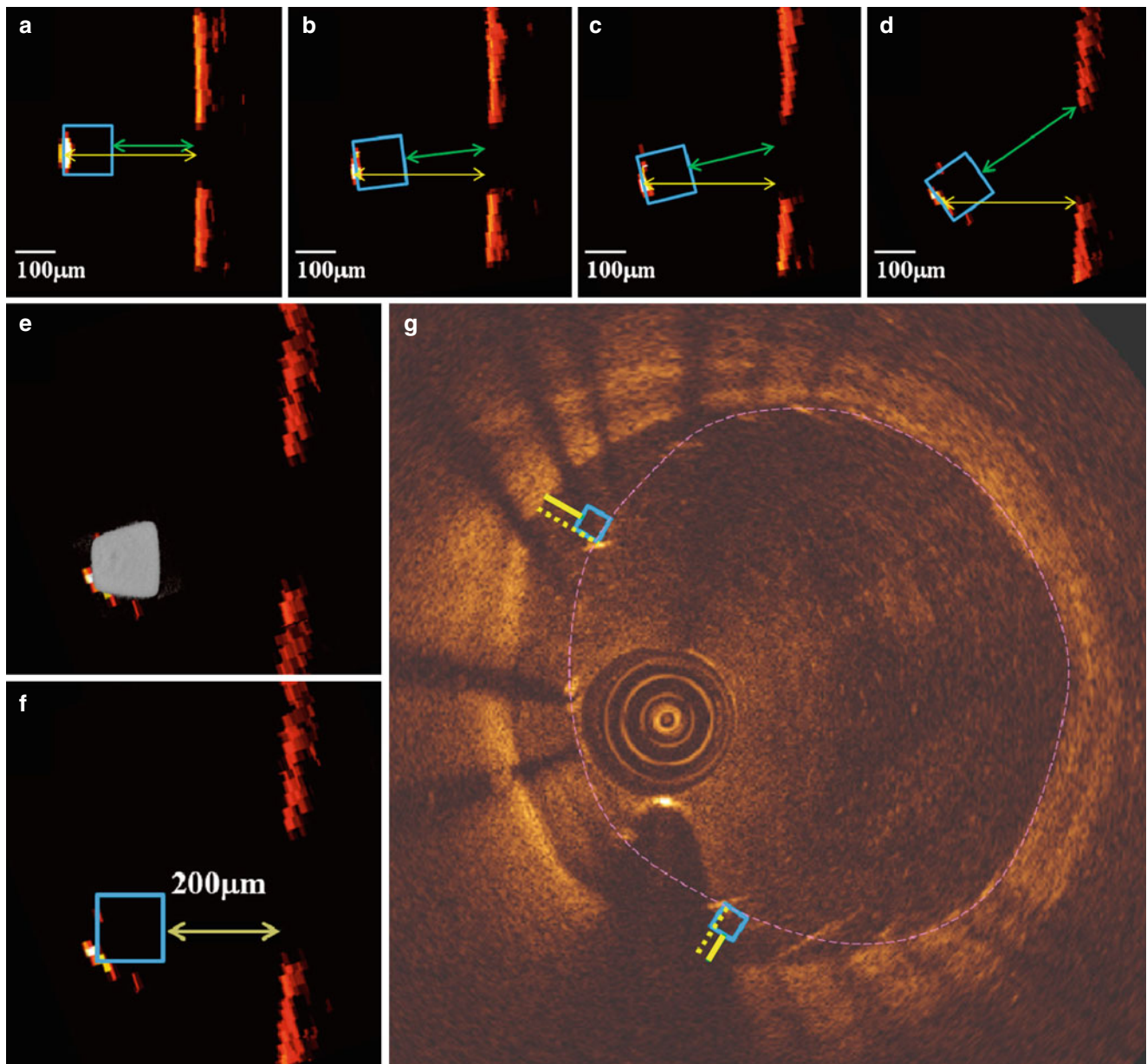
Fig. 5.15 Stent apposition measurement. (**a–d**) Simulation showing visualization of sunflower effect on struts as eccentricity of catheter increases. *Green* and *yellow arrows* show incorrect and correct methods, respectively, of measuring malapposition. (**e**) True strut shape and associated light reflection. (**f**) Proper measurement method of strut malapposition accounting for strut thickness (*yellow arrow*). (**g**) OCT image of malapposed CYPHER stent in vessel with sunflowering. Correct measurements from light reflection (*dotted line*) and back of strut (*solid line*) are shown. [From Elahi et al. [16]]

reflects from a small region of the edge of the strut back to the catheter, not the entire strut. This reflection is primarily specular and is the dominant signal returning to the catheter. As subsequent OCT A-scans reflect from this same point as the catheter rotates, the image reconstruction draws the strut as linear and perpendicular to the catheter.

Elahi et al. [16] demonstrated how the sunflower effect can artifactually increase the distance between the stent strut and the vessel wall if the above mechanism is not properly understood. Since eccentric catheter positions produce light reflections only from a small area on the stent struts, it is critical to correctly draw the stent strut relative to the light reflection (Fig. 5.15). By doing so correctly, it is apparent that simply drawing the shortest line-segment between the center of the strut blooming in the IVOCT image to the luminal wall will provide the true distance of the stent from the vessel wall. Using this technique correctly also requires that the thickness of each manufacture's stent strut is known, and this thickness must be subtracted from the measurement above.
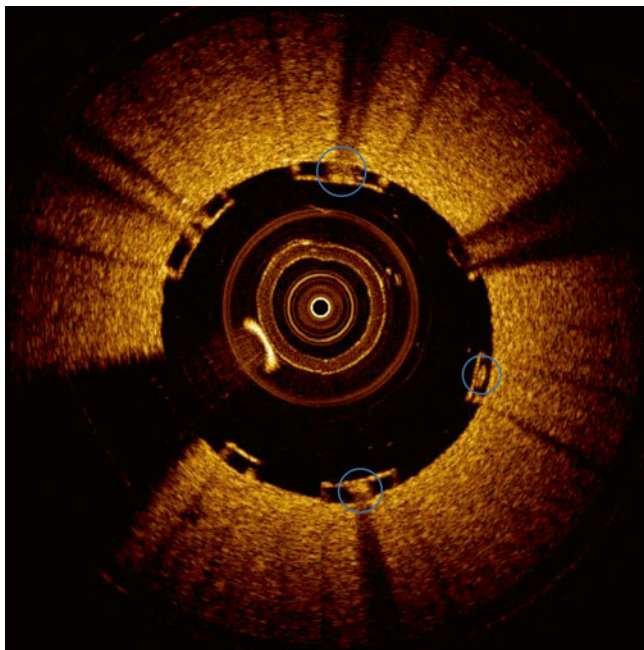
Fig. 5.16 Flare spots. OCT image of bioabsorbable stents demonstrating flare spots artifacts due to normal crazing that occurs with stent expansion (*blue circles*)

5.4.5 Bioabsorbable Stents

Bioabsorbable stents do not exhibit the sunflower artifact. With metallic stents, detected light only reflects from a small region of the strut back to the catheter, not the entire strut, when the light source is in an eccentric position. This localized region of specular reflection is the dominant signal returning to the catheter in the case of metallic stents. But, with bioabsorbable stents, diffuse reflections dominate and specular reflections are weaker than in metal stents. Thus the signal returning to the OCT catheter from bioabsorbable stents may originate from many areas of the strut surface as diffuse reflections that are not dwarfed by the specular signal. Incident OCT light propagates into the polymer struts that refract the light and returns to the photo-receiver. Because light reflections return to the catheter from many regions of the strut surface, the sunflower artifact does not occur and the strut is reconstructed correctly. Also, bioabsorbable struts appear "hollow" (all edges can be seen) in OCT images while only the leading edge of metallic struts are reconstructed in OCT images. The appearance of hollow struts is because light can transmit through the bioabsorbable strut with minimal scattering and reflect off of subsequent optical interfaces. In metallic struts, light cannot refract through the metal so this is not observed.

Bright "flares" sometimes appear in bioabsorbable stent struts when visualized by OCT (Fig. 5.16). Gutiérrez-Chico et al. [19] proposed that flare spots were located at hinge points where the highest strain is experienced during deployment, suggesting that they represent micro-crazes (fine lines) in the polymer. Nonetheless, the mechanism for the presence of flare spots in IVOCT images, and the large variation in their appearance where no two are alike was unclear. Elahi et al. [20] have demonstrated that flare spots observed in IVOCT images correspond to gaps observed in micro-crazes on the arterial side of the stent. The appearance of flare spots in IVOCT images is consistent with light reflecting from surfaces formed at these gap boundaries before returning to the catheter. Thus, flare spots are optical artifacts and consistent with the normal deployment of biodegradable stents, without clinical significance.

Conclusion

In conclusion, numerous optical artifacts are recognized when imaging vessels with and without stents. These include ghost lines, saturation artifact, NURD, fold over artifact, tangential light drop out, sew up artifact, merry-go-round, blooming, ghost struts and flare spots. As the mechanism of these artifacts is determined, physicians will have a better ability to recognize these artifacts and prevent them from causing clinical misinterpretations. As a result, this chapter has attempted to provide not only a comprehensive list of all coronary OCT imaging artifacts, but also describe their mechanisms to better recognize and account for their appearance in recorded images.

References

1. Tearney GJ, Regar E, Akasaka T, Adriaenssens T, Barlis P, Bezerra HG, et al. Consensus standards for acquisition, measurement, and reporting of intravascular optical coherence tomography studies a report from the international working group for intravascular optical coherence tomography standardization and validation. J Am Coll Cardiol. 2012;59(12):1058–72.
2. Bezerra HG, Costa MA, Guagliumi G, Rollins AM, Simon DI. Intracoronary optical coherence tomography: a comprehensive review clinical and research applications. JACC Cardiovasc Interv. 2009;2(11):1035–46.
3. Ferrante G, Presbitero P, Whitbourn R, Barlis P. Current applications of optical coherence tomography for coronary intervention. Int J Cardiol. 2013;165(1):7–16.
4. Lowe HC, Narula J, Fujimoto JG, Jang IK. Intracoronary optical diagnostics current status, limitations, and potential. JACC Cardiovasc Interv. 2011;4(12):1257–70.
5. Mehanna EA, Attizzani GF, Kyono H, Hake M, Bezerra HG. Assessment of coronary stent by optical coherence tomography, methodology and definitions. Int J Cardiovasc Imaging. 2011;27(2):259–69.
6. Suzuki N, Guagliumi G, Bezerra HG, Sirbu V, Rosenthal N, Musumeci G, et al. The impact of an eccentric intravascular ImageWire during coronary optical coherence tomography imaging. EuroIntervention. 2011;6(8):963–9.
7. Li X, Villard JW, Ouyang Y, Michalek JE, Jabara R, Sims D, et al. Safety and efficacy of frequency domain optical coherence tomography in pigs. EuroIntervention. 2011;7(4):497–504.

8. Frick K, Michael TT, Alomar M, Mohammed A, Rangan BV, Abdullah S, et al. Low molecular weight dextran provides similar optical coherence tomography coronary imaging compared to radiographic contrast media. Catheter Cardiovasc Interv. 2013 June 27.

9. Ozaki Y, Kitabata H, Tsujioka H, Hosokawa S, Kashiwagi M, Ishibashi K, et al. Comparison of contrast media and low-molecular-weight dextran for frequency-domain optical coherence tomography. Circ J. 2012;76(4):922–7.

10. Phipps JE, Vela D, Hoyt T, Halaney D, Mancuso JJ, Buja LM, et al. Macrophages and intravascular optical coherence tomography bright spots: a quantitative study. JACC Cardiovasc Imaging. 2014. In press.

11. Nadra I, Mason JC, Philippidis P, Florey O, Smythe CD, McCarthy GM, et al. Proinflammatory activation of macrophages by basic calcium phosphate crystals via protein kinase C and MAP kinase pathways: a vicious cycle of inflammation and arterial calcification? Circ Res. 2005;96(12):1248–56.

12. Rajamaki K, Lappalainen J, Oorni K, Valimaki E, Matikainen S, Kovanen PT, et al. Cholesterol crystals activate the NLRP3 inflammasome in human macrophages: a novel link between cholesterol metabolism and inflammation. PLoS One. 2010;5(7):e11765.

13. Delachartre P, Cachard C, Finet G, Gerfault FL, Vray D. Modeling geometric artefacts in intravascular ultrasound imaging. Ultrasound Med Biol. 1999;25(4):567–75.

14. Finet G, Cachard C, Delachartre P, Maurincomme E, Beaune J. Artifacts in intravascular ultrasound imaging during coronary artery stent implantation. Ultrasound Med Biol. 1998;24(6):793–802.

15. Halaney D, Mancuso JJ, Ho D, Wang T, Elahi S, Dijkstra J, et al. Ghost Struts: A New IV-OCT Artifact. Paper presented at American Heart Scientific Sessions; 2014.

16. Elahi S, Feldman MD, Dijkstra J, Milner TE. Intravascular optical coherence tomography measurement of size and apposition of metallic stents. Biomed Opt Express. 2013;4(10):1876–82.

17. Prati F, Guagliumi G, Mintz GS, Costa M, Regar E, Akasaka T, et al. Expert review document part 2: methodology, terminology and clinical applications of optical coherence tomography for the assessment of interventional procedures. Eur Heart J. 2012;33(20): 2513–20.

18. Elahi S, Mancuso JJ, Milner TE, Feldman MD. Sunflower artifact in OCT. JACC Cardiovasc Imaging. 2011;4(11):1220–1.

19. Gutierrez-Chico JL, Radu MD, Diletti R, Sheehy A, Kossuth MB, Oberhauser JP, et al. Spatial distribution and temporal evolution of scattering centers by optical coherence tomography in the poly(L-lactide) backbone of a bioresorbable vascular scaffold. Circ J. 2012;76(2):342–50.

20. Elahi S, Milner TE, Rapoza RJ, Dijkstra J, Feldman MD. Flare spots in IVOCT images of bioabsorbable stents. JACC Cardiovasc Imaging. 2014. In press.

Clinical Presentations and Coronary Plaque Characteristics

Rocco Vergallo and Ik-Kyung Jang

Abstract

Despite a marked decline in cardiovascular mortality over the last several decades, ischemic coronary artery disease (CAD) still remains one of the leading causes of morbidity and mortality in the United States. This has prompted efforts to improve our understanding of the pathophysiology of CAD using in vivo imaging modalities. Due to its high resolution (10–15 μm), optical coherence tomography (OCT) enables an "optical biopsy" of the coronary artery wall, in vivo and in real time, and represents the modality of choice for the assessment of thin-cap fibroatheroma and other important microstructures such as neovascularization, macrophage density, microcalcifications, and cholesterol crystals. The present chapter focuses on the utility of intracoronary OCT, both as a diagnostic modality and as a research tool, in the detailed characterization of coronary atherosclerosis, in relation to the different clinical presentations (i.e., stable angina vs. acute coronary syndromes), and to the traditional cardiovascular risk factors (i.e., diabetes mellitus, dyslipidemia, smoking, hypertension) and other predisposing conditions (i.e., metabolic syndrome, chronic kidney disease).

Keywords

Optical coherence tomography • Clinical presentation • Acute coronary syndrome • Stable angina • Risk factors • Vulnerable plaque • Thin-cap fibroatheroma

Despite a marked decline in cardiovascular mortality in recent years, which can be attributed both to the advancements in the diagnosis and therapy of cardiovascular disease and to the risk factor modification, coronary artery disease (CAD) still remains one of the leading causes of morbidity and mortality, with more than 2,150 deaths per day (i.e., an average of 1 death every 40 s) in the United States [1]. Over the last several decades, this awareness has prompted tremendous efforts to improve our understanding of the pathophysiology of CAD using in vivo imaging modalities, with the ultimate goal of aiding the diagnosis, developing therapies, and further improving the prognosis of these patients. Although several non-invasive imaging techniques have been proposed, such as multidetector computerized tomography [2], a number of invasive imaging tools have been implemented that are able to better characterize atherosclerotic plaques, by taking advantage of the higher signal-to-noise ratio achievable by positioning an intracoronary probe adjacent to the plaque [3–6]. Since its introduction in the early 1990s, intravascular ultrasound (IVUS) has become a valuable tool enabling an accurate assessment of the atherosclerotic burden in left main

R. Vergallo, MD
Division of Cardiology,
Massachusetts General Hospital,
Harvard Medical School,
55 Fruit Street GRB 800,
Boston, MA 02114, USA

I.-K. Jang, MD, PhD (✉)
Department of Cardiology,
Massachusetts General Hospital,
Harvard Medical School,
Boston, MA 02114, USA
e-mail: ijang@mgh.harvard.edu

disease and in intermediate coronary lesions, as well as to evaluate the vessel morphology [3]. However, its limited spatial resolution (~100–200 μm) does not enable a detailed plaque characterization and visualization of microstructures, which are crucial for the identification of vulnerable plaques. Virtual histology (VH)-IVUS has attempted to overcome this limitation, by providing a color-coded map of the atherosclerotic plaques composition through a spectral radiofrequency analysis of the raw backscattered ultrasound signal, but it does not achieve the precision required to visualize microscopic plaque features [4]. From a different perspective, near-infrared spectroscopy (NIRS) has been designed to assess the lipid content of plaques in the form of a "chemogram" [5], while sacrificing the ability to detect all other plaque characteristics. Due to its higher resolution (10–15 μm), optical coherence tomography (OCT) enables an "optical biopsy" of the coronary artery wall, in vivo and in real time, and represents the modality of choice for the assessment of thin-cap fibroatheroma (TCFA) and of other important microstructures such as neovascularization, macrophage density, microcalcifications, and cholesterol crystals [6, 7].

The present chapter focuses on the utility of intracoronary OCT, both as a diagnostic modality and as a research tool, in the detailed characterization of coronary atherosclerosis, in relation to the different clinical presentations (i.e., stable angina vs. acute coronary syndromes), and to the traditional cardiovascular risk factors (i.e., diabetes mellitus, dyslipidemia, smoking, hypertension) and other predisposing conditions (i.e., metabolic syndrome, chronic kidney disease).

6.1   In Vivo Characterization of Coronary Atherosclerosis by OCT

Intracoronary OCT has allowed us to discover the intricate pathophysiology of coronary atherosclerosis, with a level of accuracy and precision that were inconceivable before its introduction in the clinical and research arena [8]. The high resolution of OCT imaging enables the visualization of the three-layer structure of the normal coronary vessel wall (i.e., intima, media, adventitia), which was not previously feasible with other imaging modalities [7]. The intima is visualized as a signal-rich layer delimiting the coronary lumen, surrounded by the media (signal-poor middle layer) and the adventitia (external signal rich layer) [7, 9]. When an atherosclerotic plaque is present, OCT shows a loss of the three-layered structure of the vessel wall, with a different appearance according to the specific plaque composition [9]. The detailed coronary plaque morphology was assessed for the first time in vivo in 2005, when our group used intracoronary OCT to observe the coronary artery architecture in patients with CAD [6]. While fibrous plaques appear as homogeneous and signal-rich regions, lipid and calcific plaques are characterized by a

signal-poor appearance with diffuse or sharp borders, respectively [6, 9] (See Fig. 6.1). Although these plaque types could also be visualized by IVUS [4], the introduction of OCT enabled interventional cardiologists and researchers to obtain additional detailed microstructural information, and most importantly to measure the thickness of the fibrous cap overlying lipid plaques [7]. This is of uttermost relevance, if we consider that TCFA, pathologically defined as a plaque with large necrotic core covered by a thin (<65 μm) fibrous cap with macrophage infiltration, is considered the prototype of vulnerable, rupture-prone plaque [10]. Using deductive inferences based on radio-frequency signal deconstruction and VH-IVUS, the PROSPECT study showed, in fact, that TCFA is the highest-risk plaque phenotype associated with 3-year major adverse cardiovascular events [11]. Traditionally, OCT-defined TCFA is a lipid-rich plaque (i.e., with a lipid arc ≥90°) with a fibrous cap thinner than 65 μm [11] (Fig. 6.1). Although this threshold has been widely used, it represents a transposition of pathology data into in vivo imaging analysis [10]. Several, independent, in vivo OCT studies have found, in fact, greater or smaller values of fibrous cap thickness (e.g., 80 μm, or 52 μm) to better discriminate ruptured plaques from non-ruptured TCFA [12, 13]. The advantages derived from such high resolution go beyond the ability to detect TCFA, and include other important microstructural features, such as neovascularization, macrophage accumulation, and cholesterol crystals, which can also be imaged by OCT [6, 9]. Neovascularization, detected by OCT as signal-poor vesicular or tubular structures (microchannels) with a diameter of 50–300 μm (See Fig. 6.1), is thought to play a role in plaque vulnerability and progression [14–16]. Uemura et al. found, in fact, that neovascularization detected by OCT, along with TCFA, was the strongest predictor of angiographic progression of non-significant coronary plaques in patients with CAD [16]. Other in vivo OCT studies have shown that plaque neovascularization was associated with larger lipid arc, greater lipid length, and higher prevalence of TCFA [14], and was a predictor of poor responsiveness to statin therapy [17]. Another potential application of OCT is the assessment of macrophage presence (appearing as bright spots with a shadow) (See Fig. 6.1) and density (measured as normalized standard deviation of the RAW OCT signal) (Fig. 6.2) [18, 19]. This method has been validated by immunohistochemistry, demonstrating high degree of positive correlation between OCT and histological measurements of macrophage density with CD68 staining (r = 0.84, P < 0.0001) [18]. However, OCT measurement of macrophage density needs to be interpreted with caution. Some observations suggest, in fact, that other plaque components creating sharp changes in the indices of refraction may sometimes be misinterpreted as macrophages [20]. OCT might also be able to identify cholesterol crystals, described as thin, linear regions with high intensity, usually in proximity of a lipid plaque (See Fig. 6.1), although there
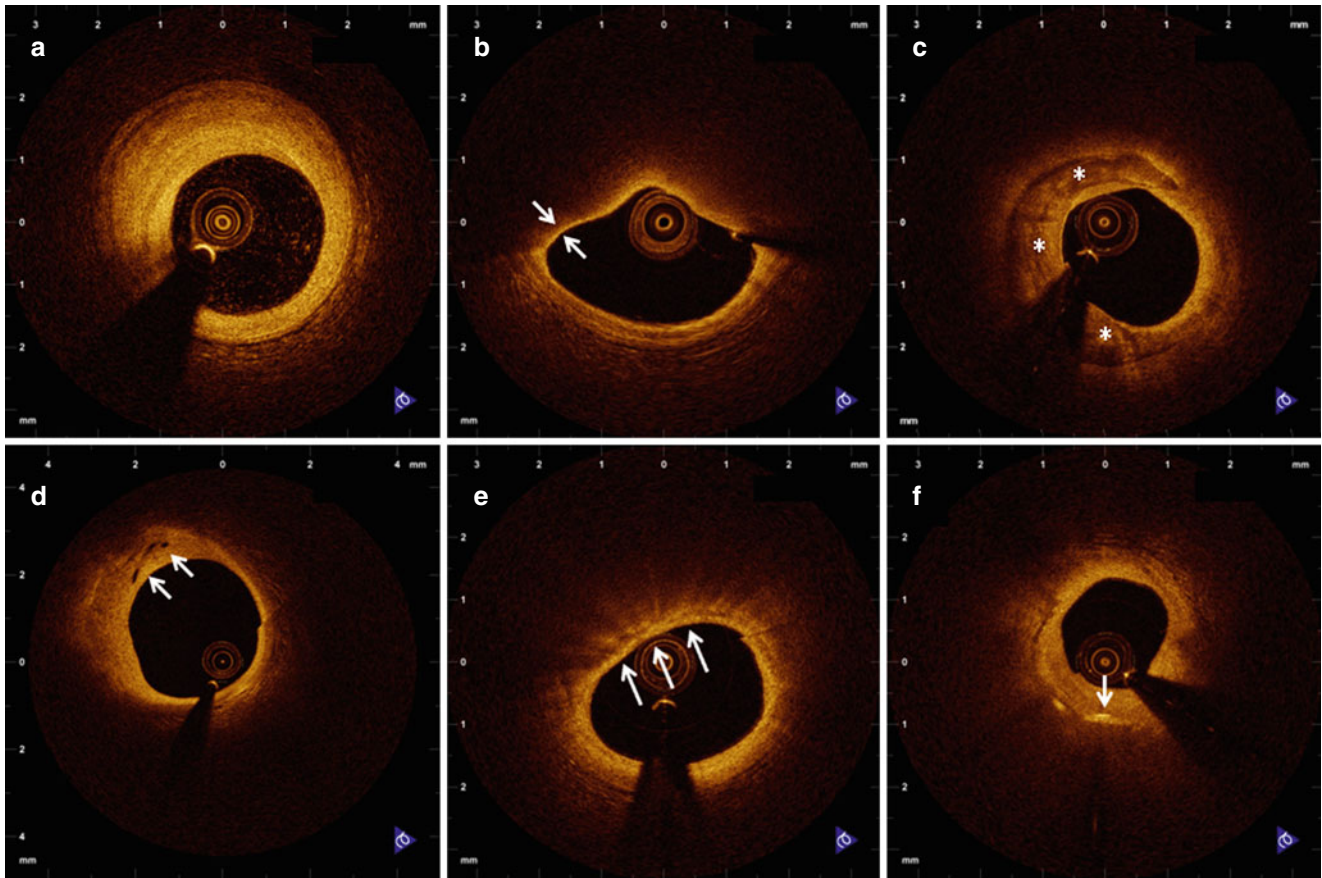
Fig. 6.1 Representative OCT images of coronary plaque characteristics. (**a**) Fibrous plaque; (**b**) Thin-cap fibroatherma: fibrous cap <65 μm (*arrows*) covering a lipid-rich plaque; (**c**) Calcification (*asterisks*); (**d**) Neovascularization (*arrows*); (**e**) Macrophage accumulation (*arrows*); (**f**) Cholesterol crystal (*arrow*)

is lack of histopathological validation for this plaque feature [9]. The emerging possible role of needle-shaped cholesterol crystals in plaque vulnerability, through a mechanical stress on thin fibrous cap [21], may promote further research to validate and improve its identification by OCT. Most of OCT research, in fact, has been recently focusing on the mechanisms triggering ACS, opening new avenues for the diagnosis and treatment of these patients. Jia et al. recently demonstrated the ability of OCT to readily identify in vivo the cause of ACS, including plaque rupture, plaque erosion, and calcified nodule [22]. While plaque rupture appears as a fibrous cap discontinuity leading to a communication between a plaque cavity and the coronary lumen, plaque erosion can be observed as thrombus contiguous to the luminal surface of a plaque with intact fibrous cap [22] (Fig. 6.3). Lastly, calcified nodule can be detected by OCT as protruding, superficial, and nodular calcium [22] (See Fig. 6.3). Therefore, it is evident how OCT represents one of the most valuable tools for plaque characterization, and the modality of choice for identifying the acute plaque complications triggering an acute event. These abilities make OCT not only a captivating research tool, but also a useful diagnostic technique in distinguishing patients with different underlying mechanisms for clinical presentations, and establishing tailored treatments.

6.2 Clinical Presentations and OCT Coronary Plaque Characteristics

Most patients presenting with ACS or dying of cardiovascular death exhibit thrombus overlying a complicated coronary plaque [22, 23]. Although plaque rupture is considered the most frequent plaque complication responsible for ACS, alternative mechanisms of plaque instability triggering coronary thrombosis have been described in pathology studies [10], and, recently, in vivo using OCT [22, 24]. Among these, plaque erosion accounts for about one third of cases, particularly in young women and smokers, and calcified nodules for 5–8 % of cases [10, 22]. However, several other mechanisms can be responsible for ACS, such as a dynamic obstruction due to spasm of an epicardial coronary artery, coronary embolism, coronary dissection, intraplaque hemorrhage or
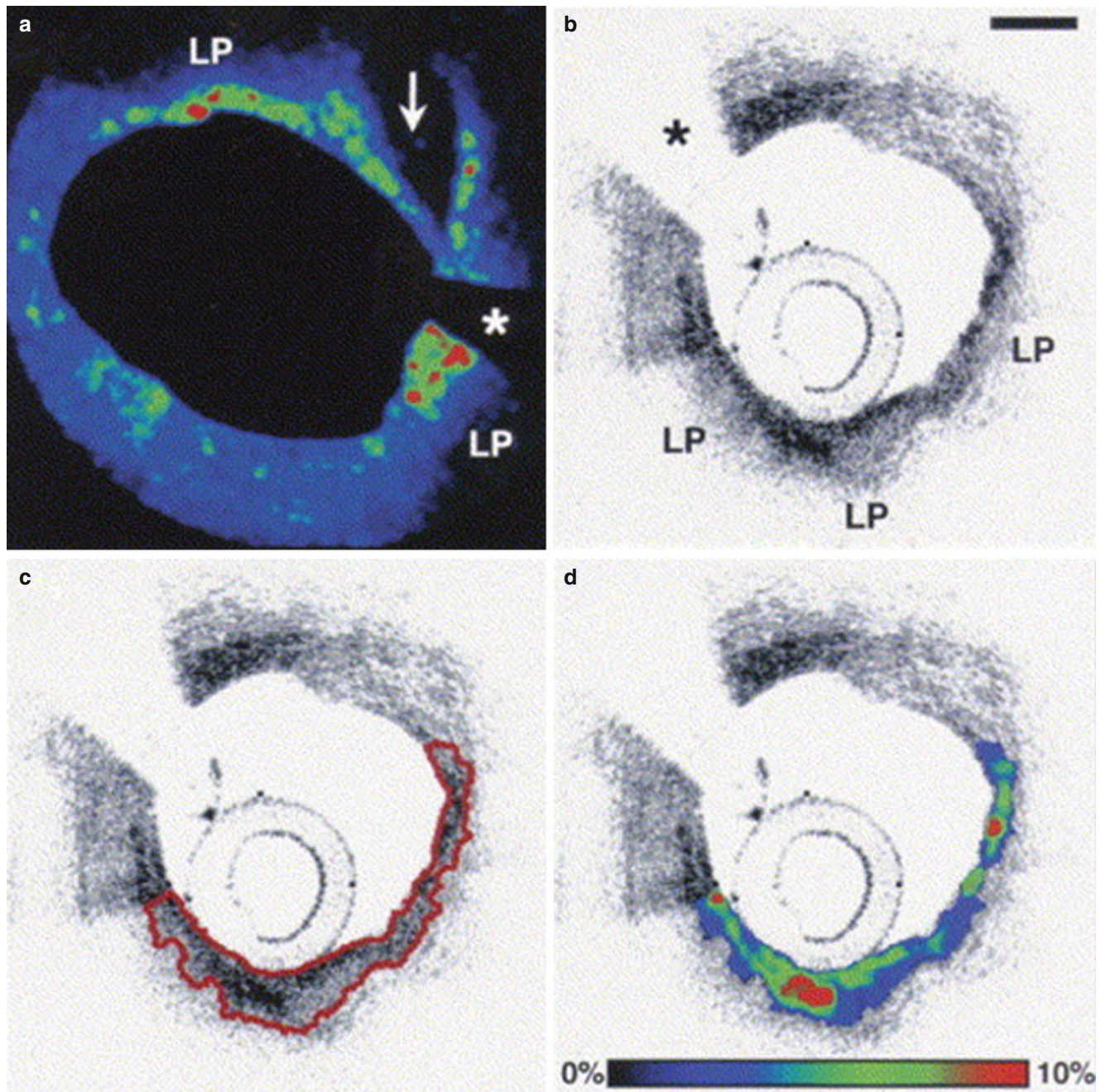
Fig. 6.2 Representative case of fibrous cap segmentation and macrophage density assessment. (**a**) Color-coded map of normalized standard deviation (NSD) values at the site of disruption (*arrow*) of a lipid-rich plaque (*LP*). The area with green-to-red colors represents a region with high macrophage density; (**b**) OCT image of lipid-rich plaque (*LP*); (**c**) Example of fibrous cap segmentation (*red line*); (**d**) Color-coded map of NSD values in the same segmented area. *Asterisks* correspond to wire artifact. Scale bare = 500 μm (From MacNeill et al. [19])

hematoma [22, 25, 26]. This considerable variety of coronary substrates, along with the grade of deriving luminal thrombosis and the myocardial vulnerability to ischemia, can determine a spectrum of clinical presentations, ranging from sudden cardiac death (SCD) or acute myocardial infarction (AMI), with or without ST-segment changes, to unstable angina pectoris (UAP) [21]. In contrast, stable angina pecto-

ris (SAP) arises from a mismatch of blood supply and demand, typically caused by a severe, flow-limiting stenosis without plaque disruption or local thrombosis [27]. Several OCT studies have tried to explore the differences among the various clinical presentations of CAD, with the goal of clarifying pathogenic mechanisms and identifying new diagnostic algorithms and therapeutic targets.
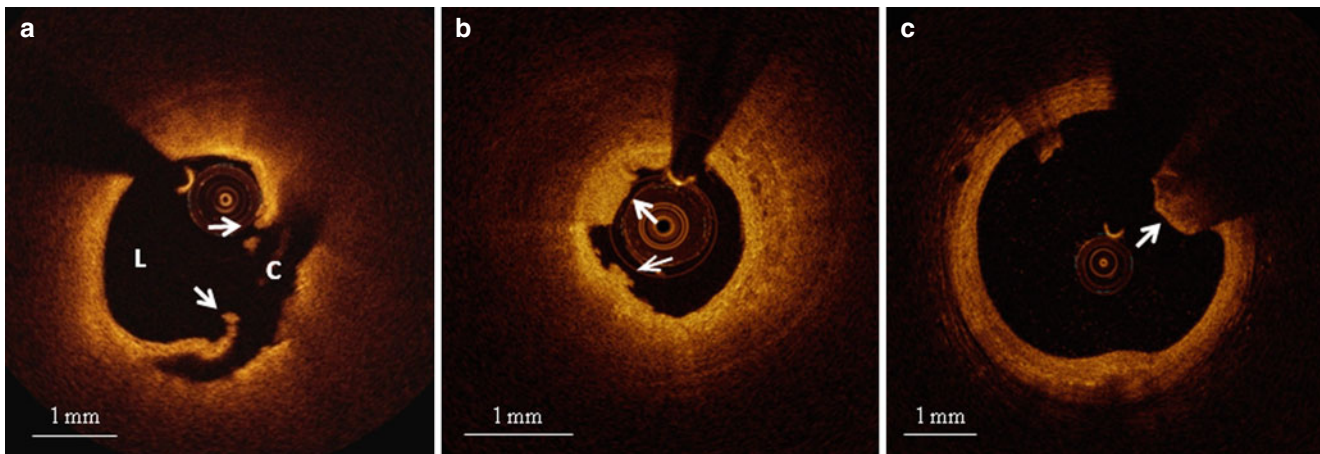
Fig. 6.3 Representative OCT images of various culprit plaque morphologies. (**a**) Plaque rupture: disrupted fibrous cap (*arrows*) leading to a communication between coronary lumen (*L*) and plaque cavity (*C*); (**b**) Plaque erosion: thrombus (*arrows*) overlying a plaque without any signs of rupture; (**c**) Calcified nodule: protruding, superficial, and nodular calcium (*arrow*)
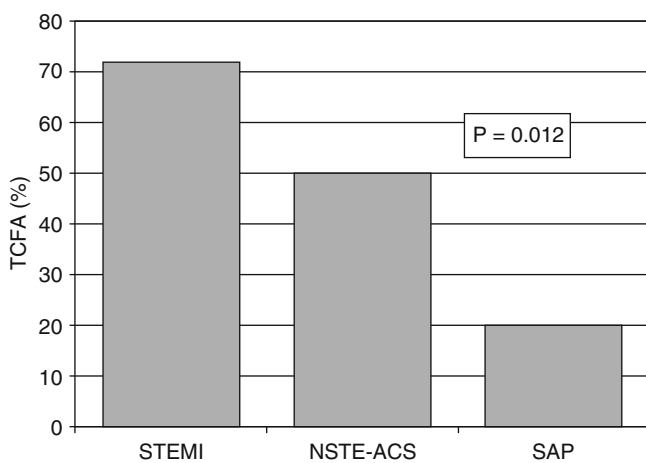

Fig. 6.4 Frequency of TCFA according to the clinical presentation. The prevalence of TCFA was higher in patients with STEMI (72 %) than in those with NSTE-ACS (50 %) and stable angina (20 %) (Adapted from Jang et al. [6])

In 2005, our group investigated, for the first time, the differences in OCT coronary plaque features in patients with various clinical coronary presentations [6]. Specifically, the detailed coronary plaque characteristics at the culprit lesion were compared among patients with ST-elevation myocardial infarction (STEMI), non-ST-elevation ACS (including NSTEMI and UAP), and SAP. That study showed that the prevalence of lipid-rich plaques tended to be higher in patients with STEMI or NSTE-ACS than in those with SAP (90 % vs. 75 % vs. 59 %, respectively, p=0.09). Importantly, there was a significant difference among the three groups in fibrous cap thickness (median value: 47.0 μm [STEMI] vs. 53.8 μm [NSTE-ACS] vs. 102.6 μm [SAP], p=0.034) and in the prevalence of TCFA (72 % [STEMI] vs. 50 % [NSTE-ACS] vs. 20 % [SAP], p=0.012) (Fig. 6.4). In contrast, patients with

SAP showed a higher prevalence of calcifications compared to those with STEMI and NSTE-ACS (10 % [STEMI] vs. 15 % [NSTE-ACS] vs. 41 % [SAP], p=0.049). These findings not only confirmed for the first time in living humans what had previously only been observed in cadavers [23], but also underscored the importance of thin fibrous cap and large lipid burden for plaque vulnerability and the development of ACS.

The degree and distribution of macrophage infiltration in relation to the clinical presentation were studied in this cohort [19]. Pathology studies had previously suggested the role of macrophages in plaque instability, with most of plaque ruptures showing high degrees of macrophage infiltration inside the fibrous cap [10]. In this in vivo OCT study, macrophage densities in culprit and non-culprit lesions were assessed in patients presenting with STEMI, UAP, and SAP, by measuring the normalized standard deviation of the RAW OCT signal, a method validated against histology by the same group [18] (See Fig. 6.2). Interestingly, lipid-rich plaques in patients with STEMI and UAP showed significantly greater macrophage density compared to those in stable patients (5.54±1.48 % vs. 5.86±2.01 % vs. 4.14±1.81 %, p=0.002 and p<0.001, respectively). When STEMI and UAP were combined into a single group of patients with unstable presentation, even the macrophage density in fibrous plaques was higher than that measured in patients with a stable presentation (5.41±1.10 % vs. 4.43±1.46 %, p=0.025). For every patient, there was significant correlation between the macrophage density at the culprit lesion and that at the non-culprit lesions (r=0.66, y=0.88x+0.43, p=0.01). Macrophage density was also greater at the ruptured sites of a plaque compared to at the adjacent non-ruptured sites (p=0.002). Superficial macrophage infiltration (<50 μm from the luminal surface) was a stronger predictor of unstable clinical presentation compared to a deeper macrophage infiltration (>50 μm) in culprit
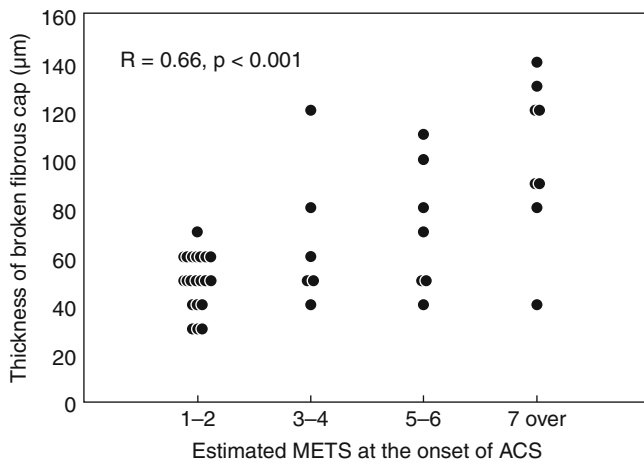
Fig. 6.5 Correlation between fibrous cap thickness and estimated MET score. Positive correlation between fibrous cap thickness and level of activity at the onset of ACS (From Tanaka A. et al. [31])

lesions (p = 0.035), but not in non-culprit lesions. These results suggested, for the first time in vivo, the correlation between macrophage density and the severity of clinical presentation, with greater densities in patients with acute presentation as compared to those with stable clinical presentation [19]. Furthermore, these data proved the multifocal nature of inflammation in symptomatic CAD, and the possible role of macrophages in the development of plaque rupture and acute coronary events [19]. The disruption of the fibrous cap is, in fact, a consequence of the imbalance between the strength of the fibrous cap and forces impinging on it [28]. In this context, activated macrophages, overexpressing matrix metalloproteinases (MMPs) and elastolytic cathepsins, may play an important role, by increasing collagen degradation, reducing collagen synthesis, and inducing the apoptosis of smooth muscle cells [29].

Inspired by pathology observations of differences in the morphology of a ruptured plaque depending on level of exertion at the time of the SCD [30], Tanaka et al. conducted an elegant study investigating the relation between the morphology of ruptured plaque and the level of patient activity at the onset of ACS [31]. Interestingly, the characteristics and location of plaque rupture appeared to correlate with the clinical scenario: specifically, patients developing ACS at rest, compared to those developing ACS during exertion, had a thicker fibrous cap (50 μm vs. 90 μm, p < 0.01), and were more likely to have a plaque ruptured at the shoulder (57 % vs. 93 %, p = 0.014), and overlying thrombus (73 % vs. 96 %, p = 0.04). In addition, fibrous-cap thickness correlated positively with the level of activity at the onset of ACS (Fig. 6.5). These results emphasized the concept that plaque rupture may not infrequently develop from thick-cap fibroatheroma, and that the level of patient activity at the time of the acute presentation may have a role in determining this event. Later on, the same group looked at the differences in culprit plaque morphologies between patients with STEMI and NSTEMI

[32]. The prevalence of plaque rupture was higher in patients with STEMI compared to those with NSTEMI (70 % vs. 47 %, p = 0.033), as well as the prevalence of TCFA (78 % vs. 49 %, p = 0.008) and red thrombus (78 % vs. 27 %, p < 0.001). Interestingly, patients with STEMI showed more frequently a plaque rupture with an aperture against the direction of coronary flow compared to those with NSTEMI (46 % vs. 17 %, p = 0.036) (Figs. 6.6 and 6.7).

Due to the heterogeneous clinical presentation of ACS, classification schemes based on clinical features can be useful to stratify risk, predict prognosis, and establish adequate treatments. For instance, in patients presenting with UAP, the Braunwald clinical classification, which includes three different classes of severity, provides valuable prognostic information [33]. To investigate the relation between clinical presentation and plaque morphology in patients with UAP, Mizukoshi et al. [34] compared the detailed OCT culprit plaque characteristics among the three different classes of severity of UAP, according to the Braunwald clinical classification:

- Class I: new onset of severe angina or accelerated angina, without pain at rest
- Class II: angina at rest within the past month, but not within the preceding 48 h
- Class III: angina at rest within 48 h

Only patients with primary angina (Braunwald class B) were included in the study; those with secondary or post-infarction angina (Braunwald class A and C, respectively) were excluded. Patients with class I showed a significantly higher prevalence of "ulcers" without any disruption compared to those with the other classes (32 % [class I] vs. 7 % [class II] vs. 8 % [class III], p = 0.003) (Fig. 6.8), and a smaller minimum lumen area (0.70 mm² [class I] vs. 1.80 mm² [class II] vs. 2.31 mm² [class III], p < 0.001). These findings may indicate a higher incidence of plaque erosion with subocclusive thrombosis in this group, and explain the typical symptoms of patients with class I, presenting with new onset angina or with a progressive crescendo pattern. In contrast, patients with class II presented more frequently with coronary spasm compared to those with class I and III (0 % [class I] vs. 33 % [class II] vs. 13 % [class III], p < 0.001) (See Fig. 6.8), suggesting that a dynamic obstruction may be the predominant mechanism in this group. Lastly, patients with class III had the thinnest fibrous cap (140 μm [class I] vs. 150 μm [class II] vs. 60 μm [class III], p < 0.001), as well as frequent plaque rupture (43 % [class I] vs. 13 % [class II] vs. 71 % [class III], p < 0.001) (See Fig. 6.8). This observation suggests that increased plaque vulnerability with subsequent disruption may be the baseline mechanism in most of patients with class III, and may explain the worse prognosis associated with this pattern of angina [35].

However, all the above mentioned studies using in vivo OCT imaging for plaque characterization were single-vessel studies, and therefore the results were derived from a limited part of the coronary vasculature. To overcome this limitation, a 3-vessel imaging study from the Massachusetts General
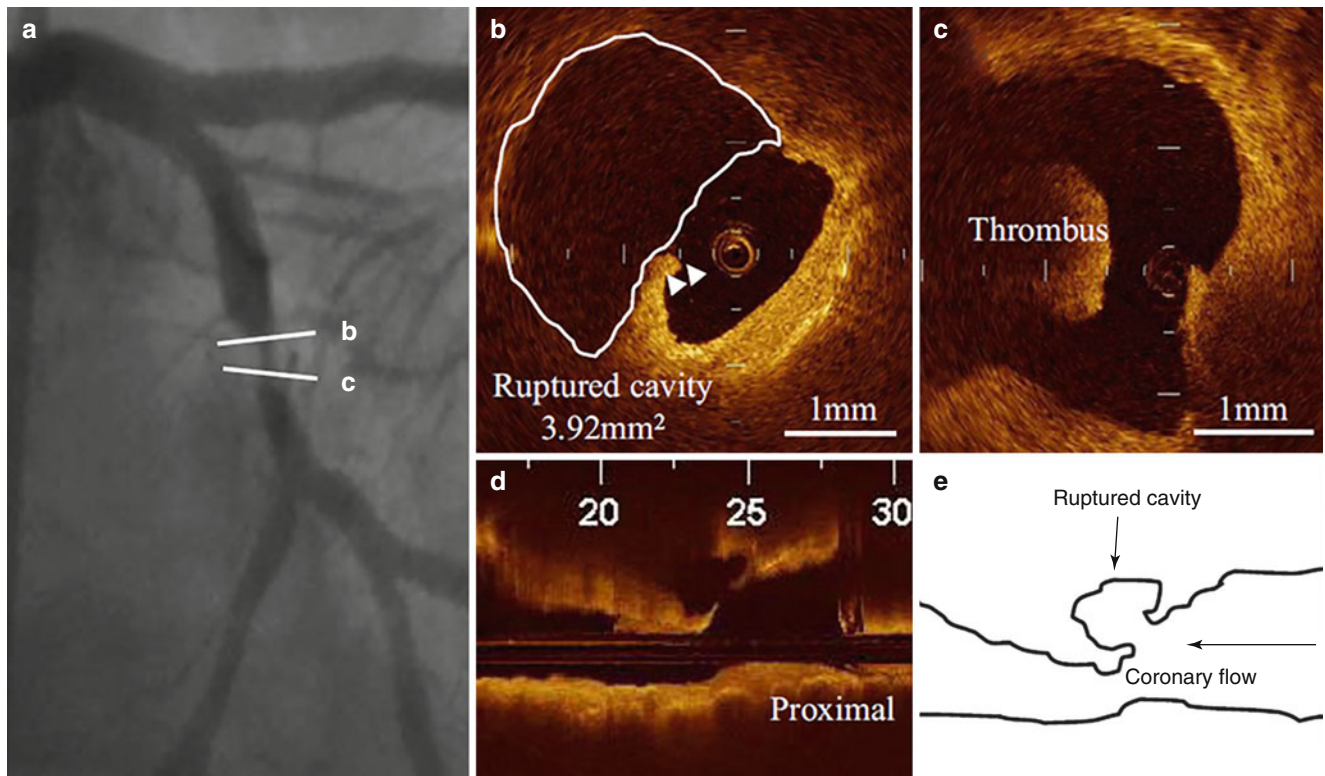
Fig. 6.6 Culprit plaque morphology in a patient with STEMI. (**a**) Coronary angiogram showing a complex lesion in the mid left circumflex artery; (**b**) Disrupted fibrous cap (*arrowheads*) with a large plaque cavity (*white line*); (**c**) Red thrombus in proximity of the ruptured plaque; (**d**) Longitudinal OCT view showing a ruptured plaque with an aperture against the direction of coronary flow; (**e**) Schematic representation of the same ruptured plaque (From Ino et al. [32])
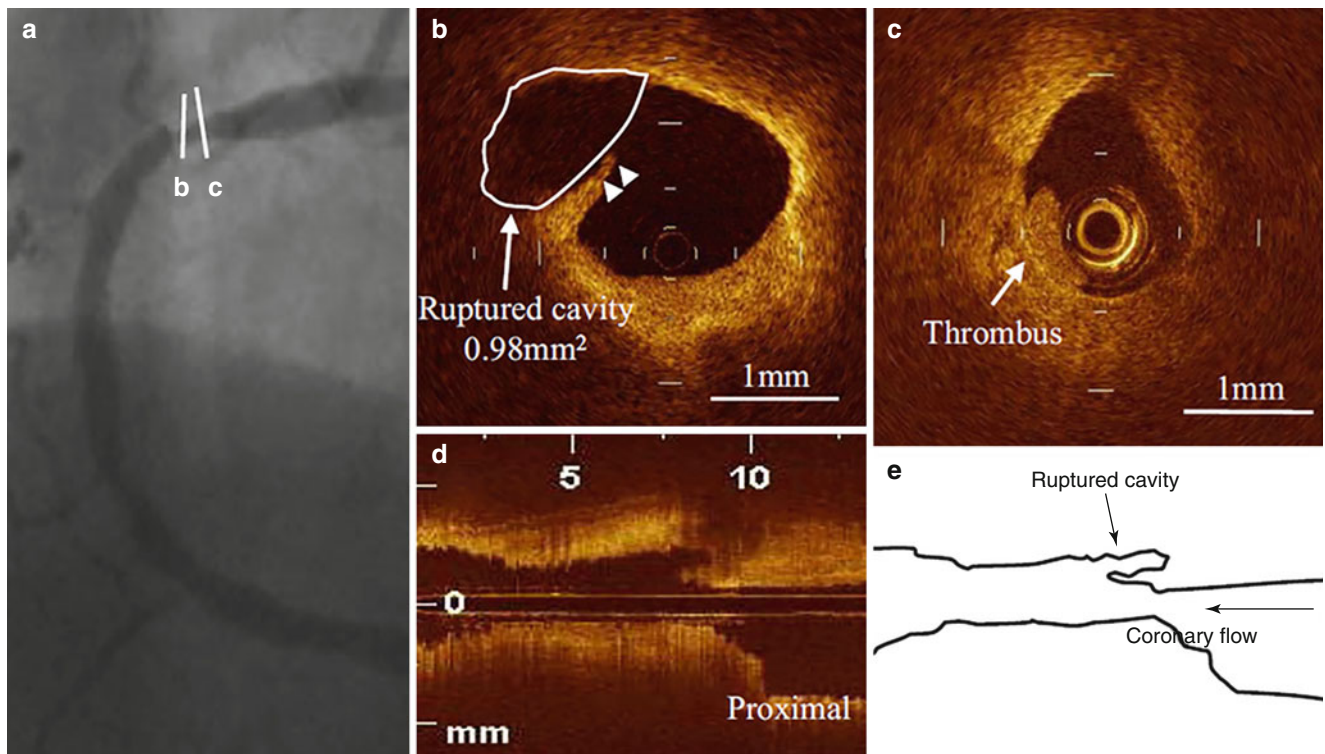

Fig. 6.7 Culprit plaque morphology in a patient with NSTE-ACS. (**a**) Coronary angiogram showing a severe stenosis in the proximal right coronary artery; (**b**) Disrupted fibrous cap (*arrowheads*) with a small plaque cavity (*white line and arrow*); (**c**) White thrombus in proximity of the ruptured plaque; (**d**) Longitudinal OCT view showing a ruptured plaque with an aperture along the direction of coronary flow; (**e**) Schematic representation of the same ruptured plaque (From Ino et al. [32])

Fig. 6.8 OCT plaque characteristics in patients with UAP according to the Braunwald clinical classification. The prevalence of lipid-rich plaque was not different between the three classes. Thrombus was significantly more frequent in patients with class I and III than in those with class II. Plaque rupture was more frequent in patients with class III, "ulcer" without disruption in those with class I, and coronary spasm in those with class II (From Mizukoshi et al. [34])
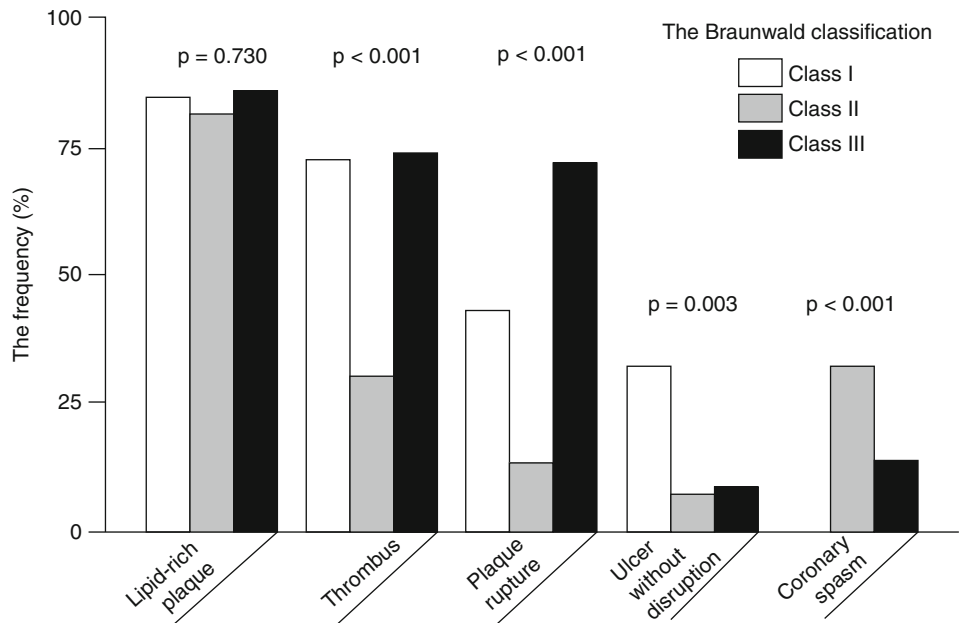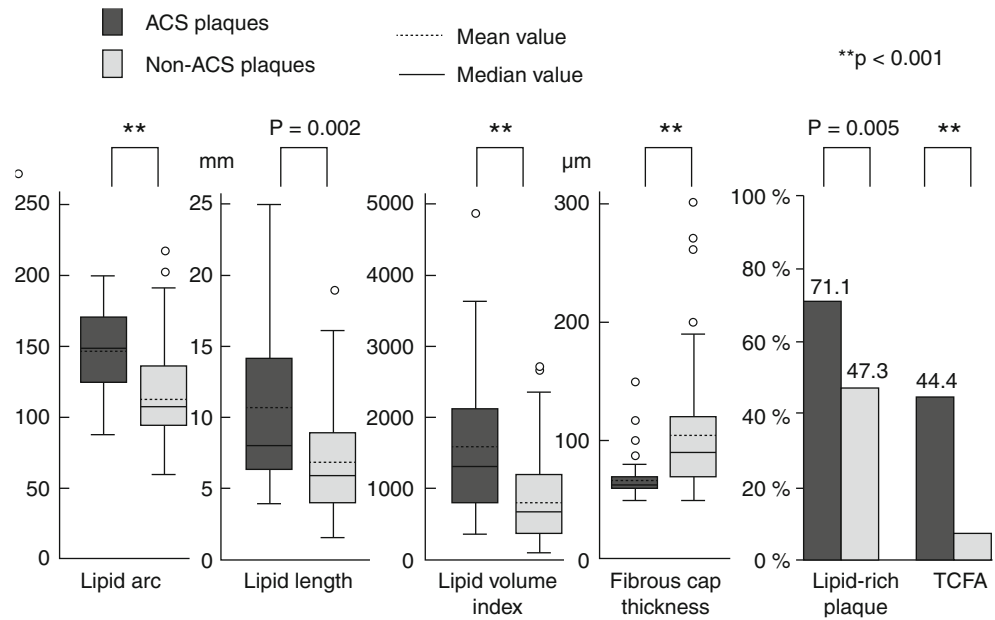

Fig. 6.9 Plaque-based analysis of OCT findings between patients with ACS and those with SAP. Compared to patients with SAP, those with ACS showed larger lipid content, thinner fibrous cap, and higher prevalence of lipid-rich plaque and TCFA (From Kato et al. [36])

Hospital (MGH) OCT Registry investigated the differences in plaque characteristics at non-culprit lesions between patients with ACS and those with a stable clinical presentation [36] (Figs. 6.9 and 6.10). Patients presenting with ACS had a larger number of lipid-rich plaques compared to the stable patients (1.9 ± 1.4 vs. 1.1 ± 1.1, p = 0.013), confirming the data from previous single-vessel OCT studies and angioscopy studies [37, 38]. In addition, lipid plaques were characterized by a wider lipid arc, greater lipid length, larger lipid volume index, and thinner fibrous cap in patients with ACS compared to those with SAP (See Fig. 6.9). Notably, the

prevalence of TCFA was significantly higher in patients with ACS than in those with SAP (64.7 % vs. 14.9 %, p < 0.001), as well as the prevalence of macrophage accumulation (82.4 % vs. 37.9 %, p = 0.001) and thrombus (29.4 % vs. 1.1 %, p < 0.001) (See Fig. 6.10). These results emphasized the panvascular nature of atherosclerosis, and the presence of greater plaque vulnerability in the coronary tree of patients with ACS than those with SAP, which may lead to higher rate of recurrent ischemic events. Interestingly, the prevalence of plaque disruption at non culprit lesions was also greater in patients with ACS than in those with stable clinical

Fig. 6.10 Patient-based analysis of OCT findings between patients with ACS and those with SAP. Compared to patients with SAP, those with ACS showed higher prevalence of TCFA, macrophage accumulation, thrombus, and a shorter distance between microchannels and coronary lumen (From Kato et al. [36])
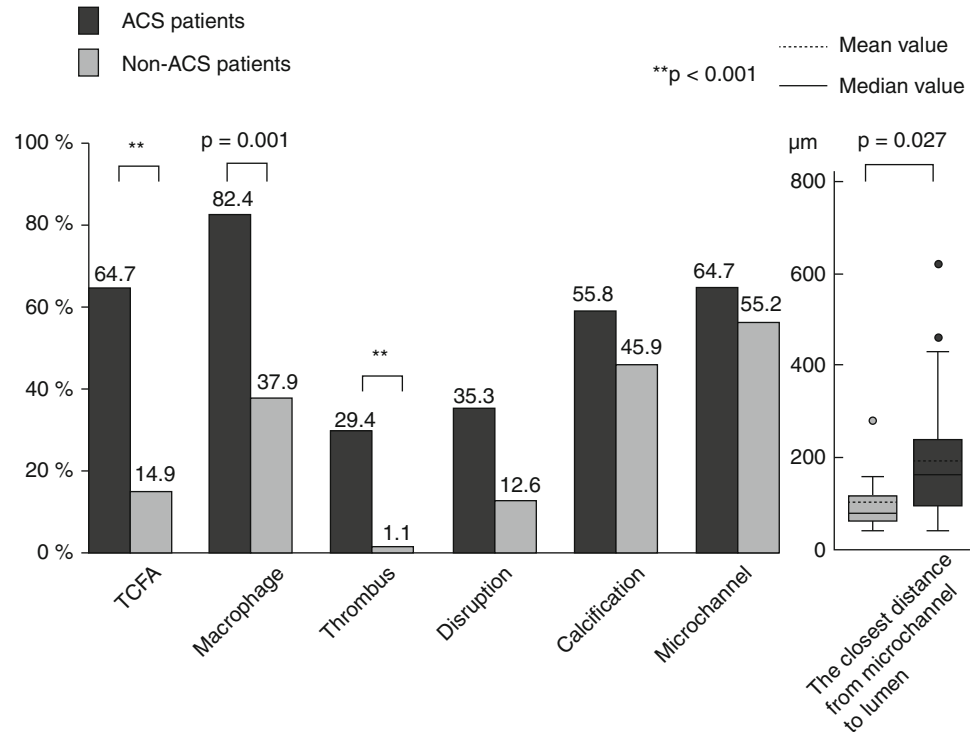
presentation, although the difference was not statistically significant. Lastly, although the prevalence of intimal neovascularization was not different between the two groups, patients with ACS had microchannels with a more superficial location (See Fig. 6.10). Neovascularization may play a role in plaque vulnerability [14] and progression [16], through the recruitment of inflammatory cells and the promotion of lipid accumulation within atherosclerotic plaque [39]. A more superficial location of neovascularization might reflect an advanced stage of atherosclerosis; however, this hypothesis needs to be confirmed in future studies. Although this study analyzed the detailed coronary plaque characteristics in patients with ACS, potential differences in non-culprit plaque characteristics in relation to various culprit plaque morphologies had not yet been investigated. As shown by pathology [10] and in vivo imaging studies [22], different types of culprit plaques are characterized by specific underlying morphologic characteristics, and are associated with different clinical presentations. In light of the systemic nature of atherosclerosis, it is reasonable to hypothesize that non-culprit plaques might have different characteristics based on the specific culprit plaque morphology. This was tested in a 3-vessel OCT study comparing the non-culprit plaque characteristics between patients with plaque rupture and those with non-ruptured plaque at the culprit lesion [40]. Patients with ACS caused by plaque rupture showed a higher prevalence of lipid-rich plaques, TCFA, and additional disruption in non-culprit lesions compared to those with a non-

ruptured culprit plaque. Patients with ACS caused by a plaque rupture had a TCFA at a remote site in 52.9 % of cases, and an additional disruption in 35.3 % of cases, which localized more frequently in the culprit artery. These data indicated the presence of pancoronary vulnerability in patients with ACS caused by plaque rupture, which may explain the multifocal instability observed during the acute phase, and may be responsible of recurrent cardiac events (Fig. 6.11). It is conceivable that this subset of high-risk patients might benefit from aggressive systemic anti-inflammatory treatments [41] or new lipid-lowering therapies (e.g., PCSK9 inhibitors) [42], in addition to the standard antiplatelet and statin therapies. Further studies are warranted to confirm this hypothesis.

6.3 OCT Coronary Plaque Characteristics and Cardiovascular Risk Factors

6.3.1 Diabetes Mellitus

Diabetes mellitus (DM) is a well recognized independent risk factor for CAD [43]. Patients with DM have increased morbidity and mortality compared to non-diabetic patients, with a two- to five-fold higher incidence of cardiac death or AMI [43, 44], and a 2-fold higher incidence of recurrent ischemic events [43]. This has been related to the presence
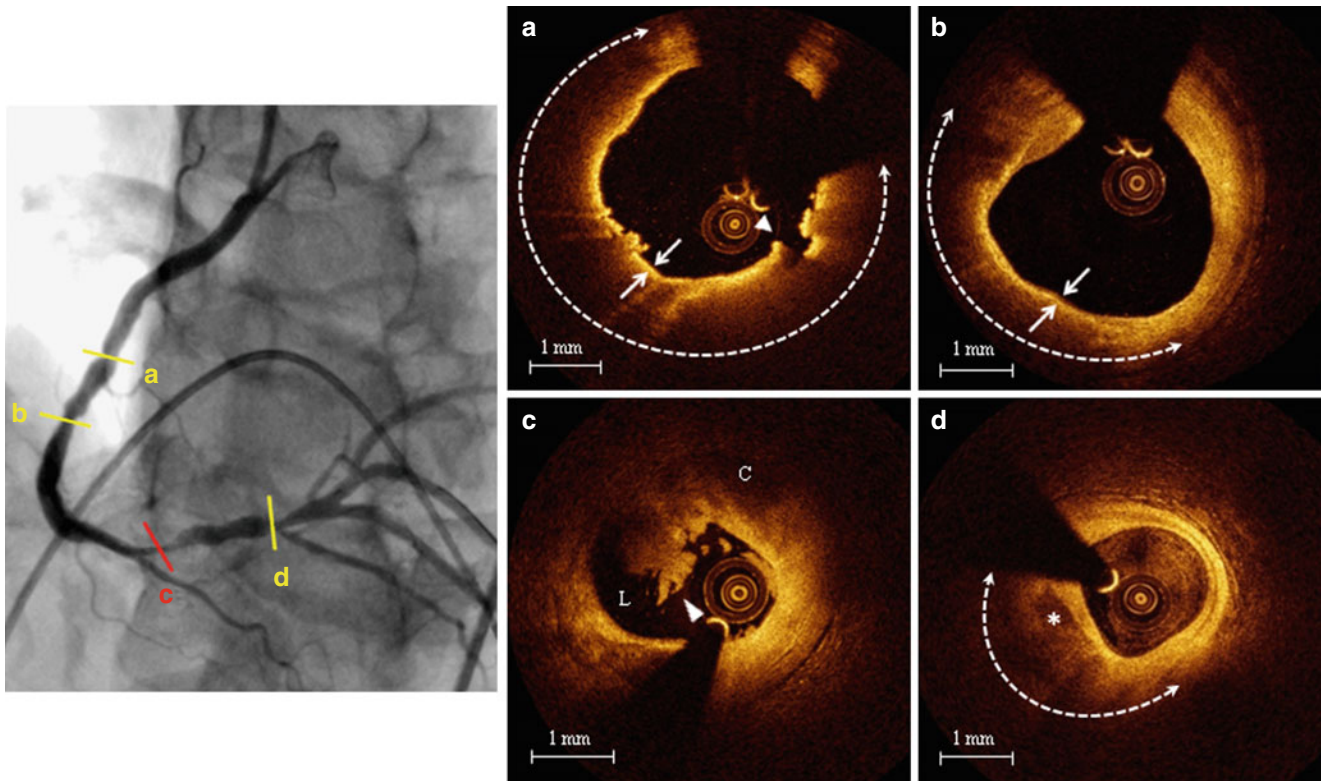
Fig. 6.11 Representative case of patient with ACS showing diffuse plaque vulnerability. *Left panel*. Coronary angiogram of the right coronary artery showing multiple lesions; (**a**) Non-culprit TCFA: large lipid arc (*dashed line*) covered by a thin (<65 μm) fibrous cap (*arrows*) with signs of disruption (*arrowhead*); (**b**) Non-culprit TCFA: large lipid arc (*dashed line*) covered by a thin (<65 μm) fibrous cap (*arrows*); (**c**) Culprit ruptured plaque with overlying thrombus (*arrowhead*). (*C* cavity, *L* lumen); (**d**) Non-culprit lipid plaque (*dashed line*) with spotty calcification (*asterisk*) (From Vergallo et al. [40])

of enhanced pro-atherosclerotic, pro-inflammatory, and pro-thrombotic stimuli in patients with DM [45]. Pathology studies have reported that subjects with DM who died of SCD had more severe atherosclerosis, larger plaque burden, greater necrotic core, and increased inflammation in their coronary arteries, as compared with non-diabetic subjects [46]. To clarify the mechanism responsible for the increased cardiovascular-risk in diabetic patients, a 3-vessel OCT study was performed comparing the detailed characteristics of non-culprit plaques between patients with DM and those without DM [47]. Although there was no difference in the prevalence of lipid-rich plaques (67.7 % [non-DM] vs. 63.9 % [DM], p=0.825) and TCFA (19.4 % [non-DM] vs. 27.8 % [DM], p=0.277) between the two groups, the non-culprit plaques of DM patients were characterized by wider lipid arc, greater lipid length and larger lipid volume index, and tended to have a thinner fibrous cap. Moreover, patients with DM showed higher prevalence of calcifications (48.4 % [non-DM] vs. 72.2 % [DM], p=0.034) and thrombus (0 % [non-DM] vs. 8.3 % [DM], p=0.047). These observations were consistent with the results from a subanalysis of the PROSPECT study showing no difference in the prevalence of VH-IVUS fibroatheroma between patients with and with-

out DM, but a higher necrotic core and calcium content in diabetic patients [48]. Interestingly, all the measures of lipid burden and fibrous cap thickness were significantly related with the hemoglobin (Hb) A_{1C} levels (Fig. 6.12), and patients with Hb A_{1C} levels ≥ 8 % showed a higher incidence of TCFA and macrophage accumulation, suggesting that diabetic patients with poor glycemic control may develop more vulnerable atherosclerotic features. Interestingly, another OCT study by Niccoli et al. [49] conducted in diabetic and non-diabetic patients at the time of a very first acute coronary event showed, consistent with previous studies, a greater number of calcified quadrants and a wider calcification arc in patients with DM compared to those without DM, but a surprisingly lower lipid content (i.e., lipid quadrants and lipid arc) at the minimum lumen area site of the culprit lesion. Another two OCT studies failed to show differences in the prevalence of lipid-rich plaques and TCFA at the culprit lesion between patients with and without diabetes [50, 51]. However, while our study [47] and the DM substudy of the PROSPECT trial [48] were 3-vessel imaging investigations, the other above-mentioned studies [49–51] performed OCT imaging only in the culprit vessel, and this may explain the contrasting results. Taken together these observations
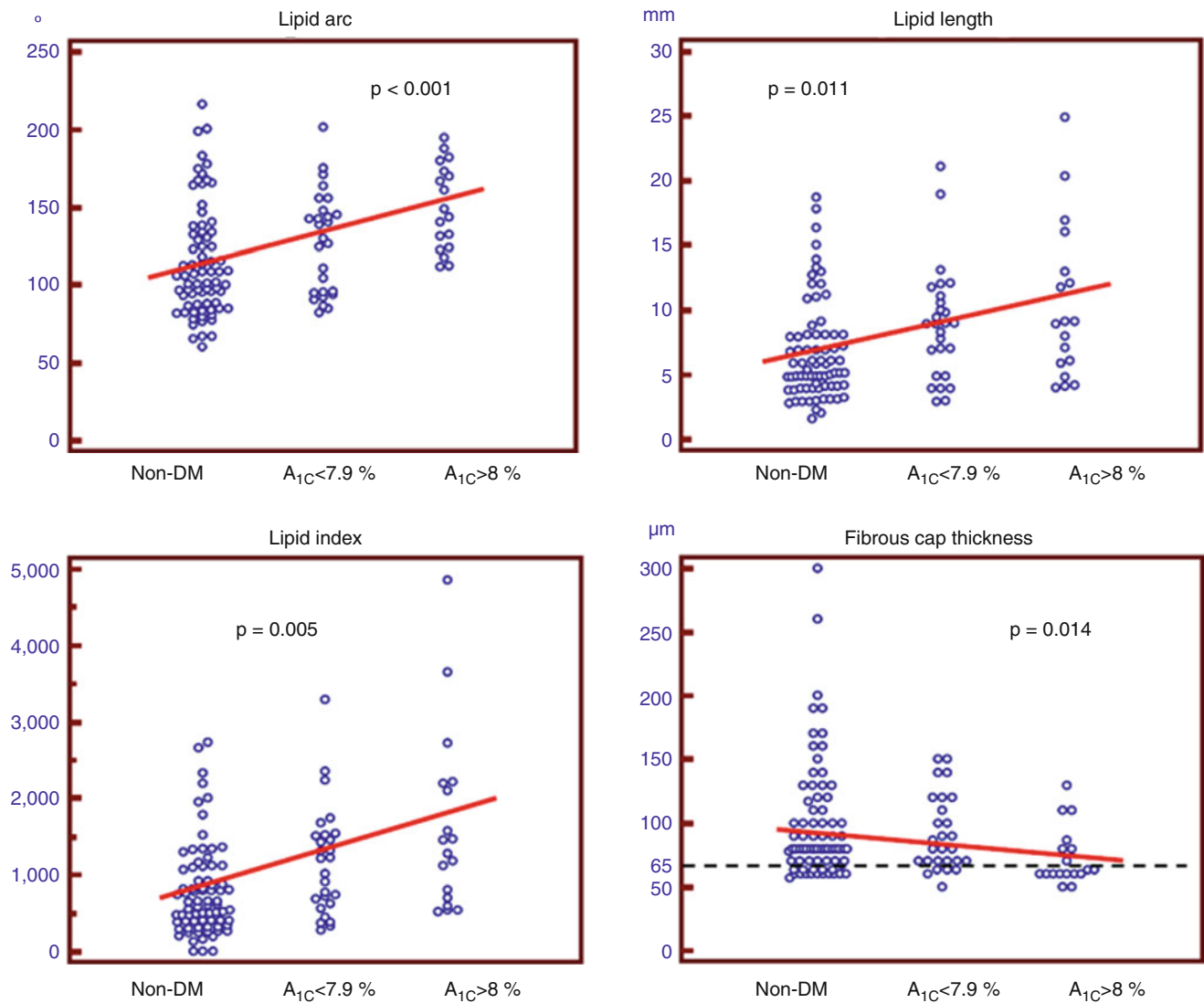
Fig. 6.12 Correlation between OCT plaque characteristics and levels of Hb A_{1C}. All OCT parameters of lipid burden correlated positively with the levels of Hb A_{1C}, whereas there was an inverse correlation between fibrous cap thickness and levels of Hb A_{1C} (From Kato et al. [47])

suggest that patients with diabetes may have increased plaque vulnerability in their coronary tree, particularly in cases of poor glycemic control, but that such differences may not necessarily be observed at the site of culprit lesion.

6.3.2   Hyperlipidemia

Hyperlipidemia represents one of the most important and best substantiated risk factors for CAD [52]. Several epidemiologic, genetic, and interventional trials have explored the causal relation between dyslipidemia and atherosclerosis, and have identified lipid-modification therapy as a risk-reducing strategy for patients with CAD [52–54]. Data from numerous large-scale trials have consistently proved the efficacy of lipid-lowering therapy with statins for the

reduction of subsequent cardiovascular events and mortality [54–56]. In addition, IVUS studies have monitored the changes in atheroma volume in relation to different intensities of lipid-lowering therapies, demonstrating the ability of statins to reduce the progression of coronary atherosclerosis [57]. This effect was significantly related to the reduction of both the levels of atherogenic lipoproteins and the systemic inflammatory status (i.e., C-reactive protein, CRP) [58]. Retrospective OCT studies have also attempted to clarify the relation between lipid profile and morphological characteristics of coronary atherosclerosis. In a study by Takarada et al. [59], 82 patients with NSTE-ACS were imaged with both IVUS and OCT at baseline and after 9 months in order to investigate the changes in non-culprit plaque composition in relation to the lipid and inflammatory profiles. The changes in total atheroma volume assessed by IVUS, but
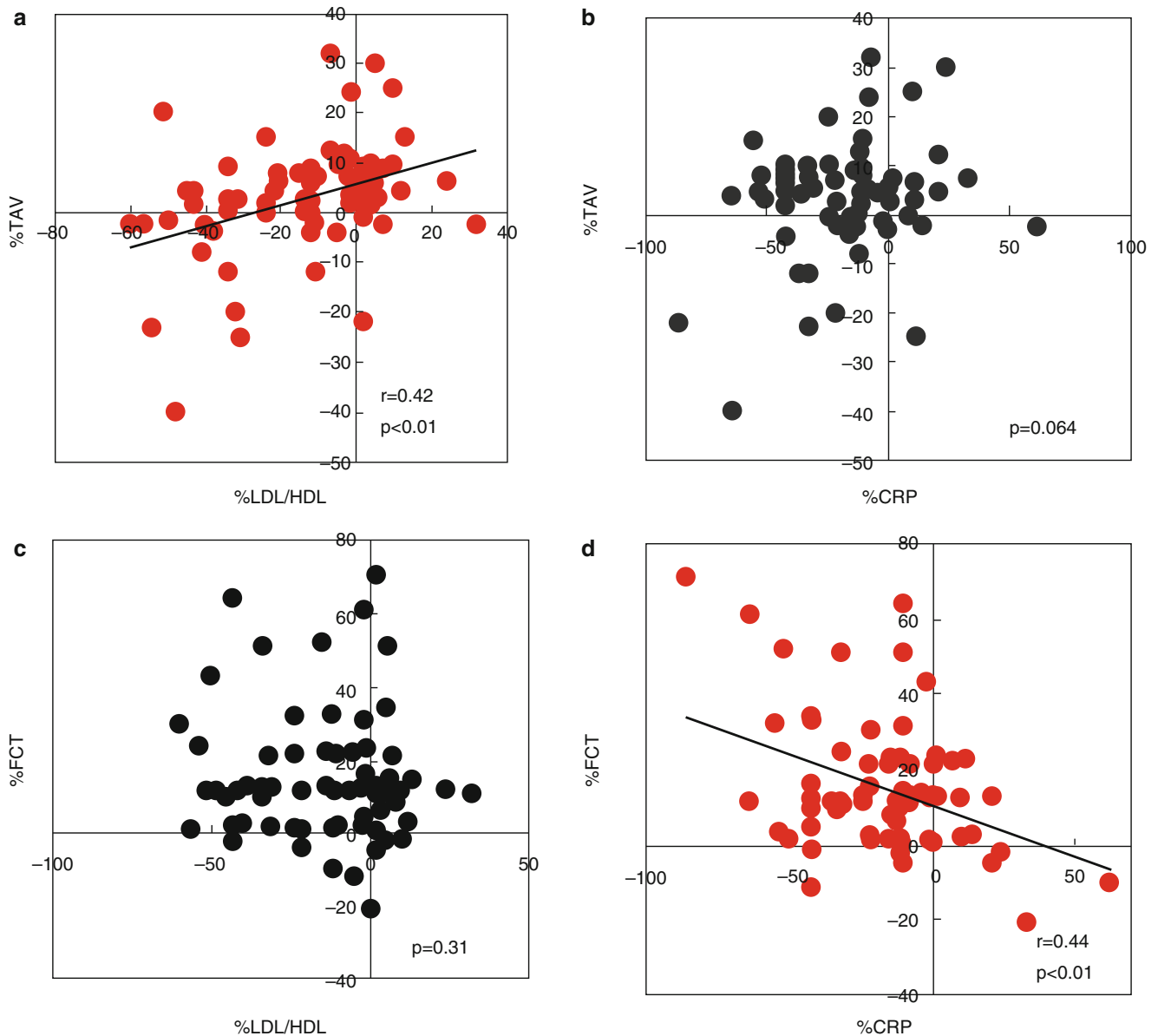
Fig. 6.13 Correlation between lipid and inflammatory profile and plaque characteristics. (**a**, **b**) IVUS-detected % total atheroma volume (*TAV*) correlated significantly with % low-density lipoprotein/high-density lipoprotein (LDL/HDL) ratio, but not with % C-reactive protein (%CRP); (**c**, **d**) In contrast, OCT-detected % fibrous cap thickness correlated significantly with %CRP, but not with %LDL/HDL ratio (From Takarada et al. [59])

not those in fibrous cap thickness assessed by OCT, were significantly correlated with the low-density lipoprotein/high-density lipoprotein (LDL/HDL) ratio. Conversely, the changes in fibrous cap thickness were inversely related to the high-sensitivity CRP levels (Fig. 6.13). Interestingly, statin therapy was an independent predictor of plaque stabilization, defined as a concomitant decrease in total atheroma volume and increase in fibrous cap thickness [59]. Another study from the same group [60] demonstrated that patients with TCFA at the culprit lesion had significantly lower HDL-cholesterol levels (39.6 ± 10.1 mg/dl vs.

46.7 ± 11.7 mg/dl, p < 0.001), higher LDL-cholesterol levels (120.7 ± 31.1 mg/dl vs. 110.0 ± 28.1 mg/dl, p = 0.004), and greater LDL/HDL ratio (3.2 ± 1.0 vs. 2.5 ± 0.8, p < 0.001), as compared with patients without TCFA at the culprit lesion. Interestingly, a study by Matsuo et al. reported higher levels of malondialdehyde-modified LDL, which is an oxidized LDL, in SAP patients with TCFA than in those without TCFA (p < 0.001) [61]. Higher levels were also detected in ACS patients with ruptured TCFA compared to those with intact TCFA (p = 0.023). Multivariate analyses proved that malondialdehyde-modified LDL levels were independently
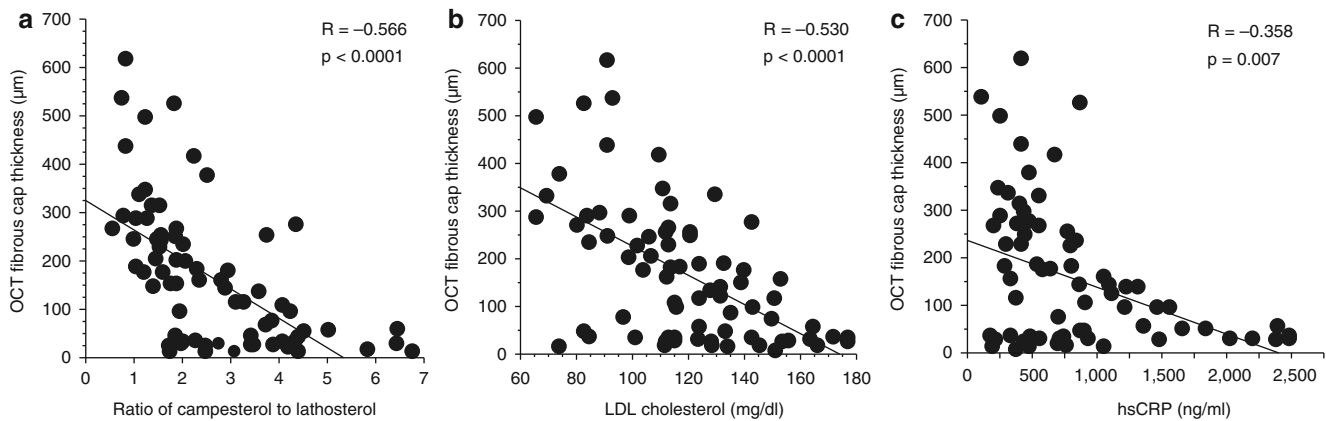
Fig. 6.14 Correlation between lipid profile and fibrous cap thickness. OCT-detected fibrous cap thickness correlated inversely with campesterol-to-lathosterol ratio (**a**), LDL-cholesterol levels (**b**), and high-sensitivity CRP levels (**c**) (Adapted from Nasu et al. [63])

associated with the presence of TCFA (odds ratio [OR]: 1.45 per 10-unit increment, 95 % confidence interval [CI]: 1.24−1.68; p<0.001). Oxidative modification of lipoproteins plays a pivotal role in the atherogenic process, through chemotactic activity on monocytes and T-cells, stimulation of MMP-1 and MMP-9 expression, promotion of CD40/CD40L signaling pathway, and direct cytotoxic activity on endothelial cells and smooth muscle cells [62]. Lastly, a recent investigation by Nasu et al. [63], using VH-IVUS and OCT, showed a correlation between fibrous cap thickness and lipid and inflammatory profiles in stable patients not receiving any lipid-lowering therapies (Fig. 6.14). Notably, campesterol-to-lathosterol ratio (OR: 3.99, 95 % CI: 1.69−9.43; p=0.002), LDL-cholesterol levels (OR: 1.42, 95 % CI: 1.02−1.98; p=0.03), and high-sensitivity CRP levels (OR: 1.02, 95 % CI: 1.00−1.05, p=0.02) independently predicted the presence of TCFA. Taken together, all these studies suggest a clear relationship between lipid profile and features of coronary plaque vulnerability. Prospective, serial OCT studies with randomization to different lipid-lowering therapy regimens are needed in order to define the best approach for coronary plaque stabilization and prevention of cardiovascular events.

6.3.3 Smoking

Smoking is a major risk factor for CAD [64], and is thought to increase cardiovascular disease burden by promoting endothelial dysfunction, atherosclerotic plaque development, and thrombosis [65]. Clinically, tobacco smoking has been reported as a predictor of new coronary atherosclerosis, and has been associated with angiographic disease severity in a dose-dependent manner [66]. In addition, current smoking independently predicts the presence of neoatherosclerosis inside the stent [67, 68]. VH-IVUS studies failed to show

a relationship between smoking and TCFA or any other plaque characteristics [69, 70]. However, VH-IVUS does not have the sufficient resolution to measure fibrous cap thickness and identify TCFA, and those studies did not use a multivessel imaging approach. A recent 3-vessel OCT study by Abtahian et al. assessed the detailed coronary plaque morphology in 182 patients with CAD, according to their smoking status [71]. Compared with former smokers and nonsmokers, current smokers were more likely to have lipid-rich plaques (45.9 % vs. 52.6 % vs. 68.0 %, respectively, p=0.002) and TCFA (7.6 % vs. 9.9 % vs. 18.4 %, p=0.018). In contrast, former smokers showed a significantly higher prevalence of calcified plaques than current and non smokers (52.9 % vs. 38.0 % vs. 32.0 %, p=0.001). Multivariate analysis showed that current smoking, presentation with ACS, and LDL-cholesterol levels were independent predictors of the presence of TCFA. The higher prevalence of ruptured-prone TCFA may explain the increased risk of future acute events observed in current smokers [72].

6.3.4 Hypertension

Hypertension represents one of the most important risk factors for cardiovascular disease, affecting 70 millions of people in the United States [73]. Approximately one half cases of CAD can be attributed to a suboptimal blood pressure [73]. Hypertension induces endothelial dysfunction, promotes atherosclerosis, and favors plaque destabilization. In addition, left ventricular hypertrophy which usually derives from hypertension promotes a reduction in coronary reserve, contributing to myocardial ischemia [74]. In this regard, a study by Tsioufis et al. investigated the correlation between coronary flow reserve and OCT-derived intimal thickness and intima-media thickness in hypertensive patients with normal coronary arteries and without left ventricular hypertrophy

Fig. 6.15 OCT plaque characteristics in patients with chronic kidney disease (*CKD*). Compared to patients without CKD, those with CKD showed larger lipid arc, greater lipid length and higher lipid index, as well as thinner fibrous cap (From Kato et al. [80])
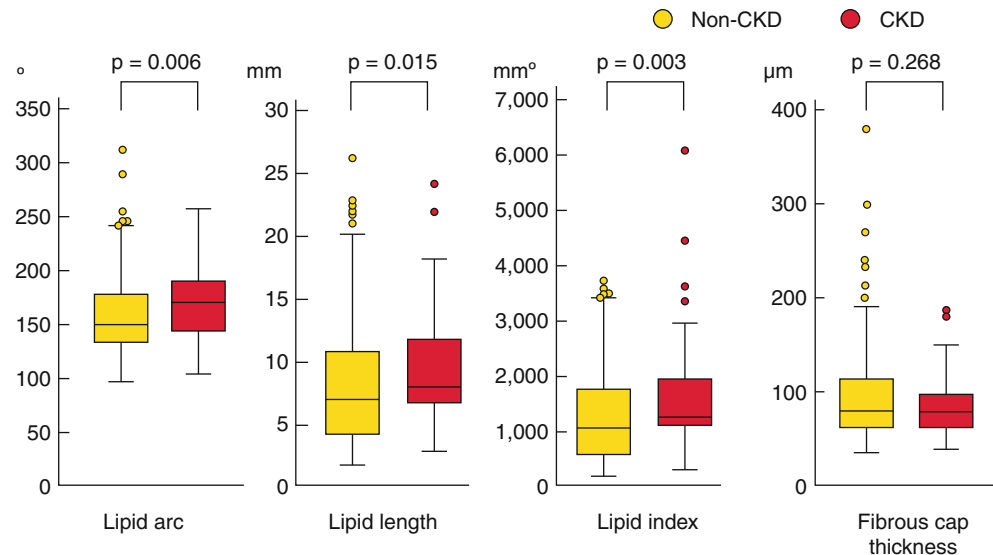
[75]. No correlation was observed between those measurements, suggesting that in hypertensive patients without left ventricular hypertrophy, adverse microcirculatory modifications assessed by CFR are not accompanied by changes in coronary intimal thickness and intima/media thickness. Aside from this observation in hypertensive patients with normal coronary arteries, no systematic OCT studies have yet been attempted in patients with CAD to investigate the correlation between hypertension and plaque morphology. However, data from VH-IVUS studies suggests the presence of associations between hypertension and an increased fibro-fatty, calcified, and necrotic plaque content [70]. In light of the global burden of hypertension, and its relevance for the pathogenesis of cardiovascular diseases, future investigations using high-resolution OCT in patients with hypertension are warranted.

6.3.5 Metabolic Syndrome (MetS)

According to the National Cholesterol Education Program Adult Treatment Panel [76], MetS is defined by the presence of at least 3 of the following 5 criteria: (1) waist circumference >102 cm in men and >88 cm in women; (2) serum triglyceride levels ≥150 mg/dL; (3) HDL-cholesterol <40 mg/dL in men and <50 mg/dL in women; (4) blood pressure ≥130/85 mmHg; and (5) serum glucose ≥110 mg/dL. The various associations and clustering of these factors have been the object of extensive investigations, and previous studies have demonstrated a higher incidence of cardiovascular events in patients with MetS [77]. However, the definition of MetS differs according to various guidelines and statements, and its concept has been a matter of concern. OCT has provided useful information to clarify the link between MetS and coronary atherosclerosis. Our group studied 451 coronary

plaques from 171 subjects who underwent 3-vessel OCT imaging [78]. Compared to a control group, patients with MetS, as well as those with DM, had coronary plaques with longer lipid-core length (7.0 ± 3.8 mm [MetS] and 7.7 ± 4.0 mm [DM] vs. 5.5 ± 2.4 mm [controls]; $p<0.001$ and $p=0.012$) and greater lipid volume index ($1,086\pm693$ [MetS] and $1,164\pm716$ [DM] vs. 796 ± 417 [controls]; $p<0.001$ and $p=0.008$). However, fibrous cap thickness and prevalence of TCFA, which are known hallmarks of plaque vulnerability, were not different among the three groups, suggesting the need for further investigations to better define the underlying pathophysiology of MetS as a cardiovascular risk factor.

6.3.6 Chronic Kidney Disease (CKD)

CKD is a worldwide public health problem, and its impact on cardiovascular morbidity and mortality is well recognized [79]. CKD favors the development of hypertension and dyslipidemia, which in turn can exacerbate renal failure. In addition, patients with CKD frequently have an enhanced inflammation and activated renin-angiotensin system, which can accelerate atherosclerosis through an increased production of reactive oxygen species [79]. An OCT study in 287 patients from the MGH OCT Registry has investigated the relationship between CKD and coronary plaque characteristics [80]. Although fibrous cap thickness and prevalence of TCFA were not different between patients with and without CKD, coronary plaques in patients with CKD had larger lipid content (Fig. 6.15), and higher prevalence of calcifications (51 % vs. 35 %, $p=0.041$), cholesterol crystals (23 % vs. 11 %, $p=0.048$), and disruptions (13 % vs. 5 %, $p=0.049$). Consistent with the subgroup analysis of the PROSPECT trial [81], which indicated the presence of larger plaque

burden, necrotic core, and dense calcium in CKD patients, these data suggest that CKD has a significant impact on coronary plaque morphology.

References

1. Go AS, Mozaffarian D, Roger VL, Benjamin EJ, Berry JD, Blaha MJ, et al. Heart disease and stroke statistics–2014 update: a report from the American Heart Association. Circulation. 2014;129(3): e28–292.

2. Motoyama S, Sarai M, Harigaya H, Anno H, Inoue K, Hara T, et al. Computed tomographic angiography characteristics of atherosclerotic plaques subsequently resulting in acute coronary syndrome. J Am Coll Cardiol. 2009;54(1):49–57.

3. Potkin BN, Bartorelli AL, Gessert JM, Neville RF, Almagor Y, Roberts WC, et al. Coronary artery imaging with intravascular high-frequency ultrasound. Circulation. 1990;81(5):1575–85.

4. Garcia-Garcia HM, Mintz GS, Lerman A, Vince DG, Margolis MP, van Es GA, et al. Tissue characterisation using intravascular radiofrequency data analysis: recommendations for acquisition, analysis, interpretation and reporting. EuroIntervention. 2009;5(2):177–89.

5. Gardner CM, Tan H, Hull EL, Lisauskas JB, Sum ST, Meese TM, et al. Detection of lipid core coronary plaques in autopsy specimens with a novel catheter-based near-infrared spectroscopy system. JACC Cardiovasc Imaging. 2008;1(5):638–48.

6. Jang IK, Tearney GJ, MacNeill B, Takano M, Moselewski F, Iftima N, et al. In vivo characterization of coronary atherosclerotic plaque by use of optical coherence tomography. Circulation. 2005;111(12):1551–5.

7. Jang IK, Bouma BE, Kang DH, Park SJ, Park SW, Seung KB, et al. Visualization of coronary atherosclerotic plaques in patients using optical coherence tomography: comparison with intravascular ultrasound. J Am Coll Cardiol. 2002;39(4):604–9.

8. Jang IK. Optical coherence tomography or intravascular ultrasound? JACC Cardiovasc Interv. 2011;4(5):492–4.

9. Di Vito L, Yoon JH, Kato K, Yonetsu T, Vergallo R, Costa M, et al. Comprehensive overview of definitions for optical coherence tomography-based plaque and stent analyses. Coron Artery Dis. 2014;25(2):172–85.

10. Virmani R, Kolodgie FD, Burke AP, Farb A, Schwartz SM. Lessons from sudden coronary death: a comprehensive morphological classification scheme for atherosclerotic lesions. Arterioscler Thromb Vasc Biol. 2000;20(5):1262–75.

11. Stone GW, Maehara A, Lansky AJ, de Bruyne B, Cristea E, Mintz GS, et al. A prospective natural-history study of coronary atherosclerosis. N Engl J Med. 2011;364(3):226–35.

12. Yonetsu T, Kakuta T, Lee T, Takahashi K, Kawaguchi N, Yamamoto G, et al. In vivo critical fibrous cap thickness for rupture-prone coronary plaques assessed by optical coherence tomography. Eur Heart J. 2011;32(10):1251–9.

13. Tian J, Ren X, Vergallo R, Xing L, Yu H, Jia H, et al. Distinct morphological features of ruptured culprit plaque for acute coronary events compared to those with silent rupture and thin-cap fibroatheroma: a combined optical coherence tomography and intravascular ultrasound study. J Am Coll Cardiol. 2014;63(21):2209–16.

14. Tian J, Hou J, Xing L, Kim SJ, Yonetsu T, Kato K, et al. Significance of intraplaque neovascularisation for vulnerability: optical coherence tomography study. Heart. 2012;98(20):1504–9.

15. Kitabata H, Tanaka A, Kubo T, Takarada S, Kashiwagi M, Tsujioka H, et al. Relation of microchannel structure identified by optical coherence tomography to plaque vulnerability in patients with coronary artery disease. Am J Cardiol. 2010;105(12):1673–8.

16. Uemura S, Ishigami K, Soeda T, Okayama S, Sung JH, Nakagawa H, et al. Thin-cap fibroatheroma and microchannel findings in optical coherence tomography correlate with subsequent progression of coronary atheromatous plaques. Eur Heart J. 2012;33(1):78–85.

17. Tian J, Hou J, Xing L, Kim SJ, Yonetsu T, Kato K, et al. Does neovascularization predict response to statin therapy? Optical coherence tomography study. Int J Cardiol. 2012;158(3):469–70.

18. Tearney GJ, Yabushita H, Houser SL, Aretz HT, Jang IK, Schlendorf KH, et al. Quantification of macrophage content in atherosclerotic plaques by optical coherence tomography. Circulation. 2003;107(1): 113–9.

19. MacNeill BD, Jang IK, Bouma BE, Iftima N, Takano M, Yabushita H, et al. Focal and multi-focal plaque macrophage distributions in patients with acute and stable presentations of coronary artery disease. J Am Coll Cardiol. 2004;44(5):972–9.

20. van Soest G, Goderie T, Regar E, Koljenovic S, van Leenders GL, Gonzalo N, et al. Atherosclerotic tissue characterization in vivo by optical coherence tomography attenuation imaging. J Biomed Opt. 2010;15(1):011105.

21. Crea F, Liuzzo G. Pathogenesis of acute coronary syndromes. J Am Coll Cardiol. 2013;61(1):1–11.

22. Jia H, Abtahian F, Aguirre AD, Lee S, Chia S, Lowe H, et al. In vivo diagnosis of plaque erosion and calcified nodule in patients with acute coronary syndrome by intravascular optical coherence tomography. J Am Coll Cardiol. 2013;62(19):1748–58.

23. Virmani R, Burke AP, Farb A, Kolodgie FD. Pathology of the vulnerable plaque. J Am Coll Cardiol. 2006;47(8 Suppl):C13–8.

24. Prati F, Uemura S, Souteyrand G, Virmani R, Motreff P, Di Vito L, et al. OCT-based diagnosis and management of STEMI associated with intact fibrous cap. JACC Cardiovasc Imaging. 2013;6(3): 283–7.

25. Tanaka A, Shimada K, Tearney GJ, Kitabata H, Taguchi H, Fukuda S, et al. Conformational change in coronary artery structure assessed by optical coherence tomography in patients with vasospastic angina. J Am Coll Cardiol. 2011;58(15):1608–13.

26. Alfonso F, Paulo M, Gonzalo N, Dutary J, Jimenez-Quevedo P, Lennie V, et al. Diagnosis of spontaneous coronary artery dissection by optical coherence tomography. J Am Coll Cardiol. 2012;59(12):1073–9.

27. Deanfield JE, Maseri A, Selwyn AP, Ribeiro P, Chierchia S, Krikler S, et al. Myocardial ischaemia during daily life in patients with stable angina: its relation to symptoms and heart rate changes. Lancet. 1983;2(8353):753–8.

28. Sukhova GK, Schonbeck U, Rabkin E, Schoen FJ, Poole AR, Billinghurst RC, et al. Evidence for increased collagenolysis by interstitial collagenases-1 and −3 in vulnerable human atheromatous plaques. Circulation. 1999;99(19):2503–9.

29. Shah PK, Falk E, Badimon JJ, Fernandez-Ortiz A, Mailhac A, Villareal-Levy G, et al. Human monocyte-derived macrophages induce collagen breakdown in fibrous caps of atherosclerotic plaques. Potential role of matrix-degrading metalloproteinases and implications for plaque rupture. Circulation. 1995;92(6):1565–9.

30. Burke AP, Farb A, Malcom GT, Liang Y, Smialek JE, Virmani R. Plaque rupture and sudden death related to exertion in men with coronary artery disease. JAMA. 1999;281(10):921–6.

31. Tanaka A, Imanishi T, Kitabata H, Kubo T, Takarada S, Tanimoto T, et al. Morphology of exertion-triggered plaque rupture in patients with acute coronary syndrome: an optical coherence tomography study. Circulation. 2008;118(23):2368–73.

32. Ino Y, Kubo T, Tanaka A, Kuroi A, Tsujioka H, Ikejima H, et al. Difference of culprit lesion morphologies between ST-segment elevation myocardial infarction and non-ST-segment elevation acute coronary syndrome: an optical coherence tomography study. JACC Cardiovasc Interv. 2011;4(1):76–82.

33. Braunwald E. Unstable angina. A classification. Circulation. 1989;80(2):410–4.

34. Mizukoshi M, Imanishi T, Tanaka A, Kubo T, Liu Y, Takarada S, et al. Clinical classification and plaque morphology determined by

optical coherence tomography in unstable angina pectoris. Am J Cardiol. 2010;106(3):323–8.

35. Scirica BM, Cannon CP, McCabe CH, Murphy SA, Anderson HV, Rogers WJ, et al. Prognosis in the thrombolysis in myocardial ischemia III registry according to the Braunwald unstable angina pectoris classification. Am J Cardiol. 2002;90(8):821–6.

36. Kato K, Yonetsu T, Kim SJ, Xing L, Lee H, McNulty I, et al. Nonculprit plaques in patients with acute coronary syndromes have more vulnerable features compared with those with non-acute coronary syndromes: a 3-vessel optical coherence tomography study. Circ Cardiovasc Imaging. 2012;5(4):433–40.

37. Asakura M, Ueda Y, Yamaguchi O, Adachi T, Hirayama A, Hori M, et al. Extensive development of vulnerable plaques as a pancoronary process in patients with myocardial infarction: an angioscopic study. J Am Coll Cardiol. 2001;37(5):1284–8.

38. Thieme T, Wernecke KD, Meyer R, Brandenstein E, Habedank D, Hinz A, et al. Angioscopic evaluation of atherosclerotic plaques: validation by histomorphologic analysis and association with stable and unstable coronary syndromes. J Am Coll Cardiol. 1996;28(1):1–6.

39. O'Brien KD, McDonald TO, Chait A, Allen MD, Alpers CE. Neovascular expression of E-selectin, intercellular adhesion molecule-1, and vascular cell adhesion molecule-1 in human atherosclerosis and their relation to intimal leukocyte content. Circulation. 1996;93(4):672–82.

40. Vergallo R, Ren X, Yonetsu T, Kato K, Uemura S, Yu B, et al. Pancoronary plaque vulnerability in patients with acute coronary syndrome and ruptured culprit plaque: a 3-vessel optical coherence tomography study. Am Heart J. 2014;167(1):59–67.

41. Charo IF, Taub R. Anti-inflammatory therapeutics for the treatment of atherosclerosis. Nat Rev Drug Discov. 2011;10(5):365–76.

42. Vogel RA. PCSK9 inhibition: the next statin? J Am Coll Cardiol. 2012;59(25):2354–5.

43. Haffner SM, Lehto S, Ronnemaa T, Pyorala K, Laakso M. Mortality from coronary heart disease in subjects with type 2 diabetes and in nondiabetic subjects with and without prior myocardial infarction. N Engl J Med. 1998;339(4):229–34.

44. Stamler J, Vaccaro O, Neaton JD, Wentworth D. Diabetes, other risk factors, and 12-yr cardiovascular mortality for men screened in the Multiple Risk Factor Intervention Trial. Diabetes Care. 1993;16(2):434–44.

45. Hess K, Grant PJ. Inflammation and thrombosis in diabetes. Thromb Haemost. 2011;105 Suppl 1:S43–54.

46. Burke AP, Kolodgie FD, Zieske A, Fowler DR, Weber DK, Varghese PJ, et al. Morphologic findings of coronary atherosclerotic plaques in diabetics: a postmortem study. Arterioscler Thromb Vasc Biol. 2004;24(7):1266–71.

47. Kato K, Yonetsu T, Kim SJ, Xing L, Lee H, McNulty I, et al. Comparison of nonculprit coronary plaque characteristics between patients with and without diabetes: a 3-vessel optical coherence tomography study. JACC Cardiovasc Interv. 2012;5(11):1150–8.

48. Marso SP, Mercado N, Maehara A, Weisz G, Mintz GS, McPherson J, et al. Plaque composition and clinical outcomes in acute coronary syndrome patients with metabolic syndrome or diabetes. JACC Cardiovasc Imaging. 2012;5(3 Suppl):S42–52.

49. Niccoli G, Giubilato S, Di Vito L, Leo A, Cosentino N, Pitocco D, et al. Severity of coronary atherosclerosis in patients with a first acute coronary event: a diabetes paradox. Eur Heart J. 2013;34(10):729–41.

50. Chia S, Raffel OC, Takano M, Tearney GJ, Bouma BE, Jang IK. Comparison of coronary plaque characteristics between diabetic and non-diabetic subjects: An in vivo optical coherence tomography study. Diabetes Res Clin Pract. 2008;81(2):155–60.

51. Feng T, Yundai C, Lian C, Zhijun S, Changfu L, Jun G, et al. Assessment of coronary plaque characteristics by optical coherence tomography in patients with diabetes mellitus complicated with unstable angina pectoris. Atherosclerosis. 2010;213(2):482–5.

52. Yusuf S, Hawken S, Ounpuu S, Dans T, Avezum A, Lanas F, et al. Effect of potentially modifiable risk factors associated with myocardial infarction in 52 countries (the INTERHEART study): case-control study. Lancet. 2004;364(9438):937–52.

53. Wilson PW, Myers RH, Larson MG, Ordovas JM, Wolf PA, Schaefer EJ. Apolipoprotein E alleles, dyslipidemia, and coronary heart disease. The Framingham Offspring Study. JAMA. 1994;272(21):1666–71.

54. Cannon CP, Braunwald E, McCabe CH, Rader DJ, Rouleau JL, Belder R, et al. Intensive versus moderate lipid lowering with statins after acute coronary syndromes. N Engl J Med. 2004;350(15):1495–504.

55. Randomised trial of cholesterol lowering in 4444 patients with coronary heart disease: the Scandinavian Simvastatin Survival Study (4S). Lancet. 1994;344(8934):1383–9.

56. Ridker PM, Danielson E, Fonseca FA, Genest J, Gotto Jr AM, Kastelein JJ, et al. Rosuvastatin to prevent vascular events in men and women with elevated C-reactive protein. N Engl J Med. 2008;359(21):2195–207.

57. Nissen SE, Tuzcu EM, Schoenhagen P, Brown BG, Ganz P, Vogel RA, et al. Effect of intensive compared with moderate lipid-lowering therapy on progression of coronary atherosclerosis: a randomized controlled trial. JAMA. 2004;291(9):1071–80.

58. Nissen SE, Tuzcu EM, Schoenhagen P, Crowe T, Sasiela WJ, Tsai J, et al. Statin therapy, LDL cholesterol, C-reactive protein, and coronary artery disease. N Engl J Med. 2005;352(1):29–38.

59. Takarada S, Imanishi T, Ishibashi K, Tanimoto T, Komukai K, Ino Y, et al. The effect of lipid and inflammatory profiles on the morphological changes of lipid-rich plaques in patients with non-ST-segment elevated acute coronary syndrome: follow-up study by optical coherence tomography and intravascular ultrasound. JACC Cardiovasc Interv. 2010;3(7):766–72.

60. Ozaki Y, Tanaka A, Komukai K, Ishibashi K, Tanimoto T, Kitabata H, et al. High-density lipoprotein cholesterol level is associated with fibrous cap thickness in acute coronary syndrome. Circ J. 2013;77(12):2982–9.

61. Matsuo Y, Kubo T, Okumoto Y, Ishibashi K, Komukai K, Tanimoto T, et al. Circulating malondialdehyde-modified low-density lipoprotein levels are associated with the presence of thin-cap fibroatheromas determined by optical coherence tomography in coronary artery disease. Eur Heart J Cardiovasc Imaging. 2013;14(1):43–50.

62. Steinberg D, Lewis A. Conner memorial lecture. Oxidative modification of LDL and atherogenesis. Circulation. 1997;95(4):1062–71.

63. Nasu K, Terashima M, Habara M, Ko E, Ito T, Yokota D, et al. Impact of cholesterol metabolism on coronary plaque vulnerability of target vessels: a combined analysis of virtual histology intravascular ultrasound and optical coherence tomography. JACC Cardiovasc Interv. 2013;6(7):746–55.

64. Ezzati M, Henley SJ, Thun MJ, Lopez AD. Role of smoking in global and regional cardiovascular mortality. Circulation. 2005;112(4):489–97.

65. Csordas A, Bernhard D. The biology behind the atherothrombotic effects of cigarette smoke. Nat Rev Cardiol. 2013;10(4):219–30.

66. Ramsdale DR, Faragher EB, Bray CL, Bennett DH, Ward C, Beton DC. Smoking and coronary artery disease assessed by routine coronary arteriography. Br Med J (Clin Res Ed). 1985;290(6463):197–200.

67. Yonetsu T, Kato K, Kim SJ, Xing L, Jia H, McNulty I, et al. Predictors for neoatherosclerosis: a retrospective observational study from the optical coherence tomography registry. Circ Cardiovasc Imaging. 2012;5(5):660–6.

68. Vergallo R, Yonetsu T, Uemura S, Park SJ, Lee S, Kato K, et al. Correlation between degree of neointimal hyperplasia and incidence and characteristics of neoatherosclerosis as assessed by optical coherence tomography. Am J Cardiol. 2013;112(9):1315–21.

69. Rodriguez-Granillo GA, Garcia-Garcia HM, Mc Fadden EP, Valgimigli M, Aoki J, de Feyter P, et al. In vivo intravascular ultrasound-derived thin-cap fibroatheroma detection using ultrasound radiofrequency data analysis. J Am Coll Cardiol. 2005; 46(11):2038–42.

70. Philipp S, Bose D, Wijns W, Marso SP, Schwartz RS, Konig A, et al. Do systemic risk factors impact invasive findings from virtual histology? Insights from the international virtual histology registry. Eur Heart J. 2010;31(2):196–202.

71. Abtahian F, Yonetsu T, Kato K, Jia H, Vergallo R, Tian J, et al. Smoking is associated with presence of vulnerable plaques: a three vessel optical coherence tomography study [abstract]. Circulation. 2013;128, A12724.

72. Hasdai D, Garratt KN, Grill DE, Lerman A, Holmes Jr DR. Effect of smoking status on the long-term outcome after successful percutaneous coronary revascularization. N Engl J Med. 1997;336(11):755–61.

73. Lawes CM, Vander Hoorn S, Rodgers A. Global burden of blood-pressure-related disease, 2001. Lancet. 2008;371(9623):1513–8.

74. Escobar E. Hypertension and coronary heart disease. J Hum Hypertens. 2002;16 Suppl 1:S61–3.

75. Tsioufis C, Latsios G, Tsiachris D, Dimitriadis K, Roussos D, Kallikazaros I, et al. Lack of correlation between coronary flow reserve and vascular remodelling in hypertensive patients without left ventricular hypertrophy: an optical coherence tomography study. Hellenic J Cardiol. 2012;53(6):426–31.

76. Grundy SM, Brewer Jr HB, Cleeman JI, Smith Jr SC, Lenfant C. Definition of metabolic syndrome: Report of the National Heart, Lung, and Blood Institute/American Heart Association conference on scientific issues related to definition. Circulation. 2004; 109(3):433–8.

77. Gami AS, Witt BJ, Howard DE, Erwin PJ, Gami LA, Somers VK, et al. Metabolic syndrome and risk of incident cardiovascular events and death: a systematic review and meta-analysis of longitudinal studies. J Am Coll Cardiol. 2007;49(4):403–14.

78. Yonetsu T, Kato K, Uemura S, Kim BK, Jang Y, Kang SJ, et al. Features of coronary plaque in patients with metabolic syndrome and diabetes mellitus assessed by 3-vessel optical coherence tomography. Circ Cardiovasc Imaging. 2013;6(5):665–73.

79. Schiffrin EL, Lipman ML, Mann JF. Chronic kidney disease: effects on the cardiovascular system. Circulation. 2007;116(1):85–97.

80. Kato K, Yonetsu T, Jia H, Abtahian F, Vergallo R, Hu S, et al. Nonculprit coronary plaque characteristics of chronic kidney disease. Circ Cardiovasc Imaging. 2013;6(3):448–56.

81. Baber U, Stone GW, Weisz G, Moreno P, Dangas G, Maehara A, et al. Coronary plaque composition, morphology, and outcomes in patients with and without chronic kidney disease presenting with acute coronary syndromes. JACC Cardiovasc Imaging. 2012;5 (3 Suppl):S53–61.

Insight into Pathogenesis of Acute Coronary Syndrome

Haibo Jia and Ik-Kyung Jang

Abstract

Over the last several decades, clinical and pathological observations have led us to a better understanding of the pathogenesis of acute coronary syndrome (ACS): coronary artery thrombosis plays a central role in the development of ACS. The three most common plaque morphologies responsible for the development of acute coronary thrombosis are plaque rupture, plaque erosion, and calcified nodules. The majority of these findings come from cross-sectional pathological studies and animal models, which are very different from living patients. *In vivo* investigation of underlying pathophysiology of ACS is of vital importance. However this has been greatly challenged by the lack of an appropriate intravascular imaging modality for studying coronary plaque morphologies *in vivo*. To date, a variety of diagnostic tools to detect underlying plaque morphology in the setting of ACS has been developed, including angiography and intravascular ultrasound (IVUS). However, an angiogram only provides a luminal outline and is not able to visualize intravascular structure, while IVUS has inadequate resolution to characterize subtle changes in the vascular wall. Optical coherence tomography (OCT), on the other hand, is an ideal intravascular imaging modality which enables us to accurately evaluate these plaque morphologies, specifically, thin fibrous cap, macrophages, and intracoronary thrombus. More importantly, OCT can potentially help us understand the underlying mechanism behind the abrupt transition from stable atherosclerotic disease to ACS by investigating the natural evolution of coronary atherosclerotic plaques, which may ultimately allow us to discover new diagnostic algorithms and therapeutic targets.

Keywords

Pathogenesis • Acute coronary syndrome • Atherosclerotic plaque • Thrombosis • Optical coherence tomography

H. Jia, MD, PhD
Department of Cardiology, Hospital of Harbin Medical University,
Laboratory of Myocardial Ischemia,
Chinese Ministry of Education, Harbin, China

Division of Cardiology, Massachusetts
General Hospital, Harvard Medical School,
55 Fruit Street GRB 800, Boston, MA 02114, USA

I.-K. Jang, MD, PhD (✉)
Division of Cardiology, Massachusetts General Hospital,
Harvard Medical School, 55 Fruit Street GRB 800,
Boston, MA 02114, USA
e-mail: ijang@mgh.harvard.edu

7.1 Pathology of Underlying Mechanism of Acute Coronary Syndrome

Insights into the pathogenesis of acute coronary syndrome (ACS) have come from detailed analyses of plaque morphologies in cases of sudden coronary death (SCD) and acute myocardial infarction (AMI). Coronary artery thrombosis is believed to be the final pathogenic pathway of most cases with ACS [1, 2]. Pathologically, coronary thrombosis is caused by three predominant plaque morphologies: plaque rupture, plaque erosion, and calcified nodule [3, 4]. (Fig. 7.1) Among these features, plaque rupture is the most
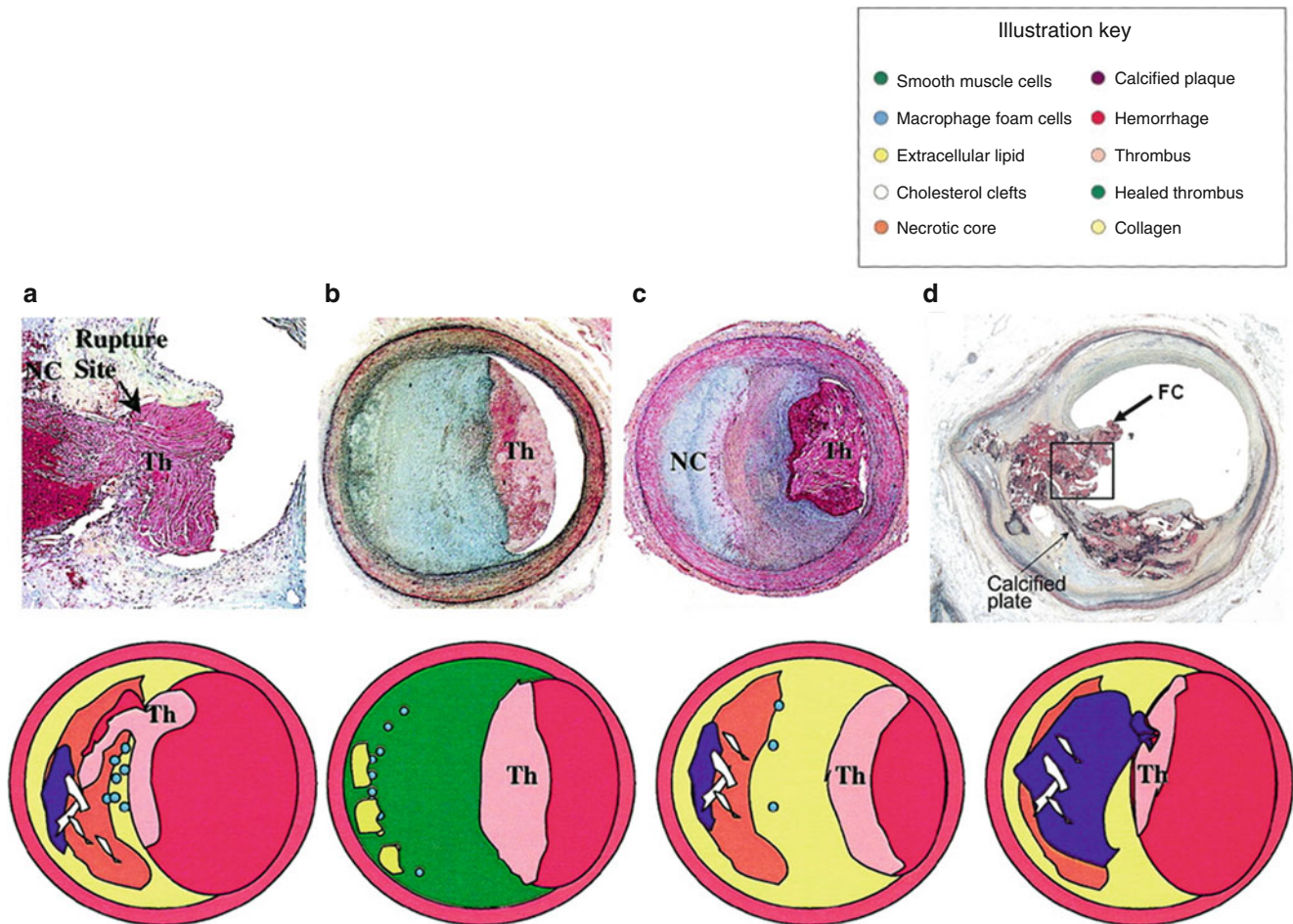
Illustration key

- 🟢 Smooth muscle cells
- 🔵 Macrophage foam cells
- 🟡 Extracellular lipid
- ⚪ Cholesterol clefts
- 🟠 Necrotic core
- 🟣 Calcified plaque
- 🔴 Hemorrhage
- 🟤 Thrombus
- 🟢 Healed thrombus
- 🟡 Collagen

Fig. 7.1 Atherosclerotic lesions with luminal thrombi. (**a**) Ruptured plaques are thin fibrous cap atheromas with luminal thrombi (*Th*). These lesions usually have an extensive necrotic core (*NC*) containing large numbers of cholesterol crystals and a thin fibrous cap (<65 μm) infiltrated by foamy macrophages and a paucity of T lymphocytes. The fibrous cap is thinnest at the site of rupture and consists of a few collagen bundles and rare smooth muscle cells. The luminal thrombus is in communication with the lipid-rich necrotic core. (**b**, **c**) Erosions occur over lesions rich in smooth muscle cells and proteoglycans. Luminal thrombus overlies areas lacking surface endothelium. The deep intima of the eroded plaque often shows extracellular lipid pools, but necrotic cores are uncommon; when present, the necrotic core does not communicate with the luminal thrombus. Inflammatory infiltrate is usually absent, but if present, is sparse and consists of macrophages and lymphocytes. (**d**) Calcified nodules protrude into the lumen through a disrupted thin fibrous cap (*FC*). There is absence of an endothelium at the site of the thrombus, and inflammatory cells (macrophages, T lymphocytes) are absent (From Virmani et al. [4])

common underlying etiology for ACS. Plaque erosion is less frequent than plaque rupture but still common, particularly in young women and smokers [5]. The least common cause is the superficial calcified nodule [4]. In pathology, plaque rupture is defined as the presence of a luminal thrombus in continuity with the large necrotic core and an overlying thin interrupted fibrous cap, measuring <65 μm and heavily infiltrated by inflammatory cells (macrophages and T-lymphocytes). In contrast, plaque erosion is characterized by a luminal thrombus in direct contact with the intimal plaque without rupture of a lipid pool. Typically, the endothelial cells are absent at the eroded area. The exposed intima is a proteoglycan-rich matrix with mostly smooth muscle cells (SMCs) and very few inflammatory cells [5, 6]. The necrotic core is not required for this form of thrombotic lesions, but if present, is usually small and present deep inside the plaque, without communication between the thrombus and lipid pool. Calcified nodule is defined as a lesion with fibrous cap disruption and thrombi associated with eruptive, dense, and calcified nodules.

7.2 Classification of Underlying Culprit Lesions in ACS

7.2.1 Evolution of the Paradigm for Atherosclerotic Lesions

The first report on the classification of atherosclerosis was proposed by the American Heart Association (AHA) in 1995 (Table 7.1) [7]. In this classification, atherosclerotic lesions were first divided into two stages (early lesion and

Table 7.1 AHA classification

Terms for atherosclerotic lesions in histological classification		Other terms for the same lesions often based on appearance to the unaided eye	
Type I lesion	Initial lesion		
Type II lesion			
IIa	Progression-prone type II lesion	Fatty dot or streak	Early lesion
IIb	Progression-resistant type II lesion		
Type III lesion	Intermediate lesion (pre-atheroma)		
Type IV lesion	Atheroma	Atheromatous plaque, fibrolipid plaque, fibrous plaque	
Va	Fibroatheroma (type V lesion)		
Vb	Calcific lesion (type VII lesion)	Calcified plaque	Advanced lesions, raised lesions
Vc	Fibrotic lesion (type VIII)	Fibrous plaque	
Type VI lesion	Lesion with surface defect and/or hematoma/hemorrhage and/or thrombotic deposit	Complicated lesion, complicated plaque	

Adapted from Virmani et al. [4]

advanced lesions), then further categorized into six types of lesions which were designated along an orderly, linear pattern of lesion progression. The perception of rupture of an advanced atherosclerotic lesion as the primary mechanism responsible for ACS was widely accepted. However, this paradigm was challenged by inconsistent findings in two pathological studies [5, 8], which showed that coronary thrombi could arise without rupture. The first study was performed by van der Wal et al. [8], who investigated 20 patients with SCD and found plaque rupture in only 60 % of lesions; the remaining 40 % showed absence of rupture with only superficial erosion which is defined as a thrombus confined to the most luminal portion of a fibrous cap in the absence of fissure or rupture after serial sectioning. The second report was from Virmani's group [5], who studied the underlying plaque morphology in more than 200 cases of SCD with luminal thrombi in at least one artery with >75 % cross-sectional area luminal narrowing. Only 31 % of lesions in their studies could be defined as plaque rupture, and over one third of lesions did not have evidence of rupture. All these data raised a critical question about the central role of plaque rupture in the previous AHA classification and subsequently led to changes in the classification of atherosclerotic lesions. To better understand the underlying mechanism of ACS, Virmani et al. [4] proposed another plaque morphological classification scheme based on their comprehensive autopsy observation (Fig. 7.2). Their categories included intimal xanthoma, intimal thickening, pathological intimal thickening, fibrous cap atheroma, thin fibrous cap atheroma, calcified nodule, and fibrocalcific plaque. The accumulation of lipid in relation to the formation of fibrous cap which changes over time, as well as thrombosis was taken into account in the classification. More importantly, their classification highlighted the importance of plaque erosion in thrombotic events. Although this classification scheme allows for easier understanding, its practical usability and application in living patients need to be confirmed.

7.2.2 *In vivo* Classification of Atherosclerotic Plaque Responsible for ACS

As mentioned above, most reports on lesion classification have been derived from autopsy studies. Not only were the sample sizes of those studies relatively small, but also the study subjects were mostly young, sudden coronary death victims, who could be significantly different from living patients. Seeing these limitations, *in vivo* classification of coronary atherosclerotic plaques is needed.

Coronary angiography has been used as a gold standard diagnostic modality for the evaluation of patients presenting with ACS. However, an angiogram shows only the luminal outline and is not able to visualize intravascular structure. Although intravascular ultrasound (IVUS) is widely used to evaluate plaque morphology, including plaque burden and remodeling, the resolution is inadequate to characterize subtle changes in the vascular wall. For example, IVUS cannot be used to detect thin fibrous cap, macrophage infiltration, mural thrombus, and irregular or eroded surface, which are key features for characterizing coronary plaque phenotype. In contrast, intravascular optical coherence tomography (OCT), with the unprecedented resolution of 10–15 μm, allows us to detect and quantify specific morphologic changes that are analogous to histological features in some circumstances, including lipid pool, thin fibrous cap, plaque rupture, throm-
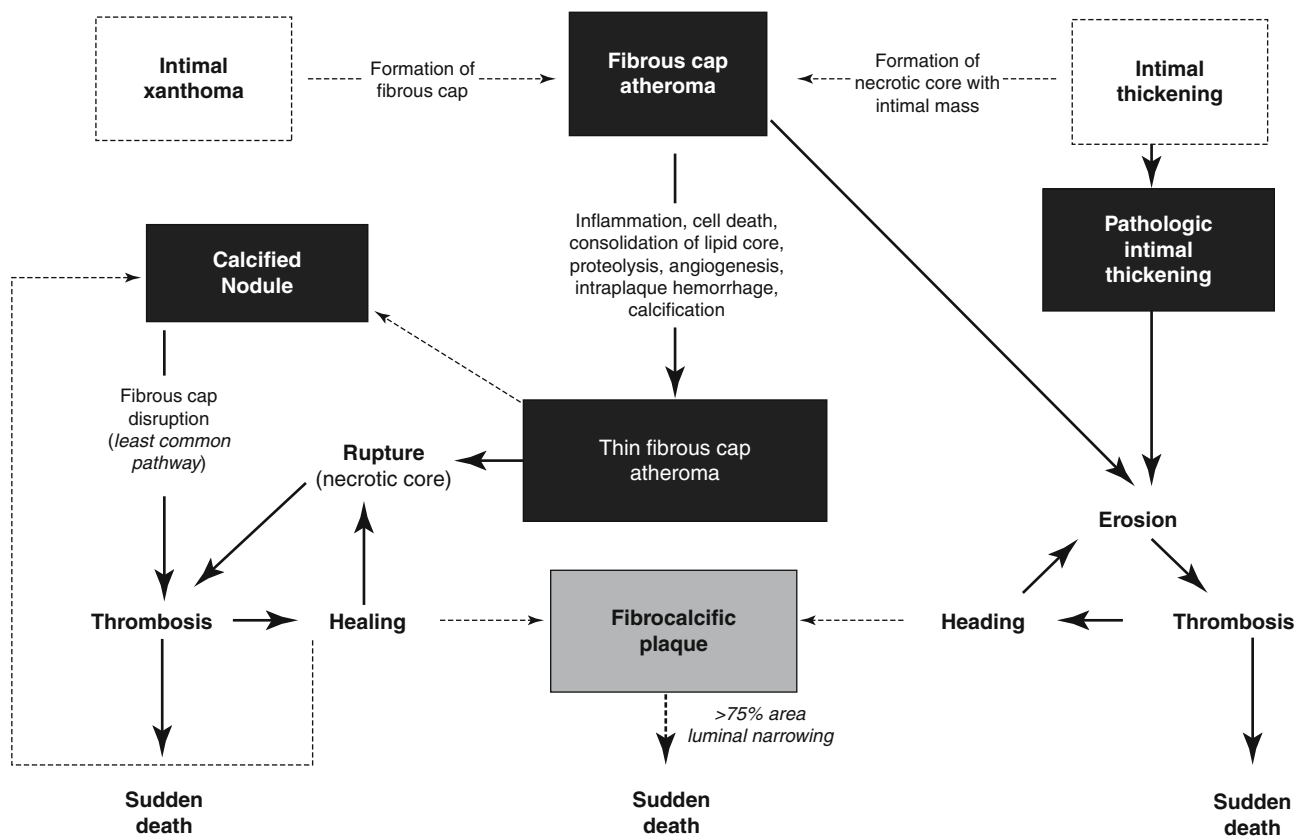
Fig. 7.2 Simplified scheme for classifying atherosclerotic lesions modified from the current AHA recommendations. The boxed areas represent the seven categories of lesion. *Dashed lines* are used for two categories because there is controversy over the role that each of them plays in the initial phase of lesion formation, and both "lesions" can exist without progressing to a fibrous cap atheroma (ie, AHA type IV lesion). The processes leading to lesion progression are listed between categories. Lines (*solid and dotted*, the latter representing the least established processes) depict current concepts of how one category may progress to another, with the thickness of the line representing the strength of the evidence that these events do occur (From Virmani et al. [4])

bus, calcification, macrophages, and microchannels (Fig. 7.3) [9–11]. Considering the limitations of OCT and the clinical situations in which patients are being treated with antithrombotics and thrombolysis, we proposed a new set of OCT diagnostic criteria for the culprit lesion classification in patients with ACS (Table 7.2 and Fig. 7.4) [12]. In order to establish this algorithm, it was critical to accurately characterize plaque erosion and calcified nodule *in vivo*, whose definitions have been well-established by autopsy studies. A few imaging studies have investigated plaque erosion and calcified nodule in patients with ACS [13, 14]. However, the definitions used in those studies were based purely on pathological findings [4] (loss of endothelial cell lines and/or dysfunction of endothelial cells) which are beyond the resolution of OCT. For this reason, we instituted new diagnostic criteria for OCT-erosion and OCT-calcified nodule (OCT-CN) based on pathologic findings and also took into account the limitations of OCT and the differences between living patient and post-mortem examinations (Fig. 7.4). Though this classification is based on only 126 patients presented with ACS, this is the first *in*

vivo study that systematically investigated and established the classification of coronary culprit atherosclerotic plaque in living patients with ACS.

7.3 Plaque Rupture

7.3.1 Definition

In a consensus statement, ruptured plaque was defined as plaque with a structural defect or gap in the fibrous cap that separates the lipid-rich necrotic core of a plaque from the flowing blood, thereby exposing the thrombogenic core of the plaque [15]. OCT characterizes plaque rupture by the presence of fibrous cap discontinuity with a clear cavity formed inside a lipid-rich plaque (Fig. 7.5). In contrast to pathology, OCT does not require the presence of overlying thrombus in the diagnosis of this type of lesion in living patients who may have already been treated with antithrombotic or thrombolytic therapy before imaging. Ruptured plaque typically has a large lipid-rich necrotic core
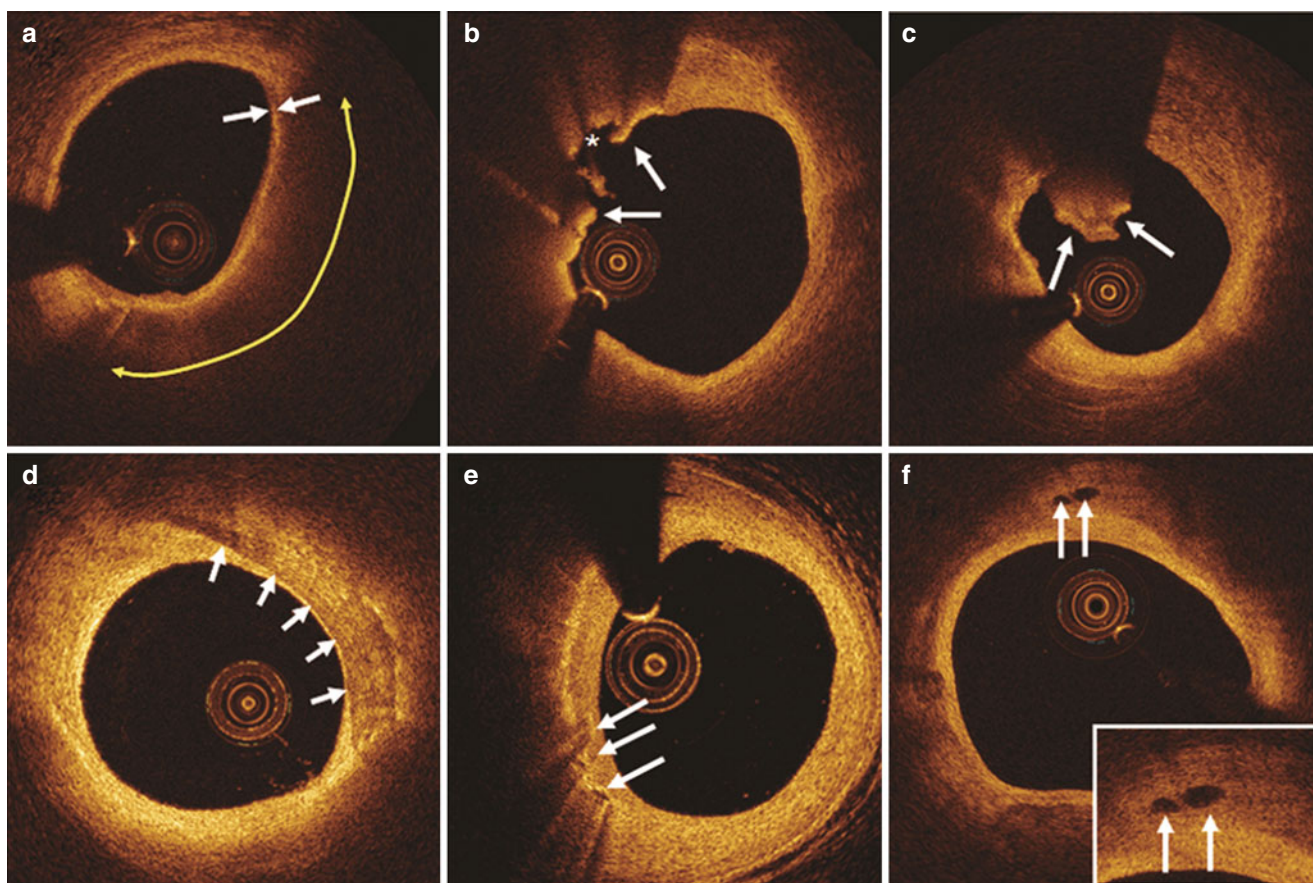
Fig. 7.3 Representative OCT images. (**a**) Thin-cap fibroatheroma is characterized by thin fibrous cap (≤65 μm, *white arrows*) and large lipid pool (*yellow double-arrow*). (**b**) Plaque rupture (*arrows* indicate rupture site, asterisk indicates cavity.). (**c**) Red thrombus is defined as a mass (diameter ≥250 μm) attached to the luminal surface or floating within the lumen, which shows high backscattering with high attenua- tion (*white arrows*). (**d**) Calcification is defined as an area with a signal- poor or heterogeneous region with a sharply delineated border. (**e**) Macrophage accumulation is defined as signal-rich, distinct or conflu- ent punctate regions that exceed the intensity of background speckle noise (*white arrows*). (**f**) Microchannels are defined as signal-poor voids that are sharply delineated in multiple contiguous frames (*arrows*)

Table 7.2 *In vivo* classification of culprit lesions in cases of ACS

Lesion type	Description
Plaque erosion	Intact fibrous cap; with or without luminal thrombosis; underlying plaque can be lipid, fibrous, or intimal thickening; calcification rare
Definite OCT-erosion	Luminal thrombus; intact fibrous cap; underlying plaque visible
Probable OCT-erosion	(a) Absence of luminal thrombus; irregular luminal surface;
	(b) Luminal thrombus; attenuation of underlying plaque by thrombus; no superficial lipid or calcification immediately proximal or distal to the site of thrombus
Plaque rupture	Lipid plaque with cap disruption; with or without luminal thrombus; cavity may exist
Calcified nodule	Disrupted fibrous cap; protruding nodular calcification with underlying fibrocalcific plaque; luminal thrombus; superficial calcium; substantive calcium proximal and/or distal to lesion

(>30 % of the plaque area) and a disrupted thin fibrous cap infil- trated by a large number of macrophages and lymphocytes, and a sparse distribution of SMCs (See Table 7.3). Although some other less-defined terms like fissure and disruption have been used by some investigators, in order to avoid confusion, plaque rupture is recommended for future OCT research work.

7.3.2   Incidence

The incidence of plaque rupture as an underlying pathology of ACS ranged from 50 to 75 % in autopsy studies depends on the population: 75 % in patients with acute myocardial infarction (AMI), 55–65 % in SCD, and 36 % in unstable

Fig. 7.4 Plaque classification algorithm by OCT (Adapted from Jia et al. [12])
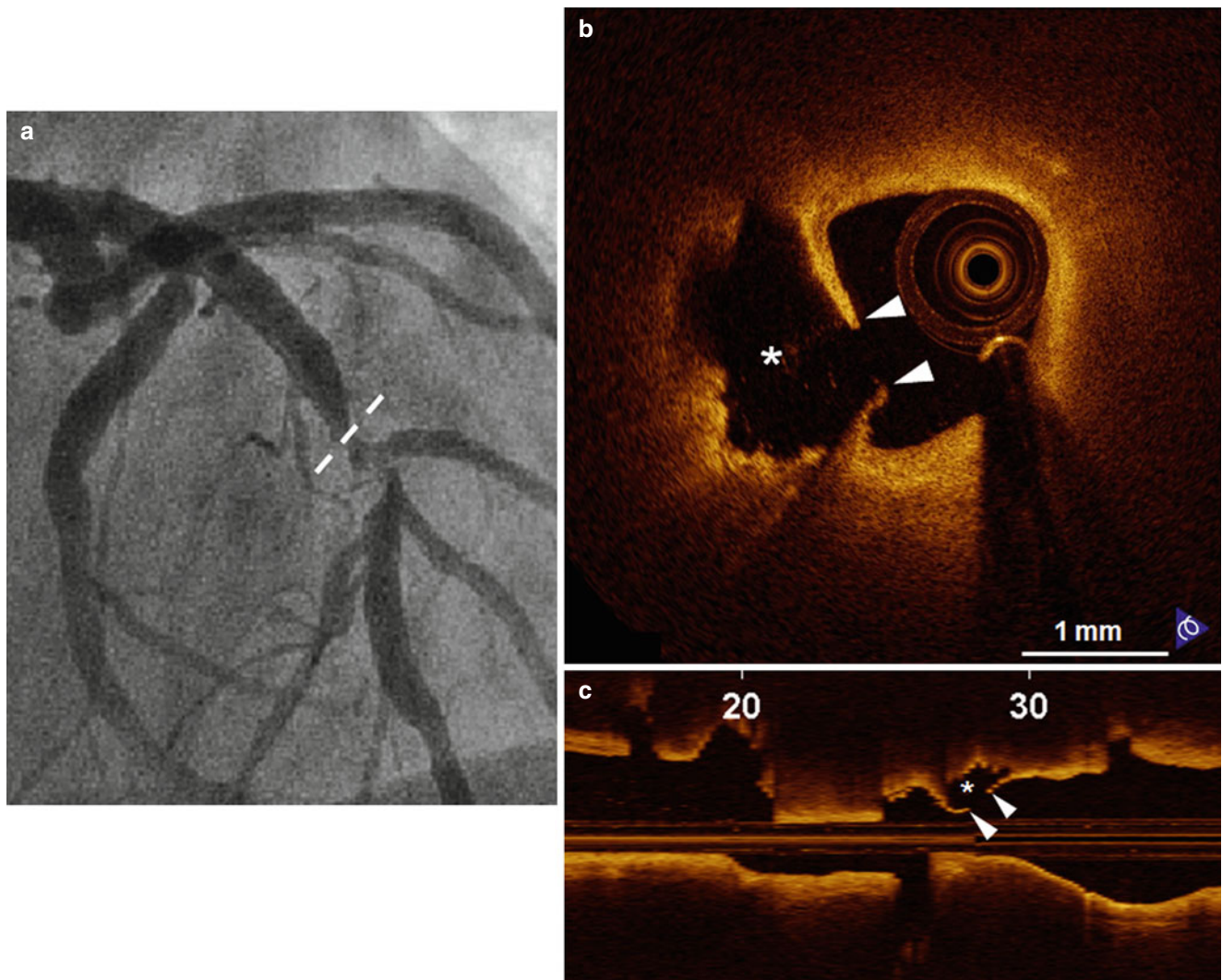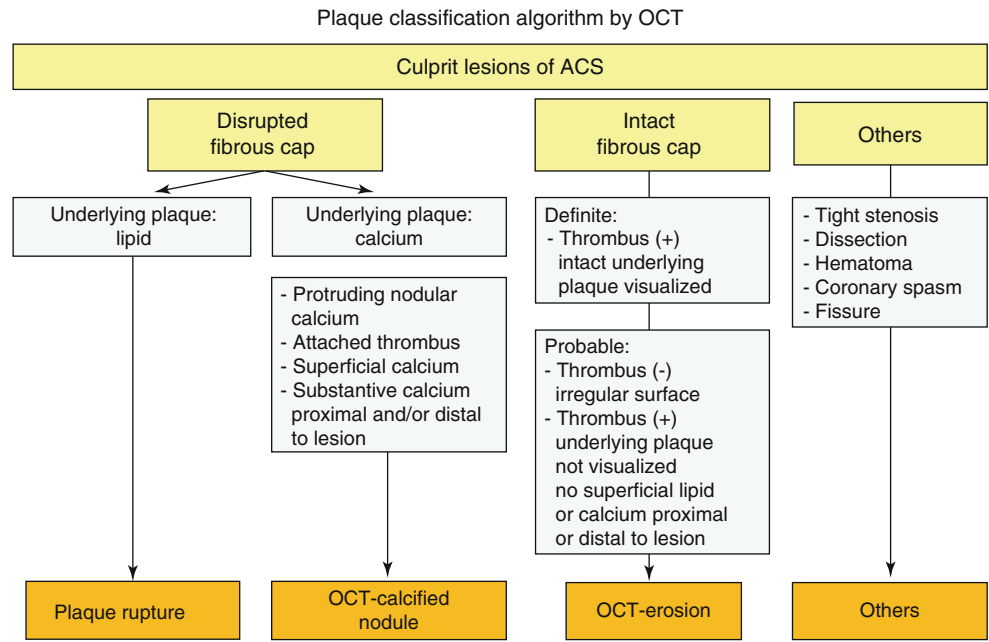
Plaque classification algorithm by OCT

Fig. 7.5 Representative case of "Plaque Rupture". A 57-year-old man presenting with STEMI was treated with thrombolysis. (**a**) The coronary angiogram shows the culprit lesion in the mid LAD (dashed line indicates the ruptured site corresponding to B). Plaque rupture is iden-

tified on cross-sectional (**b**) and longitudinal (**c**) OCT images by the disrupted fibrous-cap (*arrowheads*) and a cavity (*asterisk*) formation inside the plaque. *STEMI* ST-segment elevation myocardial infarction, *LAD* left anterior descending coronary artery (From Jia et al. [12])

angina (UA) [4, 6, 16–20]. Based on the most recent data from a worldwide survey (See Table 7.4) including 22 autopsy studies in which 1,847 coronary arteries were studied with the purpose of characterizing the underlying atherosclerotic plaques [21], plaque rupture was the primary cause of coronary thrombi in approximately 73 % of these fatal events, regardless of clinical presentation (myocardial infarction: 79 %; or sudden death: 65 %), age (>60 years: 77 %; <60 years: 64 %), sex (male: 76 %; female: 55 %) and

geographic origin (Asia: 81 %; Europe: 72 %; USA: 68 %.) [4, 6, 8, 17, 22–39]. (Fig. 7.6) Several *in vivo* studies confirmed that plaque rupture is the most common cause of acute coronary events. The very first *in vivo* OCT study to evaluate culprit lesion morphology in the setting of ACS was conducted by our group [9]: we found the frequency of thin-cap fibroatheroma (TCFA), a precursor of plaque rupture, was significantly higher in ACS, in comparison to stable angina pectoris (SAP) (72 % in AMI, 50 % in UAP, and 20 % in SAP; p=0.012). Interestingly, the frequency of thrombus and plaque rupture was not significantly different between the groups and generally lower, relative to previous pathological studies [4, 40]. This could be caused by the discrete sampling method used in this study and the time delay between symptom onset and imaging, and antithrombotic therapy before imaging. Following this study, another group from Japan used multimodality imaging including OCT, IVUS, and angioscopy, to assess underlying plaque characteristics [13]. This study highlighted the advantages of OCT for the detection of plaque rupture (73 % versus 40 % versus 43 %, p=0.021), erosion (23 % versus 0 % versus 3 %, p=0.003), and thrombus (100 % versus 33 % versus 100 %, p<0.001), in comparison to IVUS and angioscopy.

Table 7.3 Features of ruptured plaques

Thrombus
Large necrotic core (>30 % of plaque)
Fibrous cap covering the necrotic core
Thin (thickness usually <65 μm)
Many macrophages (inflammation)
Few smooth muscle cells (apoptosis)
Expansive remodelling preserving the lumen
Neovascularization from vasa vasorum
Plaque hemorrhage
Adventitial/perivascular inflammation
'Spotty' calcification

Table 7.4 Plaque rupture underlying 1,345 (73 %) of 1,847 fatal coronary thrombi worldwide

Patients	Age,[a] years	Cases, n	Rupture, %	Study
Hospital, -	—	19	19/19 = 100	Chapman [23]
Hospital, -	—	17	17/17 = 100	Constantinides [24]
Hospital, AMI + SCD	58	40	39/40 = 98	Friedman and Van den Bovenkamp [25]
Hospital, AMI	62	88	71/88 = 81	Bouch and Montgomery [26]
Hospital, AMI	66	91	68/91 = 75	Sinapius [27]
Coroner, SCD	53	20	19/20 = 95	Friedman et al. [28]
Hospital, AMI	67	76	69/76 = 91	Horie et al. [29]
Hospital, AMI	67	49	40/49 = 82	Falk [30]
Coroner, SCD	<65	32	26/32 = 81	Tracy et al. [31]
Med. Exam, SCD	<70	61	39/61 = 64	El Fawal et al. [17]
Hospital, AMI	—	83	52/83 = 63	Yutani et al. [32]
Coroner, -	—	85	71/85 = 84	Richardson et al. [33]
Hospital, AMI	63	20	12/20 = 60	van der Wal et al. [8]
Coroner, SCD	—	202	143/202 = 71	Davies [34]
Hospital, AMI	69	291	218/291 = 75	Arbustini et al. [6]
Hospital, AMI	61	61	56/61 = 92	Shi et al. [35]
Hospital, AMI	69	100	81/100 = 81	Kojima et al. [22]
Med. Exam, SCD	48	360	212/360 = 59	Virmani et al. [4]
Med. Exam, AMI + SCD	—	31	26/31 = 84	Murai et al. [36]
Hospital, SCD	—	58	34/58 = 59	Giannoukas andcoworkers [37]
Hospital, AMI	—	14	10/14 = 71	Sato et al. [38]
Coroner, SCD	54	49	23/49 = 47	Subirana et al. [39]
AMI + SCD	—	1,847	1,345/1,847 = 73	Worldwide

From Falk et al. [21]
— not reported, *AMI* acute myocardial infarction, *SCD* sudden coronary death
[a]Mean

Fig. 7.6 Frequency of plaque rupture
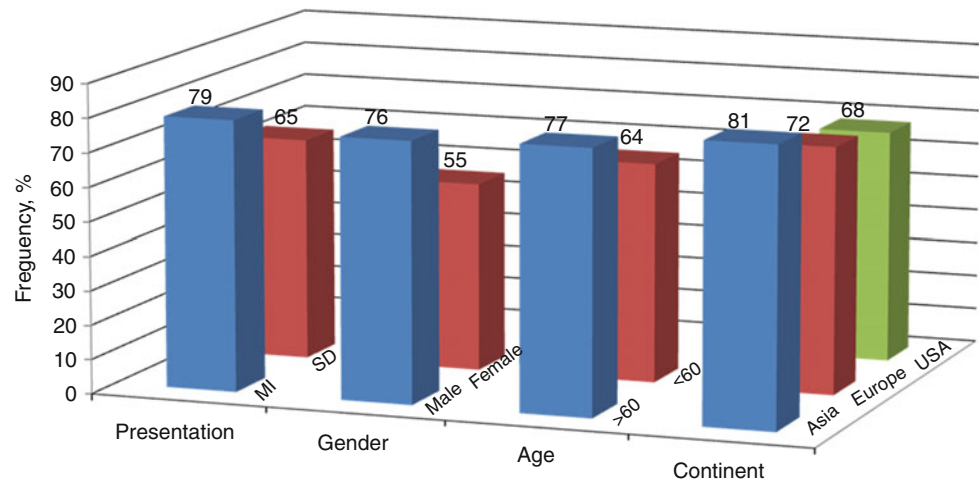
7.3.3 Plaque Ruptures in STEMI and Non–ST-segment Elevation Acute Coronary Syndrome

The paradigm proposed by pathologists is that the underlying mechanism is identical between STEMI and non–ST-segment elevation acute coronary syndrome (NSTEACS). However, this is not the case in living patients presenting with ACS. In our clinical study, we investigated the underlying plaque characteristics in over 200 cases with ACS using intravascular OCT [12]. Plaque rupture was found to be responsible for the culprit lesion in 44 % of patients, while 31 % had plaque erosion. Plaque rupture was more frequently observed in patients with STEMI (72 %) than in those with NSTEACS (32 %). Another OCT study by Ino et al. [41] found consistent results in frequency of plaque rupture (70 % versus 47 %, p=0.033); its precursor lesion-TCFA (78 % versus 49 %, p=0.008) was also significantly higher in patients with STEMI than in those with NSTEACS. Moreover, they found that patients with STEMI had different ruptured plaque morphologies as compared to those with NSTEACS. Although the minimum lumen area was similar in both groups, the ruptured cavity size was significantly larger in those with STEMI as compared to those with NSTEACS. Lastly, the ruptured plaque of which aperture was open wide against the direction of coronary flow, was more often seen in STEMI compared to NSTEACS (46 % versus 17 %, p=0.036).

7.3.4 Plaque Rupture and Exertion

Burke et al. [42] compared the frequency and morphology of plaque rupture in 116 men whose deaths occurred at rest to that of 25 men who died during strenuous activity or emotional stress. Plaque rupture was observed in 17 (68 %) of 25

men dying during exertion versus 27 (23 %) of 116 men dying at rest (p<0.001). The mean minimum thickness of the fibrous cap in exertion-related plaque ruptures was thinner compared with that in rest-related plaque ruptures. Exertion-related plaque rupture was more frequent in the center of the plaque, while rest-related rupture was more frequent in the shoulder of the plaque (Fig. 7.7). However, one OCT study reported opposite results that fibrous cap thickness (FCT) was thinner in rest-onset ACS compared with exertion-triggered ACS (50 μm versus 90 μm, p=0.002), and the rupture at plaque shoulder was more frequent in the latter (57 % versus 93 %, p=0.017) (Fig. 7.8) [43]. Furthermore, not only TCFA but also thick cap fibroatheroma (ThCFA) might rupture. The findings from this study suggested that FCT was a more important determinant of plaque instability than the shoulder region where the greatest stress was exerted, and fibrous cap rupture could occur at the site of plaque shoulder even in ThCFA up to 150 μm during exertion.

7.4 Plaque Erosion

7.4.1 Definition

Pathologically, plaque erosion is defined as a plaque with loss and/or dysfunction of the luminal endothelial cells leading to thrombosis [5]. There is usually no additional defect or gap in the plaque architecture except that proteoglycans and smooth muscle cells are exposed to circulation. The absence of endothelial cells is a critical pathological criterion for plaque erosion; however, despite its high resolution, current OCT technique cannot detect individual endothelial cells. Therefore, the OCT definition of plaque erosion is based primarily on a diagnosis of exclusion requiring the absence of a fibrous cap rupture. Since the presence of thrombus overlying the culprit lesion can hinder the ability to reliably assess

Fig. 7.7 Plaque ruptures in relation to exertion. (**a**) Plaque Rupture at the Shoulder Region of the Fibrous Cap. A 38-year-old man collapsed suddenly during an altercation. *Left*, The rupture site is toward the center of the fibrous cap (*arrows*) (Movat pentachrome, original magnification ×15). *Right*, A higher magnification demonstrating rupture site with acute thrombus. Note areas of thinning of fibrous cap (*arrowheads*) (Movat pentachrome, original magnification ×45). (**b**) Plaque Rupture at the Center of the Fibrous Cap. A 60-year-old man was found dead in bed. *Left*, The site of rupture is present at the junction of the fibrous cap with the mildly thickened intima of the relatively normal arterial wall (shoulder region) (*arrows*) (Movat pentachrome, original magnification ×15). *Right*, A higher magnification of the shoulder area showing rupture site and overlying thrombus (Movat pentachrome, original magnification ×30) (Adapted from Burke et al. [42])
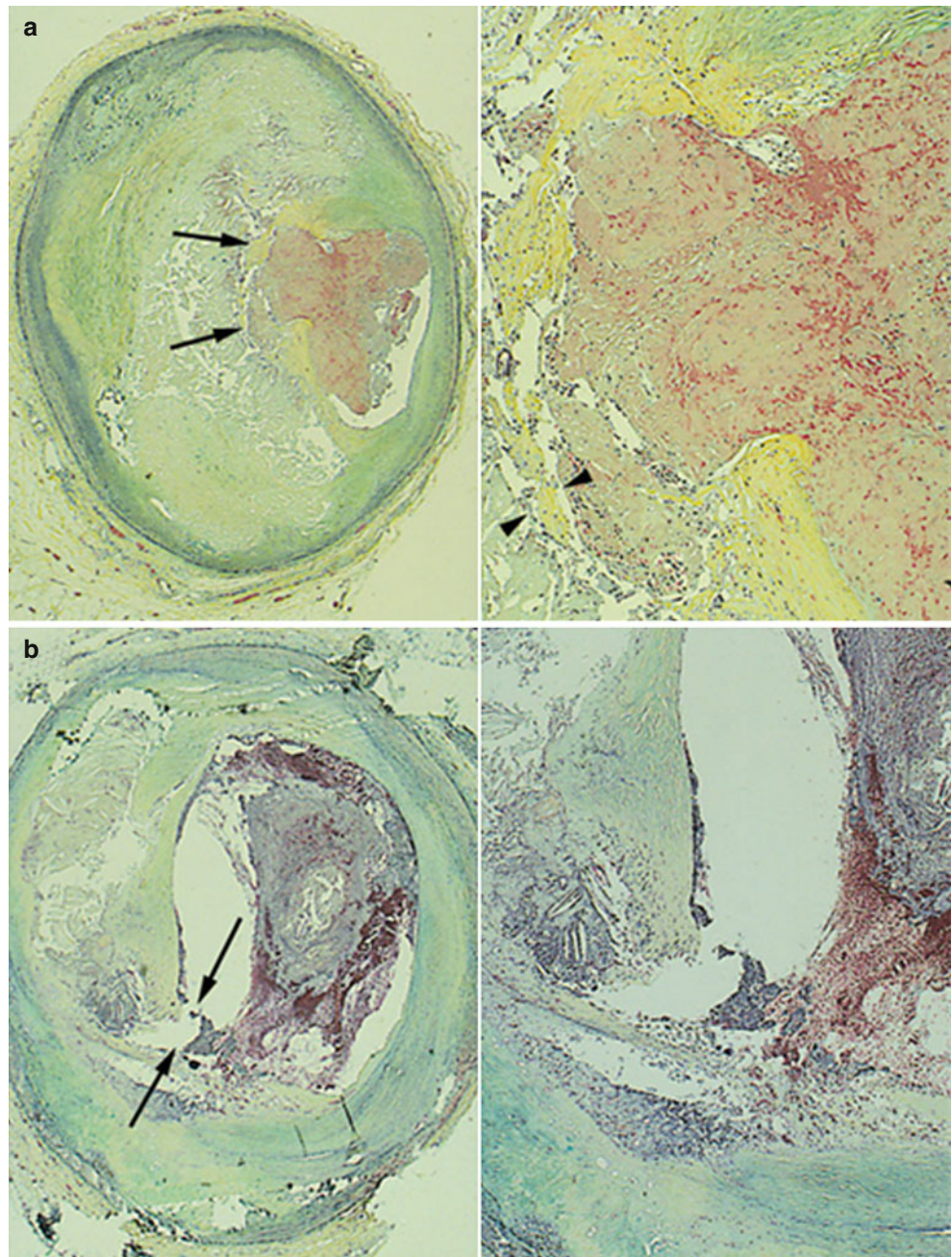
the underlying plaque characteristics by OCT, we proposed the use of definite OCT-erosion and probable OCT-erosion to describe this subset of thrombotic lesions according to the presence of thrombus and visibility of underlying plaque surface: (1) Definite OCT-erosion is defined as the presence of attached thrombus overlying an intact and visualized plaque (Fig. 7.9); (2) Probable OCT-erosion is defined by: (a) luminal surface irregularity at the culprit lesion in the absence of thrombus; or (b) attenuation of underlying plaque by thrombus without superficial lipid, or calcification immediately proximal or distal to the site of thrombus (Fig. 7.10).

7.4.2   Incidence

Plaque erosion accounts for 25–40 % of coronary thrombosis in patients dying from AMI or SCD. In 1994, van der Wal [8] introduced the generic term "plaque erosion" for coronary thrombosis without plaque rupture. Plaque erosion was observed in 8 (40 %) patients and rupture in 12 (60 %) patients who died of AMI. However, in a larger autopsy study (n=298) among patients with AMI not treated with thrombolysis or percutaneous coronary intervention, the incidence of plaque erosion was 25 % and plaque rupture,
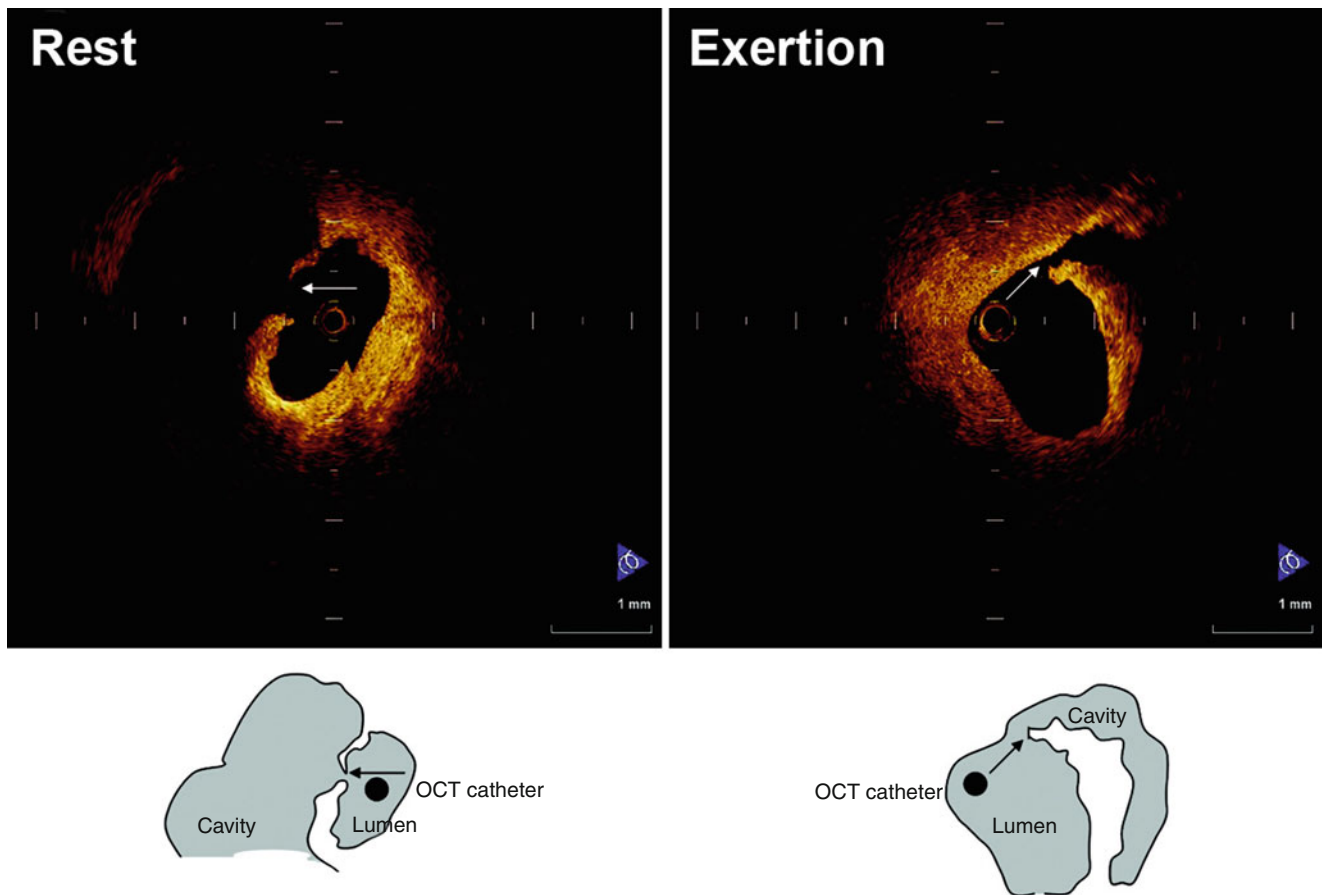
Fig. 7.8 Representative cases of plaque rupture occurring at rest or with exertion. *Left*, Plaque rupture that occurred at rest. Fibrous cap was broken at the midportion, and a thin fibrous cap could be observed.

Right, Plaque rupture that occurred during heavy farm work. Thick fibrous cap was broken at shoulder of plaque (From Tanaka et al. [43])

75 %. Plaque erosion was more common in women than in men (37.4 % versus 18.5 %; p=0.0004) [6]. Farb et al. [5] studied 96 cases of sudden coronary death to compare the incidence and morphological characteristics of coronary thrombosis in plaque rupture versus plaque erosion. Out of 50 cases with acute thrombus, plaque erosion was defined in 22 (44 %) cases versus plaque rupture in 28 (56 %). Plaque erosion was more often seen in younger individuals and women, who have less luminal narrowing and less calcification, and less frequently have foci of macrophages and T cells as compared to plaque ruptures (See Table 7.5). Another study with 241 cases of SCD reported that plaque erosion constituted approximately 40 % of cases. Again, plaque erosions were more common in young women and men <50 years old, and were associated with smoking, especially in premenopausal women [4].

In vivo imaging data on the mechanism of plaque erosion is very limited. Using OCT, our analysis of 126 patients with ACS indicated that the incidence of OCT-erosion was 31 % (definite: 18 %; probable: 13 %) [12]. Excluding the cases

caused by other uncommon lesions, the incidence was 37.5 % which is much more consistent with pathology studies. Additionally, patients with OCT-erosion were younger, had less severe stenosis, and more frequently presented with NSTEACS than those with plaque rupture. Another OCT study reported the incidence of 23 % [13]. However, the definition of erosion used in this study was taken directly from pathology which is not suitable for OCT, and therefore the incidence of plaque erosion may have been underestimated in this study.

7.4.3 Plaque Erosion and Underlying Plaque Morphology

Unlike plaque rupture, the underlying plaque feature of plaque erosion primarily involves early lesions which consist of pathological intimal thickening, fibrous plaque, or fibroatheromas with thick fibrous cap and less extensive necrotic core, less calcification, and less plaque burden [4, 5, 44].
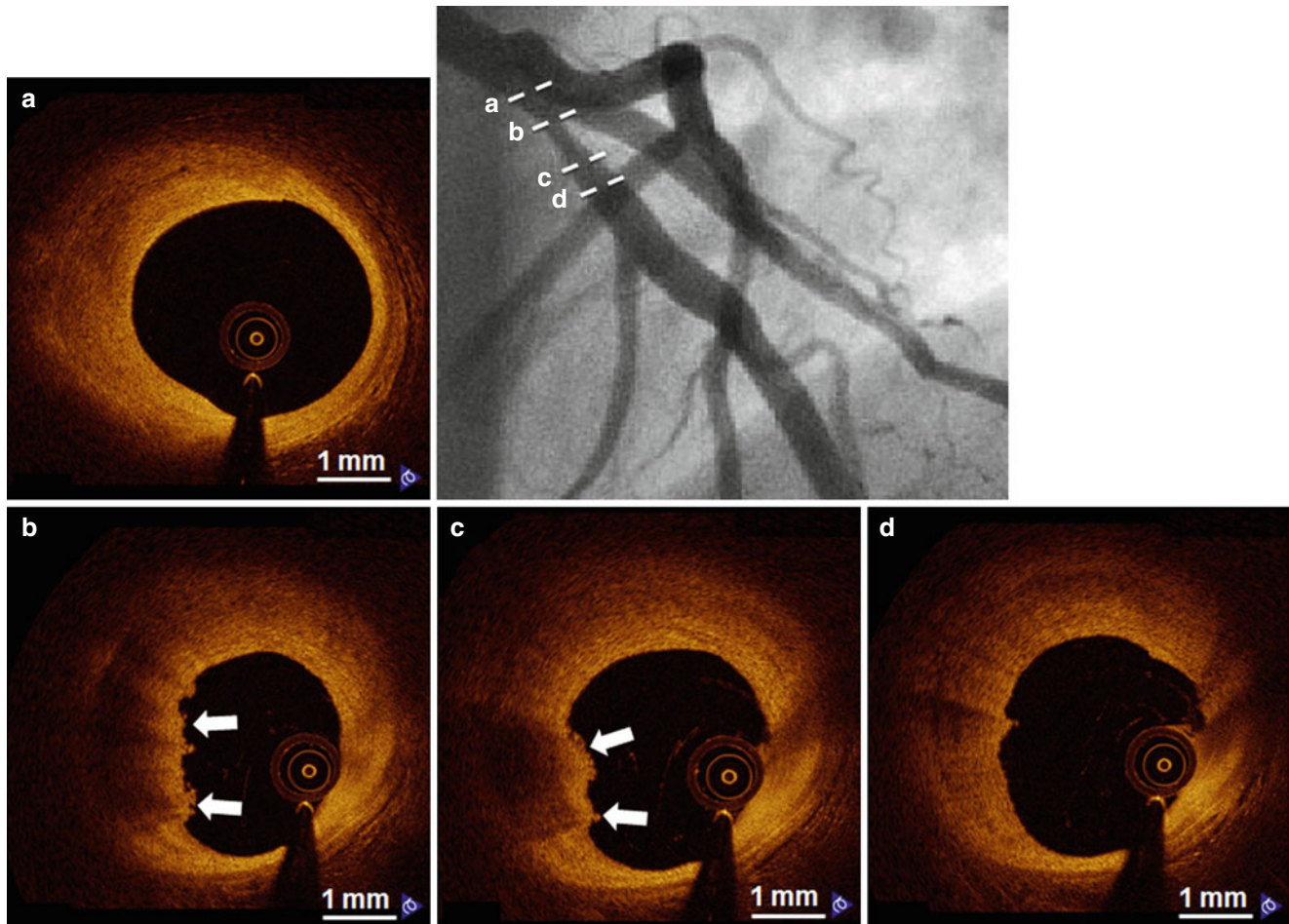
Fig. 7.9 Representative case of "Definite OCT-erosion". A 31-year-old man presented with NSTEMI. Angiographic image (*upper right*) shows a moderate stenosis in the proximal LAD. Serial OCT cross-sectional images from proximal to distal of the culprit lesion indicate that no rupture is detected. Cross-sectional images indicate fibrous plaque (homogeneous high signal region) proximal (**a**) and distal (**d**) to thrombus. OCT-erosion is identified as an irregular lumen surface with attached mural thrombus (*arrows*) overlying a fibrous plaque (**b**, **c**). *NSTEMI* non-ST-segment elevation myocardial infarction, *LAD* left anterior descending coronary artery (From Jia et al. [12])

Those findings were also confirmed by an imaging study which showed that lipid plaque was less frequently detected in OCT-erosion than in plaque rupture. Of note, the distribution of OCT-erosion in fibrous plaque and lipid plaque was similar (44 % in fibrous versus 56 % in lipid plaques) (Fig. 7.11). However, when lipid plaque was present in OCT-erosion, overlying fibrous cap was thicker, lipid arc was smaller, and lipid length was shorter, as compared to those involved in plaque rupture [12]. The eroded site often displays an absence or minimal inflammation characterized by few macrophages and lymphocytes [4, 5], in contrast to a previous study that reported inflammation at the site of erosion [8]. The intima underneath thrombus is rich in smooth muscle cells. Unlike plaque rupture which is rich in type I collagen and biglycan and decoroin, the plaque adjacent to the thrombus in plaque erosion is often rich in type III collagen, versican, and hyaluronan of which selective accumulation may promote deendothelialization and platelet aggregation [5, 45, 46].

An autopsy study has shown that more than 85 % of coronary thrombi in erosions exhibited late stages of healing characterized by inflammatory cell lysis, invasion by SMCs and/or endothelial cells, or organized layers of SMCs and proteoglycans with varying degrees of platelet/fibrin layering. In contrast, in ruptures nearly one-half of thrombi didn't show any healing, implying that thrombus maturation in fatal lesions is highly dependent on the underlying lesion morphology [44]. Clot embolization was more frequently observed in erosions (71 %) than in plaque rupture (42 %), most commonly affecting microvessels <120 μm in diameter, particularly in the left anterior descending coronary artery [47]. In another autopsy study, coronary thrombi in eroded plaques have been shown to contain a higher density of myeloperoxidase-positive cells than those of ruptured
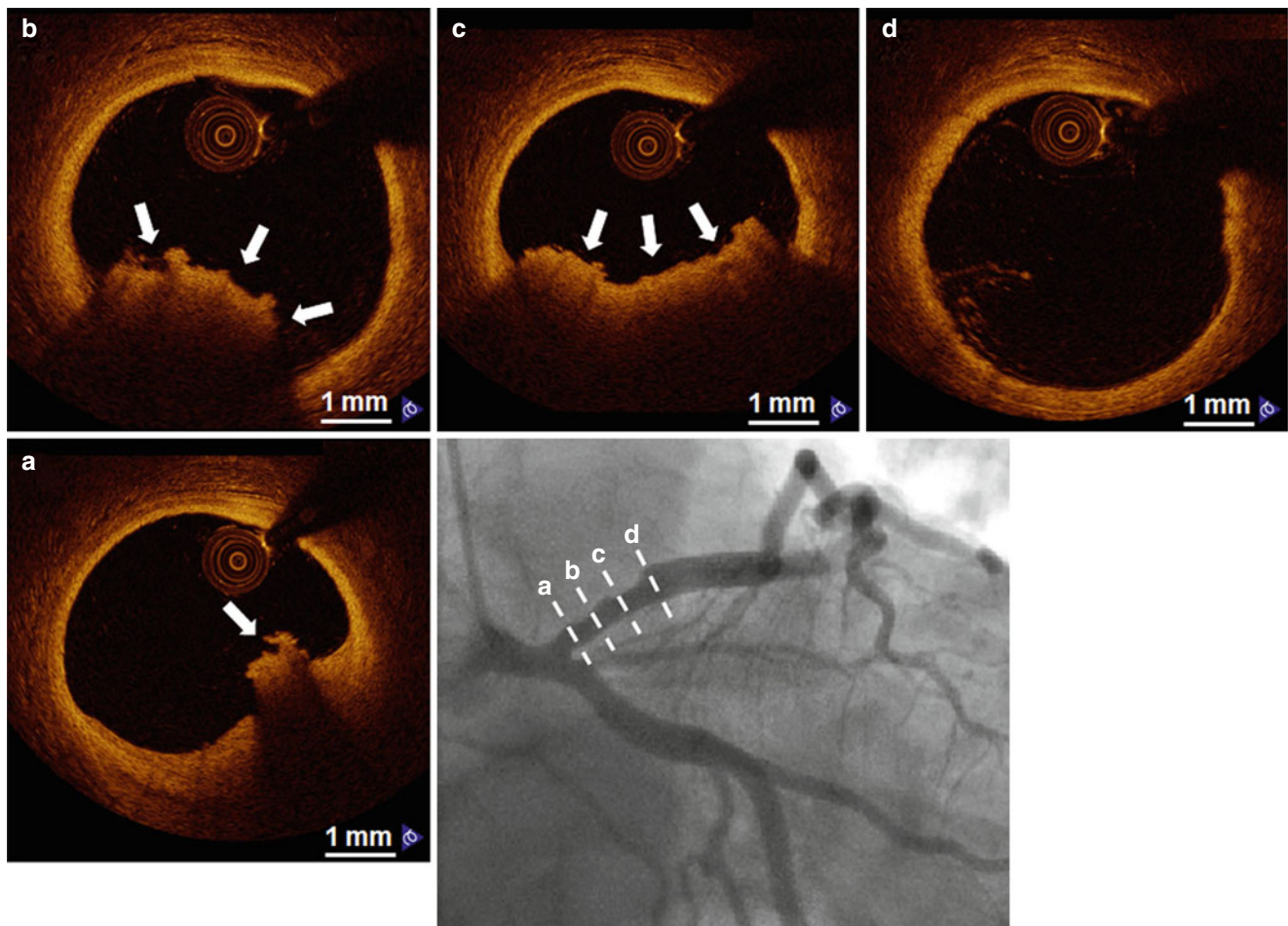
Fig. 7.10 Representative case of "Probable OCT-erosion". A 37-year-old male smoker presented with STEMI. The angiographic image (*bottom right*) shows a mild stenosis in the proximal LAD. Serial OCT cross-sectional images from proximal to distal of the culprit lesion show absence of detectable rupture (**a** through **d**). Underlying plaque morphology is not well visualized due to the presence of residual red thrombus (**a–c**, *arrows*). OCT images in the distal and proximal segments of the thrombotic lesions show the absence of superficial lipid and calcification (**a**, **d**). *STEMI* ST-segment elevation myocardial infarction, *LAD* left anterior descending coronary artery (From Jia et al. [12])

Table 7.5 Plaque rupture compared with plaque erosion

	Plaque rupture (n = 28)	Plaque erosion (n = 22)	P
Male: female	23:5	11:11	0.03
Age, year	53 ± 10	44 ± 7	<0.02
% Stenosis	78 ± 12	70 ± 11	<0.03
Calcified plaque	19 (69)	5 (23)	0.002
Occlusive: nonocclusive thrombus	12:16 (43:57)	4:18 (18:82)	0.08
Concentric: eccentric	13:15 (46:54)	4:18 (18:82)	0.07
Macrophages	28 (100)	11 (50)	<0.0001
T cells	21 (75)	7 (32)	<0.004
Smooth muscle cells	11 (33)	21 (95)	<0.0001
HLA-DR positive	25 (89)	8 (36)	0.0002

From Farb et al. [5]

plaques [48]. Moreover, patients with ACS caused by plaque erosion had higher levels of myeloperoxidase in circulation blood as compared to those by plaque rupture, suggesting that it may be possible to make a diagnosis of plaque erosion by testing inflammatory biomarkers without invasive imaging examination. However, large prospective studies are needed to find more distinguishing and sensitive potential biomarkers for plaque erosion.

Based on these observations, there are distinct pathological features and clinical characteristics that are associated with
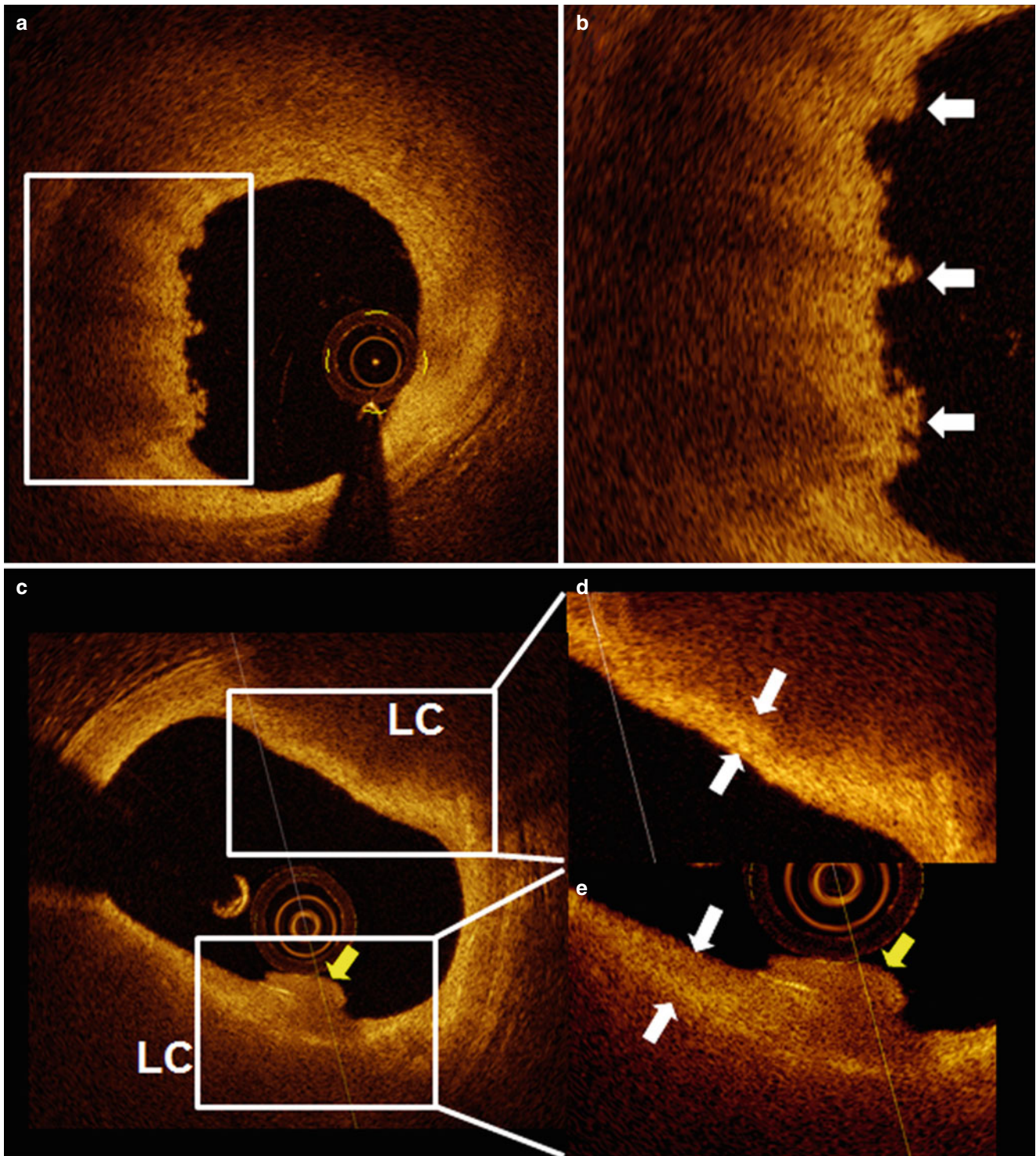
Fig. 7.11 Representative images of OCT-erosion overlying fibrous plaque and lipid-rich plaque. (**a**) OCT-erosion overlying a fibrous plaque is identified as an irregular lumen surface with attached mural thrombus (*arrows*). (**b**) Magnification of the eroded site corresponded to the region in *box* in (**a**). (**c**) A 63-year-old man presented with unstable angina. Serial OCT cross-sectional images from distal to proximal of the culprit lesion showed no evidence of fibrous cap rupture. Lipid-rich plaque with white thrombus (*yellow arrows*) attached was detected in the culprit lesion. Thick fibrous cap (*white arrows*) overlying the deep lipid core (*LC*) observed on both eroded region (**e**) and non-eroded region (**d**). (**d**, **e**) Corresponded to the region in *box* in (**c**)

plaque rupture and erosion, which suggests that they might be caused by different pathophysiologic mechanisms and therefore may need distinct treatment. Plaque rupture induces massive thrombus formation at the culprit site. In contrast, erosion often causes less thrombus burden, preserved vascular structure, and larger lumen. It is conceivable that patients with erosion might be stabilized more effectively by antithrombotic treatment without stent implantation if the lumen is not significantly compromised after thrombectomy. However, further evidence is needed to support this hypothesis.

7.5 Calcified Nodule

7.5.1 Definition

As the least common cause of coronary thrombosis, "calcified nodule" was first introduced by Virmani et al. in 2000 [4]. It refers to a lesion that occurs in disruptive nodular calcification protruding into the lumen with overlying thrombus.

It consists of areas of fragmented calcified sheets that form small calcified nodules that are mixed with fibrin and have a small luminal thrombus. Based on the pathological morphologies discussed above, OCT-CN is defined when fibrous cap disruption is detected over a calcified plaque characterized by protruding calcification, superficial calcium, and the presence of substantive calcium proximal and/or distal to the lesion (Fig. 7.12) [12]. Of note, calcified nodule, by definition requires an overlying thrombus and disruptive luminal surface, and should not be confused with nodular calcification with thin fibrous cap which does not induce thrombosis.

7.5.2 Incidence and Underlying Plaque Characteristics

Pathology study showed that calcified nodules are responsible for 2–7 % of coronary thrombosis in patients with SCD and AMI [4]. A similar finding was reported by an *in vivo* study showing 8 % in patients with ACS [12]. Using distinct
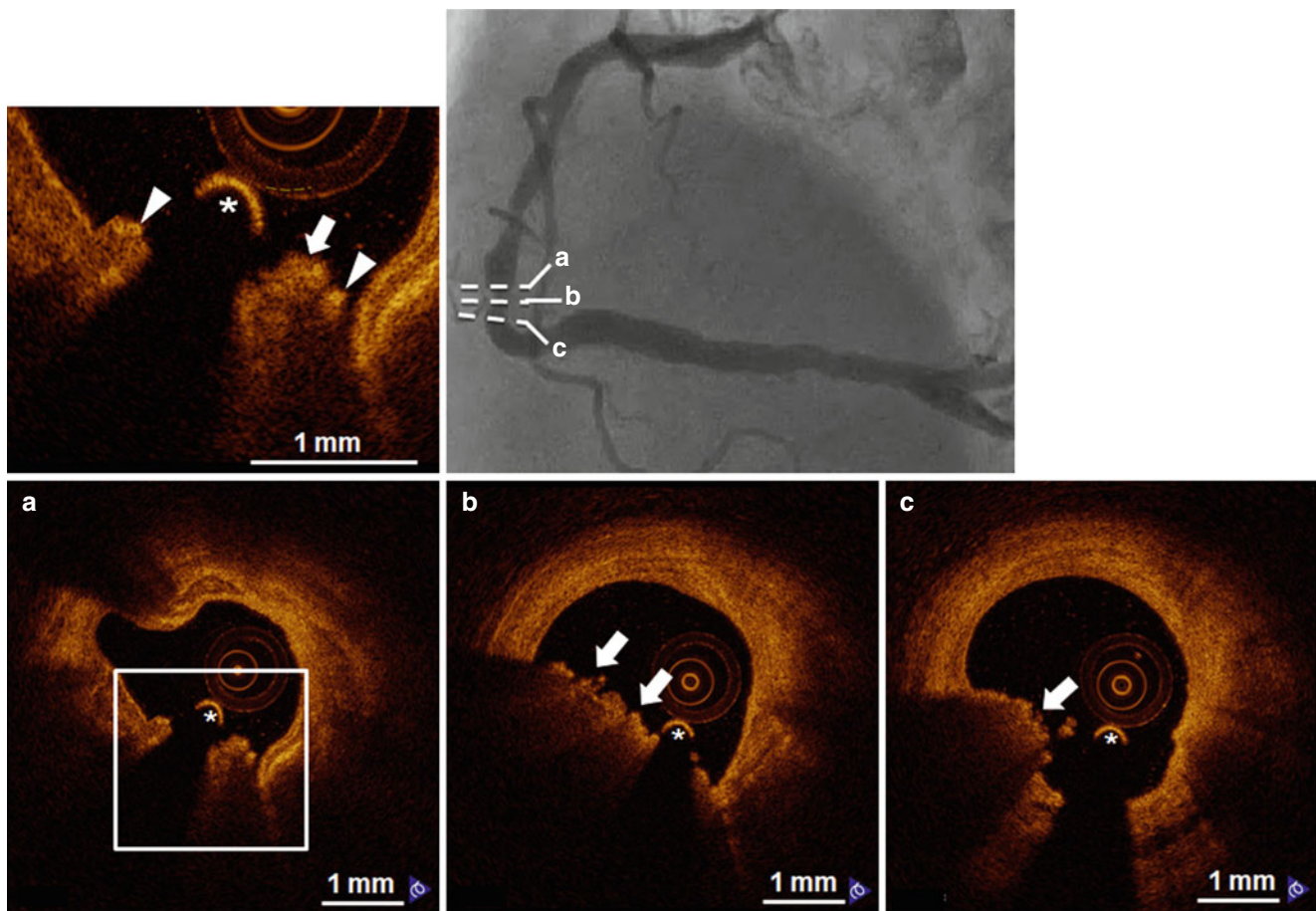
Fig. 7.12 Representative case of "OCT-calcified nodule". A 75-year-old male smoker with unstable angina. Coronary angiogram angiography (*upper right*) demonstrated a complex lesion in the distal right coronary artery. OCT-calcified nodule is identified as a nodular calcification (**a**) protruding into lumen through a disrupted fibrous cap (*arrowheads*) overlying superficial calcification with red thrombus (**b**, **c**, *arrows*) attached to the disrupted site. The *asterisk* (*) indicates the guide wire (From Jia et al. [12])

features (irregular and convex luminal surface) to define calcified nodule on IVUS, the PROSPECT (Providing Regional Observations to Study Predictors of Events in the Coronary Tree) study showed an even higher prevalence of calcified nodule in patients with ACS who underwent three-vessel gray-scale and virtual histology IVUS (VH-IVUS) [49]. Overall, 314 calcified nodules were found in 250 of 1,573 analyzable arteries, with a prevalence of 17 % per artery and 30 % per patient. However, caution should be exercised when interpreting these results, as the PROSPECT study did not distinguish a "thrombotic calcified nodule" from a "non-thrombotic nodular calcification." The previously reported calcified nodules in the autopsy studies required the presence of luminal thrombus. Moreover, VH-IVUS is unable to detect the presence of thrombus. "Non-thrombotic calcified nodules" which have been described by pathology as "nodular calcification" should be discriminated from "calcified nodules." Therefore it is not surprising that lesions with IVUS-defined "calcified nodule" in the PROSPECT study are frequent but are unlikely to cause future coronary events.

Although the true mechanisms of calcified nodules remain incompletely understood, fibrin is often present between the calcified spicules, along with rare osteoclasts and inflammatory cells, suggesting that cracking and fragmentation of calcified plate with intraplaque hemorrhage may be the key mechanism of calcified nodule [4]. Lesions with eruptive nodular calcification are more common in highly calcified tortuous arteries, in older individuals, in males, and are commonly found in the mid right coronary or the left anterior descending coronary arteries. Calcified nodules are often eccentric, and occur in the absence of endothelium overlying nodular calcium and are associated with non-occlusive thrombus.

7.6 Concept of Vulnerable Plaque

The term "vulnerable plaque" is used to describe thrombosis-prone plaques. Our understanding of vulnerable plaque is mostly derived from comprehensive examination of plaque rupture. Precursors of plaque erosion and calcified nodule have not been identified. Traditionally, TCFA is designated as vulnerable plaque which is characterized by a thin fibrous cap heavily infiltrated by macrophages and an underlying large lipid core. Compared to ruptured plaques, TCFA has a smaller necrotic core, fewer macrophages within the fibrous cap, less plaque burden, and less luminal stenosis [50, 51]. (Fig. 7.13) Virmani et al. [4] defined vulnerable plaque based on the actual thickness of the histological section from measurements made on plaque ruptures. TCFA is defined as a lesion with a fibrous cap <65 μm thick. A thickness of 65 μm was chosen as the criterion of instability because in rupture the mean cap thickness was 23 ± 19 μm; 95 % of caps measured less than 65 μm within a limit of only two standard deviations. As illustrated in Fig. 7.14, it is believed that lipid accumulation, thinning of fibrous cap with local loss of smooth muscle inflammation with many macrophages and few mast cells, and intraplaque hemorrhage, destabilize plaques, making them vulnerable to rupture [52]. FCT and size of necrotic core are the most important determinants of vulnerable
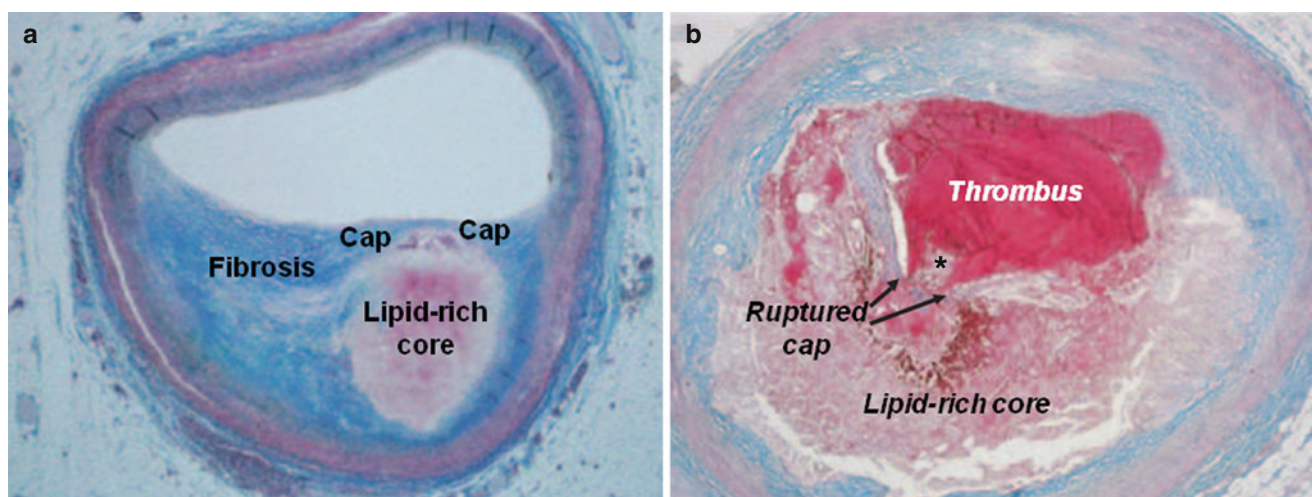
Fig. 7.13 Vulnerable plaque and ruptured plaque. (**a**) Cross-section of a coronary artery containing a plaque assumed to be rupture-prone, consisting of a relatively large lipid-rich core covered by a thin and fragile fibrous cap. Trichrome stain, rendering collagen blue and lipid colorless. (**b**) Plaque rupture. Cross-sectioned coronary artery containing a lipid-rich atherosclerotic plaque with occlusive thrombosis superimposed. The fibrous cap covering the lipid-rich core is ruptured (between *arrows*) exposing the thrombogenic core to the blood in the lumen. Athermanous plaque content is displaced through the gap in the cap into the lumen (cholesterol crystals at *asterisk*), clearly indicating the sequence of events: plaque rupture preceded thrombus formation. Trichrome stain, rendering luminal thrombus and intraplaque haemorrhage red and collagen blue (Adapted from Camm et al. [52])

Fig. 7.14 Plaque vulnerability, rupture and thrombosis. Lipid accumulation, cap thinning, macrophage infiltration, and local loss of smooth muscle cells destabilize plaques, making them vulnerable to rupture. It is unknown whether rupture of a vulnerable plaque is a random (spontaneous) or triggered event. The thrombotic response to plaque rupture is dynamic and depends on local (e.g. exposed substrate and shear forces) as well as systemic factors (e.g. platelets, coagulation and fibrinolysis) (From Camm et al. [52])
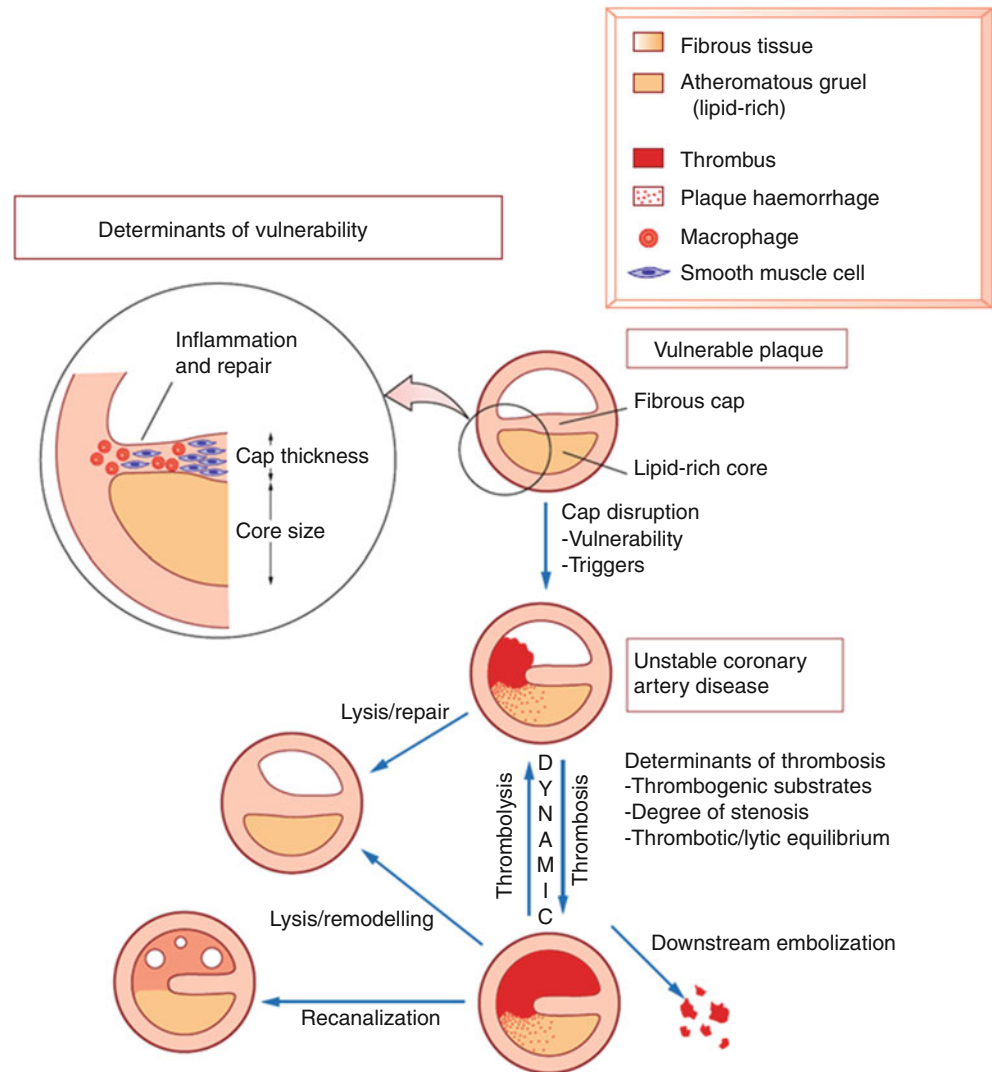
plaque, although the mechanism of thinning or weakening of fibrous cap is still unknown. This concept has been further confirmed by two important studies published recently [51, 53]. One study from our group investigated the morphological characteristics of ruptured culprit plaques (RCP) responsible for acute events, and compared them with ruptured non-culprit plaques (RNCP) and non-ruptured TCFA in patients presenting with ACS. The results indicated that RCP had larger plaque burden and smaller lumen area, when compared with RNCP and TCFA. Morphologic plaque features were not significantly different between RNCP and TCFA except for a thinner FCT observed in RNCP. The FCT <52 μm was the best cut-off value to discriminate ruptured plaque from TCFA (AUC=0.857, p<0.001), and plaque burden >76 % and lumen area <2.6 mm^2 were the best cut-off values to discriminate RCP from RNCP and TCFA (AUC=0.923, p<0.001 and AUC=0.881, p<0.001, respectively) [51]. In another study, Narula et al. [53] analyzed 195 coronary

plaques (105 fibroatheroma, 88 TCFA, and 102 ruptured plaque) from sudden cardiac death cases to determine the hierarchical importance of various pathological characteristics (including FCT, luminal stenosis, plaque area, necrotic core area, inflammation, and calcification) that might differentiate stable plaque from TCFA and ruptured plaque. They found FCT was the most important plaque characteristic when discriminating between these different plaque morphologies [53]. These findings suggest that TCFA has to progress more with a larger plaque size and greater stenosis before it is likely to rupture leading to an acute coronary event.

Currently, OCT is believed to be the ideal intravascular imaging tool to identify TCFA *in vivo* because OCT is the only modality that can accurately measure FCT. By OCT, TCFA is defined as a plaque with thin fibrous cap (≤65 μm) overlying a large lipid pool (lipid arc >2 quadrants on cross-sectional image) (Fig. 7.15). Indeed, OCT has been used in several studies to detect plaque vulnerability. Almost
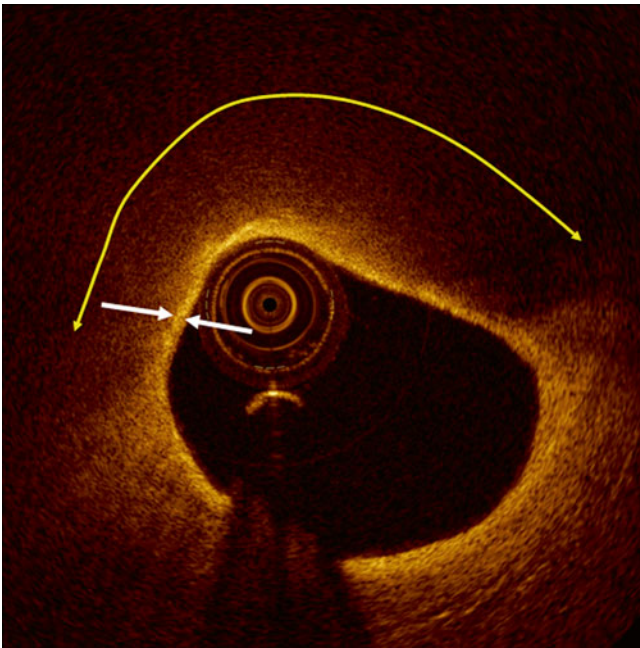
Fig. 7.15 Optical coherence tomography image of thin-capped fibroatheroma. Thin-cap fibroatheroma is characterized by thin fibrous cap (*white arrows*) and large lipid pool (*double-arrow*)

consistently, those OCT studies demonstrated that TCFA is more frequently observed in patients with ACS than in those with SAP [9, 54]. However, the challenge is whether these dangerous plaques defined by OCT can really cause future clinical events. It should be noted that contrary to common perception, there is compelling evidence that plaque rupture and thrombosis most often do not lead to clinical coronary events [55, 56]. Rather, these subclinical plaque rupture and thrombus formations are fairly frequent events that lead to plaque progression and the development of lumen stenosis [57]. These observations suggest that identifying plaques that are prone to rupture (TCFA) may not be as significant as previously held. This concept was recently confirmed in the PROSPECT study, which followed up 697 patients with ACS after VH-IVUS for 3 years for the occurrence of adverse cardiac events [58]. Although 595 TCFA were identified by IVUS in 313 of 623 patients, only 26 of these plaques were responsible for subsequent events at 3 years. Notably, over 3,000 non-culprit lesions were identified at baseline in 673 patients with ACS but only 6 were subsequently related to MI and death after 3 years.

The evidence from these clinical studies suggests that plaque vulnerability may be temporary and is dynamically changing, which may further invalidate the use of plaque characteristic identification at any point in time to predict future events. Kubo et al. [59] performed serial (baseline and 12-month follow-up) VH-IVUS studies and examined 216 non-culprit lesions (plaque burden ≥40 %) in 99 patients. They found that the majority of TCFA evolved into ThCFA

after 12 months of follow-up. Conversely, some ThCFA and some mild plaques described as intimal thickening at baseline changed into TCFA over 12 months. However, serial imaging studies are needed to conclusively establish the concept of temporal instability of plaque morphology.

Conclusions

The primary cause of ACS is plaque rupture, followed by plaque erosion, and least frequently, by calcified nodule. Intravascular OCT provides unprecedented insight into mechanism of ACS. Distinct underlying plaque morphology between plaque rupture and plaque erosion defined by OCT suggests that different treatment should be considered for patients with plaque erosion. Although further clinical research with more subjects is needed, OCT will undoubtedly play a critical role in understanding the underlying mechanisms of ACS and ultimately, the future of ACS treatment.

References

1. DeWood MA, Spores J, Notske R, Mouser LT, Burroughs R, Golden MS, et al. Prevalence of total coronary occlusion during the early hours of transmural myocardial infarction. N Engl J Med. 1980;303(16):897–902.
2. Falk E. Unstable angina with fatal outcome: dynamic coronary thrombosis leading to infarction and/or sudden death. Autopsy evidence of recurrent mural thrombosis with peripheral embolization culminating in total vascular occlusion. Circulation. 1985;71(4):699–708.
3. Virmani R, Burke AP, Farb A, Kolodgie FD. Pathology of the vulnerable plaque. J Am Coll Cardiol. 2006;47(8 Suppl):C13–8.
4. Virmani R, Kolodgie FD, Burke AP, Farb A, Schwartz SM. Lessons from sudden coronary death: a comprehensive morphological classification scheme for atherosclerotic lesions. Arterioscler Thromb Vasc Biol. 2000;20(5):1262–75.
5. Farb A, Burke AP, Tang AL, Liang TY, Mannan P, Smialek J, et al. Coronary plaque erosion without rupture into a lipid core. A frequent cause of coronary thrombosis in sudden coronary death. Circulation. 1996;93(7):1354–63.
6. Arbustini E, Dal Bello B, Morbini P, Burke AP, Bocciarelli M, Specchia G, et al. Plaque erosion is a major substrate for coronary thrombosis in acute myocardial infarction. Heart. 1999;82(3):269–72.
7. Stary HC, Chandler AB, Dinsmore RE, Fuster V, Glagov S, Insull Jr W, et al. A definition of advanced types of atherosclerotic lesions and a histological classification of atherosclerosis. A report from the Committee on Vascular Lesions of the Council on Arteriosclerosis, American Heart Association. Circulation. 1995;92(5):1355–74.
8. van der Wal AC, Becker AE, van der Loos CM, Das PK. Site of intimal rupture or erosion of thrombosed coronary atherosclerotic plaques is characterized by an inflammatory process irrespective of the dominant plaque morphology. Circulation. 1994;89(1):36–44.
9. Jang IK, Tearney GJ, MacNeill B, Takano M, Moselewski F, Iftima N, et al. *In vivo* characterization of coronary atherosclerotic plaque by use of optical coherence tomography. Circulation. 2005;111(12):1551–5.
10. Tearney GJ, Yabushita H, Houser SL, Aretz HT, Jang IK, Schlendorf KH, et al. Quantification of macrophage content in atherosclerotic plaques by optical coherence tomography. Circulation. 2003;107(1):113–9.

11. Yabushita H, Bouma BE, Houser SL, Aretz HT, Jang IK, Schlendorf KH, et al. Characterization of human atherosclerosis by optical coherence tomography. Circulation. 2002;106(13):1640–5.

12. Jia H, Abtahian F, Aguirre AD, Lee S, Chia S, Lowe H, et al. *In vivo* diagnosis of plaque erosion and calcified nodule in patients with acute coronary syndrome by intravascular optical coherence tomography. J Am Coll Cardiol. 2013;62(19):1748–58.

13. Kubo T, Imanishi T, Takarada S, Kuroi A, Ueno S, Yamano T, et al. Assessment of culprit lesion morphology in acute myocardial infarction: ability of optical coherence tomography compared with intravascular ultrasound and coronary angioscopy. J Am Coll Cardiol. 2007;50(10):933–9.

14. Rathore S, Terashima M, Matsuo H, Kinoshita Y, Kimura M, Tsuchikane E, et al. Association of coronary plaque composition and arterial remodelling: a optical coherence tomography study. Atherosclerosis. 2012;221(2):405–15.

15. Schaar JA, Muller JE, Falk E, Virmani R, Fuster V, Serruys PW, et al. Terminology for high-risk and vulnerable coronary artery plaques. Report of a meeting on the vulnerable plaque, June 17 and 18, 2003, Santorini, Greece. Eur Heart J. 2004;25(12):1077–82.

16. Burke AP, Farb A, Malcom GT, Liang Y, Smialek J, Virmani R. Effect of risk factors on the mechanism of acute thrombosis and sudden coronary death in women. Circulation. 1998;97(21): 2110–6.

17. el Fawal MA, Berg GA, Wheatley DJ, Harland WA. Sudden coronary death in Glasgow: nature and frequency of acute coronary lesions. Br Heart J. 1987;57(4):329–35.

18. Davies MJ, Bland JM, Hangartner JR, Angelini A, Thomas AC. Factors influencing the presence or absence of acute coronary artery thrombi in sudden ischaemic death. Eur Heart J. 1989;10(3): 203–8.

19. Burke AP, Farb A, Malcom GT, Liang YH, Smialek J, Virmani R. Coronary risk factors and plaque morphology in men with coronary disease who died suddenly. N Engl J Med. 1997;336(18): 1276–82.

20. Kragel AH, Gertz SD, Roberts WC. Morphologic comparison of frequency and types of acute lesions in the major epicardial coronary arteries in unstable angina pectoris, sudden coronary death and acute myocardial infarction. J Am Coll Cardiol. 1991;18(3): 801–8.

21. Falk E, Nakano M, Bentzon JF, Finn AV, Virmani R. Update on acute coronary syndromes: the pathologists' view. Eur Heart J. 2013;34(10):719–28.

22. Kojima S, Nonogi H, Miyao Y, Miyazaki S, Goto Y, Itoh A, et al. Is preinfarction angina related to the presence or absence of coronary plaque rupture? Heart. 2000;83(1):64–8.

23. Chapman I. Morphogenesis of occluding coronary artery thrombosis. Arch Pathol. 1965;80:256–61.

24. Constantinides P. Plaque fissures in human coronary thrombosis. J Atheroscler Res. 1966;6(1):1–17.

25. Friedman M, Van den Bovenkamp GJ. The pathogenesis of a coronary thrombus. Am J Pathol. 1966;48(1):19–44.

26. Bouch DC, Montgomery GL. Cardiac lesions in fatal cases of recent myocardial ischaemia from a coronary care unit. Br Heart J. 1970;32(6):795–803.

27. Sinapius D. Relationship between coronary-artery thrombosis and myocardial infarction. Dtsch Med Wochenschr. 1972;97(12): 443–8.

28. Friedman M, Manwaring JH, Rosenman RH, Donlon G, Ortega P, Grube SM. Instantaneous and sudden deaths. Clinical and pathological differentiation in coronary artery disease. JAMA. 1973; 225(11):1319–28.

29. Horie T, Sekiguchi M, Hirosawa K. Coronary thrombosis in pathogenesis of acute myocardial infarction. Histopathological study of coronary arteries in 108 necropsied cases using serial section. Br Heart J. 1978;40(2):153–61.

30. Falk E. Plaque rupture with severe pre-existing stenosis precipitating coronary thrombosis. Characteristics of coronary atherosclerotic plaques underlying fatal occlusive thrombi. Br Heart J. 1983;50(2): 127–34.

31. Tracy RE, Devaney K, Kissling G. Characteristics of the plaque under a coronary thrombus. Virchows Arch A Pathol Anat Histopathol. 1985;405(4):411–27.

32. Yutani C, Ishibashi-Ueda H, Konishi M, Shibata J, Arita M. Histopathological study of acute myocardial infarction and pathoetiology of coronary thrombosis: a comparative study in four districts in Japan. Jpn Circ J. 1987;51(3):352–61.

33. Richardson PD, Davies MJ, Born GV. Influence of plaque configuration and stress distribution on fissuring of coronary atherosclerotic plaques. Lancet. 1989;2(8669):941–4.

34. Davies MJ. The composition of coronary-artery plaques. N Engl J Med. 1997;336(18):1312–4.

35. Shi H, Wei L, Yang T, Wang S, Li X, You L. Morphometric and histological study of coronary plaques in stable angina and acute myocardial infarctions. Chin Med J (Engl). 1999;112(11):1040–3.

36. Murai T, Baba M, Ro A, Murai N, Matsuo Y, Takada A, et al. Sudden death due to cardiovascular disorders: a review of the studies on the medico-legal cases in Tokyo. Keio J Med. 2001;50(3):175–81.

37. Michalodimitrakis M, Mavroforou A, Giannoukas AD. Lessons learnt from the autopsies of 445 cases of sudden cardiac death in adults. Coron Artery Dis. 2005;16(6):385–9.

38. Sato Y, Hatakeyama K, Marutsuka K, Asada Y. Incidence of asymptomatic coronary thrombosis and plaque disruption: comparison of non-cardiac and cardiac deaths among autopsy cases. Thromb Res. 2009;124(1):19–23.

39. Subirana MT, Juan-Babot JO, Puig T, Lucena J, Rico A, Salguero M, et al. Specific characteristics of sudden death in a mediterranean Spanish population. Am J Cardiol. 2011;107(4):622–7.

40. Naghavi M, Libby P, Falk E, Casscells SW, Litovsky S, Rumberger J, et al. From vulnerable plaque to vulnerable patient: a call for new definitions and risk assessment strategies: part I. Circulation. 2003;108(14):1664–72.

41. Ino Y, Kubo T, Tanaka A, Kuroi A, Tsujioka H, Ikejima H, et al. Difference of culprit lesion morphologies between ST-segment elevation myocardial infarction and non-ST-segment elevation acute coronary syndrome: an optical coherence tomography study. JACC Cardiovasc Interv. 2011;4(1):76–82.

42. Burke AP, Farb A, Malcom GT, Liang Y, Smialek JE, Virmani R. Plaque rupture and sudden death related to exertion in men with coronary artery disease. JAMA. 1999;281(10):921–6.

43. Tanaka A, Imanishi T, Kitabata H, Kubo T, Takarada S, Tanimoto T, et al. Morphology of exertion-triggered plaque rupture in patients with acute coronary syndrome: an optical coherence tomography study. Circulation. 2008;118(23):2368–73.

44. Kramer MC, Rittersma SZ, de Winter RJ, Ladich ER, Fowler DR, Liang YH, et al. Relationship of thrombus healing to underlying plaque morphology in sudden coronary death. J Am Coll Cardiol. 2010;55(2):122–32.

45. Kolodgie FD, Burke AP, Wight TN, Virmani R. The accumulation of specific types of proteoglycans in eroded plaques: a role in coronary thrombosis in the absence of rupture. Curr Opin Lipidol. 2004;15(5):575–82.

46. Kolodgie FD, Burke AP, Farb A, Weber DK, Kutys R, Wight TN, et al. Differential accumulation of proteoglycans and hyaluronan in culprit lesions: insights into plaque erosion. Arterioscler Thromb Vasc Biol. 2002;22(10):1642–8.

47. Schwartz RS, Burke A, Farb A, Kaye D, Lesser JR, Henry TD, et al. Microemboli and microvascular obstruction in acute coronary thrombosis and sudden coronary death: relation to epicardial plaque histopathology. J Am Coll Cardiol. 2009;54(23):2167–73.

48. Ferrante G, Nakano M, Prati F, Niccoli G, Mallus MT, Ramazzotti V, et al. High levels of systemic myeloperoxidase are associated with

coronary plaque erosion in patients with acute coronary syndromes: a clinicopathological study. Circulation. 2010;122(24):2505–13.

49. Xu Y, Mintz GS, Tam A, McPherson JA, Iniguez A, Fajadet J, et al. Prevalence, distribution, predictors, and outcomes of patients with calcified nodules in native coronary arteries: a 3-vessel intravascular ultrasound analysis from Providing Regional Observations to Study Predictors of Events in the Coronary Tree (PROSPECT). Circulation. 2012;126(5):537–45.

50. Kolodgie FD, Burke AP, Farb A, Gold HK, Yuan J, Narula J, et al. The thin-cap fibroatheroma: a type of vulnerable plaque: the major precursor lesion to acute coronary syndromes. Curr Opin Cardiol. 2001;16(5):285–92.

51. Tian J, Ren X, Vergallo R, Xing L, Yu H, Jia H, et al. Distinct morphological features of ruptured culprit plaque for acute coronary events compared to those with silent rupture and thin-cap fibroatheroma: a combined optical coherence tomography and intravascular ultrasound study. J Am Coll Cardiol. 2014;63(21):2209–16.

52. Camm AJ, Lüscher TF, Serruys PW. ESC Textbook of Cardiovascular Medicine. 1st ed. Blackwell Publishing; 2006. Chapter 12, Acute Coronary Syndromes: Pathophysiology, Diagnosis and Risk Stratification; p.333–365.

53. Narula J, Nakano M, Virmani R, Kolodgie FD, Petersen R, Newcomb R, et al. Histopathologic characteristics of atherosclerotic coronary disease and implications of the findings for the invasive and noninvasive detection of vulnerable plaques. J Am Coll Cardiol. 2013;61(10):1041–51.

54. Kubo T, Imanishi T, Kashiwagi M, Ikejima H, Tsujioka H, Kuroi A, et al. Multiple coronary lesion instability in patients with acute myocardial infarction as determined by optical coherence tomography. Am J Cardiol. 2010;105(3):318–22.

55. Davies MJ. The contribution of thrombosis to the clinical expression of coronary atherosclerosis. Thromb Res. 1996;82(1):1–32.

56. Finn AV, Nakano M, Narula J, Kolodgie FD, Virmani R. Concept of vulnerable/unstable plaque. Arterioscler Thromb Vasc Biol. 2010;30(7):1282–92.

57. Burke AP, Kolodgie FD, Farb A, Weber DK, Malcom GT, Smialek J, et al. Healed plaque ruptures and sudden coronary death: evidence that subclinical rupture has a role in plaque progression. Circulation. 2001;103(7):934–40.

58. Stone GW, Maehara A, Lansky AJ, de Bruyne B, Cristea E, Mintz GS, et al. A prospective natural-history study of coronary atherosclerosis. N Engl J Med. 2011;364(3):226–35.

59. Kubo T, Maehara A, Mintz GS, Doi H, Tsujita K, Choi SY, et al. The dynamic nature of coronary artery lesion morphology assessed by serial virtual histology intravascular ultrasound tissue characterization. J Am Coll Cardiol. 2010;55(15):1590–7.

Spontaneous Coronary Artery Dissection

8

Karl Poon

Abstract

Spontaneous coronary artery dissection (SCAD) is an infrequent cause of coronary artery disease. Whilst a recognized disease entity since 1930s, its pathogenesis remains unclear and various hypotheses have been postulated from clinical and clinic-pathological association. Whilst angiography alone has traditionally been perceived to significantly under diagnose this condition, recent development in intravascular imaging, particularly optical coherence tomography (OCT), have seen significant advances in the understanding of SCAD. From a histopathological perspective, OCT has shown that there may be distinct pathological subsets in SCAD in reference to a dissection flap and an intramural hematoma. Early data also suggests that OCT may be important in optimizing PCI results in SCAD. The future is particularly promising if a collaborative approach is undertaken to utilize OCT as an *in vivo* microscope to shed more light in this poorly understood disease entity.

8.1 Introduction

Spontaneous coronary artery dissection (SCAD) is an infrequent cause of acute coronary syndrome. Given its infrequency much of the knowledge on the subject matter has been gained through case reports and case series. SCAD appears to be associated with specific clinical and pathogenetic characteristics dissimilar to conventional atherosclerotic coronary artery disease. The advent of optical coherence tomography (OCT) has provided the opportunity of an "in-vivo microscope" to better detail this poorly understood disease process. OCT has been shown to better characterize and confirm the diagnosis of acute SCAD, guide percutaneous treatment option, assess acute stent implant complication in SCAD, and follow up on SCAD treatment outcome. This chapter will briefly review the clinical characteristics of SCAD patients from major registries, review some of the postulated pathogenetic processes, examine previous knowledge gained from angiography and intravascular ultrasound studies, and detail the OCT findings of SCAD and some of its potential clinical use in SCAD.

8.2 Pathogenesis

Pretty, originally using the term "dissecting aneurysm of coronary artery", first described SCAD in 1931 in an autopsy study [1]. A larger definitive eight patient autopsy series was published in 1982 by Robinowitz et al. [2]. This histological series demonstrated a common pathological feature of focal adventitial inflammatory infiltrate, predominantly composed of esosinophils. The infiltrate was only seen in dissected arterial segments and the authors postulated that eosinophilic infiltrate may be primarily responsible for SCAD in these patients, potentially causing lysis in the arterial wall leading to intramural hematoma formation.

K. Poon, MBBS, FRACP
Interventional Cardiologist, Cardiology Program,
The Prince Charles Hospital, Rode Road,
Brisbane, Chermside, QLD 4032, Australia
e-mail: Karl.poon@health.qld.gov.au

A second pathogenetic hypothesis was that of cystic medial necrosis (CMN), such as associated with such connective tissue disorder (CTD) as Marfan's syndrome. An interesting case report by Briguori et al. [3] documented cystic medial necrosis on thromboaspirated material in a patient with angiographic SCAD. The association with (CTD) remains somewhat controversial. Patients with Marfan's syndrome rarely develop SCAD, apart from that related to aortic dissection extension. There was also no CMN demonstrated in the eight patient autopsy histological examination. Indeed some more recent large single center angiographic clinical studies by Saw et al. [4] and Alfonso et al. [5] found no increased incidence of CTD in SCAD presentation.

A more recent association was reported to be fibromuscular dysplasia (FMD), first suggested in 2005 by Pate et al. [6] and followed later in a 50 patient series by Saw et al. [4] where all these patients with non atherosclerotic SCAD were retrospectively identified and then investigated for possible noncoronary FMD such as renal, iliac or cerebrovascular involvement. The study showed 86 % of SCAD patients had at least one non-coronary FMD on screening (58.1 % had involvement renal, 48.8 % iliac and 46.5 % cerebrovascular). This led the researchers to hypothesize a potential pathogenetic association – that SCAD may be the culmination of coronary FMD. The association with FMD was also replicated in the largest SCAD registry to date of 87 patients by Tweet et al. [7], in which 8 out of angioraphic SCAD 16 patients, who had femoral angiography for vascular closure device, were shown to have concomitant femoral FMD. The association seems more than coincidental and further definitive autopsy data will be important atherosclerotic.

8.3 Clinical Characteristics

Over the years there had been hundreds of case reports in the literature on SCAD. Over the recent decade there had been several large single center case series (Table 8.1) [4, 5, 7–10] from which there had been a better appreciation of the common clinical characteristics that differentiate SCAD from conventional coronary artery disease. These clinical associations are important to recognize as a high index of suspicion is crucial in not missing the diagnosis, particularly in the absence of intracoronary imaging.

The true incidence is hard to ascertain and the reported incidence varies significantly. A review by Giacoppo et al. [11] showed an incidence of between 0.03 and 1.1 %. It should however be noted the diagnostic means varied widely in the numerous series included with varying denominator. An interesting recent series by Nishiguchi et al. [12] utilized OCT for diagnosis and this saw a 4 % incidence amongst acute coronary syndrome presentations, the highest incidence reported in the literature. It is therefore likely if coronary angiography or even intravascular ultrasound were the only modality used for diagnosis a significant portion of SCAD patients will be missed.

Young females are disproportionately represented in SCAD (see Table 8.1). Almost all cases presented with acute coronary syndrome, and possibly a significant portion which culminated in sudden cardiac death were never captured further adding to the common perception of underdiagnosis. Temporally there has also been a strong association of SCAD with peripartum or postpartum state [11], thought to be related to the impact of hormonal variation on arterial wall integrity.

Most SCAD patients had fewer cardiovascular risk factors than conventional acute coronary syndrome patients. All coronary branches have been reported to be affected by SCAD as had reports of multivessel involvement in the same index presentation. Recent observational data [5, 7] suggested a favourable outcome with a conservative approach, particularly in the presence of adequate or normal coronary blood flow in the affected artery; and that percutaneous coronary interventions are not infrequently unsuccessful even in experienced centers, requiring almost always more than one stent [7]. In the largest single center series by Tweet et al. [7], the 10-year recurrence rate was estimated at 29.4 %.

The recognition of such clinical factors is very important as SCAD occurs with such infrequency unless one is mindful of such clinical associations, SCAD can often be missed particularly when an angiographic radiolucent flap is not present.

Table 8.1 Large case series of SCAD

Study investigator	Number	Female (%)	Age	LM	LAD (%)	LCX (%)	RCA (%)	STEMI (%)	NSTEMI/USA (%)	Thrombolysis (%)	Medical (%)	PCI (%)	CABG (%)
Romero-Rodriguez et al. [8]	19	79	47.7	0	63	26	11	68.4	31.6	16	58	26	0
Vanzetto et al. [9]	23	74	46.3	13 %	52	22	13	60.0	40.0	0	43	35	22
Mortensen et al. [10]	22	82	48.7	9 %	86	5	14	72.0	28.0	0	32	59	9
Tweet et al. [7]	87	82	43	9 %	71	18	31	49.4	50.6	13	36	45	5
Alfonso et al. [5]	45	58	51	N/A	53	16	29	40.0	60.0	0	69	29	20
Saw et al. [4]	50	98	51	N/A	40	34	32	30	70	0	82	14	4

8.4   Coronary Angiography

Traditionally it is recognized that coronary angiography grossly under diagnoses SCAD. Whilst this is not particularly true when a dissection or intimal flap is clearly visible on angiography, this occurs most particularly in SCAD which has resulted in diffuse stenosis with an intramural hematoma without a flap. There are many case reports in the literature where SCAD was "invisible" on angiography and the diagnosis was elucidated only on intravascular imaging.

An angiographic classification for SCAD has recently been proposed by Saw [13], with three types of angiographic subtypes. Type 1 is the stereotypical angiographic appearance with a radiolucent flap (Fig 8.1a). Type 2 involves usually the mid to distal segments with often an abrupt change in vessel calibre, often extending into the terminal segment (Fig. 8.1b). Type 3 describes a focal segment of "atherosclerotic" lesion, usually in a localized segment of an artery, with compromise of side branches but usually otherwise no atherosclerotic lesion in other segments (Fig. 8.1c).

Most conventional angiography series tend to suggest an under-diagnosis when there is a low index of suspicion amongst angiographers. However, in an unusual twist, when OCT was systemically employed for angiographically suspected SCAD lesions [14], some cases transpired to be intracoronary thrombus manifesting as filling defect, even diffuse atherosclerotic lesions. In short, when a radiolucent dissection flap is seen angiographically, the diagnosis of SCAD is reasonably specific; in the absence of a dissection flap, angiography alone is not sufficiently sensitive enough to rule out SCAD, particularly the "diffuse stenosis" subtype caused by intramural hematoma mimicking atherosclerosis (Table 8.2).

8.5   Intravascular Ultrasound

The appearance of SCAD on IVUS was first reported by Maehara et al. [15] in 2002. These IVUS studies were important in establishing the two cardinal and pathognomonic features for SCAD on intravascular imaging: intimal dissection flap and intramural hematoma. As originally suggested from autopsy studies, spontaneous intramural hematoma was the first diagnostic feature for SCAD. The finding of an intimal flap progressed the understanding of SCAD, and raised several pathogenetic mechanism. One, a spontaneous separation developed between the arterial layers, allowing the development of a false lumen, eventually leading to the dual lumen. Second, a hematoma occurred spontaneously, with the expanding hematoma eventually rupturing into true lumen causing an intimal tear from the pressurized cavity.

The enhanced resolution of OCT over IVUS has now meant however that OCT may be the intracoronary imaging of choice in SCAD, although a definitive comparison between IVUS and OCT in SCAD is yet to be performed. The first comparison between the two modalities was reported by Poon et al. [16], who suggested potential superiority of OCT over IVUS. A subsequent eight patient series by Paulo et al. [17] demonstrated that the two modalities may be complementary.

The biggest limitation to OCT in the use of SCAD is the depth of penetration, particularly in the setting of thrombus and significant intramural hematoma where the external reference diameter is difficult if not impossible to assess. Indeed, in two recent OCT SCAD series (Paulo [17] and Nishiguchi [12]), thrombus and significant residual blood render OCT uninterpretable. In Paulo's eight patient series,
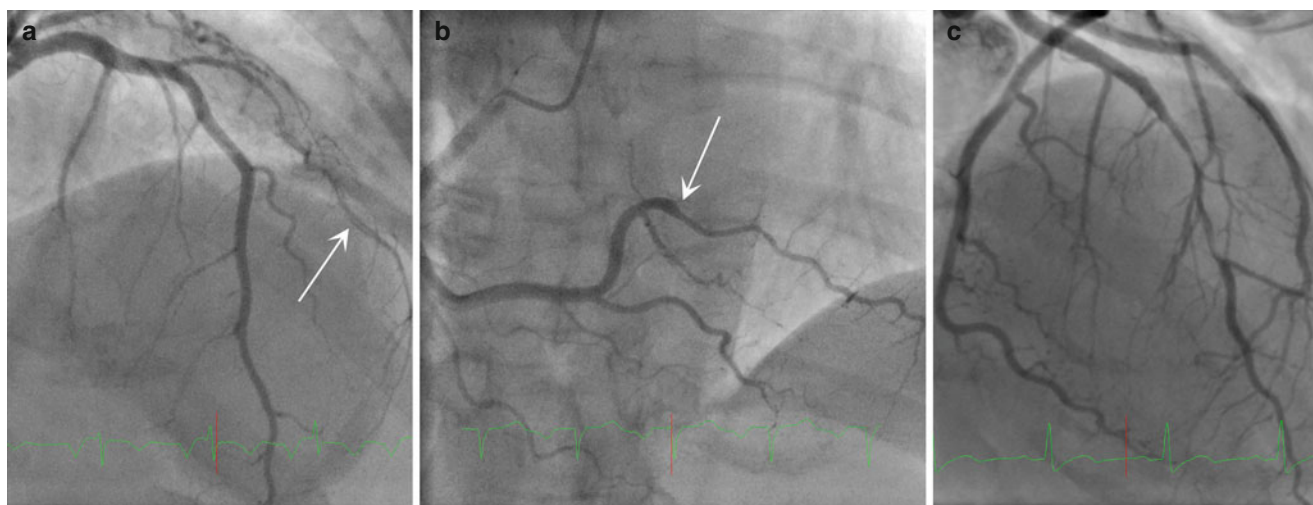
Fig. 8.1 Angiographic classification of SCAD. (**a**, **b**) Multi-vessel involvement in the same patient. (**a**) Radiolucent dissection flap (*arrow*) in the diagonal artery; (**b**) abrupt change in calibre (*arrow*) affecting the posterolateral branch. (**c**) Atherosclerotic type lesion affecting the mid LAD. Note unusual diffuse side branch compromise

Table 8.2 Characteristics of angiography vs. IVUS vs. OCT

	Coronary angiography	IVUS	OCT
Diagnosis	+	++	+++
Radiolucent intimal flap	+++	++	+++
Microscopic intimal flap	−	+	+++
Diffuse intramural hematoma/stenosis	−	++	+++
Longitudinal extent of hematoma	+	+++	+++
Intimal flap thickness	−	−	+++
Overlying thrombus	−	+	+++
Red vs. white thrombus	−	−	+++
Side branch involvement	++	++	++
Associated atherosclerotic plaque	+	++	+++
Intramural hematoma characterization	−	+++	+
Image quality with thrombus	−	+++	+
Depth of penetration	N/A	+++	+
Large vessel assessment	+++	+++	++
Percutaneous intervention			
Reference diameter/external lamina	+	+++	+
Entry and Exit ports	−	+	+++
Residual stenosis/hematoma	−	++	+++
Trapped hematoma/complication assessment	+	++	+++

IVUS provided better definition on the external layer, better assessment of the heterogeneity within the intramural hematoma, and allowed for longer segments to be imaged. A summary of the characteristics of each imaging modality is presented in Table 8.2.

8.6 Optical Coherence Tomography

8.6.1 Diagnosis and Examination of SCAD

To date much of the data on OCT in SCAD had been accumulated from case reports and 3 larger single center case series (Table 8.3), representing no more than 50 cases of SCAD on OCT altogether. The use of OCT in the diagnosis of SCAD was first reported in 2009 by Alfonso et al. [18] and Ishibashi et al. [19] separately.

OCT is now arguably the gold standard for the diagnosis of SCAD, with its near tissue level definition providing unprecedented specificity and sensitivity compared to angiography or intravascular ultrasound. Intravascular imaging, particularly with OCT, is instrumental in confirming diagnosis in angiographically silent SCAD lesions, as shown in many anecdoctal reports [20].

The observational data accumulated thus far corroborated the two distinctive intravascular features of SCAD lesions demonstrated on IVUS studies, namely that of the intimal flap and intramural hematoma. OCT has however provided further interesting insights into the pathology of SCAD.

8.6.1.1 Typical OCT SCAD Characteristics

The first pathognomonic signature of SCAD by definition, at least on angiography, is a dissection flap that is not iatrogenic, especially in otherwise normal vessel segment with no atherosclerosis or intrinsic vessel wall pathology. The finding of an intimal/dissection flap, assuming no wire trauma prior to the acquisition of OCT images, is diagnostic. The unique resolution advantage of OCT [21, 22] seems to improve the diagnosis of intimal flaps. In Alfonso's 11 patient series [14], a rupture site was identified in 74 % of cases, otherwise angiographically invisible. In Paulo's series [17], IVUS failed to demonstrate 4/6 rupture sites demonstrated on OCT. From the limited data, it would appear that OCT has a diagnostic accuracy for intimal flap or rupture sites superior to both angiography and IVUS. The localization of an intimal flap, particular in its relationship to the intramural hematoma and resultant stenosis, also facilitates and guides coronary intervention (see later).

The second diagnostic feature is that of an intramural hematoma (Figs. 8.2 and 8.3), which formed a pathological sine qua non for SCAD in the autopsy era. It has been previously suggested that there may be two pathogenetic processes for SCAD. First an initmal tear that propagates and causes dual lumen and hence luminal compromise. Second, a medial spontaneous hematoma that may not necessarily be associated with an intimal flap but may culminate as a diffuse luminal narrowing without the typical angiographic appearance of dual lumen. An intimal flap confirms the diagnosis but this may therefore not always be present. The presence of a spontaneous intramural hematoma is a powerful diagnostic feature. In the angiographic classification proposed

Table 8.3 OCT SCAD case series

Study	Year published	OCT	STEMI: NSTEMI	Dissection flap seen (%)	Thrombus	Atherosclerosis	Comments
Alfonso et al. [14]	2012	11	9:2	74	100 %	27 %	First systematic OCT study in SCAD. Intimomedial dissection discovered; common thrombus association
Paulo et al. [17]	2013	8	N/A	75	N/A	N/A	IVUS vs. OCT in SCAD. IVUS better thrombus penetration, longer lesion evaluated, longer false lumen imaged
Nishiguchi et al. [12]	2013	13	8:3	77	69 %	N/A	Systematic evaluation fo SCAD incidence in ACS patients. Entry door and hematoma patients may present with different clinical characteristics
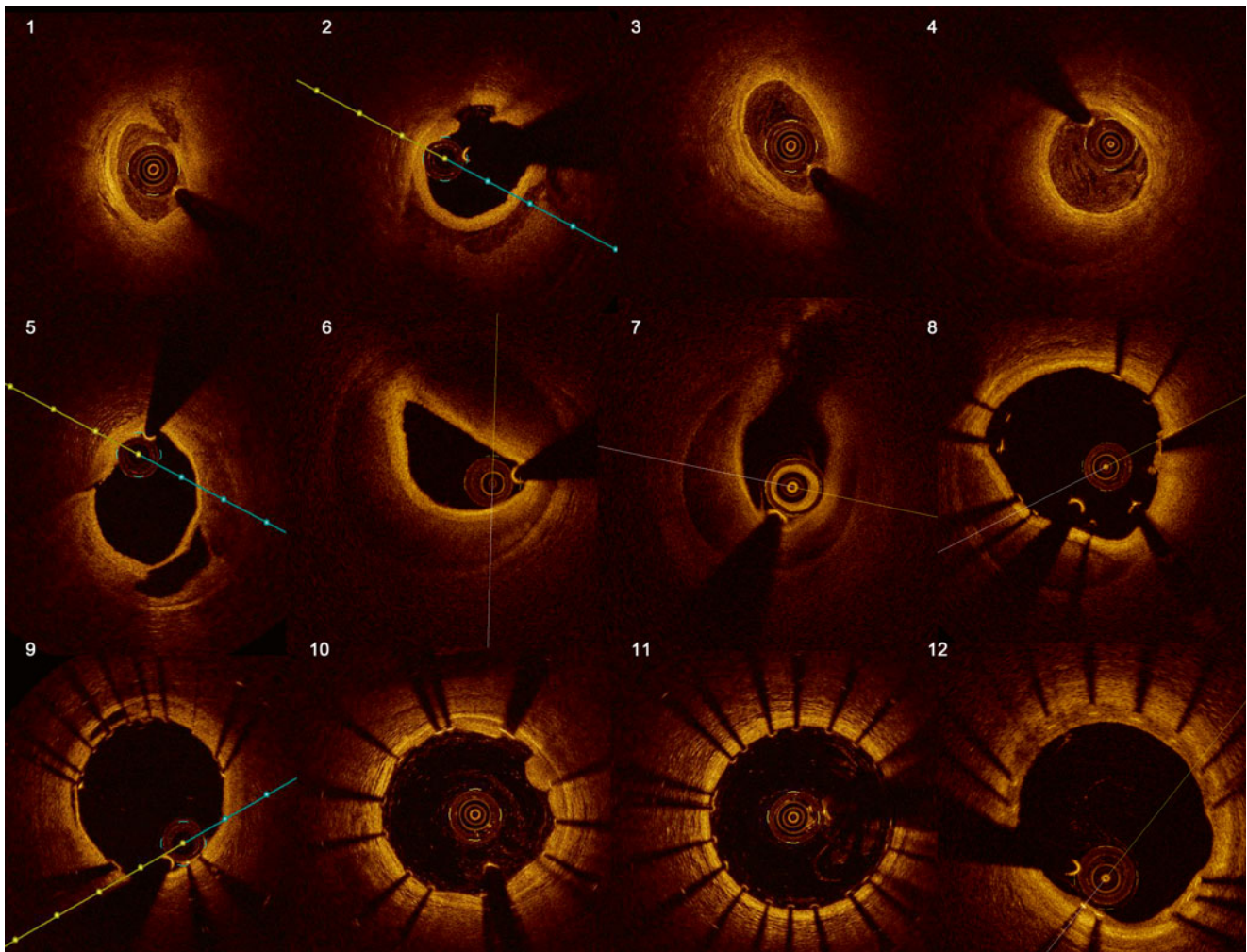
Fig. 8.2 Characteristic SCAD findings on OCT. *1* Distal "exit" flap, note poor contrast clearing creating artefact; *2* dissection flap, with communication to false lumen, note heterogeneous hematoma at 6 o'clock; *3* near circumferential hematoma, however external lamina not seen at all; *4* significant volume of hematoma with external lamina visualized; *5* relatively thin intimal flap compared to 2, complex heterogeneous hematoma; *6* pressurized hematoma compartment causing true lumen compression from hematoma propagation; *7* side branch from perfused through true lumen with contralateral false lumen; *8* stent struts malapposed, suggesting further judicious postdilatation needed; *9* apposed stent struts, with underlying dissection flap re-adhered; *10* plaque prolapse at 2 o'clock as commonly seen acute coronary lesions; *11* well expanded struts with no residual hematoma; *12* 6 month follow up of well endothelialized struts
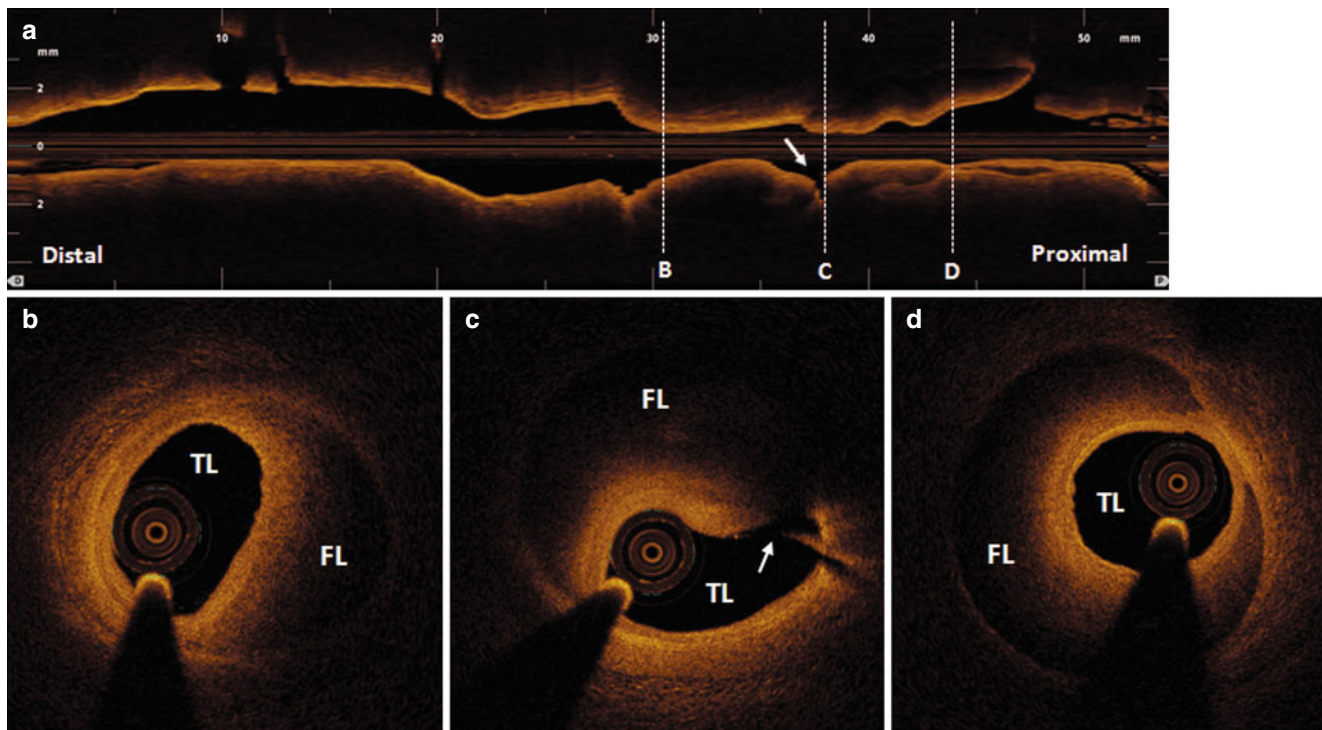
Fig. 8.3 Longitudinal cross section of OCT SCAD. Longitudinal cross section (**a**) of SCAD lesion. Note in optimally attained images the external lamina layer could be well seen (*b, c, d*). Homogenous intramural hematoma seen in false lumen (FL), against the compromised lumen in the true lumen (TL). Note again different morphology of "intimomedial" dissected layer between various segments (**b–d**). Subtle ruptures site (**c**, *arrow*). Note the rupture site is roughly midway longitudinally in the entire length of intramural hematoma (Image courtesy of Prof. IK Jang)

by Saw [13], the diffuse atherosclerotic subtype of SCAD (Type III) is most easily mistaken or misdiagnosed otherwise without intravascular imaging.

8.6.1.2 Unique OCT Insights

Intimo-Medial Flap and FMD

One of the interesting findings from the biggest single center series is the thickness of the so-called intimal flap (Fig. 8.2). It has been previously perceived that the dissection plane exists between the intima and the media. In Alfonso's 11 patient series [18], the average thickness of this flap was between 175 and 348 μm. This would hence be beyond the conventional thickness expected of the intima. This led the researchers to coin the term "intimomedial dissection". The discovery represents somewhat of a paradigm shift in the understanding of the pathology. Even more interesting is the finding that the thinnest part of this dissection often occurred at the "shoulder", somewhat akin to acute atherosclerotic plaque rupture at the shoulder of thin capped fibroatheroma. The clinical implication of this interesting finding has yet to be fully established. It is purely hypothesis generating whether such thickened flap may be related to the thickened intimal layer in fibromuscular dysplasia [23], further lending weight to the potential pathogenetic role of FMD.

Intimomedial Dissection in Relation to Intramural Hematoma

The presence of either a dissection flap or spontaneous intramural hematoma is usually sufficient for the diagnosis of SCAD, and these may not be present concomitantly. Nevertheless, one may surmise that the flap thickness would have been beyond the resolution of IVUS and hence the exact incidence of the dissection flap may have been under-diagnosed in previous studies. In Alfonso's series (see Table 8.3) [14], the dissection was identified concomitantly with intramural hematoma in 7/11 patients (74 %). This raises the possibility of two distinct pathogenetic processes. First, a dissection flap occurs spontaneously, allowing ante-grade propagation and then the formation of dual lumen, to lead to subsequent intramural hematoma. It would therefore be logical to expect the luminal compromise to be the worst when there is no "exit" flap/dissection although this may be more a function of the pressure hemodynamics between the false and true lumen. Second, a spontaneous hematoma occurs within the media, or its interface with either the intima or adventitia, and a tubular luminal stenosis results from compression of a pressurized hematoma volume, without necessarily a dissection flap if the pressure within the false lumen is relatively low or tolerated, i.e. no rupture into the true lumen.

Associated Thrombus

The incidence of associated thrombus in SCAD has never been fully appreciated. OCT has provided unique resolution advantage over IVUS. In Alfonso's 11 patient series (see Table 8.3) [14], all 11 patients had associated thrombus on their SCAD lesions. In Nishiguchi's series (see Table 8.3) [12], thrombus was only seen with the entry door subtype of SCAD but not the false lumen thrombosis type. The differential incidence is logical as the dissection flap type is more likely thrombogenic. Whilst OCT has been crucial to identify this difference, the exact pathological implication of associated thrombus remains unknown. It is unclear if SCAD lesions with associated thrombus are more prone to ischemia or even occlude, and thus maybe more justifiable for percutaneous treatment. From Alfonso's long-term data [5], it would appear conservative treatment, may be preferable to stent placement.

Associated Atherosclerosis

Several OCT registries (see Table 8.3) have examined the incidence of co-existing atherosclerosis. Hoshi et al. [21] postulated that lipid plaque adjacent to SCAD entry point may be responsible for SCAD dissection. The presence of co-existing atherosclerosis may have implication on the length of stents required or even the likelihood of SCAD recurrence.

8.6.2 Treatment Guidance in SCAD

Whilst the use of OCT in the diagnosis of SCAD is very useful, its role guiding percutaneous treatment in SCAD is indispensable. This is particularly in light of recent registries demonstrating favourable outcomes in conservative treatment in non-ischemic non-occlusive SCAD [5, 7]. From a purely clinical perspective, the use of OCT purely to confirm SCAD some would argue may be redundant: if a conservative approach is to be pursued regardless and the diagnosis is certain with the presence of a radiolucent flap.

However, PCI in SCAD can often be difficult, unsuccessful and occasionally complicated by worsening coronary flow. If PCI is to be undertaken for SCAD lesions, the use of OCT is highly recommended. This is far more than purely to confirm the wire position in the true lumen as was once suggested in the use of IVUS. If a wire was in the false lumen and an OCT catheter had traversed the false lumen, it would very likely propagate in the false lumen amongst other problems [24].

On the contrary, the biggest benefit of OCT is more related to a complete evaluation of the SCAD lesion – its longitudinal and circumferential extent, the presence or otherwise [22] of an "entry or exit door", as well as reference diameters before and after the lesion. As discussed previously, OCT can be limited by thrombus and intramural hematoma such that the external elastic lamina is not well seen compared to IVUS. As shown in Fig. 8.3, whilst the depth of penetration could sometimes be compromised by either overlying thrombus or large intramural hematoma, occasionally the longitudinal cross section of the SCAD segment can provide very important insights into the burden of SCAD disease to be treated percutaneously. There have been several case reports [24–26] documenting the complications of PCI in unsuspected SCAD. Indeed, PCI in the largest SCAD registry to date showed an unacceptably high failure rate even in an experienced center [7].

Most of the registries suggest when PCI is undertaken for SCAD, frequently more than one stent is required. The most likely reason is that the stent chosen, whilst apparently sufficient to cover the "angiographic disease", often leads to "squeezing" of the angiographic silent intramural hematoma proximally and distally [24]. This complication is well described even from the IVUS era. Often this propagating hematoma is exacerbated by conventional techniques of distal to proximal stenting. In situations where there is no proximal flap or to the main bulk of intramural hematoma, entry door, the dire consequence could be therefore ongoing propagation in the hematoma. This may even propagate all the way to the ostium of an artery if the operator is not cognizant of the vicious cycle, especially in arteries denude of significant side branches.

There are several strategies to prevent this problem when using OCT for guidance. A careful evaluation of the SCAD lesion will allow identification of the entry and potentially exit door in relation to the lesion, and the length and "volume" of intramural hematoma. The stenting strategy should be determined based on this.

Intimal flap identified in relation to hematoma – depending on the location of the intimal flap the stenting strategy may need to be tailored [22]. The location of the rupture site/intimal flap seems unpredictable and may be multiple (Figs. 8.3 and 8.4). One concern of PCI is trapping of hematoma after a stent has been placed across the exit/entry door. If a flap is proximal then the conventional technique of ballooning and stenting from distal to proximal can be undertaken with likely no concern of trapping the hematoma. If the flap is purely an exit door, then it would be advisable to consider adequate lesion preparation with 1:1 balloon predilatation and observe the response of the hematoma on a second OCT acquisition. It may be considered the stents are placed *proximal to distally* to avoid hematoma propagation (Fig. 8.4) and squeeze the hematoma distally out of the exit door. In addition, the OCT can provide important information on the length of stent(s) needed. It's almost always advisable to choose a stent longer than one might measure on OCT or angiography. The reason is the hematoma is likely to be squeezed and propagated proximally and distally.

Intramural hematoma only – when no intimal flap is identified at all with the presence of only an intramural hematoma, particularly a large and long hematoma, then caution needs to be exercised for any stent placement. With nowhere for the hematoma to move apart from into side branches, the
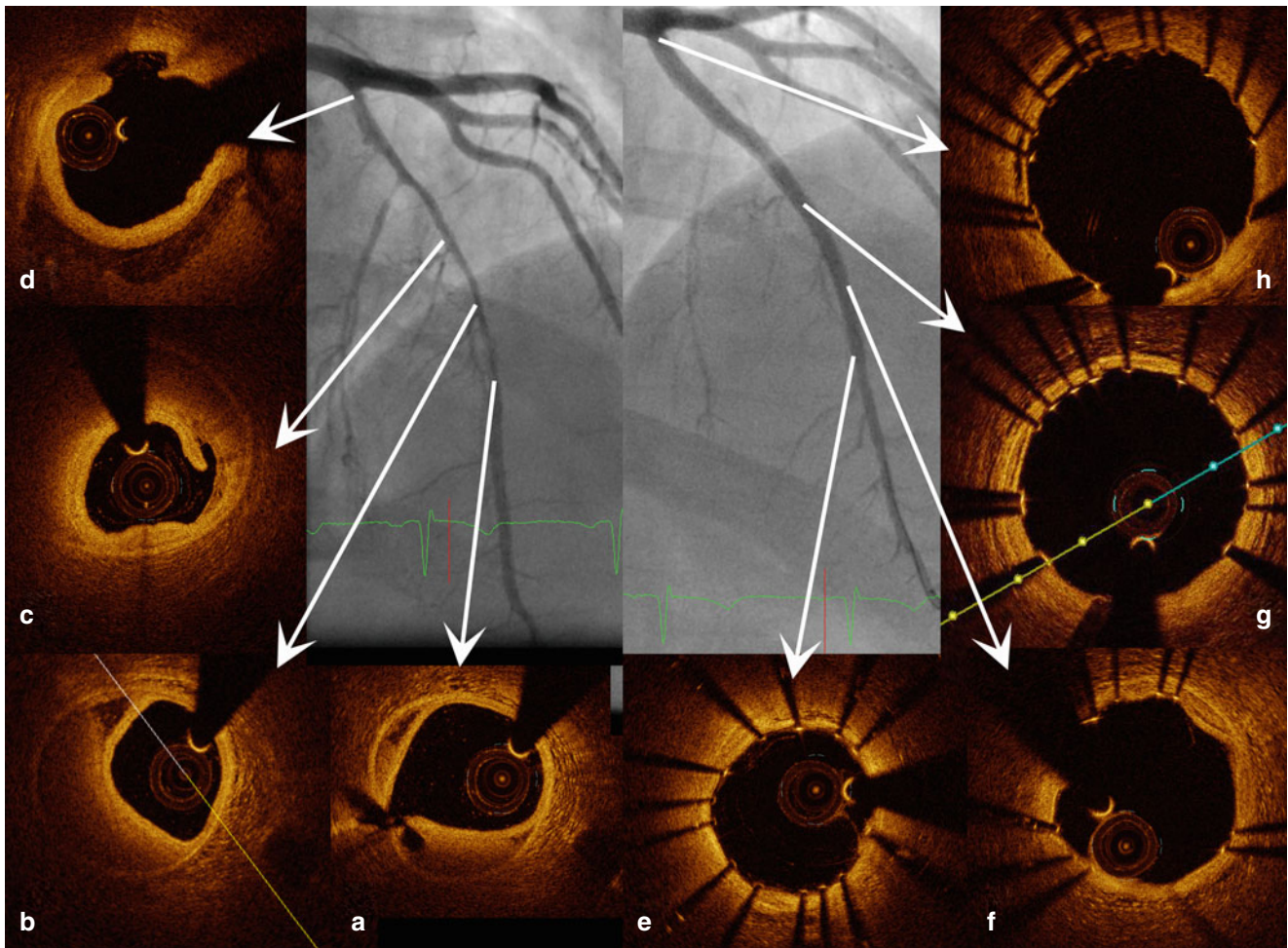
Fig. 8.4 Using OCT to guide PCI. 41 year-old female with anterior STEMI. *Left*: angiography after wiring and predilatation with a 2.0 mm balloon; *right*: angiography showing result after two overlapping stents placed with OCT guidance. OCT pre stents demonstrated interesting findings: three distinct rupture sites at (**a**, **c** and **d**). (**b**) Frame showing significant luminal compression from hematoma. Note different morphology at each rupture site. Note heterogeneous hematoma at the ostium of the LAD artery. Stents were placed from the ostium to distal – to allow for distal extrusion of hematoma given multiple exit ports, in doing so avoid trapping hematoma. OCT post stents: (**e**, **g**) – remarkably little residual hematoma. (**f**) Interesting pressurized hematoma indenting between stent strut at 2 o'clock. (**h**) Complex intramural hematoma covered by struts, but heterogeneity still visible at 11 o'clock

hematoma is likely to propagate proximally and distally. Again, it's advisable to use a long balloon and mould the hematoma and observe whether significant shift and displacement of the hematoma may occur. Such propagation of the hematoma with no exit can be dire. It's therefore advisable to use a longer stent than anticipated, and certainly to deploy the stent at low to nominal pressure and observe the impact on the hematoma. If a significant hematoma shift occurs then another stent maybe necessary, it's advisable to avoid 6 or 8 mm short stents as this tends not to be sufficient length to cover the squeezed hematoma in our experience.

Long Dissection Flap with No Significant Hematoma

Occasionally an extensive dissection may be seen angiographically. In the absence of obvious ischemia and stenosis, this may be best treated conservatively. Nevertheless, if the patient continues to have symptoms or evidence of ischemia, then a relatively short stent may be placed hopefully to tack down dissection plane. OCT may be used prior to stent placement to select the position most likely to achieve satisfactory re-apposing the dissection planes, i.e. the area of worst displacement between the dissected planes.

Assessment of Stent Implantation

OCT had been used to assess acute stent implantation outcomes in conventional coronary artery disease. The experience of stent assessment in SCAD remains relatively limited. Nevertheless, several case reports had demonstrated the superiority of OCT in assessing stent apposition as well as demonstrating the acute complications from stents in SCAD such as hematoma propagation [24–26]. An interesting finding on OCT is that often even when the stent struts are fully

apposed to the intima there is small residual hematoma in the vessel wall (Fig. 8.2).

In one case report by Poon et al. [24] such residual hematoma has been shown to disappear on follow up angiography and OCT. The trapped hematoma presumably resorbs over time as has been shown in angiography. A small circumferential rim is expected, particularly in the distal segment. One should therefore avoid the tendency to completely obliterate the circumferential rim of hematoma by continually post dilating, but rather focus on ensuring strut apposition. Continually post dilating to ensure no residual hematoma may likely propagate hematoma in an unfavourable manner, either into side branches or worse proximally into important main branches such as the left main artery (Fig. 8.4, Poon et al. [24]).

8.7   OCT in SCAD

8.7.1   When to Avoid: Practical Consideration

There are only very few instances where OCT may be relatively contraindicated in SCAD. Particularly, the use of OCT in a diffusely dissected small artery with a small residual lumen may not be advisable. An example would be a small diagonal artery (Fig. 8.1a) with angiographically definite SCAD where the incremental yield is questionable but potential harm may be caused to the small artery. Indeed, it has often been cautioned that OCT may cause harm in a dissected artery although there had been no published literature on OCT complication in SCAD lesions, possibly due to publication bias. It's generally advisable nevertheless to avoid OCT in small calibre arteries, or in distal segments where it's potentially too distal to image.

Another potential contraindication may be lesions with significant thrombus burden precluding adequate blood clearing and OCT analysis. OCT should only be performed after satisfactory aspiration with restoration of flow.

8.7.2   Future Potential

There remains significant gap in the understanding of SCAD. Given the relative infrequency, the interventional community may need a more collaborative approach to expand the collective understanding than the current single center case series in the literature. SCAD may be rare, rarer still are centers readily capable to perform OCT in such infrequent presentations in a systematic manner for scientifically robust analysis.

Pathogenesis
There seems different pathological subtypes to SCAD as demonstrated on both OCT and IVUS, a spontaneous hematoma vs. spontaneous dissection with an intimal or intimomedial flap. There does not seem to be significant clinical difference between these two subsets and indeed they may represent different time points in a continual disease process shown by Nishiguchi et al. [12]. Whilst the method of percutaneous treatment may differ between the two, more OCT data on the differing presentation and outcome between the two subsets may provide significant insights.

Pathogenesis – FMD
Given the purported association of the two conditions, the OCT appearance of "FMD-SCAD" is yet to be defined. Saw et al. [23] published interesting findings of FMD OCT, with fibrotic thickening of the intima, which seemed to correlate with the thickness of the intimo-medial dissection flap. Whether FMD is a pathogenetic compoenent or a mere a association remains to be further evaluated.

Conservative Treatment
There may be OCT findings which may favour a more conservative treatment approach as opposed to stenting. Examples may be the thrombotic burden, circumferential extent of dissection flap, signal intensity of hematoma, etc., some purely hypothetical factors which may predict the success or otherwise of conservative treatment.

Bare Metal Stents, Drug Eluting Stents, or Others
It remains unknown the ideal stent to use in such non-atherosclerotic lesions. It would be an interesting idea to even just perform balloon angioplasty to restore luminal patency, guided by OCT, and obviate the need to stent if sufficient lumen is restored. It remains unclear how SCAD lesions respond to stent placement, and how issues such as restenosis may be different in stented SCAD lesions.

Some commentators favour the use of short BMS to tack down the dissection flap, minimize the stent length, rather than stenting the entire intramural hematoma segment. Others favour the choice of stent to be guide by traditional factors particularly the length of lesion, which commonly means long DESs are needed, and occasional multiple stents. There is extremely limited medium to long-term data on stent outcome in SCAD (Fig. 8.2). A report by Poon et al. [24] suggested that at 6 months the DES was fully endothelized as would be expected and residual hematoma was completely resorbed. Perhaps the most exciting hypothesis is the use of bioabsorbable scaffold in SCAD, an attractive idea for generally young SCAD patients. There is to date no such reported use, and the thicker strut and deliverability of such stents may pose challenges in SCAD lesions.

Follow Up
There is as yet no long-term OCT follow-up of SCAD lesions, whether treated with stents or conservatively (Fig. 8.2). This is probably a very important area as whilst

there is a general trend nowadays for conservative treatment if possible, it remains unclear why some patients represent with SCAD, if there are in-vivo characteristics that may predispose to recurrence. Similarly there is also very limited data on the long-term outcome of various stents in SCAD and whether stents may respond completely differently in non-atherosclerotic lesions.

Conclusion

Often a "triumphant" but elusive diagnosis, over the past decades, SCAD has been extensively reported in a large body of namely case reports and case series. Despite these, SCAD remains poorly understood a disease process. The pathogenesis remains poorly defined despite the stereotypical clinical characteristics. Despite these recognized associated factors, SCAD can still be misdiagnosed on angiography. OCT may be the key for further insights in SCAD with its revolutionary resolution allowing in-vivo detailed assessment. It has already been shown to better the diagnostic accuracy over angiography and even IVUS in small studies. Its bigger clinical role however may be in the guidance for percutaneous treatment, by revealing the intimomedial dissection location, the longitudinal extent of the intramural hematoma, as well as assessing complications and adequacy of percutaneous treatment. Aside from clinical applications, the most promising potential application for OCT in SCAD may yet be its research application in this poorly known entity. OCT has already contributed significantly in furthering the understanding on this disease suggesting similarity between FMD and SCAD intimomedial dissection flap. A multicenter collaborative initiative may be worthwhile in capturing this often-missed diagnosis.

References

1. Pretty HC. Dissecting aneurysm of coronary artery in woman aged 42: rupture. Br Med J. 1931;1:667.
2. Robinowitz M, Virmani R, McAllister HA. Spontaneous coronary artery dissection and eosinophilic inflammation: a cause and effect relationship? Am J Med. 1982;72:923–8.
3. Briguori C, Bellevicine C, Visconti G, Focaccio A, Aprile V, Troncone G. In vivo histological assessment of a spontaneous coronary artery dissection. Circulation. 2010;10:1044–6.
4. Saw J, Ricci D, Starovoytov A, Fox R, Buller CE. Spontaneous coronary artery dissection: prevalence of predisposing conditions including fibromuscular dysplasia in a tertiary center cohort. J Am Coll Cardiol Intv. 2013;6:44–52.
5. Alfonso F, Paulo M, Lennie V, Dutary J, Bernado E, Jiménez-Quevedo P, et al. Spontaneous coronary artery dissection: long-term follow-up of a large series of patients prospectively managed with a "conservative" therapeutic strategy. J Am Coll Cardiol. 2012;5:1062–70.
6. Pate GE, Lowe R, Buller CE. Fibromuscular dysplasia of the coronary and renal arteries? Catheter Cardiovasc Interv. 2005;64:138–45.
7. Tweet MS, Hayes SN, Pitta SR, Simari RD, Lerman A, Lennon RJ, et al. Clinical features, management, and prognosis of spontaneous coronary artery dissection. Circulation. 2012;126:579–88.
8. Romero-Rodríguez N, Fernández-Quero M, Villa Gil-Ortega M, Urbano del Moral JA, Ballesteros Prada S. Spontaneous coronary dissection and its long-term prognostic implications in a cohort of 19 cases. Rev Esp Cardiol. 2010;9:1088–91.
9. Venzetto G, Berger-Coz E, Barone-Rochette G, Chavanon O, Bouvaist H, Hacini R, et al. Prevalence, therapeutic management and medium-term prognosis of spontaneous coronary artery dissection: results from a database of 11,605 patients. Eur J Cardiothorac Surg. 2009;2:250–4.
10. Mortensen KH, Thusen L, Kristensen IB, Christiansen EH. Spontaneous coronary artery dissection: a western Denmark Heart Registry Study. Catheter Cardiovasc Interv. 2009;74:710–7.
11. Giacoppo D, Capodanno D, Dangas G, Tamburino C. Spontaneous coronary artery dissection. Int J Cardiol. 2014;175(1):8–20. http://dx.doi.org/10.1016/j.ijcard.2014.04.178.
12. Nishiguchi T, Tanaka A, Ozaki Y, Taruya A, Fukuda S, Taguchi H, Iwaguro T, Ueno S, Okumoto Y, Akasaka T. Prevalence of spontaneous coronary artery dissection in patients with acute coronary syndrome. Eur Heart J Acute Cardiovasc Care. 2013 [Epub ahead of print]. doi:10.1177/2048872613504310.
13. Saw J. Coronary angiogram classification of spontaneous coronary artery dissection. Catheter Cardiovasc Interv. 2013. doi:10.1002/ccd.25293.
14. Alfonso F, Paulo M, Gonzalo N, Jimenez-Quevedo P, Lennie V, Escaned J, et al. Diagnosis of spontaneous coronary artery dissection by optical coherence tomography. J Am Coll Cardiol. 2012;12:1073–9.
15. Maehara A, Mintz GS, Castagna MT, Pichard AD, Satler LF, Waksman R, et al. Intravascular ultrasound assessment of spontaneous coronary artery dissection. Am J Cardiol. 2002;89:466–8.
16. Poon K, Bell B, Raffel OC, Walters DL, Jang IK. Spontaneous coronary artery dissection: utility of intravascular ultrasound and optical coherence tomography during percutaneous coronary intervention. Catheter Cardiovasc Interv. 2011;2:e5–7.
17. Paulo M, Sandoval J, Lennie V, Dutary J, Medina M, Gonzalo N, et al. Combined use of OCT and IVUS in spontaneous coronary artery dissection. JACC Cardiovasc Imaging. 2013;7:830–2.
18. Alfonso F, Canales E, Aleong G. Spontaneous coronary artery dissection: diagnosis by optical coherence tomography. Eur Heart J. 2009;30:385.
19. Ishibashi K, Kitabata H, Akasaka T. Intracoronary optical coherence tomography assessment of spontaneous coronary artery dissection. Heart. 2009;95:818.
20. Alfonso F, Paulo M, Dutary J. Endovascular imaging of angiographically invisible spontaneous coronary artery dissection. JACC Cardiovasc Interv. 2012;4:452–3.
21. Hoshi T, Sato A, Hiraya D, Kimura T, Wang Z, Aonuma K. Multimodality intracoronary imaging in spontaneous coronary artery dissection: impacts of intravascular ultrasound, optical coherence tomography, and coronary angioscopy. Catheter Cardiovasc Interv. 2013;3:E151–4.
22. Nakagawa M, Shite J, Shinke T, Otake H, Okada K, Okita Y, Hirata K. Ability of optical coherence tomography to visualize the entry port of spontaneous coronary artery dissection. Circ J. 2011;10:2505–7.
23. Saw J, Poulter R, Fung A. Intracoronary imaging of coronary fibromuscular dysplasia with OCT and IVUS. Catheter Cardiovasc Interv. 2013;82:E879–83.
24. Poon K, Incani A, Small A, Raffel OC. Drug eluting stents trapping intramural hematoma in spontaneous coronary artery dissection and healing pattern at six months: optical coherence tomography findings. Cardiovasc Revasc Med. 2013;3:183–6.
25. Combaret N, Souteyrand G, Amonchot A, Coupez E, Motreff P. Contribution of guidance by optical coherence tomography (OCT) in rescue management of spontaneous coronary artery dissection. Eur Heart J Cardiovasc Imaging. 2013;7:714.
26. Ruiz-García J, Jiménez-Valero S, Salinas P, Sánchez-Recalde A, Galeote G, Moreno R. Optical coherence tomography in spontaneous coronary dissection and in the complications following percutaneous treatment. Rev Esp Cardiol. 2013;1:72–3.

Soo-Jin Kang and Seung-Jung Park

Abstract

Even though catheter-based intravascular ultrasound has been generally used in evaluating coronary artery disease, optical coherence tomography (OCT) with a better resolution allows us to more precisely assess the morphologic characteristics of both native and stented lesions in the various clinical settings. With regard to early stent assessment, OCT has a unique role in identifying minor degrees of neointimal proliferation, malapposition and the presence of strut coverage that may represent a surrogate marker of stent safety and efficacy. Recently, frequency-domain (vs. time-domain) OCT system has higher frame rates that make pullback speeds faster. With a shorter procedural time and a higher acquisition rate of clear images, OCT has provided the accurate visualization of underlying pathophysiologic mechanisms of early and late stent failure.

Keywords

Optical coherence tomography • Early stent assessment • Stent coverage • Intimal hyperplasia

9.1 Introduction

Although a drug-eluting stent has an inhibitory effect on intimal hyperplasia compared with a bare metal stent, early and late stent failure, including in-stent restenosis and stent thrombosis, are still concerns. Many clinical studies of unselected populations have reported a rate of restenosis greater than 10 % following procedure [1–3]. In addition, recent registry data suggested that the rate of late stent thrombosis was 0.6 % per year and steadily increased to 3 % over 4 years in patients treated with first-generation drug-eluting stents [4, 5].

Procedural factors such as stent underexpansion and inflow/outflow tract disease are the primary cause of early stent thrombosis, while biological mechanisms are involved in stent thrombosis in the later phase. Late stent thrombosis may be related to delayed arterial healing with incomplete stent coverage and associated with late stent malapposition

[6–8]. In addition, characterization of neointimal tissue is important to the understanding of the pathophysiologic mechanisms of stent failure.

With its excellent resolution, catheter-based optical coherence tomography (OCT) has been useful for precisely assessing both native and stented coronary arteries in various clinical conditions. OCT has a unique value in identifying the presence of strut coverage and in detecting mild degrees of neointimal proliferation that may represent a surrogate marker of stent safety and efficacy. Moreover, OCT has been used to identify the underlying mechanisms of early and late stent thrombosis and restenosis. Thus, this chapter focuses on early stent evaluation (within 1 year) with the use OCT.

9.2 Quantitative and Qualitative Stent Measurements

Neointimal thickness is defined as the distance between the strut and luminal surface of neointima and is measured inside all struts as a line perpendicular to the neointima and the strut [9].

S.-J. Kang, MD, PhD (✉) • S.-J. Park, MD, PhD (✉)
Division of Cardiology, Asan Medical Center, Seoul, South Korea
e-mail: sjkang@amc.seoul.kr; sjpark@amc.seoul.kr
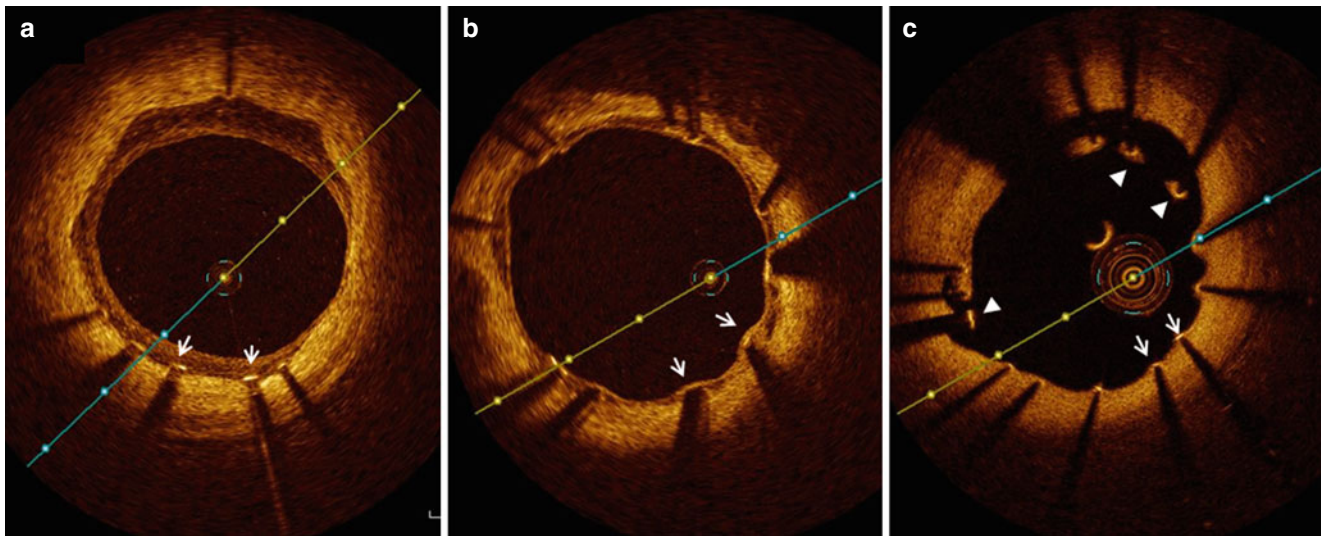
Fig. 9.1 Classification of strut apposition by OCT. (**a**) Embedded struts (*arrows*), (**b**) protruding-covered struts (*arrows*), (**c**) protruding-uncovered (*arrows*) and malapposed struts (*arrow heads*)

Struts are termed '*covered*' by OCT when intimal tissue can be detected above the struts, while struts are '*uncovered*' when no intimal tissue is identified above the struts. Thus, an uncovered strut is defined as a strut with neointimal thickness=0 μm. The ratio of malapposed (or uncovered) struts is calculated as the number of malapposed (or uncovered) struts divided by the total strut number in all sections of the lesion. Even though OCT can measure the tissue overlying a strut, clinical implication of the OCT-measured strut coverage thickness that is allowed by the axial resolution of the OCT system remains unclear.

Consensus OCT quantitative stent measurements are parallel to the JACC IVUS Consensus Document, and are partly modified [10]. Stent cross-sectional area (CSA) is the area bounded by the stent border; Minimum stent diameter is the shortest diameter through the center of the stent; Maximum stent diameter is the longest diameter through the center of the stent; Stent eccentricity is calculated as the difference in diameter length between the maximal stent diameter and the minimal stent diameter, divided by the maximal stent diameter. Stent and lumen CSAs are measured, and the neointimal CSA is calculated as the difference between stent CSA and lumen CSA. The percentage of intimal hyperplasia is calculated as [neointimal CSA/ stent CSA×100].

The stent surface is designated as being located at the center of the stent strut blooming. Strut malapposition distance is measured as the distance between the abluminal surface of the strut and the luminal surface of vessel wall. Stent malapposition is defined as the maximal distance (from the stent surface to the lumen contour) which is greater than the total thickness of the stent strut and polymer or spatial resolution of OCT [10, 11].

Strut-level analysis is classified into the following categories: covered-embedded, covered-protruding (into the lumen but covered), uncovered-apposed, and malapposed (Fig. 9.1), [11, 12]. A semi-automated stent contour algorithm applies 360 radial chords for detailed quantification of neointimal thickness at every degree of the cross section (Fig. 9.2).

9.3 OCT Findings During PCI

With parallels to IVUS predictors of stent failure, OCT is useful for precisely assessing stent expansion and edge problems. In addition, OCT is more beneficial for detecting even minor degrees of strut malapposition, tissue prolapse, thrombus, and edge dissections as compared to intravascular ultrasound (IVUS) [13]. Therefore, OCT helps us understand the underlying pathophysiology of coronary artery disease and to make better clinical decisions.

9.3.1 Thrombus

Thrombi in target lesions can protrude between stent struts. As previously described in native coronary lesions, thrombi can be classified as red, white and mixed forms by using OCT.

9.3.2 Tissue Protrusion

Plaque or thrombus protrusion is defined as the projection of tissue into the lumen between stent struts. On OCT, plaque protrusion is characterized by a smooth surface without signal attenuation, whereas thrombus protrusion appears as an irregular surface associated with significant signal attenuation [14]. Tissue protrusion is more frequently observed in
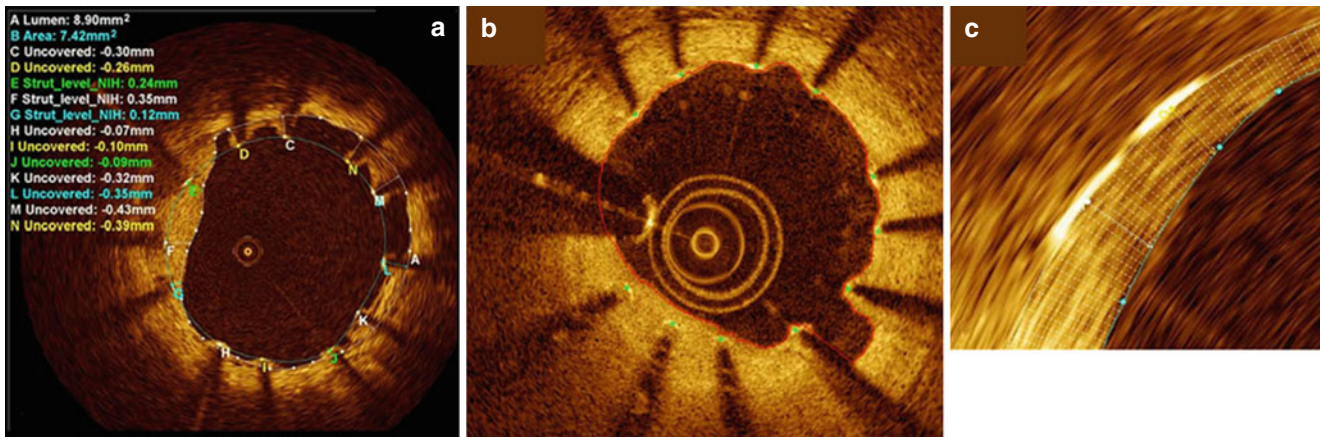
Fig. 9.2 Strut level analysis including qualitative assessment for strut coverage and quantitative measurement. (**a**) Heterogeneity of strut coverage (*C–N* refer to labeled struts): covered struts (*E–G*), uncovered apposed struts (*H–J*), and malapposed struts (*K–N, C, D*). (**b**) Automatic lumen and stent detection: stent struts (*green dots*) and lumen contour (*red line*). (**c**)Magnification of the automatic 360° chord system, applied between the stent and lumen contours (From Bezerra et al. [12])

the culprit lesion of acute coronary syndrome, because the stent is likely placed over the unstable lesion containing thrombi, lipid-rich tissue or necrotic core. Sometimes, it may be difficult to differentiate tissue prolapsed from other pathologic conditions such as thrombus, neointima, intimal or intra-stent dissection. A significant relationship between OCT-detected tissue protrusion and stent failure has not been demonstrated [15].

9.3.3 Dissection

Dissections are frequently seen especially at the edge of a stent. Compared to IVUS, OCT more sensitively detects even small dissections [14]. Gonzalo et al. evaluated OCT-defined plaque types at stent edges that were related to edge dissection. Edge dissection was more common at distal than at proximal portions. Distal edge dissection was more frequently occurred when the plaque type at the edge was fibro-calcific (43.8 %) or lipid-rich (37.5 %) than when the plaque was fibrous (10 %) (P=0.009), [15]. Kume et al. evaluated the natural history of stent edge dissection detectable only on OCT (not on IVUS) [16]. The lesions with OCT-dissection, detected only by OCT, showed relatively short maximal length of dissection and were mostly healed without restenosis or thrombus formation at follow-up (median 188 days). When there is no narrowing of the true lumen, an additional procedure may not be recommended for the treatment of dissection. Moreover, acute stent complications such as tissue protrusion, and incomplete stent apposition that were detectable only by OCT, tended to be smaller than those seen on both OCT and IVUS. The majority of OCT-detected minor complications healed or were resolved at follow-up.

9.4 OCT Versus Intravascular Ultrasound for Stent Assessment

Even though IVUS has been the standard imaging tool for the assessment of coronary stents, its poor resolution has limited its evaluation of the morphology of stented lesions. Conversely, OCT has a resolution of 10–20 μm which is much better than IVUS.

When a small degree of in-stent neointima was histologically defined as occupying <30 % of the stent area, diagnostic accuracy of OCT for detecting the small degree of neointima (area under the receiver operating characteristic curve=0.967, 95 % confidence intervals=0.914–1.019) was higher than that of IVUS (area under curve=0.781, 95 % confidence intervals=0.621–0.838) [17]. The data suggested that OCT is more accurate for identifying neointimal coverage of stent struts. As determined by OCT, the optimal cutoff value of the percent of neointimal hyperplasia to be detected by IVUS was >14.7 %, (sensitivity=0.887, specificity=0.790) [18]. For the assessments of neointimal morphology, OCT and IVUS showed a moderate correlation, while approximately 30 % of the lesions showed a discrepancy.

As compared to time-domain OCT, frequency-domain OCT system has higher frame rates that allow faster pullback speeds. As a result, frequency-domain OCT showed a shorter procedural time (3.2±0.8 min vs. 11.2±2.5 min, $p<0.01$) and a higher acquisition rate of clear images (99.4 % vs. 80.8 %, $p<0.01$) than those of time-domain OCT [19]. Frequency-domain (FD) OCT also showed better detection of incomplete stent apposition (malapposition) or uncovered strut compared with IVUS [20, 21]. Immediately post-PCI, in-stent minimal lumen areas

(MLAs) were similar between FD-OCT and IVUS. However, both FD-OCT and time-domain-OCT detected smaller MLAs at follow-up than did IVUS, probably due to the better detection of neointimal hyperplasia by OCT [20]. Post-PCI malapposition and tissue prolapse were more frequently identified by OCT which generates similar reference lumen dimensions but higher degrees of disease severity and intimal hyperplasia as well as better detection of malapposition and tissue prolapse compared with those of IVUS [9]. When compared with histology, the correlation of minimum neointimal thickness was inferior in IVUS ($R^2 = 0.39$) than that in OCT ($R^2 = 0.67$) [21]. Similarly, IVUS showed a weak correlation of the ratio of uncovered to total stent struts per section ($R^2 = 0.24$), whereas OCT was superior ($R^2 = 0.66$). In a more detailed analysis, OCT identification of individual uncovered struts demonstrated a sensitivity of 77.9 % and a specificity of 96.4 % [20].

9.5   Strut Coverage

After stent implantation, intimal hyperplasia is considered a wound healing process following vascular injury [22]. Anti-proliferative drugs inhibit the migration and proliferation of smooth-muscle cells that result in delayed arterial healing and uncovered struts of drug-eluting stents [23, 24].

The low axial resolution of IVUS (100–150 μm) and frequent artifacts around stent struts, preclude IVUS as the proper modality for a precise assessment of vascular microstructures, such as thin layers of neointima over the struts. Conversely, the high-resolution properties of OCT can detect histologically defined minor structures and quantification of thin neointima overlying struts. Strut coverage thickness can be measured as the distance between the luminal surface of the covering neointima and the luminal surface of the strut.

Strut-level analysis with an accurate assessment and quantification of neointimal coverage over stents has been adopted as a surrogate end point in numerous clinical trials of DES and as an important parameter for the safety profile of drug-eluting stents and the approval of new drug-eluting stent technologies.

OCT has been validated as a reliable and reproducible method for assessing neointimal formation and strut coverage. Prati et al. reported on the capacity of OCT for assessing arterial healing after stenting [25]. The histological and OCT measurements of mean neointimal thickness were similar and closely related (r = 0.85, p < 0.001) to an excellent intra- and interobserver reproducibility of OCT measurements ($r^2 = 0.90$ and 0.88, respectively). Murata et al. showed that there was a high correlation between OCT and histology in the evaluation of neointimal area ($r^2 = 0.804$), luminal area ($r^2 = 0.825$) and neointimal thickness ($r^2 = 0.789$) [26]. These results were independent of the stent type. In the ODESSA

trial [27], OCT was more sensitive to a small amount of neointimal hyperplasia compared to IVUS. However, OCT has not yet visualized the endothelium.

9.6   *In Vivo* OCT Data for Stent Coverage

Strut coverage patterns and the degrees of intimal hyperplasia have varied amongst different types of drug-eluting stents. For the first generation drug-eluting stents, a previous study reported that only 16 % of sirolimus-eluting stents showed complete coverage at 6 months post-intervention [24]. Kim et al. demonstrated that the incidence of completely covered stents at 9 months follow-up was 29.6 % for paclitaxel-eluting stents and 9.1 % for sirolimus-eluting stents [28]. Uncovered struts were frequently observed in sirolimus-eluting stents, whereas the pattern of neointima was more heterogeneous in paclitaxel-eluting stents.

Newer generation drug-eluting stents have been developed using a more advanced strut platform, polymer, and new anti-proliferative agents. The frequency of uncovered struts as well as malapposed struts was significantly lower in zotarolimus-eluting stents than in sirolimus-eluting stents (0.3 % vs 12.3 %, p < 0.001 and 0.1 % vs. 2.6 %, p < 0.001) [29]. Resolute zotarolimus-eluting stents also showed higher rates of strut coverage than sirolimus-eluting stents at 9 months follow-up [30]. The percentage of uncovered struts and malapposed struts at 9 months after resolute zotarolimus-eluting stent implantation was only 4.4 ± 4.8 % and 0.1 ± 0.4 %, respectively, which was significantly lower than that seen in sirolimus-eluting stents. Intracoronary thrombus was less frequently detected in lesions treated with resolute zotarolimus-eluting stents than in sirolimus-eluting stents at the 9-month follow-up. Everolimus-eluting stents also showed better vascular responses compared to sirolimus-eluting stents [31]. The percentage of uncovered struts was significantly smaller in the lesions with everolimus-eluting stents than that in lesions with sirolimus-eluting stents (4.4 ± 4.7 % vs. 10.5 ± 12.7 %, P = 0.016, respectively). There was no significant difference in the percentage of malapposed struts between the two groups (0.4 ± 0.8 % in everolimus-eluting stents vs. 1.7 ± 4.5 % in sirolimus-eluting stents, P = 0.344). Biolimus-eluting stents with the unique property of a biodegradable polymer and abluminal coating showed more frequent OCT-defined strut coverage compared to sirolimus-eluting stents at 9 months [32].

With regard to clinical outcomes, delayed neointimal healing of implanted stents was associated with the occurrence of late stent thrombosis. The ratio of uncovered to total stent struts per section >30 % was related to stent thrombosis (odds ratio 9.0, 95 % confidence intervals 3.5–22) [25]. Moreover, the length of an uncovered stent strut segment was significantly associated with stent thrombosis [33]. In a recent OCT

study, independent predictors for major adverse cardiac events were post-intervention minimal lumen diameter (odds ratio 0.019, 95 % CI=0.001–0.513, p=0.018) and the percentage of uncovered struts ≥5.9 % (odds ratio 19.781, 95 % CI=2.071–188.968, p=0.010) [34]. A greater percentage of uncovered struts ≥5.9 % as the cut-off value was significantly associated with a high rate of major adverse cardiac events after DES implantation. More favorable biological properties and vascular responses may contribute to greater clinical safety, which possibly explains the less frequent stent thrombosis after newer generation drug-eluting stent implantation as well as after biolimus-eluting stents, compared to the older generation drug-eluting stents [35, 36].

9.7 Malapposition

In IVUS studies, incomplete stent apposition is defined as a separation of at least one stent strut from the intimal surface of the arterial wall that is not overlapping a side branch, and has evidence of blood flow behind the strut [37]. Apposition of the stent struts to the vessel wall can be seen using OCT by way of its high resolution and capability to identify the tissues surrounding the struts. Malapposed stent struts seen on OCT are defined as the distance between the strut marker and the lumen contour greater than the strut thickness plus the polymer (if present) and the axial resolution of OCT [10]. Thus, the definitions of malapposed struts differ depending on the type of coronary stent and in turn, the thickness of struts and the applied polymer. For the various types of drug-eluting stents, malapposed stent struts have been defined as the struts with detachment from the vessel wall that is: ≥160 μm for sirolimus-eluting stents (Cypher Select™, Cordis, Miami Lake, FL, USA), ≥130 μm for paclitaxel-eluting stents (TaxusLiberte™, Boston Scientific, Natick, MA, USA), ≥110 μm for zotarolimus-eluting stents (Endeavor™ and Resolute™, Medtronic, Santa Rosa, CA, USA), ≥100 μm for everolimus-eluting stents (Xience™, Abbott Vascular, Santa Clara, CA, USA), and ≥130 μm for biolimus-eluting stents (Nobori™, Terumo Corporation, Tokyo, Japan or BioMatrix™, Biosensors Interventional, Singapore) [30, 31, 38]. Apposition can be described on a per-strut, per–cross-sectional area and on a per-stent basis.

With the better resolution, OCT provides a more accurate visualization of stent struts with a small malapposition which is detected by OCT but not by IVUS. As neointimal tissue proliferates over time, the majority of malapposed struts usually disappears or decreases on the follow-up OCT, especially when the malapposition was small [38–40]. The percent of malapposed struts significantly decreased from 12.2±11.0 % post-stent to 1.0±2.2 % at the 6-month follow-up (P<0.001). In those lesions with minimal malapposition, there was a significant decrease in the mean extra-stent malapposition area from 0.35±0.16 mm^2 post-stent to 0.04±0.11 mm^2 at follow-up (P<0.001) [38].

On the other hand, there are persistent malappositions and newly developed late stent malappositions detected at follow-up. A recent study showed that 11 % of the struts with acute malapposition remained malapposed at 8-month follow-up [40]. The mean distance between the strut and the vessel wall of persistent malapposed struts on post-stenting OCT images was significantly longer than that of resolved malapposed struts (342±99 μm vs. 210±49 μm; p<0.01). Based on receiver-operating characteristic curve analysis, the distance between strut and the vessel wall ≤260 μm seen on post-stenting OCT images was the best cut-off value for predicting resolved malapposed struts (sensitivity: 89.3 %, specificity: 83.7 %, area under the curve=0.884). Coverage of the incomplete stent apposition and nonapposed side-branch struts is delayed with respect to well-apposed struts in drug-eluting stents, as assessed by OCT at the 9–13 months follow-up after drug-eluting stent implantation [41]. Kim et al. reported that the lesions with the median value of the percentage of malapposed struts ≥1.3 % showed a significantly larger percentage of uncovered struts compared to those with malapposed struts <1.3 % or without malapposition [42]. There was a significant correlation between malapposed and uncovered struts in lesions with malapposed struts ≥1.3 % (r=0.393, p=0.016), while no relationship was found in the lesions with minimally malapposed struts <1.3 % (r=−0.007, p=0.965). A recent OCT analysis showed that the percentage of uncovered struts at 6 months varied significantly with post-stent strut apposition (i.e. 0 % [0, 11.4 %] in embedded, 16.3 % [8.1, 31.3 %] in apposed, and 26.8 % [0, 56.3 %] in malapposed, p<0.001) [43]. The data suggested that OCT-guided optimization of stent strut apposition enhances the strut coverage seen at follow-up.

9.8 OCT Characteristics of Neointima

In-stent neointima containing smooth-muscle cells and proteoglycan-rich extra-cellular matrices represented various patterns of OCT characteristics, such as homogenous, heterogeneous and layered patterns [42]. Figure 9.3 demonstrated various vascular responses on follow-up OCT images. Nakano et al. suggested that the important morphological features reflecting fibrin accumulation, excessive inflammation (hypersensitivity) and in-stent atherosclerosis were characterized by OCT [21]. However, the similarly dark appearance of these tissues did not allow for precise discrimination for the tissue compositions. Even though heterogeneous or layered patterns of neointima were more likely to be seen in restenotic lesions than in non-restenotic lesions [44], the clinical implications of the diverse features remain unclear. The relationship between the signal intensity of OCT and the tissue composition of the restenotic lesions is not yet known.
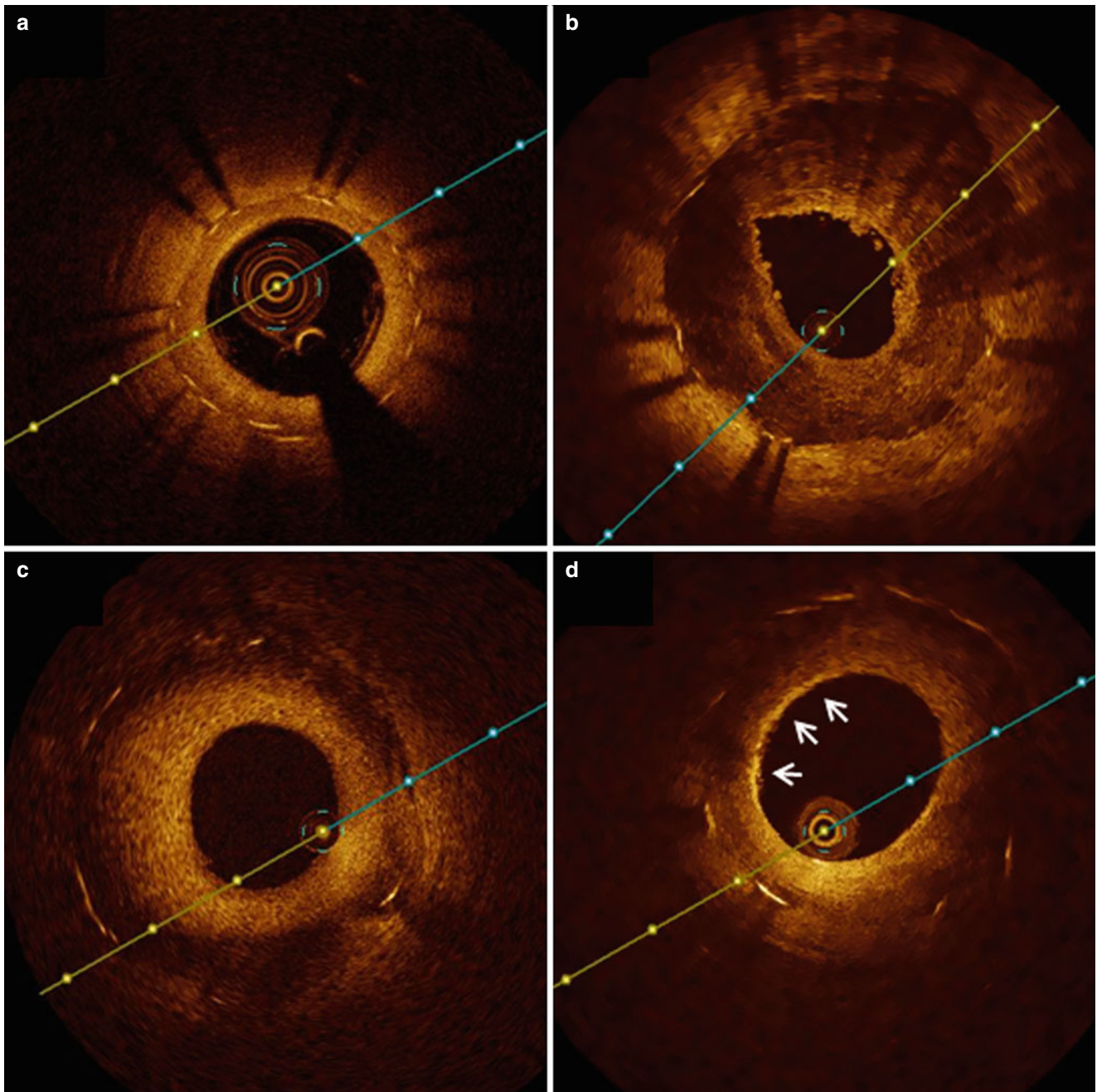
Fig. 9.3 Variousneointimal characteristics after drug-eluting stent implantation. (**a**) Uniform stent coverage and homogenous pattern of neo-intima, (**b**) heterogenous pattern of neointima, (**c**) layered pattern of neointima, (**d**) lipid-rich neointima with thin-cap fibroatheroma (*arrows*)

9.9   In-stent Neoatherosclerosis

Histopathologic studies have suggested that neointimal components following drug-eluting stent implantation were similar to those in bare metal stent lesions in that the neointima was mainly composed of smooth-muscle cells with proteoglycans-rich extracellular matrices [45]. In the early phase, neointimal tissue seems to be benign. Nevertheless, there is emerging evidence suggesting that chronic inflammation

and/or incompetent endothelial function induce late de-novo neoatherosclerosis inside both bare metal and drug-eluting stents, which may be an important mechanism to in-stent restenosis and late stent thrombosis.

Nakazawa et al. [46] reviewed autopsy cases from the CVPath (Gaithersburg, Maryland) stent registry and compared 66 Sirolimus-eluting stent lesions to 77 bare metal stent lesions where they discovered that neoatherosclerotic changes including the presence of lipid-laden, foamy

macrophages, was more frequently identified in the drug-eluting stent lesions than in the bare metal stent lesions (35 % vs. 10 %, p<0.001). The earliest atherosclerotic change with foamy macrophage infiltration began 4 months after drug-eluting stent implantation, while the same change in bare metal stent lesions occurred more than 2 years later and remained a rare finding until 4 years following stent implantation. Another observation also demonstrated that the incidence of neoatherosclerosis was greater in drug-eluting stent lesions (31 %) than in bare metal stent lesions (16 %) and the median stent duration with neoatherosclerosis was shorter in drug-eluting stents compared to bare metal stetns (420 days [361–683 days] vs. 2,160 days [1,800–2,880 days]) [47]. These observations indicate that neoatherosclerosis is more frequent in drug-eluting stents and occurs earlier than in bare metal stent, most likely due to the different pathogenesis.

Conclusion

With the excellent resolution, OCT allows us to precisely assess minor degrees of neointimal proliferation, malapposition and strut coverage that may represent a surrogate marker of stent safety and efficacy. OCT also provides important insights of underlying mechanisms of early and late stent failure. With regard to the morphological findings that can be detected only by OCT (not by IVUS), clinical impacts need to be more clarified.

References

1. Zahn R, Hamm CW, Schneider S, et al. Incidence and predictors of target vessel revascularization and clinical event rates of the sirolimus eluting coronary stent (results from the prospective multicenter German Cypher Stent Registry). Am J Cardiol. 2005; 95:1302–8.
2. Mauri L, Silbaugh TS, Wolf RE, et al. Long-term clinical outcomes after drug-eluting and bare-metal stenting in Massachusetts. Circulation. 2008;118:1817–27.
3. Lemos PA, Serruys PW, van Domburg RT, et al. Unrestricted utilization of sirolimus-eluting stents compared with conventional bare stent implantation in the "real world": the Rapamycin-Eluting Stent Evaluated at Rotterdam Cardiology Hospital (RESEARCH) registry. Circulation. 2004;109:190–5.
4. Daemen J, Wenaweser P, Tsuchida K, et al. Early and late coronary stent thrombosis of sirolimus-eluting and paclitaxel-eluting stents in routine clinical practice: data from a large two-institutional cohort study. Lancet. 2007;369:667–78.
5. Wenaweser P, Daemen J, Zwahlen M, et al. Incidence and correlates of drug-eluting stent thrombosis in routine clinical practice. 4-year results from a large 2-institutional cohort study. J Am Coll Cardiol. 2008;52:1134–40.
6. Virmani R, Guagliumi G, Farb A, et al. Localized hypersensitivity and late coronary thrombosis secondary to a sirolimus-eluting stent: should we be cautious? Circulation. 2004;109:701–5.
7. Nakazawa G, Finn AV, Vorpahl M, Ladich ER, Kolodgie FD, Virmani R. Coronary responses and differential mechanisms of late stent thrombosis attributed to first-generation sirolimus- and paclitaxel-eluting stents. J Am Coll Cardiol. 2011;57:390–8.
8. Cook S, Wenaweser P, Togni M, et al. Incomplete stent apposition and very late stent thrombosis after drug-eluting stent implantation. Circulation. 2007;115:2426–34.
9. Kim BK, Kim JS, Park J, et al. Comparison of optical coherence tomographic assessment between first- and second-generation drug-eluting stents. Yonsei Med J. 2012;53:524–9.
10. Tearney GJ, Regar E, Akasaka T, et al. Consensus standards for acquisition, measurement, and reporting of intravascular optical coherence tomography studies: a report from the International Working Group for Intravascular Optical Coherence Tomography Standardization and Validation. J Am Coll Cardiol. 2012;59:1058–72.
11. Guagliumi G, Sirbu V. Optical coherence tomography: high resolution intravascular imaging to evaluate vascular healing after coronary stenting. Catheter Cardiovasc Interv. 2008;72:237–47.
12. Bezerra HG, Costa MA, Guagliumi G, Rollins AM, Simon DI. Intracoronary optical coherence tomography: a comprehensive review clinical and research applications. JACC Cardiovasc Interv. 2009;2:1035–46.
13. Kubo T, Tanaka A, Kitabata H, Ino Y, Tanimoto T, Akasaka T. Application of optical coherence tomography in percutaneous coronary intervention. Circ J. 2012;76:2076–83.
14. Kubo T, Imanishi T, Kitabata H, et al. Comparison of vascular response after sirolimus-eluting stent implantation between patients with unstable and stable angina pectoris: a serial optical coherence tomography study. JACC Cardiovasc Imaging. 2008;1:475–84.
15. Gonzalo N, Serruys PW, Okamura T, et al. Relation between plaque type and dissections at the edges after stent implantation: an optical coherence tomography study. Int J Cardiol. 2011;150:151–5.
16. Kume T, Okura H, Miyamoto Y, et al. Natural history of stent edge dissection, tissue protrusion and incomplete stent apposition detectable only on optical coherence tomography after stent implantation: preliminary observation. Circ J. 2012;76:698–703.
17. Suzuki Y, Ikeno F, Koizumi T, et al. In vivo comparison between optical coherence tomography and intravascular ultrasound for detecting small degrees of in-stent neointima after stent implantation. JACC Cardiovasc Interv. 2008;1:168–73.
18. Kwon SW, Kim BK, Kim TH, et al. Qualitative assessment of neointimal tissue after drug-eluting stent implantation: comparison between follow-up optical coherence tomography and intravascular ultrasound. Am Heart J. 2011;161:367–72.
19. Takarada S, Imanishi T, Liu Y, et al. Advantage of next-generation frequency-domain optical coherence tomography compared with conventional time-domain system in the assessment of coronary lesion. Catheter Cardiovasc Interv. 2010;75:202–6.
20. Bezerra HG, Attizzani GF, Sirbu V, et al. Optical coherence tomography versus intravascular ultrasound to evaluate coronary artery disease and percutaneous coronary intervention. JACC Cardiovasc Interv. 2013;6:228–36.
21. Nakano M, Vorpahl M, Otsuka F, et al. Ex vivo assessment of vascular response to coronary stents by optical frequency domain imaging. JACC Cardiovasc Imaging. 2012;5:71–82.
22. Forrester JS, Fishbein M, Helfant R, Fagin J. A paradigm for restenosis based on cell biology: clues for the development of new preventive therapies. J Am Coll Cardiol. 1991;17:758–69.
23. Finn AV, Joner M, Nakazawa G, et al. Pathological correlates of late drug-eluting stent thrombosis: strut coverage as a marker of endothelialization. Circulation. 2007;115:2435–41.
24. Matsumoto D, Shite J, Shinke T, et al. Neointimal coverage of sirolimus-eluting stents at 6-month follow-up: evaluated by optical coherence tomography. Eur Heart J. 2007;28:961–7.
25. Prati F, Zimarino M, Stabile D, et al. Does optical coherence tomography identify arterial healing after stenting? An in vivo comparison with histology on a rabbit carotid model. Heart. 2008;94:217–21.
26. Murata A, Wallace-Bradley D, Tellez A, et al. Accuracy of optical coherence tomography in the evaluation of neointimal coverage after stent implantation. JACC Cardiovasc Imaging. 2010;3:76–84.

27. Guagliumi G, Musumeci G, Sirbu V, et al. Optical coherence tomography assessment of in vivo vascular response following implantation of overlapping bare-metal and drug-eluting stents. JACC Cardiovasc Interv. 2010;3:531–9.

28. Kim JS, Kim JS, Kim TH, et al. Comparison of neointimal coverage of sirolimus-eluting stents and paclitaxel-eluting stents using optical coherence tomography at 9 months after implantation. Circ J. 2010;74:320–6.

29. Kim JS, Jang IK, Kim JS, et al. Optical coherence tomography evaluation of zotarolimus-eluting stents at 9-month follow-up: comparison with sirolimus-eluting stents. Heart. 2009;95:1907–12.

30. Kim JS, Kim JS, Shin DH, et al. Optical coherence tomographic comparison of neointimal coverage between sirolimus- and resolute zotarolimus-eluting stents at 9 months after stent implantation. Int J Cardiovasc Imaging. 2012;28:1281–7.

31. Choi HH, Kim JS, Yoon DH, et al. Favorable neointimal coverage in everolimus-eluting stent at 9 months after stent implantation: comparison with sirolimus-eluting stent using optical coherence tomography. Int J Cardiovasc Imaging. 2012;28:1–497.

32. Barlis P, Regar E, Serruys PW, et al. An optical coherence tomography study of a biodegradable vs. durable polymer-coated limus-eluting stent: a LEADERS trial sub-study. Eur Heart J. 2010;31:165–76.

33. Guagliumi G, Sirbu V, Musumeci G, et al. Examination of the in vivo mechanisms of late drug-eluting stent thrombosis: findings from optical coherence tomography and intravascular ultrasound imaging. JACC Cardiovasc Interv. 2012;5:12–20.

34. Won H, Shin DH, Kim BK, et al. Optical coherence tomography derived cut-off value of uncovered stent struts to predict adverse clinical outcomes after drug-eluting stent implantation. Int J Cardiovasc Imaging. 2013;29:1255–63.

35. Stefanini GG, Kalesan B, Serruys PW, et al. Long-term clinical outcomes of biodegradable polymer biolimus-eluting stents versus durable polymer sirolimus-eluting stents in patients with coronary artery disease (LEADERS): 4 year follow-up of a randomised non-inferiority trial. Lancet. 2011;378:1940–8.

36. Sarno G, Lagerqvist B, Fröbert O, et al. Lower risk of stent thrombosis and restenosis with unrestricted use of 'new-generation' drug-eluting stents: a report from the nationwide Swedish Coronary Angiography and Angioplasty Registry (SCAAR). Eur Heart J. 2012;33:606–13.

37. Hong MK, Mintz GS, Lee CW, et al. Late stent malapposition after drug-eluting stent implantation: an intravascular ultrasound analysis with long-term follow-up. Circulation. 2006;113:414–9.

38. Kim WH, Lee BK, Lee S, et al. Serial changes of minimal stent malapposition not detected by intravascular ultrasound: follow-up optical coherence tomography study. Clin Res Cardiol. 2010;99:639–44.

39. Gutiérrez-Chico JL, Wykrzykowska J, Nüesch E, et al. Vascular tissue reaction to acute malapposition in human coronary arteries: sequential assessment with optical coherence tomography. Circ Cardiovasc Interv. 2012;5:20–9. S1–S8.

40. Kawamori H, Shite J, Shinke T, et al. Natural consequence of post-intervention stent malapposition, thrombus, tissue prolapse, and dissection assessed by optical coherence tomography at mid-term follow-up. Eur Heart J Cardiovasc Imaging. 2013;14:865–75.

41. Gutiérrez-Chico JL, Regar E, Nüesch E, et al. Delayed coverage in malapposed and side-branch struts with respect to well-apposed struts in drug-eluting stents: in vivo assessment with optical coherence tomography. Circulation. 2011;124:612–23.

42. Kim BK, Hong MK, Shin DH, et al. Relationship between stent malapposition and incomplete neointimal coverage after drug-eluting stent implantation. J Interv Cardiol. 2012;25:270–7.

43. Kim JS, Ha J, Kim BK, et al. The relationship between post-stent strut apposition and follow-up strut coverage assessed by a contour plot optical coherence tomography analysis. JACC Cardiovasc Interv. 2014;7:641–51.

44. Lee SJ, Kim BK, Kim JS, et al. Evaluation of neointimal morphology of lesions with or without in-stent restenosis: an optical coherence tomography study. Clin Cardiol. 2011;34:633–9.

45. Chieffo A, Foglieni C, Nodari RL, et al. Histopathology of clinical coronary restenosis in drug-eluting versus bare metal stents. Am J Cardiol. 2009;104:1660–7.

46. Nakazawa G, Vorpahl M, Finn AV, Narula J, Virmani R. One step forward and two steps back with drug-eluting-stents: from preventing restenosis to causing late thrombosis and nouveau atherosclerosis. JACC Cardiovasc Imaging. 2009;2:623–8.

47. Nakazawa G, Otsuka F, Nakano M, et al. The pathology of neoatherosclerosis in human coronary implants bare-metal and drug-eluting stents. J Am Coll Cardiol. 2011;57:1314–22.

Jung-Sun Kim, Myeong-Ki Hong, and Yangsoo Jang

Abstract

Optical coherence tomography (OCT) is a useful intravascular modality for evaluating changes in the coronary artery after stent implantation. With the application of light rather than ultrasound, OCT can provide high-resolution *in vivo* images of the coronary artery and evaluate the stent status and neointimal tissue after coronary stent implantation more accurately than intravascular ultrasound. Novel findings on OCT assessment include the detection of strut coverage, malapposition, and the characterization of neointimal tissue during stent follow-up. In addition, clinical implications of OCT based findings at follow-ups after implantation of drug eluting stents (DES) have been reported. Several studies have suggested that stent strut coverage and neointimal characteristics post DES implantation are associated with late stent thrombosis. Therefore, late stent-based changes may serve as crucial developments to be evaluated by OCT.

This comprehensive review on the role of OCT during stent implantation follow-up will provide both relevant technical information on OCT and further insight into the clinical utility of OCT.

Keywords

Optical coherence tomography • Stent • Stent strut coverage • Malapposition • Neointimal characteristics

Optical coherence tomography (OCT) is the most useful intravascular modality for evaluating the pathology of the coronary artery before and after stent implantation [1–3]. Compared to intravascular ultrasound (IVUS), OCT can provide 10 times higher resolution for visualizing vascular structures and the stent more clearly [4, 5]. Several investigations have indicated that OCT is more accurate than IVUS in evaluating neointimal tissue and apposition after coronary stent implantation [3, 4, 6]. In the preclinical and clinical setting, OCT is the established intravascular modality for assessing the healing status of coronary stents specifically with regard to the stent strut coverage, malapposition and characteristics of neointimal tissue [6–8]. In previous studies, incomplete neointimal healing after stent strut was the sole pathologic determinant for late stent thrombosis in patients treated with drug-eluting stent (DES) [9, 10]. Several observational OCT studies have suggested that stent strut coverage and the neointimal characteristics defined by OCT are associated with late stent thrombosis after DES implantation [11, 12]. Therefore, late stent changes may be a crucial development to be evaluated by OCT and will be further discussed in this chapter.

J.-S. Kim, MD, PhD • M.-K. Hong, MD, PhD
Division of Cardiology, Severance Cardiovascular Hospital, Yonsei University College of Medicine, 250 Seongsanno, Seodaemun-gu, Seoul 120-752, South Korea

Y. Jang, MD, PhD (✉)
Division of Cardiology, Massachusetts General Hospital, Harvard Medical School, Boston, MA 02114, USA
e-mail: jang1212@yuhs.ac

10.1 Stent Strut Coverage

DES are currently the standard treatment modality for patients with symptomatic coronary artery disease [13, 14]. However, incomplete neointimal coverage is regarded as an important pathologic parameter of late stent thrombosis in patients treated with DES implantation [9].

OCT has a resolution of 10–20 μm, which is about 10 times higher than that of IVUS (80–120 μm) and is therefore able to detect neointimal tissue *in vivo* [5, 15]. Several validation studies have shown that OCT is more accurate in evaluating neointimal tissue after coronary stent implantation than intravascular ultrasound [2, 6]. Compared to IVUS, OCT showed better diagnostic accuracy for detecting a small degree of in-stent neointima, which was defined as occupying <30 % of the stent area measured with histology [6]. The optical cutoff value of percent neointimal hyperplasia (NIH) cross-sectional area (CSA) for detecting NIH by IVUS was 14.7 %; OCT-measured neointimal tissue of percent NIH CSA <14.7 % cannot be detected with IVUS [4].

Moreover, our previous observation clearly demonstrated the limitations of IVUS resolution by directly comparing the rate of strut coverage assessed by OCT versus IVUS in the same stents (25.8 % with IVUS vs. 99.9 % with OCT) [16].

Neointimal formation is considered a general wound healing response that occurs in vascular tissue after stent implantation [17]. The neointimal proliferative response to injury with stent implantation is caused by the interaction of platelet-fibrin thrombus and smooth muscle cells, release of mitogens, followed by the secretion of an extracellular matrix [17].

This response generally occurs in three temporal phases: inflammation (platelet aggregation and inflammatory cell infiltration), granulation (migration and proliferation of endothelial cells, fibroblasts or smooth muscle cells) and extracellular matrix remodeling (production of an extracellular matrix including proteoglycan from fibroblasts and smooth muscle cells) [17]. Through these processes, it is well known that the neointima completely covers the stent for bare metal stents (BMS) around 1 month after stent implantation and excessive neointimal formation results in in-stent restenosis (ISR) [18]. This finding was also shown in OCT examination, which demonstrated complete stent strut coverage in BMS in both the early and late periods, irrespective of clinical presentation (Table 10.1) [19–22]. DES remarkably reduced the rate of ISR and subsequent target lesion revascularization (TLR) [13, 14]. However, excessive inhibition of neointimal formation and induction of vascular inflammation caused delayed vascular healing with incomplete endothelialization and thrombus formation, which has been associated with an increased risk of late stent thrombosis (LST) [23, 24].

The incomplete stent coverage was frequently observed in several OCT investigations within 12 months after the 1st generation DES including sirolimus- (SES, Cypher Select™, Cordis, Miami Lake, FL, USA) and paclitaxel- eluting stent (PES, Taxus Liberte™, Boston Scientific, Natick, MA, USA) (see Table 10.1) [21, 22, 25–27]. These findings support the current guideline that patients treated with 1st-generation DES receive dual anti-platelet therapy (aspirin and clopidogrel) for at least 12 months. To enhance the stent healing process and resolve the safety concerns of 1st generation DES, new-generation DES have been developed with thin strut platform, biocompatible polymer and an optimal dose of anti-proliferative drugs [16, 20, 26, 28–30].

Table 10.1 summarizes the rate of stent strut coverage of various DES and BMS in each period after stent implantation (Fig. 10.1). Comparing SES and PES at 9 months, the frequency of uncovered strut was significantly higher in SES (12.5 ± 15.2 vs. 4.9 ± 7.9 %, p = 0.01) [27]. For the early period group at 3 months, the follow-up OCT data revealed that 15 % of stent struts were uncovered with neointima in SES [25]. Endeavor zotarolimus-eluting stents (E-ZES, Endeavor™, Medtronic, Santa Rosa, CA, USA) have been developed to resolve the safety issue, by adding a cobalt chromium based thin-strut with a phosphorylcholine biocompatible polymer and a shorter drug elution time (within 2 weeks) [31]. Compared to SES, the coverage of Endeavor ZES was almost complete irrespective of clinical presentation at 6–9 months [20, 22, 26]. The ODESSA (Optical Coherence Tomography for Drug-Eluting Stent Safety) study showed that ZES had a significantly lower incidence of uncovered stent struts than SES at both the overlapping and non-overlapping sites (0.02 vs. 5.8 % in overlapping sites and 0.01 vs. 6.0 % in non-overlapping sites) [22]. Furthermore, our observation showed that most stent struts (99.9 %) in Endeavor ZES were covered with neointima and were well-apposed at 3 months [16]. Other 2nd generation DES were developed to improve the safety concerns while maintaining the efficacy of 1st generation DES. Everolimus-eluting stents (EES, Xience™, Abbott Vascular, Santa Clara, CA, USA) and Resolute zotarolimus-eluting stents (R-ZES, Resolute™, Medtronic, Santa Rosa, CA, USA) are a cobalt chromium-based thin strut stent with a biocompatible polymer (Biolinx polymer in R-ZES and Fluorinated copolymer in EES) and a reduced dosage of drug [29]. EES and R-ZES also showed higher rates of strut coverage than SES at 9 months but were comparable [29]. The early stent strut coverage based on serial OCT evaluations was comparable between ZES-R and EES at 3 months (EES vs. ZES-R: 4.7 ± 5.1 vs. 6.2 ± 6.9 %, p = 0.62) [30]. The presence of permanent polymers of 1st generation DES is thought to be responsible for a hypersensitivity reaction which might cause incomplete re-endothelialization [32]. To overcome these issues, the development of new-generation DES utilizing a biodegradable polymer has been introduced. Biolimus-eluting stents (BES, Nobori™, Terumo Corporation, Tokyo, Japan or BioMatrix™, Biosensors Interventional, Singapore) have the unique property of a biodegradable polymer with an abluminal drug coating. A recent OCT study comparing SES demonstrated that OCT-defined coverage of BES was greater than that of SES at

Table 10.1 Proportions of uncovered stent struts and malapposition observed by optical coherence tomography

Type of stent	3 months		6 months		9 months		12 months		≥2 years	
	Uncovered stent (%)	Malapposition	Uncovered stent (%)	Malapposition	Uncovered stent (%)	Malapposition	Uncovered stent (%)	Malapposition	Uncovered stent (%)	Malapposition
BMS	0.1	1.1	0.3–0.6 (OLP: 3.4 %)	0.1–0.17	2.0	0	1.1	0.1	0.3	0
SES	15	16	10.4–25.1 (OLP: 9.6)	1.1–1.3	7.0–11.7	1.5–2.6	5.7–11.6	1.4–1.8	3.2–6.5 0.9 (48 months)	0.6–3.3
PES	3.8	1.5	5.0–10.9 (OLP: 16.5)	1.2–5.7	3.0–4.9	0.6–1.5	5.7–7.1	0.9–3.5	3.7	0.3
ZES-P	0.1	0.2	0.02–1.2 (OLP: 0.37)	0.001–0.2	0.3	0.1				
EES	4.7	0.7	2.3–3.2	0.7–2.1	1.6–4.4	0.4–1.8	1.9–5.8	0.1–1.4		
ZES-R	6.2	0.7			4.4	0.1	7.4	1.8		
BES	21.3	1.9	15.9–21.8	0.5–9.4			4.1	0.1		

Other values are for single layered stents

The values, which were derived from Bayesian hierarchical models, were excluded in this table

BMS bare metal stent, *SES* sirolimus-eluting stent, *PES* paclitaxel-eluting stent, *ZES-P* sprint zotarolimus-eluting stent, *ZES-R* resolute zotarolimus-eluting stent, *EES* everolimus-eluting stent, *BES* biolimus eluting stent, *OLP* overlapped
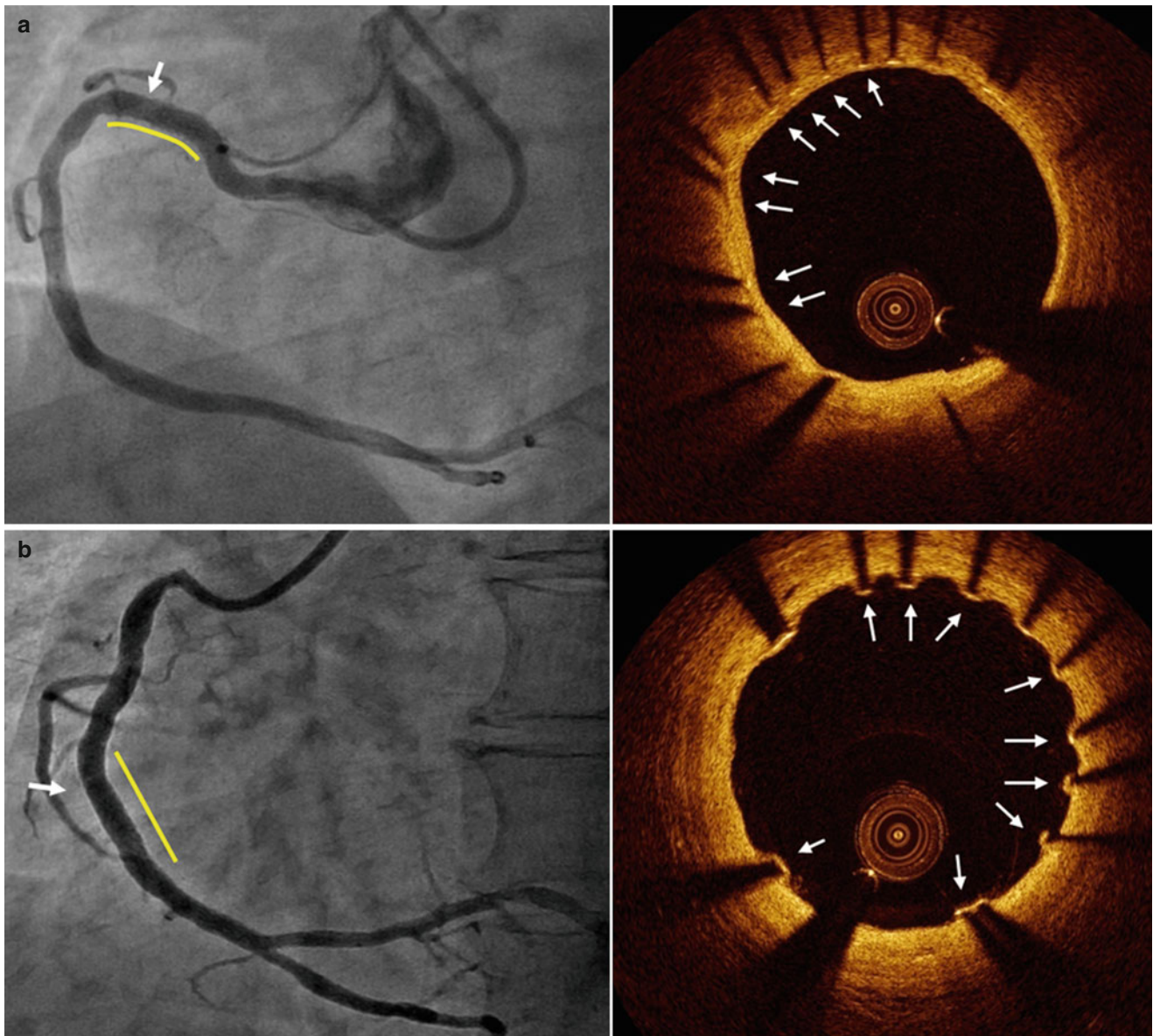
Fig. 10.1 Representative images of stent strut coverage. Optical coherence tomography showed the complete stent strut coverage at 12 months after everolimus eluting stent implantation (*arrows*) (**a**) and incomplete stent strut coverage with frequent detected uncovered struts at 3 months after biolimus eluting stent (*arrows*) (**b**)

6–9 months [33]. Serial assessment of stent strut coverage and malapposition may provide further insight into understanding clinical situations (Fig. 10.2). In serial observations of BES and SES between 3 and 12 months, both BES and SES showed a high percentage of incomplete strut coverage without any significant changes at 3 months. However, BES showed a significantly lower percentage of uncovered struts at 12 months compared to SES [34]. This was achieved by improved strut coverage from 3 to 12 months. Another study assessed the serial changes between 9 and 2 years and showed that the percentage of uncovered struts significantly decreased from 4.4 % at 9 months to 2.3 % at 2 years (p<0.001) [35]. Completely covered lesions were also more frequently observed at 2 years (44.7–59.2 %, p=0.07), although approximately half of the stented lesions were still not completely covered during

extended follow-up [35]. Based on these observations, strut thickness may be a crucial factor to stent struts coverage during the early period (3–6 months).

For the clinical manifestation, the pattern of neointimal coverage after DES implantations were different between acute coronary syndrome (ACS) including ST elevation myocardial infarction (STEMI) and stable angina pectoris (SAP), and variable among the DES types between two groups [36–38]. Therefore, the current study suggests that the vascular response after DES implantation might be influenced by both clinical presentation and the type of DES.

The next task is in the application of these findings to a real clinical situation. A recent autopsy study revealed that delayed and incomplete neointimal coverage of DES was associated with occurrence of late stent thrombosis; the
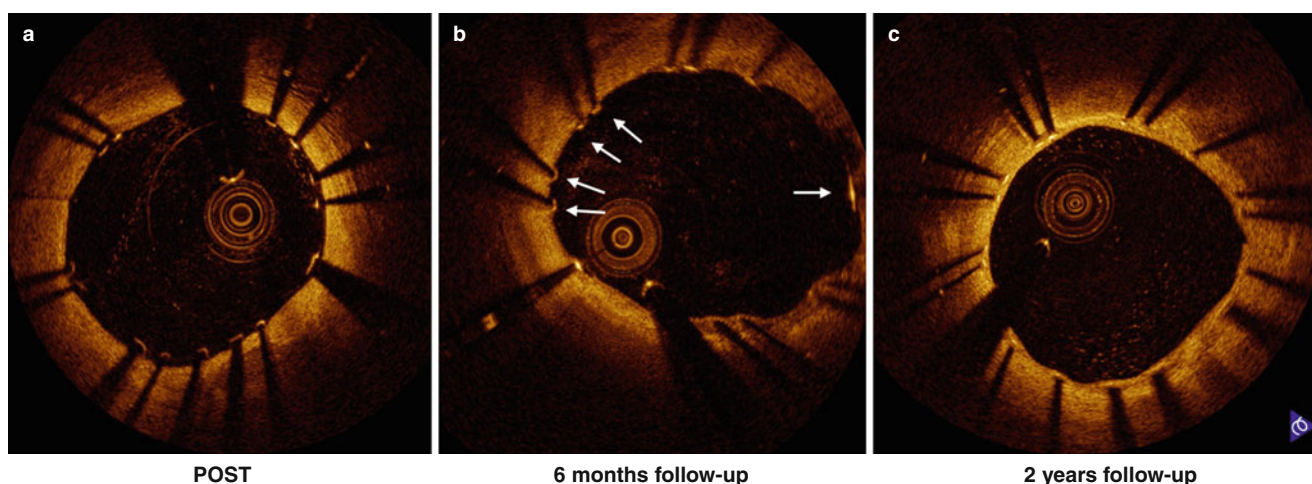
Fig. 10.2 Serial change of stent strut coverage at post intervention (**a**), 6 months (**b**) and 2 years (**c**). Some struts were not covered at 6 months (**b**, *white arrow*) and stent struts coverage completed at 2 years (**c**)

odds ratio for stent thrombosis in a stent with a ratio of uncovered to total stent struts per section >30 % was 9.0 (95 % confidence interval, 3.5–22) [10]. In a case-control study in which OCT was performed at the onset of stent thrombosis, the length of an uncovered stent strut segment was significantly associated with stent thrombosis [39]. Another cross-sectional analysis with 18 patients that experienced very late stent thrombosis showed that for 14 stents which developed very late stent thrombosis (VLST) without neointimal rupture, uncovered struts were observed in 9 stents (64.3 %) [40]. Based on these observations, strut coverage assessed by OCT may be a surrogate marker for predicting serious cardiovascular events in daily clinical practice. A recent OCT study suggested that a greater percentage of uncovered struts (a cut-off value of ≥5.9 % uncovered struts), as assessed by OCT at the 6–18 months follow-up, in asymptomatic DES-treated patients might predict the increase in major adverse cardiac events which is very relevant to stent safety in the future [41].

Current OCT analysis with conventional methods may have a challenge to compare the change of strut coverage and malapposition at the strut level during serial follow-up at different time points. Recently a contour plot OCT analysis was proposed as a possible method of assessing individual stent struts at the strut level practically; this comprehensive monitoring of stent strut status at different time points would then provide useful information regarding vascular healing status after DES implantation (Fig. 10.3) [42, 43].

10.2   Malapposition

During follow-up, the definition of malapposed struts that is applied is the same that is used immediately post stent implantation, namely one distinguishing the various types of coronary stents based on differences in the thickness of struts and the polymer (Fig. 10.4). The following are the criteria of malapposed struts for several DES: ≥160 μm for sirolimus-eluting stents (Cypher Select™, Cordis, Miami Lake, FL, USA), ≥130 μm for paclitaxel-eluting stents (Taxus Liberte™, Boston Scientific, Natick, MA, USA), ≥110 μm for zotarolimus-eluting stents (Endeavor™ and Resolute™, Medtronic, Santa Rosa, CA, USA), ≥100 μm for everolimus-eluting stents (Xience™, Abbott Vascular, Santa Clara, CA, USA) and ≥130 μm for biolimus-eluting stents (Nobori™, Terumo Corporation, Tokyo, Japan or BioMatrix™, Biosensors Interventional, Singapore) [26, 27, 29, 33, 44, 45].

As neointimal formation proceeds after stent implantation, the rate of malapposed struts significantly decreases when the detachment distance between the stent strut and vessel wall is within a certain distance, which is different depending on the type of stent [46–48]. A previous OCT report demonstrated that the percentage of malapposed struts remarkably decreased from 12.2±11.0 % post-intervention to 1.0±2.2 % at the 6 month follow-up [48]. However, during serial follow-ups between 2 and 4 years, the one study with SES reported a significant increase in the percentage of malapposed struts from 2.2 % at 2 years to 3.0 % at 4 years (p=0.044) in SES and our study revealed similar findings including 1st and 2nd generation DES that malapposed struts were similarly detected between 9 months and 2 years (0.6–0.9 %) [49, 50]. These findings were usually observed in 1st generation DES and could be possibly explained by long-term vascular inflammation. Malapposed struts could be classified into persistent (persistently malapposed after an index procedure) and late-acquired malapposition (newly detected at follow-up). Recent follow-up OCT examinations indicated that the percentage of late-persistent malapposed struts was 2.5±3.6 %, and most (72 %) late-persistent stent malappositions were located within the edges of the stents. For late acquired malapposition, the percentage of

Fig. 10.3 Representative images of contour plot images post-intervention and at follow-up. Using a contour map OCT analysis, each stent struts can be tracked appropriately
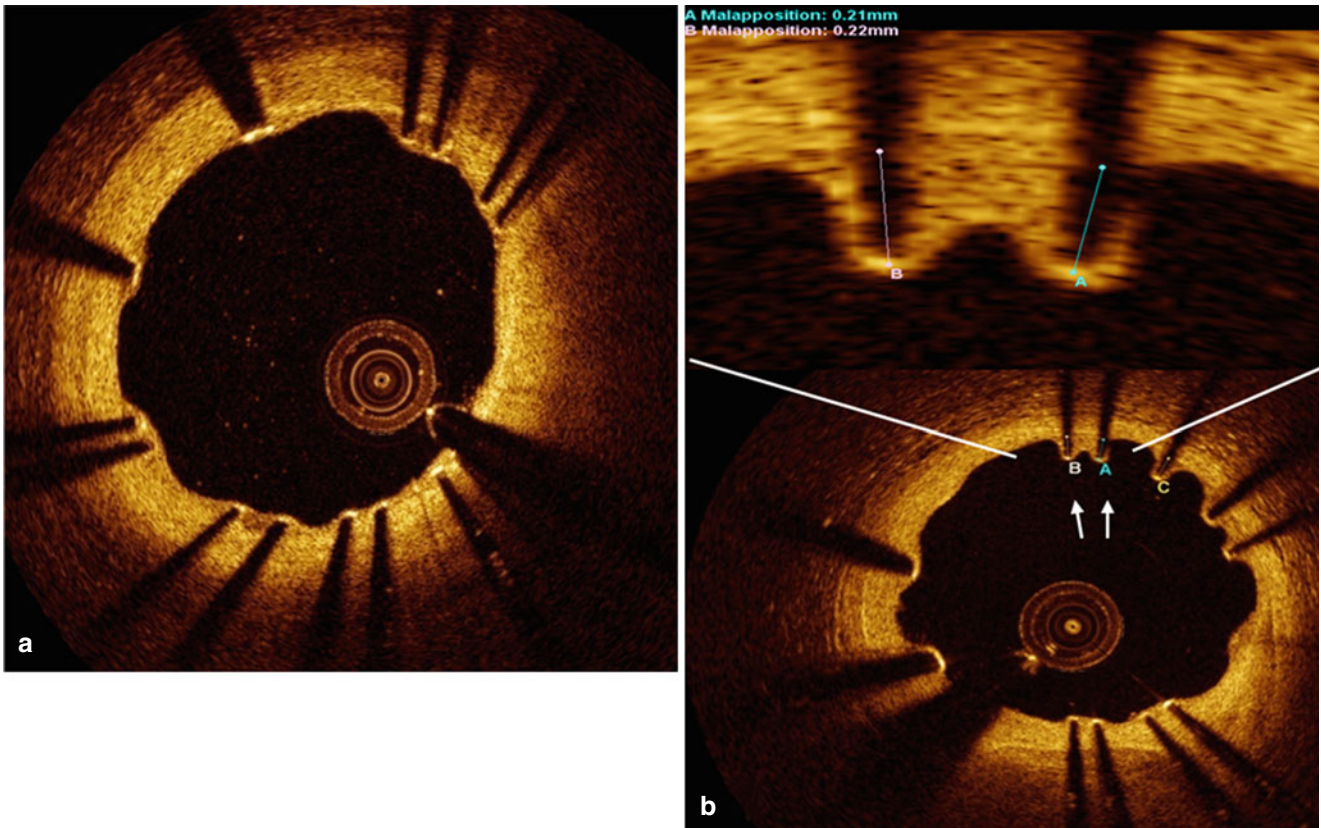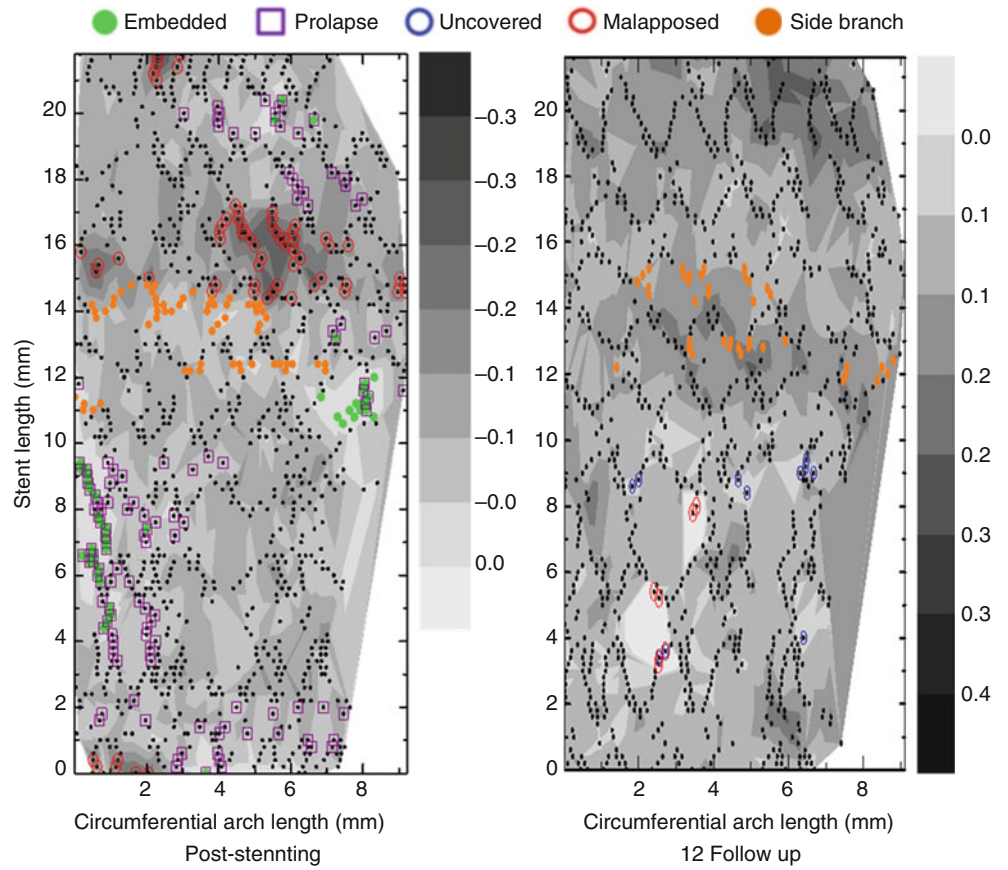
Fig. 10.4 Representative images of stent strut apposition. Optical coherence tomography showed the well apposed stent strut with complete coverage at 6 months after biolimus eluting stent implantation (**a**) and malapposition with uncovered struts in part of stent at 6 months after resolute zotarolimus eluting stent (*arrow*) (**b**)

late-acquired malapposed struts was 3.8±4.5 %, which were predominantly distributed within stent bodies (61 %) rather than stent edges (39 %). The plaque/thrombus prolapse was observed more frequently by poststent OCT examinations in patients with late-acquired stent malapposition lesions compared with those who did not have late-acquired stent malapposition lesions. In their 2013 paper Kawamori et al. suggest a the strut-to-vessel distance of ≤260 m on post-stenting OCT images as a cut-off value for resolved malapposed struts (sensitivity of 89.3 % and a specificity of 83.7 %) for 1st generation DES (SES or PES) [51]. In their more recent paper, Foin et al. studied the 2nd generation DESs and drug eluting balloon in combination with a bare metal stent, demonstrating that malapposed segments with detachment from the vessel wall of <100 m at baseline showed complete strut coverage at follow-up, whereas segments with a maximal malapposed detachment distance of 100–300 m and >300 μm had 6.1 and 15.7 % of their struts still uncovered at follow-up, respectively (P<0.001) [46]. Additionally, in another study, coverage of malapposed struts was delayed with respect to well-apposed struts at the 9–13 months post DES implantation follow-up [52]. Although overall malapposed struts were positively correlated with uncovered struts, a subgroup of lesions with minimal stent malapposition showed similar rates of uncovered struts to those without malapposition [53, 54]. The coverage of malapposed struts was also affected by DES type, namely between the first- and new-generation DES in the initial clinical presentation [55]. The incidence of malapposed stent struts was significantly higher in ACS at 9 months (2.2±5.6 vs 0.5±2.0 %, p=0.02) [36]. Especially in STEMI, the incidence of malapposed struts was significantly higher in SES and PES than ZES (SES vs PES vs ZES: 4.0±8.2 % vs 2.1±4.5 % vs 0±0 %, p=0.001) [37].

The next logical step was then to identify the clinical implication of stent malapposition during follow-up. A recent OCT study reported that severe stenosis, calcified lesions, and longer stent length were predictors for acute stent malapposition. Predictors of late-persistent stent malapposition were the presence of acute stent malapposition within the stent edge and a larger volume of acute stent malapposition. Late-acquired stent malapposition was associated with plaque/thrombus prolapse detected on poststent OCT images. Long-term clinical outcomes of late stent malapposition detected by OCT were favorable [44]. However (Using "but" at the beginning of a sentence is strongly discouraged), this investigation was a cross-sectional study and moreover, was limited by the small number of clinical events in this study.

10.3 Neointimal Characteristics

Pathological studies have demonstrated that neointima within a stent are comprised of various tissue components including collagen, proteoglycan, smooth muscle, fibrin, or thrombus [56, 57]. Previous imaging modalities, such as angiography and intravascular ultrasound, have been limited by their low resolution, in detecting crucial neointimal characteristics. However, intravascular OCT, with its higher resolution, is useful for both the qualitative as well as quantitative evaluation of neointimal tissue [35, 58]. Recent OCT studies have reported differential morphological characteristics of neointimal tissue, which were well-correlated with histological findings [7, 59]. The stented segments at the minimal lumen CSA were assessed qualitatively to characterize the neointimal tissue as (1) homogeneous neointima, a uniform signal-rich band without focal variation or attenuation; (2) heterogeneous neointima, focally changing optical properties and various backscattering patterns; and (3) layered neointima, layers with different optical properties, namely an adluminal high scattering layer and an abluminal low scattering layer (Fig. 10.5) [7, 35, 58]. Heterogeneous neointima were frequently detected in 21.7 % of DES-treated lesions in the Yonsei OCT registry. The occurrence of neointimal tissue within this group was significantly associated with both old age and initial clinical presentation of ACS [60].

Comparing different OCT morphological characteristics with different in-stent neointimal tissue types analyzed by histology with swine in-stent restenosis models, the optical characteristics of neointimal formation seen in OCT were consistent with the histological studies on stent healing [7]. Fibrous connective tissue deposition was more frequently present in the homogeneous pattern (71.6 %, P<0.001), whereas significant fibrin deposits were more commonly seen in the heterogeneous pattern (56.9 %, P=0.007). Peri-strut inflammation was less frequently found in the homogeneous pattern (19.8 %, P<0.001) in comparison with the layered (73.9 %) or heterogeneous patterns (43.1 %). The presence of external elastic lamina (EEL) rupture was also more commonly seen in layered (73.9 %) and heterogeneous (46.6 %) patterns than in the homogeneous pattern (22.4 %, P<0.001) [7].

However, the detailed relationship between different OCT-based neointimal tissues regardless of neoatherosclerosis and clinical outcomes has not yet been investigated. It was recently reported however that major adverse cardiac events including cardiac death, MI, target vessel revascularization and stent thrombosis occurred more frequently in patients in the heterogeneous group compared with those in non-heterogeneous group during the average 31 month follow-up period (11.8 % vs. 2.9 % in the homogeneous group vs. 8.8 % in the layered group, p=0.003) [60]. In addition, our group found that inclusion in the heterogeneous group and minimal lumen CSA at the follow-up OCT examination were independent risk factors for future MACE [60].

Conclusion

Stent evaluations using OCT have been well addressed in previous investigations and provide important information for clinical decisions post DES implantation. OCT-derived assessments of stent strut coverage, malapposition
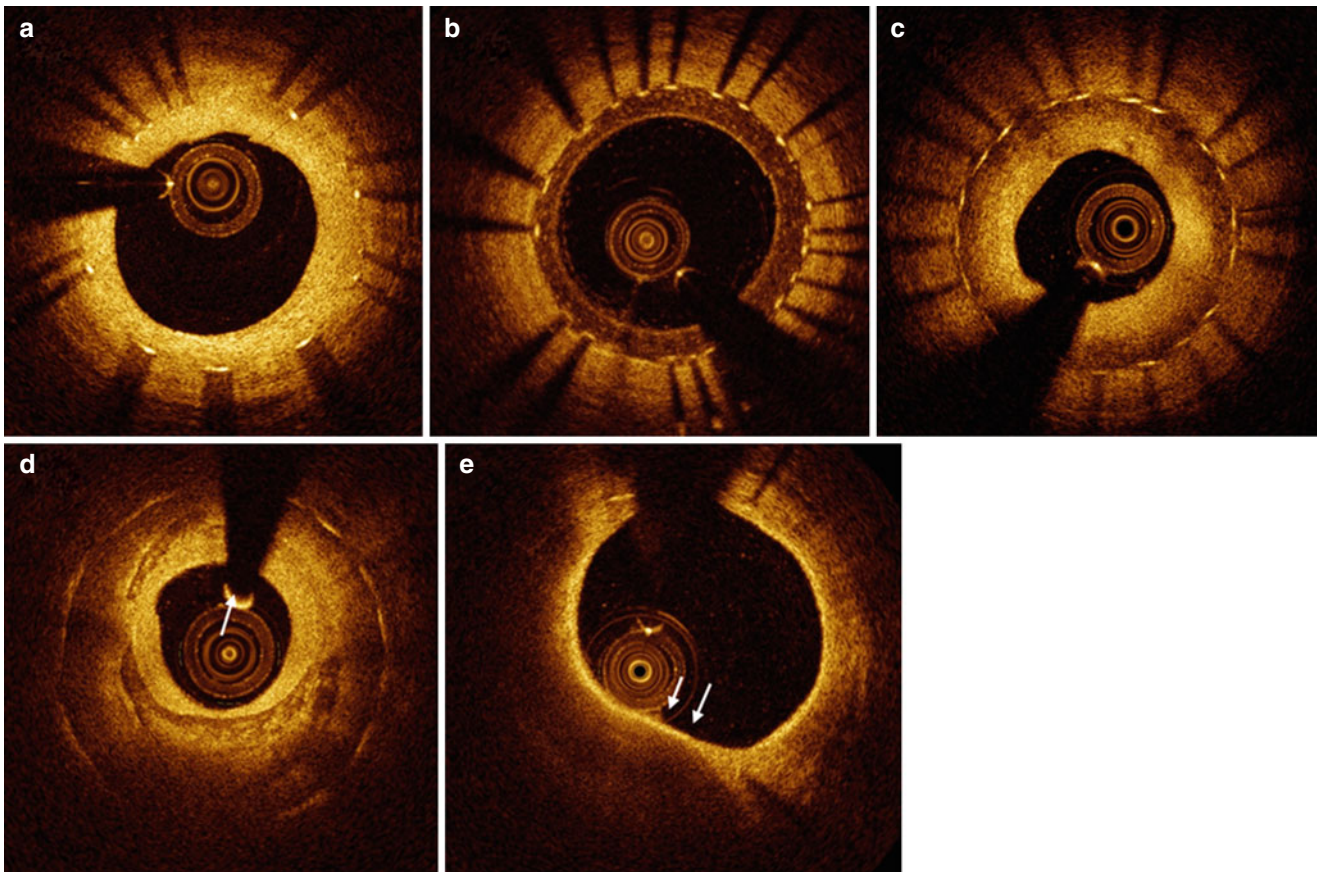
Fig. 10.5 Representative images of neointimal characteristics. Homogeneous (**a**); heterogeneous (**b**); layered (**c**); neointimal calcification (**d**); thin cap fibroatheroma like neointima (**e**)

or neointimal characteristics may also be very useful for predicting and preventing future adverse cardiac events. Moreover, advances in OCT technology and developments in its applications will likely provide further information on coronary stents and improve their practical usefulness in future clinical practice.

References

1. Prati F, Guagliumi G, Mintz GS, Costa M, Regar E, Akasaka T, et al. Expert review document part 2: methodology, terminology and clinical applications of optical coherence tomography for the assessment of interventional procedures. Eur Heart J. 2012;33(20):2513–20.
2. Bezerra HG, Attizzani GF, Sirbu V, Musumeci G, Lortkipanidze N, Fujino Y, et al. Optical coherence tomography versus intravascular ultrasound to evaluate coronary artery disease and percutaneous coronary intervention. JACC Cardiovasc Interv. 2013;6(3):228–36.
3. Bouma BE, Tearney GJ, Yabushita H, Shishkov M, Kauffman CR, DeJoseph Gauthier D, et al. Evaluation of intracoronary stenting by intravascular optical coherence tomography. Heart. 2003;89(3):317–20.
4. Kwon SW, Kim BK, Kim TH, Kim JS, Ko YG, Choi D, et al. Qualitative assessment of neointimal tissue after drug-eluting stent implantation: comparison between follow-up optical coherence tomography and intravascular ultrasound. Am Heart J. 2011;161(2):367–72.
5. Jang IK, Bouma BE, Kang DH, Park SJ, Park SW, Seung KB, et al. Visualization of coronary atherosclerotic plaques in patients using optical coherence tomography: comparison with intravascular ultrasound. J Am Coll Cardiol. 2002;39(4):604–9.
6. Suzuki Y, Ikeno F, Koizumi T, Tio F, Yeung AC, Yock PG, et al. In vivo comparison between optical coherence tomography and intravascular ultrasound for detecting small degrees of in-stent neointima after stent implantation. JACC Cardiovasc Interv. 2008;1(2):168–73.
7. Kim JS, Afari ME, Ha J, Tellez A, Milewski K, Conditt G, et al. Neointimal patterns obtained by optical coherence tomography correlate with specific histological components and neointimal proliferation in a swine model of restenosis. Eur Heart J Cardiovasc Imaging. 2014;15(3):292–8.
8. Kim JS, Wallace-Bradley D, Alviar CL, Conditt G, Milewski K, Afari ME, et al. Correlation of angiographic late loss with neointimal proliferation in stents evaluated by OCT and histology in porcine coronary arteries. JACC Cardiovasc Imaging. 2011;4(9):1002–10.
9. Farb A, Burke AP, Kolodgie FD, Virmani R. Pathological mechanisms of fatal late coronary stent thrombosis in humans. Circulation. 2003;108(14):1701–6.
10. Finn AV, Joner M, Nakazawa G, Kolodgie F, Newell J, John MC, et al. Pathological correlates of late drug-eluting stent thrombosis: strut coverage as a marker of endothelialization. Circulation. 2007;115(18):2435–41.
11. Takano M, Yamamoto M, Inami S, Murakami D, Ohba T, Seino Y, et al. Appearance of lipid-laden intima and neovascularization after implantation of bare-metal stents extended late-phase observation by intracoronary optical coherence tomography. J Am Coll Cardiol. 2009;55(1):26–32.

12. Kang SJ, Mintz GS, Akasaka T, Park DW, Lee JY, Kim WJ, et al. Optical coherence tomographic analysis of in-stent neoatherosclerosis after drug-eluting stent implantation. Circulation. 2011;123(25):2954–63.

13. Stone GW, Ellis SG, Cox DA, Hermiller J, O'Shaughnessy C, Mann JT, et al. A polymer-based, paclitaxel-eluting stent in patients with coronary artery disease. N Engl J Med. 2004;350(3):221–31.

14. Moses JW, Leon MB, Popma JJ, Fitzgerald PJ, Holmes DR, O'Shaughnessy C, et al. Sirolimus-eluting stents versus standard stents in patients with stenosis in a native coronary artery. N Engl J Med. 2003;349(14):1315–23.

15. Jang IK, Tearney GJ, MacNeill B, Takano M, Moselewski F, Iftima N, et al. In vivo characterization of coronary atherosclerotic plaque by use of optical coherence tomography. Circulation. 2005;111(12):1551–5.

16. Kim JS, Jang IK, Fan C, Kim TH, Park SM, Choi EY, et al. Evaluation in 3 months duration of neointimal coverage after zotarolimus-eluting stent implantation by optical coherence tomography: the ENDEAVOR OCT trial. JACC Cardiovasc Interv. 2009;2(12):1240–7.

17. Forrester JS, Fishbein M, Helfant R, Fagin J. A paradigm for restenosis based on cell biology: clues for the development of new preventive therapies. J Am Coll Cardiol. 1991;17(3):758–69.

18. Virmani R, Farb A. Pathology of in-stent restenosis. Curr Opin Lipidol. 1999;10(6):499–506.

19. Xie Y, Takano M, Murakami D, Yamamoto M, Okamatsu K, Inami S, et al. Comparison of neointimal coverage by optical coherence tomography of a sirolimus-eluting stent versus a bare-metal stent three months after implantation. Am J Cardiol. 2008;102(1):27–31.

20. Guagliumi G, Sirbu V, Bezerra H, Biondi-Zoccai G, Fiocca L, Musumeci G, et al. Strut coverage and vessel wall response to zotarolimus-eluting and bare-metal stents implanted in patients with ST-segment elevation myocardial infarction: the OCTAMI (Optical Coherence Tomography in Acute Myocardial Infarction) Study. JACC Cardiovasc Interv. 2010;3(6):680–7.

21. Guagliumi G, Costa MA, Sirbu V, Musumeci G, Bezerra HG, Suzuki N, et al. Strut coverage and late malapposition with paclitaxel-eluting stents compared with bare metal stents in acute myocardial infarction: optical coherence tomography substudy of the Harmonizing Outcomes with Revascularization and Stents in Acute Myocardial Infarction (HORIZONS-AMI) Trial. Circulation. 2011;123(3):274–81.

22. Guagliumi G, Musumeci G, Sirbu V, Bezerra HG, Suzuki N, Fiocca L, et al. Optical coherence tomography assessment of in vivo vascular response after implantation of overlapping bare-metal and drug-eluting stents. JACC Cardiovasc Interv. 2010;3(5):531–9.

23. Jeremias A, Sylvia B, Bridges J, Kirtane AJ, Bigelow B, Pinto DS, et al. Stent thrombosis after successful sirolimus-eluting stent implantation. Circulation. 2004;109(16):1930–2.

24. Daemen J, Wenaweser P, Tsuchida K, Abrecht L, Vaina S, Morger C, et al. Early and late coronary stent thrombosis of sirolimus-eluting and paclitaxel-eluting stents in routine clinical practice: data from a large two-institutional cohort study. Lancet. 2007;369(9562):667–78.

25. Takano M, Inami S, Jang IK, Yamamoto M, Murakami D, Seimiya K, et al. Evaluation by optical coherence tomography of neointimal coverage of sirolimus-eluting stent three months after implantation. Am J Cardiol. 2007;99(8):1033–8.

26. Kim JS, Jang IK, Kim TH, Takano M, Kume T, Hur NW, et al. Optical coherence tomography evaluation of zotarolimus-eluting stents at 9-month follow-up: comparison with sirolimus-eluting stents. Heart. 2009;95(23):1907–12.

27. Kim JS, Kim TH, Fan C, Lee JM, Kim W, Ko YG, et al. Comparison of neointimal coverage of sirolimus-eluting stents and paclitaxel-eluting stents using optical coherence tomography at 9 months after implantation. Circ J. 2010;74(2):320–6.

28. Kim BK, Kim JS, Park J, Ko YG, Choi D, Jang Y, et al. Comparison of optical coherence tomographic assessment between first- and second-generation drug-eluting stents. Yonsei Med J. 2012;53(3):524–9.

29. Kim JS, Kim BK, Jang IK, Shin DH, Ko YG, Choi D, et al. ComparisOn of neointimal coVerage betwEen zotaRolimus-eluting stent and everolimus-eluting stent using Optical Coherence Tomography (COVER OCT). Am Heart J. 2012;163(4):601–7.

30. Kim S, Kim JS, Shin DH, Kim BK, Ko YG, Choi D, et al. Comparison of early strut coverage between zotarolimus- and everolimus-eluting stents using optical coherence tomography. Am J Cardiol. 2013;111(1):1–5.

31. Kandzari DE, Leon MB, Popma JJ, Fitzgerald PJ, O'Shaughnessy C, Ball MW, et al. Comparison of zotarolimus-eluting and sirolimus-eluting stents in patients with native coronary artery disease: a randomized controlled trial. J Am Coll Cardiol. 2006;48(12):2440–7.

32. Joner M, Finn AV, Farb A, Mont EK, Kolodgie FD, Ladich E, et al. Pathology of drug-eluting stents in humans: delayed healing and late thrombotic risk. J Am Coll Cardiol. 2006;48(1):193–202.

33. Kim BK, Ha J, Mintz GS, Kim JS, Shin DH, Ko YG, et al. Randomised comparison of strut coverage between Nobori biolimus-eluting and sirolimus-eluting stents: an optical coherence tomography analysis. EuroIntervention. 2014;9(12):1389–97.

34. Kim BK, Hong MK, Shin DH, Kim JS, Ko YG, Choi D, et al. Optical coherence tomography analysis of strut coverage in biolimus- and sirolimus-eluting stents: 3-month and 12-month serial follow-up. Int J Cardiol. 2013;168(5):4617–23.

35. Kim JS, Hong MK, Shin DH, Kim BK, Ko YG, Choi D, et al. Quantitative and qualitative changes in DES-related neointimal tissue based on serial OCT. JACC Cardiovasc Imaging. 2012;5(11):1147–55.

36. Kim JS, Fan C, Choi D, Jang IK, Lee JM, Kim TH, et al. Different patterns of neointimal coverage between acute coronary syndrome and stable angina after various types of drug-eluting stents implantation; 9-month follow-up optical coherence tomography study. Int J Cardiol. 2011;146(3):341–6.

37. Fan C, Kim JS, Lee JM, Kim TH, Park SM, Wi J, et al. Different vascular healing patterns with various drug-eluting stents in primary percutaneous coronary intervention for ST-segment elevation myocardial infarction: optical coherence tomographic findings. Am J Cardiol. 2010;105(7):972–6.

38. Gonzalo N, Barlis P, Serruys PW, Garcia-Garcia HM, Onuma Y, Ligthart J, et al. Incomplete stent apposition and delayed tissue coverage are more frequent in drug-eluting stents implanted during primary percutaneous coronary intervention for ST-segment elevation myocardial infarction than in drug-eluting stents implanted for stable/unstable angina: insights from optical coherence tomography. JACC Cardiovasc Interv. 2009;2(5):445–52.

39. Guagliumi G, Sirbu V, Musumeci G, Gerber R, Biondi-Zoccai G, Ikejima H, et al. Examination of the in vivo mechanisms of late drug-eluting stent thrombosis: findings from optical coherence tomography and intravascular ultrasound imaging. JACC Cardiovasc Interv. 2012;5(1):12–20.

40. Ko YG, Kim DM, Cho JM, Choi SY, Yoon JH, Kim JS, et al. Optical coherence tomography findings of very late stent thrombosis after drug-eluting stent implantation. Int J Cardiovasc Imaging. 2012;28(4):715–23.

41. Won H, Shin DH, Kim BK, Mintz GS, Kim JS, Ko YG, et al. Optical coherence tomography derived cut-off value of uncovered stent struts to predict adverse clinical outcomes after drug-eluting stent implantation. Int J Cardiovasc Imaging. 2013;29(6):1255–63.

42. Ha J, Kim BK, Kim JS, Shin DH, Ko YG, Choi D, et al. Assessing neointimal coverage after DES implantation by 3D OCT. JACC Cardiovasc Imaging. 2012;5(8):852–3.

43. Kim JS, Ha J, Kim BK, Shin DH, Ko YG, Choi D, et al. The relationship between post-stent strut apposition and follow-up strut

coverage assessed by a contour plot optical coherence tomography analysis. JACC Cardiovasc Interv. 2014;7(6):641–51.

44. Im E, Kim BK, Ko YG, Shin DH, Kim JS, Choi D, et al. Incidences, predictors, and clinical outcomes of acute and late stent malapposition detected by optical coherence tomography after drug-eluting stent implantation. Circ Cardiovasc Interv. 2014; 7(1):88–96.

45. Gutierrez-Chico JL, Juni P, Garcia-Garcia HM, Regar E, Nuesch E, Borgia F, et al. Long-term tissue coverage of a biodegradable polylactide polymer-coated biolimus-eluting stent: comparative sequential assessment with optical coherence tomography until complete resorption of the polymer. Am Heart J. 2011;162(5):922–31.

46. Foin N, Gutierrez-Chico JL, Nakatani S, Torii R, Bourantas CV, Sen S, et al. Incomplete stent apposition causes high shear flow disturbances and delay in neointimal coverage as a function of strut to wall detachment distance: implications for the management of incomplete stent apposition. Circ Cardiovasc Interv. 2014;7(2): 180–9.

47. Gutierrez-Chico JL, Wykrzykowska J, Nuesch E, van Geuns RJ, Koch KT, Koolen JJ, et al. Vascular tissue reaction to acute malapposition in human coronary arteries: sequential assessment with optical coherence tomography. Circ Cardiovasc Interv. 2012;5(1): 20–9. S1-8.

48. Katoh H, Shite J, Shinke T, Matsumoto D, Tanino Y, Ogasawara D, et al. Delayed neointimalization on sirolimus-eluting stents: 6-month and 12-month follow up by optical coherence tomography. Circ J. 2009;73(6):1033–7.

49. Takano M, Yamamoto M, Mizuno M, Murakami D, Inami T, Kimata N, et al. Late vascular responses from 2 to 4 years after implantation of sirolimus-eluting stents: serial observations by intracoronary optical coherence tomography. Circ Cardiovasc Interv. 2010;3(5):476–83.

50. Kim TH, Kim JS, Kim BK, Ko YG, Choi D, Jang Y, et al. Long-term (≥2 years) follow-up optical coherence tomographic study after sirolimus- and paclitaxel-eluting stent implantation: comparison to 9-month follow-up results. Int J Cardiovasc Imaging. 2011;27(6):875–81.

51. Kawamori H, Shite J, Shinke T, Otake H, Matsumoto D, Nakagawa M, et al. Natural consequence of post-intervention stent malapposition, thrombus, tissue prolapse, and dissection assessed by optical coherence tomography at mid-term follow-up. Eur Heart J Cardiovasc Imaging. 2013;14(9):865–75.

52. Gutierrez-Chico JL, Regar E, Nuesch E, Okamura T, Wykrzykowska J, di Mario C, et al. Delayed coverage in malapposed and sidebranch struts with respect to well-apposed struts in drug-eluting stents: in vivo assessment with optical coherence tomography. Circulation. 2011;124(5):612–23.

53. Kim BK, Hong MK, Shin DH, Kim JS, Ko YG, Choi D, et al. Relationship between stent malapposition and incomplete neointimal coverage after drug-eluting stent implantation. J Interv Cardiol. 2012;25(3):270–7.

54. Ozaki Y, Okumura M, Ismail TF, Naruse H, Hattori K, Kan S, et al. The fate of incomplete stent apposition with drug-eluting stents: an optical coherence tomography-based natural history study. Eur Heart J. 2010;31(12):1470–6.

55. Kim BK, Shin DH, Kim JS, Ko YG, Choi D, Jang Y, et al. Optical coherence tomography-based evaluation of malapposed strut coverage after drug-eluting stent implantation. Int J Cardiovasc Imaging. 2012;28(8):1887–94.

56. Farb A, Kolodgie FD, Hwang JY, Burke AP, Tefera K, Weber DK, et al. Extracellular matrix changes in stented human coronary arteries. Circulation. 2004;110(8):940–7.

57. Nakano M, Vorpahl M, Otsuka F, Taniwaki M, Yazdani SK, Finn AV, et al. Ex vivo assessment of vascular response to coronary stents by optical frequency domain imaging. JACC Cardiovasc Imaging. 2012;5(1):71–82.

58. Gonzalo N, Serruys PW, Okamura T, van Beusekom HM, Garcia-Garcia HM, van Soest G, et al. Optical coherence tomography patterns of stent restenosis. Am Heart J. 2009;158(2):284–93.

59. Malle C, Tada T, Steigerwald K, Ughi GJ, Schuster T, Nakano M, et al. Tissue characterization after drug-eluting stent implantation using optical coherence tomography. Arterioscler Thromb Vasc Biol. 2013;33(6):1376–83.

60. Kim JS, Lee JH, Shin DH, Kim BK, Ko YG, Choi D, et al. Long-term outcomes of neointimal hyperplasia without features of neoatherosclerosis after drug-eluting stent implantation. JACC Cardiovasc Imaging. 2014;7(8):788–95.

Stent Thrombosis

11

Giulio Guagliumi, Chiara Bernelli, Kenichi Komukai,
and Vasile Sirbu

Abstract

The occurrence of stent thrombosis (ST) is rare but it remains one of the most dreadful complications following Percutaneous Coronary Intervention (PCI), due to the possible risk of death and extensive myocardial infarction. OCT contributes critically in the assessment of ST with substantial clinical implications through: (1) a better mechanistic understanding of the different processes involved; (2) the identification of surrogate markers anticipating the risk of ST; (3) a tailored and more effective approach for the acute treatment of ST. The high level of accuracy in the measurements and separation of the plaque and thrombus components along the entire vessel, and in the fine details on tissue coverage at the stent strut level, makes OCT a unique intracoronary imaging modality for assessing stent failures and guiding appropriate interventions during ST.

Keywords

Optical coherence tomography • Stent thrombosis • Myocardial infarction • Inadequate stent implantation • Stent malapposition • Uncovered struts • Neoatherosclerosis

11.1 Introduction

The increased burden of coronary artery disease (CAD) represents a major challenge to the global health care system. Over the last decades the number of patients undergoing percutaneous coronary interventions (PCI) substantially increased, with more complex clinical and anatomical settings treated with stent implantation. Acute myocardial infarction, unprotected left main disease and complex bifurcation are regularly treated with coronary stents. This approach was made possible by the development and widespread use of drug-eluting stents (DES) that effectively reduced the limit of in-stent restenosis following bare metal

stent implantation [1, 2]. Nevertheless, the extensive use of DES in high risk cohorts was plagued by an increasing number of stent thrombosis (ST), especially in the late and very late phases after the DES implantation, associated with a high rate of mortality [3–5].

11.2 Definition and Incidence

The definition of ST varies from an "angiographically proven" to a "clinically suspected" event with the inclusion of acute myocardial infarction (MI) involving the target vessel, and unexplained death (within 30 days or anytime). The Academic Research Consortium (ARC) divided ST according to the level of certainty in source documentation and frequency of occurrence compared to the index procedure [6]. Definite ST (highest level of certainty) requires either angiographic or postmortem evidence of thrombotic stent occlusion that has to be in the stent or in the 5 mm segment immediately apart from the stent. Conversely, probable ST

G. Guagliumi, MD, FESC (✉) • C. Bernelli, MD
K. Komukai, MD • V. Sirbu, MD
Cardiovascular Department, A.O. Papa Giovanni
XXIII Hospital, Piazza OMS 1, Bergamo 24127, Italy
e-mail: guagliumig@gmail.com

encompasses any unexplained death within 30 days of stent implantation or any MI in the territory of the implanted stent, regardless of the time span. Finally, possible ST includes any unexplained death beyond 30 days. All these entities are subdivided temporally into acute (<24 h), sub-acute (1–30 days), late (between 30 days and 1 year) and very late ST (>1 year after stent implantation).

ST limited during the early phase of bare-metal-stent (BMS) the rate of ST was as high as 20 % [7]. Following the introduction of high pressure balloon post- dilatation and the combined use of dual antiplatelet therapy (DAPT), a significant decrease of ST was observed [8–14], with a range between 0.5 and 4 %. In the Dutch registry that included more than 21,000 patients treated with BMS and first generation DES, the vast majority of ST (>70.0 %) occurred in the first month after stent implantation, with a cumulative rate of 2.1 % in definite ST over a 3-years follow-up period [15]. A similar occurrence of ST was observed in the Bern-Rotterdam registry, that followed 8,146 patients treated with first generation DES (paclitaxel eluting stent [PES] and sirolimus eluting stent [SES]), with 3.3 % of cumulative incidence of ST at 3-years [16]. Furthermore, the specific concern for additional risk of very late ST observed in the first generation DES at an annual rate of 0.5 % [16–18] was addressed by these studies. More recently, following the widespread adoption of current generation DES, with thinner struts and a more biocompatible polymer, a substantial reduction of ST has been reported [19, 20].

11.3 Clinical Outcomes

Very few studies have been published on the long-term clinical outcomes following a first episode of definite ST. Some series reported a mortality rate associated with ST of up to 45 % [13, 21–23]. Interestingly, the observed rate of recurrent episodes of ST was approximately 20 %. In a recent meta-analysis of 23 studies that evaluated 7,315 cases of definite ST, this event was associated with an in hospital mortality of 8 % and an in–hospital new or recurrent MI rate of 6 % (not counting for the ST event). Notably, the stent type had no significant effect on in-hospital or 30-day mortality [24].

11.4 Associated Factors

Several studies have confirmed the multifactorial nature of ST. ST may depend on: (1) patient characteristics and risk factors, (2) treated lesion and procedural-related factors, including the stent type and (3) DAPT compliance and responsiveness [13, 21–33]. Patients clinical characteristics associated with ST include diabetes mellitus, acute coronary

syndromes (in particular ST-elevation myocardial infarction [STEMI]) as indication for PCI, left ventricular dysfunction, renal failure, younger age, smoking status, malignancy and presence of bleeding. Moreover some angiographic characteristics of the stented lesion, including small vessel diameter, bifurcations, heavy calcified lesions, ostial and long lesions have been associated with increased risk of ST. In addition, procedural characteristics (multiple stents implantation, stent undersizing and under expansion, total stent length, balloon/stent size ratio, bivalirudin administration, and stent type) may also predict the individual risk to develop ST. Among the technical aspects more critically involved in early ST the presence of residual dissection and stent underexpansion seem to play major roles. Finally, individual DAPT responsiveness may substantially contribute to ST occurrence. Indeed, both BMS and DES implantation induce platelet adhesion, activation and thrombus formation [32, 33]. Therefore, effective anti-platelet therapy is strongly recommended during and after stent implantation. The awareness of the potential for late and very late ST has prompted a shift towards prolonged (12 months or more) duration of DAPT, which is in turn is associated with increased bleeding risk, entails increased costs and interferes with invasive and surgical procedures, if required.

11.5 The Pathology View

Different pathological mechanisms are associated with ST. The information on coronary vessel response after stent implantation was essentially derived from two sources – translational preclinical models and human autopsy series. Different factors are involved in the pathogenesis of early and late ST. Nakano et al. recently reported the histopathology features of early ST in 34 patients presenting with Acute Coronary Syndrome (ACS), who underwent an implant with BMS, first or second generation DES. Interestingly, the authors found that the underlying plaque morphology (prolapse of the necrotic core), the thrombus burden, medial tear and incomplete apposition were more frequently observed at the level of cross-sections containing thrombus compared with patent cross-sections in the same stent [34]. These findings support the concept that plaque morphology as well as procedural and mechanical-related factors play a role in acute/subacute ST. These pathological findings are also in line with the results of the previous angiographic and intravascular ultrasound (IVUS) studies which demonstrated that the presence of residual edge dissection and significant remaining stenosis in proximal and/or distal reference segments can significantly increase the risk of early ST [31].

Histopathology has also demonstrated delayed healing and incomplete endothelial stent coverage as the most

Fig. 11.1 Histology and OCT. (**a**) and (**b**) Magnified histology sections (Movat pentachrome stain) and corresponding OCT image (**c, d**) of a specimen of stented coronary artery with implant duration of 48 h. (**a**) Uncovered struts at 9 o'clock (*arrowhead*) and calcium deposition (*arrow*); (**c**) corresponding OCT image. (**b**) Thrombus deposition (*) on top of the uncovered strut at 6 o'clock and (**d**) corresponding OCT image
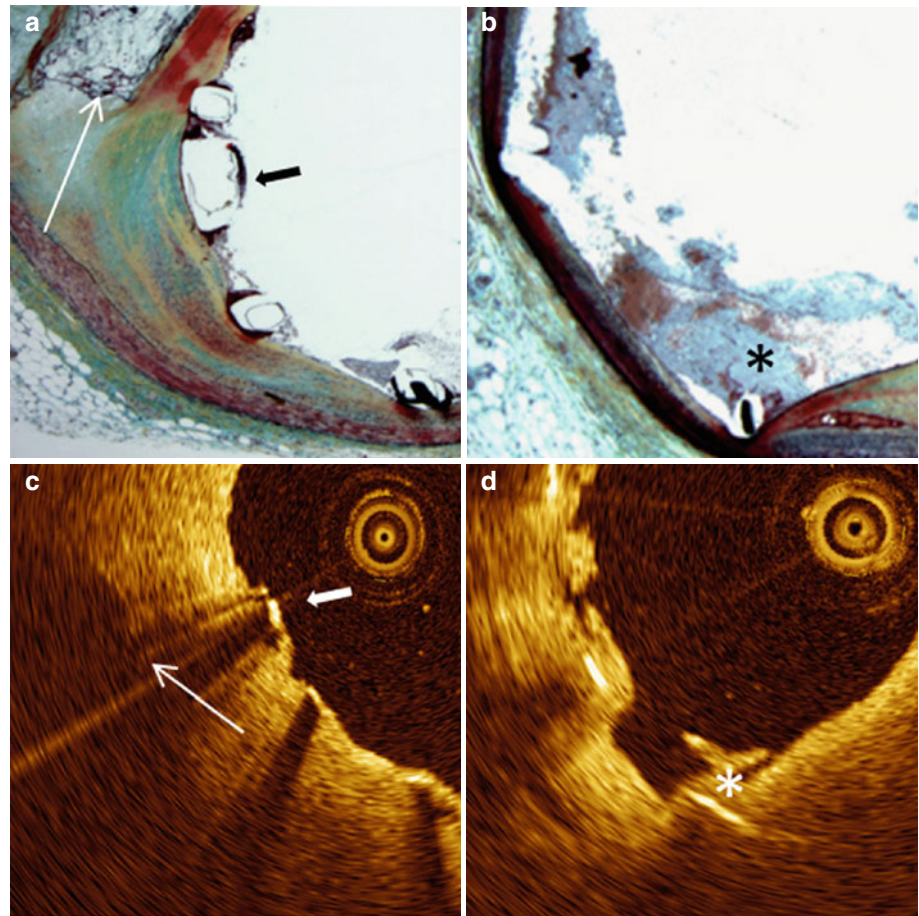
important factors for late ST after DES implantation [35, 36], (Fig. 11.1). These studies suggested hypersensitivity, with chronic inflammation and late acquired stent malapposition, as possible contributing factors [35–38]. In an *ex-vivo* study comparing DES vs. BMS cases of ST at different time points, endothelialization was nearly complete in BMS examined beyond 6 months, whereas incomplete endothelialization persisted in DES beyond 40 months [34]. More recently neo-atherosclerosis, characterized as clusters of lipid-laden foamy macrophages within the neointima, with or without necrotic core [39], has been identified as a frequent cause of late stent failure, including ST. Moreover, pathological reports have demonstrated that neoatherosclerosis is more common and occurs earlier with DES as compared to BMS [40].

ence of thrombus, rupture plaques, thin-cap fibroatheroma (TCFA) and pools of superficial macrophages [41, 42]. In addition, OCT provides superior details on the immediate results of stent implantation (vessel injury, tissue prolapse, stent malapposition and stent geometry distortion). Finally, OCT at the follow-up time is more accurate in assessing the remaining thrombus and the amount and type of tissue growing into the stent, discriminating between covered and uncovered struts, neointimal formation and newly developing atherosclerosis [42–44]. Based on these unique characteristics OCT can critically contribute to a better mechanistic understanding of the pathophysiology of ST and to the identification of surrogate markers, anticipating the risk.

11.6 The Role of Intravascular Imaging to Assess Stent Thrombosis

Intracoronary imaging techniques have been developed to provide complementary, more accurate measurements and details to coronary angiography in patients undergoing complex PCI. Compared with IVUS, OCT is superior in the assessment of unstable plaque features, including the pres-

11.7 OCT in Stent Thrombosis: Not All Stent Thrombosis Are Created Equal

The multi-factorial nature of ST and the high risk related to this event favors a fully informative, accurate assessment of the culprit lesion and vessel at time of acute presentation, through high resolution intravascular imaging modalities. Similarly to any acute MI, ST requires immediate thrombus removal and quick restoration of an

effective TIMI flow as the goals of primary interventions. After vessel recanalization, OCT may be used for guiding a more effective thrombus removal, via mechanical and/or additional pharmacological treatments. Further, OCT may help to recognize the stent-related factors (if any) responsible for ST (malapposition, under expansion, incomplete coverage, lipid laden neointima) and to select, based upon the imaging details, the most effective treatment to avoid recurrences. Indeed, while stent under-sizing, under-expansion and other suboptimal PCI results are usually observed in the acute/subacute ST cases, the main mechanisms involved in both late/very late ST are usually linked to the presence of uncovered stent struts and/or neoatherosclerosis.

11.8　How to Perform OCT in the Acute Setting of Stent Thrombosis

The planning for imaging in a patient arriving at the hospital with possible ST should start before the patient's arrival at the Cath Lab. If the patient was treated with stent(s) in the same hospital all clinical and procedural information (comorbidities, clinical presentation at the index procedure, stent type and size, eventually complications at the stent implant) has to be made available to the operator before primary PCI. In patients arriving with ST and TIMI 0–1 flow grade or large filling defect, thrombus aspiration is at the frontline of treatment for reestablishing the flow and allowing subsequent histopathology analysis of the aspirated thrombotic material. In this case thrombus aspiration has to be performed until coronary flow is reestablished and in any case before the OCT imaging pullback. It is relevant to the safety of the patient and equally relevant for having high quality OCT imaging, not to proceed with the OCT scan when the vessel is occluded with no distal flow or in the presence of an extremely high thrombus burden anticipated at the angiography views. Major arrhythmias and images unreadable due to the excess of remaining thrombus are the main reasons for adopting a dedicated strategy. In the presence of a large remaining thrombus the imaging catheter can be occlusive. One possible trick to anticipating if an OCT pullback can be performed with enough quality is a quick check in angiography with a few cc of contrast, maintaining the aspiration catheter at the culprit site. If the contrast passes freely the probability that it will not be occlusive with the image catheter is high and you may proceed with the OCT pullback. A combined use of IVUS and OCT when possible is recommended, since both imaging techniques may provide complementary data on mechanisms of ST. In these cases it seems wise to start with IVUS, since no contrast flushing and no selective coronary intubation is required. IVUS may add unique information on vessel remodeling that cannot be provided by OCT. It is important to remember that OCT imaging may increase the overall amount of procedural contrast. In the presence of hemodynamic instability, frequently observed during ST, the total amount of contrast needs to be strictly monitored. When flow is reestablished the operator should take time to analyze the imaging data, understand the main causative mechanism and the possible contributing factors and to tailor the treatment strategy. Since the time interval between the baseline assessment and the final post-intervention pullbacks can be wide, the OCT catheter should be maintained wet in saline solution to avoid fibrin deposition on the imaging element and contrast medium crystallization.

11.9　Information Provided by OCT

11.9.1　Thrombus Assessment

OCT is able to assess the presence and type of thrombus and the effectiveness of coronary thrombus removal through mechanical and or pharmacological interventions. With OCT, intracoronary thrombus is identified as any abnormal mass protruding into the lumen, with a sharp gap in the underlying tissue, signal backscattering and various degrees of attenuation. White thrombus is characterized by homogeneous signal rich with low-backscattering attenuation, while red thrombus, that contains red blood cells and a network of fibrin, is defined by a highly backscattering and highly attenuated light signal (resembling blood). The presence of a large amount of residual thrombus may preclude a reliable assessment of strut coverage (Fig. 11.2). In these cases additional potent pharmacologic agents, such as GP IIb/IIIa receptor blockers, can be used to allow an accurate assessment of the underlying stent, and to detect possible segmental malapposition or consecutive frames with largely uncovered struts (Fig. 11.3).

11.9.2　Inadequate Stent Implantation

Inadequate stent implantation can be due to a mismatch between lumen dimensions and the selected stent size, or be the consequence of stent under expansion in spite of an adequate stent/artery ratio. Providing automatic lumen profile measurements, novel OCT systems allow for the online detection of inadequate stent implantation.

In a small-scale OCT study evaluating patients with subacute ST [45], a smaller minimal stent area was observed in these patients compared to the uneventful controls, with minimum stent area preferentially located at the thrombus site, indicating stent under expansion as a possible mechanism of
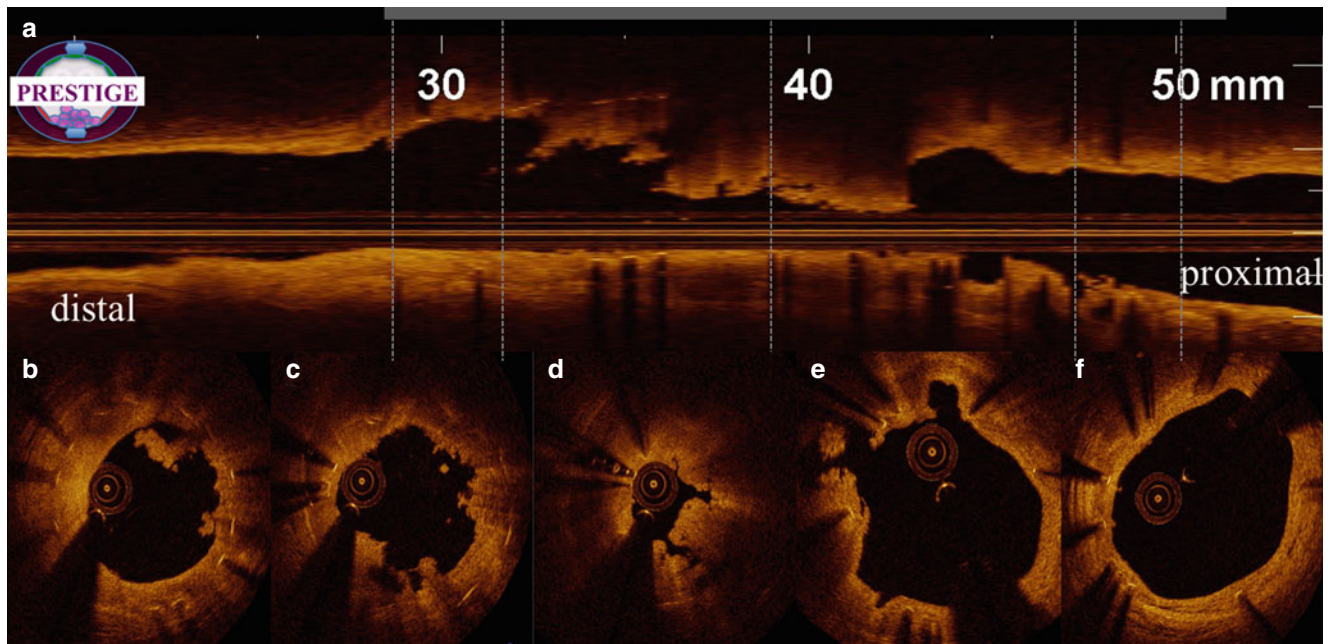
Fig. 11.2 Large amount of residual thrombus after manual thrombus aspiration. OCT longitudinal view (**a**) and multiple cross-sections (**b**–**f**) images during a ST case after thrombus aspiration. Large residual thrombus remained inside the stent (**b**, **c**, **d**). Struts are clearly visible due to shadowing. Proximal (**f**) and distal (**b**) sections indicate complete strut coverage. White thrombus mainly in (**b**, **c**), mixed thrombus in (**d**)

early ST. In addition, the percentage of both uncovered and malapposed struts was significantly higher at the thrombus site compared with their respective control patients.

Illustrative Case 1

Stent Under-Expansion as Primary Cause of Late Stent Thrombosis

A 60 years-old patient underwent a complex PCI procedure on a highly calcified right coronary artery (RCA), requiring rotational atherectomy (Fig. 11.4). Five years later the patient was admitted with diagnosis of inferior STEMI. Coronary angiography revealed an in stent thrombotic occlusion of the RCA. After wire crossing and thrombus aspiration, OCT and IVUS pullbacks were performed. IVUS showed a large amount of residual thrombus and severe stent under expansion at the culprit segment. OCT pullback confirmed stent under expansion in the absence of any uncovered/malapposed struts or abnormal neointima (Fig. 11.5). Severe under expansion was treated with larger balloons and a short EES implanted at high pressure. Final intracoronary imaging confirmed an adequate acute gain in the previously unexpanded stent segment (Fig. 11.6).

11.9.3 Incomplete Stent Apposition

There is increasing interest in the role of incomplete stent apposition (ISA) as a causative factor of ST. ISA is normally defined as the separation of one or more stent struts from the arterial wall, with evidence of blood speckles behind the strut, in the absence of any side branch. According to the time of occurrence, ISA is labeled as acute (post-procedure), persistent (diagnosed at post-procedure and still present at follow-up), and acquired (not present at post-procedure but identified at follow-up). In the absence of any intravascular imaging assessment at the index procedure, ISA is usually classified as late incomplete stent apposition. The role of stent malapposition in the pathogenesis of late ST has been continuously debated advocated as a possible causative factor in some studies and neglected in others. Cook et al. reported an increased incidence of stent malapposition and positive vessel remodeling in patients presenting with very late ST after first generation DES, compared with uneventful controls [46]. ISA was detected in 77 % of patients with very late ST with a wide area of malapposition. Similarly, in a study conducted by Guagliumi and coll. on consecutive cases of late and very late ST assessed with OCT, stent malapposition was observed in 78 % of the all cases, with maximal area of malapposition significantly greater compared to the uneventful matched controls [43]. Recently, the "Mechanism Of Stent Thrombosis" MOST study also demonstrated a three times higher rate of malapposed struts in patients with late ST as compared to controls [45]. Late acquired ISA may essentially be due to two different mechanisms: (a) positive vessel remodeling, as a marker of vessel toxicity in response to the drug and or to the polymer; (b) resolution or reabsorption of a pre-existing soft plaque or thrombus behind the stent struts.
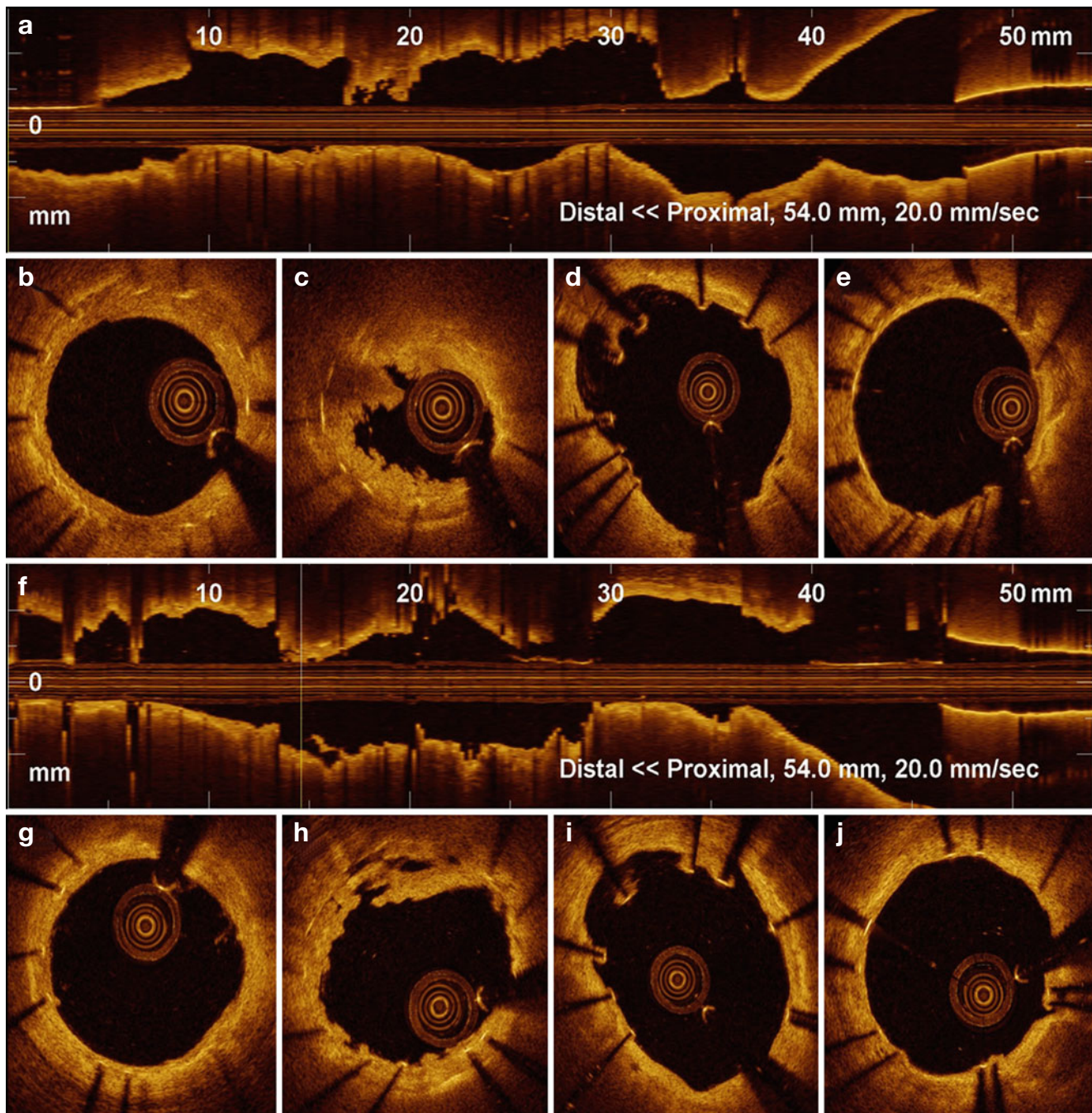
Fig. 11.3 OCT in Late Stent Thrombosis, Immediately After Thrombus Aspiration. OCT Longitudinal view (**a**) and multiple cross-sections (**b–e**) images obtained in very late stent thrombosis, immediately after manual thrombus aspiration. Large residual thrombus is observed inside the stent, dominantly white in signal characteristics (**c**). Struts malapposition can be observed (**d**). Same vessel after intracoronary injection of GP IIb/IIIa inhibitors. A substantial reduction of the remaining thrombus can be recognized in long (**f**) and cross-sectional (**h**) images. Incompleteley apposed stent struts can be identified in the cross sections proximal to thrombus burden (**d, i**). Healthy looking distal (**g**) and proximal (**j**) stent segment

Illustrative Case 2
Persistent Malapposition as Causative Factor of Stent Thrombosis

Brief summary: Two everolimus-eluting-stent (EES) were implanted to treat an occluded left descending coronary artery (LAD) during an anterior STEMI. The proximal stent was bordering a small aneurysm (arrow, Fig. 11.7). After 4 years, the patient was urgently hospitalized due to a recurrent anterior STEMI. Coronary angiography showed a thrombotic occlusion at the stent entrance. After wiring the occluded vessel and an effective manual thrombus aspiration, coronary angiography displayed only a small filling

Fig. 11.4 Coronary angiography at the index procedure. (**a**) Rotational atherectomy at mid RCA. (**b**) Optimal result after DES implantation
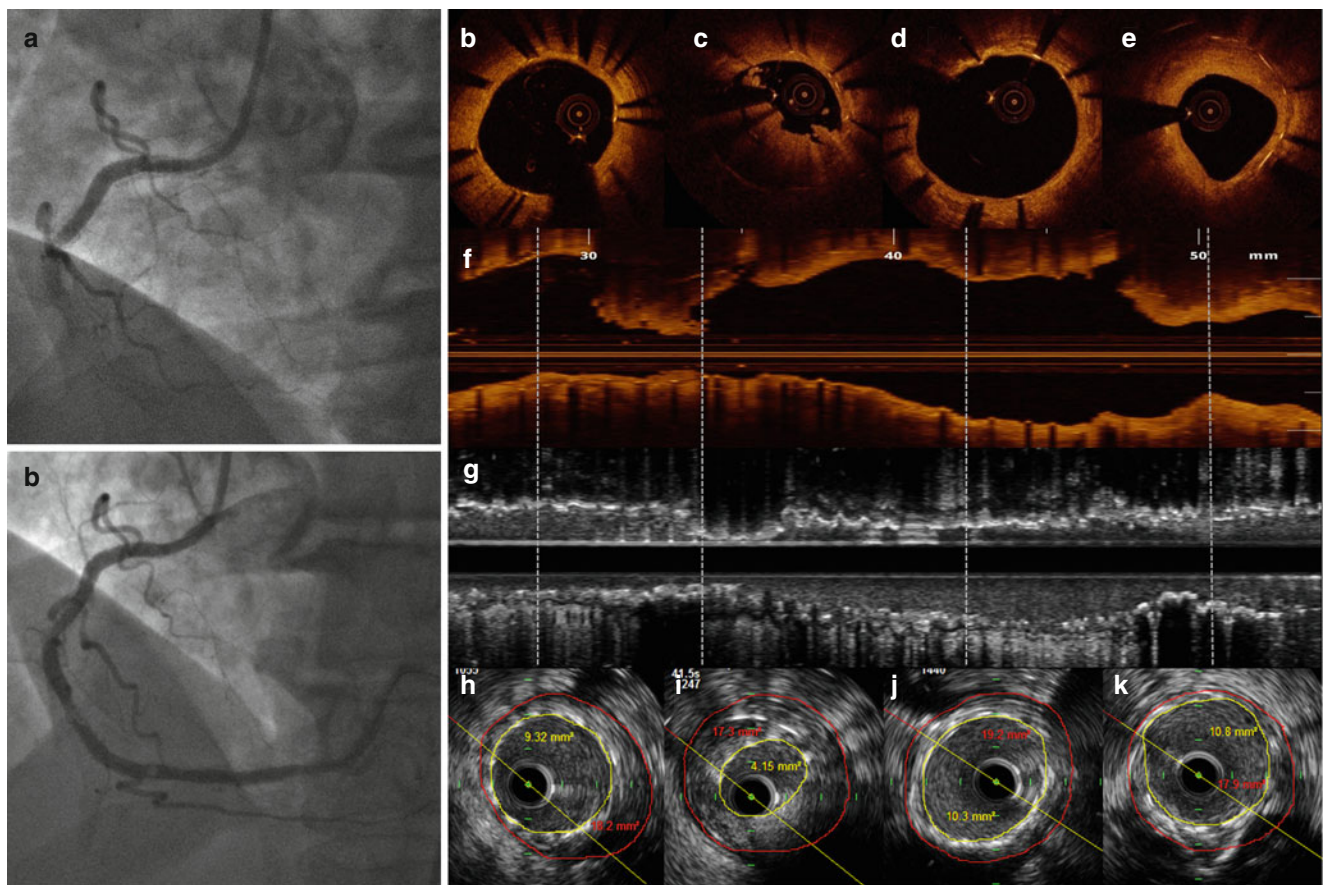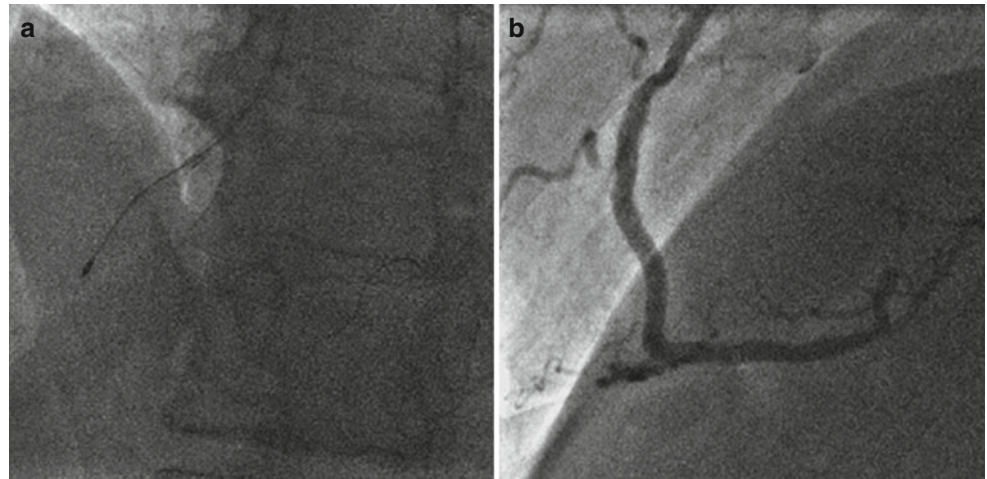
Fig. 11.5 OCT and IVUS findings at time of very late ST. (**a**, **b**) coronary angiography showing stent thrombosis at mid RCA (**a**) and lumen profile after reestablishing of the vessel patency with thrombus aspiration (with small persisting filling defects). (**b**, **d**, **e**) OCT cross sectional views at multiple levels. Distal and proximal stent segments demonstrated complete strut coverage, no malposition and only mild tissue deposition (**e**). (**c**) OCT cross section with stent under-expansion at the site of protruding thrombus, remaining after manual aspiration. The thrombus was not detected at the corresponding IVUS section (**i**). (**f**, **g**) Longitudinal OCT and IVUS views. Distal (**h**) and proximal (**j**, **k**) to the culprit lesion (**i**) IVUS cross sectional images, show good stent expansion and moderate vessel remodeling

defect, with irregular borders at the level of a small aneurysm (Fig. 11.8). An IVUS pullback, sequentially performed after OCT, excluded the presence of positive vessel remodeling, confirming the persistent nature of malapposition. Large malapposition associated with lack of coverage was identi-fied as the causative mechanism in this EES ST (Fig. 11.9). To further expand the entrance of the existing stent, and pro-mote the strut coverage in this small aneurysm, a large BMS was implanted at malapposition site and finally expanded at high pressure (Fig. 11.10).

Fig. 11.6 IVUS and OCT assessment post-treatment. (**a–e**) IVUS and (**f–j**) OCT multiple cross-sectional views. Large MLA, even at site of multiple strut layers
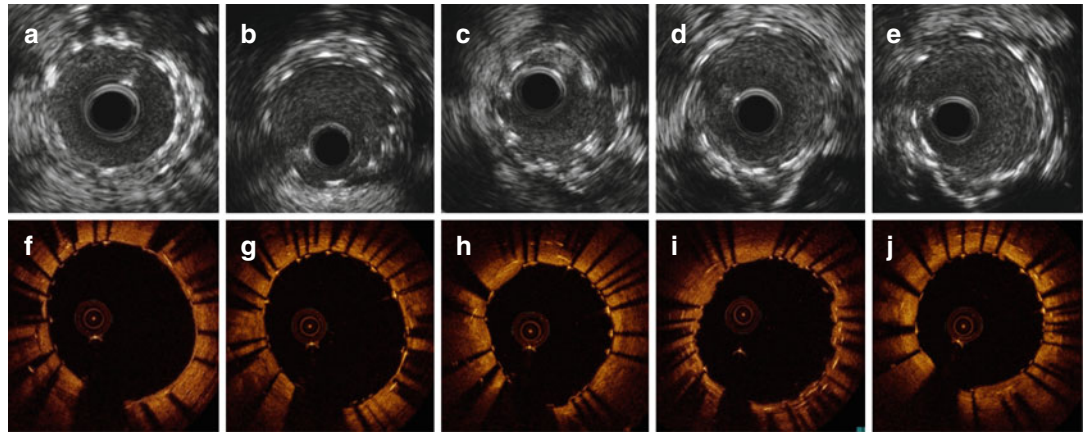
Fig. 11.7 Index primary PCI on LAD during an anterior STEMI. (**a**) Coronary angiography at the index procedure (primary PCI) with LAD occlusion. A small aneurysm was visible (*arrow*) immediately before the occlusion point. (**b**) Coronary angiography immediately after stent implantation with a reestablished lumen profile and effective coronary flow. (**b'**) Magnification at the stented segment with evidence of contrast staining bordering the small aneurysm (*arrow*)
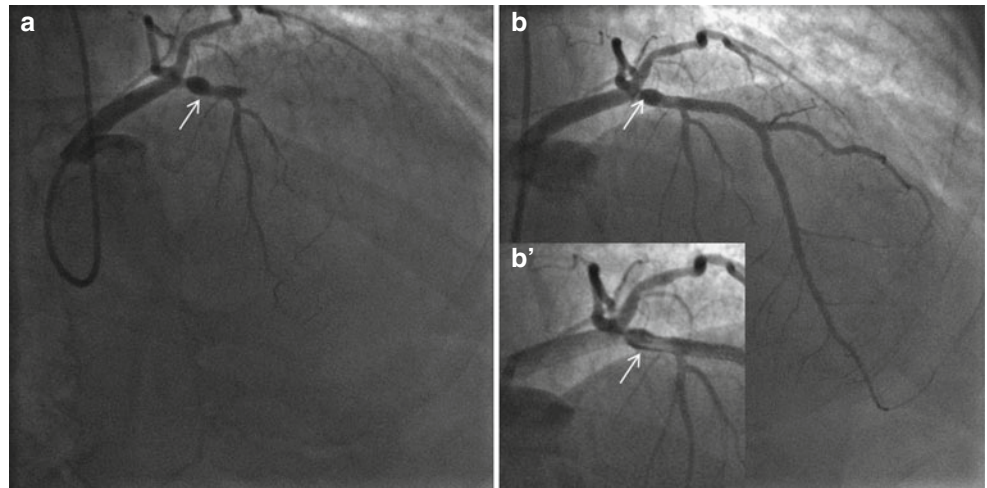
Fig. 11.8 Coronary angiography performed during very late ST. (**a**) Coronary angiography showing an in stent thrombotic occlusion. (**b**) After thrombus aspiration and restored vessel patency. (**b'**) Magnification at proximal LAD after thrombus aspiration: persistent haziness at the level of the aneurysm located at the stent entrance (*arrows*)
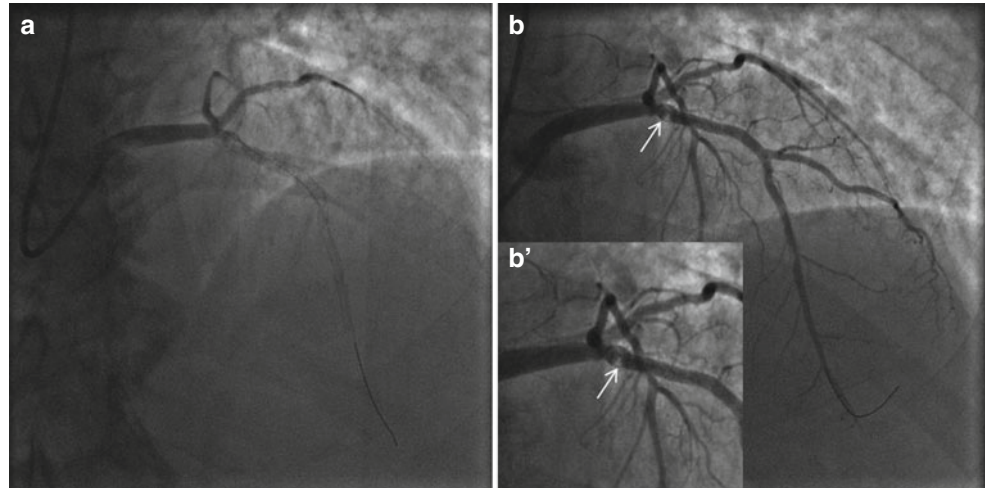
This case shows some of the issues with stent implantation during acute myocardial infarction, when the presence of thrombus and the increased vasoconstriction make difficult the stent size selection and the identification of the proper landing zone, facilitating stent malapposition to remain undetected by angiography. In such cases a large seg-ment of malapposed/uncovered struts may persist asymptomatic for years until a triggering factor may precipitate ST.

Finally, as demonstrated by Gutierrez-Chico and coll., the larger the acute malapposition, the greater the likelihood of persistent malapposed segments at FU and delayed healing [47].
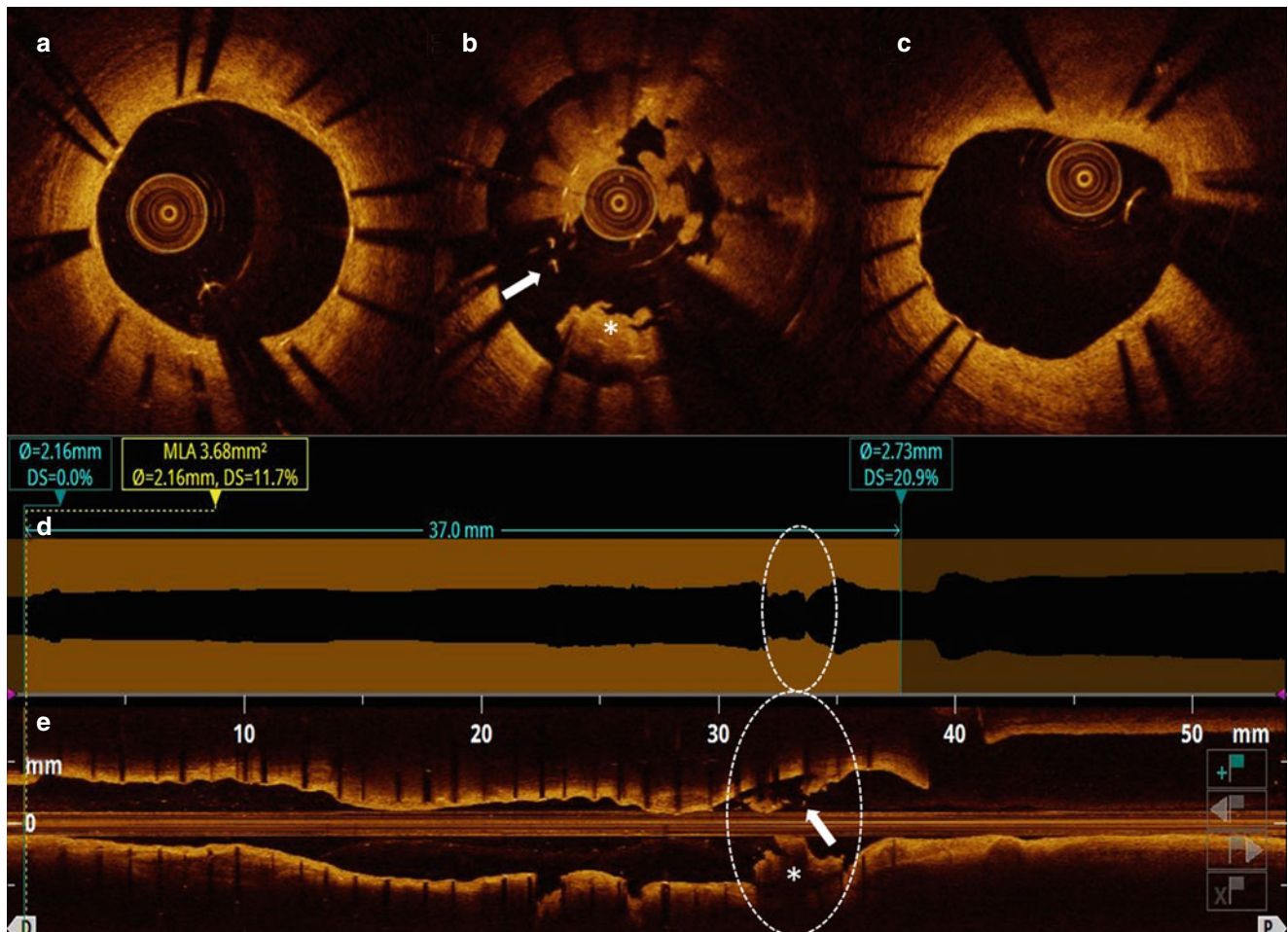
Fig. 11.9 OCT longitudinal and cross-sectional views after thrombus aspiration. Cross-sectional views: (**a**, **c**) optimal healing and coverage of the stented segment at both distal and proximal sites. (**b**) Cluster of grossly malapposed and uncovered struts (*arrow*) with large remaining thrombus (*). Automatic lumen border detection (**d**) and long view (**e**) showing overall uniform and good stent expansion, except for the segment at the aneurysm level (*circle*)

Illustrative Case 3

Acquired Malapposition in Current Generation DES as Cause of Stent Thrombosis

A 50 year old man presented with an anterior STEMI and cardiogenic shock. The proximal LAD was then treated by implantation of a 3.5/24 mm everolimus eluting stent (Fig. 11.11). Two months later, despite an adequate DAPT, the patient experienced recurrent chest pain and was admitted with diagnosis of non ST elevation myocardial infarction (NSTEMI). Coronary angiography revealed invariable stenosis in the left circumflex artery (LCX) and a barely noticeable in stent hazy lesion in the previous stented LAD. Fractional Flow Reserve (FFR) investigation of LCX resulted in a non-ischemic value. OCT revealed uncovered and malapposed stent struts, and a luminal protruding mass combining the characteristics of both organized and fresh thrombus (Fig. 11.12). The diagnosis of late ST as the culprit lesion was therefore made. Interestingly, the MULTIPLATE analyzer testing platelet reactivity revealed sufficient platelet inhibition by ongoing therapy. Thus the hypothesis of persistent or acquired ISA, was considered as the possible substrate for this complication. Application of high pressure balloon (4.5/12 mm at 20 atm) dilatation resulted in a larger cross-section area and corrected stent apposition (Fig. 11.13).

This case illustrates that secondary thrombus resolution in the contest of STEMI may cause ST due to acquired stent malapposition even in patients responsive to DAPT therapy. The use of OCT helped in the identification of mechanisms underlying ST and guided a customized treatment with a high pressure balloon dilatation. Combined use of imaging technology with platelet reactivity tests are sometimes needed to detect the mechanism underlying ST events.

ISA after stent implantation may also present with acquired in-stent aneurysm(s) formation and largely uncovered/malapposed struts. This results mainly from a toxic reaction to a drug and/or polymer creating extensive coronary wall inflammation with in stent extra-cavities formation. The segment involved has a significant damping of the
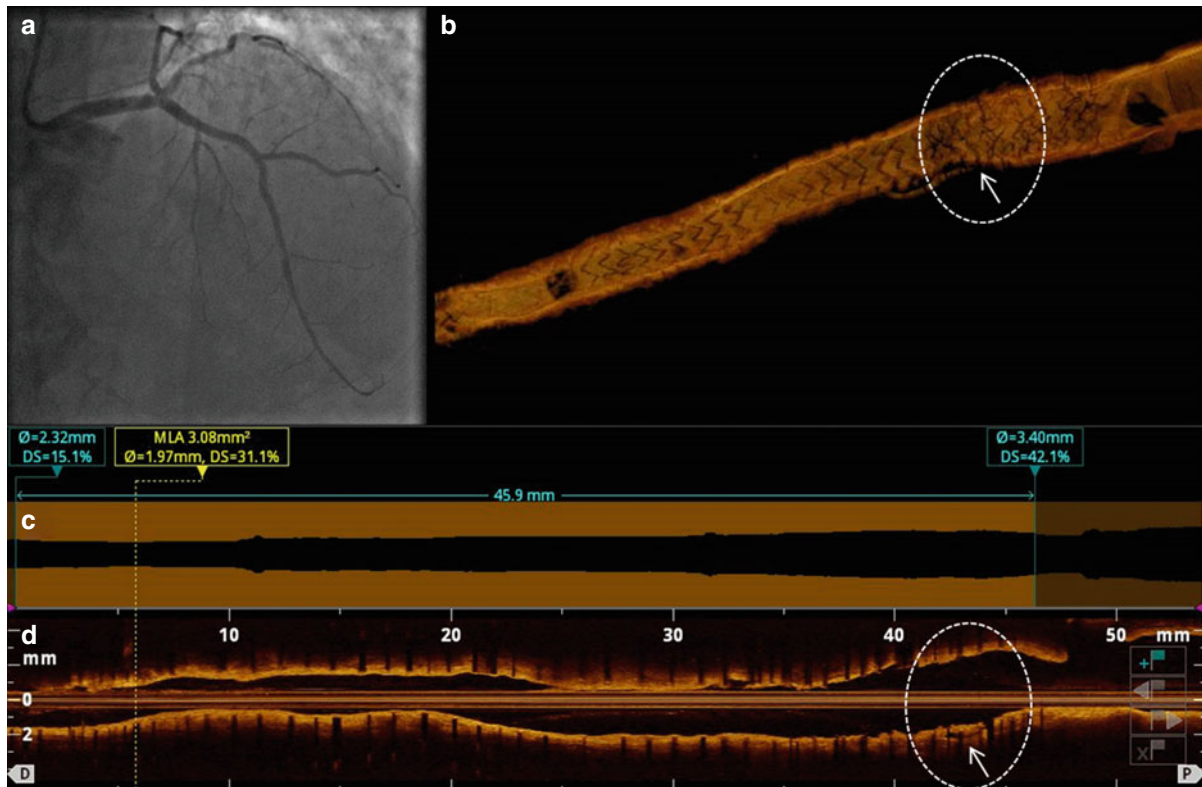
Fig. 11.10 OCT pullback after BMS implantation at the malapposed site. Coronary angiography (**a**) and OCT at post-treatment. The 3D OCT reconstruction (**b**), automatic lumen profile (**c**) and longitudinal view (**d**) confirmed optimal stent expansion with no residual malapposition (*arrow*) in the segment of interest (*circle*)

Fig. 11.11 Baseline procedure. (**a**) Coronary angiography during index primary-PCI showed thrombotic occlusion of left anterior descending artery (*arrow*). (**b**) Coronary angiography after stent implantation showing acceptable result
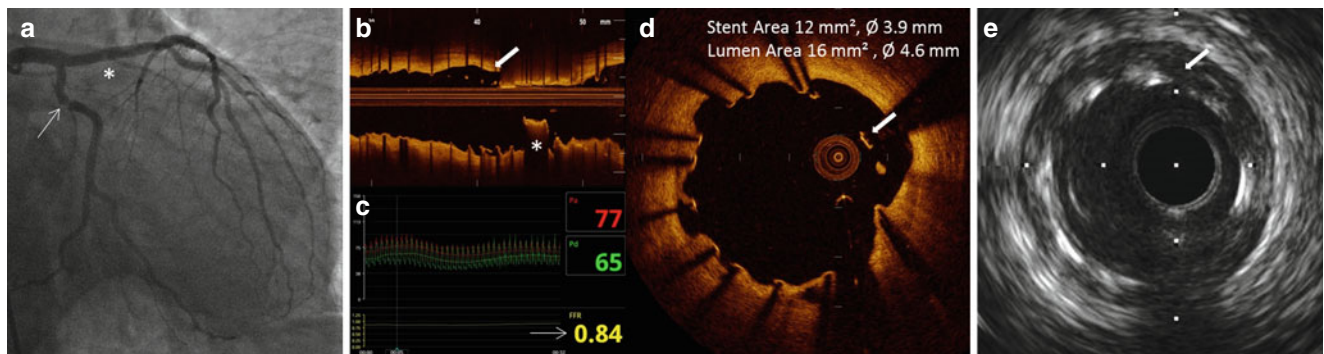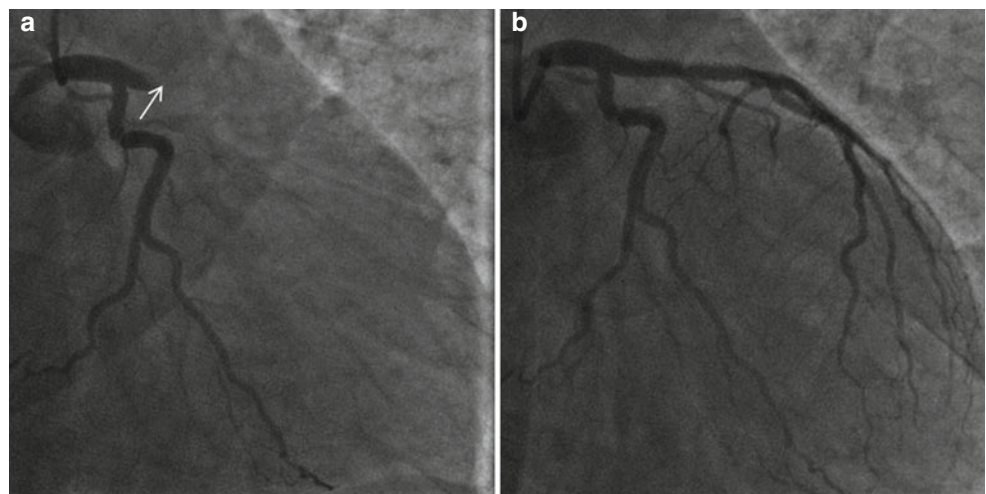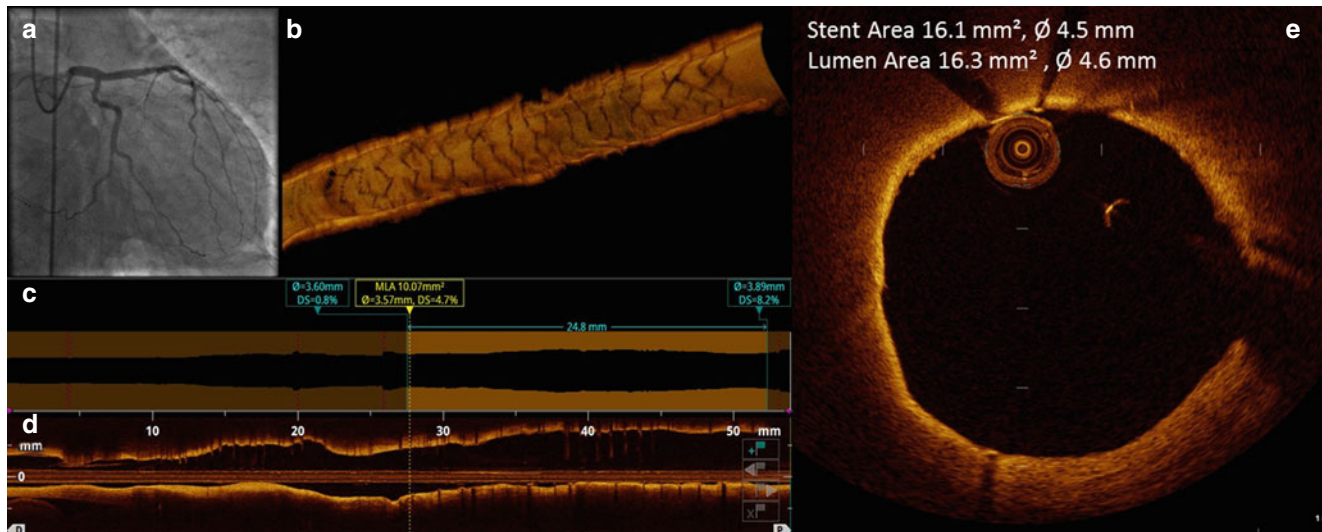
Fig. 11.13 OCT pullback after high pressure dilatation. (**a**) Final coronary angiography demonstrated good angiographic results of high pressure balloon dilatation. (**b**) 3D OCT reconstruction showed perfect result with optimal stent strut geometry; (**c, d**) Lumen profile tool and longitudinal reconstruction did not revealed residual stenosis and stent edge dissection after high pressure balloon stent expansion. (**e**) Cross-section analysis at the proximal stent edge showed resolution of the strut malapposition

optical signal (dark segmental appearance) compared to the uninvolved segments that normally have a mature neointima. These aspects were recently substantiated in an OCT study assessing different degrees of maturity on top of the stent struts, in various preclinical and clinical contexts (*ex-vivo* animals and humans, and *in-vivo* animals and humans) [48].

Illustrative Case 4
Very Late Stent Thrombosis due to Late Acquired Malapposition
Fifty-seven years old male presenting with multi-vessel coronary artery disease was treated with PCI and two PES implanted in overlap on the proximal LAD. Three years later the patient was readmitted for an anterior STEMI in cardiogenic shock complicated by cardiac arrest. Emergency angiography, under external cardiopulmonary resuscitation, documented very late ST on the proximal LAD, prompt balloon dilation immediately restored vessel patency. Extracorporeal support (ECMO) was immediately initiated. A few days later, with haemodynamic stability, an OCT pullback displayed the presence of an acquired in-stent aneurysm with extra-cavities around the entire circumference of the vessel, and largely uncovered and malapposed struts (Fig. 11.14). As treatment, a PCI with a bare metal "stent in stent implantation" was performed in an attempt to promote strut coverage and seal these extra-cavities. The patient was then discharged on the 30th day with complete left ventricular

function recovery. At the 6 months OCT follow-up a complete sealing of the in-stent aneurysm with homogeneous stent coverage was observed (Fig. 11.15).

11.9.4 Uncovered Struts

Uncovered struts, the most important pathologic predictor of late and very late ST following DES placement, can be identified by OCT with high specificity, [49]. However, the sensitivity of OCT in detecting uncovered struts is reduced when fibrin and inflammatory cells are present around the struts. Uncovered struts are an indirect marker of delayed stent healing and poor endothelialization, more frequently observed in DES compared to BMS, [50]. Uncovered struts detected by OCT in DES may persist for several years and, in line with pathology data, may be an independent factor for predicting late and very late ST [43]. Compared with matched uneventful patients, ST patients showed a significantly higher percentage of uncovered struts and a higher number of sections with >30 % uncovered struts. Interestingly, the length of the segment with consecutive uncovered struts was the only OCT predictive factor for ST selected at the multivariate analysis. Similarly, the MOST [45] study demonstrated that the number and percentage of uncovered stent struts were particularly high at the site of ST, with similar values to pathological findings. However, it is still unknown

Fig. 11.12 Angiographic and OCT findings of late stent thrombosis. (**a**) Coronary angiography shows an area of haziness inside the EES previously implanted in the left anterior descending artery (*), and a tight focal stenotic lesion in mid circumflex artery (*arrow*). (**b**) Longitudinal reconstruction after thrombus aspiration revealed the thrombotic nature of the intraluminal hazy lesion (*). (**c**) FFR performed on circumflex artery was negative (**d**) close review of cross-section OCT reveals clusters of uncovered and malapposed struts. (**e**) IVUS pullback revealed absence of positive vessel remodeling and free space behind stent struts
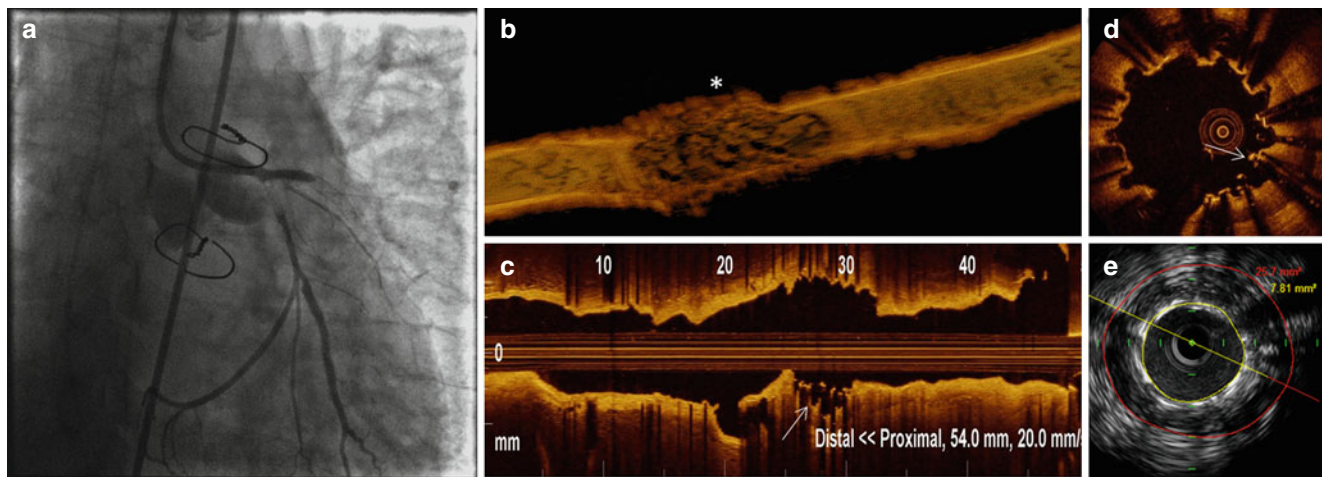
Fig. 11.14 Coronary angiography, OCT and IVUS during very late ST with cardiac arrest. (**a**) Coronary angiography during cardiac arrest showing thrombotic occlusion of proximal LAD and LCX. (**b**) 3D OCT reconstruction after primary-PCI and hemodynamic stabilization revealed a segmental in-stent aneurysm at site of overlap (*asterisk*). (**c**, **d**) Long view OCT and cross section analyses showed clusters of uncovered and malapposed struts (*arrow*). (**e**) IVUS pullback confirmed large positive remodeling at the stent overlap, (*arrow*).
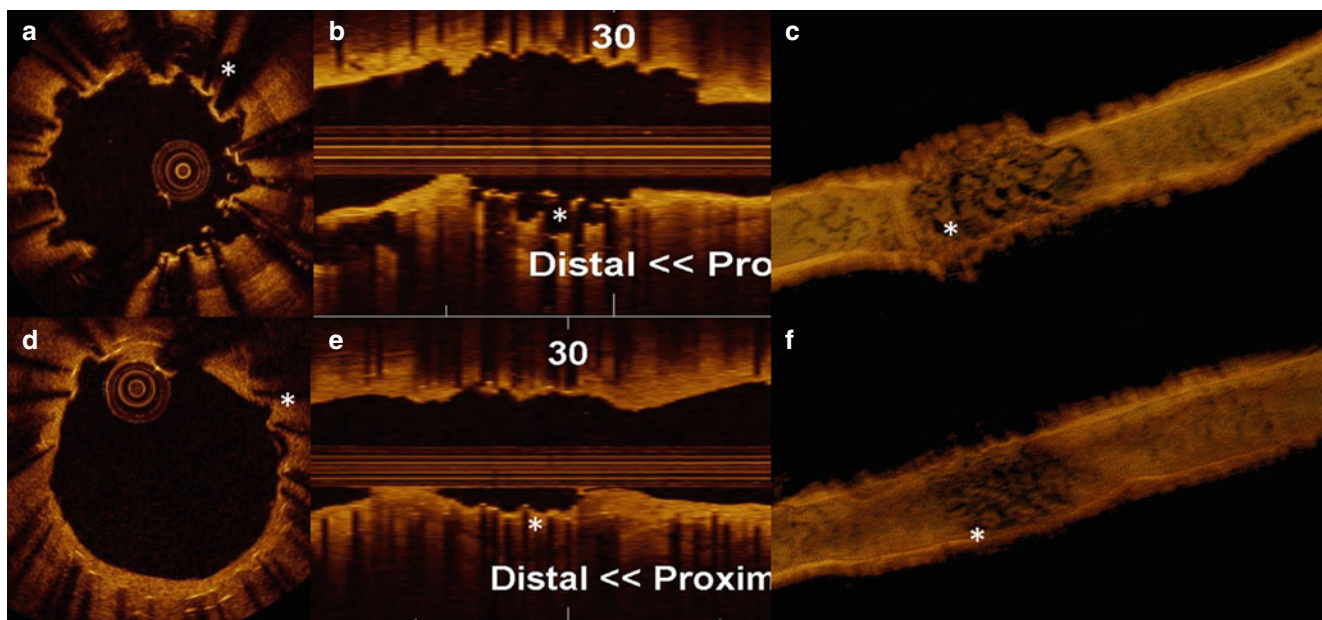
Fig. 11.15 Post PCI with BMS OCT Findings after very late ST. (**a–c**) cross section, longitudinal and OCT 3D reconstruction after very late ST with localized in-stent extra cavities and largely uncovered/malapposed struts at the stent overlap (*asterisk*). (**d–f**) OCT findings 9 months after focal BMS implantation (*asterisk*). showing sealing of the in-stent extra-cavities with complete strut coverage

which extent of lack of struts coverage promotes ST and should be considered unsafe. In the absence of any additional factor(s), the presence of uncovered struts is probably acting only as a risky substrate, requiring a precipitating factor to trigger thrombus formation, [51]. This hypothesis has been substantiated by the fact that many uncovered stents remain asymptomatic for years. Coverage of the stent struts depends also on the underlying plaque composition. Lüscher et al. demonstrated that DES implantation in lesions with a large necrotic core might result in delayed endothelialization or absent healing [52]. This observation is consistent with the

OCT finding reported by Guagliumi et al. which showed that acute coronary syndrome at the index procedure was more frequently observed in patients with ST as compared with the controls [43].

Uncovered struts may be found in several circumstances:

(a) Uncovered struts due to malapposition to the vessel wall at time of initial implant
(b) Uncovered struts due to acquired malapposition, secondary to positive vessel remodeling
(c) Uncovered struts in the presence of a stent completely apposed to the vessel wall (inadequate healing)
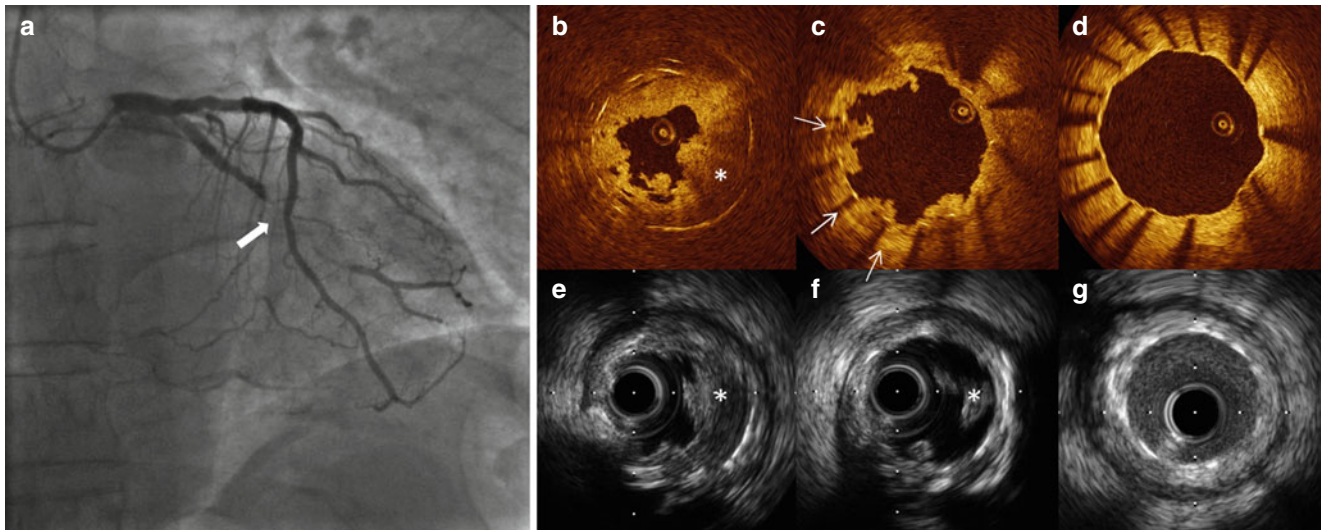
Fig. 11.16 Role of isolated uncovered struts promoting ST. (**a**) Coronary angiography after thrombus aspiration (*arrow*); (**b–d**) cross sections substantiate stent thrombotic occlusion (**b** *), thrombus attached on top of uncovered stent struts (**c**-*arrows*); (**d**) uniform tissue coverage of the stent in the proximal segment. (**e–g**) corresponding IVUS cross-sections obtained with contrast flushing to enhance lumen visualization with no evidence of positive remodeling

The association with different types of malapposition has already been discussed and presented in prior clinical cases. The following figure reports a clinical example of the role of isolated uncovered struts promoting ST even in the presence of a stent completely apposed to the vessel wall (Fig. 11.16).

11.9.5 Neoatherosclerosis

Neoatherosclerosis is pathologically recognized as clusters of lipid pools within the neointima, representing the entire spectrum from lipid rich plaque with or without necrotic core, to TCFA with foamy macrophages, to plaque rupture and calcium deposition [40]. Optical imaging techniques contributed in a substantial way to the identification and characterization of this abnormal neointima growth as a possible causative factor for ST. With intracoronary angioscopy, Higo et al. observed a 35 % increase of intra-stent yellow neointima, 10 months after DES implantation and hypothesized that neoatherosclerosis within the stent might serve as a possible substrate for late ST [53]. At OCT images, lipid-laden neointima, compared to non-lipid stent segments, is more frequently associated with intimal disruption, neovascularization and thrombus formation, all possibly implied in late ST [54]. Guagliumi et al. found that in 17 % of late/very late ST in DES patients (median time from initial stent implant being 20 months) neoatherosclerosis was the likely mechanism [43]. Kang et al. recently demonstrated from a series of 33 patients suffering from very late ST that neoatherosclerosis was the primary mechanism in almost 70 % of patients (median time from initial stent implant being 62 months), while malapposition was observed in only 25 % of all cases [44]. The frequency of the in-stent neoath-

erosclerosis is time dependent and is not normally observed as a consistent finding until approximately 1.5–2 years post-DES implantation [55].

Illustrative Case 5
Very Late Stent Thrombosis due to Neoatherosclerosis
A 63 year old male previously treated with two PES on LCX-OM, and LAD was readmitted 4 years later for NSTEMI. Coronary angiography showed a complete occlusion of both the LCX and OM branches (Fig. 11.17). After manual thrombus aspiration, OCT pullback revealed an heterogeneous vessel response in the stents implanted in the LCX. In-stent segments with lipid laden neointima with segments presented a lack of tissue coverage. More specifically, lipid laden neointima presented patterns of light attenuation and bright lines with an important shadow suggestive of foamy macrophage accumulation at the culprit segment (Fig. 11.18). A current generation DES was implanted in the segment with significant stenosis, but not the whole segment that presented lipid laden neointima (Fig. 11.19).

Despite the fact that neoatherosclerosis is a well-known phenomenon in first generation DES, recent reports have demonstrated that this in stent abnormal tissue proliferation may also be involved in new generation DES [56].

11.9.6 Other Mechanisms Involved in Stent Thrombosis

ST may be also the consequence of other mechanisms including disease progression at the stent edges, plaque rupture underneath the stent, poor responsiveness to DAPT, or a combination of multiple causative factors.

Fig. 11.17 Coronary angiography at time of very late stent thrombosis. (**a**) Coronary angiography: in stent thrombotic occlusion of the marginal obtuse branch (*arrow*); (**b**) After thrombus aspiration and restoration of vessel patency
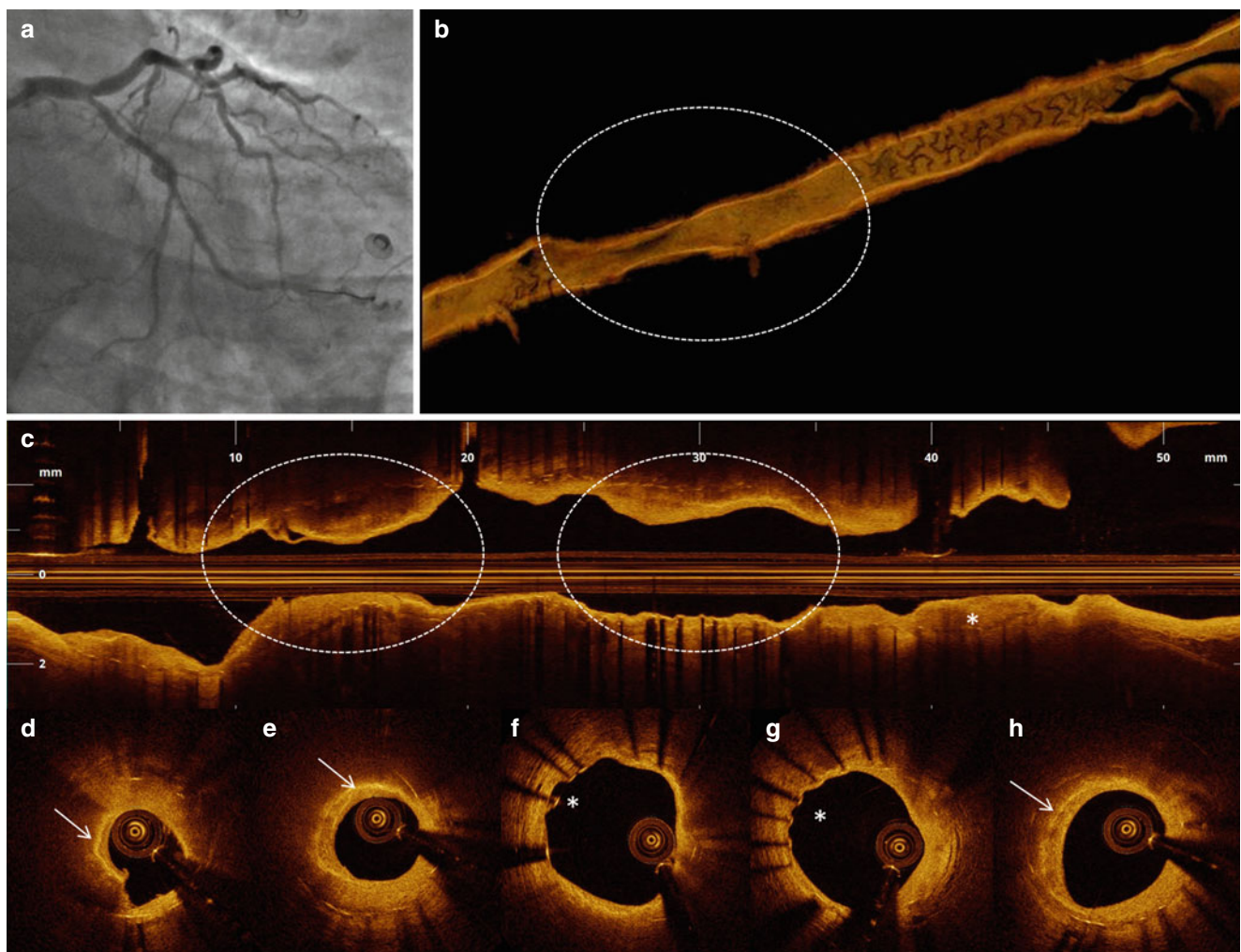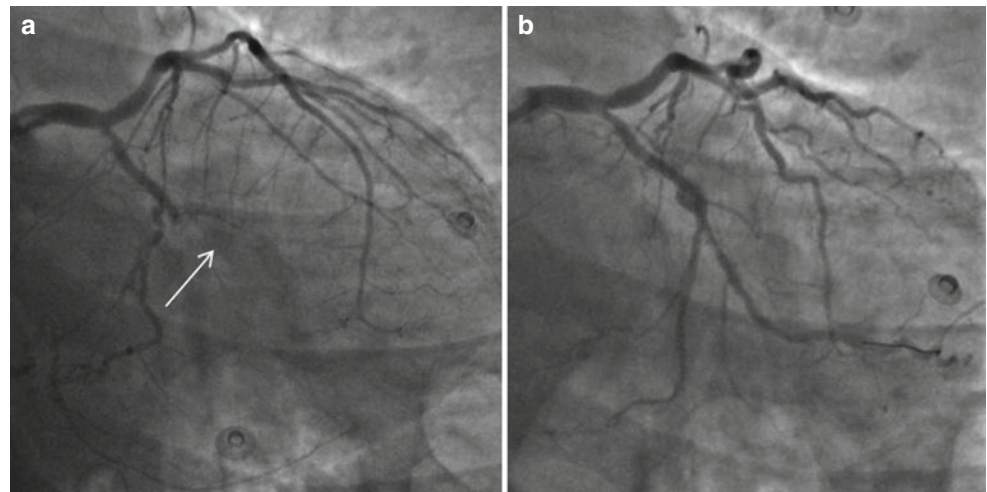
Fig. 11.18 OCT findings of the in-stent neoatherosclerosis. (**a**) Coronary angiography after thrombus aspiration; (**b**, **c**) 3D and Longitudinal OCT view displayed multiple in-stent segments infiltrated by lipid laden neointima (*circle*). Cross sections substantiate different patterns of coexisting lipid infiltration within the stent lipid rich plaques (**d**, **e**, **h**), signals of foamy macrophage accumulation (**d**, **e**, **h**-*arrows*) and uncovered stent struts (**f**, **g**-*)
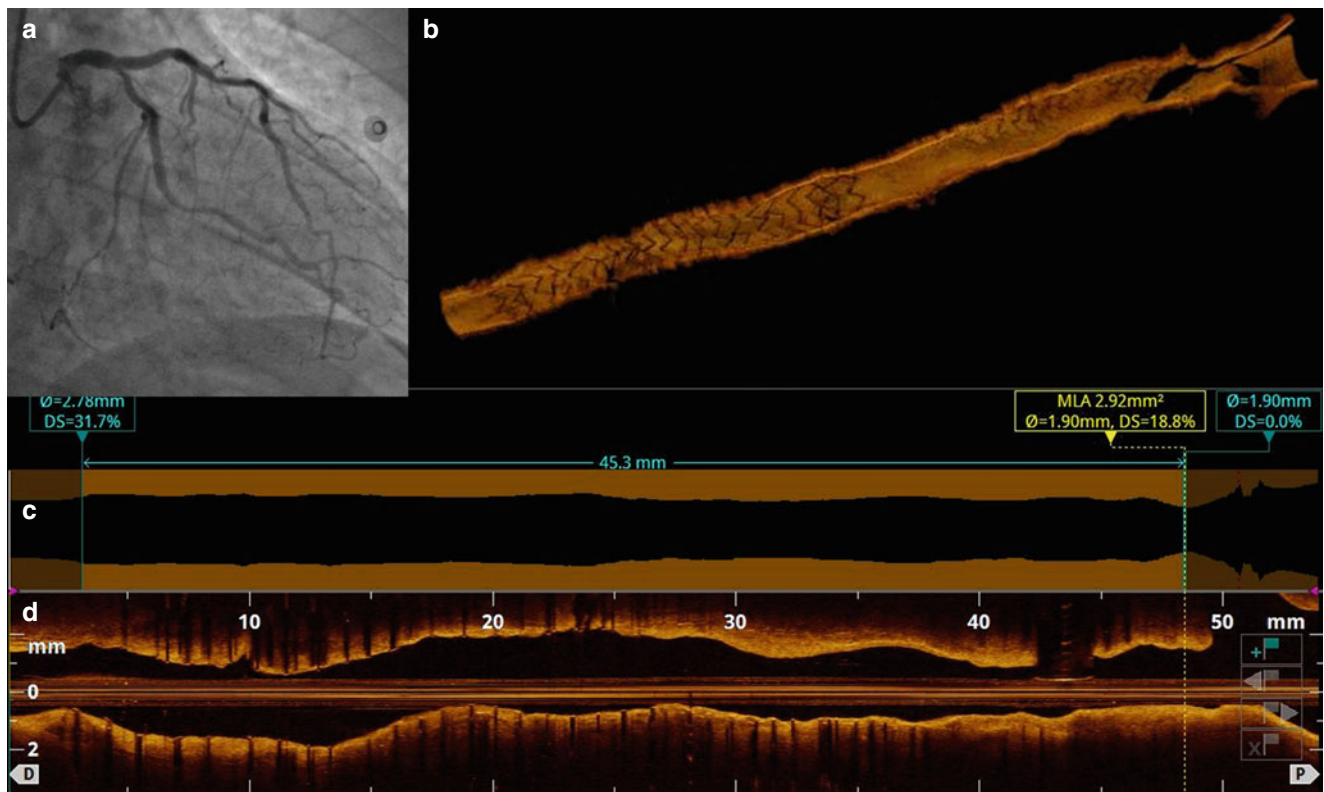
Fig. 11.19 Final angiography and OCT images after novel generation EES implantation. (**a**) Coronary angiography after the implantation of a current generation EES stent. (**b**) 3D OCT reconstruction with optimal stent strut geometry and no cell deformation; (**c**, **d**) automatic lumen border and longitudinal views displayed uniform stent in stent expansion, no residual stenosis and no stent edge dissection after high pressure stent expansion
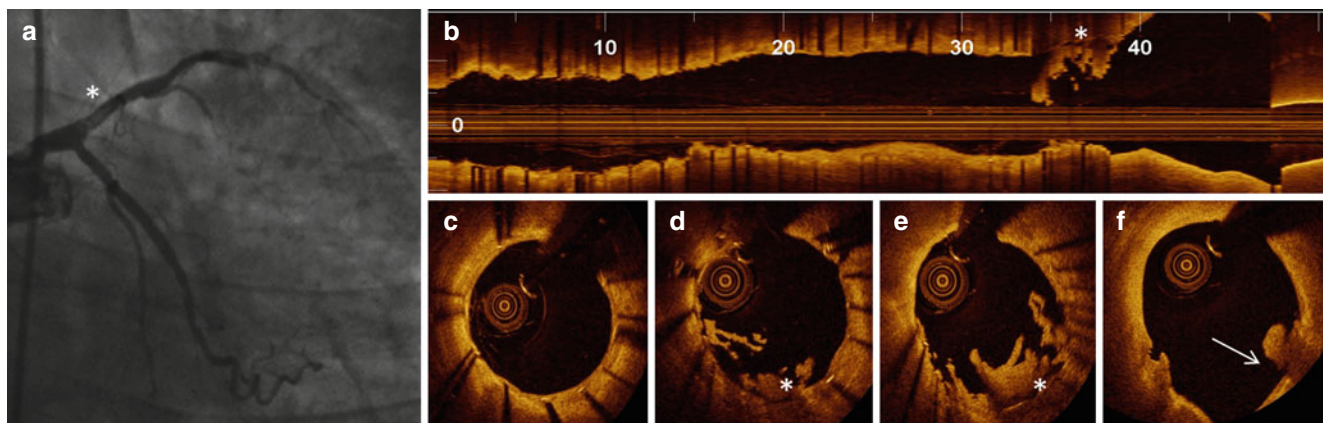
Fig. 11.20 Coronary angiography and OCT during very late ST. (**a**) Coronary angiography showing haziness and filling defect at the proximal LAD (* *asterisk*). (**b**) OCT longitudinal view: optimal result of the previously implanted PES with complete strut coverage and protruding thrombus at the LAD ostium (**asterisk*). (**d**, **e**) White thrombus tail extending into the proximal stent edge (*). (**f**) Ruptured plaque located at the ostium of the LAD at the stent proximal edge (*arrow*)

Illustrative Case 6
Rupture Plaque at the Edge of the Stent as Causative Factor of Late ST

A 88-years old man with stable angina received 2 PES in the proximal LAD. After 2 years the patient was readmitted with an anterior STEMI. At the time of coronary angiography the LAD was opened, with a filling defect at the proximal stent entrance. OCT revealed complete strut coverage with minimal neointimal deposition across the entire stented segment. A white thrombus on top of a new ruptured plaque at the ostium of the LAD was easily detected by OCT (Fig. 11.20). New ruptured plaque was sealed by an additional EES
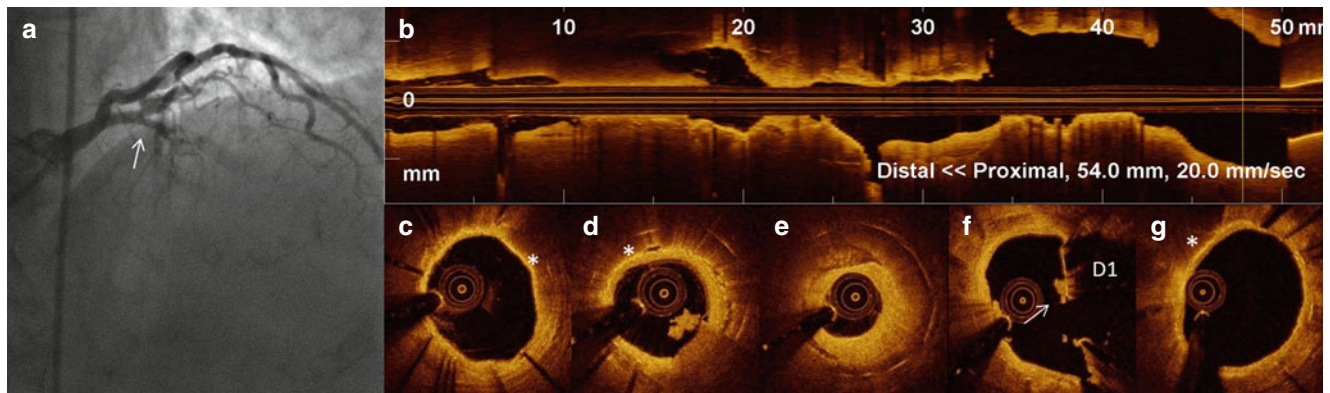
Fig. 11.21 Angiographic and OCT images during primary PCI performed for very late ST. (**a**) coronary angiography before thrombus aspiration showed a thrombotic stent occlusion at proximal LAD, involving the first diagonal branch (*arrow*). (**b**) OCT long view demonstrated an irregular lumen contour with some degree of stenosis and atherosclerotic lipid laden neointima. (**c–g**) cross sectional views from the distal to the proximal stent segments. (**c, g**) the cross sections at the stent edges showed an early pattern of neoatherosclerosis with thin cap lipid rich plaques and foamy macrophage (*). (**d, e**) Body of the stents presenting with more advanced stages of neoatherosclerosis with mixed thrombus (**d**- 4–6 o'clock) and calcified plaque (**e**- 10–12 o'clock). (**f**) cross-section at the level of the D1 bifurcation showing stent under-expansion and cell strut deformation (*arrow*)
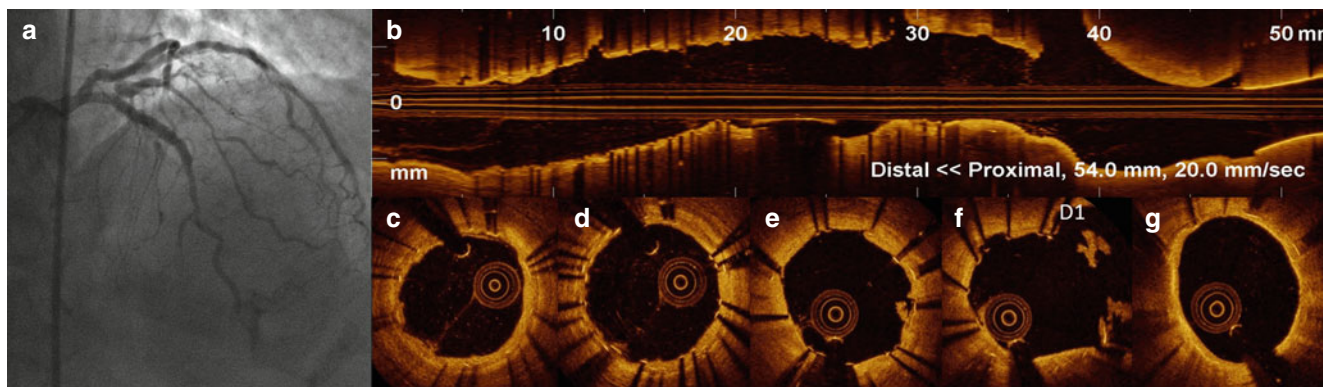
Fig. 11.22 Angiography and OCT after treatment. (**a**) Final coronary angiography with no residual stenosis and TIMI 3 flow grade. (**b**) Longitudinal OCT view showing a large lumen area across the entire stented segments, with no residual stenosis and no stent edge dissection. (**c–g**) OCT cross-sectional views confirming complete stent expansion, a full compression of the lipid laden neoitima and a wide access to the *D1* branch (**f**)

implanted at the ostial LAD. Progression of disease at the inflow/outflow tract can be responsible for late DES failure. Late ST may be observed even in the presence of an optimal DES result, with complete stent healing.

Illustrative Case 7
ST with Coexisting Multiple Causative Factors

Due to its high level of accuracy OCT can detect multiple mechanisms implicated in ST at the same time. In the following case ST was associated with the presence of stent under-expansion and geometry deformation at the bifurcation lesion, combined with atherosclerotic neointima deposition. A 63-year old patient had two PES implanted in the proximal LAD, as provisional stents across the LAD-first diagonal (D1). bifurcation. Five years later the patient was readmitted to the hospital with an anterior STEMI. Coronary angiography showed a complete occlusion at the stent entrance, with TIMI 0 flow grade. The flow was reestablished with thrombus aspiration performed in both branches. OCT detected multiple coexisting causative factors bystanders, with lipid laden neointima (*) and calcium deposition (arrow) in some cross sections, severe stent deformation and under-expansion with fragments of thrombus in other sections (Fig. 11.21).

Current generation EES were implanted inside the two PES, and post-dilated at high pressure. A final OCT pullback confirmed the full lumen/stent expansion, the absence of any remaining stent deformation and wide open access to D1 (Fig. 11.22).

11.10 Limitations of OCT Imaging During Stent Thrombosis

Whenever thrombus is present, a reliable assessment of strut coverage with OCT during ST is difficult. Current OCT cannot differentiate between neointimal and other tissue types.

Endothelial cell dimensions are below the resolution of even OCT, and it is possible that some struts that appear bare in fact is covered by a thin layer of tissue. Futhermore, ST it cannot be excluded that thrombus aspiration might have partially removed this thin layer of material covering the stent struts. Moreover OCT, unlike IVUS cannot always provide information on vessel size (media to media), and therefore is not possible to judge the presence of a stent under expansion and vessel remodeling.

11.11 New Perspectives for in Stent Thrombosis

The low frequency occurrence of ST with paucity of sparse data collected by different interventional groups and the possible catastrophic clinical consequences of this complication has attracted the attention of the Heath Care Authorities to have a more global approach to solve this problem. Therefore, very large cohorts of ST patients need to be recruited in order to substantiate the main mechanisms involved and to possibly demonstrate the impact of a given intervention. Moreover, the evaluation of patients with ST needs to include a comprehensive evaluation using combined clinical, high resolution intracoronary imaging, blood platelet function data and genes. Large-scale clinical trials with long-term follow-up as well as detailed mechanistic assessments are warranted. In pursuit of these goals, the "PREvention of Stent Thrombosis by an Interdisciplinary Global European effort" PRESTIGE project, supported by a financial grant of the EU Community (FP7-Seventh Health Program, Health 2010.2.4.2-1, Reducing in-stent thrombosis) represents an advanced and unique multidisciplinary project, involving world –leading European specialists and centers, in the study of all the contributing factors to ST in five different working packages. The five fields of actions in the PRESTIGE project are: (1) Assessment of the basic mechanisms leading to ST (2) Bio-engineering approaches to reduce ST (3) Novel imaging approaches to assess healing and thrombotic processes after stenting (4) Multimodal characterization of patients with late ST (5) Exploitation of the results. In this project the PRESTIGE-registry (WP4) is the joint effort to collect data regarding all patients presenting with ST. An extensive clinical and procedural database, integrated with blood platelet functional tests, OCT/IVUS intracoronary imaging, DNA-sampling and histopathological and immunohistochemical analyses of aspirated thrombus was prospectively collected. Between April 2011 and April 2014, all patients with angiographic confirmed ST were enrolled into the PRESTIGE Registry, in 14 centers and compared to control patients without ST who underwent a PCI with stent implantation on the same date (±14 days) and with the same indication. At present more than 200 consecutive ST were assessed with OCT (±IVUS) combined with histopathology of aspirated thrombus. The PRESTIGE project is anticipated to result in significant improvement in the understanding, prediction and treatment of ST, providing surrogate marker(s) identification and tailored therapeutic and interventional strategies.

Conclusions

The occurrence of ST is rare; however it remains one of the most dreadful complications following PCI, due to potential catastrophic clinical events. The prevention of ST represents a major challenge in interventional cardiology, due to the multiple causative and contributing factors. The limited value of coronary angiography in differentiating causative factors responsible for ST has been recently updated/ameliorated by with the amazingly informative content of OCT, detecting thrombus, plaque, tissues and stent components. The use of OCT in the acute phase of ST, when the flow has been reestablished, allows to promptly identifying the main causative mechanisms (incomplete stent expansion, uncovered/malapposed struts, toxic vessel response with extra-cavities formation, disease progression, neoatherosclerosis). Furthermore, by addressing the implicated mechanisms, OCT may allow individualized treatment through targeted mechanical or pharmacological interventions. Finally, the use of OCT at different time points of follow-up after ST allows for the unique opportunity to verify the long term vessel response (coverage, sealing of in-stent aneurysm), and possibly reduce the risk of ST recurrences.

References

1. Stone GW, Ellis SG, Cox DA, Hermiller J, O'Shaughnessy C, Mann JT, et al.; TAXUS-IV Investigators. A polymer-based, paclitaxel-eluting stent in patients with coronary artery disease. N Engl J Med. 2004;350(3):221–31.
2. Moses JW, Leon MB, Popma JJ, Fitzgerald PJ, Holmes DR, O'Shaughnessy C, et al.; SIRIUS Investigators. Sirolimus-eluting stents versus standard stents in patients with stenosis in a native coronary artery. N Engl J Med. 2003;349(14):1315–23.
3. Kuchulakanti PK, Chu WW, Torguson R, Ohlmann P, Rha SW, Clavijo LC, et al. Correlates and long-term outcomes of angiographically proven stent thrombosis with sirolimus- and paclitaxel-eluting stents. Circulation. 2006;113(8):1108–13.
4. Daemen J, Wenaweser P, Tsuchida K, Abrecht L, Vaina S, Morger C, et al. Early and late coronary stent thrombosis of sirolimus-eluting and paclitaxel-eluting stents in routine clinical practice: data from a large two-institutional cohort study. Lancet. 2007;369(9562):667–78.
5. Cook S, Meier B. Have we been misled by the ESC DES firestorm? EuroIntervention. 2008;3(5):535–7.
6. Cutlip DE, Windecker S, Mehran R, Boam A, Cohen DJ, van Es GA, et al.; Academic Research Consortium. Clinical end points in coronary stent trials: a case for standardized definitions. Circulation. 2007;115(17):2344–51.
7. Serruys PW, Strauss BH, Beatt KJ, Bertrand ME, Puel J, Rickards AF, et al. Angiographic follow-up after placement of a self-expanding coronary-artery stent. N Engl J Med. 1991;324(1):13–7.

8. Colombo A, Hall P, Nakamura S, Almagor Y, Maiello L, Martini G, et al. Intracoronary stenting without anticoagulation accomplished with intravascular ultrasound guidance. Circulation. 1995;91(6):1676–88.

9. Karrillon GJ, Morice MC, Benveniste E, Bunouf P, Aubry P, Cattan S, et al. Intracoronary stent implantation without ultrasound guidance and with replacement of conventional anticoagulation by antiplatelet therapy. Circulation. 1996;94(7):1519–27.

10. Moussa I, Di Mario C, Reimers B, Akiyama T, Tobis J, Colombo A. Subacute stent thrombosis in the era of intravascular ultrasound-guided coronary stenting without anticoagulation: frequency, predictors and clinical outcome. J Am Coll Cardiol. 1997;29(1):6–12.

11. Schühlen H, Kastrati A, Dirschinger J, Hausleiter J, Elezi S, Wehinger A, et al. Intracoronary stenting and risk for major adverse cardiac events during the first month. Circulation. 1998;98(2):104–11.

12. De Servi S, Repetto S, Klugmann S, Bossi I, Colombo A, Piva R, et al. Stent thrombosis: incidence and related factors in the R.I.S.E. Registry (Registro Impianto Stent Endocoronarico). Catheter Cardiovasc Interv. 1999;46(1):13–8.

13. Cutlip DE, Baim DS, Ho KK, Popma JJ, Lansky AJ, Cohen DJ, Carrozza Jr JP, et al. Stent thrombosis in the modern era: a pooled analysis of multicenter coronary stent clinical trials. Circulation. 2001;103(15):1967–71.

14. Ong AT, Hoye A, Aoki J, van Mieghem CA, Rodriguez Granillo GA, Sonnenschein K, et al. Thirty-day incidence and six-month clinical outcome of thrombotic stent occlusion after bare-metal, sirolimus, or paclitaxel stent implantation. J Am Coll Cardiol. 2005;45(6):947–53.

15. van Werkum JW, Heestermans AA, de Korte FI, Kelder JC, Suttorp MJ, Rensing BJ, et al. Long – term clinical outcome after a first angiographically confirmed coronary stent thrombosis: an analysis of 431 cases. Circulation. 2009;119(6):828–34.

16. Wenaweser P, Daemen J, Zwahlen M, van Domburg R, Jüni P, Vaina S, et al. Incidence and correlates of drug-eluting stent thrombosis in routine clinical practice. 4-year results from a large 2-institutional cohort study. J Am Coll Cardiol. 2008;52(14):1134–40.

17. Moreno R, Fernández C, Hernández R, Alfonso F, Angiolillo DJ, Sabaté M, et al. Drug-eluting stent thrombosis: results from a pooled analysis including 10 randomized studies. J Am Coll Cardiol. 2005;45(6):954–9.

18. Kastrati A, Dibra A, Eberle S, Mehilli J, Suárez de Lezo J, Goy JJ, et al. Sirolimus-eluting stents vs paclitaxel-eluting stents in patients with coronary artery disease: meta-analysis of randomized trials. JAMA. 2005;294(7):819–25.

19. Sarno G, Lagerqvist B, Fröbert O, Nilsson J, Olivecrona G, Omerovic E, et al. Lower risk of stent thrombosis and restenosis with unrestricted use of 'new-generation' drug-eluting stents: a report from the nationwide Swedish Coronary Angiography and Angioplasty Registry (SCAAR). Eur Heart J. 2012;33(5):606–13.

20. Palmerini T, Kirtane AJ, Serruys PW, Smits PC, Kedhi E, Kereiakes D, et al. Stent thrombosis with everolimus-eluting stents: meta-analysis of comparative randomized controlled trials. Circ Cardiovasc Interv. 2012;5(3):357–64.

21. Holmes Jr DR, Kereiakes DJ, Garg S, Serruys PW, Dehmer GJ, Ellis SG, et al. Stent thrombosis. J Am Coll Cardiol. 2010;56(17):1357–65.

22. Iakovou I, Schmidt T, Bonizzoni E, Sangiorgi GM, Stankovic G, Airoldi F, et al. Incidence, predictors, and outcome of thrombosis after successful implantation of drug-eluting stents. JAMA. 2005;293(17):2126–30.

23. van Werkum JW, Heestermans AA, Zomer AC, Kelder JC, Suttorp MJ, Rensing BJ, et al. Predictors of coronary stent thrombosis: the Dutch Stent Thrombosis Registry. J Am Coll Cardiol. 2009;53(16):1399–409.

24. Kohn CG, Kluger J, Azeem M, Coleman CI. Short-term consequences of angiographically-confirmed coronary stent thrombosis. PLoS One. 2013;8(10):e77330.

25. Parodi G, Memisha G, Bellandi B, Valenti R, Migliorini A, Carrabba N, et al. Effectiveness of primary percutaneous coronary interventions for stent thrombosis. Am J Cardiol. 2009;103(7):913–6.

26. Chechi T, Vecchio S, Vittori G, Giuliani G, Lilli A, Spaziani G, et al. ST-segment elevation myocardial infarction due to early and late stent thrombosis a new group of high-risk patients. J Am Coll Cardiol. 2008;51(25):2396–402.

27. Parodi G, Marcucci R, Valenti R, Gori AM, Migliorini A, Giusti B, et al. High residual platelet reactivity after clopidogrel loading and long-term cardiovascular events among patients with acute coronary syndromes undergoing PCI. JAMA. 2011;306(11):1215–23.

28. Rinaldi MJ, Kirtane AJ, Piana RN, Caputo RP, Gordon PC, Lopez JJ, et al. Clinical, procedural, and pharmacologic correlates of acute and subacute stent thrombosis: results of a multicenter case-control study with 145 thrombosis events. Am Heart J. 2008;155(4):654–60.

29. de la Torre-Hernández JM, Alfonso F, Hernández F, Elizaga J, Sanmartin M, Pinar E, et al. ESTROFA Study Group. Drug-eluting stent thrombosis: results from the multicenter Spanish registry ESTROFA (Estudio ESpanol sobre TROmbosis de stents FArmacoactivos). J Am Coll Cardiol. 2008;51(10):986–90.

30. Roy P, Torguson R, Okabe T, Pinto Slottow TL, Steinberg DH, Smith K, et al. Angiographic and procedural correlates of stent thrombosis after intracoronary implantation of drug-eluting stents. J Interv Cardiol. 2007;20(5):307–13.

31. Park DW, Park SW, Park KH, Lee BK, Kim YH, Lee CW, et al. Frequency of and risk factors for stent thrombosis after drug-eluting stent implantation during long-term follow-up. Am J Cardiol. 2006;98(3):352–6.

32. Pinto Slottow TL, Bonello L, Gavini R, Beauzile P, Sushinsky SJ, Scheinowitz M, et al. Prevalence of aspirin and clopidogrel resistance among patients with and without drug-eluting stent thrombosis. Am J Cardiol. 2009;104(4):525–30.

33. Gurbel PA, Bliden KP, Samara W, Yoho JA, Hayes K, Fissha MZ, et al. Clopidogrel effect on platelet reactivity in patients with stent thrombosis: results of the CREST Study. J Am Coll Cardiol. 2005;46(10):1827–32.

34. Nakano M, Yahagi K, Otsuka F, Sakakura K, Finn AV, Kutys R, et al. Causes of early stent thrombosis in patients presenting with acute coronary syndrome: an ex vivo human autopsy study. J Am Coll Cardiol. 2014;63(23):2510–20.

35. Virmani R, Guagliumi G, Farb A, Musumeci G, Grieco N, Motta T, et al. Localized hypersensitivity and late coronary thrombosis secondary to a sirolimus-eluting stent: should we be cautious? Circulation. 2004;109(6):701–5.

36. Nebeker JR, Virmani R, Bennett CL, Hoffman JM, Samore MH, Alvarez J, et al. Hypersensitivity cases associated with drug-eluting coronary stents: a review of available cases from the Research on Adverse Drug Events and Reports (RADAR) project. J Am Coll Cardiol. 2006;47(1):175–81.

37. Joner M, Finn AV, Farb A, Mont EK, Kolodgie FD, Ladich E, et al. Pathology of drug-eluting stents in humans: delayed healing and late thrombotic risk. J Am Coll Cardiol. 2006;48(1):193–202.

38. Cook S, Ladich E, Nakazawa G, Eshtehardi P, Neidhart M, Vogel R, et al. Correlation of intravascular ultrasound findings with histopathological analysis of thrombus aspirates in patients with very late drug-eluting stent thrombosis. Circulation. 2009;120(5):391–9.

39. Park SJ, Kang SJ, Virmani R, Nakano M, Ueda Y. In-stent neoatherosclerosis: a final common pathway of late stent failure. J Am Coll Cardiol. 2012;59(23):2051–77.

40. Nakazawa G, Otsuka F, Nakano M, Vorpahl M, Yazdani SK, Ladich E, et al. The pathology of neoatherosclerosis in human coronary implants bare-metal and drug-eluting stents. J Am Coll Cardiol. 2011;57(11):1314–22.

41. Mintz GS. Clinical utility of intravascular imaging and physiology in coronary artery disease. J Am Coll Cardiol. 2014;64(2):207–22.

42. Prati F, Guagliumi G, Mintz GS, Costa M, Regar E, Akasaka T, et al. Expert review document part 2: methodology, terminology and clinical applications of optical coherence tomography for the assessment of interventional procedures. Expert's OCT Review Document. Eur Heart J. 2012;33(20):2513–20.

43. Guagliumi G, Sirbu V, Musumeci G, Gerber R, Biondi-Zoccai G, Ikejima H, et al. Examination of the in vivo mechanisms of late drug-eluting stent thrombosis: findings from optical coherence tomography and intravascular ultrasound imaging. JACC Cardiovasc Interv. 2012;5(1):12–20.

44. Kang SJ, Lee CW, Song H, Ahn JM, Kim WJ, Lee JY, et al. OCT analysis in patients with very late stent thrombosis. JACC Cardiovasc Imaging. 2013;6(6):695–703.

45. Parodi G, La Manna A, Di Vito L, Valgimigli M, Fineschi M, et al. Stent-related defects in patients presenting with stent thrombosis: differences at optical coherence tomography between subacute and late/very late thrombosis in the Mechanism Of Stent Thrombosis (MOST) study. EuroIntervention. 2013;9(8):936–44.

46. Cook S, Wenaweser P, Togni M, Billinger M, Morger C, Seiler C, et al. Incomplete stent apposition and very late stent thrombosis after drug-eluting stent implantation. Circulation. 2007;115(18): 2426–34.

47. Gutiérrez-Chico JL, Wykrzykowska J, Nüesch E, van Geuns RJ, Koch KT, Koolen JJ, et al. Vascular tissue reaction to acute malapposition in human coronary arteries: sequential assessment with optical coherence tomography. Circ Cardiovasc Interv. 2012;5(1): 20–9.

48. Malle C, Tada T, Steigerwald K, Ughi GJ, Schuster T, Nakano M, et al. Tissue characterization after drug-eluting stent implantation using optical coherence tomography. Arterioscler Thromb Vasc Biol. 2013;33(6):1376–83.

49. Nakano M, Vorpahl M, Otsuka F, Taniwaki M, Yazdani SK, Finn AV, et al. Ex vivo assessment of vascular response to coronary stents by optical frequency domain imaging. JACC Cardiovasc Imaging. 2012;5(1):71–82.

50. Guagliumi G, Costa MA, Sirbu V, Musumeci G, Bezerra HG, Suzuki N, et al. Strut coverage and late malapposition with paclitaxel-eluting stents compared with bare metal stents in acute myocardial infarction: optical coherence tomography substudy of the Harmonizing Outcomes with Revascularization and Stents in Acute Myocardial Infarction (HORIZONS-AMI) Trial. Circulation. 2011;123(3):274–81.

51. Zwart B, van Werkum JW, Heestermans AA, Kelder JC, Zomer AC, van't Hof AW, et al. Triggering mechanisms of stent thrombosis. EuroIntervention. 2011;6(6):722–8.

52. Lüscher TF, Steffel J, Eberli FR, Joner M, Nakazawa G, Tanner FC, et al. Drug-eluting stent and coronary thrombosis: biological mechanisms and clinical implications. Circulation. 2007;115(8): 1051–8.

53. Higo T, Ueda Y, Oyabu J, Okada K, Nishio M, Hirata A, et al. Atherosclerotic and thrombogenic neointima formed over sirolimus drug-eluting stent: an angioscopic study. JACC Cardiovasc Imaging. 2009;2(5):616–24.

54. Takano M, Yamamoto M, Inami S, Murakami D, Ohba T, Seino Y, et al. Comparison of incidence and time course of neoatherosclerosis between bare metal stents and drug-eluting stents using optical coherence tomography. J Am Coll Cardiol. 2009;55(1): 26–32.

55. Yonetsu T, Kim JS, Kato K, Kim SJ, Xing L, Yeh RW, et al. Comparison of incidence and time course of neoatherosclerosis between bare metal stents and drug-eluting stents using optical coherence tomography. Am J Cardiol. 2012;110(7):933–9.

56. Otsuka F, Vorpahl M, Nakano M, et al. Pathology of second-generation everolimus-eluting stents versus first-generation sirolimus- and paclitaxel-eluting stents in humans. Circulation 2014;129:211–23.

Shiro Uemura

Abstract

Percutaneous coronary intervention with drug-eluting stents has now gained worldwide acceptance for the treatment of patients with coronary artery disease. However, according to the results of recent clinical studies, late recurrence of cardiovascular events relating to previously implanted coronary stents has emerged as an important issue in current cardiovascular medicine. The mechanism of late stent failure has not been elucidated, but the introduction of intravascular optical coherence tomography has demonstrated that atherosclerotic changes with vulnerable characteristics occur within the neointima not only of drug-eluting stents but also of bare metal stents in the late post-implantation phase, and that this pathological process is important in the development of stent-related late cardiovascular adverse events.

In this chapter, the basic mechanisms, morphological characteristics, and clinical impact of neoatherosclerosis are described.

Keywords

Neoatherosclerosis • Neointima • Restenosis • Bare metal stent • Drug eluting stent • Very late stent thrombosis • Optical coherence tomography

12.1 Introduction

Medical treatment of coronary artery disease (CAD) has progressed significantly during the last several decades since the introduction of percutaneous coronary intervention (PCI). In particular, PCI with drug-eluting stents (DES) has now become the standard of care for patients with CAD because of the significantly lower rates of both restenosis and target lesion revascularization (TLR) compared with either plain balloon angioplasty or bare metal stents (BMS) [1–3]. However, there are concerns regarding the potential development of stent-related major adverse cardiovascular events (MACE) during extended follow-up. One of the established underlying mechanisms of late or very late stent failure in DES is thrombus formation at the sites of uncovered stent struts, which occurs due to drug- or polymer-related oversuppression of neointimal growth [4, 5]. On the other hand, accumulated data from clinical studies using intravascular optical coherence tomography (OCT) has shown that the occurrence of neoatherosclerosis inside both BMS and DES is also important in the development of MACE, especially in the very late phase after coronary stent implantation.

12.2 Neointima Formation After Coronary Stent Implantation

The clinical introduction of BMS has significantly reduced the incidence of restenosis, mainly by preventing acute elastic recoil and the chronic process of negative remodeling at culprit coronary lesions that are the main causes of restenosis of plain balloon angioplasty. However, even the placement of BMS cannot eliminate neointimal overgrowth within the metal scaffold due

S. Uemura, MD, PhD
First Department of Internal Medicine, Nara Medical University, 840 Shijo-cho, Kashihara, Nara 634-8522, Japan
e-mail: suemura@naramed-u.ac.jp

to the proliferation of vascular smooth muscle cells and the production of extracellular matrix. In fact, the restenosis rate of BMS within 6 months to 1 year is approximately 13–30 % [6, 7], but the long-term outcome is believed to be benign, with an increase in luminal diameter within stented segments when BMS has escaped from initial restenosis [8]. However, a more recent study with an extended follow-up duration demonstrated [9] that neointima within BMS exhibits a triphasic luminal response characterized by an early restenosis phase until 6 months, an intermediate-term regression phase from 6 months to 3 years, and a late luminal renarrowing phase beyond 4 years. These findings suggest that in the late phase the neointimal tissue of BMS is susceptible not only to dimensional changes but also qualitative ones, specifically development of atherosclerosis inside stent struts. Development of atheromatous changes in BMS neointima was previously thought to be uncommon, but studies with intravascular imaging revealed that the development of vulnerable atherosclerotic changes is not rare in BMS following at least 5 years of implantation [10, 11].

In comparison, DES inhibit neointimal growth by pharmacologically suppressing vascular smooth muscle cell proliferation and extracellular matrix production. Use of DES has significantly reduced the rates of both restenosis and TLR compared with BMS over mid-term follow-up [1, 2]. However, a recent long-term follow-up study of sirolimus-eluting stents (SES), first-generation DES, revealed that very late stent thrombosis (VLST) and late TLR beyond 1 year after implantation occurred consistently and without decline for up to 7 years at annual rates of 0.24 and 2.0 % per year, respectively, as compared with annual rates of 0.05 % per year and 0.7 % per year after BMS implantation [12]. Furthermore, the clinical presentation of acute coronary syndrome (ACS) was more common at the time of late versus early TLR after SES implantation. Supporting these observations, it has recently been shown that DES are accompanied by delayed and progressive neointimal proliferation during long-term follow-up, termed the "late catch up" phenomenon [13–15]. Although the mechanism by which continuous growth of the DES neointima eventually results in MACE has not been elucidated, continuous endothelial cell injury by both cytotoxic drug effects and polymer-related chronic inflammation plays an important role in both destabilization and proliferation of neointimal tissue within DES in the very late post-implantation phase. In addition, it is possible that unstable and proliferative neointima may constitute the pathological background for the subsequent development of atherosclerotic changes.

12.3 Pathohistological Background of Neoatherosclerosis

The term "neoatherosclerosis" refers to pathohistological findings of de novo development of atheromatous changes in the neointimal tissue of both BMS and DES, similar to those

that develop intrinsically in native coronary arteries. Although the pathogenesis of neoatherosclerosis is not fully understood, both systemic risk factors for general atherosclerosis and local factors relating to the stent itself are likely to be involved in this process. Recent studies using human autopsy samples have shown that neointimal tissue from BMS within 1 year after implantation is composed mainly of vascular smooth muscle cells and collagen fibers. However, unlike the vascular response after plain balloon angioplasty, the vascular tissue around BMS demonstrates prolonged chronic inflammation characterized by accumulation of blood cells, including macrophages, T cells, and giant cells [16]. These findings suggest that a foreign-body inflammatory reaction to the metal occurs even in patients with stable clinical course. Particularly in BMS implanted for more than 4 years, probably relating to continuous inflammation around stent struts, decreased smooth muscle cell density has been observed around stent struts with evidence of foamy macrophage infiltration and initial findings of atherosclerosis [16, 17]. Accordingly, neointimal tissue covering BMS struts is subject to stent-related specific vascular reaction in addition to systemic atherosclerotic stimuli that affect native coronary arteries, and this tissue then transforms into a neoatherosclerotic lesion with unstable features that include plaque rupture, erosion, and subsequent thrombus formation. Yamaji et al. [18] performed histological analysis of aspirated thrombus material obtained in BMS with VLST (>1 year). Supporting previous autopsy findings, they found that evidence of atherosclerotic plaques such as foamy macrophages, cholesterol crystals, and thin fibrous caps, was more commonly seen in very late thrombosis cases (31 %) than in those in which stent thrombosis occurred during the intermediate follow-up period (<1 year) (10 %).

Neointimal tissue within DES is exposed to a more aggravated inflammatory milieu compared to BMS, probably due to a complex vascular response that includes an allergic reaction to polymers as well as pharmacological insult to vascular cells. It has been shown that chronic inflammation around DES struts directly impairs the normal vascular healing process and thus induces inadequate endothelial coverage of the stent [19], and that chronic and high-grade inflammation accelerates the spatial heterogeneity of the vascular healing process, which in turn correlates with the subsequent development of both impaired and excess neointimal growth.

Nakazawa et al. [20] reported the pathohistological characteristics of neointimal tissue in 197 BMS and 209 DES in 299 autopsy cases. In their study, almost two-thirds of lesions had features of advanced atherosclerotic changes in total (Fig. 12.1). Although there were differences in patient backgrounds between the two stent arms, the study indicated that neoatherosclerotic changes occurred in both BMS and DES, with the incidence more frequent in DES (31 % vs 16 %, p < 0.001), and these changes occurred significantly earlier in
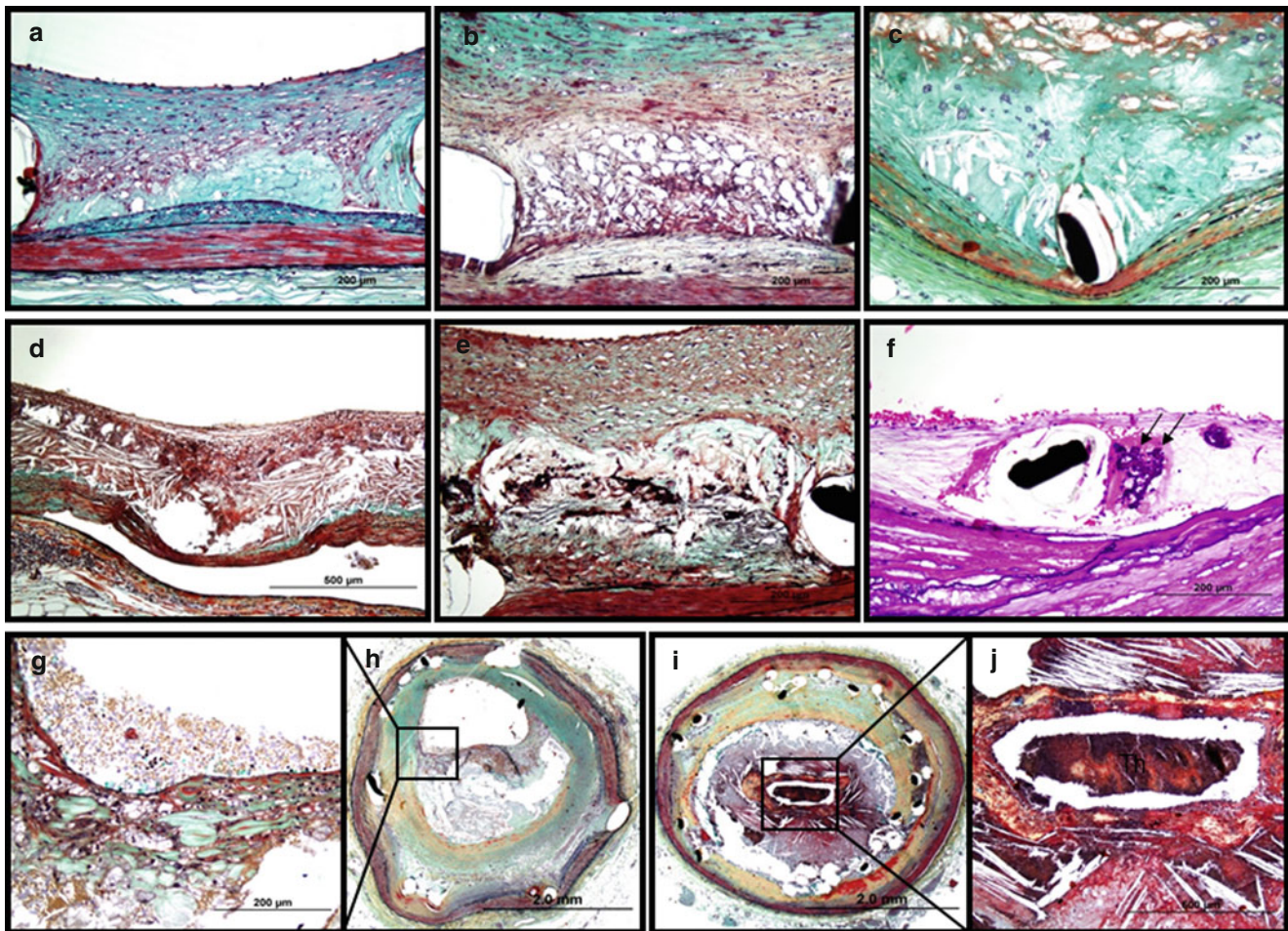
Fig. 12.1 Representative images of various stages of newly formed atherosclerotic changes within neointima after stent implantation. (**a**) Foamy macrophage clusters in the peristrut region of sirolimus-eluting stents (SES) implanted for 13 months antemortem. (**b**) Fibroatheroma with a foamy macrophage-rich lesion and early necrotic core formation in SES of 13 months' duration. (**c**) Fibroatheroma with peristrut early necrotic core, cholesterol clefts, surface foamy macrophages, and early calcification (*arrows*) in SES at 13 months. (**d**) Peristrut late necrotic core in the neointima characterized by a large aggregate of cholesterol clefts in SES at 17 months. (**e**) Fibroatheroma with calcification in the necrotic core in SES of 10 months' duration. (**f**) Peristrut calcification (*arrows*) with fibrin in SES of 7 months' duration. (**g**, **h**) A low-power magnification image (**h**) of a severely narrowed bare-metal stent (BMS) implanted for 61 months with a thin-cap fibroatheroma. Note macrophage infiltration and a discontinuous thin fibrous cap in a high-power magnification image (**g**). (**i**) A low-power magnification image shows a plaque rupture with an acute thrombus totally occluding the lumen in a BMS implanted for 61 months antemortem. (**j**) A high-power magnification image shows a discontinuous thin-cap fibroatheroma with occlusive luminal thrombus (Reprinted with permission from Dr. Nakazawa with permission from the publisher (From Nakazawa et al. [20]))

DES compared with BMS (420 days vs 2,260 days, $p < 0.001$) with no evidence of neoatherosclerotic changes in BMS within 2 years of implantation. In detail, for implants of <2 years, DES demonstrated a greater incidence of any type of neoatherosclerosis (DES 29 % vs BMS 0 %, $p < 0.001$), as shown by a greater incidence of foamy macrophage clusters (DES 14 % vs BMS 0 %, $p < 0.001$) and fibroatheromas (DES 13 % vs BMS 0 %, $p < 0.001$). For durations between 2 and 6 years, DES still showed a higher incidence of neoatherosclerosis (DES 41 % vs BMS 22 %, $p < 0.001$). These results suggest that (1) neoatherosclerosis was progressive in both types of stents, and (2) neoatherosclerosis in DES had more aggressive and unstable characteristics compared with BMS. Interestingly, the incidence of atherosclerotic changes was significantly higher when BMS were implanted in proximal segments compared with mid/distal segments of coronary arteries (27 % vs 12 %, $p < 0.001$). In contrast, such differences were not seen in DES (33 % vs 30 %, ns).

More aggressive development of neoatherosclerotic changes in DES compared with BMS might be explained by the delayed and incomplete recovery of endothelial cells covering the neointimal surface due to cytotoxic or cytostatic drugs. It is possible that dysfunctioning endothelial cells or a denuded endothelial cell layer over the neointima stimulates the interaction between circulating monocytes and the vascular wall, which then leads to earlier development of

unstable atherosclerotic changes in the neointima through cell adhesion and cell migration mechanisms.

One pathological study examined neoatherosclerosis that developed in second-generation DES. Otsuka et al. [21] studied 204 lesions that included 46 everolimus-eluting stents (EES) from 149 autopsy cases. As expected, EES demonstrated greater strut coverage with less inflammation, less fibrin deposition, and less late and very late stent thrombosis compared with the first-generation DES. Nevertheless, the observed frequency of neoatherosclerosis was comparable between these devices, indicating that careful long-term follow-up is still mandatory even after second-generation DES implantation.

Up to this point, there have been no reports on the patho-histological characteristics of neoatherosclerosis in bioabsorbable vascular scaffolds (BVS).

12.4 IVUS and Angioscopic Findings of Neoatherosclerosis

It has been difficult to precisely identify the characteristics of neointimal tissue using intravascular ultrasound (IVUS) because of this technique's relatively low spatial resolution. However, several studies have used gray-scale IVUS to evaluate the development of atherosclerotic changes within the neointima [22, 23]. In particular, Hakim et al. [23] studied 47 patients (54 lesions) who received serial IVUS examinations for more than 1.5 years after coronary stenting. Calcified neointima was observed in 20 % (12 lesions) of patients during follow-up, but the possibility of lipid accumulation was not assessed in this study. Researchers have begun to evaluate changes in neointimal tissue characteristics using new-generation IVUS with spectral analysis of ultrasound intensity and frequency [24–26]. Kang et al. [24] examined tissue characteristics of restenotic in-stent neointima after DES and BMS using virtual histology intravascular ultrasound (VH-IVUS) in 117 lesions (70 DES and 47 BMS). During mean follow-up durations of 43.5 months for BMS and 11.1 months for DES, they observed time-dependent development and progression of both necrotic cores and dense calcium deposits within the neointima in both stent types.

Coronary angioscopy is able to differentiate neointimal characteristics by semi-quantitatively grading yellow color tones. A recent study involving serial angioscopic examinations of 26 patients [27] showed that the incidence of yellow plaque and thrombus in BMS increased from the first (6–12 months) to second (>4 years) follow-up visits (58 and 31 %, P<0.05). In addition, all of the yellow plaques at the second follow-up visit protruded from the vessel wall into the lumen. Higo et al. [28] used angioscopy to compare BMS with 57 cases of SES in terms of changes in neointimal characteristics. SES promoted more frequent formation of atherosclerotic yellow neointima in stent-implanted lesions at 10-month follow-up compared with BMS. In addition, intraluminal thrombus was detected more often on yellow areas than on white ones, and was never detected where a stent was buried under white neointima. It is possible that the increased risk of late stent thrombosis in DES lesions may be due to newly formed yellow neointima, which is indicative of cholesterol accumulation.

12.5 OCT Findings of Neoatherosclerosis

Intravascular OCT is a newly developed intravascular imaging modality with a maximum spatial resolution of 10 μm, which is approximately ten times higher than that of conventional IVUS imaging [29–31]. In addition to plaque characterization of native coronary arteries [32, 33], OCT provides detailed morphological information about neointimal tissue within coronary stents [34–36]. Indeed, innovations in the application of OCT to coronary imaging have promoted our understanding of neoatherosclerosis after coronary stent implantation.

Morphological characteristics of the neointima within 1 year after stent implantation can be categorized into three patterns based on OCT appearance [37]. Figure 12.2 shows representative pictures. The homogeneous pattern is characterized by a uniformly signal-rich and low-attenuation appearance. This OCT feature is predominantly observed in early-stage BMS neointima, and represents stable fibrous tissue. The layered pattern has a signal-poor appearance with a high-signal band adjacent to the luminal surface. The heterogeneous pattern is mainly signal-poor with islands of various signal intensities. In some cases there were mixed neointimal patterns. The latter two patterns are frequently observed in DES neointima, and represent the deposition of fibrin, platelets, or extracellular matrix proteoglycans during the acute phase of implantation. Accordingly, such OCT pattern observed within early phase of implantation should be distinguished from neoatherosclerosis developing in the chronic phase. Figure 12.3 depicts representative findings of a variety of neoatherosclerotic changes within the neointima of either BMS or DES.

12.5.1 BMS

Using intravascular OCT, Takano et al. [11] for the first time demonstrated that fibrous neointima could transform into lipid-laden neointima in the chronic phase after BMS implantation. In their study, 67 % of BMS demonstrated conversion to lipid-laden neointima after 5 years of implantation, and plaque angiogenesis (neovascularization) was also observed significantly more frequently in the late phase (>5 years) than in the early phase (<1 year). Remarkably,
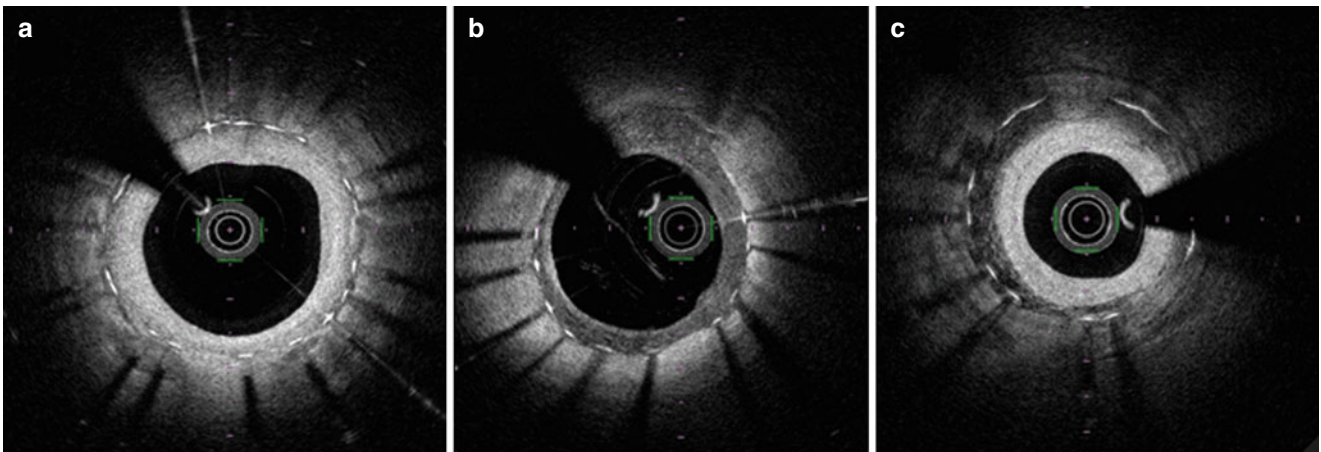
Fig. 12.2 OCT characteristics of neointimal tissue observed in the early post-implantation stage (<1 year). (**a**) Homogenous, (**b**) heterogenous, and (**c**) layered patterns. (**b**) and (**c**) are more frequently observed in DES than BMS
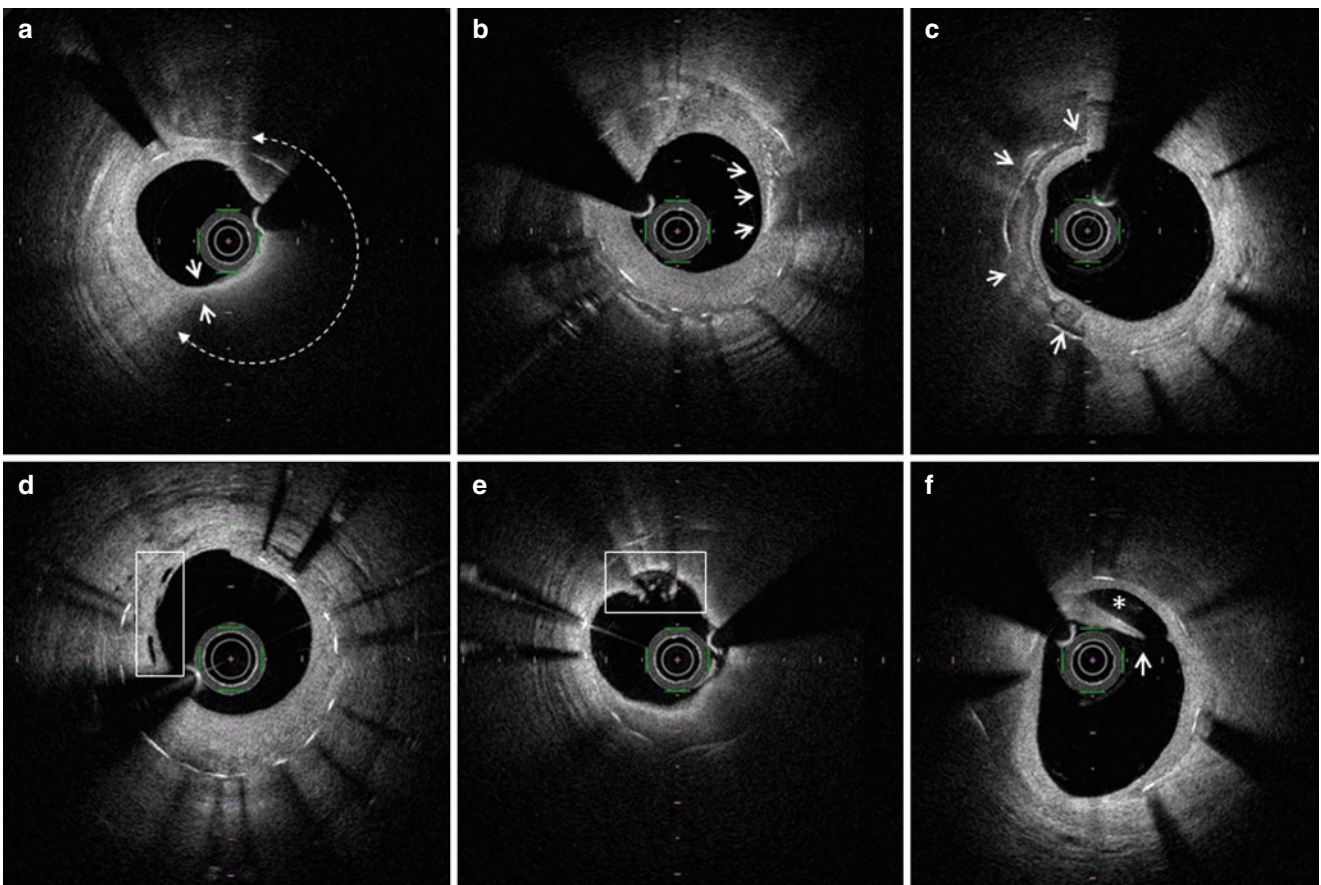
Fig. 12.3 OCT characteristics of neoatherosclerosis observed in the intermediate and late post-implantation phases. (**a**) Lipid-laden neo-intima showing a diffusely bordered, signal-poor region with overlying signal-rich homogeneous band (*bidirectional arc*). The minimal thickness of the fibrous cap is 60 m (between the two *white arrows*). (**b**) Macrophage infiltration with high signal accumulation accompanied by heterogeneous back shadows (*white arrows*). (**c**) Calcium deposition within the stented segment showing a sharply delineated region with a mixture of signal-poor and signal-rich areas (*white arrows*). (**d**) Neovascularization showing small vesicular or tubular structures of 50- to 300 μm diameters (*rectangular box*). (**e**) Neointimal laceration showing irregularities or disruption of the superficial intimal lining without fibrous cap rupture (*rectangular box*). (**f**) Intra-stent plaque rupture showing disrupted fibrous membrane (*white arrow*) with an underlying empty cavity (*)
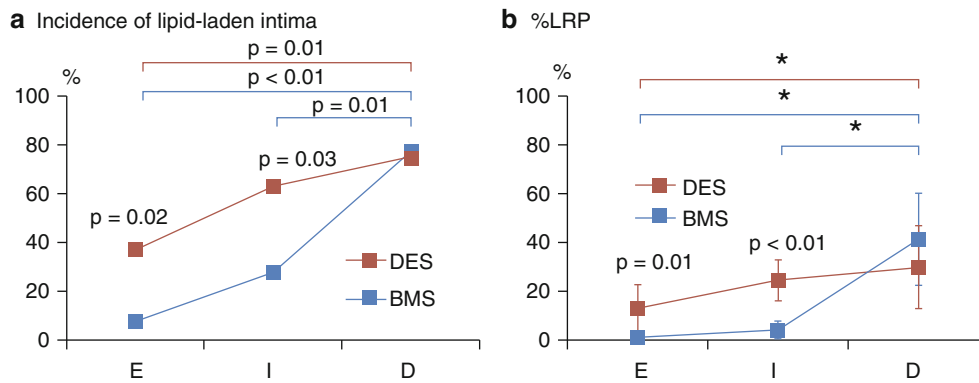
Fig. 12.4 Oct comparison of different neoatherosclerosis parameters between DES and BMS over time. (**a**) Incidence of lipid-laden plaque and (**b**) % lipid-rich plaque (LRP). LRP is defined as a plaque with a lipid arc >90°, and %LRP is calculated as the number of cross-sections with LRP divided by the total number of analyzed cross-sections of plaque × 100. *Significant difference using Duncan's multiple range post hoc test at a 5 % significance level. *E* early phase (<9 months), *I* intermediate phase (>9 to <48 months), *D* delayed phase (>48 months) (Reprinted with permission from the publisher (From Yonetsu et al. [40]))

neoatherosclerotic changes were observed in the BMS without angiographic restenosis. They also found disruption of the fibrous cap and thrombus formation associated with neoatherosclerotic changes, suggesting a potential role of neoatherosclerosis in late stent failure. In selected cases with restenosis, Habara et al. [38] compared the morphological characteristics of neointima either very late (>5 years) or early after BMS implantation. Almost 90 % of the BMS restenotic lesions that occurred in the very late phase were accompanied by neoatherosclerotic changes, and peri-stent and intra-neointimal microvessels were more frequently observed in in-stent restenosis occurring in the very late phase.

12.5.2 DES

Neoatherosclerosis occurs more evidently in DES compared with BMS. Kang et al. [39] showed that of 50 restenotic lesions in DES that were on average 32 months old, 90 % of neointima contained lipid accumulation, and 10 % demonstrated calcium deposits. In addition, 52 % showed in-stent thin-cap fibroatheroma (TCFA) and 29 (58 %) had at least one in-stent neointimal rupture. Patients presenting with unstable angina showed a significantly thinner fibrous cap (55 m vs 100 m, P<0.006) and higher incidence of TCFA (75 % vs 37 %, P<0.008), intimal rupture (75 % vs 47 %, P<0.044), and intraluminal thrombus (80 % vs 43 %, P<0.010) than stable patients. Interestingly, fibrous cap thickness negatively correlated with follow-up time (r=−0.318, P<0.024) after stent implantation. Compared with DES implanted more recently than 20 months, those placed at least 20 months prior to the study had a higher incidence of TCFA (69 % vs 33 %, P<0.012) and red thrombus (27 % vs 0 %, P<0.007). Patients with unstable angina dem-

onstrated an increasing number of unstable findings on OCT, including TCFA, neointima rupture, and thrombus. The authors showed that in-stent neoatherosclerosis possibly correlates with DES failure, especially late after implantation.

12.5.3 BMS vs DES

As previously mentioned, there are substantial differences between BMS and DES in terms of the incidence and time course of neoatherosclerosis development. Yonetsu et al. [40] recently used OCT to compare the characteristics of neoatherosclerosis in 56 BMS and 82 DES cases. They categorized 138 stents with neointima (>100 μm) based on time since implantation: early phase (<9 months), intermediate phase (9–48 months), and delayed phase (>48 months) [40]. In the early phase, a greater incidence of lipid-laden plaque (37 % vs 8 %, p<0.02) was found in DES than in BMS. This relation was also evident in the intermediate phase. In the delayed phase, however, incidence of neoatherosclerosis was similar between the two stent types in total. A similar pattern was observed regarding the incidence of lipid-rich plaque (LRP), defined as a plaque with a lipid arc >90° (Fig. 12.4). These findings support previous pathological data showing earlier development of neoatherosclerosis in DES than in BMS [20]. In addition, in both stent types the incidence of lipid-laden plaque, intra-intimal neovascularization, and TCFA were significantly greater in cases with symptomatic restenosis than in those with asymptomatic restenosis. Thus, lipid-rich neoatherosclerosis develops inside stents earlier in DES than in BMS. After 48 months, most restenotic stents will have developed lipid-laden neointima in both groups. The same group [41] demonstrated that cutoff durations for the development of neoatherosclerosis in DES and BMS were 14 and 55 months, respectively.

Fig. 12.5 Time course and relation between neointimal hyperplasia and neoatherosclerosis. (**a**) In the BMS group, there is no difference in mean NIT among stents in different phases. However, the prevalence of NA differs among stents in different phases, with significantly higher values in stents in the late phase compared with those in the early and intermediate phases. (**b**) In the DES group, mean NIT and prevalence of NA are progressively greater across the three groups. † Indicates significance after adjustment with Bonferroni's correction (Reprinted with permission from the publisher (From Vergallo et al. [43]))
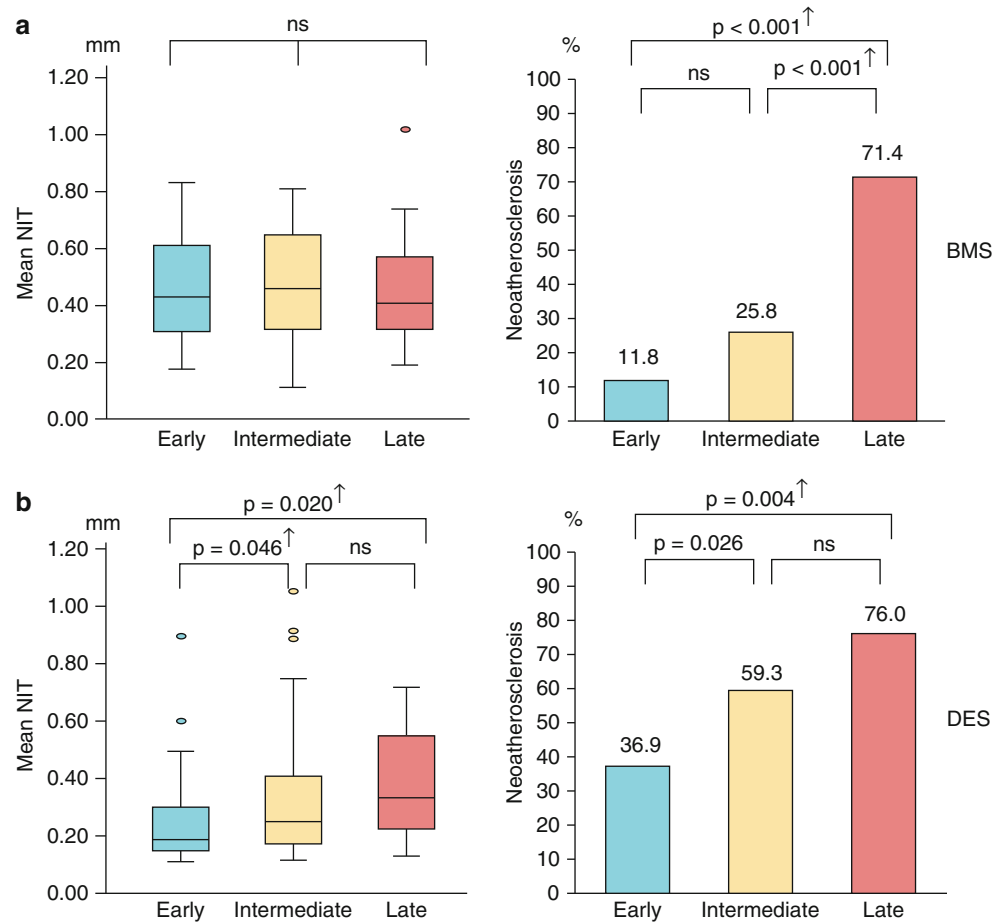
12.5.4 OCT-Derived Insight into the Pathogenesis of Neoatherosclerosis

The precise mechanism of neoatherosclerosis development remains unknown, but recent OCT studies have provided important clues in this regard.

Tian et al. [42] studied the spatial distribution of neoatherosclerotic changes and evaluated the relation between neoatherosclerosis and tissue characteristics around the stent edge reference segment. In their study, neoatherosclerosis was (1) more frequent in the proximal and distal sections than in the mid-sections of stents, (2) more frequently observed in stents with neointimal formation of microvessels, and (3) significantly more frequent when the adjacent plaque in the edge reference segment was rich in lipid content. These findings suggest that introduction of microvessels into neointima plays an important role in the formation of neoatherosclerosis, and that lipid-rich segments adjacent to stent edges are important in the formation of microvessels that supply blood during neointimal and neoatherosclerotic development.

Furthermore, a recent study by Vergallo et al. showed a positive correlation between the degree of neointimal hyperplasia and the presence of neointimal lipid accumulation [43]. They observed that stents of both types with greater neointimal thickness had a significantly greater prevalence of lipid-laden neointima, but the time course of neoatherosclerotic changes were different between BMS and DES (Fig. 12.5). Additionally, in DES, the magnitude of lipid accumulation was positively related to the degree of neointimal hypertrophy. This association was independent of stent type and time since implantation, and suggests a possible pathogenic link between the two processes. These results agree with data from a previous OCT study, in which neoatherosclerosis was more frequently identified in patients with restenosis than without restenosis [27]. Neointimal hypertrophy and neoatherosclerosis might share similar underlying mechanisms involving chronic inflammation and endothelial dysfunction, as suggested by the involvement of proinflammatory cytokines and the impairment of the nitric oxide pathway. In addition, the extensive neointimal hypertrophy that typically develops inside BMS likely maintains and amplifies flow disturbances inside the stent (restenosis-induced low endothelial shear stress: ESS), favoring further neointimal proliferation and ultimately resulting in neoatherosclerotic degeneration. This "ESS hypothesis" could explain the late occurrence of neoatherosclerosis and its preferential edge location observed in BMS. In contrast, incompetent and incomplete

Table 12.1 Predictors for neoatherosclerosis

	Final multivariate model (n = 179)		
	Adjusted odds ratio	95 % CI	P
Stent age >48 months	10.45	3.71–29.41	<0.001
DES			
SES	3.86	1.44–10.38	0.007
PES	24.17	6.02–97.02	<0.001
ZES	7.18	1.51–34.21	0.013
EES	6.46	1.65–25.34	0.007
BMS	1	–	–
Age >65 years	1.84	0.85–3.97	0.121
Hypertension	1.87	0.77–4.52	0.166
Hyperlipidemia	1.01	0.39–2.61	0.982
Diabetes mellitus	1.12	0.53–2.43	0.765
Smoking	7.03	2.46–20.04	<0.001
LDL-C >100 mg/dL			
TG >150 mg/dL			
CKD	3.69	1.10–12.35	0.035
Statin use	0.46	0.14–1.55	0.213
ACE-I/ARB use	0.39	0.17–0.91	0.028

From Yonetsu et al. [41]

DES drug-eluting stents, *SES* sirolimus-eluting stents, *PES* paclitaxel-eluting stent, *ZES* zotarolimus-eluting stents, *EES* everolimus-eluting stents, *BMS* bare metal stents, *LDL-C* low-density lipoprotein cholesterol, *TG* triglyceride, *CKD* chronic kidney disease (estimated glomerular filtration rate <60 mL/min per 1.73 m²), *ACE-I* angiotensin-converting enzyme inhibitors, and *ARB* angiotensin receptor blocker

endothelialization after DES implantation induces an inflammatory response stimulating neointimal growth and lipid deposition into the subendothelial space, causing earlier development of neoatherosclerosis compared with BMS.

12.5.5 Risk Factors for Neoatherosclerosis

The predictive factors for the development of neoatherosclerosis have not been established. Yonetsu et al. [41] examined 179 stents in 151 patients and evaluated the influence of patient characteristics, stent type, and time since stent implantation (stent age) on the development of lipid-laden neointima or calcification inside the stents (Table 12.1). In multivariate analysis, stent age ≥48 months, all subtypes of DES, current smoking, chronic kidney disease, and use of angiotensin-converting enzyme inhibitors (ACE-I) or angiotensin II receptor blockade (ARB) remained independent predictors for neoatherosclerosis. Because current smoking and chronic kidney disease are established risk factors for native coronary atherosclerosis, a similar mechanism is likely to be involved in neoatherosclerosis formation. In addition, these results may support the importance of secondary prevention after stent implantation regardless of stent type. It is interesting that ACE-I and ARB were protectively correlated with neoatherosclerosis. These drugs are widely used to reduce cardiovascular events in the secondary prevention of coronary heart disease [44, 45]. Moreover, it has been reported that pharmacologic therapy with ACE-I or ARB reduces neointima proliferation and restenosis after stent implantation [46, 47]. Prospective studies to evaluate the effects of ACE-I and ARB on the prevention of neoatherosclerosis are warranted.

12.5.6 Neoatherosclerosis in Second-Generation DES

Previous data on neoatherosclerosis were mostly available only for BMS and first-generation DES. Newer generation DES have not been adequately investigated. The OCT study by Tian et al. [42] showed that neoatherosclerosis occurred in 25.6 % of EES by 12.3 months after stent implantation. These results were comparable to those of a recent pathohistological study on second-generation DES [21], and demonstrate that neoatherosclerosis occurs earlier even in second-generation DES than in BMS, especially in restenotic lesions after DES implantation. It should be noted that at this time there are no studies examining neoatherosclerosis in bioabsorbable vascular scaffolds.

12.6 Clinical Significance of Neoatherosclerosis

A recent multicenter clinical study, PROSPECT [48], demonstrated that secondary MACE occur almost equally at the sites of stent-implanted culprit lesions and non-culprit lesions in ACS patients, and that the 3-year cumulative rate of MACE attributable to culprit lesions with previous stent implantation was 12.9 %. Furthermore, a recent large cohort study revealed that the incidence of TLR and VLST in patients treated with first-generation DES continued to increase up to 7-year follow-up (12.4 and 1.43 %, respectively) [12]. These observations strongly indicate the importance of neoatherosclerosis in triggering stent-related MACE in the chronic post-implantation phase.
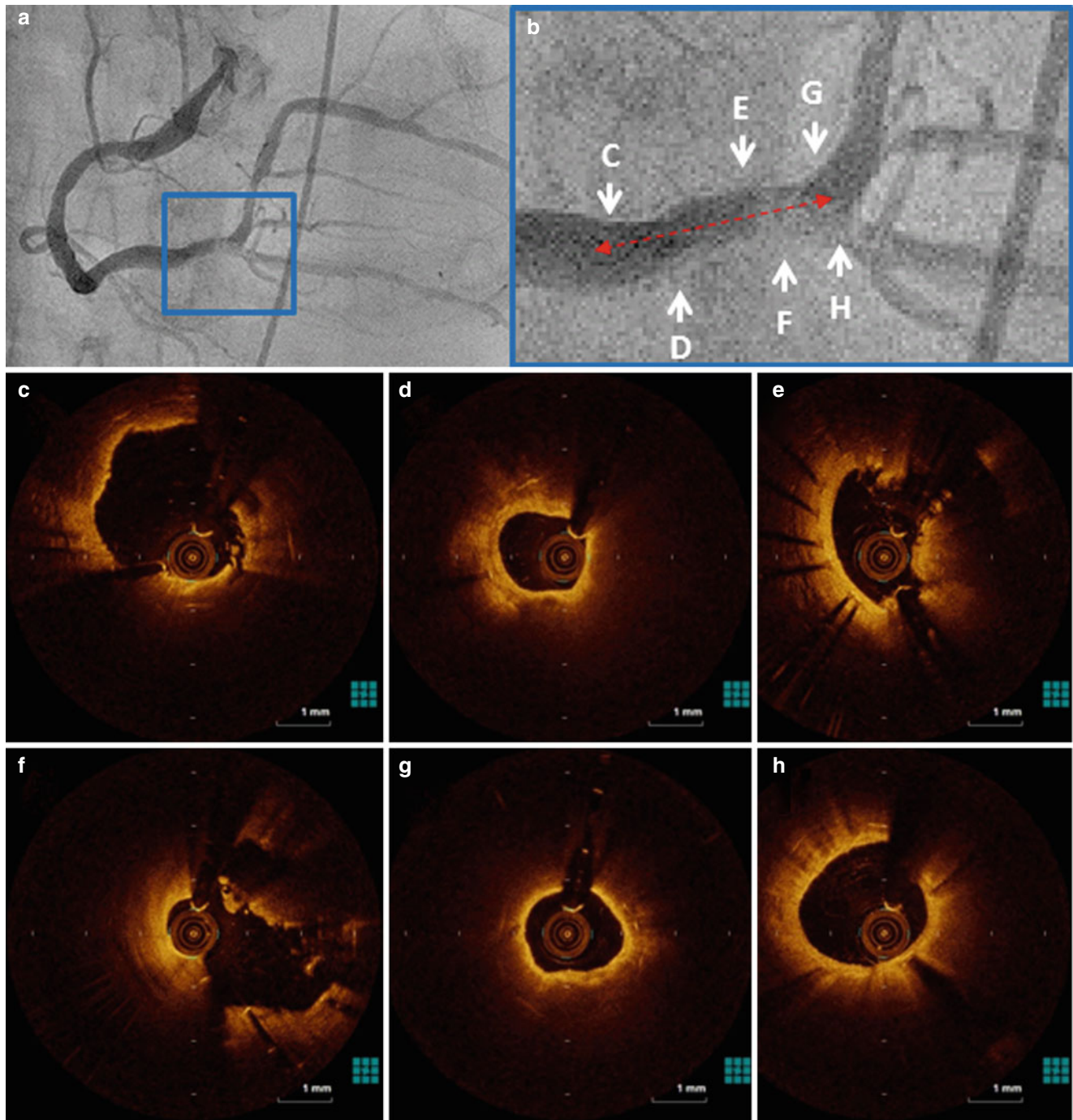
Fig. 12.6 Acute coronary syndrome due to thrombus formation at a neo-atherosclerotic lesion. A 73-year-old man was admitted with a diagnosis of ST-elevation myocardial infarction. Eight years earlier he had been treated with a bare metal stent at the distal RCA. Coronary angiography (**a**) shows subtotal thrombotic occlusion at the center of the BMS (**b**, *bidirectional arrow*). OCT examination was performed after thrombus aspiration. (**c**) Proximal stent edge showing macrophage infiltration. (**d**) Neointimal proliferation with lipid accumulation. (**e**) Intra-stent red thrombus formation. (**f**) Neointimal fibrous cap rupture and thrombus formation. (**g**) Circumferential lipid accumulation. (**h**) Distal stent edge showing fibrous neointima with macrophage infiltration

Indeed, Amabile et al. [49] used OCT to identify the presence of neoatherosclerosis in patients who suffered from VLST. In 20 coronary segments with definite VLST, 10 cases were revealed to have neoatherosclerosis. OCT analysis revealed significantly thicker neointimal coverage as well as a lower number of uncovered struts in neoatherosclerotic lesions compared with non-VLST patients, suggesting that neoatherosclerosis plays an important role in stent-related MACE in the very late phase by itself. Figure 12.6 shows a case of ACS who developed thrombus formation at the plaque rupture site in a neoatherosclerotic lesion.

Furthermore, the development of neoatherosclerotic changes correlated with the occurrence of periprocedural myocardial infarction. In addition, Ali et al. [50] used OCT and near-infrared spectroscopy to characterize neoatherosclerosis in 65 stents in consecutive symptomatic patients with in-stent restenosis. They found that neoatherosclerotic changes were associated with increased risk of periprocedural myocardial infarction in DES compared with BMS.

As of now, the incidence of and the event rate for neoatherosclerosis have been estimated based on retrospective observational studies. In order to clarify the natural history of neoatherosclerosis as well as a causative relation with late MACE, prospective cohort studies are necessary.

Conclusions

The clinical utilization of OCT has provided insight into the development of neoatherosclerosis within the neo-intima of both BMS and DES, a process important in the mechanism of late and very late adverse outcomes in CAD patients with previous coronary metal stents. It is expected that further improvements and new innovations in intravascular imaging will enhance our understanding of the complex vascular response to intravascular devices, and will improve the long-term prognosis in patients with CAD.

References

1. Morice MC, Serruys PW, Sousa JE, Fajadet J, Ban Hayashi E, Perin M, et al. A randomized comparison of a sirolimus-eluting stent with a standard stent for coronary revascularization. N Engl J Med. 2002;346(23):1773–80.
2. Stone GW, Ellis SG, Cox DA, Hermiller J, O'Shaughnessy C, Mann JT, et al. A polymer-based, paclitaxel-eluting stent in patients with coronary artery disease. N Engl J Med. 2004;350(3):221–31.
3. Stone GW, Midei M, Newman W, Sanz M, Hermiller JB, Williams J, et al. Comparison of an everolimus-eluting stent and a paclitaxel-eluting stent in patients with coronary artery disease: a randomized trial. JAMA. 2008;299(16):1903–13.
4. McFadden EP, Stabile E, Regar E, Cheneau E, Ong AT, Kinnaird T, et al. Late thrombosis in drug-eluting coronary stents after discontinuation of antiplatelet therapy. Lancet. 2004;364(9444):1519–21.
5. Cook S, Eshtehardi P, Kalesan B, Raber L, Wenaweser P, Togni M, et al. Impact of incomplete stent apposition on long-term clinical outcome after drug-eluting stent implantation. Eur Heart J. 2012;33(11):1334–43.
6. Kimura T, Nosaka H, Yokoi H, Iwabuchi M, Nobuyoshi M. Serial angiographic follow-up after Palmaz-Schatz stent implantation: comparison with conventional balloon angioplasty. J Am Coll Cardiol. 1993;21(7):1557–63.
7. Fischman DL, Leon MB, Baim DS, Schatz RA, Savage MP, Penn I, et al. A randomized comparison of coronary-stent placement and balloon angioplasty in the treatment of coronary artery disease. Stent Restenosis Study Investigators. N Engl J Med. 1994;331(8):496–501.
8. Kimura T, Yokoi H, Nakagawa Y, Tamura T, Kaburagi S, Sawada Y, et al. Three-year follow-up after implantation of metallic coronary-artery stents. N Engl J Med. 1996;334(9):561–6.
9. Kimura T, Abe K, Shizuta S, Odashiro K, Yoshida Y, Sakai K, et al. Long-term clinical and angiographic follow-up after coronary stent placement in native coronary arteries. Circulation. 2002;105(25):2986–91.
10. Ramcharitar S, Garcia-Garcia HM, Nakazawa G, Kukreja N, Ligthart J, Virmani R, et al. Ultrasonic and pathological evidence of a neo-intimal plaque rupture in patients with bare metal stents. EuroIntervention. 2007;3(2):290–1.
11. Takano M, Yamamoto M, Inami S, Murakami D, Ohba T, Seino Y, et al. Appearance of lipid-laden intima and neovascularization after implantation of bare-metal stents extended late-phase observation by intracoronary optical coherence tomography. J Am Coll Cardiol. 2009;55(1):26–32.
12. Natsuaki M, Morimoto T, Furukawa Y, Nakagawa Y, Kadota K, Yamaji K, et al. Late adverse events after implantation of sirolimus-eluting stent and bare-metal stent: long-term (5–7 years) follow-up of the coronary revascularization demonstrating outcome study-kyoto registry cohort-2. Circ Cardiovasc Interv. 2014;7(2):168–79.
13. Nakazawa G, Finn AV, Vorpahl M, Ladich ER, Kolodgie FD, Virmani R. Coronary responses and differential mechanisms of late stent thrombosis attributed to first-generation sirolimus- and paclitaxel-eluting stents. J Am Coll Cardiol. 2011;57(4):390–8.
14. Grube E, Dawkins K, Guagliumi G, Banning A, Zmudka K, Colombo A, et al. TAXUS VI final 5-year results: a multicentre, randomised trial comparing polymer-based moderate-release paclitaxel-eluting stent with a bare metal stent for treatment of long, complex coronary artery lesions. EuroIntervention. 2009;4(5):572–7.
15. Ishigami K, Uemura S, Morikawa Y, Soeda T, Okayama S, Nishida T, et al. Long-term follow-up of neointimal coverage of sirolimus-eluting stents–evaluation with optical coherence tomography. Circ J. 2009;73(12):2300–7.
16. Inoue K, Abe K, Ando K, Shirai S, Nishiyama K, Nakanishi M, et al. Pathological analyses of long-term intracoronary Palmaz-Schatz stenting; Is its efficacy permanent? Cardiovasc Pathol. 2004;13(2):109–15.
17. Farb A, Burke AP, Kolodgie FD, Virmani R. Pathological mechanisms of fatal late coronary stent thrombosis in humans. Circulation. 2003;108(14):1701–6.
18. Yamaji K, Inoue K, Nakahashi T, Noguchi M, Domei T, Hyodo M, et al. Bare metal stent thrombosis and in-stent neoatherosclerosis. Circ Cardiovasc Interv. 2012;5(1):47–54.
19. Finn AV, Joner M, Nakazawa G, Kolodgie F, Newell J, John MC, et al. Pathological correlates of late drug-eluting stent thrombosis: strut coverage as a marker of endothelialization. Circulation. 2007;115(18):2435–41.
20. Nakazawa G, Otsuka F, Nakano M, Vorpahl M, Yazdani SK, Ladich E, et al. The pathology of neoatherosclerosis in human coronary implants bare-metal and drug-eluting stents. J Am Coll Cardiol. 2011;57(11):1314–22.
21. Otsuka F, Vorpahl M, Nakano M, Foerst J, Newell JB, Sakakura K, et al. Pathology of second-generation everolimus-eluting stents versus first-generation sirolimus- and paclitaxel-eluting stents in humans. Circulation. 2014;129(2):211–23.
22. Fineschi M, Carrera A, Gori T. Atheromatous degeneration of the neointima in a bare metal stent: intravascular ultrasound evidence. J Cardiovasc Med. 2009;10(7):572–3.
23. Hakim DA, Mintz GS, Sanidas E, Rusinova R, Weisz G, Leon MB, et al. Serial gray scale intravascular ultrasound findings in late drug-eluting stent restenosis. Am J Cardiol. 2013;111(5):695–9.
24. Kang SJ, Mintz GS, Park DW, Lee SW, Kim YH, Lee CW, et al. Tissue characterization of in-stent neointima using intravascular

ultrasound radiofrequency data analysis. Am J Cardiol. 2010; 106(11):1561–5.

25. Araki T, Nakamura M, Sugi K. Characterization of in-stent neointimal tissue components following drug-eluting stent implantation according to the phase of restenosis using a 40-MHz intravascular ultrasound imaging system. J Cardiol. 2014. doi 10.1016/j.jjcc.2014.03.001

26. Kitabata H, Loh JP, Pendyala LK, Omar A, Ota H, Minha S, et al. Intra-stent tissue evaluation within bare metal and drug-eluting stents >3years since implantation in patients with mild to moderate neointimal proliferation using optical coherence tomography and virtual histology intravascular ultrasound. Cardiovasc Revasc Med. 2014;15(3):149–55.

27. Yokoyama S, Takano M, Yamamoto M, Inami S, Sakai S, Okamatsu K, et al. Extended follow-up by serial angioscopic observation for bare-metal stents in native coronary arteries: from healing response to atherosclerotic transformation of neointima. Circ Cardiovasc Interv. 2009;2(3):205–12.

28. Higo T, Ueda Y, Oyabu J, Okada K, Nishio M, Hirata A, et al. Atherosclerotic and thrombogenic neointima formed over sirolimus drug-eluting stent: an angioscopic study. JACC Cardiovasc Imaging. 2009;2(5):616–24.

29. Fujimoto JG, Boppart SA, Tearney GJ, Bouma BE, Pitris C, Brezinski ME. High resolution in vivo intra-arterial imaging with optical coherence tomography. Heart. 1999;82(2):128–33.

30. Huang D, Swanson EA, Lin CP, Schuman JS, Stinson WG, Chang W, et al. Optical coherence tomography. Science. 1991;254(5035):1178–81.

31. Brezinski ME, Tearney GJ, Bouma BE, Izatt JA, Hee MR, Swanson EA, et al. Optical coherence tomography for optical biopsy. Properties and demonstration of vascular pathology. Circulation. 1996;93(6):1206–13.

32. Yabushita H, Bouma BE, Houser SL, Aretz HT, Jang IK, Schlendorf KH, et al. Characterization of human atherosclerosis by optical coherence tomography. Circulation. 2002;106(13):1640–5.

33. Jang IK, Tearney GJ, MacNeill B, Takano M, Moselewski F, Iftima N, et al. In vivo characterization of coronary atherosclerotic plaque by use of optical coherence tomography. Circulation. 2005;111(12):1551–5.

34. Bouma BE, Tearney GJ, Yabushita H, Shishkov M, Kauffman CR, DeJoseph Gauthier D, et al. Evaluation of intracoronary stenting by intravascular optical coherence tomography. Heart. 2003;89(3):317–20.

35. Kume T, Akasaka T, Kawamoto T, Watanabe N, Toyota E, Sukmawan R, et al. Visualization of neointima formation by optical coherence tomography. Int Heart J. 2005;46(6):1133–6.

36. Takano M, Jang IK, Mizuno K. Neointimal proliferation around malapposed struts of a sirolimus-eluting stent: optical coherence tomography findings. Eur Heart J. 2006;27(15):1763.

37. Gonzalo N, Serruys PW, Okamura T, van Beusekom HM, Garcia-Garcia HM, van Soest G, et al. Optical coherence tomography patterns of stent restenosis. Am Heart J. 2009;158(2):284–93.

38. Habara M, Terashima M, Nasu K, Kaneda H, Inoue K, Ito T, et al. Difference of tissue characteristics between early and very late restenosis lesions after bare-metal stent implantation: an optical coherence tomography study. Circ Cardiovasc Interv. 2011;4(3):232–8.

39. Kang SJ, Mintz GS, Akasaka T, Park DW, Lee JY, Kim WJ, et al. Optical coherence tomographic analysis of in-stent neoatherosclerosis after drug-eluting stent implantation. Circulation. 2011;123(25):2954–63.

40. Yonetsu T, Kim JS, Kato K, Kim SJ, Xing L, Yeh RW, et al. Comparison of incidence and time course of neoatherosclerosis between bare metal stents and drug-eluting stents using optical coherence tomography. Am J Cardiol. 2012;110(7):933–9.

41. Yonetsu T, Kato K, Kim SJ, Xing L, Jia H, McNulty I, et al. Predictors for neoatherosclerosis: a retrospective observational study from the optical coherence tomography registry. Circ Cardiovasc Imaging. 2012;5(5):660–6.

42. Tian J, Ren X, Uemura S, Dauerman H, Prasad A, Toma C, et al. Spatial heterogeneity of neoatherosclerosis and its relationship with neovascularization and adjacent plaque characteristics: optical coherence tomography study. Am Heart J. 2014;167(6):884–92.e2.

43. Vergallo R, Yonetsu T, Uemura S, Park SJ, Lee S, Kato K, et al. Correlation between degree of neointimal hyperplasia and incidence and characteristics of neoatherosclerosis as assessed by optical coherence tomography. Am J Cardiol. 2013;112(9):1315–21.

44. Pfeffer MA, Braunwald E, Moye LA, Basta L, Brown Jr EJ, Cuddy TE, et al. Effect of captopril on mortality and morbidity in patients with left ventricular dysfunction after myocardial infarction. Results of the survival and ventricular enlargement trial. The SAVE Investigators. N Engl J Med. 1992;327(10):669–77.

45. Yusuf S, Sleight P, Pogue J, Bosch J, Davies R, Dagenais G. Effects of an angiotensin-converting-enzyme inhibitor, ramipril, on cardiovascular events in high-risk patients. The Heart Outcomes Prevention Evaluation Study Investigators. N Engl J Med. 2000;342(3):145–53.

46. Powell JS, Clozel JP, Muller RK, Kuhn H, Hefti F, Hosang M, et al. Inhibitors of angiotensin-converting enzyme prevent myointimal proliferation after vascular injury. Science. 1989;245(4914):186–8.

47. Yoshida O, Hirayama H, Nanasato M, Watanabe T, Murohara T. The angiotensin II receptor blocker candesartan cilexetil reduces neointima proliferation after coronary stent implantation: a prospective randomized study under intravascular ultrasound guidance. Am Heart J. 2005;149(1):e2.

48. Stone GW, Maehara A, Lansky AJ, de Bruyne B, Cristea E, Mintz GS, et al. A prospective natural-history study of coronary atherosclerosis. N Engl J Med. 2011;364(3):226–35.

49. Amabile N, Souteyrand G, Ghostine S, Combaret N, Slama MS, Barber-Chamoux N, et al. Very late stent thrombosis related to incomplete neointimal coverage or neoatherosclerotic plaque rupture identified by optical coherence tomography imaging. Eur Heart J Cardiovasc Imaging. 2014;15(1):24–31.

50. Ali ZA, Roleder T, Narula J, Mohanty BD, Baber U, Kovacic JC, et al. Increased thin-cap neoatheroma and periprocedural myocardial infarction in drug-eluting stent restenosis: multimodality intravascular imaging of drug-eluting and bare-metal stents. Circ Cardiovasc Interv. 2013;6(5):507–17.

Bioabsorbable Stent

13

Nienke Simone van Ditzhuijzen, Antonios Karanasos,
Jors Nicolaas van der Sijde, Gijs van Soest,
and Evelyn Regar

Abstract

Fully bioresorbable scaffolds are a promising approach to the treatment of coronary artery disease. The absence of residual foreign material and subsequent restoration of endothelial coverage may address the safety concerns associated with metallic drug-eluting stents such as permanent caging of the artery with or without malapposition, jailing of side branches and late stent thrombosis.

Currently, numerous bioresorbable scaffolds – the majority composed of bioresorbable polymers, and some of absorbable metals – are being developed. Coronary angiography is limited in its ability to visualize the scaffold, because of its low spatial resolution and the radiolucence of the scaffold's polymer backbone.

Angiography alone cannot diagnose scaffold expansion, its interaction with the vessel wall or scaffold degradation over time.

Intracoronary imaging techniques such as intravascular ultrasound (IVUS) or optical coherence tomography (OCT) can overcome these limitations and allow for the evaluation of coronary arteries and scaffolds in great detail. OCT is particularly well suited for the assessment of atherosclerotic plaque, the scaffold and tissue coverage, and allows for detailed evaluation on the individual strut level.

Keywords

Bioresorbable scaffold • BRS • Optical coherence tomography • OCT

13.1 Introduction and Rationale for the Use of Bioresorbable Scaffolds

In the past decades, the applications of percutaneous coronary intervention (PCI) have expanded steadily from balloon angioplasty, the use of bare metal stents, their refinement to drug-eluting stents, and currently fully bioresorbable (drug-eluting) stents are being developed. Fully bioresorbable scaffolds potentially allow for late luminal enlargement, late expansive remodelling and the return of vasomotion. The absence of residual foreign material and the subsequent restoration of endothelial coverage may address currently used stents' limitations including permanent caging with or without malapposition, jailing of side branches and late stent thrombosis [1].

Today, numerous bioresorbable polymer or metal scaffolds are undergoing preclinical and clinical testing (Table 13.1). The most frequently used polymer is Poly-l-Lactide Acid (PLLA), which is widely used in clinical applications such as surgical sutures for wound closure, orthopaedic implants and dialysis media. The application of polymers as scaffolds in coronary arteries, however, still faces several challenges.

N.S. van Ditzhuijzen, MSc • A. Karanasos, MD
J.N. van der Sijde, MD • E. Regar, MD, PhD, FESC (✉)
Department of Cardiology, Erasmus University
Medical Center, s-Gravendijkwal 230, Rotterdam
3015 CE, The Netherlands
e-mail: e.regar@erasmsumc.nl

G. van Soest, PhD
Department of Biomedical Engineering, Erasmus
University Medical Center, Rotterdam, The Netherlands

Table 13.1 Bioresorbable scaffolds under clinical evaluation

Scaffold	Manufacturer	Design	Drug-elution	Strut thickness (μm)	Resorption time (months)
Polymeric					
Igaki-Tamai	Kyoto medical	Zigzag hoops	No	170	24–36
BVS1.0	Abbott vascular	Circumferential hoops	Everolimus	150	24–48
BVS1.1	Abbott vascular	In-phase zigzag hoops linked by bridges	Everolimus	150	36–60
DESolve gen 1	Elixir medical	In-phase zigzag hoops linked by bridges	Myolimus	150	12–25
DESolve gen 2	Elixir medical	In-phase zigzag hoops linked by bridges	Novolimus	150	12–25
REVA	Reva medical	Slide-and-lock	No	114–228	4–6
ReZolve	Reva medical	Slide-and-lock	Sirolimus	114–228	4–6
ReZolve2	Reva medical	Slide-and-lock	Sirolimus	114–228	4–6
ART	Arterial remodeling technologies	Zigzag hoops	No	170	18–24
IDEAL	Xenogenics	In-phase zigzag hoops linked by bridges	Sirolimus	200	Unknown
Xinsorb	Huaan biotech	Zigzag hoops	Sirolimus	160	12–24
ON-ABS	OrbusNeich	Zigzag hoops	Abluminal Sirolimus and luminal+CD34	150	Unknown
FORTITUDE	Amaranth	In-phase zigzag hoops linked by bridges	No	120	12–24
FORTITUDE gen 2	Amaranth	In-phase zigzag hoops linked by bridges	Sirolimus	120	12–24
Metallic					
AMS	Biotronik	Tubular slotted	No	Unknown	4–6
DREAMS gen 1	Biotronik	Zigzag hoops	Paclitaxel	120	12
DREAMS gen 2	Biotronik	In-phase zigzag hoops	Sirolimus	140	12

13.2 Challenges for the Evaluation of Bioresorbable Scaffolds

Bioresorbable scaffolds should possess a variety of key characteristics that are set by metallic stents, such as widespread availability, storage under standard conditions in the catheterization laboratory, fast preparation of the device, wide ranges of available sizes and lengths, a low crossing profile, good visibility under X-ray and a controlled and predictable expansion range. Polymeric scaffolds have however different material characteristics than metallic stents. The first polymeric scaffolds had to be stored under special conditions and had a shorter shelf-life than metallic stents. Today's bioresorbable scaffolds have similar storage conditions and shelf-lives to metallic stents.
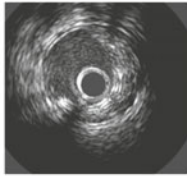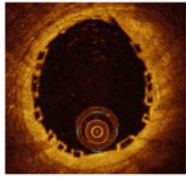
Compared to metallic stents, bioresorbable materials are relatively rigid and non-elastic, resulting in the weakening of the polymeric scaffold by expansion and deformation, thus requiring careful sizing to the coronary artery dimensions. The majority of scaffolds have a balloon-expandable design, but there are also scaffolds with a self-expanding design (Igaki-Tamai) [2] or a slide-and-lock design (REVA), that is deployed by sliding open and is locked into place [3].

Another important difference between the stent types lies in the fact that polymers are invisible under X-ray and thus suffer from poor visualization by coronary angiography. Most of the scaffolds are equipped with radio-opaque markers on both ends of the scaffold or on both ends of the delivery balloon [2, 4, 5], whereas in the REVA bioresorbable scaffold a proprietary iodinated material is added to the polymer that allows visualization of the entire scaffold under X-ray [3].

Coronary angiography is limited to assess scaffold expansion or scaffold degradation over time due to the poor spatial resolution and the radiolucence of the scaffold's polymer backbone. Furthermore, coronary angiography tends to underestimate the vessel dimensions (Fig. 13.1) [6, 7]. Intracoronary imaging techniques such as intravascular ultrasound (IVUS) or optical coherence tomography (OCT) can overcome these limitations [8, 9]. IVUS can provide real-time high-resolution cross-sectional images of the vessel wall and scaffold. IVUS, however, has a tendency to

Fig. 13.1 Advantages of optical coherence tomography (OCT)

	QCA	IVUS	OCT
Dimension measurement	Underestimation	Overestimation	Correct
Detection of scaffold expansion and apposition	Not possible	Poor	Optimal
Detection of scaffold strut distribution	Not possible	Poor	Optimal
Detection of scaffold coverage	Poor	Poor	Optimal
Detection of scaffold strut degradation	Not possible	Poor	Optimal
Extra costs	No	Yes	Yes
Extra procedure time	No	Yes	Yes

slightly overestimate vessel dimensions (Fig. 13.1) and is hampered by the echogenic blooming effect caused by the polymeric struts (Fig. 13.2). Additionally, the limited resolution of IVUS (80–150 μm) compared to OCT (10–15 μm) and the speckled echo signal from blood – that decreases the contrast between the lumen and vessel wall – make the assessment of scaffold expansion and especially the diagnosis of malapposition difficult by IVUS.

The high resolution of intracoronary OCT and the high contrast between lumen and vessel wall (Fig. 13.2) offers advantages for the assessment of atherosclerotic plaque [10], scaffold apposition (Fig. 13.3) and tissue coverage [11, 12] and demonstrated consistently high accuracy and reproducibility in the assessment of coronary stents and scaffolds, irrespective of the analysis method or software used [13–18].

13.3 Intracoronary OCT Imaging of Bioresorbable Scaffolds

Intracoronary OCT enables high-resolution, *in-vivo*, serial imaging of the scaffold and has proven beneficial for the straight-forward detailed evaluation of atherosclerotic lesions and their composition, the vascular injury caused by the implantation procedure, the expansion, the apposition (Fig. 13.3) and mechanical integrity of the scaffold over time, the effect of the underlying plaque on the performance of the scaffold, and the position of the scaffold relative to the side branches [19–23].

13.3.1 OCT Can Reliably Guide Treatment Strategy

Currently available bioresorbable scaffolds have relatively thick struts (114–228 μm), resulting in a relatively high crossing profile. This means that adequate lesion preparation, e.g. by Pre-dilatation, or another appropriate technique, is crucial to pass the device for implantation. Accurate determination of the lumen size and lesion characteristics prior to bioresorbable scaffold implantation is important to ensure appropriate sizing of the device. For instance, the Absorb bioresorbable vascular scaffold (BVS) (Abbott Vascular, Santa Clara, CA) allows for a maximum over-expansion of 0.5 mm compared to the nominal scaffold diameter. Post-dilatation with balloons inflated >0.5 mm above the indicated scaffold diameter increases the risk of fracture. OCT can accurately determine lumen and vessel dimensions as well as lesion characteristics and thus guide treatment strategy, in terms of the selection of an appropriate balloon and scaffold diameter and length [6].

13.3.2 OCT Can Precisely Assess Scaffold Expansion and Strut Apposition

The major concern in inadequate scaffold expansion and incomplete strut apposition is that it can cause non-laminar and turbulent blood flow that can trigger platelet activation, thrombosis or restenosis [24, 25]. OCT allows for the assessment of
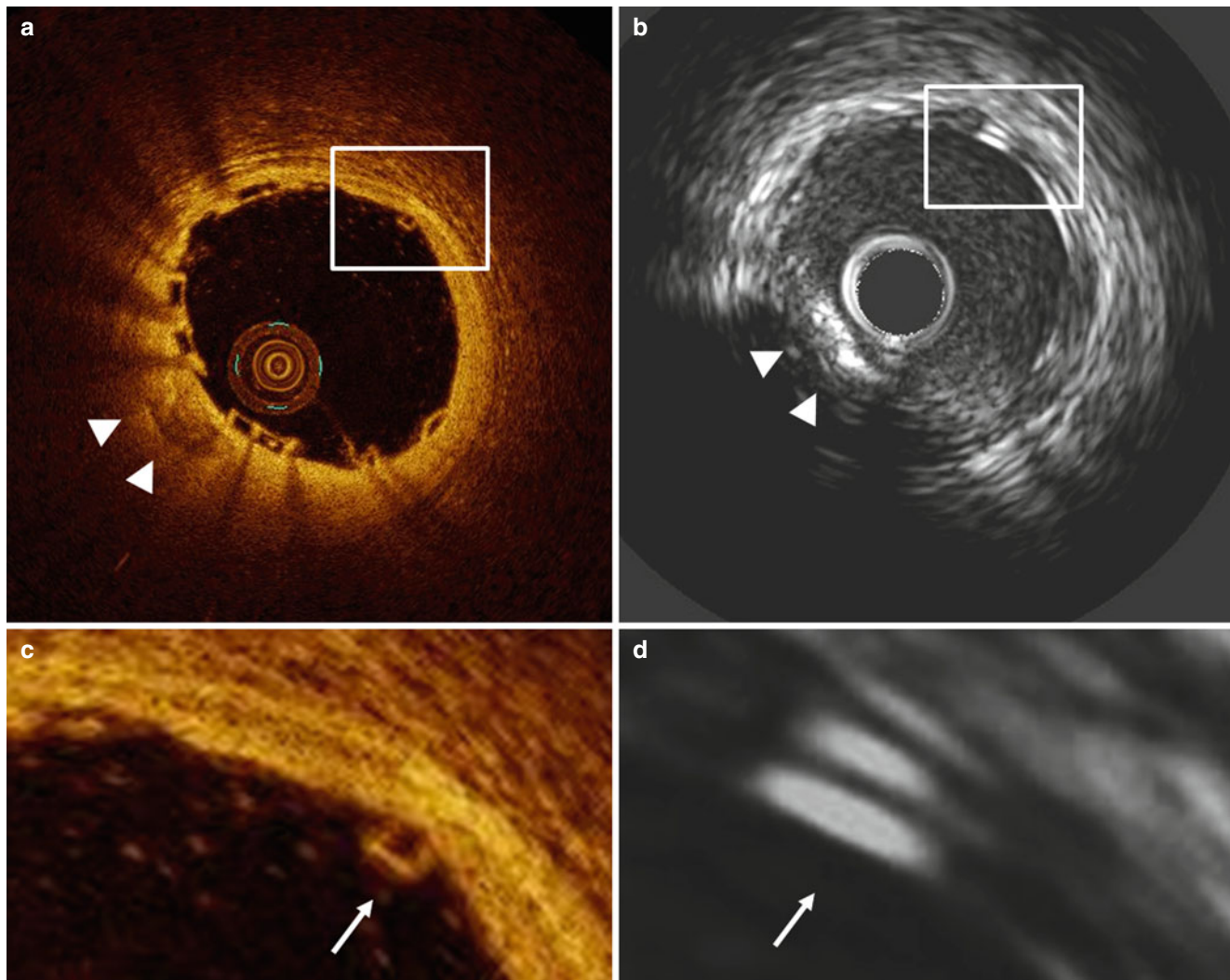
Fig. 13.2 OCT and IVUS immediately after Absorb BVS-implantation in a patient with stable angina. The OCT cross-section (**a**) and magnification (**c**) demonstrate a box-shaped appearance of the scaffold struts (*arrow*), while in the IVUS cross-section (**b**) and magnification (**d**) the scaffold struts have a double-strut appearance due to the echogenic blooming effect of the polymeric struts of the Absorb bioresorbable vascular scaffold (Abbott Vascular, Santa Clara, USA). The *arrowheads* indicate a calcified region visible in both the OCT (**a**) and IVUS (**b**) cross-section

scaffold expansion in relation to the distal and proximal reference segments and to side branches, as well as strut apposition against the vessel wall. The accurate evaluation of scaffold expansion and apposition decreases the risk of incomplete scaffold expansion, recoil, fracture or thrombosis [26, 27].

13.3.3 OCT Can Reliably Assess Scaffold Strut Distribution

Scaffold strut distribution can influence the concentrations of drug reached within the vessel wall, the radial support of the vessel wall and the access to side branches. Therefore, assessment of the scaffold strut distribution is important. Non-uniform strut distribution, which is hypothesized to be caused by calcified deposits occupying >75° of the vessel circumference

[28], may cause non-uniform drug-concentrations within the vessel wall, potentially affecting long-term outcome [29]. OCT allows for detailed analysis of the composition of the atherosclerotic lesion, including the size and extent of calcium, and of the strut distribution pattern, including the assessment of the maximum circular unsupported surface area as well as the assessment of side branch access through the scaffold struts and the impact of struts on side branch patency [30–33].

13.3.4 OCT Can Accurately Assess Scaffold Strut Coverage

The absence and the exaggerated development of neointimal coverage, potentially with the subsequent development of neo-atherosclerosis, have been related to late (drug-eluting) stent
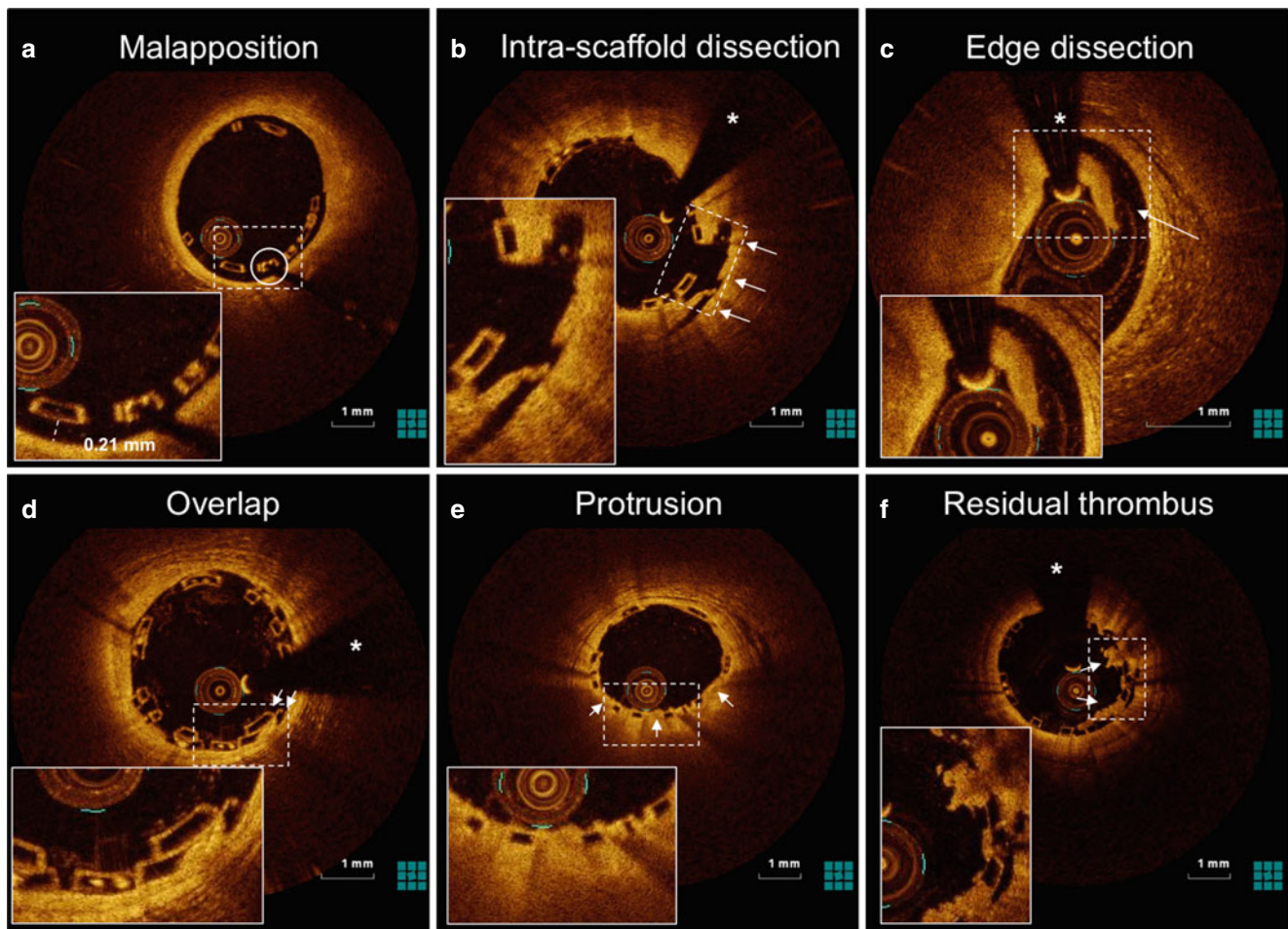
Fig. 13.3 OCT can accurately detect scaffold apposition and periprocedural vessel injury. OCT cross-sections of Absorb BVS demonstrate mild malapposition (**a**), intra-scaffold dissection (**b**; *arrows*), edge dissection (**c**; *arrow*), scaffold overlap (**d**; *arrows*), tissue protrusion between the scaffold struts (**e**; *arrows*) and residual thrombus on top of the struts (**f**; *arrows*) after implantation of an Absorb BVS for ST-elevation myocardial infarction. The *asterisk* (*) indicates the guidewire artefact, the *circle* indicates the platinum marker of the scaffold strut. The *dotted rectangles* indicates the magnification

thrombosis [34, 35]. OCT can reliably detect early and very thin layers of coverage on top of scaffold struts and permits the quantification of the coverage with high reliability [27, 36]. OCT allows the assessment of scaffold area, neointimal area and symmetry as well as lumen area [37–39] and permits the qualitative characterization of neointimal tissue [40, 41].

13.3.5 OCT Allows for Detailed Assessment of Scaffold Strut Degradation

Scaffold strut degradation is of growing clinical interest. OCT can visualize with detail the appearance of the scaffold struts and changes in the strut-appearance over time [4]. In the first-in-man evaluation of the Absorb bioresorbable vascular scaffold (BVS), OCT demonstrated changes in the optical properties of the scaffold struts.

Preclinical observations in coronary arteries of healthy swine demonstrated that OCT can accurately diagnose indi-

vidual struts as well as the strut/vessel wall interaction acutely (Fig. 13.4) and over time. At the 4 year follow-up, OCT demonstrated absence of struts in the vascular wall, with complete degradation of the scaffold confirmed by histology. It is important to note that at the mid-term follow-up (2 years) OCT demonstrated a box-shaped appearance of the scaffold strut that can be associated with strut replacement by proteoglycan [42].

13.3.6 Advantage of Three-Dimensional OCT

The unique ability of OCT to reconstruct three-dimensional (3D) images allows better visualization of the scaffold surface and can provide additive information on the result of PCI, particularly in complex lesions [43, 44]. The application of 3D OCT within the coronary bifurcation seems promising, as the visualization of the complex anatomy of the bifurcation and the effects of intervention
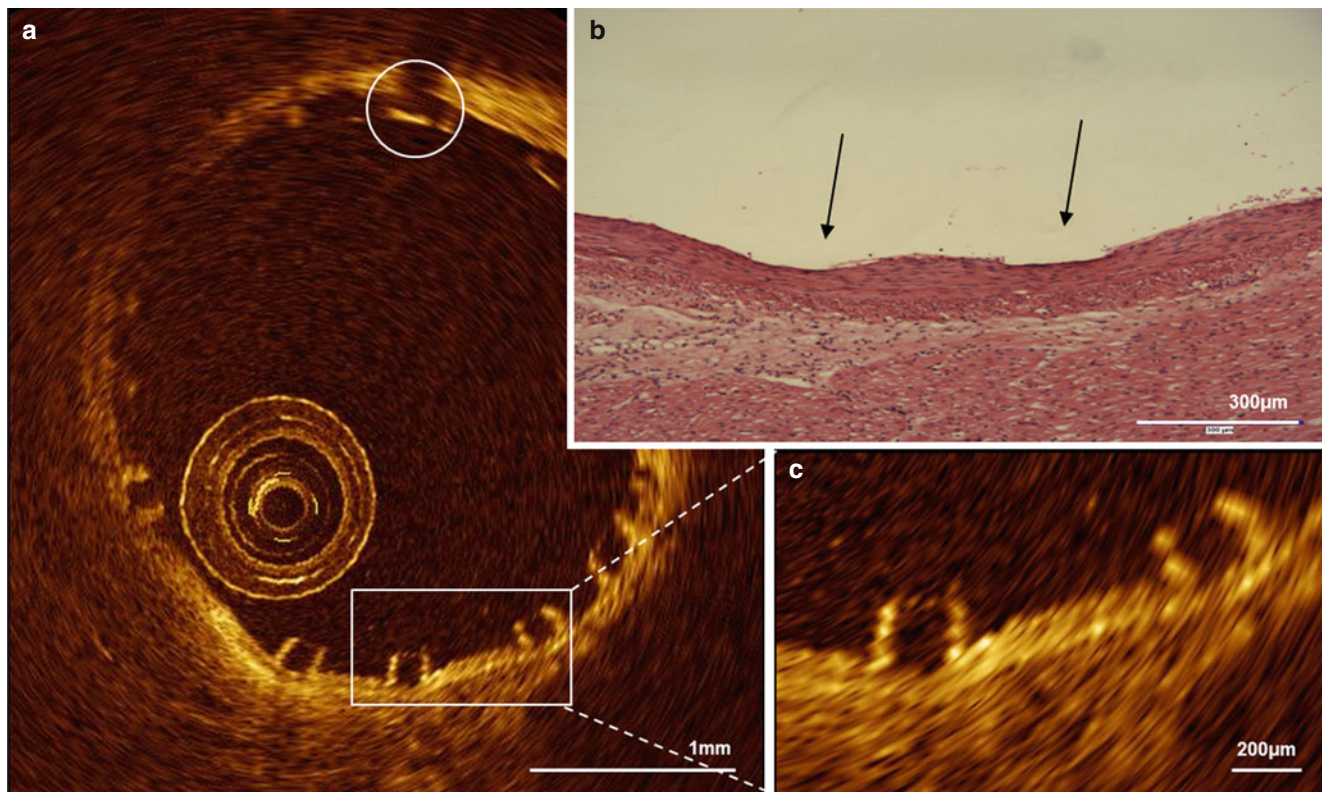
Fig. 13.4 OCT and histology of the Absorb BVS immediately after implantation in a healthy, young swine. OCT (**a**, **c**) can accurately visualize the vessel/ wall interaction after implantation of an Absorb bioresorbable vascular scaffold (Abbott Vascular, Santa Clara, CA, USA) in a coronary artery of a healthy, young swine. In the magnification the typical box-shaped appearance of the scaffold struts can be appreciated, which slightly compress the media (**c**), as confirmed by the histological cross-section (**b**). The *circle* indicates the platinum marker of the scaffold strut. The *arrows* indicate the indentation of the scaffold on histology

are difficult and not always reliable with two-dimensional imaging [32, 45]. 3D-OCT can identify the configuration of overhanging struts in front of the side branch ostium and can be helpful to assess and correctly position the guide wire.

13.4 Clinical Experience

Numerous bioresorbable scaffolds have been investigated in humans [46]. Some have demonstrated disappointing first findings [47], while others, e.g. the ABSORB trials, have proven more encouraging findings [4].

13.4.1 Polymeric Bioresorbable Scaffolds

13.4.1.1 Igaki-Tamai

The Igaki-Tamai (Igaki Medical Planning Co., Kyoto, Japan) represents the first fully biodegradabable scaffold tested in humans in the 1990's [2]. It was a self-expanding, poly-l-lactic acid (PLLA) based, non drug-eluting scaffold with a zigzag design and a strut thickness of 170 μm. The scaffold was compatible with 8 F guide catheters and required storage and expansion at a pre-specified temperature.

A clinical trial in 15 patients proved feasibility and demonstrated remarkable results with a target lesion revascularization rate per patient of 6.7 % at 6 months [2]. Six-month intravascular imaging demonstrated no degradation of the scaffold and the absence of scaffold shrinkage. At the 10-year follow-up, similar major adverse cardiac event (MACE) rates to those of bare metal stents (MACE-free survival was 50 % at 10 years) were documented [48] and OCT demonstrated that just the scaffold markers were still visible (Fig. 13.5). Despite the good results, however, further use of the scaffold for treatment of coronary disease was put on hold, mainly because of the pre-specified temperatures required for storage and expansion.

13.4.1.2 Absorb BVS

The Absorb bioresorbable vascular scaffold (Abbott Vascular, Santa Clara, CA) represents the scaffold with the vastest clinical experience. The scaffold is constructed of a poly-L-lactic acid (PLLA) backbone coated with poly-D,L-lactic acid (PDLLA) that contains the antiproliferative drug everolimus and controls its release (Fig. 13.4) [49].

In the *ABSORB Cohort A trial*, a prospective, multi-center registry in 30 patients with a single, *de-novo* target lesion in
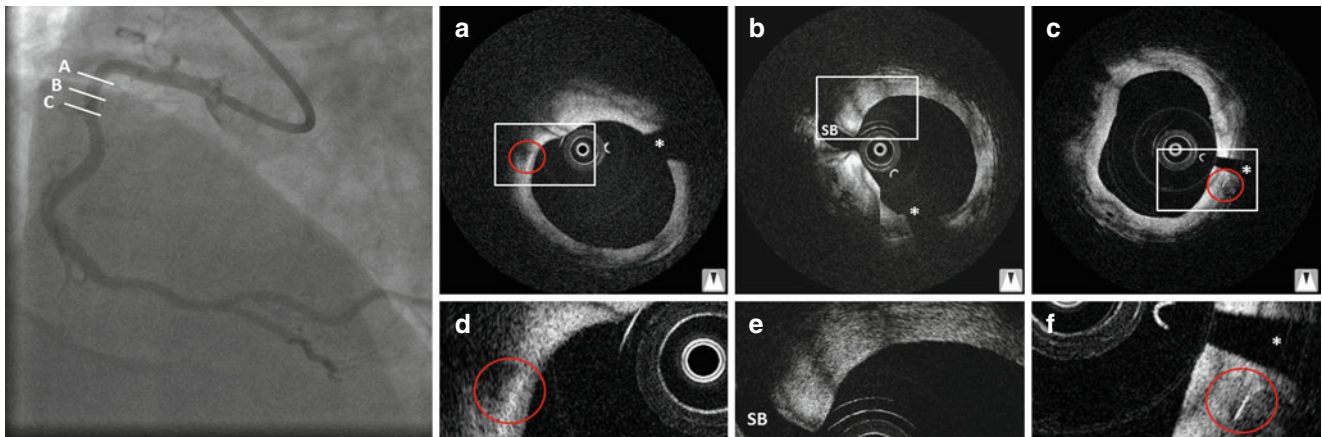
Fig. 13.5 Angiography and OCT 10 year after implantation of an Igaki-Tamai scaffold in a patient with stable angina. Optical coherence tomography cross-sections (**a**–**f**) demonstrate that only the markers of the scaffold are still visible (**a**, **c**), while the remaining struts are not. The *asterisk* (*) indicates the guidewire artifact, *SB* side branch. The *rectangles* indicate the magnifications on the bottom and the *red circles* indicate the markers of the scaffold

a native coronary artery, the first-generation BVS (BVS1.0) was investigated [4]. The majority of patients received a 3.0×12.0 mm scaffold, two patients received a 3.0×18 mm scaffold. The BVS1.0 was designed with a crossing profile of 1.4 mm in circumferential hoops and a strut thickness of 150 μm that were either directly joined or linked by straight bridges. The scaffolds had to be kept at a minimum temperature of −20 °C to prevent physical aging of the polymer and to ensure device stability.

This first-in-man-trial trial demonstrated the feasibility of the everolimus-eluting BVS1.0. Procedural success was 100 %, and device success 94 % [4, 50, 51]. At 1 year, the MACE-rate was 3.3 % of 30 patients. One patient suffered a non-Q wave myocardial infarction. There were no late stent thromboses. At 2 years vasomotion restored, and the scaffold was clinically safe without cardiac death, ischaemia-driven target lesion revascularisation, or stent thrombosis [4, 50]. Long-term results up to 5 years confirmed favourable clinical outcomes, without any cardiac death or scaffold thrombosis and ischaemia-driven MACE rate remained unchanged (3.4 % of 29 patients) [52]. Furthermore, late luminal enlargement (Fig. 13.6) without adaptive vessel remodelling was observed up to 5 year follow-up [53–56].

The OCT substudy of this first-in-man trial, including 13 patients, described changes of the strut appearance at follow-up that were thought to be associated with degradation of the scaffold over time.

In the preclinical study of the BVS1.0 implanted in healthy young swine, however, the assessment of polymer degradation by chemical analysis demonstrated that the preservation of the box-shaped appearance did not exclude resorption of polymeric struts [42]. Two years after implantation, the polymer was no longer accurately quantifiable by chemical degradation analysis, but the structures observed with OCT represented regions corresponding to the location of the scaffold struts. At the 4 year follow-up, OCT demonstrated an absence of struts in the vascular wall, indicating its ability to assess complete degradation of the scaffold in-vivo.

In the *ABSORB Cohort B trial*, a prospective, multi-centre registry of patients with a single, *de-novo* target lesion in a native coronary artery, the second-generation Absorb BVS (BVS 1.1) was investigated. The BVS1.1 is similar to the BVS1.0 with the same polymer mass, strut thickness and drug coating. The manufacturing process of the BVS1.1 has however been modified to enhance the mechanical strength and durability of the struts [30]. The BVS1.1 has in-phase zigzag hoops linked by bridges that allow for more uniform strut distribution, reducing the maximum circular unsupported surface area and providing more uniform vessel wall support and drug transfer [33].

Clinical results demonstrated a low MACE-rate at 6 months (4.4 %), representing one myocardial infraction and one target lesion revascularization. No death or thrombosis occurred [57]. At 1 year, the MACE-rate was 7.1 %, representing two myocardial infarctions and 2 target lesion revascularizations, whereas no cardiac death occurred. At 3 years, the MACE-rate was 10.0 % without any scaffold thrombosis. The return of vasomotion was observed at 12 months and more pronounced at 24 months, suggesting a link between scaffold degradation and restoration of vasomotion in the treated segments [58].

The OCT substudy demonstrated preservation of the box-shaped appearance of the scaffold struts at 6 months [30], which is in line with preclinical observations in atherosclerotic swine [59] 6 months after Absorb BVS1.1 implantation (Fig. 13.7).

In the *ABSORB EXTEND trial*, a non-randomized, single-arm, continued access trial, 800 patients with up to two *de novo* lesions in a native coronary artery were treated with

Fig. 13.6 Angiography and OCT of an Absorb BVS immediately after, 6 months and 2 and 5 year after implantation in a patient with stable angina. The distal and proximal edge of the scaffold are depicted by white lines in the coronary angiogram (*left*). The box-shaped appearance of the scaffold struts can be clearly visualized by OCT immediately after implantation. At 5 year follow-up, the marker of the scaffold strut is visible (*red circle*), while the remaining scaffold struts are not. The *asterisk* (*) indicates the guidewire artefact
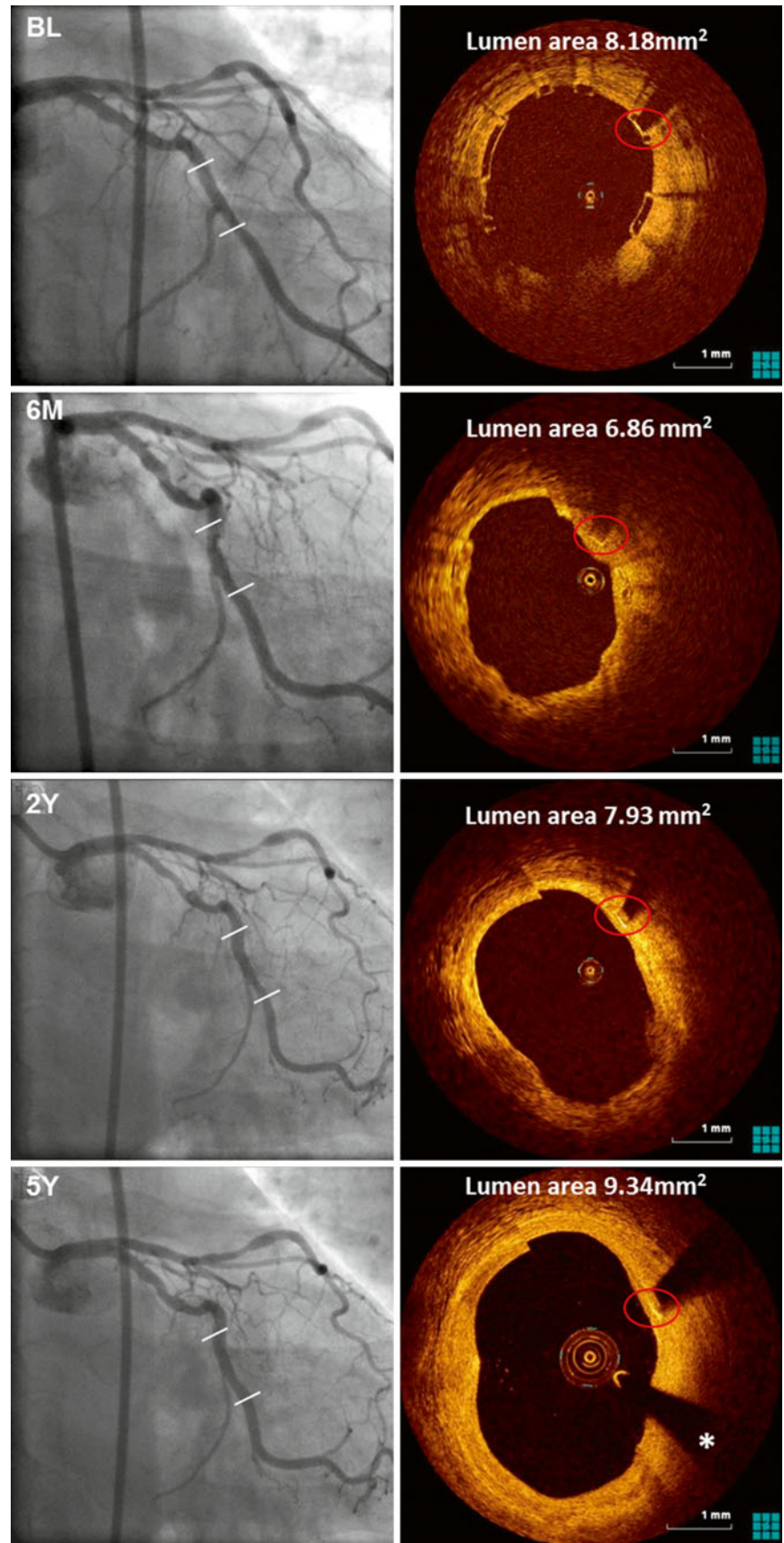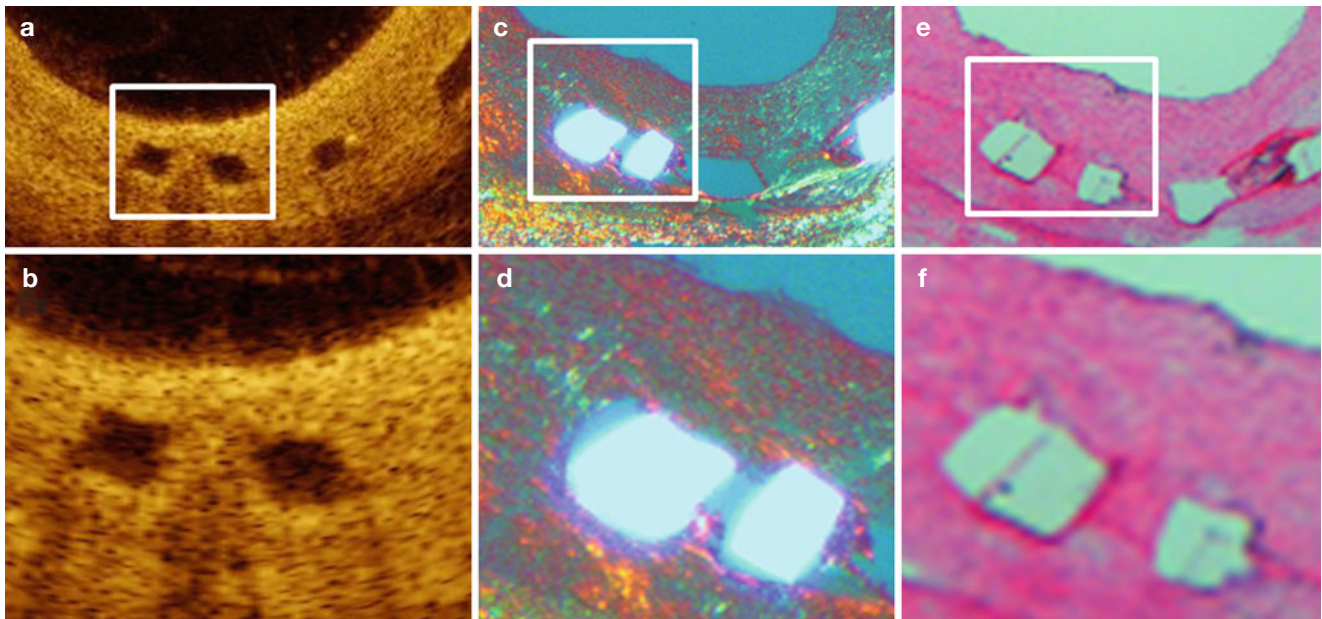
Fig. 13.7 OCT and histology 6 months after Absorb BVS1.1 implantation in an atherosclerotic swine. The OCT cross-sections (**a**, magnification in **b**) clearly demonstrate the box-shaped appearance of the scaffold struts. Preservation of the scaffold struts is confirmed by histology, demonstrating presence of the polymeric struts under polarization light microscopy (**c**, magnification in **d**) and of the strut voids on haematoxylin eosin staining (**e**, magnification in **f**)

BVS 1.1 to continue the assessment of the safety and performance of the BVS1.1 in a large and more complex population. The preliminary report of the 12-month clinical outcomes for the first 512 patients demonstrated that the composite endpoints of ischaemia-driven MACE and ischaemia-driven target vessel failure were low (4.3 and 4.9 %, respectively). The cumulative rate of definite and probable scaffold thrombosis was 0.8 % [60].

Other clinical trials that are underway include the *ABSORB II* and *the ABSORB III and IV pivotal clinical trial programs*. The *ABSORB II trial* is the first randomized trial designed to compare the safety and efficacy of the BVS1.1 versus Xience prime in 500 patients with stable angina and single or two vessel disease [61]. The *ABSORB III and IV pivotal clinical trial programs* are randomized trials designed to achieve approval of BVS1.1 in the United States of America and to demonstrate the superiority of BVS1.1 compared to drug-eluting stents [62].

13.4.1.3 DESolve

The DESolve (Elixir Medical, Sunnyvale, USA) scaffold is a PLLA-based scaffold that contains the anti-proliferative drug myolimus, has a strut thickness of 150 μm, 2 platinum-based radiopaque markers at either end of the scaffold, provides vessel support for 3–4 months and fully resorbs in about 1 year.

In *the DESolve First-in-Man* study, a prospective, non-randomized, multi-centre study, 16 patients with *de novo* native coronary artery lesions were included and the feasibility and efficacy of the DESolve scaffold were demonstrated

[5]. Acute procedural success was 100 %. At 12 months, no scaffold thrombosis or MACE directly attributable to the scaffold occurred and invasive imaging demonstrated low neointimal hyperplasia and no evidence of scaffold recoil or late malapposition [5].

In *the DESolve Nx study*, a prospective, multi-centre study presented at the transcatheter-therpeutic-interventions (TCT) conference in San Francisco in 2013, the second iteration of the DESolve containing the antiproliferative drug novolimus was evaluated. In the first 126 patients included, a 1-year MACE rate of 5.69 % was observed, representing 2 cardiac deaths, 1 target vessel myocardial infarction and 4 clinically indicated target lesion revascularizations. No scaffold thrombosis was documented [63].

13.4.1.4 REVA

The first-generation REVA (REVA Medical Inc., San Diego, USA) was a non-drug-eluting scaffold composed of tyrosine-derived polycarbonate, with a unique radio-opaque slide-and-lock mechanism to allow for safe expansion and visualization under X-ray (Fig. 13.8) [3].

In *the RESORB study*, a non-randomized, multicentre registry that assessed the safety and performance of the scaffold, 25 patients with a *de novo* coronary lesion were included. Radial strength was sufficient during the first 3 months following implantation without appreciable shrinkage. However, focal mechanical failures led to a high rate of target lesion revascularization (66.7 %) between the 4 and 6 months follow-up [64].
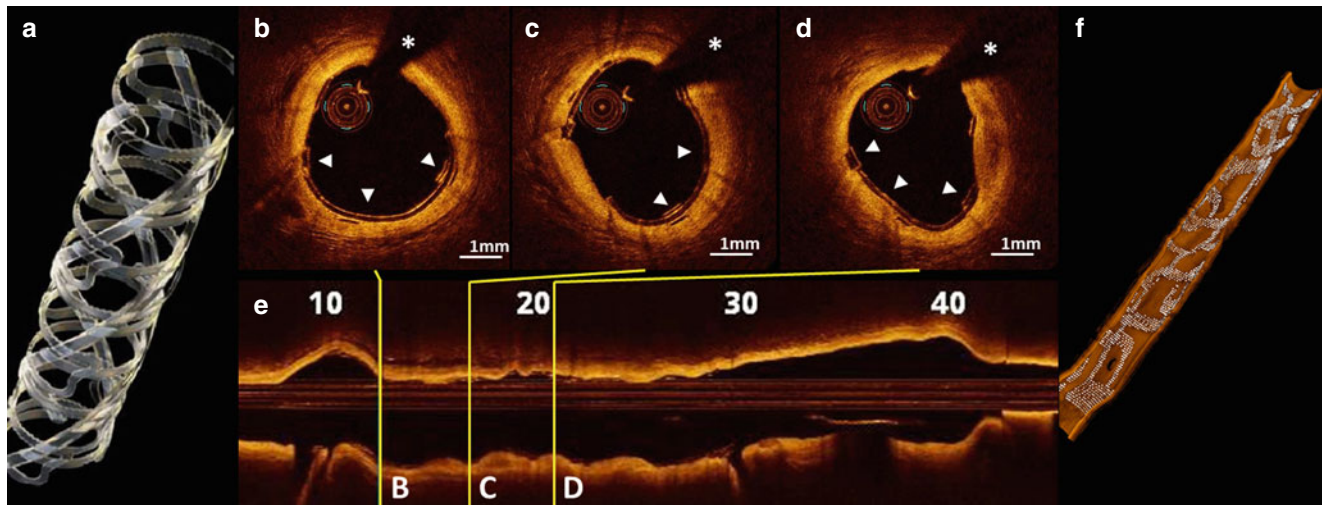
Fig. 13.8 OCT immediately after REVA scaffold implantation in a patient with stable angina. The REVA is designed with a unique slide-and-lock design, as can be visualized in the cartoon (**a**), the OCT cross-sections (*arrowheads* in **b–d**) that correspond to the letters *B*, *C* and *D* in the longitudinal view (**e**) of the OCT-pullback and the three-dimensional reconstruction (**f**). The *asterisk* (*) indicates the guide wire artifact

In *the RESTORE trial*, the ReZolve Sirolimus-eluting bioresorbable coronary scaffold clinical trial, a new iteration of the REVA scaffold, the ReZolve, was evaluated for its safety and performance in 26 patients. The 12 months results, presented at the TCT conference in Miami in 2012, demonstrated safety and good performance. Two MACE, one target lesion revascularization for focal in-stent restenosis, and one directly related to protocol deviation at implant were documented up through the 6 months follow-up [65].

In *the RESTORE II trial*, the second-generation ReZolve (ReZolve2), which has a lower profile and is sheathless, will be evaluated in 125 patients with the aim of attaining Conformité Européenne (CE) mark approval.

13.4.1.5 ART

The ART (Arterial Remodeling Technologies, Noisy le Roi, France) is a drug-free, flexible, bioresorbable PDLLA-polymer scaffold. Dismantling starts at 3 months with recovery of arterial function, and full resorption expected within 18–24 months.

In *the ARTDIVA* (Arterial Remodelling Transient Dismantling Vascular Angioplasty) trial, a prospective, multicentre, single-arm investigation, 30 patients with single *de novo* native coronary artery lesions with mandatory balloon predilatation were included. Preliminary results, presented at the TCT conference in San Francisco in 2013, demonstrated 100 % procedural and 94 % device success, good apposition, 30-day event-free survival and 4.0 % angiographic recoil at 30 days [66].

13.4.1.6 IDEAL

The IDEAL (Xenogenics Corp., Canton, MA, USA) is a fully bioresorbable balloon-expandable scaffold that consists of a polylactide, anhydride and a trimer of two salicyclic acid molecules joined by a sebacic acid, while the top coat is comprised of salicylate and the antiproliferative drug sirolimus [67].

In *the WHISPER study*, a prospective, first-in-man, the safety and efficacy of the scaffold was evaluated. Although the study has not been fully reported, an increased neointimal formation, attributed to an inadequate drug dose and fast drug-elution, was documented in 11 patients, and a new iteration of the scaffold was developed.

The revised scaffold, the IDEAL BioStent, has a higher drug dose with slower release kinetics and is currently under preclinical evaluation.

13.4.1.7 Xinsorb

The Xinsorb (Shandong Huaan Biotechnology Co., Ltd, China) is a sirolimus-eluting, balloon-expandable, PLLA scaffold that has radiopaque markers to facilitate its expansion. The scaffold has a strut thickness of 160 µm and is available in sizes ranging from 2.75 to 4.0 mm in diameter, and from 12 to 28 mm in length [68].

In the first-in-man, prospective, bi-center trial, the feasibility, safety and efficacy of the Xinsorb will be evaluated in 30 patients at 1, 3, 6, 9 and 12 months. The 6-months angiography of the first 6 patients demonstrates effective suppression of neointimal hyperplasia [69].

13.4.1.8 ON-ABS

The ON-ABS BRS is composed of three distinct bioabsorbable polymer systems: Poly-D-lactide, PLLA, and L-lactide-co-ε-caprolactone, and incorporates a partitioned coating technology that allows the scaffold to be covered by abluminal sirolimus and luminal endothelial progenitor cell capture (+CD34) antibodies. Preliminary preclinical data presented at the TCT conference in San Francisco in 2013 demonstrated optimal device implantation without evidence of fracture [70].

The first-in-man evaluation of the ON-ABS is underway.

13.4.1.9 FORTITUDE

The FORTITUDE (Amaranth Medical Inc Mountain View, CA, USA) is a non-drug-eluting PLLA-based scaffold that contains structural integrity for 3–6 months and completely resorbs within 1–2 years. The scaffold was evaluated in a study of 13 patients with single *de novo* coronary artery lesions and, as presented at the TCT conference in San Francisco in 2013, demonstrated maintained mechanical integrity with late lumen loss comparable to that observed for bare metal stents at the 6 months follow-up [71].

Currently, the second-generation FORTITUDE, which has thinner struts and sirolimus drug-elution capabilities, is already in advanced development.

13.4.2 Metallic Bioresorbable Scaffolds

13.4.2.1 AMS

The absorbable metal stent (AMS) (Biotronik, Berlin, Germany) is a tubular, slotted, magnesium-based balloon-expandable scaffold, available in 10 and 15 mm lengths with 3.0 and 3.5 mm diameters, respectively.

In the first-in-man *PROGRESS-AMS trial*, a prospective, non-randomised, multicentre clinical trial, 63 patients with single *de novo* native coronary artery lesions were enrolled [72]. No myocardial infarction, subacute or late thrombosis, or death was documented. Target lesion revascularization rates were, however, high: 23.8 % after 4 months, and 45 % after 1 year.

In *the BIOSOLVE-1 trial*, a prospective, multi-centre study, a new generation drug-eluting absorbable metal scaffolds (DREAMS), characterized by a prolonged scaffolding time and the anti-proliferative drug paclitaxel, was evaluated in 46 patients with single *de novo* native coronary artery lesions. One-year results demonstrated feasibility and safety of the DREAMS with 100 % procedural and device success, a target lesion revascularization rate of 7 % and no cardiac death or scaffold thrombosis [73].

In *the BIOSOLVE-II trial*, a prospective, international, multi-centre study, the safety and clinical performance of the second-generation sirolimus-eluting DREAMS will be evaluated.

13.5 Other Bioresorbable Scaffolds Currently Under Investigation

Several other bioresorbable scaffolds that are currently under development include the MeRes (Meril Life Science, India), Lifetech Iron (Lifetech Scientific, Shenzhen, China), Sahajanand (Sahajanand Medica Technologies, India), Avatar (S3V Vascular Technologies, India), FADES (Zorion Medical, Indianapolis, IN, USA) and Arterius (Arterius Ltd, Bradford, UK).

13.6 OCT Imaging of Bioresorbable Scaffolds – A Step Towards Routine Clinical Practice

Bioresorbable scaffolds are increasingly used in clinical practice, with the extension to patients with more complex lesions [60], including ST-elevation myocardial infarction patients [74], patients with long lesions requiring overlapping scaffolds, or patients with small vessels and bifurcation lesions [75–78]. The detailed evaluation of the behaviour and performance of bioresorbable scaffolds – such as the expansion, apposition and degradation of the scaffolds as well as the vascular response to the scaffold – is of growing clinical interest and thus the longitudinal, *in-vivo* intracoronary OCT, which has proven safe, highly accurate and reliable, is more widely used. Additionally, with the development of 3D OCT and software that allows co-registration of quantitative coronary angiography and OCT [79], OCT can accurately guide treatment strategy (Fig. 13.9) and assess treatment outcome (Fig. 13.10) and thus provide advantages for the evaluation of scaffold behaviour and performance in routine clinical practice.
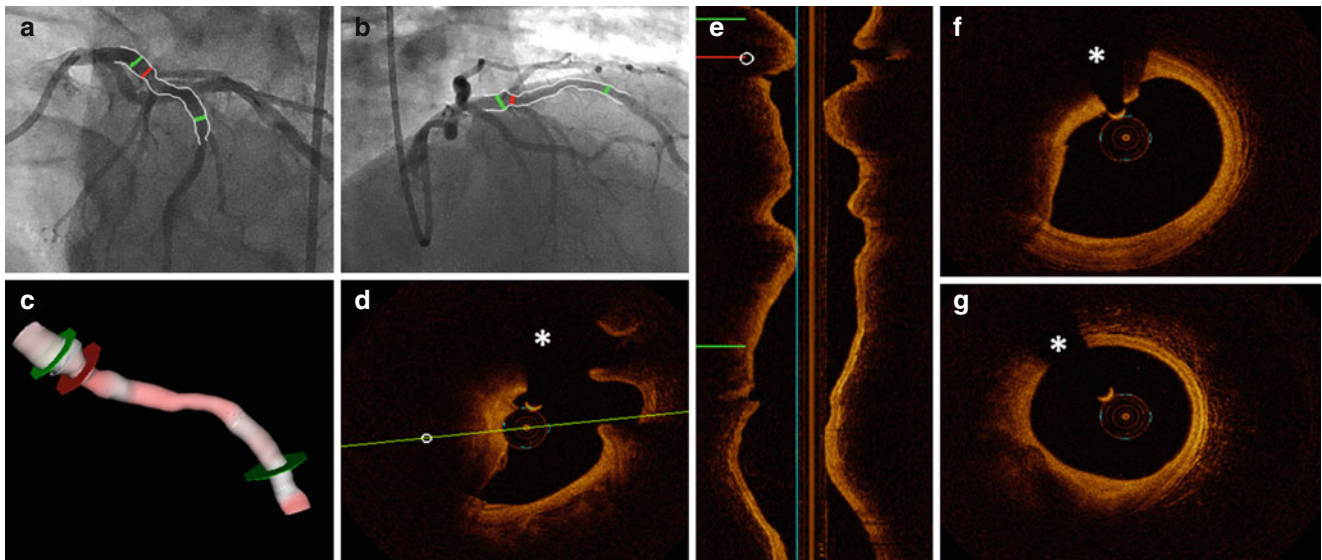
Fig. 13.9 Three-dimensional (3D) QCA and OCT for optimal scaffold selection. Two angiographic views (**a**, **b**) were used to reconstruct the color-coded vessel segment (**c**) [79]. The *red line* corresponds to the OCT cross-section that is used as landmark (**d**), also visible in the longitudinal view of the OCT pullback (**e**). The *green lines* indicate the distal (**f**) and proximal (**g**) landing zones. After the registration, the corresponding markers in the different views (**a–g**) were synchronized, allowing the assessment of lumen dimensions from both imaging modalities at every corresponding position along the vessel segment (QAngioOCT; Medis Specials, Leiden, Netherlands). The *asterisk* (*) indicates the guide wire artifact
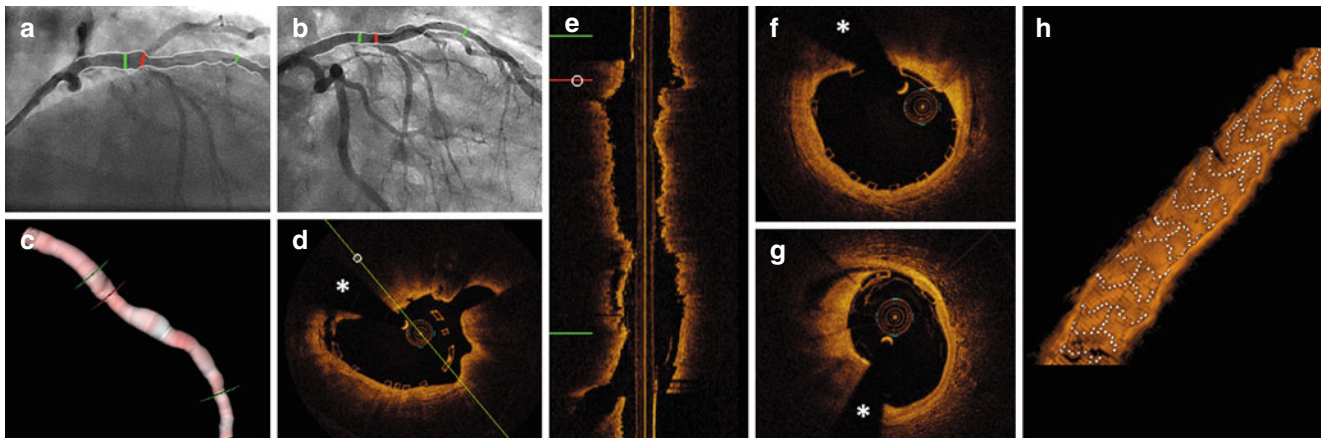
Fig. 13.10 Three-dimensional QCA and OCT to assess scaffold-implantation. Two angiographic views (**a**, **b**) were used to reconstruct the color-coded vessel segment (**c**) [79]. The *red line* corresponds to the OCT cross-section that is used as landmark (**d**), also visible in the longitudinal view of the OCT pullback (**e**). The *green lines* indicate the distal (**f**) and proximal (**g**) landing zones. After the registration, the corresponding markers in the different views (**a–g**) were synchronized, allowing for assessment of the scaffold from both imaging modalities. The 3D reconstruction of the scaffold clearly demonstrates the in-phase zigzag hoops that are linked by bridges (**h**) (QAngioOCT; Medis Specials, Leiden, Netherlands). The *asterisk* (*) indicates the guide wire artifact

References

1. Serruys PW, Garcia-Garcia HM, Onuma Y. From metallic cages to transient bioresorbable scaffolds: change in paradigm of coronary revascularization in the upcoming decade? Eur Heart J. 2012; 33(1):16–25b.
2. Tamai H, Igaki K, Kyo E, Kosuga K, Kawashima A, Matsui S, et al. Initial and 6-month results of biodegradable poly-l-lactic acid coronary stents in humans. Circulation. 2000;102(4):399–404.
3. Pollman MJ. Engineering a bioresorbable stent: REVA programme update. EuroIntervention. 2009;5(Suppl F):F54–7.
4. Ormiston JA, Serruys PW, Regar E, Dudek D, Thuesen L, Webster MW, et al. A bioabsorbable everolimus-eluting coronary stent system for patients with single de-novo coronary artery lesions (ABSORB): a prospective open-label trial. Lancet. 2008;371(9616): 899–907.
5. Verheye S, Ormiston JA, Stewart J, Webster M, Sanidas E, Costa R, et al. A next-generation bioresorbable coronary scaffold system: from bench to first clinical evaluation: 6- and 12-month clinical and multi-modality imaging results. JACC Cardiovasc Interv. 2014;7(1):89–99.
6. Gutierrez-Chico JL, Serruys PW, Girasis C, Garg S, Onuma Y, Brugaletta S, et al. Quantitative multi-modality imaging analysis of a

fully bioresorbable stent: a head-to-head comparison between QCA, IVUS and OCT. Int J Cardiovasc Imaging. 2012;28(3):467–78.

7. Tsuchida K, van der Giessen WJ, Patterson M, Tanimoto S, Garcia-Garcia HM, Regar E, et al. *In vivo* validation of a novel three-dimensional quantitative coronary angiography system (CardiOp-B): comparison with a conventional two-dimensional system (CAAS II) and with special reference to optical coherence tomography. EuroIntervention. 2007;3(1):100–8.

8. Huang D, Swanson EA, Lin CP, Schuman JS, Stinson WG, Chang W, et al. Optical coherence tomography. Science. 1991;254(5035):1178–81.

9. Sarno G, Bruining N, Onuma Y, Garg S, Brugaletta S, De Winter S, et al. Morphological and functional evaluation of the bioresorption of the bioresorbable everolimus-eluting vascular scaffold using IVUS, echogenicity and vasomotion testing at two year follow-up: a patient level insight into the ABSORB A clinical trial. Int J Cardiovasc Imaging. 2012;28(1):51–8.

10. Van Ditzhuijzen NS, Van Beusekom HM, Ligthart JM, Regar E. Invasive imaging of the coronary atherosclerotic plaque. Minerva Cardioangiol. 2012;60(3):305–29 [Review].

11. Regar E, van Leeuwen AMGJ, Serruys PW. Optical coherence tomography in cardiovascular research. London: Informa Healthcare; 2007.

12. Gonzalo N, Serruys PW, Garcia-Garcia HM, van Soest G, Okamura T, Ligthart J, et al. Quantitative *ex vivo* and *in vivo* comparison of lumen dimensions measured by optical coherence tomography and intravascular ultrasound in human coronary arteries. Rev Esp Cardiol. 2009;62(6):615–24.

13. van Ditzhuijzen NS, Karanasos A, Bruining N, van den Heuvel M, Sorop O, Ligthart J, et al. The impact of Fourier-Domain optical coherence tomography catheter induced motion artefacts on quantitative measurements of a PLLA-based bioresorbable scaffold. Int J Cardiovasc Imaging. 2014;16.

14. Jamil Z, Tearney G, Bruining N, Sihan K, van Soest G, Ligthart J, et al. Interstudy reproducibility of the second generation, Fourier domain optical coherence tomography in patients with coronary artery disease and comparison with intravascular ultrasound: a study applying automated contour detection. Int J Cardiovasc Imaging. 2013;29(1):39–51.

15. Okamura T, Onuma Y, Garcia-Garcia HM, van Geuns RJ, Wykrzykowska JJ, Schultz C, et al. First-in-man evaluation of intravascular optical frequency domain imaging (OFDI) of Terumo: a comparison with intravascular ultrasound and quantitative coronary angiography. EuroIntervention. 2011;6(9):1037–45.

16. Gonzalo N, Tearney GJ, Serruys PW, van Soest G, Okamura T, Garcia-Garcia HM, et al. Second-generation optical coherence tomography in clinical practice. High-speed data acquisition is highly reproducible in patients undergoing percutaneous coronary intervention. Rev Esp Cardiol. 2010;63(8):893–903.

17. Okamura T, Gonzalo N, Gutierrez-Chico JL, Serruys PW, Bruining N, de Winter S, et al. Reproducibility of coronary Fourier domain optical coherence tomography: quantitative analysis of *in vivo* stented coronary arteries using three different software packages. EuroIntervention. 2010;6(3):371–9.

18. Zahnd G, Karanasos A, Van Soest G, Regar E, Niessen WJ, Gijsen FJ, et al. Semi-automated quantification of fibrous cap thickness in intra- coronary optical coherence tomography. International Conference on Information Processing in Computer-Assisted Interventions (IPCAI), 2014.

19. Takarada S, Imanishi T, Liu Y, Ikejima H, Tsujioka H, Kuroi A, et al. Advantage of next-generation frequency-domain optical coherence tomography compared with conventional time-domain system in the assessment of coronary lesion. Catheter Cardiovasc Interv. 2010;75(2):202–6.

20. Prati F, Regar E, Mintz GS, Arbustini E, Di Mario C, Jang IK, et al. Expert review document on methodology, terminology, and clinical applications of optical coherence tomography: physical principles, methodology of image acquisition, and clinical application for assessment of coronary arteries and atherosclerosis. Eur Heart J. 2010;31(4):401–15.

21. Prati F, Guagliumi G, Mintz GS, Costa M, Regar E, Akasaka T, et al. Expert review document part 2: methodology, terminology and clinical applications of optical coherence tomography for the assessment of interventional procedures. Eur Heart J. 2012; 33(20):2513–20.

22. Tanimoto S, Bruining N, van Domburg RT, Rotger D, Radeva P, Ligthart JM, et al. Late stent recoil of the bioabsorbable everolimus-eluting coronary stent and its relationship with plaque morphology. J Am Coll Cardiol. 2008;52(20):1616–20.

23. Tearney GJ, Regar E, Akasaka T, Adriaenssens T, Barlis P, Bezerra HG, et al. Consensus standards for acquisition, measurement, and reporting of intravascular optical coherence tomography studies: a report from the International Working Group for Intravascular Optical Coherence Tomography Standardization and Validation. J Am Coll Cardiol. 2012;59(12):1058–72.

24. Foin N, Gutierrez-Chico JL, Nakatani S, Torii R, Bourantas CV, Sen S, et al. Incomplete stent apposition causes high shear flow disturbances and delay in neointimal coverage as a function of strut to wall detachment distance: implications for the management of incomplete stent apposition. Circ Cardiovasc Interv. 2014;7(2):180–9.

25. Karanasos A, van Geuns RJ, Zijlstra F, Regar E. Very late bioresorbable scaffold thrombosis after discontinuation of dual antiplatelet therapy. Eur Heart J. 2014;19.

26. Gomez-Lara J, Diletti R, Brugaletta S, Onuma Y, Farooq V, Thuesen L, et al. Angiographic maximal luminal diameter and appropriate deployment of the everolimus-eluting bioresorbable vascular scaffold as assessed by optical coherence tomography: an ABSORB cohort B trial sub-study. EuroIntervention. 2012;8(2):214–24.

27. Gomez-Lara J, Radu M, Brugaletta S, Farooq V, Diletti R, Onuma Y, et al. Serial analysis of the malapposed and uncovered struts of the new generation of everolimus-eluting bioresorbable scaffold with optical coherence tomography. JACC Cardiovasc Interv. 2011;4(9):992–1001.

28. Sato K, Latib A, Naganuma T, Panoulas VF, Miyazaki T, Colombo A, editors. Impact of calcified plaque for stent struts distribution of the bioabsorbable everolimus-eluting device – optical coherence tomography analysis. Paris: EuroPCR; 2014.

29. Suzuki Y, Ikeno F, Yeung AC. Drug-eluting stent strut distribution: a comparison between Cypher and Taxus by optical coherence tomography. J Invasive Cardiol. 2006;18(3):111–4.

30. Gomez-Lara J, Brugaletta S, Diletti R, Garg S, Onuma Y, Gogas BD, et al. A comparative assessment by optical coherence tomography of the performance of the first and second generation of the everolimus-eluting bioresorbable vascular scaffolds. Eur Heart J. 2011;32(3):294–304.

31. Burzotta F, De Vita M, Sgueglia G, Todaro D, Trani C. How to solve difficult side branch access? EuroIntervention. 2010;6(Suppl J):J72–80.

32. Okamura T, Onuma Y, Garcia-Garcia HM, Regar E, Wykrzykowska JJ, Koolen J, et al. 3-Dimensional optical coherence tomography assessment of jailed side branches by bioresorbable vascular scaffolds: a proposal for classification. JACC Cardiovasc Interv. 2010;3(8):836–44.

33. Okamura T, Garg S, Gutierrez-Chico JL, Shin ES, Onuma Y, Garcia-Garcia HM, et al. In vivo evaluation of stent strut distribution patterns in the bioabsorbable everolimus-eluting device: an OCT ad hoc analysis of the revision 1.0 and revision 1.1 stent design in the ABSORB clinical trial. EuroIntervention. 2010;5(8):932–8.

34. Cook S, Wenaweser P, Togni M, Billinger M, Morger C, Seiler C, et al. Incomplete stent apposition and very late stent thrombosis after drug-eluting stent implantation. Circulation. 2007;115(18):2426–34.

35. Park SJ, Kang SJ, Virmani R, Nakano M, Ueda Y. In-stent neoatherosclerosis: a final common pathway of late stent failure. J Am Coll Cardiol. 2012;59(23):2051–7.

36. Gutierrez-Chico JL, Regar E, Nuesch E, Okamura T, Wykrzykowska J, di Mario C, et al. Delayed coverage in malapposed and side-branch struts with respect to well-apposed struts in drug-eluting stents: in vivo assessment with optical coherence tomography. Circulation. 2011;124(5):612–23 [Research Support, Non-U.S. Gov't].

37. Tanimoto S, Rodriguez-Granillo G, Barlis P, de Winter S, Bruining N, Hamers R, et al. A novel approach for quantitative analysis of intracoronary optical coherence tomography: high inter-observer agreement with computer-assisted contour detection. Catheter Cardiovasc Interv. 2008;72(2):228–35.

38. Gonzalo N, Garcia-Garcia H, Serruys PW, Commissaris K, Bezerra H, Gobbens P, Costa MA, Regar E. Reproducibility of quantitative optical coherence tomography for stent analysis. EuroIntervention. 2009;5(2):224–32.

39. Brugaletta S, Radu MD, Garcia-Garcia HM, Heo JH, Farooq V, Girasis C, et al. Circumferential evaluation of the neointima by optical coherence tomography after ABSORB bioresorbable vascular scaffold implantation: can the scaffold cap the plaque? Atherosclerosis. 2012;221(1):106–12.

40. Gomez-Lara J, Brugaletta S, Farooq V, Onuma Y, Diletti R, Windecker S, et al. Head-to-head comparison of the neointimal response between metallic and bioresorbable everolimus-eluting scaffolds using optical coherence tomography. JACC Cardiovasc Interv. 2011;4(12):1271–80.

41. Gonzalo N, Serruys PW, Okamura T, van Beusekom HM, Garcia-Garcia HM, van Soest G, et al. Optical coherence tomography patterns of stent restenosis. Am Heart J. 2009;158(2):284–93.

42. Onuma Y, Serruys PW, Perkins LE, Okamura T, Gonzalo N, Garcia-Garcia HM, et al. Intracoronary optical coherence tomography and histology at 1 month and 2, 3, and 4 years after implantation of everolimus-eluting bioresorbable vascular scaffolds in a porcine coronary artery model: an attempt to decipher the human optical coherence tomography images in the ABSORB trial. Circulation. 2010;122(22):2288–300.

43. Farooq V, Gogas BD, Okamura T, Heo JH, Magro M, Gomez-Lara J, et al. Three-dimensional optical frequency domain imaging in conventional percutaneous coronary intervention: the potential for clinical application. Eur Heart J. 2013;34(12):875–85.

44. van Geuns RJ, Gogas BD, Farooq V, Regar E, Serruys PW. 3-Dimensional reconstruction of a bifurcation lesion with double wire after implantation of a second generation everolimus-eluting bioresorbable vascular scaffold. Int J Cardiol. 2011;153(2):e43–5.

45. Okamura T, Serruys PW, Regar E. Cardiovascular flashlight. The fate of bioresorbable struts located at a side branch ostium: serial three-dimensional optical coherence tomography assessment. Eur Heart J. 2010;31(17):2179 [Case Reports].

46. Van Ditzhuijzen N, Ligthart J, Bruining N,ER, Van Beusekom HMM. Invasive imaging of bioresorbable coronary scaffolds – a review. Intervent Cardiol Review. 2013;8(1):23–35.

47. Erbel R, Di Mario C, Bartunek J, Bonnier J, de Bruyne B, Eberli FR, et al. Temporary scaffolding of coronary arteries with bioabsorbable magnesium stents: a prospective, non-randomised multicentre trial. Lancet. 2007;369(9576):1869–75.

48. Nishio S, Kosuga K, Igaki K, Okada M, Kyo E, Tsuji T, et al. Long-Term (>10 Years) clinical outcomes of first-in-human biodegradable poly-l-lactic acid coronary stents: Igaki-Tamai stents. Circulation. 2012;125(19):2343–53.

49. Oberhauser J, Hossainy S, Rapoza R. Design principles and performance of bioresorbable polymeric coronary scaffolds. EuroIntervention. 2009;5(Supplement F):F15–23.

50. Serruys PW, Ormiston JA, Onuma Y, Regar E, Gonzalo N, Garcia-Garcia HM, et al. A bioabsorbable everolimus-eluting coronary stent system (ABSORB): 2-year outcomes and results from multiple imaging methods. Lancet. 2009;373(9667):897–910.

51. Onuma Y, Serruys PW, Ormiston JA, Regar E, Webster M, Thuesen L, et al. Three-year results of clinical follow-up after a bioresorbable everolimus-eluting scaffold in patients with de novo coronary artery disease: the ABSORB trial. EuroIntervention. 2010;6:447–53.

52. Onuma Y, Dudek D, Thuesen L, Webster M, Nieman K, Garcia-Garcia HM, et al. Five-year clinical and functional multislice computed tomography angiographic results after coronary implantation of the fully resorbable polymeric everolimus-eluting scaffold in patients with de novo coronary artery disease: the ABSORB cohort A trial. JACC Cardiovasc Interv. 2013;6(10):999–1009.

53. Brugaletta S, Heo JH, Garcia-Garcia HM, Farooq V, van Geuns RJ, de Bruyne B, et al. Endothelial-dependent vasomotion in a coronary segment treated by ABSORB everolimus-eluting bioresorbable vascular scaffold system is related to plaque composition at the time of bioresorption of the polymer: indirect finding of vascular reparative therapy? Eur Heart J. 2012;33(11):1325–33.

54. Karanasos A, Simsek C, Serruys P, Ligthart J, Witberg K, van Geuns RJ, et al. Five-year optical coherence tomography follow-up of an everolimus-eluting bioresorbable vascular scaffold: changing the paradigm of coronary stenting? Circulation. 2012;126(7):e89–91.

55. Garcia-Garcia HM, Schultz C, Duckers E, Regar E, Ligthart J, Serruys PW, et al. Five-year follow-up of the ABSORB bioresorbable everolimus-eluting vascular scaffold system: multimodality imaging assessment. EuroIntervention. 2013;8(10):1126–7 [Case Reports].

56. Simsek C, Karanasos A, Magro M, Garcia-Garcia HM, Onuma Y, Regar E, Boersma E, Serruys P, van Geuns R-J. Long-term invasive follow-up of the everolimus-eluting bioresorbable vascular scaffold: five-year results of multiple invasive imaging modalities. EuroIntervention. 2014; in press.

57. Serruys PW, Onuma Y, Ormiston JA, de Bruyne B, Regar E, Dudek D, et al. Evaluation of the second generation of a bioresorbable everolimus drug-eluting vascular scaffold for treatment of de novo coronary artery stenosis: six-month clinical and imaging outcomes. Circulation. 2010;122(22):2301–12.

58. Serruys PW, Onuma Y, Dudek D, Smits PC, Koolen J, Chevalier B, et al. Evaluation of the second generation of a bioresorbable everolimus-eluting vascular scaffold for the treatment of de novo coronary artery stenosis: 12-month clinical and imaging outcomes. J Am Coll Cardiol. 2011;58(15):1578–88.

59. van Ditzhuijzen NS, Kurata M, Sorop O, van den Heuvel M, van Duin R, Krabbendam-Peters I, et al. Diabetes mellitus does not influence long-term coverage of the everolimus-eluting bioresorbable scaffold. Circulation 2013;128(22) (Supplement S):17519.

60. Abizaid A, Costa JR, Jr., Bartorelli AL, Whitbourn R, van Geuns RJ, Chevalier B, et al. The ABSORB EXTEND study: preliminary report of the twelve-month clinical outcomes in the first 512 patients enrolled. EuroIntervention. 2014.

61. Diletti R, Serruys PW, Farooq V, Sudhir K, Dorange C, Miquel-Hebert K, et al. ABSORB II randomized controlled trial: a clinical evaluation to compare the safety, efficacy, and performance of the Absorb everolimus-eluting bioresorbable vascular scaffold system against the XIENCE everolimus-eluting coronary stent system in the treatment of subjects with ischemic heart disease caused by de novo native coronary artery lesions: rationale and study design. Am Heart J. 2012;164(5):654–63 [Comparative Study Multicenter Study Randomized Controlled Trial].

62. Stone GW, editor. ABSORB III and IV: pivotal clinical trial program. Miami: Transcatheter Cardiovascular Therapeutics; 2012.

63. Abizaid A, Schofer J, Maeng M, Witzenbichler B, Botelho R, Ormiston JA, Costa RA, Costa Jr JD, Chamie D, Castro JP, Abizaid A, John Y, Bhat V, Morrison L, Toyloy S, Verheye S, editors. Prospective, multi-center evaluation of the DESolve Nx Novolimus-Eluting bioresorbable coronary scaffold: first report of one year clinical and imaging outcomes. San Francisco: Transcatheter Cardiovascular Therapeutics (TCT); 2013.

64. Grube E, editor. Bioabsorbable stents: the Boston Scientific & REVA technology. Barcelona: EuroPCR; 2009.

65. Costa RA, editor. REVA ReZolve clinical program update. Miami: Transcatheter Cardiovascular Therapeutics; 2012.

66. Fajadet J, editor. The ART BRS: design and FIH experiences: can a polymer-only scaffold do it alone? San Francisco: Transcatheter Cardiovascular Therapeutics; 2013.

67. Jabara R, Pendyala L, Geva S, Chen J, Chronos N, Robinson K. Novel fully bioabsorbable salicylate-based sirolimus-eluting stent. EuroIntervention. 2009;5(Suppl F):F58–64.

68. Wu Y, Shen L, Wang Q, Ge L, Xie J, Hu X, et al. Comparison of acute recoil between bioabsorbable poly-L-lactic acid XINSORB stent and metallic stent in porcine model. J Biomed Biotechnol. 2012;2012:413956.

69. Ge J, Chen Y, Qian J, Ge L, Wang Q, Yao K, et al., editors. A first-in-man study of XINSORB scaffold for patients with single de-novo coronary lesions. Paris: EuroPCR; 2014.

70. Cottone RJ, editor. Pre-clinical evaluations of combination drug eluting and CD34 antibody – coated bioabsorbable scaffold – program update. San Francisco: Transcatheter Cardiovascular Therapeutics; 2013.

71. Granada JF, editor. The Amaranth PLLA Based Bioresorbable Scaffold (ABRS) – experimental and early human results. San Fransisco: Transcatheter Cardiovascular Therapeutics; 2013.

72. Erbel R, Di Mario C, Bartunek J, Bonnier J, de Bruyne B, Eberli FR, et al. Temporary scaffolding of coronary arteries with bioabsorbable magnesium stents: a prospective, non-randomised multicentre trial. Lancet. 2007;369(9576):1869–75.

73. Haude M, Erbel R, Erne P, Verheye S, Degen H, Bose D, et al. Safety and performance of the drug-eluting absorbable metal scaffold (DREAMS) in patients with de-novo coronary lesions: 12 month results of the prospective, multicentre, first-in-man BIOSOLVE-I trial. Lancet. 2013;14.

74. Diletti R, Karanasos A, Muramatsu T, Nakatani S, Van Mieghem NM, Onuma Y, et al. Everolimus-eluting bioresorbable vascular scaffolds for treatment of patients presenting with ST-segment elevation myocardial infarction: BVS STEMI first study. Eur Heart J. 2014;35(12):777–86 [Research Support, Non-U.S. Gov't].

75. Van Mieghem N, Wilschut J, Ligthart J, Witberg K, Van Geuns RJ, Regar E. Modified T-technique with bioresorbable scaffolds ensures complete carina coverage – an optical coherence tomography study. JACC Cardiovasc Interv. 2014;7:e109–10.

76. Ruzsa Z, van der Linden M, Van Mieghem NM, Regar E, Ligthart JM, Serruys P, et al. Culotte stenting with bioabsorbable everolimus-eluting stents. Int J Cardiol. 2013;168(2):e35–7.

77. Diletti R, Onuma Y, Farooq V, Gomez-Lara J, Brugaletta S, van Geuns RJ, et al. 6-month clinical outcomes following implantation of the bioresorbable everolimus-eluting vascular scaffold in vessels smaller or larger than 2.5 mm. J Am Coll Cardiol. 2011;58(3):258–64 [Multicenter Study].

78. Diletti R, Farooq V, Girasis C, Bourantas C, Onuma Y, Heo JH, et al. Clinical and intravascular imaging outcomes at 1 and 2 years after implantation of absorb everolimus eluting bioresorbable vascular scaffolds in small vessels. Late lumen enlargement: does bioresorption matter with small vessel size? Insight from the ABSORB cohort B trial. Heart. 2013;99(2):98–105.

79. Reiber JH, Tu S, Tuinenburg JC, Koning G, Janssen JP, Dijkstra J. QCA, IVUS and OCT in interventional cardiology in 2011. Cardiovasc Diagn Ther. 2011;1(1):57–70 [Review].

Consensus Documents

14

Luca Di Vito, Valeria Marco, Mario Albertucci,
and Francesco Prati

Abstract

Optical coherence tomography is a novel technique capable of studying coronary plaques and stented segments with superb resolution. Two consensus documents focused on the clinical applications of OCT for baseline or post-intervention assessment have been released. As the first goal of this chapter, we summarized the conclusion reached by the consensus documents, updating the statements that were made at that time, with new concepts.

The assessment of both atherosclerotic plaque and stent deployment using OCT, and the study of vessel healing require an extensive knowledge of the pertinent definitions. In all three published consensus documents, the authors tried to provide a complete list of definitions needed for conducting appropriate OCT based plaque and stent analyses.

However, researchers still continue to use different definitions especially in cases of plaque erosion and intra-stent thrombus. We first addressed the role of OCT in assessing coronary plaque morphology and vulnerability, then we focused on OCT guidance of coronary interventions.

14.1 Current Available OCT Technologies

The main obstacle in the adoption of optical coherence tomography (OCT) imaging in clinical practice is that OCT cannot image through a blood field, and therefore requires clearing or flushing of blood from the lumen [1]. While the previous OCT system called time-domain (TD) OCT, performed by either a vessel occlusion or a non occlusive technique, required a large amount of iso-osmolar contrast [2, 3], the latest technology called frequency-domain (FD) OCT allows us to acquire clear and multiple images simultaneously, reducing the amount of needed contrast.

The acquisition of FD-OCT pullback requires a bolus of crystalloid solution (usually contrast or dextran [3]) injected through the guiding catheter. The quality of OCT images depends on an accurate acquisition technique and proper guiding catheter engagement, a fundamental maneuver to optimizing directional contrast flushing [1].

Currently, there are two FD-OCT catheters on the market: the DragonflyTM© catheter (St. Jude Medical) and the FastView© OCT catheter (Terumo). They have similar functions as they are advanced over a regular guide wire, distal to the region of interest and are provided with a dedicated marker, located 10 mm distal to the OCT lens, which enables the pull-back starting point selection.

L. Di Vito, MD, PhD • V. Marco, RN
CLI Foundation, Rome, Italy

M. Albertucci, MD
Department of Surgery, San Giovanni Addolorata Hospital
and CLI Foundation, Rome, Italy

F. Prati, MD (✉)
Interventional Cardiology Unit, San Giovanni
Addolorata Hospital, Via dell'Amba Aradam 8, Rome 00184, Italy
e-mail: fprati@hsangiovanni.roma.it

The acquisition speed of the DragonflyTM© and FastView© OCT catheters can be set up in a range between 5 and 40 mm/s, enabling the study of vessel segments with lengths of 50 mm or 75 mm. In the former option the system permitted the study of arteries with cross sectional thickness up to 100 μm [1, 4].

In the past decade, intravascular ultrasound (IVUS) was the most used intravascular imaging technique. Unlike IVUS, OCT cannot penetrate the whole plaque thickness; however, OCT can image coronary arteries at a very high resolution (20 μm). Due to the thinner profile of FD-OCT probes, and the faster pull-back imaging speed of OCT, many severely diseased target lesions can be safely imaged without causing luminal obstruction, thus making symptomatic ischemia much less likely [5]. As a main technical drawback, FD-OCT cannot study plaques located at the very ostium of the left or right coronary arteries. Also, in the presence of very tight stenosis, image quality can be sub-optimal [5].

In previous years, TD OCT technology was found to be safe [2, 6, 7], effective [2, 6, 7] and highly reproducible. Later studies carried with the FD OCT technique, confirmed data on the safety and effectiveness and showed that luminal areas and vessel length can be measured with high reproducibility [8–10]. A fair correlation between OCT and IVUS quantitative measurements of the lumen areas was reported [8–10] despite comparative studies showing that IVUS tends to slightly overestimate lumen areas, while stent and neo-intimal areas are slightly higher on OCT [8–10].

14.2   Impact of Plaque Composition on Coronary Intervention

14.2.1   Calcification and Lipid Pool

Identification of calcium can affect an interventional cardiologist's decision making. In fact, in the presence of circumferential calcification, direct stenting should be avoided and strategy can span from a careful pre-dilatation to test expansion, to cutting balloons for very short calcific rings or to pre-treatment with a rotational atherectomy [11, 12].

Both IVUS and OCT can identify calcium with accuracy [13]. However, IVUS is unable to measure its thickness due to a shadowing effect [14]. Infrared light penetrates calcium better, enabling measurement of superficial calcific components with a thickness less than 1.0–1.3 mm [15, 16]. Only the less common deep intra-plaque calcium deposits cannot be addressed with OCT.

As a relatively new concept stent positioning should be performed by aiming for complete coverage of the lipid pool [17], avoiding the placement of stent edges over lipid formations, that can potentially lead to stent thrombosis and plaque embolization [18]. OCT identifies lipid pools with high

accuracy and its pre-intervention use can also be encouraged to reduce the risk of embolization of plaque components.

14.2.2   Assessment of Ambiguous Angiographic Lesions and Deferral of Interventions

Hazy and intermediate lesions on angiogram are considered a grey-zone for interventional cardiologists [19]. OCT allows detailed analysis of plaque morphology and lumen area, being therefore very instrumental in guiding interventions and helping decide whether to treat coronary narrowings. Unlike other intravascular imaging modalities, OCT has the unique ability to identify thrombi and measure the amount of thrombus. The "OCT defined thrombus score" is a semi-quantitative assessment of a thrombus [20, 21], that can be used in cases of angiographically hazy lesions. These kinds of lesions often appear as ruptured plaques with large amounts of thrombus attached to the site of disruption [19].

Coronary angiograms of patients with acute coronary syndrome may show one or more non-significant lesions, exhibiting only haziness on angiogram. This can pose a problem for the interventional cardiologist. In fact, misinterpretation of culprit lesions may cause ischemic events in the short and mid-term follow-up. Under these circumstances the decision to proceed with treatment rests more on morphologic observations than on the absolute measurement of lumen area.

The fact that lumen contours are easily obtained enables the on-line application of an automated algorithm, that facilitates operator decision making by displaying the reconstructed segment in a longitudinal view.

14.2.3   Identification of Vulnerable Plaques

A number of IVUS studies attempted to characterize the appearance of vulnerable plaque. Recently, the PROSPECT trial, based on a signal radiofrequency analysis of the IVUS backscatter, for the first time showed that intravascular imaging modalities can identify plaque with a higher risk of events at 3 years [22]. OCT, due to its high accuracy in the detection of superficial plaque components, can potentially identify plaque at risk of rupture. In fact, OCT can address many features that have been related to plaque vulnerability such as the presence of thin fibrous cap, extension of lipid pools [5], micro-vessels [23] and inflammatory cells [24]. However dedicated soft-wares, based on the acoustic properties of the OCT signal, are needed to improve identification of the local signs of inflammation [24].

To better understand the change of plaque composition in response to specific treatment, serial studies should be

carried out with the specific goal of identifying the same location at different time points. For this task, dedicated three-dimensional soft-wares can be adopted. The recently developed "carpet view software" which unfolds the vessel segment, reconstructing it as an open structure, will likely improve the off-line serial comparisons of target plaques and enable the matching of different imaging modalities [25]. Many experts have suggested that the identification of a vulnerable plaque requires the combination of OCT and other imaging modalities such as IVUS or near infrared spectroscopy to better characterize the plaque and obtain information on deep lesion components [26, 27].

14.3 OCT-Guided PCI Guidance

The main drawback of OCT is its inability, unlike IVUS, to outline the vessel architecture, and measure the external elastic membrane, and the longitudinal extent of plaque burden in lesions with thicknesses exceeding 1.0–1.5 mm. Some interventional cardiologists may argue that measurement of plaque burden has a role in selecting reference segments. Therefore, the pre-intervention use of OCT to select the appropriate stent size and length is mainly based on the assessment of lumen areas. Furthermore, pre-intervention OCT assessment of plaque composition is helpful for predicting the subsequent risk of complications. In fact, calcified and lipid plaques carry an increased risk of stent edge dissections [28], while thin cap fibro-atheroma is more frequently associated with a significant tissue prolapse inside the stent [29].

Recent meta-analysis stressed the role of IVUS in guiding stenting procedures, showing that the rate of stent thrombosis and major adverse clinical outcomes can be significantly reduced [30, 31]. According to these findings, the large IVUS sub-study of the ADAPT-DES registry showed that the presence of attenuated plaque, tissue protrusion, reference segment plaque burden, and edge dissection were significant predictors of stent thrombosis [32]. Lastly, IVUS guidance proved to be useful for treatment of complex lesions such as left main PCI [33]. Due to the improved resolution of OCT, it is reasonable to believe that OCT guidance can also improve the outcome of percutaneous coronary interventions (PCIs). However, the two techniques are different, particularly in their resolutions and penetrations. Therefore, IVUS accepted criteria that require an assessment of vessel architecture, specifically with a measurement of the external elastic membrane and plaque burden, cannot be adopted for OCT use.

On the other hand, OCT can identify details such as stent under-expansion, malapposition, asymmetric stent strut distribution, intra-stent thrombotic formations, and dissections at the edges and inside the stents, with a level of accuracy unmatched by IVUS.

14.3.1 Frequency of OCT Findings of Sub-Optimal Stenting and Clinical Role of OCT Guidance

The multicenter CLI-OPCI study [34], addressed the role of OCT guidance. The registry compared the clinical outcome of 335 patients with OCT guided intervention to those from a control group by means of a propensity score adjustment. OCT guidance was found to improve the 1-year composite event of cardiac death or non-fatal myocardial infarction after PCI in a real-world population. The study also addressed the issue of how to treat OCT findings indicative of suboptimal stent deployment. In 34.7 % of the stented segments, it was determined, based on the OCT results, that further intervention with either balloon dilation (22.3 %) or additional stenting (12.4 %) was needed. The final conclusion of the study was that explicit quantitative OCT thresholds are required in order to improve clinical outcome of patients undergoing PCI.

OCT studies, in patients with acute coronary syndrome, have shown that in-stent tissue protrusion due to the presence of residual thrombus, is a common finding [29]. Recent data revealed that residual intra-stent thrombus is related to peri-procedural myocardial infarction if left untreated [29]. Preliminary data showed that additional OCT-driven in-stent balloon dilatation can significantly reduce the in-stent thrombus area percentage without worsening the microcirculatory indexes [35].

As another crucial application, OCT can clarify mechanisms of restenosis and thrombosis early or late after the index procedure, guiding repeat revascularization and thus minimizing the risk of additional adverse events.

Assessment of stent under-expansion by OCT can be obtained by comparing the minimal stent area with the reference lumen area. Additionally, a threshold of absolute minimum lumen cross-sectional area within the stent could be applied, with an area of at least 5.0–5.5 mm² previously advocated as the target minimum stent area to prevent failure [36].

A recent study from our group, addressed the incidence of suboptimal OCT results in 21 consecutive patients exhibiting sub-acute thrombosis. The patients were matched 1:2 with a control group of 42 patients from the Rome Heart Research core-lab database [37]. OCT showed that minimum lumen area and minimum stent area measurements were significantly smaller in the stent thrombosis group together with a higher frequency of stent under-expansion, edge dissection and reference lumen narrowing.

Stent follow-up, delayed healing and poor endothelialization are common findings in the pathological specimens of vessels treated with drug eluting stent (DES) [38], and recent post-mortem studies demonstrated that late-stent thrombosis was strongly associated with the ratio of uncovered/total stent struts [39].

Several experimental and clinical studies have demonstrated the high correlation between OCT and histological measurements of tissue coverage of stent struts [40, 41], although OCT is unable to identify the endothelium [5]. In a sub-analysis of the ODESSA trial, 8 % of the stented segments with no detectable neo-intima by IVUS were found to have neo-intimal coverage by OCT [42]. Follow-up OCT data revealed that most drug eluting stents, including those with a biodegradable polymer, were covered with thin neointima, but few revealed complete coverage [42–44]. Incomplete stent apposition without neo-intimal hyperplasia was significantly associated with the presence of an OCT-detected thrombus at the follow-up, and may constitute a potent substrate for late-stent thrombosis [45]; however, so far a sub-clinical thrombus has not been related to the risk of major adverse cardiac events [46]. Furthermore, incomplete stent apposition and the absence of tissue coverage detected by OCT are more frequently found in the setting of acute coronary syndromes, particularly after DES deployment [47].

Optical coherence tomography can be applied for the treatment of late in-stent restenosis because the strong reflective power of the stent struts allows their detection through thick layers of hyperplasia, allowing optimal sizing of high-pressure balloons to correct under-expansion and facilitating the use of cutting balloons [48].

OCT can image neo-intimal tissue distinguishing among several types on the base of OCT signal attenuation and backscattering. The most common type is the homogeneous form that is characterized by uniform optical properties without focal variations in the backscattering pattern [49–51].

14.4 Fields of Controversy for OCT Definitions

Although three expert review documents have been published, there is not yet an agreed upon definition among researchers for OCT based plaque and stent analyses. This paragraph aims to highlight the major differences in the definitions used for OCT analyses. OCT can address plaque composition with high accuracy. Lipid-rich plaques have been defined by researchers in several ways: (1) Plaques with lipid material extending for more than 90° [52, 53] or 120° [54, 55] or (2) Lipid plaque with a thin fibrous cap (<400 μm) [56]. A fibrous cap is identified as a signal-rich homogenous band overlying a lipid core [54]. The thickness of the fibrous cap, measured as the distance from the arterial lumen to the luminal border of the lipid pool [56], can be calculated with different methods and there is no general agreement on the number of repeated cap thickness measurements for an accurate value.

Some authors have used a single measure of the thinnest portion of the cap [57], while others have proposed the use of the mean of the three [54, 56, 58, 59] or five [52] separate measurements.

OCT has the ability to identify vulnerable plaque such as thin cap fibro-atheroma (TCFA) which is thought to account for 60–70 % of coronary events [60, 61].

OCT research groups have used different definitions to identify TCFA. TCFA was defined as: (1) plaque with more than 2 lipid quadrants and a cap thickness of less than 65 μm [60]; (2) plaque with more than 1 lipid quadrant and a cap thickness of less than 70 μm [17], or (3) lipid plaque with a cap thickness of less than 80 μm [56]. The comparison with histological studies provided the first [60] and second [17] definitions, whereas an *in vivo* study of plaque rupture provided the third definition [56].

OCT is also very instrumental in studying the pathophysiology of plaque instability leading to intracoronary thrombus. Complicated plaques can lead to one of the following three different outcomes: plaque rupture, erosion or calcified nodule.

While the presence of plaque rupture can be easily identified by OCT assessment for the presence of fibrous cap disruption and the formation of a cavity inside the plaque [54], there is no agreement on the ability of OCT for identifying erosion and calcified nodules.

Fibrous cap erosion is an endothelial damage or denudation associated with thrombus, but without a clear fibrous cap disruption [58, 62]. Recently a plaque classification algorithm for identifying OCT-defined erosion has been proposed. This approach differentiates definite erosion (superficial thrombus and intact fibrous cap) from probable erosion (either the absence of superficial thrombus and the presence of an irregular surface or large intra-coronary thrombus impairing accurate plaque visualization without associated calcium or lipid in the close proximal and distal cross-sections) [13].

Calcific nodules are considered superficial deposits of calcium that may lead to thrombus formation. OCT has been proposed for identifying these tiny structures, since they appear as nodules protruding into the lumen. These nodules may have an irregular surface [63]. Some authors have identified their prevalence before thrombus formation [14]; others, after fibrous cap rupture and thrombus formation [13].

OCT can investigate strut apposition and coverage and other features indicative of suboptimal deployment, such as edge dissections, thrombus and tissue prolapse.

Two different methods have been used for assessing stent strut malapposition:

1. Measurements of the distance from the center of the blooming artifact to the vessel wall [64, 65].
2. Measurements of the distance from the outer surface of the blooming artifact to the vessel wall and correcting for half of the thickness of the blooming (18 μm) [66–68] or the axial resolution of the OCT instrument used (20 μm) [45].

Tissue prolapse and intra-stent thrombus are difficult to distinguish. Tissue prolapse is defined as tissue protrusion

between stent struts. It has a typical convex-shaped appearance without disruption of the continuity of the luminal vessel surface [69]. It does not extent for more than 250 µm inside the lumen [70]. On the contrary, thrombus is considered an irregular mass protruding for more than 250 µm, that can appear attached to or separate from the stent surface [43].

Stent edge dissection are often imaged by OCT as a disruption of the luminal vessel surface in the edge segments [69] (within 5 mm proximal and distal to the end of the stent) [71, 72]. However, there is no agreement on how to define a significant edge dissection. Some authors have used a dissection angle greater than 60° [73], while others have applied a longitudinal extension greater than >0.67 mm [72].

Conclusions

OCT enables the accurate assessment of coronary atherosclerosis and offers unique insights into stenting procedures. It has many fields of potential application such as the investigation of an ambiguous lesion or the assessment of a suboptimal stent deployment.

Recent, studies proved the efficacy of IVUS to guide PCI, especially in the setting of complex procedures such as left main PCI or bifurcations. OCT, due to a much higher resolution at expense of a limited penetration, promise to have an important role in this setting. However, there is limited data available on the clinical impact of OCT guided PCI, with only one large registry being published.

Importantly, operators should avoid misinterpretation of OCT images keeping in mind that the high resolution of the technique may induce to over treat plaque-stent features unlikely affecting the clinical outcomes.

Three consensus documents have been recently released to guide investigators in their OCT based plaque and stent analyses. However, some fields of controversy such as the definition of vulnerable plaque and the assessment of strut malapposition still remain open leading to different criteria and definitions.

There is need for better general agreement on the best OCT definitions that should be adopted to address plaque anatomy and stented segments in order to identify the clinical significance of OCT findings.

References

1. Prati F, Regar E, Mintz GS, Arbustini E, Di Mario C, Jang IK, et al. Expert review document on methodology, terminology, and clinical applications of optical coherence tomography: physical principles, methodology of image acquisition, and clinical application for assessment of coronary arteries and atherosclerosis. Eur Heart J. 2010;31:401–15 [Research Support, Non-U.S. Gov't Review].
2. Imola F, Mallus MT, Ramazzotti V, Manzoli A, Pappalardo A, Di Giorgio A, et al. Safety and feasibility of frequency domain optical coherence tomography to guide decision making in percutaneous coronary intervention. EuroIntervention. 2010;6:575–81.
3. Ozaki Y, Kitabata H, Tsujioka H, Hosokawa S, Kashiwagi M, Ishibashi K, et al. Comparison of contrast media and low-molecular-weight dextran for frequency-domain optical coherence tomography. Circ J. 2012;76:922–7 [Comparative Study].
4. Okamura T, Onuma Y, Garcia-Garcia HM, van Geuns RJ, Wykrzykowska JJ, Schultz C, et al. First-in-man evaluation of intravascular optical frequency domain imaging (OFDI) of Terumo: a comparison with intravascular ultrasound and quantitative coronary angiography. EuroIntervention. 2011;6:1037–45 [Comparative Study Randomized Controlled Trial].
5. Prati F, Guagliumi G, Mintz GS, Costa M, Regar E, Akasaka T, et al. Expert review document part 2: methodology, terminology and clinical applications of optical coherence tomography for the assessment of interventional procedures. Eur Heart J. 2012;33:2513–20.
6. Takarada S, Imanishi T, Liu Y, Ikejima H, Tsujioka H, Kuroi A, et al. Advantage of next-generation frequency-domain optical coherence tomography compared with conventional time-domain system in the assessment of coronary lesion. Catheter Cardiovasc Interv. 2010;75:202–6 [Comparative Study Evaluation Studies].
7. Barlis P, Gonzalo N, Di Mario C, Prati F, Buellesfeld L, Rieber J, et al. A multicentre evaluation of the safety of intracoronary optical coherence tomography. EuroIntervention. 2009;5:90–5 [Evaluation Studies Multicenter Study Research Support, Non-U.S. Gov't].
8. Fedele S, Biondi-Zoccai G, Kwiatkowski P, Di Vito L, Occhipinti M, Cremonesi A, et al. Reproducibility of coronary optical coherence tomography for lumen and length measurements in humans (The CLI-VAR [Centro per la Lotta contro l'Infarto-VARiability] study). Am J Cardiol. 2012;110:1106–12.
9. Bezerra HG, Costa MA, Guagliumi G, Rollins AM, Simon DI. Intracoronary optical coherence tomography: a comprehensive review clinical and research applications. JACC Cardiovasc Interv. 2009;2:1035–46 [Review].
10. Capodanno D, Prati F, Pawlowsky T, Cera M, La Manna A, Albertucci M, et al. Comparison of optical coherence tomography and intravascular ultrasound for the assessment of in-stent tissue coverage after stent implantation. EuroIntervention. 2009;5:538–43 [Comparative Study].
11. Tanigawa J, Barlis P, Di Mario C. Heavily calcified coronary lesions preclude strut apposition despite high pressure balloon dilatation and rotational atherectomy: in-vivo demonstration with optical coherence tomography. Circ J. 2008;72:157–60 [Case Reports Research Support, Non-U.S. Gov't].
12. Tenaglia AN, Buller CE, Kisslo KB, Phillips HR, Stack RS, Davidson CJ. Intracoronary ultrasound predictors of adverse outcomes after coronary artery interventions. J Am Coll Cardiol. 1992;20:1385–90 [Comparative Study].
13. Jang IK, Bouma BE, Kang DH, Park SJ, Park SW, Seung KB, et al. Visualization of coronary atherosclerotic plaques in patients using optical coherence tomography: comparison with intravascular ultrasound. J Am Coll Cardiol. 2002;39:604–9 [Clinical Trial Comparative Study Research Support, Non-U.S. Gov't].
14. Mintz GS, Nissen SE, Anderson WD, Bailey SR, Erbel R, Fitzgerald PJ, et al. American College of Cardiology Clinical Expert Consensus Document on Standards for Acquisition, Measurement and Reporting of Intravascular Ultrasound Studies (IVUS). A report of the American College of Cardiology Task Force on Clinical Expert Consensus Documents. J Am Coll Cardiol. 2001;37:1478–92.
15. Jia H, Abtahian F, Aguirre AD, Lee S, Chia S, Lowe H, et al. In vivo diagnosis of plaque erosion and calcified nodule in patients with acute coronary syndrome by intravascular optical coherence tomography. J Am Coll Cardiol. 2013;62(19):1748–58.
16. Niccoli G, Giubilato S, Di Vito L, Leo A, Cosentino N, Pitocco D, et al. Severity of coronary atherosclerosis in patients with a first acute coronary event: a diabetes paradox. Eur Heart J. 2012;34(10):729–41.

17. Tanaka A, Imanishi T, Kitabata H, Kubo T, Takarada S, Tanimoto T, et al. Lipid-rich plaque and myocardial perfusion after successful stenting in patients with non-ST-segment elevation acute coronary syndrome: an optical coherence tomography study. Eur Heart J. 2009;30:1348–55.

18. Imola F, Occhipinti M, Biondi-Zoccai G, Di Vito L, Ramazzotti V, Manzoli A, et al. Association between proximal stent edge positioning on atherosclerotic plaques containing lipid pools and post-procedural myocardial infarction (from the CLI-POOL Study). Am J Cardiol. 2013;111:526–31.

19. Koo BK, Yang HM, Doh JH, Choe H, Lee SY, Yoon CH, et al. Optimal intravascular ultrasound criteria and their accuracy for defining the functional significance of intermediate coronary stenoses of different locations. JACC Cardiovasc Interv. 2011;4:803–11 [Comparative Study Multicenter Study Randomized Controlled Trial Research Support, Non-U.S. Gov't].

20. Capodanno D, Prati F, Pawlowsky T, Ramazzotti V, Albertucci J, La Manna A, et al. ClearWayRX system to reduce intracoronary thrombus in patients with acute coronary syndromes according to optical coherence tomography after abciximab intracoronary local infusion trial (COCTAIL): study rationale and design. J Cardiovasc Med (Hagerstown). 2010;11:130–6 [Randomized Controlled Trial].

21. Prati F, Capodanno D, Pawlowski T, Ramazzotti V, Albertucci M, La Manna A, et al. Local delivery versus intracoronary infusion of abciximab in patients with acute coronary syndromes. JACC Cardiovasc Interv. 2010;3:928–34 [Comparative Study Multicenter Study Randomized Controlled Trial Research Support, Non-U.S. Gov't].

22. Stone GW, Maehara A, Lansky AJ, de Bruyne B, Cristea E, Mintz GS, et al. A prospective natural-history study of coronary atherosclerosis. N Engl J Med. 2011;364:226–35 [Clinical Trial Multicenter Study Research Support, Non-U.S. Gov't].

23. Takano M, Yamamoto M, Inami S, Murakami D, Ohba T, Seino Y, et al. Appearance of lipid-laden intima and neovascularization after implantation of bare-metal stents extended late-phase observation by intracoronary optical coherence tomography. J Am Coll Cardiol. 2009;55:26–32.

24. Tearney GJ, Yabushita H, Houser SL, Aretz HT, Jang IK, Schlendorf KH, et al. Quantification of macrophage content in atherosclerotic plaques by optical coherence tomography. Circulation. 2003;107:113–9 [Evaluation Studies Research Support, Non-U.S. Gov't].

25. Gabriele A, Marco V, Gatto L, Paoletti G, Di Vito L, Castriota F, et al. Reproducibility of the Carpet View system: a novel technical solution for display and off line analysis of OCT images. Int J Cardiovasc Imaging. 2014;30(7):1225–33.

26. Sawada T, Shite J, Garcia-Garcia HM, Shinke T, Watanabe S, Otake H, et al. Feasibility of combined use of intravascular ultrasound radiofrequency data analysis and optical coherence tomography for detecting thin-cap fibroatheroma. Eur Heart J. 2008;29:1136–46 [Evaluation Studies Research Support, Non-U.S. Gov't].

27. Manfrini O, Mont E, Leone O, Arbustini E, Eusebi V, Virmani R, et al. Sources of error and interpretation of plaque morphology by optical coherence tomography. Am J Cardiol. 2006;98:156–9 [Comparative Study In Vitro].

28. Gonzalo N, Serruys PW, Okamura T, Shen ZJ, Garcia-Garcia HM, Onuma Y, et al. Relation between plaque type and dissections at the edges after stent implantation: an optical coherence tomography study. Int J Cardiol. 2011;150:151–5 [Comparative Study].

29. Porto I, Di Vito L, Burzotta F, Niccoli G, Trani C, Leone AM, et al. Predictors of periprocedural (type IVa) myocardial infarction, as assessed by frequency-domain optical coherence tomography. Circ Cardiovasc Interv. 2012;5(89–96):S1–6 [Research Support, Non-U.S. Gov't].

30. Roy P, Steinberg DH, Sushinsky SJ, Okabe T, Pinto Slottow TL, Kaneshige K, et al. The potential clinical utility of intravascular ultrasound guidance in patients undergoing percutaneous coronary intervention with drug-eluting stents. Eur Heart J. 2008;29:1851–7 [Evaluation Studies].

31. Sonoda S, Morino Y, Ako J, Terashima M, Hassan AH, Bonneau HN, et al. Impact of final stent dimensions on long-term results following sirolimus-eluting stent implantation: serial intravascular ultrasound analysis from the sirius trial. J Am Coll Cardiol. 2004;43:1959–63 [Evaluation Studies].

32. Witzenbichler B, Maehara A, Weisz G, Neumann FJ, Rinaldi MJ, Metzger DC, et al. Relationship between intravascular ultrasound guidance and clinical outcomes after drug-eluting stents: the assessment of dual antiplatelet therapy with drug-eluting stents (ADAPT-DES) study. Circulation. 2014;129:463–70 [Clinical Trial Comparative Study Multicenter Study Research Support, Non-U.S. Gov't].

33. Park SJ, Kim YH, Park DW, Lee SW, Kim WJ, Suh J, et al. Impact of intravascular ultrasound guidance on long-term mortality in stenting for unprotected left main coronary artery stenosis. Circ Cardiovasc Interv. 2009;2:167–77 [Comparative Study Multicenter Study Research Support, Non-U.S. Gov't].

34. Prati F, Di Vito L, Biondi-Zoccai G, Occhipinti M, La Manna A, Tamburino C, et al. Angiography alone versus angiography plus optical coherence tomography to guide decision-making during percutaneous coronary intervention: the Centro per la Lottacontrol'Infarto-Optimisation of Percutaneous Coronary Intervention (CLI-OPCI) study. EuroIntervention. 2012;8:823–9 [Research Support, Non-U.S. Gov't].

35. Di Giorgio A, Capodanno D, Ramazzotti V, Imola F, Mallus MT, Stazi F, et al. Optical coherence tomography guided in-stent thrombus removal in patients with acute coronary syndromes. Int J Cardiovasc Imaging. 2013;29:989–96 [Research Support, Non-U.S. Gov't].

36. de Jaegere P, Mudra H, Figulla H, Almagor Y, Doucet S, Penn I, et al. Intravascular ultrasound-guided optimized stent deployment. Immediate and 6 months clinical and angiographic results from the Multicenter Ultrasound Stenting in Coronaries Study (MUSIC Study). Eur Heart J. 1998;19:1214–23 [Multicenter Study].

37. L Gatto, A Chisari, A La Manna, F Burzotta, L Di Vito, MT Tallus, A Cremonesi, A Pappalardo, M Albertucci, F Prati. Comparative incidence of optical coherence tomography features indicative of uncorrected stent deployment in patients with and without major adverse cardiac events in the OCT guided arm of the CLI-OPCI study. Journal of the American College of Cardiology, 2013/10/29; Vol: 62; N: 18_S1; Pagine: B167–B167.

38. Parodi G, La Manna A, Di Vito L, Valgimigli M, Fineschi M, Bellandi B, et al. Stent-related defects in patients presenting with stent thrombosis: differences at optical coherence tomography between subacute and late/very late thrombosis in the Mechanism of Stent Thrombosis (MOST) study. EuroIntervention. 2013;9:936–44 [Research Support, Non-U.S. Gov't].

39. Guagliumi G, Sirbu V, Musumeci G, Gerber R, Biondi-Zoccai G, Ikejima H, et al. Examination of the in vivo mechanisms of late drug-eluting stent thrombosis: findings from optical coherence tomography and intravascular ultrasound imaging. JACC Cardiovasc Interv. 2012;5:12–20 [Research Support, Non-U.S. Gov't].

40. Prati F, Zimarino M, Stabile E, Pizzicannella G, Fouad T, Rabozzi R, et al. Does optical coherence tomography identify arterial healing after stenting? An in vivo comparison with histology, in a rabbit carotid model. Heart. 2008;94:217–21 [Comparative Study].

41. Suzuki Y, Ikeno F, Koizumi T, Tio F, Yeung AC, Yock PG, et al. In vivo comparison between optical coherence tomography and intravascular ultrasound for detecting small degrees of in-stent neointima after stent implantation. JACC Cardiovasc Interv. 2008;1:168–73 [Comparative Study Evaluation Studies].

42. Guagliumi G, Costa MA, Sirbu V, Musumeci G, Bezerra HG, Suzuki N, et al. Strut coverage and late malapposition with paclitaxel-eluting stents compared with bare metal stents in acute myocardial infarction: optical coherence tomography substudy of the Harmonizing Outcomes with Revascularization and Stents in Acute Myocardial Infarction (HORIZONS-AMI) Trial. Circulation.

2011;123:274–81 [Comparative Study Multicenter Study Randomized Controlled Trial Research Support, Non-U.S. Gov't].

43. Matsumoto D, Shite J, Shinke T, Otake H, Tanino Y, Ogasawara D, et al. Neointimal coverage of sirolimus-eluting stents at 6-month follow-up: evaluated by optical coherence tomography. Eur Heart J. 2007;28:961–7.

44. Takano M, Murakami D, Yamamoto M, Kurihara O, Murai K, Inami T, et al. Six-month follow-up evaluation for everolimus-eluting stents by intracoronary optical coherence tomography: comparison with paclitaxel-eluting stents. Int J Cardiol. 2011;166(1):181–6.

45. Ozaki Y, Okumura M, Ismail TF, Naruse H, Hattori K, Kan S, et al. The fate of incomplete stent apposition with drug-eluting stents: an optical coherence tomography-based natural history study. Eur Heart J. 2010;31:1470–6 [Research Support, Non-U.S. Gov't].

46. Otake H, Shite J, Ako J, Shinke T, Tanino Y, Ogasawara D, et al. Local determinants of thrombus formation following sirolimus-eluting stent implantation assessed by optical coherence tomography. JACC Cardiovasc Interv. 2009;2:459–66.

47. Gonzalo N, Barlis P, Serruys PW, Garcia-Garcia HM, Onuma Y, Ligthart J, et al. Incomplete stent apposition and delayed tissue coverage are more frequent in drug-eluting stents implanted during primary percutaneous coronary intervention for ST-segment elevation myocardial infarction than in drug-eluting stents implanted for stable/unstable angina: insights from optical coherence tomography. JACC Cardiovasc Interv. 2009;2:445–52 [Comparative Study].

48. Miyazaki S, Hiasa Y, Takahashi T, Yano Y, Minami T, Murakami N, et al. In vivo optical coherence tomography of very late drug-eluting stent thrombosis compared with late in-stent restenosis. Circ J. 2012;76:390–8 [Comparative Study].

49. Gonzalo N, Serruys PW, Okamura T, van Beusekom HM, Garcia-Garcia HM, van Soest G, et al. Optical coherence tomography patterns of stent restenosis. Am Heart J. 2009;158:284–93.

50. Kwon SW, Kim BK, Kim TH, Kim JS, Ko YG, Choi D, et al. Qualitative assessment of neointimal tissue after drug-eluting stent implantation: comparison between follow-up optical coherence tomography and intravascular ultrasound. Am Heart J. 2011;161:367–72.

51. Lee SJ, Kim BK, Kim JS, Ko YG, Choi D, Jang Y, et al. Evaluation of neointimal morphology of lesions with or without in-stent restenosis: an optical coherence tomography study. Clin Cardiol. 2011;34:633–9.

52. Fujii K, Kawasaki D, Masutani M, Okumura T, Akagami T, Sakoda T, et al. OCT assessment of thin-cap fibroatheroma distribution in native coronary arteries. JACC Cardiovasc Imaging. 2010;3:168–75.

53. Kato K, Yonetsu T, Kim SJ, Xing L, Lee H, McNulty I, et al. Non-culprit plaques in patients with acute coronary syndromes (ACS) have more vulnerable features compared to those with non-ACS: a 3-vessel optical coherence tomography study. Circ Cardiovasc Imaging. 2012;5(4):433–40.

54. Ino Y, Kubo T, Tanaka A, Kuroi A, Tsujioka H, Ikejima H, et al. Difference of culprit lesion morphologies between ST-segment elevation myocardial infarction and non-ST-segment elevation acute coronary syndrome an optical coherence tomography study. JACC Cardiovasc Interv. 2011;4:76–82.

55. Lee T, Kakuta T, Yonetsu T, Takahashi K, Yamamoto G, Iesaka Y, et al. Assessment of echo-attenuated plaque by optical coherence tomography and its impact on post-procedural creatine kinase-myocardial band elevation in elective stent implantation. JACC Cardiovasc Interv. 2011;4:483–91.

56. Yonetsu T, Kakuta T, Lee T, Takahashi K, Kawaguchi N, Yamamoto G, et al. In vivo critical fibrous cap thickness for rupture-prone coronary plaques assessed by optical coherence tomography. Eur Heart J. 2011;32:1251–9.

57. Feng T, Yundai C, Lian C, Zhijun S, Changfu L, Jun G, et al. Assessment of coronary plaque characteristics by optical coherence tomography in patients with diabetes mellitus complicated with unstable angina pectoris. Atherosclerosis. 2010;213:482–5.

58. Yonetsu T, Kakuta T, Lee T, Takahashi K, Yamamoto G, Iesaka Y, et al. Impact of plaque morphology on creatine kinase-MB elevation in patients with elective stent implantation. Int J Cardiol. 2011;146:80–5.

59. Tian J, Hou J, Xing L, Kim SJ, Yonetsu T, Kato K, et al. Does neovascularization predict response to statin therapy? Optical coherence tomography study. Int J Cardiol. 2012;158:469–70.

60. Jang IK, Tearney GJ, MacNeill B, Takano M, Moselewski F, Iftima N, et al. In vivo characterization of coronary atherosclerotic plaque by use of optical coherence tomography. Circulation. 2005;111:1551–5 [Research Support, N.I.H., Extramural Research Support, Non-U.S. Gov't Research Support, U.S. Gov't, P.H.S.].

61. Virmani R, Burke AP, Farb A, Kolodgie FD. Pathology of the vulnerable plaque. J Am Coll Cardiol. 2006;47(8 Suppl):C13–8.

62. Mizukoshi M, Imanishi T, Tanaka A, Kubo T, Liu Y, Takarada S, et al. Clinical classification and plaque morphology determined by optical coherence tomography in unstable angina pectoris. Am J Cardiol. 2010;106:323–8.

63. Karanasos A, Ligthart JM, Witberg KT, Regar E. Calcified nodules: an underrated mechanism of coronary thrombosis? JACC Cardiovasc Imaging. 2012;5:1071–2 [Letter Research Support, Non-U.S. Gov't].

64. Miyoshi N, Shite J, Shinke T, Otake H, Tanino Y, Ogasawara D, et al. Comparison by optical coherence tomography of paclitaxel-eluting stents with sirolimus-eluting stents implanted in one coronary artery in one procedure. - 6-month follow-up. Circ J. 2010;74:903–8.

65. Ishigami K, Uemura S, Morikawa Y, Soeda T, Okayama S, Nishida T, et al. Long-term follow-up of neointimal coverage of sirolimus-eluting stents–evaluation with optical coherence tomography. Circ J. 2009;73:2300–7.

66. Gutierrez-Chico JL, Wykrzykowska J, Nuesch E, van Geuns RJ, Koch KT, Koolen JJ, et al. Vascular tissue reaction to acute malapposition in human coronary arteries: sequential assessment with optical coherence tomography. Circ Cardiovasc Interv. 2012;5(1):20–9.

67. Tanigawa J, Barlis P, Di Mario C. Intravascular optical coherence tomography: optimisation of image acquisition and quantitative assessment of stent strut apposition. EuroIntervention. 2007;3:128–36.

68. Mehanna EA, Attizzani GF, Kyono H, Hake M, Bezerra HG. Assessment of coronary stent by optical coherence tomography, methodology and definitions. Int J Cardiovasc Imaging. 2011;27:259–69.

69. Kawamori H, Shite J, Shinke T, Otake H, Sawada T, Kato H, et al. The ability of optical coherence tomography to monitor percutaneous coronary intervention: detailed comparison with intravascular ultrasound. J Invasive Cardiol. 2010;22:541–5.

70. Lee SW, Park SW, Kim YH, Yun SC, Park DW, Lee CW, et al. A randomized comparison of sirolimus- versus paclitaxel-eluting stent implantation in patients with diabetes mellitus 4-year clinical outcomes of DES-DIABETES (drug-eluting stent in patients with DIABETES mellitus) trial. JACC Cardiovasc Interv. 2011;4:310–6.

71. Gonzalo N, Serruys PW, Okamura T, Shen ZJ, Onuma Y, Garcia-Garcia HM, et al. Optical coherence tomography assessment of the acute effects of stent implantation on the vessel wall: a systematic quantitative approach. Heart. 2009;95:1913–9.

72. Kume T, Okura H, Miyamoto Y, Yamada R, Saito K, Tamada T, et al. Natural history of stent edge dissection, tissue protrusion and incomplete stent apposition detectable only on optical coherence tomography after stent implantation. Circ J. 2012;76(3):698–703.

73. Choi SY, Witzenbichler B, Maehara A, Lansky AJ, Guagliumi G, Brodie B, et al. Intravascular ultrasound findings of early stent thrombosis after primary percutaneous intervention in acute myocardial infarction: a Harmonizing Outcomes with Revascularization and Stents in Acute Myocardial Infarction (HORIZONS-AMI) substudy. Circ Cardiovasc Interv. 2011;4:239–47 [Multicenter Study Randomized Controlled Trial Research Support, Non-U.S. Gov't].

Joseph M. Schmitt, Desmond C. Adler, and Chenyang Xu

Abstract

This chapter gives an overview of on-going research and development (R&D) work that is likely to impact the future of cardiovascular OCT. Addressed first are the influences of macrotrends in healthcare delivery on R&D investment and the need for advances that lead to improvements in patient outcomes. The remainder of the chapter reviews recent work in selected topic areas: ultra-high-speed OCT technologies, 3D segmentation and visualization, angiographic co-registration, functional lesion assessment, multimodality imaging, and novel blood-clearing methods.

Keywords

FFR • Co-registration • 3D rendering • Image processing • Segmentation • Multimodality • Ultrasound • Spectroscopy • Fluorescence • Laser • Micromotor • Contrast • Blood substitute

15.1 Introduction

Predicting the future development of a rapidly emerging technology such as intravascular OCT poses a unique challenge. Often the unanticipated, disruptive advances—not the foreseeable incremental advances—have the largest influence on the development trajectory of new medical technologies. For example, just 10 years ago, the sudden emergence of fast Fourier-domain methods propelled intravascular OCT out of the research lab into mainstream clinical use. It is impossible to know whether other similar unanticipated advances will shape the future of OCT. In spite of these inherent difficulties of prediction, the potential influence of on-going R&D efforts on the future of intravascular OCT imaging is worthwhile to contemplate.

15.2 Intravascular Imaging in the Era of Evidence-Based Medicine

Before taking a closer look at OCT R&D and emerging technologies, it is important to examine how trends in healthcare delivery and in the practice of interventional cardiology are influencing R&D investment decisions. In an era of healthcare delivery motivated by cost efficiency and better patient outcomes, investments in small technological advances that are unlikely to yield demonstrable patient benefits or cost reductions can no longer be justified. Designers and manufacturers are being challenged to think beyond the incremental addition of 'bells and whistles' with every generation of a medical device.

Table 15.1 lists a few of the macro trends in the practice of interventional cardiology and their potential consequences on the development of new diagnostic technologies. The trends that are most relevant to the future development of OCT include the increased emphasis on the cost effectiveness of PCI and the imperative to demonstrate patient benefits in well-controlled clinical studies. Two of the consequences of these trends have been to compel lower costs of production of imaging catheters and to restrict applications of intravascular imaging to complex cases for which

J.M. Schmitt, PhD (✉) • D.C. Adler, PhD • C. Xu, PhD
Advanced Technology, St. Jude Medical Inc.,
4 Robbins Road, Westford, MA 01886, USA
e-mail: jschmitt@sjm.com

Table 15.1 Macro trends in interventional cardiology: potential consequences related to the development of new diagnostic technologies

Macro trend	Potential consequences
Emphasis on cost effectiveness of PCI	Earlier triage via non-invasive testing
	Selective use of invasive diagnostics
	Lower disposable costs
	Emphasis on functional assessment
	Preference for rapid, easy-to-use technologies
Increased emphasis on patient outcomes	Reimbursement restricted to devices with proven outcome benefit
	Selective use of invasive diagnostics in complex cases with highest complication rates
	Need for well-conducted clinical trials to gain wide acceptance of new devices
Economic penalties for repeat procedures	Increased use of therapeutic guidance in complicated cases
	Need for new diagnostic methods to guide preventative therapies
Personalized medicine	Emphasis on quantitative risk assessment to appropriately tailor therapy
Fewer open-heart surgical procedures	Need for better real-time visualization in structural heart procedures

angiography provides inadequate information to make informed clinical decisions.

Another equally important consequence has been an increased emphasis on functional assessment of coronary lesion severity by fractional flow reserve (FFR) as an adjunct to the conventional anatomical assessment by angiography. Measurement of FFR with a pressure wire has been shown in well-controlled clinical trials to be a powerful tool for detecting ischemia-producing coronary lesions [1, 2]. Stenting in lesions with FFR readings above a threshold of 0.80 can be safely deferred, with an associated reduction of procedural complications [3]. The relatively weak correlation that has been observed between FFR and IVUS- or OCT-derived anatomical measures in recent studies [4] has called into question the role of intravascular imaging in decisions to stent intermediate coronary lesions. How can OCT-guided PCI improve a patient's chances of a good outcome beyond that expected when stenting decisions are made by FFR assessment alone? This is one of the key questions being addressed as the application of optical coherence tomography in interventional cardiology expands.

Counterbalancing the trend toward cost-containment in PCI, which tends to discourage the widespread use of intravascular imaging, is the need to obtain reliable and comprehensive information for making the right treatment decisions so that complications and repeat procedures can be avoided. There will continue to be a clinical demand for advances in imaging that give cardiologists a more detailed look at vascular morphology than angiography alone can provide.

15.3 Research Areas

Optical coherence tomography is a very active research area for engineers and scientists, with hundreds of journal articles published each year on topics ranging from the principles of tunable lasers to new applications of OCT in clinical

ophthalmology [5–7]. Although a relatively small fraction of the published research literature pertains specifically to coronary imaging, these publications serve as a valuable resource for innovation in intravascular OCT. In particular, the latest generation of intravascular OCT instruments has benefited from the accelerated commercialization of R&D advances in laser and photonics technologies, image processing, and computing power. Industry has the primary responsibility to translate these advances into affordable products with clear patient benefits. Toward this end, efforts to improve future generations of OCT imaging systems are focused on the reliability of image acquisition, rapid extraction of relevant clinical information, and ease of use for real-time decision-making in the catheterization lab. In the following sections, work in several specific research areas is discussed under separate headings.

15.3.1 OCT Image Acquisition Within a Single Cardiac Cycle

Since the first frequency-domain OCT systems were introduced for coronary imaging in 2009, the benefits of increasing the speed of OCT image acquisition have been recognized: longer vessel surveys with lower injected contrast volume, fewer cardiac motion artifacts in 3D vessel reconstruction, and shortened therapeutic decision times. It is now possible to complete an intravascular OCT pullback in less than 1 s, enabling 3D image acquisition within a single cardiac cycle. The transition to markedly higher imaging speeds has been made possible by concurrent advances in three areas: rapidly swept laser light sources; distally actuated micromotors; and high-speed electronics for data acquisition.

Swept lasers form the heart of intravascular OCT systems. Laser sweep rate, tuning range, and coherence length directly map into OCT system imaging speed, axial resolution, and imaging range, respectively. Hence, academic and industrial research groups have focused heavily on improving laser

performance in recent years. Fourier-Domain Mode-Locked (FDML) lasers have increased in sweep rate from 290 kHz in 2006 [8] to 5.2 MHz in 2010 [9], while the use of dispersion-compensating filters has allowed FDML coherence lengths to extend beyond 2 cm [10], thereby enabling longer scan ranges for intravascular imaging. At the same time, vertical cavity surface-emitting laser (VCSEL) technology has progressed rapidly and can now reach sweep rates up to 1 MHz, with coherence lengths in the multi-cm range [11]. Other classes of lasers have also been demonstrated for high-speed OCT imaging, such as fiber ring lasers that operate at rates up to 240 kHz [12] and external cavity lasers based on polygon rotational filters that operate at rates as high as 400 kHz [13]. Many high-speed OCT laser systems now incorporate internal or external optical buffering [14] to replicate time-delayed copies of each wavelength scan and thereby multiply the effective sweep rate.

To make productive use of their fast line rates, high-speed OCT laser systems must be coupled to correspondingly high-speed imaging catheters. Intravascular OCT requires line densities of 500–1,000 image lines per frame; fewer lines per frame lead to spatially under sampled images, while more lines per frame lead to spatially oversampled images. State-of-the-art lasers operating at speeds of 1–5 MHz should therefore be operated with catheters capable of generating images at speeds of 1,000–10,000 fps. A conventional intravascular imaging catheter is actuated at its proximal end using an external motor coupled to a torque wire via a fiber-optic rotary joint (FORJ). Rotational motion is transmitted to the lens assembly at the distal tip of the catheter. Due to the mechanical constraints of the torque coil, FORJ, and motor, as well as the requirement to translate motion over the entire length of the catheter (1.5–2.0 m), commercial catheter speeds are currently limited to about 200 fps. High-precision research systems that employ custom-made FORJ assemblies and catheters have achieved rotational speeds up to 350 rotations per second (rps), which enables frame capture at the equivalent rate of 350 frames per second [12]. Emerging catheter designs that feature micromotors mounted at the distal end of the catheter eliminate the need for external motors and torque coils. High-speed catheter operation has been demonstrated with piezoelectric devices at rotational speeds up to 960 rps [15] and with rotary micromotors at 400 rps [16] and 3,200 rps [17]. While these revolutionary catheter technologies remain slightly too large for clinical deployment and pose fabrication and cost challenges, moderate reductions in actuator size may soon enable their use in vivo without compromising device deliverability or safety.

The final technology required for intravascular OCT imaging within a single cardiac cycle is high-speed data acquisition and signal-processing electronics. To preserve system dynamic range, OCT systems require relatively high-resolution digitizers, particularly when imaging samples with highly variable signal levels common to pathologic or stented arteries. The availability of gigasample-class digitizer integrated circuits, combined with high-bandwidth digital bus architectures and the signal-processing capabilities of graphic processing units (GPUs) has opened the door for real-time 3D OCT imaging. Currently, the highest speeds achieved to date for an intravascular OCT imaging system have been obtained by pairing a high-speed signal processing system with a 1.6 MHz FDML laser source and a micromotor catheter operating at 3200 rps, culminating in a total pullback time of under 1 s [17]. In the future, intravascular OCT acquisition speeds will continue to increase as laser, catheter, and signal processing technologies advance in parallel.

15.3.2 3D Segmentation and Visualization

The increase in the volume of image data acquired by successive generations of OCT imaging systems has outpaced the ability of the systems to extract clinically relevant information and display it in a format that can be readily interpreted by cardiologists during PCI procedures. In a typical OCT procedure, several gigabytes of data are acquired to generate cross-sectional images of an artery in three dimensions before and after intervention. Fortunately, software is being developed for the latest generation of OCT systems that eases the information processing burden by automating the main tasks involved in treatment planning and evaluation.

Earliest to emerge have been automated software tools that take advantage of the clear delineation of the lumen boundary provided by OCT [18–20]. Figure 15.1 shows an example of the information displayed by the latest generation of a commercial intravascular imaging system (ILUMIEN OPTIS™, St. Jude Medical, Westford, MA). In addition to the conventional transverse and longitudinal (L)-mode cross sections (upper right and lowermost panels of Fig. 15.1), a volumetric reconstruction of the lumen is displayed (upper left panel). Generated by a fully automatic software routine that traces the 3D contour of the inner surface of the artery, this representation of the artery is intended to give cardiologists views of lumen morphology similar to those provided by coronary angiograms reconstructed from projections acquired at multiple angles. The algorithms that underlie the automated boundary detection must be computationally efficient for real-time operation and must operate in the presence of guidewire shadows and other image artifacts.

Although they give an impression of the severity and longitudinal extension of flow-limiting lesions, 3D lumen reconstructions are not well-suited for quantitative planning. The lumen profile display, shown in Fig. 15.1 above the L-mode image, is designed to serve this function. Derived from the 3D lumen contour, the lumen profile shows the mean diameter or area of the vessel lumen along the entire
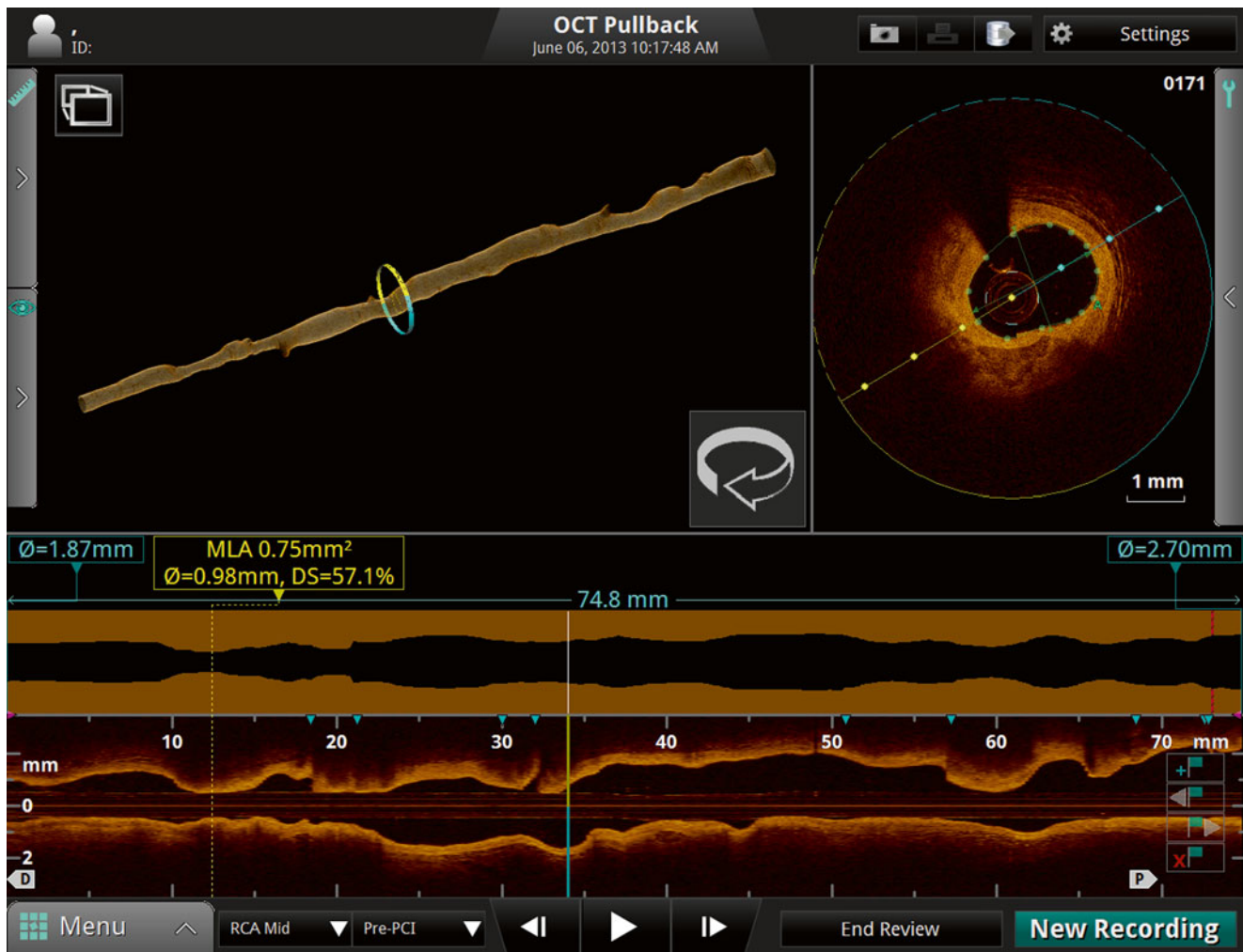
Fig. 15.1 Volumetric data display on the ILUMIEN OPTIS™ OCT system console

length of the imaged segment of the artery (7.5 cm, in this example). Unlike the L-mode display, the lumen profile is calculated as an average over all angles, allowing the variations of the flow-limiting diameter or area of the artery to be quantified independent of lesion eccentricity. This information facilitates the choice of the appropriate stent diameter and length for restoration of the lumen profile.

Recently, the scope of research in volumetric imaging has extended beyond lumen reconstruction to automated segmentation and visualization of stents for volumetric assessment of malapposition and neointimal thickness [21–24]. One of the objectives of this work is to provide clinical researchers with new off-line tools for evaluation of stent performance in large patient trials; another objective is to facilitate real-time assessment of stent deployment.

When a beam of light impinges on a metallic stent strut, it reflects light strongly and casts a shadow. These basic optical properties are the primary signatures of stents in OCT images. One might imagine that computer recognition of stent struts

would then be simple exercise of searching for regions of the OCT image with bright reflections with associated shadows. In practice, however, the image-processing task is not so straightforward. Since the reflection of light from the surface of most stent struts tends to be specular, the intensity of light reflected back to the lens at the tip of the OCT catheter depends strongly on the angular orientation of the strut relative to the incident OCT beam. Consequently, the apparent brightness of the image of a stent strut, as well as the appearance of its shadow, both depend on the position of the OCT catheter in the artery. Moreover, the radial position of the strut relative to the focus of the incident OCT beam and the presence of overlying tissue or residual blood adds to intensity variations. Finally, other bright and highly attenuating structures in the artery (e.g., foam cell clusters) can masquerade as stent struts.

In spite of the challenges imposed by these variables, significant progress has been made in the development of robust image-processing methods for automated stent detection in OCT images. Figure 15.2 shows an example of
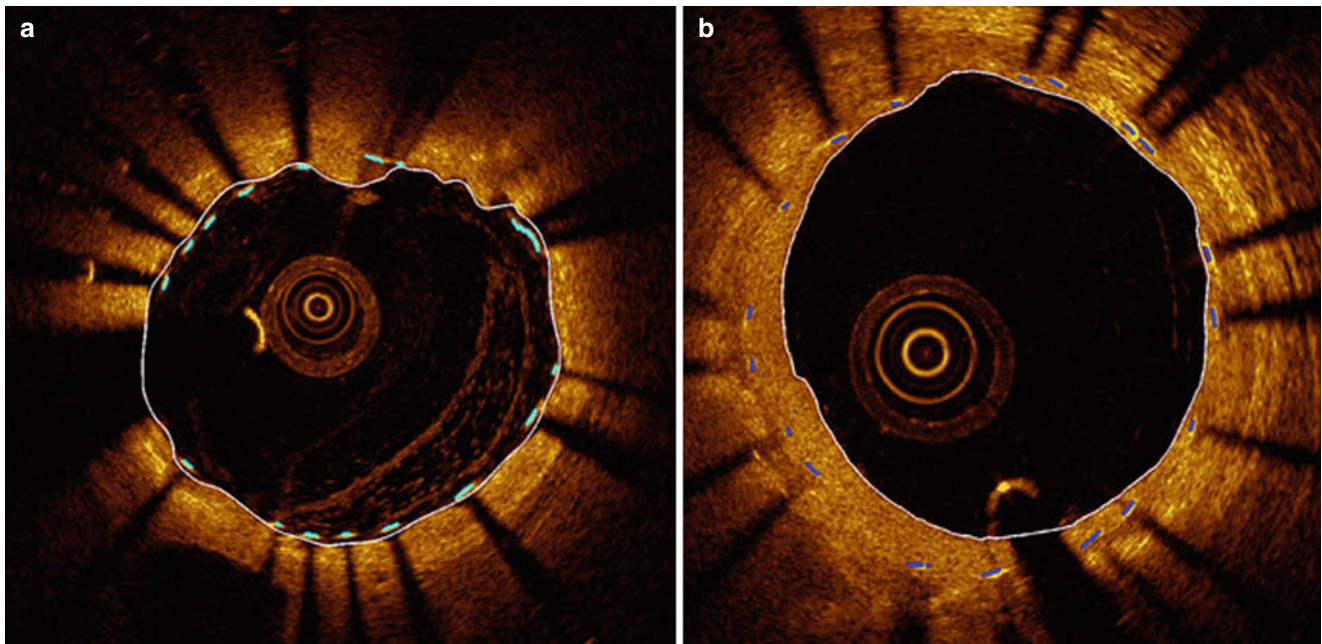
Fig. 15.2 Examples of automatic detection of stent struts in OCT image cross sections. (**a**) Freshly implanted stent with residual blood in lumen. (**b**) Stent at follow-up with eccentric neointimal growth console (From Ughi et al. [23])

Fig. 15.3 3-D rendering of calcified plaque in an OCT image segment (**a**) manually segmented, and (**b**) automatically segmented (From Wang et al. [30])
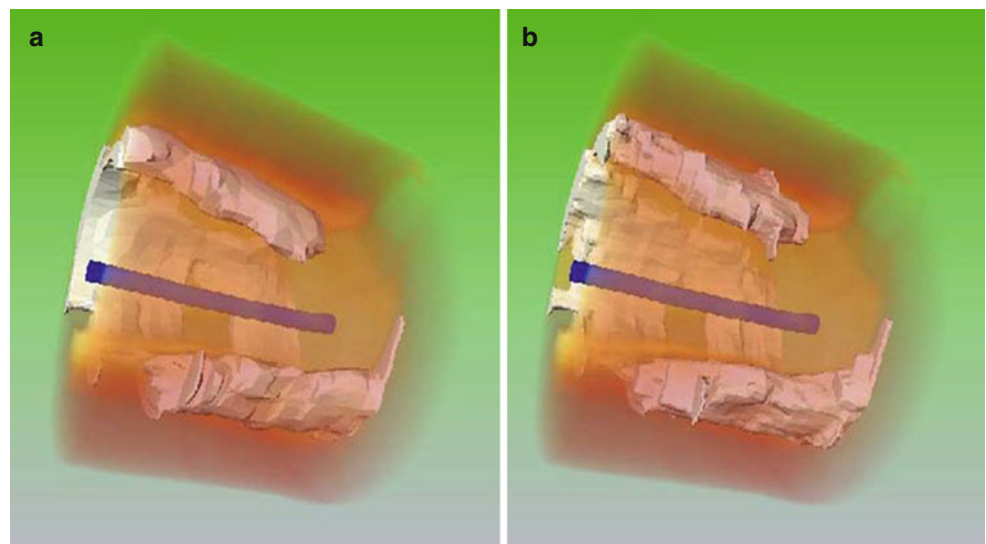
computer-detected stent struts in OCT images of a freshly implanted stent and of a stent at follow-up [23]. Based on the computer-generated distribution of stent reflections relative to the lumen boundary, the boundary of the malapposed region or the volume of tissue coverage can be quantified and displayed. The potential clinical benefits of volumetric stent imaging with intravascular OCT is currently being investigated for assessing the risks of stent restenosis and thrombosis after implantation of bare metal and drug-eluting stents [25, 26].

Perhaps the longest-standing and most challenging objective of OCT software developers has been the automated delineation and characterization of plaque within long arterial segments. Although early work by Yabushita and others [27–29] established the relationship between the optical characteristics of the most common vascular tissues and their appearances in OCT images, an algorithm for fully automated tissue classification is not yet available for clinical use. Recently, computer-assisted segmentation of calcified plaques and thin-capped fibroatheromas has been demonstrated in a research setting. Figure 15.3 is an example of a 3D rendering of a large calcium deposit in an artery imaged by OCT in vivo [31]. Such reconstructions, made

possible by the unique ability of OCT to image calcium, may facilitate real-time planning of stent placement and deployment, especially in complicated cases for which use of rotational atherectomy or a cutting balloon is indicated. A semi-automatic algorithm has also been developed for volumetric reconstruction of fibrous caps overlying lipid-rich plaque [30]. Quantitation of thickness variation based on the 3D structure of the plaque may lead to a better understanding of the mechanisms of plaque rupture.

The rapid development of 3D visualization techniques for CT, MR and other non-invasive imaging modalities is likely to engender parallel developments in intravascular imaging. By reducing the steepness of the learning curve for image interpretation, computer-assisted processing and display of image data promises to improve the clinical utility of OCT for non-expert users.

15.3.3 Angiographic Co-Registration

While intravascular OCT images enable visualization of coronary anatomy with unprecedented levels of detail, only a segment of one coronary branch can be interrogated within a single acquisition. Additionally, OCT imaging cannot be performed in real time during delivery of stents or other therapeutic devices. Therefore, cardiologists continue to rely on X-ray angiography for assessment of the complete coronary system and for real-time guidance of intravascular therapy. Recently, technologies have begun to emerge that allow co-registration of OCT and angiography image data to overcome these limitations.

Two general software techniques for OCT-angiography co-registration currently exist: landmark-based and tracking-based. Landmark-based co-registration techniques rely on identification of a known feature that is visible in both the OCT and angiographic images to anchor the position of the images. Landmark features are typically large side branches, which are readily detectable with both OCT and X-ray imaging. Although identification of the landmark is currently performed by a trained user, this technique could conceivably be automated in the future. Once a landmark has been selected, a priori knowledge about the OCT pullback speed, length, and starting position can be used to project the OCT frame positions onto an angiographic image. This class of techniques has the advantage that an OCT pullback can be co-registered to an angiogram acquired at a different point in time, as long as there was no change in the position of the OCT catheter between the acquisition of the two datasets. Industrial research teams have demonstrated full 3D reconstruction and co-registration of OCT with angiography using multi-planar X-ray imaging and landmark-based techniques [32].

Tracking-based co-registration techniques rely on detection of a radio-opaque feature on the OCT catheter, such as a marker band, in a series of angiography frames acquired at the same time as the OCT pullback. If the radio-opaque feature is positioned at a known distance from the catheter's imaging lens, the OCT image position can be localized directly on the corresponding angiography frame. This class of techniques has the advantage of generally requiring less user input, as there is no need for identification of landmarks on the OCT or angiography images. Tracking-based co-registration has the drawback of requiring the OCT and angiography datasets to be acquired simultaneously. However, this requirement provides the benefit of inherent compensation of motion artifacts, as the true position of the OCT imaging lens can be inferred on every angiography frame.

Figure 15.4 shows an example screenshot of tracking-based OCT co-registration software developed by St. Jude Medical. The left panel shows an angiography frame acquired at the same time as the OCT frame displayed in the right panel. The white bar on the X-ray image indicates the spatial location of the OCT frame. The side branch visible at 8 o'clock in the OCT image is also visible directly underneath the white angiography marker. This type of display is useful for localizing features detected by OCT within the wide field of view provided by angiography.

15.3.4 Functional Lesion Assessment

The increasing acceptance of FFR as the gold standard for functional assessment of the hemodynamic significance of coronary stenoses has called into question the role of imaging in stenting decisions [2]. Minimum lumen area (MLA) and percent diameter or area stenosis (%DS or %AS) are the anatomical measures of lesion significance by which the significant of intermediate lesions have been evaluated by angiography and IVUS. Recent studies have shown weak correlations of these measures with FFR for both imaging modalities [33, 34]. MLA and %AS measured using OCT has not fared much better, except in small-diameter arteries [4, 35].

Since narrowing of the epicardial coronary branches is the predominant contributor to the pressure drop measured by a pressure FFR, why do MLA and %AS, as measured by OCT and other existing imaging modalities, fail to correspond well with FFR measurements? This discordance has both physiological and methodological origins [36]: (1) simple anatomic indices fail to represent the volumetric nature of flow-limiting lesions, (2) very high measurement accuracy is critical, because the flow resistance or a stenosis varies in inverse proportion to the fourth power of its radius, (3) since the pressure drops across stenoses are flow dependent, shunting of flow by side branches and collateral vessels can alter the physiological significance of the same stenosis at different locations, and (4) the hyperemic microvascular
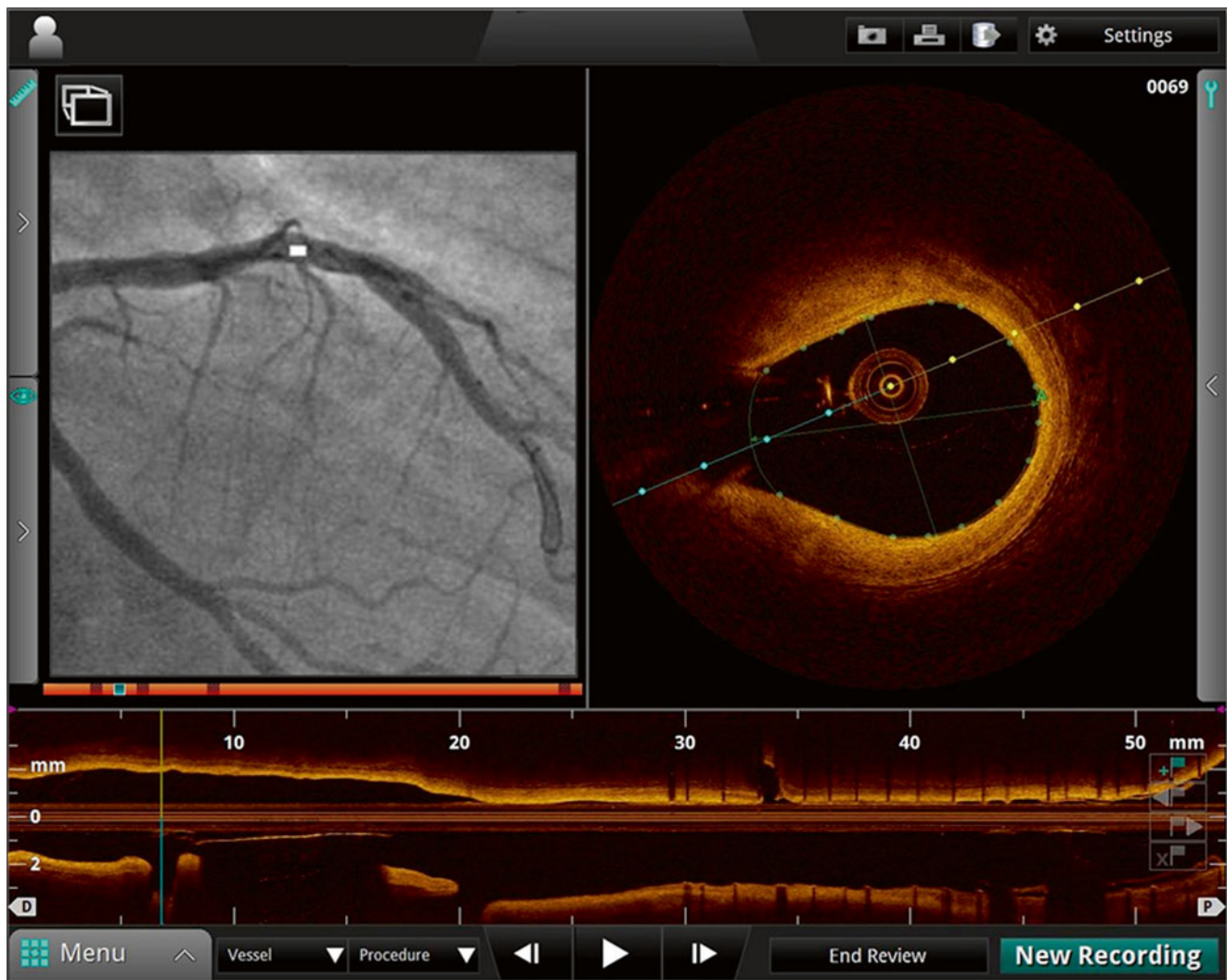
Fig. 15.4 Co-registration of OCT (*right hand panel*) and angiographic (*left hand panel*) images. White marker on angiogram indicates position of OCT frame. Side branch visible on OCT at 8 o'clock position is also visible directly beneath white marker on angiogram

resistance, which sets the upper limit on blood flow in a given branch, and hence, the pressure drop across a stenosis, varies according to the volume of myocardium perfused by a given coronary branch.

New methods are being developed for modeling blood flow resistance of coronary arteries that aim to improve the ability of image-derived anatomical measurements to predict the functional significance of coronary lesions [37]. Although most of the publications on this topic pertain to non-invasive assessment of FFR using computed tomography angiography [38, 39], investigations of methods to estimate FFR from 3D OCT models have been active for a number of years [40, 41]. High-quality 3D lumen reconstructions generated from OCT images contain detailed information about lumen morphology, normal reference diameters, branch locations and other variables from which patient-specific models of coronary blood flow can be built.

The feasibility of estimating FFR using a computationally efficient model of flow resistance derived from OCT images was demonstrated recently in a small clinical study [41]. This study showed the benefits of incorporating information about the volumetric properties of a coronary lesion, in addition to its minimum cross-sectional dimensions. Figure 15.5 shows the diameter profile of a diffusely stenosed coronary artery (upper panel) and the corresponding pressure drop along its length (lower panel) calculated by the analytical flow model employed in the study. The numerical values shown in the figure are the hyperemic blood flow rates estimated by the flow model for each of the branches. Based on these flow rates and the flow resistances calculated from the lumen areas measured along the length of the vessel, the model estimates the FFR for the main branch. In this example, the '1 – VRR' value (0.66) displayed in the top panel of the figure is an estimate of the distal FFR that would be measured by a pressure

Fig. 15.5 (*Top*) Mean-diameter profile of the lumen of a stenosed coronary branch derived from an OCT pullback image. The '1 – VRR" value (0.66) in the upper left corner of the panel is the estimated FFR. The other numerical values are the estimated blood flows in ml/s. (*Bottom*) Calculated pressure drop along the length of the vessel for the branched and hypothetical unbranched artery (From Guagliumi et al. [41])
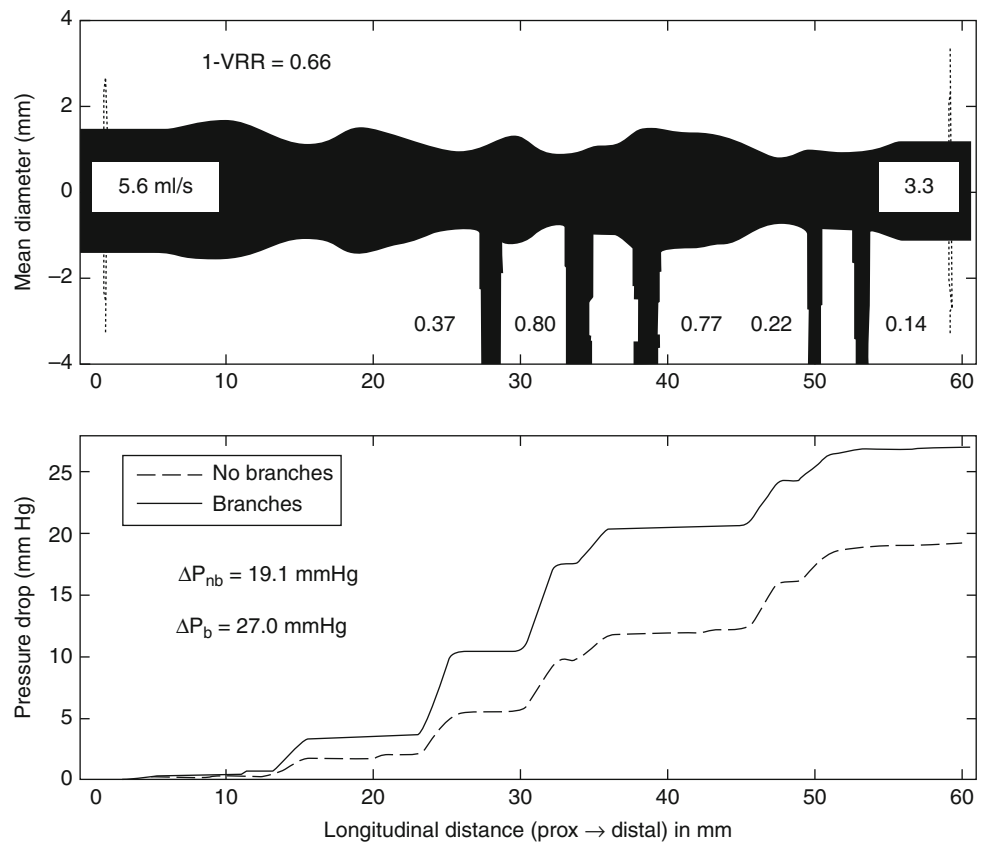
wire. Flow modeling opens the potential for optimization of PCI according to anatomical and physiological information derived from pullbacks. If future studies support the clinical utility of OCT-derived FFR estimates, this approach may encourage the development of interactive stent planning tools to facilitate treatment of complex coronary lesions.

15.3.5 Multimodal Imaging

Since the first intravascular OCT studies were carried out nearly 15 years ago, a growing number of intravascular imaging modalities have been demonstrated in pre-clinical studies: near-infrared spectroscopy (NIRS), intracoronary MRI, elastography, molecular fluorescence, and photoacoustic imaging [42–44]. Given that each modality has its particular strengths and weaknesses, it is natural to contemplate whether there are synergistic combinations of modalities that can provide unique clinical diagnostic capabilities for cardiovascular application. In 2013, the TVC™ NIRS-IVUS Imaging System (Infraredx, Burlington, MA) was the first intravascular imaging system with a dual-modality catheter to gain FDA approval. It is likely that other multimodal intravascular imaging technologies will be introduced into clinical practice in the coming decade. This section reviews on-going investigations of multimodal intravascular diagnostics in which OCT plays a central role.

15.3.5.1 OCT-IVUS

Although the superior contrast, resolution, and near-field image quality of OCT compared to IVUS make the interpretation of arterial morphology easier [45], the deeper tissue penetration of IVUS has advantages in applications that require a long far-field scan range, such as ostial left main imaging and the measurement of lipid plaque burden.

Efforts to combine OCT and IVUS functionality on the same catheter and console have been reported by several research groups [46–48]. The main challenge of these efforts has been to maintain state-of-the-art performance of both modalities without adding significant complexity or cost. Without sacrificing crossing profile and deliverability, the catheter must accommodate the IVUS transducer with the interconnecting RF and OCT fiber optics within a single sheath. Several different catheter-tip configurations have been reported to align the OCT and IVUS beams with only a small longitudinal, lateral or angular offset. To date, prototype catheters with outer diameters as small as 3.6 F have been developed and tested in animal models [48]. Figure 15.6 shows an example of the construction of the internal catheter-tip assembly at the tip of a 4 F OCT-IVUS catheter [47]. Further improvements in catheter design and manufacturing are required to meet the clinical requirements for imaging performance, deliverability and reliability.
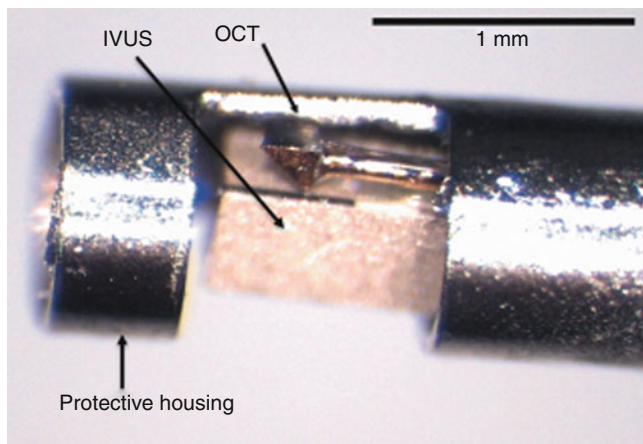
Fig. 15.6 Imaging assembly at the tip of a prototype OCT- IVUS catheter before insertion in a 4 F transparent nylon sheath (not shown) (From Li et al. [47])

Fig. 15.7 A diagram of one configuration of a combined OCT and pressure-sensing catheter (From Schmitt et al. [50])

Hybrid OCT-IVUS imaging has the potential to differentiate and characterize plaque morphology more precisely than either modality alone. In particular, hybrid imaging may allow more comprehensive assessment of atherosclerotic lesions by combining the ability of OCT to assess lumen dimensions, estimate fibrous cap thickness, identify thrombus, and delineate the boundaries of calcified plaque with the ability of IVUS to image through lipid-rich plaques and thrombus [44].

15.3.5.2 OCT-Pressure

OCT is regarded as one of the most accurate structural imaging methods for coronary arteries, while FFR is the gold standard for function assessment of stenosis relevance during maximum flow conditions [49]. PCI guidance may benefit from access to complementary information from both modalities.

The first effort to combine OCT and FFR was St Jude Medical's Ilumien™ PCI Optimization™ system, which integrates wireless FFR measurement into the St Jude Medical OCT platform, using separate pressure wires and OCT catheters. FFR can be used for making PCI decisions, while OCT can be used for optimizing PCI procedures. In the ideal case, together with the angiographic co-registration, the cardiologist first uses FFR to decide if and roughly where stents are needed. He or she can then use an OCT catheter to observe the plaque characteristics and measure lumen dimensions for the stenting procedure. After the stents are placed, the physician can then optionally use OCT to check the stent placement results and use FFR to assure revascularization success.

Despite the theoretical advantage of using both OCT and FFR in the same patient, the combined usage remains low, even in large medical centers. In the current US medical and reimbursement environment, the time and cost of employing two separate diagnostic catheters in the same procedure are significant limitations. To enhance the clinical workflow and to mitigate the cost, one future solution may be to combine the OCT and FFR together on a single catheter, although catheter dimensions are critical.
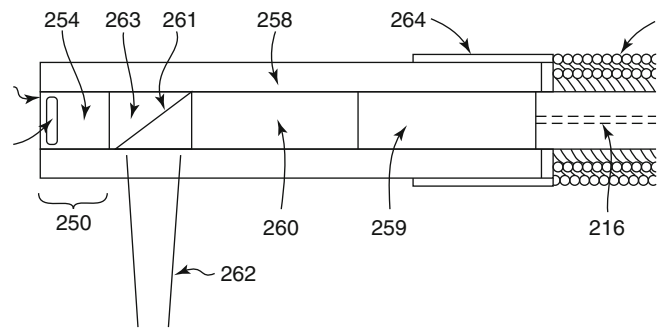
Figure 15.7 shows a schematic diagram of one possible design of a combination OCT and FFR catheter [50, 51]. This device uses an optical pressure transducer mounted on the OCT lens assembly, both sharing the same optical fiber and other catheter components. The light travels through the core of a single-mode fiber into the lens assembly where it is separated into two paths by a fiber prism. The portion of the beam that is directed into the tissue is used for OCT imaging. The other portion of the beam, which reflects from the optical pressure sensor, is used for FFR recording. Because most of the catheter components and other optical system components are shared, the cost of the combination device may not be significantly higher than that of a single-function OCT catheter.

Multi-modal catheters that enable co-registered OCT images and FFR recordings are not yet available commercially, nor have large-scale clinical studies been conducted that show the advantages of combining OCT imaging and FFR measurements in the same patient. Future research is needed to evaluate potential synergic effects on outcomes in different patient populations.

15.3.5.3 OCT-Spectroscopy

Although it provides high-resolution images of coronary anatomy, OCT does not provide direct information about the chemical or molecular composition of tissue. While some compositional information may be inferred from image analysis, such inferences are prone to inaccuracy, especially in plaque composed of mixed tissue types. To increase the diagnostic accuracy, it may be advantageous to combine molecular-sensitive imaging techniques with OCT.

One of the most developed imaging methods that take advantage of molecular contrast is the intravascular near-infrared reflectance spectroscopy (NIRS). NIRS is a spectroscopic method that uses a portion of the near-infrared spectrum to detect and quantify chemical compounds that have characteristic vibrational absorption spectra [52]. A NIRS system designed for lipid detection is now commercially available
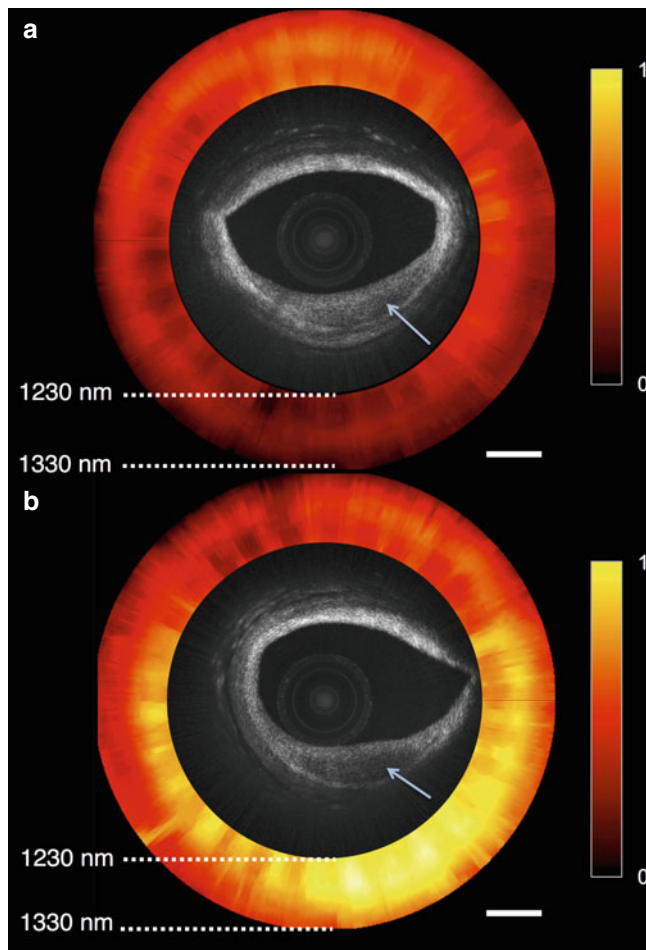
Fig. 15.8 OCT-NIRS images of cadaver coronary artery ex vivo. Both OCT images show lesions with reduced backscattering. NIRS image shows absorption spectra of tissue versus wavelength, representing the total attenuation normalized for the entire data set; '1' and '0' correspond to the maximum and minimum absorption within the data set, respectively. The NIRS signal in (**a**) does not demonstrate a high lipid signal, while the NIRS signal in (**b**) shows the presence of abundant lipid. These findings suggest that the lesion in (**a**) does not contain much lipid whereas the lesion in (**b**) is lipid-rich. Scale bars, 500 μm (From Fard et al. [53])

(Infraredx, Inc., Burlington, MA). NIRS has also been combined with intravascular ultrasound (IVUS) to provide co-registered structural and chemical information [44].

Recently, Fard et al. described a prototype OCT-NIRS system with a dual-modality catheter [53]. The system used a swept laser source (1,229–1,335 nm) for both OCT and NIRS. A double-clad fiber (DCF) was used to transmit and receive the optical signals between the electro-optic unit and catheter. The OCT and NIRS excitation light traveled along the core of the DCF. The backscattered OCT signal returned through the core of the DCF, while the NIRS signal traveled through the inner cladding of the DCF. The signals were then detected separately by an OCT console and an NIRS console. Using this apparatus, the authors were able to simultaneously obtain OCT and NIRS data sets (Fig. 15.8).

By exploiting the negative absorption slope of lipid in the near-infrared region (1,200–1,400 nm), the authors claim that it is possible to obtain both a lipid composition map and OCT images. In principle, NIRS principles can also be applied to the measurement of other organic compounds, including proteins and carbohydrates.

Both NIRS and OCT have been shown to be sensitive to lipid in histological studies; however, the relative improvement in detection sensitivity and selectivity that can be expected by combining the two technologies is still unknown. Recently, reports have been published that show discrepancies among the available technologies for in vivo lipid detection. Pu et al. reported that by comparing grayscale IVUS, VH-IVUS and NIRS, a positive relationship was found between VH-derived and the NIRS-derived lipid cores in non-calcified plaques, but not in calcified plaques [54]. By comparing the OCT and NIRS imaging data, poor overall agreement between NIRS and OCT was reported for detection of lipid [55]. Although it is unclear what could be the gold standard for these clinical studies, further investigation of NIRS technology is warranted to establish the potential clinical utility of OCT-NIRS catheter for routine intravascular diagnostics.

15.3.5.4 OCT-Fluorescence (Molecular Tagging)

Fluorescence imaging is potentially one of the most sensitive and specific methods for obtaining information about the molecular composition of arterial tissues. Some tissue constituents, such as type I collagen and NADH, have intrinsic fluorescence properties that can be imaged directly by measuring auto-fluorescence signals. Barton et al. demonstrated an endoscope for pre-clinical imaging that combines OCT and fluorescence spectroscopy [56]. Multiple UV-visible light bands were used for fluorescence excitation and fluorescence signals were recorded from several wavelength bands. The correct classification rates were 97 % and 91 %, respectively, for normal and plaque regions of excised aortic specimens. The same group also developed a multimodality catheter for mouse colon cancer imaging [57]. The catheter contains three parallel fibers, two multimode fibers for the fluorescence channel and one single-mode fiber for the OCT channel. It was found that OCT could be used as the primary method for identifying abnormal tissue by detecting epithelial thickening and structure deformation, while auto-fluorescence signals could be used for matching the fluorescence spectra of chemical compounds associated with the lesions. However, although statistically significant differences was found between normal and diseased tissues, the sensitivity and specificity were limited by variations of the fluorescence signal.

It may be possible to obtain better diagnostic accuracy by imaging specific biomarkers instead of common tissue types. Cardiac biomarkers have been identified for assessing inflammation, endothelial dysfunction, thrombosis, oxidative and ischemia stress, metabolic dysregulation and other pathological disorders [58]. Because most natural biomarkers do not

OFDI
thrombus segmentation

OFDI-NIRF
overlay
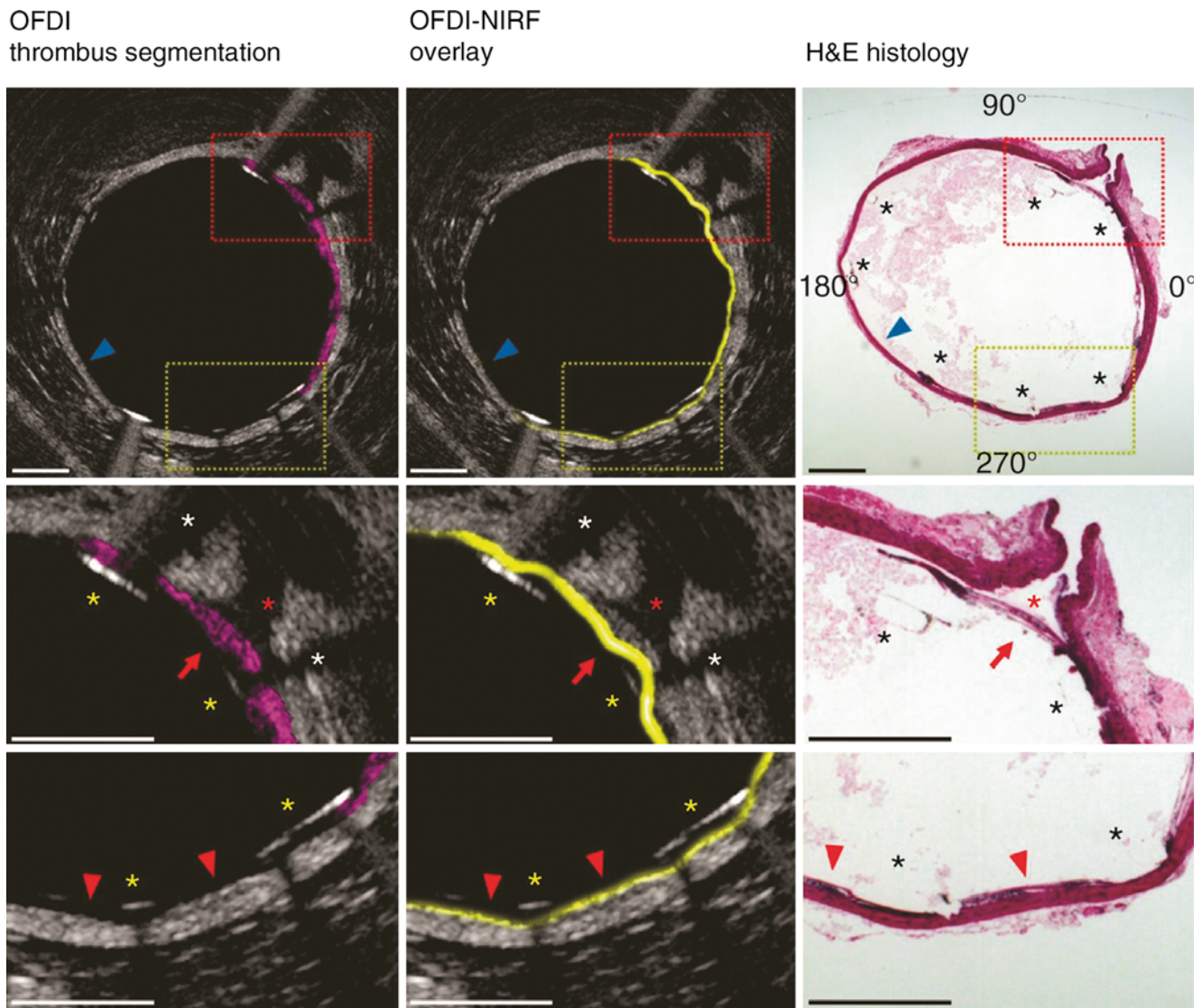
H&E histology

Fig. 15.9 OFDI (*gray scale*) with thrombus segmentation (*purple*) (*left column*), overlaid OFDI (*gray scale*) and NIRF (*yellow scale*) images (*middle column*), and corresponding H&E histology (Original magnification×25) (*right column*). The top row and the insets demonstrate OFDI, NIRF, and histology data showing corresponding microstructural features, such as a side branch (*red asterisk*), stent struts (*yellow asterisks* in OFDI, *black asterisks* in H&E), and thrombi (*red arrow*). Areas (*blue arrowhead*) without NIRF signal were devoid of fibrin by histology. Strong NIRF was observed where thrombus was detected by OFDI and histology (*middle row*, *red arrow*). In another area (*lower row*), a weaker fluorescence signal was detected corresponding to fibrin as confirmed by histology, but without evidence of protruding thrombus by OFDI (*red arrowheads*). *White asterisks*-stent strut shadows (From Yoo et al. [60])

have intrinsic optical properties that allow detection at low concentrations, contrast agents have been designed to bind with them and emit fluorescence signals [59]. To avoid the strong autofluorescence background in the visible region of the spectrum, the biomarkers are typically imaged using contrast agents that fluorescence in the near infrared.

Yoo et al. recently described a system and catheter that is capable of simultaneous OFDI (another acronym for FD-OCT) and near-infrared fluorescence (NIRF) imaging [60]. Instead of using multiple fibers, a single double-clad fiber was employed, which enabled the outer diameter of the catheter to be reduced to 0.8 mm. The OFDI axial resolution was 7 µm and the transverse resolution was 30 µm, while the NIRF resolution was about 100 µm. The NIRF measurements were precisely co-registered to OFDI and provided highly sensitive detection of nanomolar concentrations of Cy7 NIR fluorochrome. Both stent-associated thrombus and inflammatory enzyme activity were imaged in human coronary arteries ex vivo and in a rabbit iliac artery in vivo. Structural features, such as the stent struts, stent-associated thrombus, macrophages, and layers of the arterial wall were imaged with OFDI. The NIRF measurements mapped the fibrin distribution via the fibrin-specific molecular tag Cy7 and the distribution of inflammatory protease via an activatable cysteine protease agent (Fig. 15.9).

The combination of intravascular OCT and molecular imaging may offer new insight into human atherosclerosis.

Although it is still in a pre-clinical stage, early studies have already demonstrated the feasibility of the combination. However, regulatory approval of contrast agents remains a key hurdle to clinical translation. Also, the clinical value of a system that combines OCT and fluorescence imaging must be demonstrated before it can expect to gain widespread application outside of the research laboratory.

15.3.6 Novel Blood Clearing Methods

Because of its ready availability and desirable physical properties, angiographic contrast is currently the medium of choice for blood clearance in OCT imaging procedures. It has low optical attenuation within the spectral band in which current intravascular OCT systems operate (1,250–1,360 nm) and its high viscosity (approximately 2 times the viscosity of blood and 3–4 times the viscosity of water) facilitates the displacement of red cells in flowing blood [61]. However, contrast increases the risk of nephropathy in patients with compromised kidney function [62].

The introduction of fast frequency-domain technology has reduced the volume of radiographic contrast required to obtain OCT images over long vessel segments. Efficient procedural workflow that coordinates cineangiography and OCT can also reduce contrast use [63]. Nonetheless, the requirement for injection of contrast media for image acquisition continues to be a limitation of OCT.

A variety of alternatives to contrast media for OCT imaging have been investigated over the past decade, including dextran [61, 64], artificial blood substitutes [65, 66], and carbon dioxide [67]. Biocompatibility and optical transparency are two of the fundamental requirements that any OCT blood-clearing medium must satisfy. To be considered biocompatible for intra-arterial injection, the medium must be sterile, non-toxic, and have a short residence time in the bloodstream. In addition, it must not cause electrolytic disturbances that induce cardiac arrhythmias when injected into the coronary arteries. Moreover, to displace red cells efficiently at the recommended injection rates of 3–4 ml/s, the viscosity of the medium should be comparable to or greater than that of blood [61].

Dextran-40 (LMD-L), a low-molecular weight dextran, has been the most extensively studied alternative to contrast media for OCT imaging [61]. LMD-L has been used in clinical practice in Japan as a flushing medium for coronary angioscopy [68] and time-domain OCT [69]. With a viscosity slightly less than that of blood, LMD displaces blood more efficiently than saline, but requires higher volumes and/or flow rates to provide blood clearance equivalent to that of contrast [61]. The optimum rates and volumes for manual and pump-assisted injection of LMD-L for FD-OCT imaging have not yet been established. To date, the feasibility and safety of Dextran-40 for OCT imaging has been demonstrated in a total of 48 patients in two studies [61, 64].

LMD-L has been associated with renal failure at high cumulative volumes (>1 l) in other studies [70], but its nephrotoxicity at low volumes is unknown. At present, the use of Dextran-40 as an alternative to contrast is regarded as an off-label approach that continues to undergo clinical investigation [63].

Artificial blood substitutes have also been investigated in pre-clinical studies as alternatives to contrast for OCT imaging [65, 66]. A potential advantage of these agents is their ability to supply oxygen to tissues during prolonged imaging periods. The two main types of oxygen-carrying blood substitutes that have been investigated are stabilized hemoglobin solutions (Oxyglobin and Hemopure; Biopure, Inc., now OPK Biotech, Cambridge, MA) and perfluorocarbon (Fluosol) emulsions. Since both of these types of blood substitutes attenuate near-infrared light much less than blood, they enable OCT imaging when blood is temporarily displaced [66]. However, their relatively low viscosities reduce flushing efficacy compared to that of contrast. Although one form of Fluosol was granted approval by the FDA in 1989 for use during cardiac angioplasty, there is currently no FDA-approved blood substitute available on the market. Questions about the safety of blood substitutes remain and safety continues to be a primary focus of development for second- and third-generation blood substitutes [71]. If these efforts prove to be successful and new products enter the market, it is likely that researchers will renew their interest in investigating oxygen-carrying blood substitutes for OCT imaging.

Carbon dioxide (CO_2) is currently used as medium for digital subtraction angiography in peripheral vascular patients with chronic renal insufficiency. In a recent case study, performed with institutional review board approval, OCT pullback images of a diseased superficial femoral artery were obtained by using hand-injected CO_2 to displace blood [67]. The authors of this study concluded that CO_2 may be a viable option to avoid nephrotoxicity in patients with chronic renal insufficiency or congestive heart failure. An additional advantage of CO_2 as a blood-clearing agent is that it expands the effective scan radius of the OCT system for imaging vessels with large lumens, because its refractive index is substantially lower than that of contrast (1.0 vs 1.45).

OCT remains an investigational modality in peripheral vascular imaging and its potential clinical role has not been defined. CO_2 is contraindicated for use in coronary, cerebral, and spinal arteries, because of the risk of air embolism [72]. Therefore, the utility of CO_2 as an alternative to angiographic contrast will depend on how the application of OCT in peripheral vascular imaging evolves.

References

1. Pijls NH, De Bruyne B, Peels K, van der Voort PH, Bonnier HJRM, Bartunek J, et al. Measurement of fractional flow reserve to assess the functional severity of coronary-artery stenosis. N Engl J Med. 1996;334:1703–8.

2. Tonino PA, De Bruyne B, Pijls NH, Siebert U, Ikeno F, van't Veer M, Klauss V, et al. Fractional flow reserve versus angiography for guiding percutaneous coronary intervention. N Engl J Med. 2009; 360:213–24.

3. Pijls NH, Van Schaardenburgh P, Manoharan G, Boersma E, Bech JW, van't Veer M, et al. Percutaneous coronary intervention of functionally nonsignificant stenosis: 5-year follow-up of the DEFER study. J Am Coll Cardiol. 2007;49:2105–11.

4. Gonzalo N, Escaned J, Alfonso F, Nolte C, Rodrigeuz V, Jimenez-Quevedo P, et al. Morphometric assessment of coronary stenosis relevance with optical coherence tomography: a comparison with fractional flow reserve. J Am Coll Cardiol. 2012;59:1080–90.

5. Schmitt JM. Optical coherence tomography (OCT): a review. IEEE J Sel Top Quant Electr. 1999;5:1205–15.

6. Fercher AF, Drexler W, Hitzenberger CK, Lasser T. Optical coherence tomography – principles and application. Rep Prog Phys. 2003;33:239–303.

7. Hamden R, Gonzales RG, Ghostine S, Caussin C. Optical coherence tomography: from physical principles to clinical applications. Arch Cardiovasc Dis. 2012;105:529–34.

8. Huber R, Wojtkowski M, Fujimoto JG. Fourier Domain Mode Locking (FDML): a new laser operating regime and applications for optical coherence tomography. Opt Express. 2006;14(8):3225–37.

9. Wieser W, Biedermann BR, Klein T, Eigenwillig CM, Huber R. Multi-megahertz OCT: high quality 3D imaging at 20 million A-scans and 4.5 GVoxels per second. Opt Express. 2010;18:14685–704.

10. Adler DC, Wieser W, Trepanier F, Schmitt JM, Huber RA. Extended coherence length Fourier domain mode locked lasers at 1310 nm. Opt Express. 2011;19:20930–9.

11. Jayaraman V, Jiang J, Potsaid B, Cole G, Fujimoto J, Cable A. Design and performance of broadly tunable, narrow line-width, high repetition rate 1310 nm VCSELs for swept source optical coherence tomography. Proc SPIE. 2012 8276:82760D-1–82760D-11.

12. Cho HS, Jang SJ, Kim K, Dan-Chin-Yu AV, Shishkov M, Bouma BE, Oh WY. High frame-rate intravascular optical frequency-domain imaging in vivo. Biomed Opt Express. 2014;5:223–32.

13. Oh WY, Vakoc BJ, Shishkov M, Tearney GJ, Bouma BE. > 400 KHz repetition rate wavelength-swept laser and application to high-speed optical frequency domain imaging. Opt Lett. 2010;35:2919–21.

14. Huber R, Adler DC, Fujimoto J. Buffered Fourier domain mode locking: unidirectional swept laser sources for optical coherence tomography imaging at 370,000 lines/s. Opt Lett. 2006;31:2975–7.

15. Tsai TH, Potsaid B, Kraus MF, Zhou C, Tao YK, Hornegger J, Fujimoto JG. Piezoelectric-transducer-based miniature catheter for ultrahigh-speed endoscopic optical coherence tomography. Biomed Opt Express. 2011;2:2438–48.

16. Tsai TH, Potsaid B, Jayaraman V, Jiang J, Heim PJ, Kraus MF, Zhou C, Hornegger J, Mashimo H, Cable AE, Fujimoto JG. Ultrahigh speed endoscopic optical coherence tomography using micromotor imaging catheter and VCSEL technology. Biomed Opt Express. 2013;4:1119–32.

17. Wang T, Weiser W, Springeling G, Beurskens R, Lancee CT, Pfeiffer T, van der Steen AF, Huber R, van Soest G. Intravascular optical coherence tomography imaging at 3200 frames per second. Opt Lett. 2013;38:1715–7.

18. Sihan K, Botha C, Post F, de Winter S, Gonzalo N, Regar E, et al. Fully automatic three-dimensional quantitative analysis of intra-coronary optical coherence tomography: method and validation. Catheter Cardiovasc Interv. 2009;74:1058–65.

19. Gogas BD, Farooq V, Serruys PW. Three-dimensional coronary tomographic reconstructions using in vivo intracoronary optical frequency domain imaging in the setting of acute myocardial infarction: the clinical perspective. Hellenic J Cardiol. 2012;53:148–51.

20. Chatzizisis YS, Koutkias VG, Toutouzas K, Giannopoulos A, Chouvardia I, Riga M, et al. Clinical validation of an algorithm for rapid and accurate automated segmentation of intracoronary optical coherence tomography images. Int J Cardiol. 2014;172:568–80.

21. Bonnema GT, O'Halloran Cardinal K, Williams SK, Barton JK. An automatic algorithm for detecting stent endothelization from volumetric optical coherence tomography datasets. Phys Med Biol. 2008;53:3082–98.

22. Tsantis S, Kagadis GC, Katsanos K, Karnabatidis D, Bourantas G, Nikiforidis GC. Automatic vessel lumen segmentation and stent strut detection in intravascular optical coherence tomography. Med Phys. 2012;39:503–13.

23. Ughi GJ, Adriaenssens T, Onsea K, Kayaert P, Dubois C, Sinnaeve P, Coosemans M, Desmet W, D'hooge J. Automatic segmentation of in-vivo intra-coronary optical coherence tomography images to assess stent strut apposition and coverage. Int J Cardiovasc Imaging. 2012;28:229–41.

24. Ughi GJ, Van Dyck CJ, Adriaenssens T, Hoymans VY, Sinnaeve P, Timmermans JP, Desmet W, Vrints CJ, D'hooge J. Automatic assessment of stent neointimal coverage by intravascular optical coherence tomography. Eur Heart J Cardiovasc Imaging. 2014;15: 195–200.

25. Gonzalo N, Serruys PW, Okamura T, van Beusekom HM, Garcia-Garcia HM, van Soest G, et al. Optical coherence tomography patterns of stent restenosis. Am Heart J. 2009;158:284–93.

26. Guagliumi G, Sirbu V, Musumeci G, Gerber R, Biondi-Zoccai G, Ikejima H, Ladich E, et al. Examination of the in vivo mechanisms of late drug eluting stent thrombosis. J Am Coll Cardiol Intv. 2012;5:12–20.

27. Yabushita H, Bouma BE, Houser SL, Aretz T, Jang IK, Schlendorf KH, Kauffman CR, Shishkov M, Kang DH, Halpern EF, Tearney GJ. Characterization of human atherosclerosis by optical coherence tomography. Circulation. 2002;106:1640–5.

28. Kume T, Akasaka T, Kawamoto T, Watanabe N, Toyota E, Neishi Y, Sukmawan R, Sadahira Y, Yoshida K. Assessment of coronary arterial plaque by optical coherence tomography. Am J Cardiol. 2006;97:1172–5.

29. Xu C, Schmitt JM, Carlier SG, Virmani R. Characterization of atherosclerosis plaques by measuring both backscattering and attenuation coefficients in optical coherence tomography. J Biomed Opt. 2008;13:034003.

30. Wang Z, Kyono H, Bezerra H, Wang H, Gargesha M, Alraies C, Xu C, Schmitt JM, Wilson DL, Costa MA, Rollins AM. Semi-automatic segmentation and quantification of calcified plaques in intra-coronary optical coherence tomography images. J Biomed Opt. 2010;15:061711.

31. Wang Z, Chamie D, Bezerra HG, Yamamoto H, Kanovsky J, Wilson DL, Costa MA, Rollins AM. Volumetric quantification of fibrous caps using intravascular optical coherence tomography. Biomed Opt Express. 2012;3:1413–26.

32. Tu S, Xu L, Ligthart J, Xu B, Witberg K, Sun Z, Koning G, Reiber JHC, Regar E. In vivo comparison of arterial lumen dimensions assessed by co-registered three-dimensional (3D) quantitative coronary angiography, intravascular ultrasound and optical coherence tomography. Int J Cardiovasc Imaging. 2012;28:1315–27.

33. Pyxaras SA, Tu S, Barbato E, Barbati G, Di Serafino L, De Vroey F, et al. Quantitative angiography and optical coherence tomography for the functional assessment of nonobstructive coronary stenosis: comparison with fractional flow reserve. Am Heart J. 2013;166:1010–8.

34. Koo BK, Yang HM, Doh JH, Choe H, Lee SY, Yoon CH, et al. Optimal intravascular ultrasound criteria and their accuracy for defining the functional significance of intermediate coronary stenosis of difference locations. J Am Coll Cardiol Intv. 2011;4:803–11.

35. Shiono Y, Kitabata H, Kubo T, Masuno T, Ohta S, Ozaki Y, et al. Optical coherence tomography-derived anatomical criteria for functionally significant coronary stenosis assessed by fractional flow reserve. Circ J. 2012;76:2218–25.

36. Johnson NP, Kirkeeide RL, Gould KL. Coronary anatomy to predict physiology. Circ Cardiovasc Imaging. 2013;6:817–32.

37. Serruys PW, Girasis C, Papadopoulou S-L, Onuma Y. Non-invasive fractional flow reserve: scientific basis, methods, and perspectives. EuroIntervention. 2012;8:511–9.

38. Koo BK, Erglis A, Doh JH, Daniels DV, Jegere S, Kim HS, et al. Diagnosis of ischemia-causing coronary stenosis by noninvasive fractional flow reserve computed from coronary computed tomographic angiograms. Results from the prospective multicenter DISCOVER-FLOW (Diagnosis of Ischemia-Causing Stenoses Obtained Via Noninvasive Fractional Flow Reserve. J Am Coll Cardiol. 2011;58:1989–97.

39. Norgaard BL, Leipsic J, Gaur S, Gaur S, Seneviratne S, Ko BS, et al. Diagnostic performance of noninvasive fractional flow reserve derived from coronary computed tomography angiography in suspected coronary artery disease. J Am Coll Cardiol. 2014;63:1145–55.

40. Schmitt JM, Friedman JM, Petroff C, Elbasiony A. Lumen morphology and vascular resistance measurements data collection systems, apparatus, and methods. US Patent Application 0071404 (24 Mar 2011).

41. Guagliumi G, Sirbu V, Petroff C, Capodanno D, Musumeci G, Yamamoto H, et al. Volumetric assessment of lesion severity with optical coherence tomography: relationship with fractional flow reserve. EuroIntervention. 2013;8:1172–81.

42. Maehara A, Mintz GS, Weissman NJ. Advances in intravascular imaging. Circ Cardiovasc Interv. 2009;2:482–90.

43. Muller JE, Weissman NJ, Tuzcu EM. The year in intracoronary imaging. J Am Coll Cardiol Imaging. 2010;3:881–91.

44. Bourantas CV, Garcia-Garcia HM, Naka KK, Sakellarios A, Athanasiou L, Fotiadis DI, et al. Hybrid intravascular imaging. Current applications and prospective potential in the study of coronary atherosclerosis. J Am Coll Cardiol. 2013;61:1369–78.

45. Jang I-K, Bouma BE, Kang D-H, Park S-J, Park S-W, Seung K-B, Choi K-B, Shishkov M, Schlendorf K, Pomerantsev E, Houser SL, Aretz HT, Tearney GJ. Visualization of coronary atherosclerotic plaques in patients using optical coherence tomography: comparison with intravascular ultrasound. J Am Coll Cardiol. 2002;39:604–9.

46. Yin J, Li X, Jing J. Novel combined miniature optical coherence tomography ultrasound probe for in vivo intravascular imaging. J Biomed Opt. 2011;16:060505.

47. Li BH, Leung SO, Soong A, Munding CE, Lee H, Thind AS, et al. Hybrid intravascular ultrasound and optical coherence tomography catheter for imaging of coronary atherosclerosis. Cath Cardiovasc Interv. 2012;81:494–507.

48. Li X, Li JW, Jing J, Ma T, Liang SS, Zhang J, et al. Integrated IVUS-OCT imaging for atherosclerotic plaque characterization. IEEE J Sel Top Quantum Electron. 2013;20:7100108.

49. Kern MJ, Samady H. Current concepts of integrated coronary physiology in the catheterization laboratory. J Am Coll Cardiol. 2010;55:173–85.

50. Schmitt JM, Petroff C. Method of determining pressure in a vessel as measured an optical pressure transducer in an optical coherence tomography system. US Patent 8,676,299 (18 Mar 2014).

51. Petroff C, Schmitt JM. Optical coherence tomography and pressure based systems and methods. U.S. Patent Application 20140094697 (3 Apr 2014).

52. Caplan JD, Waxman S, Nesto RW, Muller JE. Near-infrared spectroscopy for the detection of vulnerable coronary artery plaques. J Am Coll Cardiol. 2006;47:C92–6.

53. Fard AM, Vacas-Jacques P, Hamidi E, Wang H, Carruth RW, Gardecki JA, Tearney GJ. Optical coherence tomography–near infrared spectroscopy system and catheter for intravascular imaging. Opt Express. 2013;21:30849–58.

54. Pu J, Mintz GS, Brilakis ES, Banerjee S, Abdel-Karim AR, Maini B, Biro S, Lee JB, Stone GW, Weisz G, Maehara A. In vivo characterization of coronary plaques: novel findings from comparing greyscale and virtual histology intravascular ultrasound and near-infrared spectroscopy. Eur Heart J. 2012;33:372–83.

55. Yonetsu T, Suh W, Abtahian F, Kato K, Vergallo R, Kim SJ, Ji H, McNulty I, Lee H, Jang IK. Comparison of near-infrared spectroscopy and optical coherence tomography for detection of lipid. Catheter Cardiovasc Interv 2013 (in press).

56. Barton JK, Guzman F, Tumlinson A. Dual modality instrument for simultaneous optical coherence tomography imaging and fluorescence spectroscopy. J Biomed Opt. 2004;9:618–23.

57. Tumlinson AR, Hariri LP, Utzinger U, Barton JK. Miniature endoscope for simultaneous optical coherence tomography and laser-induced fluorescence measurement. Appl Opt. 2004;43:113–21.

58. Vasan RS. Biomarkers of cardiovascular disease: molecular basis and practical considerations. Circulation. 2006;113:2335–62.

59. Qureshi A, Gurbuz Y, Niazi JH. Biosensors for cardiac biomarkers detection: a review. Sens Actuators B. 2012;171–172:62–76.

60. Yoo H, Kim JW, Shishkov M, Namati E, Morse T, Shubochkin R, McCarthy JR, Ntziachristos V, Bouma BE, Jaffer FA, Tearney GJ. Intra-arterial catheter for simultaneous microstructural and molecular imaging in vivo. Nat Med. 2011;17:1680–4.

61. Ozaki Y, Kitabata H, Tsujioka H, Hosokawa S, Kashiwagi M, Ishibashi K, et al. Comparison of contrast media and low-molecular-weight dextran for frequency-domain optical coherence tomography. Circ J. 2012;76:922–7.

62. Hou SH, Bushinsky DA, Wish JB, Cohen JJ, Harrington JT. Hospital-acquired renal insufficiency: a prospective study. Am J Med. 1983;74:243–8.

63. Lopez JJ, Arain SA, Madder R, Parekh N, Shroff AR, Westerhausen MD. Techniques and best practices for optical coherence tomography. Cath Cardiovasc Interv. 2014 (on-line publication; article in press).

64. Frick K, Michael TT, Alomar M, Mohammed A, Abdullah S, Grodin J, Hastings JL, et al. Low molecular weight dextran provides similar optical coherence tomography coronary imaging compared to radiographic contrast media. Cath Cardiovasc Interv. 2013. doi:10.1002/ccd.25092. Epub.

65. Villard J, Feldman M, Kim J, Milner T, Freeman G. Use of a blood substitute to determine instantaneous murine right ventricular thickening with optical coherence tomography. Circulation. 2002;105:1843–9.

66. Hoang KC, Edris A, Su J, Mukai DS, Mahon S, Petrov AD, Kern M, Ashan C, Chen Z, Tromberg BJ, Narula J, Brenner M. Use of an oxygen-carrying blood substitute to improve intravascular optical coherence tomography imaging. J Biomed Opt. 2009;14:034028.

67. Allemang MT, Lakin RO, Kanaya T, Eslahpazir BA, Bezerra HG, Kashyap VS. The use of dextran and carbon dioxide for optical coherence tomography in the superficial femoral artery. J Vasc Surg. 2014;59:238–40.

68. Ueda Y, Asakura M, Hirayama A, Komamura K, Hori M, Komada K. Intracoronary morphology of culprit lesions after reperfusion in acute myocardial infarction: serial angioscopic observations. J Am Coll Cardiol. 1996;27:606–10.

69. Kataiwa H, Tanaka A, Kitabata H, Matsumoto H, Kashiwagi M, Kuroi A, et al. Head to head comparison between the conventional balloon occlusion method and the non-occlusion method for optical coherence tomography. Int J Cardiol. 2011;146:186–90.

70. Kato A, Yonemura K, Matsushima H, Ikegaya N, Hishida A. Complication of oliguric acute renal failure in patients treated with low-molecular weight dextran. Ren Fail. 2001;23:679–84.

71. Alayash AI. Setbacks in blood substitutes research and development: a biochemical perspective. Clin Lab Med. 2010;30:381–9.

72. Voorhies RM, Fraser RA. Cerebral air embolism occurring at angiography and diagnosed by computerized tomography. Case report. J Neurosurg. 1984;60:177–8.

Index